Takashi Suzuki
Clair Poignard
Mark Chaplain
Vito Quaranta   *Editors*

Methods of Mathematical Oncology

Fusion of Mathematics and Biology,
Osaka, Japan, October 26–28, 2020

Springer

Springer Proceedings in Mathematics & Statistics

Volume 370

This book series features volumes composed of selected contributions from workshops and conferences in all areas of current research in mathematics and statistics, including operation research and optimization. In addition to an overall evaluation of the interest, scientific quality, and timeliness of each proposal at the hands of the publisher, individual contributions are all refereed to the high quality standards of leading journals in the field. Thus, this series provides the research community with well-edited, authoritative reports on developments in the most exciting areas of mathematical and statistical research today.

More information about this series at http://www.springer.com/series/10533

Takashi Suzuki · Clair Poignard ·
Mark Chaplain · Vito Quaranta
Editors

Methods of Mathematical Oncology

Fusion of Mathematics and Biology,
Osaka, Japan, October 26–28, 2020

Editors
Takashi Suzuki
Centre for Mathematical Modeling
& Data Science
Osaka University
Toyonaka, Japan

Clair Poignard
Research Team MONC
Institut de Mathématiques de Bordeaux
(CNRS UMR 5251)
Talence, France

Mark Chaplain
School of Mathematics and Statistics
University of St Andrews, MI
St Andrews, UK

Vito Quaranta
Quantitative Systems Biology Center
Vanderbilt University School of Medicine
Nashville, TN, USA

Preface

Following recent developments in computational biology, a research project entitled "Establishing International Research Networks of Mathematical Oncology" has been carried out for five years and nine months since April 2015 as a part of the Core-to-Core Program of the Japan Society for the Promotion of Science (JSPS). This project has established a permanent and collaborative network, to foster research leaders in mathematical oncology and to strive to build an international research base.

In this project, the Center for Mathematical Modeling and Data Science (MMDS) at Osaka University (Professor Takashi Suzuki, representative researcher) has engaged in collaborative research with the following prestigious organizations: INRIA Research Center of Bordeaux-Sud-Ouest in France (Professor Clair Poignard, representative coordinator); University of St. Andrews in the UK (Professor Mark Chaplain, representative coordinator); and Vanderbilt University in the USA (Professor Vito Quaranta, representative coordinator). The Program has also been supported by the following renowned institutions in Japan: The Institute of Medical Science, The University of Tokyo, and Kanagawa Cancer Center Research Institute. By utilizing their respective strength and realizing the fusion of life science and mathematical science, the base organization has achieved the cooperation of "mathematical analysis," "verification by biomedical experiments," and "statistical analysis of a chemical database."

As the core event for the final year of the project, the international symposium entitled "Fusion of Mathematics and Biology" and organized by Professor Takashi Suzuki at MMDS was held during October 26–28, 2020, at Osaka University in Japan to provide valuable opportunities for researchers to share their innovative ideas with eminent speakers. The international symposium was originally scheduled to take place in March 2020, but it was postponed due to the worldwide outbreak of COVID-19.

All sessions were basically delivered live through the Zoom webinar. Furthermore, we set up a hybrid conference platform combined with a real venue and online meetings. Speakers from eight countries led 20 sessions and provided 62 talks. The total number of session chairs and speakers was 82, and they attended as

panelists. In addition, 91 participants registered as an audience through the JSPS 2020 website. The number of participants by Zoom was continuously 50–70. Despite the differences in time zones of the participants, there was an enthusiastic exchange of questions, comments, and discussions.

This book consists of original manuscripts offered by speakers who have contributed to the symposium and researchers who are dedicated to mathematical oncology and mathematical biology, among other topics. In addition to the proceedings of the international symposium, this book includes an attractive review of the latest in mathematical science.

Individual contributions were all reviewed by authoritative, credible researchers in the field. We hope that this contribution is valuable and useful for a wide range of researchers and scientists.

Acknowledgments

March 2021   Takashi Suzuki

Organization

List of Participants

Organizer

Takashi Suzuki	Osaka University

Session Chairs

Mark Chaplain	University of St Andrews, UK
Naoya Fujita	The Cancer Institute of JFCR, Japan
Hao Gao	University of Glasgow, UK
Alexander Hoffmann	University of California, Los Angeles, USA
Junichiro Inoue	The University of Tokyo, Japan
Yoh Iwasa	Kwansei Gakuin University, Japan
Hiroyuki Kubota	Medical Institute of Bioregulation, Kyushu University, Japan
Naotoshi Nakamura	Osaka University, Japan
Fumiko Ogushi	Osaka University, Japan
Mariko Okada	Osaka University, Japan
Clair Poignard	Inria Research Center of Bordeaux-Sud Ouest, France
Vito Quaranta	Vanderbilt University, USA
Satoshi Sawai	The University of Tokyo, Japan
Tatsuya Sawasaki	Ehime University, Japan
Mutsuhiro Takekawa	The University of Tokyo, Japan
Sohei Tasaki	Kyoto University Institute for the Advanced Study of Human Biology, Japan
Tetsuji Tokihiro	The University of Tokyo, Japan

Fuminori Tokunaga   Osaka City University, Japan
Tetsuo Yasugi   Kanazawa University, Japan

Speakers

Mohd Ariff Bin Admon   Universiti Teknologi Malaysia, Malaysia
Nobuhiko Asakura   Osaka University, Japan
Samantha Beik   Vanderbilt University, USA
Ryoma Bise   Kyushu University, Japan
Mark Chaplain   University of St Andrews, UK
Eric Deeds   University of California, Los Angeles, USA
Shinichiro Ei   Hokkaido University, Japan
Christèle Etchegaray   Inria Research Center of Bordeaux-Sud Ouest,
                              France
Hao Gao   University of Glasgow, UK
Sarah M. Groves   Vanderbilt University, USA
Hiroshi Haeno   The University of Tokyo, Japan
Leonard Harris   University of Arkansas, USA
Alexander Hoffmann   University of California, Los Angeles, USA
Junichi Ikenouchi   Kyushu University, Japan
Masamichi Imajo   Hokkaido University, Japan
Yusuke Imoto   Kyoto University, Japan
Junichiro Inoue   The University of Tokyo, Japan
Takeshi Ito   The University of Tokyo, Japan
Yuki Ito   Kyushu University, Japan
Yukinobu Ito   Akita University, Japan
Shingo Iwami   Kyushu University, Japan
Pedro Jaramillo   Inria Research Center of Bordeaux-Sud Ouest,
                              France
Ryuichiro Kageyama   Kyoto University, Japan
Eiryo Kawakami   Chiba University/RIKEN, Japan
Jae Kyong Kim   Korea Advanced Institute of Science
                              and Technology /KAIST, South Korea
Tetsuya Kobayashi   The University of Tokyo, Japan
Mizuka Komatsu   Kobe University, Japan
Naohiko Koshikawa   Kanagawa Cancer Center Research Institute,
                              Japan
Hiroyuki Kubota   Medical Institute of Bioregulation, Kyushu
                              University, Japan
S. Seirin-Lee   Hiroshima University, Japan
Carlos Lopez   Vanderbilt University, USA
Keiji Miura   Kwansei Gakuin University, Japan
Takashi Miura   Kyushu University, Japan
Yoichiro Mori   University of Pennsylvania, USA

Masashi Muramatsu   Kumamoto University, Japan
Masaharu Nagayama   Hokkaido University, Japan
Naotoshi Nakamura   Osaka University, Japan
Takanori Nakamura   The University of Tokyo, Japan
Shinji Nakaoka   Hokkaido University, Japan
Daisuke Nanba   Tokyo Medical and Dental University, Japan
Tsuyoshi Osawa   The University of Tokyo, Japan
Nuha Loling Othman   Universiti Malaysia Sarawak, Malaysia
Masaaki Oyama   The University of Tokyo, Japan
Sungsu Park   Sungkyunkwan University, South Korea
Clair Poignard   Inria Research Center of Bordeaux-Sud Ouest,
                             France
Luigi Preziosi   Politecnico di Torino, Italy
Vito Quaranta   Vanderbilt University, USA
Don Pietro Saldajeno   Nara Institute of Science and Technology, Japan
Satoshi Sawai   The University of Tokyo, Japan
Tatsuya Sawasaki   Ehime University, Japan
Nikolaos Sfakianakis   University of St Andrews, UK
Fuaada Binti Mohd Siam   Universiti Teknologi Malaysia, Malaysia
Yudi Soeharyadi   Institut Teknologi Bandung, Indonesia
Hiroshi Suito   Tohoku University, Japan
Kei Takahashi   The University of Tokyo, Japan
Mutsuhiro Takekawa   The University of Tokyo, Japan
Sohei Tasaki   Kyoto University Institute for the Advanced
                             Study of Human Biology, Japan
Fuminori Tokunaga   Osaka City University, Japan
Masahiro Tomioka   The University of Tokyo, Japan
Koji Tsuda   The University of Tokyo, Japan
Darren Tyson   Vanderbilt University, USA
Tasuku Ueno   The University of Tokyo, Japan
Tetsuo Yasugi   Kanazawa University, Japan

Contents

Mathematical Modeling

Constitutive Modelling of Soft Biological Tissue from Ex Vivo to in Vivo: Myocardium as an Example

Debao Guan, Xiaoyu Luo, and Hao Gao[(✉)]

School of Mathematics and Statistics, University of Glasgow, Glasgow, UK
d.guan.1@research.gla.ac.uk, {xiaoyu.luo,hao.gao}@glasgow.ac.uk

Abstract. Imbalance of stress/strain microenvironment can lead to adverse remodelling and pathogenesis in various soft tissues, tumour included. Therefore, there is a critical need for accurate quantification of the biomechanical homeostasis in soft tissue through mathematical modelling, which is critically dependent on constitutive models, the mathematical descriptions that approximate the mechanical behaviours of material under specific conditions by considering information from subcellular, cellular and tissue levels. In most soft biological tissue, collagen is the major component of the extracellular matrix, its architecture largely determines the material property (stiffness). In this work, we will use myocardium as an example to show how we can develop a constitutive law from various ex vivo experiments within the continuum mechanics framework, and demonstrate the applications to real patient data. We will further focus on parameter calibrations from ex/in vivo measurements. We believe this approach of constitutive modelling and calibration can be applied to various soft biological tissues and shed light on physiological and pathological mechanobiology.

1 Introduction

Imbalance of stress/strain micro-environment can lead to adverse remodelling in various organs and further causing functional deterioration. For example, imbalance of stress/strain can regulate tumour immunity and even promote metastasis [6]. The kinematics of soft tissue can be quantitatively measured by various experimental techniques [4,17,20]. However, direct measurements of in vivo solid stress have not been achieved, and still challenging in in vivo situation. To overcome this difficulty, a common way is to compute stresses by using constitutive models which characterize the relation between kinematics and stresses. In this respect, there is a critical need for accurate quantification of the biomechanical micro-environment in soft tissue through mathematical modelling, which is essentially dependent on constitutive models. Constitutive models are

mathematical descriptions that approximate the mechanical behaviours of material under specific conditions, which can further take into account information from different scales [12]. In most soft biological tissue, collagen is the major component of the extracellular matrix, and largely determines the material property (stiffness), cancerous tissue included [6].

In this study, we will use myocardium as an example to show how we can develop a constitutive law from various ex vivo experiments, and further show the applications to real patient data by encompassing a wide range of cross-scale soft tissue mathematical models. In the past several decades, a few constitutive models have been proposed for myocardium [12]. Myocardium is usually treated as an anisotropic, hyper-elastic material with layered collagen network [8,10,11]. One of very widely used model is the Holzapfel and Ogden (HO) model and its variations [12]. To account for fine structures of collagen fibres, general structural tensors were further introduced to describe fibre dispersion by Eriksson et al.[5]. Calibrating unknown parameters in the HO model has been investigated in [10] using three different sets of ex vivo experiment data, and inverse estimation of its unknown parameters from in vivo data was first reported in [8] by using magnetic resonance imaging.

2   Constitutive Modelling of Soft Biological Tissue

In this section, we will briefly introduce the essential continuum mechanics for soft tissue mechanics. Consider a soft tissue under certain external loading, and the material point $\mathbf{X}$ in the reference configuration will move to a new position $\mathbf{x} = \mathbf{x}(\mathbf{X}, t)$ at time t. The deformation gradient associated with the soft tissue is defined as $\mathbf{F} = \partial \mathbf{x}/\partial \mathbf{X}$, the shape change in 3-dimension. By assuming the soft tissue is hyperelastic and incompressible, then there exists a constitutive law $\mathcal{W}$, and the Cauchy stress is $\sigma = \mathbf{F} \frac{\partial \mathcal{W}}{\partial \mathbf{F}} - p\mathbf{I}$, where the Lagrange multiplier p enforces incompressibility and $\mathbf{I}$ is the identity tensor. In addition, associated with $\mathbf{F}$ are the left and right Cauchy-Green tensors, they are $\mathbf{B} = \mathbf{F}\mathbf{F}^T$ and $\mathbf{C} = \mathbf{F}^T\mathbf{F}$, respectively, and the Green-Lagrange strain tensor is $\mathbf{E} = (\mathbf{C} - \mathbf{I})/2$.

Invariants of the right Cauchy–Green deformation tensor $\mathbf{C}$ are commonly used in formulating the strain energy function $\mathcal{W}$, likewise $I_1 = \text{tr}(\mathbf{C})$, $I_2 = \frac{1}{2}\{[\text{tr}(\mathbf{C})]^2 - \text{tr}(\mathbf{C}^2)\}$, $I_3 = \det(\mathbf{C})$. An example is the incompressible Neo-Hooken material $W = C_1(I_1 - 3)$, in which C_1 is a material constant. Strain invariant-based constitutive laws can be widely found for characterizing and modelling various soft tissues, such as myocardium [12] and solid cancer [23].

In order to characterize anisotropic hyperelastic myocardium, for example, to take into account the stiffening effects of the collagen network and its preferred orientation, extra strain invariants are needed. Transversely isotropic models were firstly proposed by assuming all fibres (mainly collagen) are aligned

perfectly in one direction and share the same mechanical properties. Denote the fibre direction $\mathbf{f}_0$ in the reference configuration, two related strain invariants can be introduced,

$$I_{4f} = \mathbf{f}_0 \cdot (\mathbf{C}\mathbf{f}_0), \qquad I_{5f} = \mathbf{f}_0 \cdot (\mathbf{C}^2\mathbf{f}_0). \tag{1}$$

The strain energy function for such one family fibre can be formulated as $\mathcal{W}(I_1, I_2, I_3, I_{4f}, I_{5f})$ with I_1, I_2, I_3 for its isotropic response and I_{4f}, I_{5f} for fibre contributions. In actual applications, reduced formula $\mathcal{W}(I_1, I_{4f})$ is often found [11]. The corresponding Cauchy stress is

$$\sigma = 2\frac{\partial \mathcal{W}}{\partial I_1}\mathbf{B} + 2\frac{\partial \mathcal{W}}{\partial I_{4f}}\mathbf{f} \otimes \mathbf{f} - p\mathbf{I}, \quad \text{and} \quad \mathbf{f} = \mathbf{F}\mathbf{f}_0. \tag{2}$$

Experimental studies have shown that myocardium has layered myofibre structure with three families of fibres, the so-called fibre ($\mathbf{f}_0$)–sheet($\mathbf{s}_0$)–normal($\mathbf{n}_0$) system, or $f - s - n$ in short. Additional strain invariants are

$$\begin{aligned} &I_{4s} = \mathbf{s}_0 \cdot (\mathbf{C}\mathbf{s}_0), \ I_{5s} = \mathbf{s}_0 \cdot (\mathbf{C}^2\mathbf{s}_0), \ I_{4n} = \mathbf{n}_0 \cdot (\mathbf{C}\mathbf{n}_0), \ I_{5n} = \mathbf{n}_0 \cdot (\mathbf{C}^2\mathbf{n}_0), \\ &I_{8fs} = \mathbf{f}_0 \cdot (\mathbf{C}\mathbf{s}_0), \ I_{8fn} = \mathbf{f}_0 \cdot (\mathbf{C}\mathbf{n}_0), \ I_{8ns} = \mathbf{n}_0 \cdot (\mathbf{C}\mathbf{s}_0). \end{aligned} \tag{3}$$

As discussed in [12], not all strain invariants are independent, thus we can omit some of these in the functional dependence of the strain energy function. Based on the simple shear data of ex vivo porcine myocardium [4], Holzapfel and Ogden proposed the micro-structure informed strain energy function for myocardium by only including I_1, I_{4f}, I_{4s}, I_{8fs} (the HO law),

$$\mathcal{W} = \frac{a}{2b}\{e^{b(I_1-3)} - 1\} + \sum_{i=f,s} \frac{a_i}{2b_i}\{e^{b_i(I_{4i}-1)^2} - 1\} + \frac{a_{fs}}{2b_{fs}}\{e^{I_{8fs}^2} - 1\}, \tag{4}$$

where a, b, a_f, b_f, a_s, b_s, a_{fs} and b_{fs} are material parameters. The corresponding Cauchy stress tensor is

$$\begin{aligned} \sigma &= a_1 e^{b_1(I_1-3)}\mathbf{B} + 2a_f(I_{4f} - 1)e^{b_f(I_{4f}-1)^2}\mathbf{f} \otimes \mathbf{f} \\ &+ 2a_s(I_{4s} - 1)e^{b_s(I_{4s}-1)^2}\mathbf{s} \otimes \mathbf{s} + a_{fs}I_{8fs}e^{I_{8fs}^2}(\mathbf{f} \otimes \mathbf{s} + \mathbf{s} \otimes \mathbf{f}), \end{aligned} \tag{5}$$

in which $\mathbf{s} = \mathbf{F}\mathbf{s}_0$. Since its introduce, the HO law in Eq. (4) has been widely used in characterizing myocardial mechanic behaviours in various ex vivo experiments [10] and in vivo cardiac function modelling [8] (Fig. 1).
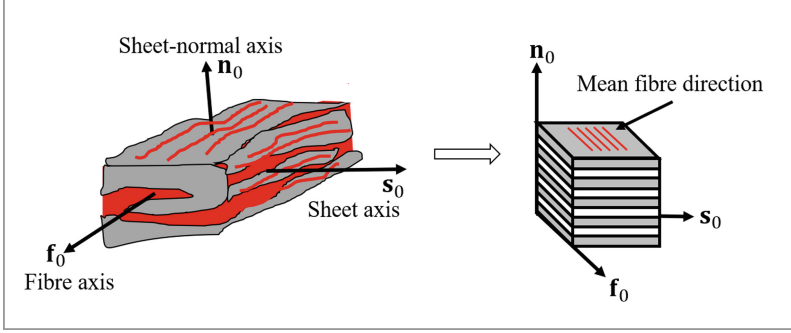
Fig. 1. The sketch of layered organization of myocytes and the collagen fibres between the sheets in the orthonormal coordinate system with fibre axis $\mathbf{f}_0$, sheet axis $\mathbf{s}_0$ and sheet-normal axis $\mathbf{n}_0$. An additional cube of layered tissue serving as the base for the constitutive model in the simulation. (Figure is cited from Holzapfel & Ogden [12])

3   Ex Vivo Calibration

Experimental tests of passive properties of the myocardium are usually performed on tissue level at ex vivo condition because of easy setup and operation compared to the experiments on the cellular level [4,20]. By assuming the experimental specimen to be homogeneous, measured stresses and strains can be used to inform the underlying formulations of constitutive behaviours. For example, simple shear tests have been found necessary for characterizing the orthotropic nonlinear behaviours of the myocardium [4], recently extended to the combination with bi-axial tests [20], and further demonstrated in [10].

In this study, we choose the simple shear experimental data from Dokos et al. [4] for inferring material constants in Eq. (4). Dokos et al. firstly reported ex vivo simple shear tests on passive myocardium from porcine hearts with six different shear modes, shown in Fig. 2(a) where (ij) refers to shearing in the j direction within the ij plane, where $i \neq j \in \{f, s, n\}$. Details of the experimental protocols can be found in [4].

The loading path in simple shear experiments can be quantified by deformation gradient tensors under homogeneous deformation assumption. For the six simple shear tests in Fig. 2(a), we have

$$
\text{(ns):} \quad \mathbf{F} = \begin{bmatrix} 1 & 0 & 0 \\ 0 & 1 & 0 \\ 0 & \gamma_{\text{ns}} & 1 \end{bmatrix}, \quad \text{(fn):} \quad \mathbf{F} = \begin{bmatrix} 1 & 0 & 0 \\ \gamma_{\text{fn}} & 1 & 0 \\ 0 & 0 & 1 \end{bmatrix}, \quad \text{(sf):} \quad \mathbf{F} = \begin{bmatrix} 1 & 0 & \gamma_{\text{sf}} \\ 0 & 1 & 0 \\ 0 & 0 & 1 \end{bmatrix},
$$

$$
\text{(nf):} \quad \mathbf{F} = \begin{bmatrix} 1 & \gamma_{\text{nf}} & 0 \\ 0 & 1 & 0 \\ 0 & 0 & 1 \end{bmatrix}, \quad \text{(fs):} \quad \mathbf{F} = \begin{bmatrix} 1 & 0 & 0 \\ 0 & 1 & 0 \\ \gamma_{\text{fs}} & 0 & 1 \end{bmatrix}, \quad \text{(sn):} \quad \mathbf{F} = \begin{bmatrix} 1 & 0 & 0 \\ 0 & 1 & \gamma_{\text{sn}} \\ 0 & 0 & 1 \end{bmatrix}, \quad (6)
$$

where γ_{ij} is the shear amount with respect to the Cartesian coordinates $\{\mathbf{e}_1, \mathbf{e}_2, \mathbf{e}_3\}$, which are coincident with the local material coordinates
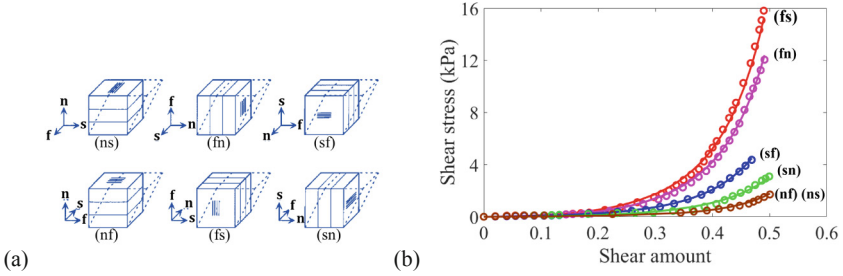
Fig. 2. Parameter inference from ex vivo experiments. (a) a sketch of all six shear modes of a cubic myocardial sample adapted from [4], **f**, **s** and **n** denote the fibre, sheet and normal direction, respectively; (b) fitted simple shear experimental data using the HO model from the optimized parameter set in Table 1.

$\{\mathbf{f}_0, \mathbf{n}_0, \mathbf{s}_0\}$. We now use the six shear experimental data [4] to inversely determine the 8 unknown parameters in Eq. (4) by using those above deformation gradients for each corresponding simple shear experiment. The inverse problem is similar as in our previous study [10] by minimising the loss function defined as the squared errors between the predicted stress from the HO law to the measured values. The goodness of fits are shown in Fig. 2(b), from which we can see that the HO law is able to capture all mechanical responses of six simple shears, and the optimised parameters are listed in Table 1.

Table 1. Optimised parameters in the HO law based on the experimental data of six simple shear tests [4] and from in vivo measurements using clinical cardiac magnetic resonance imaging [9]

Parameters	a (kPa)	b	a_f (kPa)	b_f	a_s (kPa)	b_s	a_{fs} (kPa)	b_{fs}
Ex vivo	0.2362	10.81	20.037	14.154	3.7245	5.1645	0.4109	11.3
In vivo	0.1	2.49	1.99456	4.92	0.243	1.188	0.1	2.6

4 Move to in Vivo

To estimate myocardial passive stiffness from in vivo data is still very challenging, there is no established approach on how to adjust parameters derived from ex vivo experiments directly to in vivo situations. Studies have found that the passive stiffness estimated from ex vivo experiments will over-estimate in vivo stiffness, thus not suitable for personalized modelling. For this reason, a few studies have tried to re-scale ex vivo experimental data to match measured in vivo dynamics. In this section, an in vivo human left ventricular (LV) model reconstructed from cardiac magnetic resonance (CMR) imaging from our previous studies [9] is used as shown in Fig. 3(a) superimposed with a CMR image.

The LV geometry is reconstructed at early-diastole when the LV pressure is at the lowest.

We previously proposed a three-step algorithm [8] to inversely infer the 8 constitutive parameters by matching the simulated LV dynamics at diastole to in vivo measured LV motion (the cavity volume and 24 segmental strains). To simulate the LV passive filling at diastole, a quasi-static biomechanical model is developed using the finite-element discretization and solved by ABAQUS. The boundary value problem of the LV passive filling is

$$\left.\begin{array}{ll}\nabla \cdot \sigma + \mathbf{b} = 0 & \text{in } \Omega \\ \sigma \cdot \mathbf{n} = \mathbf{t} & \text{in } \Gamma^{\text{N}} \\ \mathbf{u} = \mathbf{u}_0 & \text{in } \Gamma^{\text{D}}\end{array}\right\}, \tag{7}$$

where Ω is the LV computational domain, σ is Cauchy stress of Eq. (5), $\mathbf{n}$ denotes the normal direction of $\partial\Omega$, $\mathbf{b}$ is the body force density per unit volume, which is zero in this study, $\mathbf{t}$ is the traction force resulted from the LV cavity pressure, Γ^{D} is the basal plane with prescribed displacements $\mathbf{u}_0$, and Γ^{N} is the endocardial surface with linearly ramped pressure from $0\,\text{mmHg}$ to $8\,\text{mmHg}$ at end-diastole. Details of the LV biomechanical model can be found in our previous studies [8,25].

Here, we introduce a modified version by taking into account ex vivo pressure–volume relationship reported by Klotz et al. [14] in the multi-step optimization procedure. In detail,

1. Optimise C_a, C_b by minimising f_{O1} using grid search within $[0.1, 1.0]$, following the widely used scaling approach by grouping the 8 parameters into two groups: $a^{\text{group}} = \{a, a_{\text{f}}, a_{\text{s}}, a_{\text{fs}}\}$, $b^{\text{group}} = \{b, b_{\text{f}}, b_{\text{s}}, b_{\text{fs}}\}$, respectively. C_a and C_b are scaling parameters as

$$a^{\text{group}} = C_a a_0^{\text{group}} \quad \text{and} \quad b^{\text{group}} = C_b b_0^{\text{group}},$$

in which a_0^{group} and b_0^{group} are from ex vivo data (see Sect. 3). The objective function is defined as

$$f_{\text{O1}} = (V^{\text{simulated}} - V^{\text{in vivo}})^2 + \sum_{i=1}^{24}(\epsilon_i^{\text{simulated}} - \epsilon^{\text{in vivo}})^2,$$

in which V is the LV cavity volume, and ϵ is the myocardial strains.

2. Refine C_a, C_b by minimising $f_{\text{O1}}^{\text{Klotz}}$, which is defined as

$$f_{\text{O1}}^{\text{Klotz}} = \left(\frac{V_8^{\text{simulate}} - V_8}{V_8}\right)^2 + \left(\frac{V_{30}^{\text{simulate}} - V_{30}}{V_{30}}\right)^2 + \sum_{i=1}^{N}(\epsilon_i^{\text{simulated}} - \epsilon^{\text{in vivo}})^2,$$

where V_8 and V_{30} are the LV cavity volumes at $8\,\text{mmHg}$ and $30\,\text{mmHg}$ derived from the Klotz relationship [14].

3. Optimise a_{f}, b_{f} by minimising f_{O2}, which is similar as $f_{\text{O1}}^{\text{Klotz}}$ by excluding the term $\left((V_{30}^{\text{simulate}} - V_{30})/V_{30}\right)^2$.

Note steps 2 and 3 use the MATLAB function *fmincon* for finding the best parameters. Details of this multistep optimization procedure can be found in [8] and its application in [9]. Figure 3 (b) compares the strains from ex vivo parameters and from the optimal set of parameters to the in vivo measured values. As pointed out in other studies [8], ex vivo parameters lead to a very stiff myocardium which has a much small strain magnitude at end-diastole, and away from the measurements (Fig. 3 (b)). The optimized parameters from this in vivo heart can be found in Table 1, which is largely different from the ex vivo values.
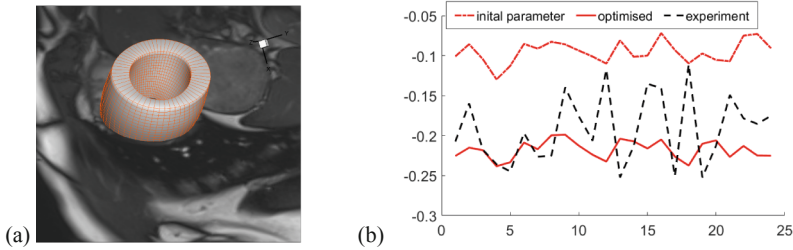
Fig. 3. Parameter calibration from in vivo data. (a) Fitted LV mesh according to the MR cine image; (b) Comparisons of regional circumferential strain at end of diastole after each optimization step.

We further compare the mechanical responses between in vivo and ex vivo parameters from Table 1 using a virtual shear experiment by shearing a cubic sample along 6 different directions up to 0.5, as shown in Fig. 4(a). Clearly, in vivo myocardium is much softer than ex vivo myocardium. We then further simulate the LV filling phase by using the optimal parameters from Table 1 using the in vivo finite-element LV model (see Fig. 3 and Eq.(7)) with a pressure of 8 mmHg at end-diastole. Figure 2(b) shows the deformed LV shape at end-diastole with in vivo estimated parameters (left) and ex vivo estimated parameters (right). A much larger end-diastolic volume is achieved for the in vivo parameter set (140 mL) compared to the ex vivo parameter set (70 mL), the corresponding filling volume is 85 mL and 15 mL, respectively. Figure 4(b) is further contoured by the maximum principal Cauchy stresses at end-diastole, again the two-parameter sets give very different stress levels and patterns. This suggests cautions are needed when using ex vivo experimental data for modelling the in vivo biomechanical environment.

5   Biomechanical Study to Cancer

There is an increased appreciation of the biomechanical environment in determining tissue development, cell differentiation and adaptation to maintain the homeostasis in healthy tissue, and the loss of this ability to maintain the local
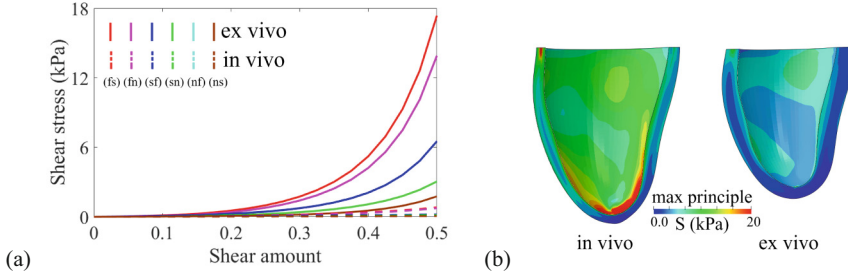
Fig. 4. Comparisons between the passive property between the ex vivo and in vivo derived parameter sets. (a) Predicted simple shear stress; (b) Simulated maximum principal stress distributions at end diastole in a human left ventricle.

biomechanical homeostasis, such as tumour cells, will potentially contribute to its progression [6]. As has been discussed in [21], the mechanical stress environment from both the solid and fluid phases of the tumour can play an important role in the progression and response to treatment. The elevated solid stress not only compresses intratumoral blood and lymphatic vessels, but also reduces perfusion, a major barrier to the delivery of chemotherapeutic agents and nanomedicine, causing low efficiency of those treatments. The reduced perfusion further promotes tumour progression and metastasis. Therefore, accurate quantification of solid stress in the tumour is critical for treatment planning, such as stress-reducing therapy [21]. Measuring stress is very difficult and challenging, especially in vivo, thus biomechanical predictions by solving conservations of mass, momentum, energy and entropy are usually employed along with the constitutive models of tumour tissue [23].

It is well known that solid tumour tissues are nonlinear, hierarchical and heterogeneous, thus very different from healthy tissues [13,19]. This inherent spatially heterogeneous and hierarchical structure with its active nature make it very difficult when developing an accurate constitutive model [23]. The interplays between tumour cells and surrounding environments further complicate the accurate stress predictions. Almost over a decade ago, Unnikrishnan et al. [23] reviewed the constitutive models of tumour tissue within the single-phase continuum models, the multiphase continuum models and the poroelastic models. Constitutive modelling of the myocardium presented in this study can be classified as a single phase continuum model. In this category, Chaplain and Sleeman [2] implemented a non-linear elastic material model for a growing tumour. Other constitutive laws include the incompressible neo-Hookean [15], the Blatz-Ko type model [1], etc.

Most of the aforementioned models of tumour tissue are isotropic [23], an oversimplification of the nonlinear, hierarchical heterogeneous tumour tissue. Except for tumour cells and blood and lymphatic vessels, the extracellular matrix is another major structural component with collagen being one of the most common constituents and the scaffold of tumour micro-environment, which not only

behaves as a barrier to tumour cell migration, but also actively regulates tumour progression [6,26]. Torzilli et al. [22] has suggested a new paradigm in which they suggested the imbalanced biomechanical force in tumour tissue, is the key trigger of Epithelial-mesenchymal transition, and further leads to tumour cell escaping. Therefore, it is essentially necessary to take into account local collagen network into the constitutive modelling of tumour tissue with its active adaption during tumour progression. Few studies have incorporated micro-structure of collagen network in modelling biomechanics in tumour tissues. The knowledge learned from modelling soft tissue in general, will benefit the biomechanics modelling of tumour, in particular including complex collage network through fibre-reinforced models presented in this study, dispersion described by probability distributions [11,18] and tension-compression switch [12], etc.

The procedures of inferring material constants for a selected tumour model can be obtained from ex/in vivo measurements in a similar way as presented in this study for myocardium, usually, an inverse problem is formulated. By conducting an unconfined compression experiment in tumour tissues, Voutouri et al. [24] found that an exponential constitutive law can better fit the experimental data compared to widely used neo-Hookean and Blatz-Ko models. Colin et al. [3] estimated the residual stress using the Ciarlet-Geymonat material model in a spherical tumour tissue combined with an in vitro incision experiment. The Ciarlet-Geymonat model describes an isotropic material consisting of four terms using the three invariants I_1, I_2 and I_3 of $\mathbf{C}$, with three material parameters. Unlike the material model used in this study, strain invariants arising from collage fibres are included for describing the anisotropic behaviours. Their parameter studies further demonstrated that with limited measurements, i.e. the opening distance of the incision, only one model parameter can be identified with confidence, and the radial stored stress could be estimated accurately. Recently, magnetic resonance elastography has been used to infer peritumoural tissue stiffness for non-invasively estimating tumour pressure through a nonlinear biomechanical model [7]. Future studies shall include different stretch modes on different types of tumour tissues at various stages and different spatial scales in order to develop competent constitutive laws, further studies shall also explore different non-invasive in vivo approaches for calibrating tumour biomechanical behaviours.

The reliability and accuracy of the biomechanical models critically depend on the model inputs, not just material properties, but also the geometry, etc. Patient-specific geometries are usually constructed by manual or semi-automatic approaches, which can have a big impact on the model predictions. While to take into account geometry uncertainty can be challenging because of its high dimension. For example, the LV geometry in this study is discretized with 133,042 nodes. The image-based geometry reconstruction procedure used in this study has recently been examined by Li et al. [16], in which an LV geometry from one patient has been reconstructed five times using the same in vivo imaging data by the same operator, and the results showed that the differences of the end-diastolic LV cavity volume and the wall volume are less than 1%. Thus, the LV

geometry reconstruction procedure is highly reproducible and reliable. Interested readers refer to [9,16] for details of image processing and geometry reconstruction. Future studies shall quantify how sensitive the geometric uncertainty affects the biomechanical environment and constitutive parameter calibration.

As discussed in [3], not all parameters can be uniquely identified from limited measured data. The identifiability issue also exists for the constitutive law used in this study, which has more parameters than the Ciarlet–Geymonat model [3]. Furthermore, parameters in the HO law is highly correlated as discussed in [8]. In our previous study [10], a repeated random initialization strategy was used for inversely estimating the parameters of the HO law using ex vivo experiments. Our results also suggest that with more measured data, more parameters can be identified. For the in vivo estimation procedure, our previous study [8] has found that even though it is very challenging to establish the uniqueness of the solution of the inverse problem because of its ill-posed nature, the same mechanical responses in the physiological range can be achieved though the parameters are somewhat different. The dilemma in the in vivo inverse problem is that fewer data makes the inverse problem more ill-posed, but more measurements not only bring in extra uncertainties but also make the experiments challenging or inapplicable in vivo. By using a Bayesian statistical approach, we recently found that a and b in the HO law are identifiable, a_f is weakly identifiable, but not for other parameters if only using circumferential strains and the cavity volume. We are currently investigating which extra measurements (i.e. radial strain, shear strain, etc.) are needed in order to identify all parameters of the HO law through a global sensitivity study and uncertainty quantification. A further limitation in the HO law is that it does not take into account collagen fibre dispersion thought it can fit the experimental data very well [11], while a complex constitutive model will further complicate the identifiability issue of the inverse problem.

6   Conclusion

Studies on the constitutive modelling of soft tissues are critical for understanding the complex mechanobiology and pathogonesis, i.e. tumour progression and heart disease. In this study, the invariant-based fibre-reinforced strain energy function is introduced first within the continuum mechanics. The myocardium is then used as an example to demonstrate how to determine unknown material parameters from limited ex vivo experimental data, and later from in vivo measurements, which still remains a great challenge in the biomechanics community. The significant differences between the ex vivo and in vivo material property suggest that future studies are needed to bridge the gap from ex vivo to in vivo by taking into account inherent spatial heterogeneity and hierarchical microstructures, and the active growth and remodelling in biological tissue.

References

1. Ambrosi, D., Mollica, F.: On the mechanics of a growing tumor. Int. J. Eng. Sci. **40**(12), 1297–1316 (2002)
2. Chaplain, M.A.J., Sleeman, B.D.: Modelling the growth of solid tumours and incorporating a method for their classification using nonlinear elasticity theory. J. Math. Biol. **31**(5), 431–473 (1993)
3. Colin, T., Dechristé, G., Fehrenbach, J., Guillaume, L., Lobjois, V., Poignard, C.: Experimental estimation of stored stress within spherical microtissues. J. Math. Biol. **77**(4), 1073–1092 (2018)
4. Dokos, S., Smaill, B.H., Young, A.A., LeGrice, I.J.: Shear properties of passive ventricular myocardium. Am. J. Physiol.-Heart Circulatory Physiol. **283**(6), H2650–H2659 (2002)
5. Eriksson, T.S.E., Prassl, A.J., Plank, G., Holzapfel, G.A.: Modeling the dispersion in electromechanically coupled myocardium. Int. J. Numer. Methods Biomed. Eng. **29**(11), 1267–1284 (2013)
6. Fang, M., Yuan, J., Peng, C., Li, Y.: Collagen as a double-edged sword in tumor progression. Tumor Biol. **35**(4), 2871–2882 (2014)
7. Fovargue, D., Fiorito, M., Capilnasiu, A., Nordsletten, D., Lee, J., Sinkus, R.: Towards noninvasive estimation of tumour pressure by utilising MR elastography and nonlinear biomechanical models: a simulation and phantom study. Sci. Rep. **10**(1), 1–13 (2020)
8. Gao, H., Li, W.G., Cai, L., Berry, C., Luo, X.Y.: Parameter estimation in a Holzapfel-Ogden law for healthy myocardium. J. Eng. Math. **95**(1), 231–248 (2015)
9. Gao, H., Aderhold, A., Mangion, K., Luo, X, Husmeier, D., Berry, C.: Changes and classification in myocardial contractile function in the left ventricle following acute myocardial infarction. J. R. Soc. Interface **14**(132), 20170203 (2017)
10. Guan, D., Ahmad, F., Theobald, P., Soe, S., Luo, X., Gao, H.: On the AIC based model reduction for the general Holzapfel-Ogden myocardial constitutive law. Biomech. Model. Mechanobiol. **18**, 1213–1232 (2019)
11. Guan, D., Yao, J., Luo, X., Gao, H.: Effect of myofibre architecture on ventricular pump function by using a neonatal porcine heart model: from DT-MRI to rule-based methods. R. Soc. Open Sci. **7**(4) (2020)
12. Holzapfel, G.A., Ogden, R.W.: Constitutive modelling of passive myocardium: a structurally based framework for material characterization. Philos. Trans. R. Soc. A: Math. Phys. Eng. Sci. **367**(1902), 3445–3475 (2009)
13. Hoyt, K., et al.: Tissue elasticity properties as biomarkers for prostate cancer. Cancer Biomarkers **4**(4–5), 213–225 (2008)
14. Klotz, S., et al.: Single-beat estimation of end-diastolic pressure-volume relationship: a novel method with potential for noninvasive application. Am. J. Physiol.-Heart Circulatory Physiol. **291**(1), H403–H412 (2006)
15. Kyriacou, S.K., Davatzikos, C.: A biomechanical model of soft tissue deformation, with applications to non-rigid registration of brain images with tumor pathology. In: Wells, W.M., Colchester, A., Delp, S. (eds.) MICCAI 1998. LNCS, vol. 1496, pp. 531–538. Springer, Heidelberg (1998). https://doi.org/10.1007/BFb0056238
16. Li, W., Gao, H., Mangion, K., Berry, C., Luo, X.: Apparent growth tensor of left ventricular post myocardial infarction - in human first natural history study. Comput. Biol. Med. **129** (2021)
17. Mangion, K., Gao, H., Husmeier, D., Luo, X., Berry, C.: Advances in computational modelling for personalised medicine after myocardial infarction. Heart **104**(7), 550–557 (2018)

18. Melnik, A.V., Luo, X., Ogden, R.W.: A generalised structure tensor model for the mixed invariant I8. Int. J. Non-Linear Mech. **107**, 137–148 (2018)
19. O'Hagan, J.J., Samani, A.: Measurement of the hyperelastic properties of tissue slices with tumour inclusion. Phys. Med. Biol. **53**(24), 7087 (2008)
20. Sommer, G., et al.: Biomechanical properties and microstructure of human ventricular myocardium. Acta Biomaterialia **24**, 172–192 (2015)
21. Stylianopoulos, T.: The solid mechanics of cancer and strategies for improved therapy. J. Biomech. Eng. **139**(2) (2017)
22. Torzilli, P.A., Bourne, J.W., Cigler, T., Theresa Vincent, C.: A new paradigm for mechanobiological mechanisms in tumor metastasis. In: Seminars in Cancer Biology, vol. 22, pp. 385–395. Elsevier (2012)
23. Unnikrishnan, G.U., Unnikrishnan, V.U., Reddy, J.N., Lim, C.T.: Review on the constitutive models of tumor tissue for computational analysis. Appl. Mech. Rev. **63**(4) (2010)
24. Voutouri, C., Mpekris, F., Papageorgis, P., Odysseos, A.D., Stylianopoulos, T.: Role of constitutive behavior and tumor-host mechanical interactions in the state of stress and growth of solid tumors. PloS One **9**(8), e104717 (2014)
25. Wang, H.M., et al.: Structure-based finite strain modelling of the human left ventricle in diastole. Int. J. Numer. Methods Biomed. Eng. **29**(1), 83–103 (2013)
26. Xu, S., et al.: The role of collagen in cancer: from bench to bedside. J. Transl. Med. **17**(1), 1–22 (2019)

Mathematical Modeling of Gastro-Intestinal Metastasis Resistance to Tyrosine Kinase Inhibitors

Thierry Colin[1], Thomas Michel[2], and Clair Poignard[3]([✉])

[1] SOPHiA GENETICS Radiomics Department, 33600 Pessac, France
[2] SAS KELI NETWORK, 92300 Levallois-Perret, France
[3] Team MONC, INRIA Bordeaux-Sud-Ouest,
Université de Bordeaux, IMB, UMR 5251, 33400 Talence, France
clair.poignard@inria.fr

Abstract. In this paper, we study a continuum mechanics model of gastrointestinal stroma tumor (GIST) evolution under the action of two specific treatments. The first-line treatment is a specific tyrosine kinase inhibitor (TKI), with a cytotoxic effect, that induces direct cell death. The second-line treatment is a multi-targeted TKI, with both cytotoxic and anti-angiogenic effect. The model is a coupled hyperbolic/elliptic system based on mass balance equations on cell densities coupled with a diffusion equation on the nutrients and oxygen concentrations. The tumor model involves 3 proliferating cell densities and a necrotic phase. Each proliferating cell density responds differently to the treatments: P_1-cells are killed by both treatments, P_2-cells are affected by the second-line treatment only, and P_3 cells are resistant to both therapies. The necrotic cells are eliminated at a rate $1/\tau$. We first prove the well-posedness of the model for any non-negative τ. Then we study the asymptotic behavior of the solution as τ goes to zero. In particular, we proved that the limit problem correspond to a tumor growth model without necrosis. This is of great interest regarding the modeling, since it proves the continuity with respect to τ of the family of τ-dependent, ensuring the consistency of the modeling.

Keywords: Tumor growth modeling · Drug resistance · Partial differential equations · Well-posedness · Asymptotic analysis

1991 Mathematics Subject Classification. Primary: 35B40, 35Q92 · Secondary: 92C10

1 Introduction

The impact of mathematical modeling in biology has increased dramatically during the last two decades. Particularly in oncology, the expansion of biological

knowledge combined with the data obtained by invasive and non-invasive techniques makes it possible to elaborate more and more accurate models of tumor growth and to study the impact of different treatments.

Many kinds of mathematical models for solid tumor growth have been developed over the last few decades. Among them, we can find discrete models, models based on ordinary differential equations (ODE models) and partial differential equations (PDE models). ODE models describe the time evolution of volume or masses of tumors, but they account neither for the spatial behavior of the tumor nor for its spatial heterogeneity. Discrete models like cellular automata and agent-based models [3,12] can reproduce the growth at the cell-scale but they fail to describe the cancer evolution at the tissue scale. To this end, macroscopic PDE models are deemed to be adequate for accounting for both time and spatial behavior of the tumor at the macroscale. This paper falls in this framework which seems more appropriate for clinical purpose.

Regarding PDEs descriptions of tumor, there is a wide spectrum of literature researches on the modeling of solid tumor growth with or without treatments and it is impossible to give an extensive list here. However, the reader can refer to [7, 14,17,22,25] and the references therein. Among PDE models, we can distinguish two families of models: the models based on reaction-diffusion equation and the models based on mass balance equations. Models based on reaction-diffusion equations are used to describe the active motion of tumor cells in invasive tumors (see [16] or [23]). Models based on mass balance equations on cell densities are used when cell proliferation is the only cause of tumor growth. Roughly speaking, on the one hand, primary tumors are composed of degenerate cells of the host organ. These cells are in their initial host organ, which is their original growing environment. This makes it hard to determine precisely the boundary of the tumor. On the other hand, metastases are composed of cells that come from a different tissue than the host organ. They are more regular, with sharp interfaces. These interfaces can be described using free boundary methods [9,11,15,20] or multiphase mixtures [8], which consider both cell densities and extracellular matrix [21,24]. The model we study comes from [4] and it is based on mass balance equations. It describes the spatial heterogeneity as a mixture of several cell populations. For the closure of the model, we assume that the tumor behaves like a fluid in a porous media and we close the system by a Darcy's law on the velocity field [2]. Other closure such as viscoelastic laws can be used (see [5]) however based on our experience, Darcy's law is sufficient as a first approximation to address some clinical issues [10].

In this paper, we consider the PDE models of gastrointestinal stroma tumor (GIST) metastases located in the liver. The model has been studied numerically in [18]. The aim of this paper is to study the mathematical properties, namely well-posedness and asymptotic behavior of the solution. Let us present briefly the heuristics of the model. It is commonly known that mutations will lead to the creation of tumor cells which are resistant to cytotoxic drugs. At the time being, it is not possible to know when such mutations appear since this may depend on several parameters (such as treatment time, patient variability, external conditions). Therefore, it has been assumed in [18] that different populations of cells

co-exist at the initial time of the model. Other models for drug resistance can be studied, by considering that the transition from being sensitive to a treatment to becoming resistant to a treatment is continuous [19]. One of the features of the model [18] is that it describes the necrosis. Such a necrosis is composed of cells that die because of drugs or hypoxia (the lack of oxygen/nutrients). This necrosis is evacuated at a given rate $1/\tau$. The main objective of this paper is to study the well-posedness of the model proposed in [18] and to study its asymptotic behavior for small τ.

The outline of the paper is as follows. In Sect. 2 we briefly present the model. The model will be considered in a bounded domain in dimension 2 or 3 in space. Then we present the model without necrosis which will be proved to be the limit model when the necrosis is immediately evacuated. In Sect. 3 we state the main results. Section 4 is devoted to preliminary results required for Sects. 5 and 6. These results use classical estimates for hyperbolic, elliptic, and parabolic equations. In Sect. 5, we prove the well-posedness of the model. The proof is based on a fixed-point method. Finally, we perform the asymptotic analysis for $\tau \to 0$ in Sect. 6. As it will be shown hereafter, it is a singular perturbation problem. The interesting fact is that, based on our analysis, we can describe the tumor growth evolution under treatment continuously with respect to τ.

Remark 1.1 (On the necrotic phase in tumor model). Besides GIST metastases, such a necrotic compartment is also important for other kinds of tumors. For example, one can cite thyroid metastases to the lung (Fig. 1.a) or meningioma (Fig. 1.b), in which few necrotic tissue is visible. Much more aggressive tumors, such as glioblastoma (Fig. 1.d), generate a rather big necrotic core. In contrast to these tumors, the necrotic cells of GIST metastases to the liver (Fig. 1.c) are more diffused inside the tumor.

2   The Model

In this section, we present the model of Lefebvre *et al.* provided in [18]. The typical evolution of the volume of GIST metastasis is provided by Fig. 2. Once the GIST metastasis has been diagnosed and the specific TKI (typically Imatinib drug) has been chosen the tumor starts its shrinkage, synonym of a good response to the treatment and the disease is under control. However, after a specific period of time, which depends on the patient, the volume stabilises and the shrinkage stops. On the image, one can see a recolonisation of the necrotic core as shown in [18]. Then the tumor restarts growing, meaning that the first-line treatment is no more efficient. The second line treatment is then a multi-targeted TKI (often Sunitinib), which is followed by a shrinkage much shorter than the previous one, and then the disease is out of control. The model proposed in [18] consists in describing the evolution of three cancer cell populations subjected to two lines of treatment. The first-line treatment denoted by $\mathcal{T}_1$ is a specific tyrosine kinase inhibitor (TKI), which has a cytotoxic effect, as reported by clinical studies. The second-line treatment denoted by $\mathcal{T}_2$ is a multi-targeted TKI, with both
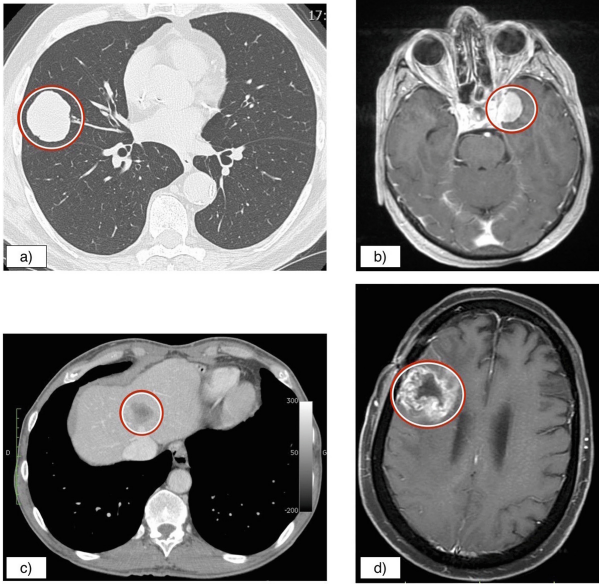
Fig. 1. a) Metastasis to the lung (Courtesy of J. Palussière, MD at Institut Bergonié, 33000 Bordeaux, France), b) brain meningioma (Courtesy of H. Loiseau, MD at Hôpital Pellegrin, CHU Bordeaux, 33000 Bordeaux, France), c) GIST metastasis to the liver (Courtesy of J. Palussière, MD at Institut Bergonié, 33000 Bordeaux, France), d) brain glioma (Courtesy of H. M. Fathallah-Shaykh, MD at University of Alabama at Birmingham, Birmingham, AL 35294, USA).
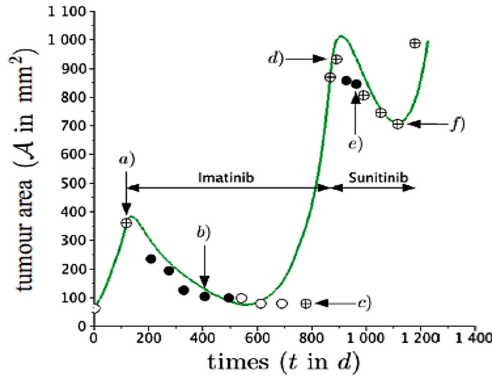
Fig. 2. The typical evolution of the volume of GIST metastasis under 2 lines of tyrosine kinase inhibitor treatment from [18]. The continuous line is the polynomial interpolation of the volumes computed from medical imaging. a) the first-line treament begins. b) the tumor shrinks and the core is dark (necrotic) on the MRI. c) The shrinkage has stops and the core of the tumor is enhanced. d) the disease if out of control: another treatment has to be chosen. e) the second line treatment seems efficient. f) In terms of volume the disease seems under control but the texture of the image is changing. One month later the disease relapse.

cytotoxic and anti-angiogenic effect. P_1 stands for the density of the proliferating cells which are assumed to be sensitive to both treatments $\mathcal{T}_1$ and $\mathcal{T}_2$. P_2 denotes the density of proliferating cells which are resistant to $\mathcal{T}_1$ and sensitive to $\mathcal{T}_2$. The density of cells that are affected neither by $\mathcal{T}_1$ nor by $\mathcal{T}_2$ is denoted by P_3.

The nutrient (and oxygen) supply, that comes from the healthy tissue, is denoted by M. It drives the cell proliferation rate $\gamma_1(M) - \gamma_2(M)$ of the three cancer cell species, where γ_1 and γ_2 are positive functions, standing respectively for the proliferation rate and the death rate due to hypoxia. In [18], they set

(1)
$$\gamma_1(M) = \frac{1 + \tanh(K_1(M - M_{hyp}))}{2}, \quad \gamma_2(M) = \frac{1 - \tanh(K_2(M - M_{hyp}))}{2},$$

where K_0, K_1 are coefficients, and M_{hyp} is the hypoxia threshold.

The treatments efficiency is described by using the smooth functions $t \rightarrow \mu_1(t)$ and $t \rightarrow \mu_2(t)$, which stand for the cytotoxic effect of the treatments $\mathcal{T}_1$ and $\mathcal{T}_2$ respectively. We assume that the absorption of these drugs is proportional to the nutrient/oxygen supply rate.

When the cells die because of the treatment or due to hypoxia, they enter to a necrotic phase, whose density is denoted by N. The necrotic compartment is assumed to be evacuated at the rate $1/\tau$ where τ is the characteristic evacuation time.

S is the density of the healthy cells, which do not divide since their metabolism is slow compared to the metabolism of proliferating cells.

The tumor grows at a speed $\mathbf{v}$ whose divergence is obtained by using the saturation assumption:

(2)
$$P_1 + P_2 + P_3 + N + S = 1.$$

The factor ξ is introduced in order to account for the VEGF signal produced by the tumor cells to involve angiogenesis (see [13]). It is assumed to be global at any time and proportional to the number of cells dying by hypoxia, which is the fraction $\frac{\gamma_2(M)}{\max \gamma_2}(P_1 + P_2 + P_3)$. The smooth function of time ν_2 stands for the anti-angiogenic effect of treatment $\mathcal{T}_2$, it can be a regularization of the time-characteristic function of treatment $\mathcal{T}_2$. The parameter λ is the coefficient of absorption of this signal by the organism. For further details concerning the modeling, the reader may refer to [18].

For the sake of conciseness, we introduce the following notations in order to write the problem in a factorized way.

Notation 2.1. For any $\alpha \in \mathbb{R}^n, \beta \in \mathbb{R}^d$ we denote by

$$(\alpha \otimes \beta)_{i,j} = \alpha_i \beta_j, \qquad \text{for } i = 1, \ldots, n, \, j = 1, \ldots, d,$$
$$\nabla \cdot (\alpha \otimes \beta) = (\nabla \cdot \beta)\alpha + (\beta \cdot \nabla)\alpha.$$

The vector $\mathbf{u}$ stands for $(P_1, P_2, P_3, S)^t$ and we denote by $\gamma(M) := \gamma_1(M) - \gamma_2(M)$. Now we define

$$A(M) := \begin{pmatrix} \gamma(M) - (\mu_1 + \mu_2)M & 0 & 0 & 0 \\ 0 & \gamma(M) - \mu_2 M & 0 & 0 \\ 0 & 0 & \gamma(M) & 0 \\ 0 & 0 & 0 & 0 \end{pmatrix},$$

$$\mathbf{b}(M) := (\gamma_1(M), \gamma_1(M), \gamma_1(M), 0)^t,$$

$$\mathbf{d}(M) := (\gamma_2(M) + (\mu_1 + \mu_2)M, \gamma_2(M) + \mu_2 M, \gamma_2(M), 0)^t,$$

$$\mathbf{p} := (1, 1, 1, 0)^t,$$

$$\mathbf{p}_{1,2} := (1, 1, 0, 0)^t,$$

$$\mathbf{s} := (0, 0, 0, 1)^t,$$

and we denote by $\mathbf{n}$ the outward normal to Ω, where Ω is a bounded domain in $\mathbb{R}^2$ or $\mathbb{R}^3$.

The model of Lefebvre *et al.* can be written as

(3a) $$\partial_t \mathbf{u} + \nabla \cdot (\mathbf{u} \otimes \mathbf{v}) = A(M)\mathbf{u},$$

(3b) $$\mathbf{u} = \mathbf{s}, \qquad \text{if } \mathbf{v} \cdot \mathbf{n} < 0 \text{ on } \partial\Omega,$$

(3c) $$\partial_t N + \nabla \cdot (\mathbf{v}N) = \mathbf{d}(M) \cdot \mathbf{u} - (1/\tau)N,$$

(3d) $$N = 0, \qquad \text{if } \mathbf{v} \cdot \mathbf{n} < 0 \text{ on } \partial\Omega,$$

(3e) $$\nabla \cdot \mathbf{v} = \mathbf{b}(M) \cdot \mathbf{u} - (1/\tau)N,$$

(3f) $$\mathbf{v} = -k\nabla\Pi,$$

(3g) $$\Pi|_{\partial\Omega} = 0,$$

(3h) $$\partial_t M - \Delta M + \nabla \cdot (M\xi\nabla(\mathbf{p} \cdot \mathbf{u})) = -\eta M \mathbf{p} \cdot \mathbf{u} + C_0 \mathbf{s} \cdot \mathbf{u}(1 - M),$$

(3i) $$M|_{\partial\Omega} = 1,$$

(3j) $$\partial_t \xi = \alpha \int_\Omega \frac{\gamma_2(M)}{\max \gamma_2}(\mathbf{p} - \nu_2\mathbf{p}_{1,2}) \cdot \mathbf{u}\,\mathrm{d}x - \lambda\xi,$$

with initial conditions on $\mathbf{u}$, N, M, and ξ given later on.

Without necrosis, similar modeling considerations lead to the following model:

(4a) $$\partial_t \mathbf{u} + \nabla \cdot (\mathbf{u} \otimes \mathbf{v}) = A(M)\mathbf{u},$$

(4b) $$\mathbf{u} = \mathbf{s}, \qquad \text{if } \mathbf{v} \cdot \mathbf{n} < 0 \text{ on } \partial\Omega,$$

(4c) $$\nabla \cdot \mathbf{v} = (\mathbf{b}(M) - \mathbf{d}(M)) \cdot \mathbf{u},$$

(4d) $$\mathbf{v} = -k\nabla\Pi,$$

(4e) $$\Pi|_{\partial\Omega} = 0,$$

(4f) $$\partial_t M - \Delta M + \nabla \cdot (M\xi\nabla(\mathbf{p} \cdot \mathbf{u})) = -\eta M \mathbf{p} \cdot \mathbf{u} + C_0 \mathbf{s} \cdot \mathbf{u}(1 - M),$$

(4g) $$M|_{\partial\Omega} = 1,$$

(4h) $$\partial_t \xi = \alpha \int_\Omega \frac{\gamma_2(M)}{\max \gamma_2}(\mathbf{p} - \nu_2\mathbf{p}_{1,2}) \cdot \mathbf{u}\,\mathrm{d}x - \lambda\xi.$$

Here again the initial conditions on $\mathbf{u}$, M, and ξ are made precise later on.

It is worth noting that for both systems (3) and (4) the Eqs. (3e)–(3f)–(3g) (resp. (4c)–(4d)–(4e)) uniquely determines the pressure Π, from which the velocity $\mathbf{v}$ is deduced thanks to the Darcy type law (3f) (resp. (4d)). Note that in both cases homogeneous Dirichlet condition is imposed to the pressure Π. This implicitly states that the tumor growth has no influence on the tissue far from the tumor location.

3 Main Results and Interpretation

In this paper, we prove the local existence and uniqueness of the solution to the problems (3) and (4), under appropriate assumptions on the initial data and the boundary, as well as the asymptotic behavior of the solution to (3) when $\tau \to 0$. In particular we prove that under high enough Sobolev regularity the two above problems are well-posed as long as the tumor does not reach the boundary of the domain.

In our study, we consider a bounded domain denoted by Ω included in $\mathbb{R}^d$, for $d = 2, 3$. For the spatial regularity, we use the algebra structure of the Sobolev space $H^s(\Omega)$ for s large enough. This algebra structure is a consequence of the two following results:

- the Sobolev embedding $H^s(\Omega) \hookrightarrow L^\infty(\Omega)$ for s integer such that $s > d/2$ (see Corollary 9.13 and Corollary 9.15 in [6]);
- the algebra structure of $H^s(\Omega) \cap L^\infty(\Omega)$ for $s > 0$ (see Chapter II. §A.2 Application to the study of products and composition, Proposition 2.1.1 in [1]).

Hypothesis 3.1. Throughout the paper, the following hypothesis hold:

- the domain Ω is a bounded domain in $\mathbb{R}^2$ or $\mathbb{R}^3$ with C^∞ boundary,
- the rates $\gamma_1(M)$ and $\gamma_2(M)$ are non-negative and C^∞ functions (this is the case for the examples given by (1)),
- the parameters μ_1, μ_2, and ν_2 are C^∞ non-negative functions of time, such as regularization of the time-characteristic functions of treatment $\mathcal{T}_1, \mathcal{T}_2$ and we assume that $\nu_2 \in [0, 1]$,
- the parameters k, η, C_0, α, and λ are non-negative.

Before stating our theoretical resulst, we introduce the following notations:

Notation 3.2. The solution of each equation belongs to specific space:

- for any $T > 0$, $p \in [1, +\infty]$, and $s \geq 0$, we denote by $L_T^p; H^s$ the space $L^p(0, T; H^s(\Omega))$ endowed with the norm

$$\|\varphi\|_{L_T^p; H^s} := \|\varphi\|_{L^p(0,T; H^s(\Omega))}, \qquad \forall \varphi \in L_T^p; H^s,$$

for the purpose of clarity, for $\mathbf{u} \in L^p(0, T; H^s(\Omega))^n$ we denote by $\|\mathbf{u}\|_{L_T^p; H^s}$ the norm of $\mathbf{u}$ components by components,

- for any $T > 0$, $p_1, p_2 \in [1, +\infty]$, and $s_1, s_2 \geq 0$, we denote by $L_T^{p_1}; H^{s_1} \cap L_T^{p_2}; H^{s_2}$ the space $L^{p_1}(0, T; H^{s_1}(\Omega)) \cap L^{p_2}(0, T; H^{s_2}(\Omega))$ endowed with the norm

$$\|\varphi\|_{L_T^{p_1}; H^{s_1} \cap L_T^{p_2}; H^{s_2}} := \|\varphi\|_{L_T^{p_1}; H^{s_1}} + \|\varphi\|_{L_T^{p_2}; H^{s_2}}, \quad \forall \varphi \in L_T^{p_1}; H^{s_1} \cap L_T^{p_2}; H^{s_2},$$

- for any $s \geq 1$, we denote by $\mathcal{E}_0^s$ the space $H^s(\Omega)^4 \times H^{s-1}(\Omega) \times \mathbb{R}$ endowed with the norm:

$$\|(\mathbf{u}_0, M_0, \xi_0)\|_{\mathcal{E}_0^s} := \|\mathbf{u}_0\|_{H^s} + \|M_0\|_{H^{s-1}} + |\xi_0|, \quad \forall (\mathbf{u}_0, M_0, \xi_0) \in \mathcal{E}_0^s,$$

- for any $T > 0$ and $s \geq 1$, we denote by $\mathcal{E}_T^s$ the space $(L_T^\infty; H^s)^4 \times L_T^2; H^s \cap L_T^\infty; H^{s-1} \times C^0([0, T])$ endowed with the norm:

$$\|(\mathbf{u}, M, \xi)\|_{\mathcal{E}_T^s} := \|\mathbf{u}\|_{L_T^\infty; H^s} + \|M\|_{L_T^2; H^s \cap L_T^\infty; H^{s-1}} + \|\xi\|_\infty, \quad \forall (\mathbf{u}, M, \xi) \in \mathcal{E}_T^s,$$

- for any $T > 0$ and $s \geq 0$, we denote by $\mathcal{E}_T^{2,s}$ the space $(L_T^2; H^s)^4 \times L_T^2; H^s \times L^2(0, T)$ endowed with the norm:

$$\|(\mathbf{u}, M, \xi)\|_{\mathcal{E}_T^{2,s}} := \|\mathbf{u}\|_{L_T^2; H^s} + \|M\|_{L_T^2; H^s} + \|\xi\|_{L^2(0, T)}, \quad \forall (\mathbf{u}, M, \xi) \in \mathcal{E}_T^{2,s}.$$

Then the local existence and uniqueness result is the following:

Theorem 3.3 (Well-posedness of problems (3) and (4)). *Assume the hypotheses 3.1 hold. Let $s \geq 3$.*

(i) *Let $\tau > 0$, $(\mathbf{u}_0, M_0, \xi_0) \in \mathcal{E}_0^s$, and $N_0 \in H^s(\Omega)$ such that $\mathbf{u}_0 - \mathbf{s}$ (where $\mathbf{s} = (0, 0, 0, 1)^t$) and N_0 are compactly supported in Ω. Let us assume that the cell densities $\mathbf{u}_0 = (P_{1,0}, P_{2,0}, P_{3,0}, S_0)^t$ and N_0 satisfy*
  - $P_{1,0}$, $P_{2,0}$, $P_{3,0}$, and N_0 have compact support in Ω,
  - $P_{1,0}, P_{2,0}, P_{3,0}, S_0, N_0 \geq 0$,
  - $P_{1,0} + P_{2,0} + P_{3,0} + N_0 + S_0 = 1$.

  Then, there exist $R \geq \|(\mathbf{u}_0, M_0, \xi_0)\|_{\mathcal{E}_0^s} + \|N_0\|_{H^s}$ and a maximal time of existence $T^\tau > 0$ such that the problem (3) has a unique solution $((\mathbf{u}, M, \xi), \mathbf{v}, N)$ in $\mathcal{E}_{T^\tau}^s \times L_T^2; H^{s+1} \cap L_T^\infty; H^s \times L_T^\infty; H^s$. This solution satisfies
  (a) $\|(\mathbf{u}, M, \xi)\|_{\mathcal{E}_{T^\tau}^s} + \|N\|_{L_{T^\tau}^\infty; H^s} \leq R$,
  (b) $\mathbf{u}$, N, $\mathbf{v} \in C^0([0, T^\tau]; H^{s-1}(\Omega))$, $M \in C^0([0, T^\tau]; H^{s-2}(\Omega))$, and $\xi \in C^1([0, T^\tau])$,
  (c) *the cell densities $\mathbf{u} = (P_1, P_2, P_3, S)^t$ and N satisfy*
    - *for all $t < T^\tau$, $P_1(t, \cdot), P_2(t, \cdot), P_3(t, \cdot), N(t, \cdot)$ have compact support in Ω (i.e. the tumor does not hit the boundary),*
    - $P_1, P_2, P_3, S, N \geq 0$,
    - $P_1 + P_2 + P_3 + N + S = 1$.
(ii) *Let $(\mathbf{u}_0, M_0, \xi_0) \in \mathcal{E}_0^s$ such that $\mathbf{u}_0 - \mathbf{s}$ (where $\mathbf{s} = (0, 0, 0, 1)^t$) is compactly supported in Ω. Let us assume that the cells densities $\mathbf{u}_0 = (P_{1,0}, P_{2,0}, P_{3,0}, S_0)^t$ satisfy*
  - $P_{1,0}, P_{2,0}, P_{3,0}$ have compact support in Ω,

- $P_{1,0}, P_{2,0}, P_{3,0}, S_0 \geq 0$,
- $P_{1,0} + P_{2,0} + P_{3,0} + S_0 = 1$.

Then, there exist $R \geq \|(\mathbf{u}_0, M_0, \xi_0)\|_{\mathcal{E}_0^s}$ and a maximal time of existence $T > 0$ such that the problem (4) has a unique solution $((\mathbf{u}, M, \xi), \mathbf{v})$ in $\mathcal{E}_T^s \times L_T^2; H^{s+1} \cap L_T^\infty; H^s$. This solution satisfies

(a) $\|(\mathbf{u}, M, \xi)\|_{\mathcal{E}_T^s} \leq R$,

(b) $\mathbf{u}, \mathbf{v} \in C^0([0, T]; H^{s-1}(\Omega))$, $M \in C^0([0, T]; H^{s-2}(\Omega))$, $\xi \in C^1([0, T])$,

(c) *the cell densities $\mathbf{u} = (P_1, P_2, P_3, S)^t$ satisfy*
  - *for all $t < T$, $P_1(t, \cdot), P_2(t, \cdot), P_3(t, \cdot)$ have compact support in Ω (i.e. the tumor does not hit the boundary),*
  - $P_1, P_2, P_3, S \geq 0$,
  - $P_1 + P_2 + P_3 + S = 1$.

Remark 3.4. For the purpose of simplicity, we prove the theorem for s integer such that $s \geq 3$, then interpolation theorem gives the result for any real $s \geq 3$. The only hypothesis needed is that $s > d/2 + 1$ (which implies that the embedding $H^{s-1}(\Omega) \hookrightarrow L^\infty(\Omega)$ is continuous).

Remark 3.5 (Continuity with respect to initial conditions)**.** Under the assumptions of Theorem 3.3 we have

(i) Let $\tau > 0$. For $i = 1, 2$, let $X_{0,i} := (\mathbf{u}_{0,i}, M_{0,i}, \xi_{0,i}) \in \mathcal{E}_0^s$ and $N_{0,i} \in H^s(\Omega)$ as in Theorem 3.3 (i) and assume that these initial conditions $X_{0,i}, N_{0,i}$ are bounded by $R > 0$. Let $((\mathbf{u}_i, M_i, \xi_i), \mathbf{v}_i, N_i)$ be the solution to problem (3) with initial conditions $\mathbf{u}_{0,i}, M_{0,i}, \xi_{0,i}$, and $N_{0,i}$. Denote by X_i the vector $(\mathbf{u}_i, M_i, \xi_i)$. Then there exists $C_R > 0$ such that

$$\|(X_1, \mathbf{v}_1, N_1) - (X_2, \mathbf{v}_2, N_2)\|_{\mathcal{E}_{T^\tau}^{2,s-1} \times L_{T^\tau}^2; H^s \times L_{T^\tau}^2; H^{s-1}}^2$$
$$\leq C_R \|(X_{0,1}, N_{0,1}) - (X_{0,2}, N_{0,2})\|_{\mathcal{E}_0^{s-1} \times H^{s-1}}^2.$$

(ii) For $i = 1, 2$, let $X_{0,i} := (\mathbf{u}_{0,i}, M_{0,i}, \xi_{0,i}) \in \mathcal{E}_0^s$ as in Theorem 3.3 (ii) and assume that these initial conditions $X_{0,i}$ are bounded by $R > 0$. Let $((\mathbf{u}_i, M_i, \xi_i), \mathbf{v}_i)$ be the solution to problem (4) with initial conditions $\mathbf{u}_{0,i}, M_{0,i}, \xi_{0,i}$. Denote by X_i the vector $(\mathbf{u}_i, M_i, \xi_i)$. Then there exists $C_R > 0$ such that

$$\|(X_1, \mathbf{v}_1) - (X_2, \mathbf{v}_2)\|_{\mathcal{E}_{T^\tau}^{2,s-1} \times L_{T^\tau}^2; H^s}^2 \leq C_R \|X_{0,1} - X_{0,2}\|_{\mathcal{E}_0^{s-1}}^2.$$

The second result states that, if the initial data are well-prepared, the solution to problem (3) converges to the solution to problem (4) when $\tau \to 0$:

Theorem 3.6 (Asymptotic behavior)**.** *For any $\tau > 0$, let $\mathbf{u}_0^\tau$, N_0^τ, M_0^τ, and ξ_0^τ be as in Theorem 3.3 (i). Let $\mathbf{u}_0$, M_0, and ξ_0 be as in Theorem 3.3 (ii). Assume that*

- $\lim\limits_{\tau \to 0^+} \dfrac{1}{\sqrt{\tau}} \|N_0^\tau\|_{H^s} = 0$,
- $\lim\limits_{\tau \to 0^+} (\mathbf{u}_0^\tau, M_0^\tau, \xi_0^\tau) = (\mathbf{u}_0, M_0, \xi_0)$ *in* $\mathcal{E}_0^{s-1}$.

Then there exists $T > 0$ (independent of τ) such that

- *for any $\tau > 0$, the problem (3) has a unique solution on $[0, T]$ denoted by $((\mathbf{u}^\tau, M^\tau, \xi^\tau), \mathbf{v}^\tau, N^\tau)$ and the problem (4) has a unique solution on $[0, T]$ denoted by $((\mathbf{u}, M, \xi), \mathbf{v})$,*
- *there exists $C > 0$ such that for any $\tau > 0$ small enough*

$$\frac{1}{\sqrt{\tau}} \|N^\tau\|_{L_T^\infty; H^s} + \frac{1}{\tau} \|N^\tau\|_{L_T^2; H^s} \leq C,$$

- $\lim\limits_{\tau \to 0^+} ((\mathbf{u}^\tau, M^\tau, \xi^\tau), \mathbf{v}^\tau) = (\mathbf{u}, M, \xi, \mathbf{v})$ *in* $\mathcal{E}_T^{2,s-1} \times L_T^2; H^s$.

4   Preliminary Results

Throughout the paper, we consider $d = 2, 3$ and $s \geq 3$. In this section, we prove estimates on the solutions to the two models. The key argument to obtain these estimates is that if the initial data of P_1, P_2, P_3, N have compact support in Ω, then any solution to (3) or (4) is compactly supported in Ω. One can obtain *a priori* estimates on the system using nonlinear estimates in high order Sobolev spaces (similarly to nonlinear hyperbolic systems, see [1]) and usual parabolic estimates on M. The strategy is therefore to construct a suitable mapping such that this property remains true. In a first step, we start to define the operators which give the solution of each equation and we construct the mappings on which we apply the fixed-point strategy.

Definition 4.1. We consider the following operators

- $\mathcal{V} : f \longmapsto \mathbf{v}$, where $\mathbf{v}$ is the solution[1] to

$$(5) \qquad \begin{cases} \nabla \cdot \mathbf{v} = f, & (\text{in } \Omega) \\ \mathbf{v} = -k\nabla\Pi, & (\text{in } \Omega) \\ \Pi = 0, & (\text{on } \partial\Omega) \end{cases}$$

- $\mathcal{U} : (\mathbf{u}_0, \mathbf{v}, M) \longmapsto \mathbf{u}$, where $\mathbf{u}$ is the solution to

$$(6) \qquad \begin{cases} \partial_t \mathbf{u} + \nabla \cdot (\mathbf{u} \otimes \mathbf{v}) = A(M)\mathbf{u}, & (\text{in } \Omega) \\ \mathbf{u} = \mathbf{s}, & (\text{if } \mathbf{v} \cdot \mathbf{n} < 0 \text{ on } \partial\Omega) \\ \mathbf{u}|_{t=0} = \mathbf{u}_0, & (\text{in } \Omega) \end{cases}$$

---

[1] Note that Π is uniquely determined as the elliptic solution to (5), ans $\mathbf{v}$ is deduced by $\mathbf{v} = -k\nabla\Pi$.

- $\mathcal{N} : (N_0, \mathbf{u}_0, \mathbf{v}, M, \tau) \longmapsto N$, where N is the solution to

(7) $\qquad \begin{cases} \partial_t N + \nabla \cdot (\mathbf{v}N) = \mathbf{d}(M) \cdot \mathbf{u} - (1/\tau)N, & \text{(in } \Omega) \\ \qquad\qquad N = 0, & \text{(if } \mathbf{v} \cdot \mathbf{n} < 0 \text{ on } \partial\Omega) \\ \qquad\qquad N|_{t=0} = N_0, & \text{(in } \Omega) \end{cases}$

with $\mathbf{u} := \mathcal{U}(\mathbf{u}_0, \mathbf{v}, M)$.

- $\mathcal{M} : (M_0, \mathbf{u}, \xi) \longmapsto M$, where M is the solution to

(8)
$\qquad \begin{cases} \partial_t M - \Delta M + \nabla \cdot (M\xi\nabla(\mathbf{p} \cdot \mathbf{u})) = -\eta M\mathbf{p} \cdot \mathbf{u} + C_0\mathbf{s} \cdot \mathbf{u}(1 - M), & \text{(on } \Omega) \\ \qquad\qquad M|_{\partial\Omega} = 1, \\ \qquad\qquad M|_{t=0} = M_0, \end{cases}$

- $\Xi : (\xi_0, \mathbf{u}, M) \longmapsto \xi$, where ξ is the solution to

(9) $\qquad \begin{cases} \partial_t \xi = \alpha \int_\Omega \dfrac{\gamma_2(M)}{\max \gamma_2}(\mathbf{p} - \nu_2\mathbf{p}_{1,2}) \cdot \mathbf{u}\mathrm{d}x - \lambda\xi, \\ \xi|_{t=0} = \xi_0. \end{cases}$

To apply the fixed-point strategy on problem (3), we define the operator Φ as follows: for any $X_0 := (\mathbf{u}_0, M_0, \xi_0)$, N_0, and $X := (\mathbf{u}, M, \xi)$, N, we define

$$(\tilde{X}, \tilde{N}) := \Phi((X, N), (X_0, N_0), \tau),$$

where $\tilde{X} := (\tilde{\mathbf{u}}, \tilde{M}, \tilde{\xi})$ with

$$\tilde{\mathbf{u}} := \mathcal{U}(\mathbf{u}_0, \mathcal{V}(\mathbf{b}(M) \cdot \mathbf{u} - (1/\tau)N), M),$$
$$\tilde{N} := \mathcal{N}(N_0, \mathbf{u}_0, \mathcal{V}(\mathbf{b}(M) \cdot \mathbf{u} - (1/\tau)N), M),$$
$$\tilde{M} := \mathcal{M}(M_0, \mathbf{u}, \xi),$$
$$\tilde{\xi} := \Xi(\xi_0, \mathbf{u}, M),$$

To apply the fixed-point strategy on problem (4), we define the operator Ψ as follows: for any $X_0 := (\mathbf{u}_0, M_0, \xi_0)$ and $X := (\mathbf{u}, M, \xi)$, we define

$$\tilde{X} := \Psi(X, X_0),$$

where $\tilde{X} := (\tilde{\mathbf{u}}, \tilde{M}, \tilde{\xi})$ with

$$\tilde{\mathbf{u}} := \mathcal{U}(\mathbf{u}_0, \mathcal{V}((\mathbf{b}(M) - \mathbf{d}(M)) \cdot \mathbf{u}), M),$$
$$\tilde{M} := \mathcal{M}(M_0, \mathbf{u}, \xi),$$
$$\tilde{\xi} := \Xi(\xi_0, \mathbf{u}, M).$$

In order to prove the well-posedness of problems (3) and (4), we use the facts that

- if it exists, the solution to (3) satisfies $(X^\tau, N^\tau) = \Phi((X^\tau, N^\tau), (X_0, N_0), \tau)$,
- if the solution to (4) exists, it satisfies $X = \Psi(X, X_0)$.

It is crucial to exhibit the stability and the Lipschitz-continuity properties of the operators Φ and Ψ. Such properties will be deduced after the analysis of the operators $\mathcal{V}, \mathcal{U}, \mathcal{N}, \mathcal{M}$, and Ξ.

4.1   Estimates for Operator $\mathcal{V}$

Since Ω is smooth, the following estimate on $\mathcal{V}$ is a consequence of classical results on linear elliptic equations that can be found in [6] (see Theorem 9.25 in [6]). For the sake of conciseness, the proof of the following property is left to the reader.

Proposition 4.2 (Estimate for $\mathcal{V}$). *Let $s' \leq s$, $p \in [1, +\infty]$, and $f \in L_T^p; H^{s'}$ be given. Then the solution $\mathbf{v}$ to (5) belongs to $L_T^p; H^{s'+1}$ and there exists $C > 0$ such that $\mathbf{v}$ satisfies*

$$\|\mathbf{v}\|_{L_T^p; H^{s'+1}}^2 \leq C\|f\|_{L_T^p; H^{s'}}^2.$$

Moreover, if $f \in C^0([0,T]; H^{s-2}(\Omega))$ then $\mathbf{v} \in C^0([0,T]; H^{s-1}(\Omega))$.

4.2   Estimates for Operators $\mathcal{U}, \mathcal{N}$

Let $\mathbf{u}_0 \in H^s(\Omega)^4$, $N_0 \in H^s(\Omega)$, $\mathbf{v} \in (L_T^2; H^{s+1})^d$, and $M \in L_T^2; H^s$ be given. We consider $\mathbf{u}$ and N the solutions to (6) and (7). In order to derive explicit formulas of $\mathbf{u}$ and N, we use the characteristic method. The difficulty lies in the fact that $\nabla \cdot \mathbf{v}$ is not necessarily non-negative and thus we must be able to move forward and backward along the characteristic curves. We use the assumption that $\mathbf{u}_0 - \mathbf{s}$ (where $\mathbf{s} = (0,0,0,1)^t$) and N_0 have compact support in Ω and we restrict T to an upper bound so that the tumor does not reach the boundary $\partial\Omega$. More precisely we introduce the following domains:

Definition 4.3. Let Ω_0 be an open set compactly embedded in Ω and assume that $\mathrm{supp}(\mathbf{u}_0 - \mathbf{s}) \cup \mathrm{supp}(N_0) \subset \Omega_0$. For $i = 1,2,3$, we define the open domain Ω_i (see Fig. 3) by

$$\Omega_i := \left\{x \in \Omega, \mathrm{d}(x, \Omega_0) < \frac{i}{4}\mathrm{d}(\partial\Omega, \Omega_0)\right\}, \qquad \text{for } i = 1,2,3.$$

In order to prevent that characteristic curves go out of Ω we assume in the following that T is small enough such that

$$(10) \qquad\qquad \sqrt{T}\|\mathbf{v}\|_{L_T^2; H^{s+1}} < \frac{1}{4}\mathrm{d}(\partial\Omega, \Omega_0).$$

The upper bound (10) on T ensures the two following points:

- The characteristic curves are well-defined for any $t, t' \in [0, T]$, and $x \in \Omega_3$ by

$$\begin{cases} \partial_{t'}\tilde{x}(t', t, x) = \mathbf{v}(t', \tilde{x}(t', t, x)), \\ \tilde{x}(t, t, x) = x, \end{cases}$$

- For $i = 0, 1, 2$, the characteristic curves coming from Ω_i at $t = 0$ stay in Ω_{i+1} for any $t \leq T$. Indeed for any $t, t' \in [0, T]$, and $x \in \Omega_2$, we have

$$|\tilde{x}(t', t, x) - x| \leq \sqrt{|t - t'|}\|\mathbf{v}\|_{L_T^2; H^{s+1}} < \sqrt{\frac{|t - t'|}{T}}\frac{1}{4}\mathrm{d}(\partial\Omega, \Omega_0).$$

Ω_0 is such that

$$\text{supp}(\mathbf{u}_0 - \mathbf{s}) \cup \text{supp}(N_0) \subset\subset \Omega_0,$$

Ω_1 satisfies

$$\bigcup_{t\in[0,T]} \big(\text{supp}(\mathbf{p}\cdot\mathbf{u}(t,\cdot))\cup\text{supp}(N(t,\cdot))\big) \subset\subset \Omega_1,$$

Ω_2 is such that $\mathbf{u}$ and N have explicit formula in Ω_2 and satisfy

$$\bigcup_{t\in[0,T]} \text{supp}(\mathbf{u}(t,\cdot) - \mathbf{s}) \subset\subset \Omega_2,$$

characteristic curves are defined in Ω_3.
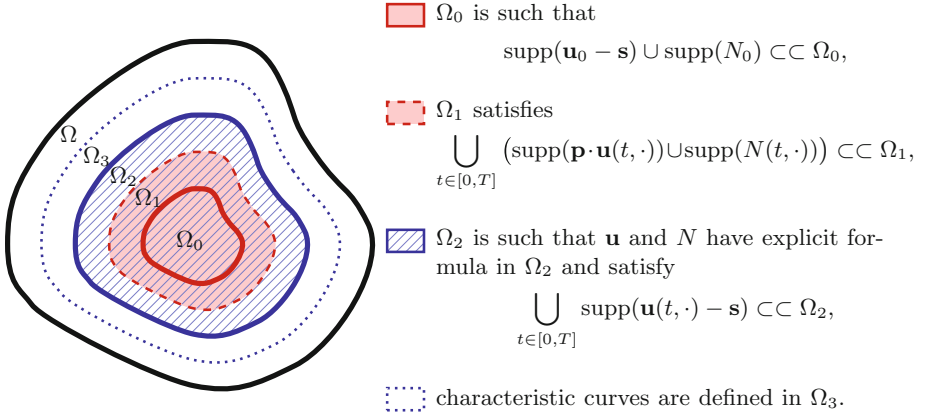
Fig. 3. The domains defined for the characteristic method.

By using the change of coordinates along the characteristic curves, we can come back from Ω_3 to Ω_2 and obtain the following explicit formulas of the solutions to (6) and (7) in Ω_2:
$\forall (t,x) \in [0,T] \times \Omega_2$,

$$(11) \quad \mathbf{u}(t,x) = \exp\Big(\int_0^t (A(M) - \nabla\cdot\mathbf{v})(t', \tilde{x}(t',t,x))\mathrm{d}t'\Big)\mathbf{u}_0(\tilde{x}(0,t,x)),$$

$$
\begin{aligned}
(12) \quad N(t,x) &= \exp\Big(-\int_0^t \big(\nabla\cdot\mathbf{v} + \tfrac{1}{\tau}\big)(t', \tilde{x}(t',t,x))\mathrm{d}t'\Big)N_0(\tilde{x}(0,t,x)) \\
&\quad + \int_0^t \exp\Big(-\int_{t'}^t \big(\nabla\cdot\mathbf{v} + \tfrac{1}{\tau}\big)(t'', \tilde{x}(t'',t,x))\mathrm{d}t''\Big)\big(\mathbf{d}(M)\cdot\mathbf{u}\big)(t', \tilde{x}(t',t,x))\mathrm{d}t'.
\end{aligned}
$$

This leads to the following property:

Proposition 4.4. *Let $\mathbf{u}_0 \in H^s(\Omega)^4$, $N_0 \in H^s(\Omega)$, $\mathbf{v} \in (L_T^2; H^{s+1})^d$, and $M \in L_T^2; H^s$. Assume the 3 following facts:*

(i) N_0 *and the components of* $\mathbf{u}_0$ *are non-negative,*
(ii) $\text{supp}(\mathbf{u}_0 - \mathbf{s}) \cup \text{supp}(N_0)$ *is compactly embedded in* Ω_0,
(iii) $\bigcup_{t\in[0,T]} \text{supp}((\nabla\cdot\mathbf{v})(t,\cdot))$ *is compactly embedded in* Ω_1.

Then $\mathbf{u} := \mathcal{U}(\mathbf{u}_0, \mathbf{v}, M)$ and $N := \mathcal{N}(N_0, \mathbf{u}_0, \mathbf{v}, M, \tau)$ satisfy

(i) N *and the components of* $\mathbf{u}$ *are non-negative,*
(ii) $\bigcup_{t\in[0,T]} \big(\text{supp}(\mathbf{p}\cdot\mathbf{u}(t,\cdot)) \cup \text{supp}(N(t,\cdot))\big)$ *is compactly embedded in* Ω_1,
(iii) $\bigcup_{t\in[0,T]} \text{supp}(\mathbf{u}(t,\cdot) - \mathbf{s})$ *is compactly embedded in* Ω_2.

Remark 4.5. The property that $\bigcup_{t\in[0,T]}\Big(\mathrm{supp}(\mathbf{p}\cdot\mathbf{u}(t,\cdot))\cup\mathrm{supp}(N(t,\cdot))\Big)$ is compactly embedded in Ω_1 implies the 2 followings points:

- $\bigcup_{t\in[0,T]}\mathrm{supp}\Big((\nabla\cdot\mathcal{V}(\mathbf{b}(M)\cdot\mathbf{u}-(1/\tau)N))(t,\cdot)\Big)$ is compactly embedded in Ω_1,
- $\bigcup_{t\in[0,T]}\mathrm{supp}\Big((\nabla\cdot\mathcal{V}((\mathbf{b}(M)-\mathbf{d}(M))\cdot\mathbf{u}))(t,\cdot)\Big)$ is compactly embedded in Ω_1,

which will be useful for the fixed point in Sect. 5.

Proof. The property that the components of $\mathbf{u}$ are non-negative is a consequence of the assumption on $\mathbf{u}_0$ and of the explicit formula (11). Then since $\mathbf{d}(M)\cdot\mathbf{u}$ is non-negative, the explicit formula (12) and the assumption on N_0 lead to the property that N is non-negative.

Denote by $\mathcal{K}_0\subset\Omega_0$ the compact $\mathrm{supp}(\mathbf{u}_0-\mathbf{s})\cup\mathrm{supp}(N_0)$ and denote by $\mathcal{K}_1\subset\Omega_1$ a compact such that

- $\bigcup_{t\in[0,T]}\mathrm{supp}\big((\nabla\cdot\mathbf{v})(t,\cdot)\big)\subset\mathcal{K}_1$,
- $\big\{x\in\Omega,\mathrm{d}(x,\mathcal{K}_0)\leq\frac{1}{4}\mathrm{d}(\partial\Omega,\Omega_0)\big\}\subset\mathcal{K}_1$.

We consider also $\mathcal{K}_2$ the compact $\big\{x\in\Omega,\mathrm{d}(x,\mathcal{K}_1)\leq\frac{1}{4}\mathrm{d}(\partial\Omega,\Omega_0)\big\}\subset\Omega_2$.

Let us focus on (11). For any $t\in[0,T]$ and $x\in\Omega_2\setminus\mathcal{K}_1$, assumption (10) on T ensures that $\mathbf{u}_0(\tilde{x}(0,t,x))=\mathbf{s}$. The fact that $A(M)\mathbf{s}=0$ implies that $\exp(A(M))\mathbf{s}=\mathbf{s}$ and leads to

$$\mathbf{u}(t,x)=\exp\Big(\int_0^t-(\nabla\cdot\mathbf{v})(t',\tilde{x}(t',t,x))\mathrm{d}t'\Big)\mathbf{s},$$

for any $t\in[0,T]$ and $x\in\Omega_2\setminus\mathcal{K}_1$. Then we obtain that $\mathbf{p}\cdot\mathbf{u}(t,\cdot)=0$ in $\Omega_2\setminus\mathcal{K}_1$ for any $t\in[0,T]$.

Since $\tilde{x}(t',t,x)\in\Omega\setminus\mathcal{K}_1$ for any $t,t'\in[0,T]$, and $x\in\Omega_2\setminus\mathcal{K}_2$, we deduce from the above formula that $\mathbf{u}(t,\cdot)=\mathbf{s}$ in $\Omega_2\setminus\mathcal{K}_2$ for any $t\in[0,T]$.

From the explicit expressions for N and $\mathbf{u}$ respectively given in (12) and (11), we deduce that $\mathbf{d}(M)\cdot\mathbf{u}(t',\tilde{x}(t',t,x))=0$ for any $t,t'\in[0,T]$, and $x\in\Omega_2\setminus\mathcal{K}_1$. Since $N_0(\tilde{x}(0,t,x))=0$ for any $t\in[0,T]$ and $x\in\Omega_2\setminus\mathcal{K}_1$, we conclude that $N(t,\cdot)=0$ in $\Omega_2\setminus\mathcal{K}_1$.

In conclusion, the solutions $\mathbf{u}$ and N given by the characteristic method in Ω_2 satisfy $\mathbf{u}=\mathbf{s}$ and $N=0$ in a neighborhood of $\partial\Omega_2$. Based on the Eqs. (6) and (7), $\mathbf{u}$ can be smoothly extended by $\mathbf{u}=\mathbf{s}$ in $\Omega\setminus\Omega_2$ and N can be smoothly extended by $N=0$ in $\Omega\setminus\Omega_2$. This concludes the proof of the Proposition. $\square$

For the purpose of clarity, hereafter we denote by ∂_x^k, for $k\in\mathbb{N}$, any partial derivative of order k (which is the partial derivative ∂_x^α for any multi-index $\alpha\in\mathbb{N}^d$ such that $|\alpha|=\alpha_1+\cdots+\alpha_d=k$). The following Lemma provides estimates on the product $\partial_x^m\nabla\cdot(\mathbf{v}u)\partial_x^m u$ in terms of $\|u\|_{H^m}$ for $u\in H^m(\Omega)$:

Lemma 4.6. *Let s' be an integer such that $s' > d/2$ and let $K \in \mathbb{R}$ be given. Let $m \in \mathbb{N}$ be such that $m \leq s'$. Let $\mathbf{v} \in H^{s'+1}(\Omega)$. We assume that $u \in H^m(\Omega)$ is such that $u = K$ in a neighborhood of $\partial\Omega$. Therefore $\partial_x^k u|_{\partial\Omega} = 0$ for any $1 \leq k \leq m$. Then there exists $C > 0$ such that the following estimate holds:*

$$\left| \int_\Omega \partial_x^m \nabla \cdot (\mathbf{v}u) \partial_x^m u \right| \leq C \|\mathbf{v}\|_{H^{s'+1}} \left(K^2 \delta_{m,0} + \|u\|_{H^m}^2 \right),$$

where $\delta_{m,0}$ is the Kronecker symbol equal to 1 for $m = 0$ and equal to 0 elsewhere.

Proof. In the proof, we use the Gagliardo-Nirenberg interpolation inequality that is a consequence of Theorem 9.9, Corollary 9.11 and Corollary 9.14 given in [6]: there exists $C > 0$ such that

$$\|u\|_{L^4} \leq C \|u\|_{H^1}, \quad \forall u \in H^1(\Omega).$$

We start by applying Leibniz formula on the left-hand side

$$\left| \int_\Omega \partial_x^m \nabla \cdot (\mathbf{v}u) \partial_x^m u \right| \leq \sum_{k=0}^m C_m^k \underbrace{\left| \int_\Omega \nabla \cdot (\partial_x^k \mathbf{v} \partial_x^{m-k} u) \partial_x^m u \right|}_{=I_m^k}.$$

- If $k = 0$,

$$I_m^0 = \int_\Omega \nabla \cdot (\mathbf{v} \partial_x^m u) \partial_x^m u = \int_\Omega (\nabla \cdot \mathbf{v})(\partial_x^m u)^2 + \int_\Omega \mathbf{v} \cdot \frac{1}{2} \nabla \left((\partial_x^m u)^2 \right),$$

then integrate by parts the second integral to obtain successively

$$I_m^0 = \int_\Omega (\nabla \cdot \mathbf{v})(\partial_x^m u)^2 + \frac{1}{2} \left(K^2 \delta_{m,0} \int_{\partial\Omega} \mathbf{v} \cdot \mathbf{n} d\sigma - \int_\Omega (\nabla \cdot \mathbf{v})(\partial_x^m u)^2 \right),$$

$$= \frac{1}{2} \int_\Omega (\nabla \cdot \mathbf{v}) \left(K^2 \delta_{m,0} + (\partial_x^m u)^2 \right).$$

By using the continuous embedding $H^{s'}(\Omega) \hookrightarrow L^\infty(\Omega)$ we infer

$$\left| I_m^0 \right| \leq C \|\mathbf{v}\|_{H^{s'+1}} \left(K^2 \delta_{m,0} + \|u\|_{H^m}^2 \right).$$

- If $1 \leq k \leq m$, the integral I_m^k can be rewritten as

$$I_m^k = \underbrace{\int_\Omega (\nabla \cdot \partial_x^k \mathbf{v}) \, \partial_x^{m-k} u \partial_x^m u}_{I_1} + \underbrace{\int_\Omega \partial_x^k \mathbf{v} \cdot \nabla \left(\partial_x^{m-k} u \right) \partial_x^m u}_{I_2}.$$

Let first estimate I_1.

(i) If $m \geq 2$ and $k = m$:

$$|I_1| \leq \|\nabla \cdot \partial_x^m \mathbf{v}\|_{L^2} \|u\|_{L^\infty} \|\partial_x^m u\|_{L^2},$$

and we use the continuous embedding $H^m \hookrightarrow L^\infty$ to obtain

$$|I_1| \leq C \|\mathbf{v}\|_{H^{s'+1}} \|u\|_{H^m}^2.$$

(ii) Otherwise I_1 satisfies

$$|I_1| \leq \|\nabla \cdot \partial_x^k \mathbf{v}\|_{L^4} \|\partial_x^{m-k} u\|_{L^4} \|\partial_x^m u\|_{L^2},$$

Gagliardo-Nirenberg inequality and using the fact that $s' + 1 \geq 3$ lead to

$$|I_1| \leq C \|\mathbf{v}\|_{H^{s'+1}} \|u\|_{H^m}^2.$$

Then we focus on I_2.

(i) If $k = 1$:

$$|I_2| \leq \|\partial_x \mathbf{v}\|_{L^\infty} \|\nabla(\partial_x^{m-1} u)\|_{L^2} \|\partial_x^m u\|_{L^2},$$

here again the embedding $H^2(\Omega) \hookrightarrow L^\infty(\Omega)$ and the fact that $s' + 1 \geq 3$ lead to

$$|I_2| \leq C \|\mathbf{v}\|_{H^{s'+1}} \|u\|_{H^m}^2.$$

(ii) Otherwise, for $k \geq 2$, the integral I_2 satisfies

$$|I_2| \leq \|\partial_x^k \mathbf{v}\|_{L^4} \|\nabla(\partial_x^{m-k} u)\|_{L^4} \|\partial_x^m u\|_{L^2},$$

and Gagliardo-Nirenberg inequality leads to

$$|I_2| \leq C \|\mathbf{v}\|_{H^{s'+1}} \|u\|_{H^m}^2.$$

$\square$

The previous Lemma makes it possible to prove the following estimate on the solution to the scalar advection Eq. (13):

Proposition 4.7. *Let* $K \in \mathbb{R}$, $u_0 \in H^s(\Omega)$, $\mathbf{v} \in (L_T^2; H^{s+1})^d$, $a, b_1, b_2 \in L_T^2; H^s$. *Let* u *be a solution to*

(13)
$$\begin{cases} \partial_t u + \nabla \cdot (\mathbf{v} u) = au + b_1 + b_2, \\ u|_{t=0} = u_0, \\ u|_{\partial\Omega} = K, \qquad \textit{if } \mathbf{v} \cdot \mathbf{n} < 0 \textit{ on } \partial\Omega \end{cases}$$

and assume that $u = K$ *in a neighborhood of* Ω. *Then for all* $s' \in \mathbb{N}$ *such that* $d/2 < s' \leq s$, *there exists* $C > 0$ *such that*

(14)
$$\|u\|_{L_T^\infty;H^{s'}}^2 \leq \left(\|u_0\|_{H^{s'}}^2 + C\sqrt{T} \left(K^2 \|\mathbf{v}\|_{L_T^2;H^{s'+1}} + \|b_1\|_{L_T^2;H^{s'}} \right) + \|b_2\|_{L_T^2;H^{s'}}^2 \right)$$
$$\times \exp \left(CT + C\sqrt{T}(\|\mathbf{v}\|_{L_T^2;H^{s'+1}} + \|a\|_{L_T^2;H^{s'}} + \|b_1\|_{L_T^2;H^{s'}}) \right).$$

Remark 4.8. *A priori*, b_1 and b_2 play the same role. However for the stability of the operator $\mathcal{N}$ and the Lipschitz continuity of $\mathcal{U}$ and $\mathcal{N}$, it is important to discriminate their roles. More precisely, the fact that the term $\|b_2\|_{L^2_T;H^{s'}}$ does not appear in the exponential term in (14) will be crucial in the following (see the proof of the Lipschitz continuity in Proposition 4.9).

Proof. Let $m \in \mathbb{N}$, $m \le s'$, apply the derivative ∂_x^m to (13), multiply by $\partial_x^m u$ and integrate over Ω. First we observe that since $H^{s'}$ is an algebra,

$$\left| \int_\Omega \partial_x^m (au) \partial_x^m u \right| \le \|au\|_{H^{s'}} \|u\|_{H^{s'}},$$
$$\le C\|a\|_{H^{s'}} \|u\|_{H^{s'}}^2.$$

Then we have

$$\left| \int_\Omega \partial_x^m b_1 \partial_x^m u \right| \le \|b_1\|_{H^{s'}} \|u\|_{H^{s'}},$$
$$\le \|b_1\|_{H^{s'}} (1 + \|u\|_{H^{s'}}^2),$$

and similarly

$$\left| \int_\Omega \partial_x^m b_2 \partial_x^m u \right| \le \frac{1}{2} (\|b_2\|_{H^{s'}}^2 + \|u\|_{H^{s'}}^2).$$

By summing the above inequalities and by using Lemma 4.6 we obtain straightforwardly

$$\partial_t \|u\|_{H^{s'}}^2 \le C \Big[(1 + \|\mathbf{v}\|_{H^{s'+1}} + \|a\|_{H^{s'}} + \|b_1\|_{H^{s'}}) \|u\|_{H^{s'}}^2$$
$$+ K^2 \|\mathbf{v}\|_{H^{s'+1}} + \|b_1\|_{H^{s'}} + \|b_2\|_{H^{s'}}^2 \Big],$$

then integrating in time between 0 and $t < T$ and applying Gronwall's inequality lead to the result. $\square$

By using Proposition 4.7, we deduce the stability and the Lipschitz continuity of the operators $\mathcal{U}$ and $\mathcal{N}$.

Proposition 4.9 (Estimate for $\mathcal{U}, \mathcal{N}$). *Operators $\mathcal{U}$ and $\mathcal{N}$ satisfy the following properties:*

(i) *(Stability) Let $\mathbf{u}_0 \in H^s(\Omega)^4$, $N_0 \in H^s(\Omega)$, $\mathbf{v} \in (L^2_T; H^{s+1})^d \cap (L^\infty_T; H^s)^d$, and $M \in L^2_T; H^s \cap L^\infty_T; H^{s-1}$ satisfying the assumptions of Proposition 4.4. Then there exists $C > 0$ such that $\mathbf{u} := \mathcal{U}(\mathbf{u}_0, \mathbf{v}, M)$ satisfies*

$$\|\mathbf{u}\|_{L^\infty_T;H^s}^2 \le \left(\|\mathbf{u}_0\|_{H^s}^2 + C\sqrt{T} \|\mathbf{v}\|_{L^2_T;H^{s+1}} \right) \exp \left(C\sqrt{T} (\|\mathbf{v}\|_{L^2_T;H^{s+1}} + \|M\|_{L^2_T;H^s}) \right),$$

and $N := \mathcal{N}(N_0, \mathbf{u}_0, \mathbf{v}, M, \tau)$ satisfies

$$\|N\|_{L^\infty_T;H^s}^2 \le \left(\|N_0\|_{H^s}^2 + C\sqrt{T} (\|\mathbf{v}\|_{L^2_T;H^{s+1}} + \|\mathbf{u}\|_{L^\infty_T;H^s} \|M\|_{L^2_T;H^s}) \right)$$
$$\times \exp \left(C\sqrt{T} (\|\mathbf{v}\|_{L^2_T;H^{s+1}} + \|\mathbf{u}\|_{L^\infty_T;H^s} \|M\|_{L^2_T;H^s}) \right).$$

moreover $\mathbf{u}, N \in C^0([0, T]; H^{s-1}(\Omega))$.

(ii) *(Lipschitz continuity) For $i = 1, 2$, let $\mathbf{u}_{0,i}$, $N_{0,i}$, $\mathbf{v}_i$, M_i be as previously and let $\mathbf{u}_i := \mathcal{U}(\mathbf{u}_{0,i}, \mathbf{v}_i, M_i)$ and $N_i := \mathcal{N}(N_{0,i}, \mathbf{u}_{0,i}, \mathbf{v}_i, M_i, \tau)$. Assume there exists $R > 0$ such that*

$$\|(\mathbf{u}_i, M_i, \xi_i)\|_{\mathcal{E}_T^s} + \|N_i\|_{L_T^\infty; H^s} \leq R,$$

then there exists $C_R > 0$ such that

$$\|\mathbf{u}_1 - \mathbf{u}_2\|_{L_T^\infty; H^{s-1}}^2 \leq C_R \Big(\|\mathbf{u}_{0,1} - \mathbf{u}_{0,2}\|_{H^{s-1}}^2$$
$$+ \|\mathbf{v}_1 - \mathbf{v}_2\|_{L_T^2; H^s}^2 + \|M_1 - M_2\|_{L_T^2; H^{s-1}}^2 \Big),$$

and

$$\|N_1 - N_2\|_{L_T^\infty; H^{s-1}}^2 \leq C_R \Big(\|N_{0,1} - N_{0,2}\|_{H^{s-1}}^2 + \|\mathbf{v}_1 - \mathbf{v}_2\|_{L_T^2; H^s}^2$$
$$+ \|M_1 - M_2\|_{L_T^2; H^{s-1}}^2 + \|\mathbf{u}_1 - \mathbf{u}_2\|_{L_T^2; H^{s-1}}^2 \Big).$$

Proof. (i) We apply Proposition 4.7 with $s' = s$, b_1, and b_2 identically null. For $1 \leq i \leq 4$, let u be the ith component of $\mathbf{u}$, and a equals to the ith diagonal component of $A(M)$ (recall that $A(M)$ is diagonal) and we apply Proposition 4.7 to obtain the estimate for $\mathbf{u}$.

Applying Proposition 4.7 with $s' = s$, b_1 equal to $\mathbf{d}(M) \cdot \mathbf{u}$, a, and b_2 identically null leads to the estimate for N.[2]

To prove the time continuity, the assumptions on $\mathbf{v}$, M, and the Eq. (6) imply that $\partial_t \mathbf{u}$ belongs to $(L_T^\infty; H^{s-1})^d$. By integrating $\partial_t \mathbf{u}$ in time between t_1 and t_2 (with $0 \leq t_1 \leq t_2 \leq T$) and using the fact that $\mathbf{u}_0 \in H^s(\Omega)$, we obtain that $\mathbf{u} \in C^0([0, T]; H^{s-1}(\Omega))$ (even Lipschitz continuous). The same result holds for N.

(ii) Let $\mathbf{u}_1$, $\mathbf{u}_2$ be as in Proposition 4.9, then $\mathbf{u}_1 - \mathbf{u}_2$ satisfies the following equation:

$$\partial_t(\mathbf{u}_1 - \mathbf{u}_2) + \nabla \cdot ((\mathbf{u}_1 - \mathbf{u}_2) \otimes \mathbf{v}_1)$$
$$= A(M_1)(\mathbf{u}_1 - \mathbf{u}_2) - \nabla \cdot (\mathbf{u}_2 \otimes (\mathbf{v}_1 - \mathbf{v}_2)) + (A(M_1) - A(M_2))\mathbf{u}_2.$$

For $1 \leq i \leq 4$, we apply Proposition 4.7 with $s' = s - 1$, $\mathbf{v} = \mathbf{v}_1$, u equal to the ith component of $\mathbf{u}_1 - \mathbf{u}_2$, a equal to the ith diagonal component of $A(M_1)$, b_1 identically null, and b_2 equal to the ith component of $-\nabla \cdot (\mathbf{u}_2 \otimes (\mathbf{v}_1 - \mathbf{v}_2)) + (A(M_1) - A(M_2))\mathbf{u}_2$. By observing that

$$\|\nabla \cdot (\mathbf{u}_2 \otimes (\mathbf{v}_1 - \mathbf{v}_2))\|_{H^{s-1}}^2 \leq \|\mathbf{u}_2 \otimes (\mathbf{v}_1 - \mathbf{v}_2)\|_{H^s}^2,$$
$$\leq C \|\mathbf{u}_2\|_{H^s}^2 \|\mathbf{v}_1 - \mathbf{v}_2\|_{H^s}^2,$$
$$\leq C_R \|\mathbf{v}_1 - \mathbf{v}_2\|_{H^s}^2,$$

---

[2] Note that the linear term $-(1/\tau)N$ in Eq. (7) is easy to handle: it provides a constant $e^{-t/\tau} \leq 1$ for any $0 \leq t \leq T$.

and by integrating in time between 0 and T, we obtain

$$\|\nabla \cdot (\mathbf{u}_2 \otimes (\mathbf{v}_1 - \mathbf{v}_2))\|^2_{L^2_T;H^{s-1}} \leq C_R \|\mathbf{v}_1 - \mathbf{v}_2\|^2_{L^2_T;H^s}.$$

Similarly, we get the following estimate on $A(M_1) - A(M_2)$:

$$\|(A(M_1) - A(M_2))\mathbf{u}_2\|^2_{L^2_T;H^{s-1}} \leq C_R \|M_1 - M_2\|^2_{L^2_T;H^{s-1}}.$$

Then we apply Proposition 4.7 to obtain

$$\|\mathbf{u}_1 - \mathbf{u}_2\|^2_{L^\infty_T;H^{s-1}}$$
$$\leq \left(\|\mathbf{u}_{0,1} - \mathbf{u}_{0,2}\|^2_{H^{s-1}} + C_R \left(\|\mathbf{v}_1 - \mathbf{v}_2\|^2_{L^2_T;H^s} + \|M_1 - M_2\|^2_{L^2_T;H^{s-1}} \right) \right)$$
$$\times \exp\left(CT + C_R \sqrt{T} \right).$$

Finally, since T is bounded by some arbitrary constant, we have proven the estimate on $\mathbf{u}_1 - \mathbf{u}_2$.
We use the same ideas to get the estimate on $N_1 - N_2$.

$\square$

4.3   Estimate for $\mathcal{M}$

To prove the estimates on $\mathcal{M}$, we start proving estimates on the following equation:

(15)
$$\begin{cases} \partial_t \tilde{M} - \Delta \tilde{M} + \nabla \cdot (\mathbf{w}_1 \tilde{M} + \mathbf{w}_2) = a\tilde{M} + b, \\ \tilde{M}|_{\partial\Omega} = 0, \\ \tilde{M}|_{t=0} = \tilde{M}_0, \end{cases}$$

where $\tilde{M}_0$ satisfies the boundary condition, $\mathbf{w}_1$, $\mathbf{w}_2$, and b have compact support in Ω. The estimates on $\tilde{M}$ make it possible to prove the stability and the Lipschitz continuity estimates on $\mathcal{M}$. To prove the estimates on $\tilde{M}$, we build $\tilde{M}$ by a Galerkin approximation using the eigenvalues of the operator $(-\Delta)$ endowed with the Dirichlet boundary conditions. This makes it possible to assume in the following computations that for any $k \in \mathbb{N}$, $(-\Delta)^k \tilde{M} = 0$ on the boundary (we can also see this from the equation satisfied by $\tilde{M}$). In order to prove the estimate on $\tilde{M}$, we need the following Lemma:

Lemma 4.10. *Let $\tilde{M}_0 \in H^{s-1}(\Omega)$. Let $\mathbf{w}_1 \in (L^2_T;H^{s-1})^d$, $a \in L^2_T;H^{s-1}$, and $\mathbf{w}_2 \in (L^2_T;L^2)^d, b \in L^2_T;L^2$. Assume that $\tilde{M}_0|_{\partial\Omega} = 0$ and that $\mathbf{w}_1$, $\mathbf{w}_2$, and b have compact support in Ω. Then the solution $\tilde{M}$ to (15) satisfies*

(i) for any $k \in \mathbb{N}$, such that $2k + 1 \leq s$ and $\mathbf{w}_2 \in (L^2_T;H^{2k})^d, b \in L^2_T;H^{2k}$, there exists $C > 0$ such that

(16)
$$\partial_t \|(-\Delta)^k \tilde{M}\|^2_{L^2} + \|(-\Delta)^k \nabla \tilde{M}\|^2_{L^2}$$
$$\leq C\left[\|\mathbf{w}_2\|^2_{H^{2k}} + \|b\|^2_{H^{2k}} + \left(1 + \|\mathbf{w}_1\|^2_{H^{s-1}} + \|a\|^2_{H^{s-1}}\right) \|(-\Delta)^k \tilde{M}\|^2_{L^2} \right],$$

(ii) *for any $k \in \mathbb{N}$, such that $2k + 2 \leq s$ and $\mathbf{w}_2 \in (L_T^2; H^{2k+1})^d, b \in L_T^2; H^{2k+1}$, there exists $C > 0$ such that*

(17)
$$\partial_t \|(-\Delta)^k \nabla \tilde{M}\|_{L^2}^2 + \|(-\Delta)^{k+1} \tilde{M}\|_{L^2}^2$$
$$\leq C\Big[\|\mathbf{w}_2\|_{H^{2k+1}}^2 + \|b\|_{H^{2k+1}}^2 + (1 + \|\mathbf{w}_1\|_{H^{s-1}}^2 + \|a\|_{H^{s-1}}^2) \|\nabla(-\Delta)^k \tilde{M}\|_{L^2}^2\Big].$$

Proof. First, we prove the result for $k = 0$ since it uses different estimates from the general case.

- For $k = 0$.
  To prove (16), multiply the Eq. (15) by $\tilde{M}$ and integrate by parts:

$$\frac{1}{2}\partial_t \|\tilde{M}\|_{L^2}^2 + \|\nabla \tilde{M}\|_{L^2}^2 \leq \left|\int_\Omega (\mathbf{w}_1 \tilde{M} + \mathbf{w}_2) \cdot \nabla \tilde{M}\right| + \left|\int_\Omega (a\tilde{M} + b)\tilde{M}\right|.$$

Using Young's inequality leads to

$$\frac{1}{2}\partial_t \|\tilde{M}\|_{L^2}^2 + \|\nabla \tilde{M}\|_{L^2}^2$$
$$\leq \frac{1}{2}\left(\|\mathbf{w}_1 \tilde{M} + \mathbf{w}_2)\|_{L^2}^2 + \|\nabla \tilde{M}\|_{L^2}^2 + \|a\tilde{M}\|_{L^2}^2 + \|\tilde{M}\|_{L^2}^2 + \|b\|_{L^2}^2 + \|\tilde{M}\|_{L^2}^2\right),$$

then we use the continuous embedding $H^2(\Omega) \hookrightarrow L^\infty(\Omega)$ for $\mathbf{w}_1$ and we get (16) for $k = 0$.
To prove (17), we apply the operator $(-\Delta)$ to (15), multiply by $\tilde{M}$ and integrate by parts:

$$\frac{1}{2}\partial_t \|\nabla \tilde{M}\|_{L^2}^2 + \|\Delta \tilde{M}\|_{L^2}^2 \leq \left|\int_\Omega \nabla \cdot (\mathbf{w}_1 \tilde{M} + \mathbf{w}_2))\Delta \tilde{M}\right| + \left|\int_\Omega \nabla(a\tilde{M} + b) \cdot \nabla \tilde{M}\right|.$$

Using Young's inequality leads to

$$\frac{1}{2}\partial_t \|\nabla \tilde{M}\|_{L^2}^2 + \|\Delta \tilde{M}\|_{L^2}^2$$
$$\leq \frac{1}{2}\left(\|\nabla \cdot (\mathbf{w}_1 \tilde{M} + \mathbf{w}_2))\|_{L^2}^2 + \|\Delta \tilde{M}\|_{L^2}^2 + \|\nabla(a\tilde{M})\|_{L^2}^2 + \|\nabla b\|_{L^2}^2 + 2\|\nabla \tilde{M}\|_{L^2}^2\right).$$

Observe that

$$\|\nabla \cdot (\mathbf{w}_1 \tilde{M})\|_{L^2} \leq \|(\nabla \cdot \mathbf{w}_1)\tilde{M}\|_{L^2} + \|\mathbf{w}_1 \cdot \nabla \tilde{M}\|_{L^2},$$
$$\leq \|(\nabla \cdot \mathbf{w}_1)\|_{L^4}\|\tilde{M}\|_{L^4} + \|\mathbf{w}_1 \cdot \nabla \tilde{M}\|_{L^2}.$$

Using Gagliardo-Nirenberg inequality on the first term and the continuous embedding $H^2(\Omega) \hookrightarrow L^\infty(\Omega)$ on the second term lead to

$$\|\nabla \cdot (\mathbf{w}_1 \tilde{M})\|_{L^2} \leq C\|\mathbf{w}_1\|_{H^2}\|\nabla \tilde{M}\|_{L^2},$$

The same idea applied to $\nabla(a\tilde{M})$ makes it possible to infer

$$\|\nabla(a\tilde{M})\|_{L^2} \leq C\|a\|_{H^2}\|\nabla M\|_{L^2}.$$

- For $k \geq 1$.

  To prove (16), apply $(-\Delta)^k$ to (15), multiply by $(-\Delta)^k \tilde{M}$ and integrate by parts:

$$\frac{1}{2}\partial_t \|(-\Delta)^k M\|_{L^2}^2 + \|(-\Delta)^k \nabla M\|_{L^2}^2$$
$$\leq \left| \int_\Omega (-\Delta)^k(\mathbf{w}_1 \tilde{M} + \mathbf{w}_2)) \cdot (-\Delta)^k \nabla \tilde{M} \right| + \left| \int_\Omega (-\Delta)^k(a\tilde{M} + b)(-\Delta)^k \tilde{M} \right|.$$

Using Young's inequality leads to

$$\frac{1}{2}\partial_t \|(-\Delta)^k \tilde{M}\|_{L^2}^2 + \|(-\Delta)^k \nabla \tilde{M}\|_{L^2}^2$$
$$\leq \frac{1}{2}\left(\|(-\Delta)^k(\mathbf{w}_1 \tilde{M} + \mathbf{w}_2))\|_{L^2}^2 + \|(-\Delta)^k \nabla \tilde{M}\|_{L^2}^2 + \|(-\Delta)^k(a\tilde{M})\|_{L^2}^2 \right.$$
$$\left. + \|(-\Delta)^k \tilde{M}\|_{L^2}^2 + \|(-\Delta)^k b\|_{L^2}^2 + \|(-\Delta)^k \tilde{M}\|_{L^2}^2 \right),$$

then use the fact that $H^{2k}(\Omega)$ is an algebra to deduce (16).

To prove (17), apply $(-\Delta)^{k+1}$ to (15), multiply by $(-\Delta)^k \tilde{M}$ and integrate by parts:

$$\frac{1}{2}\partial_t \|(-\Delta)^k \nabla \tilde{M}\|_{L^2}^2 + \|(-\Delta)^{k+1} \tilde{M}\|_{L^2}^2$$
$$\leq \left| \int_\Omega (-\Delta)^k \nabla \cdot (\mathbf{w}_1 \tilde{M} + \mathbf{w}_2))(-\Delta)^{k+1} \tilde{M} \right|$$
$$+ \left| \int_\Omega (-\Delta)^k \nabla(a\tilde{M} + b) \cdot (-\Delta)^k \nabla \tilde{M} \right|.$$

Using Young's inequality leads to

$$\frac{1}{2}\partial_t \|(-\Delta)^k \nabla \tilde{M}\|_{L^2}^2 + \|(-\Delta)^{k+1} \tilde{M}\|_{L^2}^2$$
$$\leq \frac{1}{2}\left(\|(-\Delta)^k \nabla \cdot (\mathbf{w}_1 \tilde{M} + \mathbf{w}_2))\|_{L^2}^2 + \|(-\Delta)^{k+1} \tilde{M}\|_{L^2}^2 + \|(-\Delta)^k \nabla(a\tilde{M})\|_{L^2}^2 \right.$$
$$\left. + \|(-\Delta)^k \nabla \tilde{M}\|_{L^2}^2 + \|(-\Delta)^k \nabla b\|_{L^2}^2 + \|(-\Delta)^k \nabla \tilde{M}\|_{L^2}^2 \right),$$

then use the fact that $H^{2k+1}(\Omega)$ is an algebra to obtain (17). $\qquad \square$

The previous Lemma leads to the following Proposition, which makes it possible to prove the estimates on $\mathcal{M}$:

Proposition 4.11. *Under the assumption of Lemma 4.10, for any $s' \in \mathbb{N}$ such that $s' \leq s$, there exists $C > 0$ such that*

(18)
$$\|\tilde{M}\|_{L_T^\infty; H^{s'-1}}^2 \leq \left(\|\tilde{M}_0\|_{H^{s'-1}}^2 + C(\|\mathbf{w}_2\|_{L_T^2; H^{s'-1}}^2 + \|b\|_{L_T^2; H^{s'-1}}^2) \right)$$
$$\times \exp\left[C\left(T + \|\mathbf{w}_1\|_{L_T^2; H^{s-1}}^2 + \|a\|_{L_T^2; H^{s-1}}^2 \right) \right].$$

$$\text{(19)} \quad \begin{aligned} \|\tilde{M}\|^2_{L^2_T;H^{s'}} &\leq \|\tilde{M}_0\|^2_{H^{s'-1}} + C\Big[\|\mathbf{w}_2\|^2_{L^2_T;H^{s'-1}} + \|b\|^2_{L^2_T;H^{s'-1}} \\ &\quad + \Big(T + \|\mathbf{w}_1\|^2_{L^2_T;H^{s-1}} + \|a\|^2_{L^2_T;H^{s-1}}\Big)\|\tilde{M}\|^2_{L^\infty_T;H^{s'-1}}\Big]. \end{aligned}$$

Proof. We use Lemma 4.10 and the facts that for $k \in \mathbb{N}$, the norm $\|\cdot\|_{L^2} + \|(-\Delta)^k\cdot\|_{L^2}$ is equivalent to $\|\cdot\|_{H^{2k}}$ and the norm $\|\cdot\|_{L^2} + \|(-\Delta)^k\nabla\cdot\|_{L^2}$ is equivalent to $\|\cdot\|_{H^{2k+1}}$.

- If $s' = 2m + 1$, with $m \in \mathbb{N}^*$, we apply (16) for $k = 0$ and $k = m$ and sum them.
- If $s' = 2m + 2$, $m \in \mathbb{N}^*$, we apply (16) for $k = 0$ and (17) for $k = m$ and sum them.

Theses calculations lead to the following estimates:

$$\text{(20)} \quad \begin{aligned} \partial_t\|\tilde{M}\|^2_{H^{s'-1}} + \|\tilde{M}\|^2_{H^{s'}} &\leq C\Big[\|\mathbf{w}_2\|^2_{H^{s'-1}} + \|b\|^2_{H^{s'-1}} \\ &\quad + \big(1 + \|\mathbf{w}_1\|^2_{H^{s-1}} + \|a\|^2_{H^{s-1}}\big)\|\tilde{M}\|^2_{H^{s'-1}}\Big]. \end{aligned}$$

We start by omitting the term $\|\tilde{M}\|^2_{H^{s'}} \geq 0$ and we integrate in time between 0 and $t \leq T$. Applying Gronwall's inequality leads to (18). To prove (19), we go back to (20), integrate in time between 0 and T and omit the term $\|\tilde{M}(T,\cdot)\|^2_{H^{s'-1}}$. □

Now we can prove the main estimates on operator $\mathcal{M}$:

Proposition 4.12. *Operator $\mathcal{M}$ satisfies the following properties:*

(i) *(Stability) Let $M_0 \in H^{s-1}(\Omega)$ such that $M_0 = 1$ on $\partial\Omega$. Let $\mathbf{u} \in (L^\infty_T;H^s)^4$ such that $\mathbf{p}\cdot\mathbf{u}$ has support in Ω, where $\mathbf{p} = (0,0,0,1)^t$. Let $\xi \in C^0([0,T])$. Then there exists $C > 0$ such that $M := \mathcal{M}(M_0, \mathbf{u}, \xi)$ satisfies*

$$\|M\|^2_{L^\infty_T;H^{s-1}} \leq 1 + \Big(\|M_0\|^2_{H^{s-1}} + CT(\|\mathbf{u}\|^2_{L^\infty_T;H^s} + \|\xi\|^2_\infty)\Big)$$
$$\times \exp\Big[CT\Big(1 + \|\mathbf{u}\|^2_{L^\infty_T;H^s} + \|\xi\|^2_\infty\Big)\Big],$$

$$\|M\|^2_{L^2_T;H^s} \leq 1 + \|M_0\|^2_{H^{s-1}} + CT\Big[\|\mathbf{u}\|^2_{L^\infty_T;H^s} + \|\xi\|^2_\infty$$
$$+ \Big(1 + \|\mathbf{u}\|^2_{L^\infty_T;H^s} + \|\xi\|^2_\infty\Big)\|M\|^2_{L^\infty_T;H^{s-1}}\Big].$$

Furthermore M belongs to $C^0([0,T]; H^{s-2}(\Omega))$.

(ii) *(Lipschitz continuity) For $i = 1, 2$, let $M_{0,i}, \mathbf{u}_i, \xi_i$ be as previously and let $M_i := \mathcal{M}(M_{0,i}, \mathbf{u}_i, \xi_i)$. Assume there exists $R > 0$ such that*

$$\|(\mathbf{u}_i, M_i, \xi_i)\|_{\mathcal{E}^s_T} \leq R,$$

then there exists $C_R > 0$ such that

$$\|M_1 - M_2\|^2_{L^2_T;H^{s-1}}$$
$$\leq C_R\Big(\|M_{0,1} - M_{0,2}\|^2_{H^{s-2}} + \|\mathbf{u}_1 - \mathbf{u}_2\|^2_{L^2_T;H^{s-1}} + \|\xi_1 - \xi_2\|^2_{L^2_T}\Big).$$

Proof. (i) The proof is a consequence of Proposition 4.11 with $s' = s$ and

$$\tilde{M} := 1 - M,$$
$$\tilde{M}_0 := 1 - M_0,$$
$$\mathbf{w}_1 := \xi \nabla(\mathbf{p} \cdot \mathbf{u}),$$
$$\mathbf{w}_2 := \mathbf{w}_1,$$
$$a := -(\eta \mathbf{p} + C_0 \mathbf{s}) \cdot \mathbf{u},$$
$$b := \eta \mathbf{p} \cdot \mathbf{u}.$$

(ii) We consider

$$\tilde{M} := M_1 - M_2,$$
$$\tilde{M}_0 := M_{0,1} - M_{0,2},$$
$$\mathbf{w}_1 := \xi_1 \nabla(\mathbf{p} \cdot \mathbf{u}_1),$$
$$\mathbf{w}_2 := -\big((\xi_1 \nabla(\mathbf{p} \cdot \mathbf{u}_1) - \xi_2 \nabla(\mathbf{p} \cdot \mathbf{u}_2))M_2\big),$$
$$a := -(\eta \mathbf{p} + C_0 \mathbf{s}) \cdot \mathbf{u}_1,$$
$$b := -(\eta \mathbf{p} + C_0 \mathbf{s}) \cdot (\mathbf{u}_1 - \mathbf{u}_2)M_2 + \eta \mathbf{p} \cdot (\mathbf{u}_1 - \mathbf{u}_2),$$

and we apply Proposition 4.11 with $s' = s - 1$. The assumptions and the equation (18) lead to

$$\|M_1 - M_2\|^2_{L^\infty_T; H^{s-2}}$$
$$\leq \big(\|M_{0,1} - M_{0,2}\|^2_{H^{s-2}} + C_R(\|\mathbf{u}_1 - \mathbf{u}_2\|^2_{L^2_T; H^{s-1}} + \|\xi_1 - \xi_2\|^2_{L^2_T})\big) \times \exp(C_R T),$$

then from (19) we infer

$$\|M_1 - M_2\|^2_{L^2_T; H^{s-1}} \leq \|M_{0,1} - M_{0,2}\|^2_{H^{s-2}}$$
$$+ C_R \Big[\|\mathbf{u}_1 - \mathbf{u}_2\|^2_{L^2_T; H^{s-1}} + \|\xi_1 - \xi_2\|^2_{L^2_T} + T\|M_1 - M_2\|^2_{L^\infty_T; H^{s-2}}\Big],$$

this ends the proof since T is bounded by some arbitrary constant. $\qquad\square$

4.4   Estimates for Ξ

Estimates on Ξ are consequences of Gronwall's inequality

Proposition 4.13. *Operator Ξ satisfies the following properties:*

(i) *(Stability) Let $\xi_0 \in \mathbb{R}$. Let $\mathbf{u} \in (L^\infty_T; H^s)^d$ and $M \in L^2_T; H^s$. Then $\xi := \Xi(\xi_0, \mathbf{u}, M)$ satisfies*

$$\|\xi\|^2_\infty \leq \Big(|\xi_0|^2 + CT\|\mathbf{u}\|^2_{L^\infty_T; L^1}\Big) \exp(CT),$$

where $C > 0$ depends only on $\alpha, \|\nu_2\|_\infty$.

(ii) *(Lipschitz continuity) For $i = 1, 2$, let $\xi_{0,i}, \mathbf{u}_i$, and M_i be as previously and let $\xi_i := \Xi(\xi_{0,i}, \mathbf{u}_i, M_i)$. Assume there exists $R > 0$ such that*

$$\|(\mathbf{u}_i, M_i, \xi_i)\|_{\mathcal{E}_T^s} \leq R,$$

then we have

$$\|\xi_1 - \xi_2\|_\infty^2 \leq C_R \Big(|\xi_{0,1} - \xi_{0,2}|^2 + \|\mathbf{u}_1 - \mathbf{u}_2\|_{L_T^2;L^1}^2 + \|M_1 - M_2\|_{L_T^2;L^1}^2 \Big),$$

where $C_R > 0$ depends only on $\alpha, \|\nu_2\|_\infty$, and R.

Proof. Multiply by ξ the equation satisfied by ξ and apply Young's inequality:

$$\frac{1}{2}\partial_t \xi^2 \leq C \left[\left(\int_\Omega |\mathbf{u}| \right)^2 + \xi^2 \right] - \lambda \xi^2,$$

integrate over time and apply Gronwall's inequality to obtain the estimate for ξ. The estimate for $\xi_1 - \xi_2$ follows the same line. □

5   Local Existence and Uniqueness for Problems (3) and (4)

Let us summarize the stability estimates for the operators $\mathcal{U}, \mathcal{N}, \mathcal{V}, \mathcal{M}$, and Ξ. Based on Proposition 4.4 and Remark 4.5, if $\mathbf{u}_0 - \mathbf{s}$, N_0, $\mathbf{p} \cdot \mathbf{u}$, $\mathbf{u} - \mathbf{s}$, and N have compact support in Ω, then the solutions $\tilde{\mathbf{u}}$ and $\tilde{N}$ defined by operators Φ or Ψ have also compact support in Ω and these solutions stay in the same compact. We obtain straightforwardly

Proposition 5.1 (Stability estimates for Φ and Ψ). *For $i = 0, 1, 2$, let Ω_i be as in Definition 4.3. Operators Φ and Ψ satisfies the following estimates:*

(i) *Let $X_0 := (\mathbf{u}_0, M_0, \xi_0) \in \mathcal{E}_0^s$ and $N_0 \in H^s(\Omega)$ be such that $\mathrm{supp}(\mathbf{u}_0 - \mathbf{s}) \cup \mathrm{supp}(N_0)$ is compactly embedded in Ω_0.*
    There exist $R \geq \|X_0\|_{\mathcal{E}_0^s} + \|N_0\|_{H^s}$ and $T_1^\tau > 0$ depending only on R and the parameters of the model (such as $\gamma_1, \gamma_2, \dots$) such that for any $X := (\mathbf{u}, M, \xi) \in \mathcal{E}_{T_1^\tau}^s$ and $N \in L_{T_1^\tau}^\infty; H^s$ satisfying
    - $\bigcup_{t \in [0,T]} \big(\mathrm{supp}(\mathbf{p} \cdot \mathbf{u}(t, \cdot)) \cup \mathrm{supp}(N(t, \cdot)) \big)$ *is compactly embedded in Ω_1,*
    - $\bigcup_{t \in [0,T]} \mathrm{supp}(\mathbf{u}(t, \cdot)) - \mathbf{s}$ *is compactly embedded in Ω_2,*
    - $\mathbf{u}(t = 0, \cdot) = \mathbf{u}_0, N(t = 0, \cdot) = N_0, M(t = 0, \cdot) = M_0, \xi(t = 0) = \xi_0$,
    - $\|X\|_{\mathcal{E}_{T_1^\tau}^s} + \|N\|_{L_{T_1^\tau}^\infty; H^s} \leq R$,
    therefore $(\tilde{X}, \tilde{N}) := \Phi((X, N), (X_0, N_0), \tau)$ satisfies
    - $\bigcup_{t \in [0,T]} \big(\mathrm{supp}(\mathbf{p} \cdot \tilde{\mathbf{u}}(t, \cdot)) \cup \mathrm{supp}(\tilde{N}(t, \cdot)) \big)$ *is compactly embedded in Ω_1,*
    - $\bigcup_{t \in [0,T]} \mathrm{supp}(\tilde{\mathbf{u}}(t, \cdot)) - \mathbf{s}$ *is compactly embedded in Ω_2,*

- $\|\tilde{X}\|_{\mathcal{E}^s_{T_1^\tau}} + \|\tilde{N}\|_{L^\infty_{T_1^\tau};H^s} \leq R$.

(ii) *Let $X_0 := (\mathbf{u}_0, M_0, \xi_0) \in \mathcal{E}^s_0$ be such that $\mathrm{supp}(\mathbf{u}_0 - \mathbf{s})$ is compactly embedded in Ω_0.*

There exist $R \geq \|X_0\|_{\mathcal{E}^s_0}$ and $T_1 > 0$ depending only on R and the parameters of the model (such as $\gamma_1, \gamma_2, \dots$) such that for any $X := (\mathbf{u}, M, \xi) \in \mathcal{E}^s_{T_1}$ satisfying

- $\bigcup\limits_{t\in[0,T]} \mathrm{supp}(\mathbf{p} \cdot \mathbf{u}(t, \cdot))$ *is compactly embedded in Ω_1,*
- $\bigcup\limits_{t\in[0,T]} \mathrm{supp}(\mathbf{u}(t, \cdot)) - \mathbf{s})$ *is compactly embedded in Ω_2,*
- $\mathbf{u}(t = 0, \cdot) = \mathbf{u}_0, M(t = 0, \cdot) = M_0, \xi(t = 0) = \xi_0$,
- $\|X\|_{\mathcal{E}^s_{T_1}} \leq R$,

we deduce that $\tilde{X} := \Psi(X, X_0)$ satisfies

- $\bigcup\limits_{t\in[0,T]} \mathrm{supp}(\mathbf{p} \cdot \tilde{\mathbf{u}}(t, \cdot))$ *is compactly embedded in Ω_1,*
- $\bigcup\limits_{t\in[0,T]} \mathrm{supp}(\tilde{\mathbf{u}}(t, \cdot)) - \mathbf{s})$ *is compactly embedded in Ω_2,*
- $\|\tilde{X}\|_{\mathcal{E}^s_{T_1}} \leq R$.

Remark 5.2. The dependence on τ of the final time T_1^τ is due to (10) and Proposition 4.9 since the speed defined by Φ satisfies

$$\|\mathbf{v}\|_{L^2_T;H^{s+1}} \leq C\Big(\|\mathbf{b}(M) \cdot \mathbf{u}\|_{L^2_T;H^s} + \frac{1}{\tau}\|N\|_{L^2_T;H^s}\Big).$$

Then Proposition 4.9 requires that $C\sqrt{T}\|\mathbf{v}\|_{L^2_T;H^{s+1}}$ is small enough to obtain

$$\|\tilde{\mathbf{u}}\|_{L^\infty_T;H^s}, \|\tilde{N}\|_{L^\infty_T;H^s} \leq R.$$

Now we summarize the Lipschitz estimates on $\mathcal{U}, \mathcal{N}, \mathcal{M}$, and Ξ:

Proposition 5.3 (Lipschitz continuity estimates for Φ and Ψ)**.** *Φ and Ψ satisfy the following estimates:*

(i) *For $i = 1, 2$, let $X_{0,i}, N_{0,i}, R, T_1^\tau$, and X_i, N_i as in Proposition 5.1 (i) and denote*

$$(\tilde{\tilde{X}}_i, \tilde{\tilde{N}}_i) := \Phi(\Phi((X_i, N_i), (X_{0,i}, N_{0,i}), \tau), (X_{0,i}, N_{0,i}), \tau).$$

Then there exists $C_R > 0$ such that for all $T \leq T_1^\tau$, one has

$$
\begin{aligned}
\|(\tilde{\tilde{X}}_1, \tilde{\tilde{N}}_1) &- (\tilde{\tilde{X}}_2, \tilde{\tilde{N}}_2)\|^2_{\mathcal{E}^{2,s-1}_T \times L^2_T;H^{s-1}} \\
&\leq C_R\Big(\|(X_{0,1}, N_{0,1}) - (X_{0,2}, N_{0,2})\|^2_{\mathcal{E}^{s-1}_0 \times H^{s-1}} \\
&\quad + T\|(X_1, N_1) - (X_2, N_2)\|^2_{\mathcal{E}^{2,s-1}_T \times L^2_T;H^{s-1}}\Big).
\end{aligned}
$$

(21)

(ii) *For $i = 1, 2$, let $X_{0,i}, R, T_1$, and X_i as in Proposition 5.1 (ii) and denote*

$$\tilde{\tilde{X}}_i := \Psi(\Psi(X_i, X_{0,i}), X_{0,i}).$$

Then there exists $C_R > 0$ such that for all $T \leq T_1$, one has

(22) $\|\tilde{\tilde{X}}_1 - \tilde{\tilde{X}}_2\|_{\mathcal{E}_T^{2,s-1}}^2 \leq C_R \Big(\|X_{0,1} - X_{0,2}\|_{\mathcal{E}_0^{s-1}}^2 + T\|X_1 - X_2\|_{\mathcal{E}_T^{2,s-1}}^2 \Big).$

Therefore, taking $X_{0,1} = X_{0,2} = X_0$ and $N_{0,1} = N_{0,2} = N_0$ in the previous Proposition leads to the following result:

Corollary 5.4. *Operators Φ and Ψ satisfy*

(i) *Under the assumptions of Proposition 5.1 (i), there exists $0 < T_2^\tau \leq T_1^\tau$ small enough such that*

$$\Lambda_\Phi : (X, N) \longmapsto \Phi((X, N), (X_0, N_0), \tau),$$

is such that Λ_Φ^2 is a contraction in the set

$$\mathcal{E}_{\Lambda_\Phi} := \Big\{ (X, N) \in \mathcal{E}_{T_2^\tau}^s \times L_{T_2^\tau}^\infty; H^s \text{ such that } \|X\|_{\mathcal{E}_{T_2^\tau}^s} + \|N\|_{L_{T_2^\tau}^\infty; H^s} \leq R) \Big\}$$

endowed with the usual norm on $\mathcal{E}_{T_2^\tau}^{2,s-1} \times L_{T_2^\tau}^2; H^{s-1}$.

(ii) *Under the assumptions of Proposition 5.1 (ii), there exists $0 < T_2 \leq T_1$ small enough such that*

$$\Lambda_\Psi : X \longmapsto \Psi(X, X_0),$$

is such that Λ_Ψ^2 is a contraction in the set

$$\mathcal{E}_{\Lambda_\Psi} := \Big\{ (\mathbf{u}, M, \xi) \in \mathcal{E}_{T_2}^s \text{ such that } \|X\|_{\mathcal{E}_{T_2}^s} \leq R) \Big\}$$

endowed with the usual norm on $\mathcal{E}_{T_2}^{2,s-1}$.

Proof. The proofs of (i) and (ii) are direct consequences of Proposition 5.3 for $T > 0$ small enough such that $C_R T < 1$.   □

Remark 5.5. The dependence of the final time T_2^τ on τ is similar to the one of T_1^τ in Proposition 5.1.

By using Proposition 5.1 and Corollary 5.4, we can prove Theorem 3.3.

Proof of Theorem 3.3. We consider $T = T_2^\tau$ and the set $\mathcal{E}_{\Lambda_\Phi}$ endowed with the usual norm on the Banach space $(L_T^2; H^{s-1})^4 \times L_T^2; H^{s-1} \times L^2(0, T) \times L_T^2; H^{s-1}$. Since the closed unit ball in $L_T^2; H^s$ is compact in the weak topology and the closed unit balls in $L_T^\infty; H^{s-1}$ and in $L_T^\infty; H^s$ are compact in the weak* topology [6], we get that $\mathcal{E}_{\Lambda_\Phi}$ is a closed subspace of $(L_T^2; H^{s-1})^4 \times L_T^2; H^{s-1} \times L^2(0, T) \times L_T^2; H^{s-1}$. Then we apply the contraction mapping theorem in $\mathcal{E}_{\Lambda_\Phi}$ to obtain

the existence and uniqueness of the fixed point $(X^\Phi, N^\Phi) \in \mathcal{E}_{\Lambda_\Phi}$ to Λ_Φ^2. Then applying Λ_Φ to $\Lambda_\Phi^2(X^\Phi, N^\Phi) = (X^\Phi, N^\Phi)$ leads to the existence and uniqueness of the fixed point (X^Φ, N^Φ) to Λ_Φ.

Propositions 4.9 and 4.12 lead to the time continuity of $\mathbf{u}$ and M stated in Theorem 3.3 (i)b. Then from Propositions 4.2 and 4.13 we infer the time continuity of $\mathbf{v}$ and ξ.

By construction of the solution, we get

$$P_1, P_2, P_3, N, S \geq 0, \qquad \text{where } (P_1, P_2, P_3, S)^t := \mathbf{u}.$$

In conclusion, the saturation $P_1 + P_2 + P_3 + N + S = 1$ is a consequence of the equation satisfied by $P_1 + P_2 + P_3 + N + S$ obtained by summing the equations on $P_1, P_2, P_3, N,$ and S and Gronwall's inequality.

The exact same reasoning holds for Λ_Ψ. □

Remark 5.6. Remark 3.5 is a consequence of Theorem 3.3 and Proposition 5.3, assuming that $C_R T \leq \frac{1}{2}$ in Proposition 5.3.

6 Asymptotic Behavior of the Solution as τ Decreases to 0

The goal of this section is to prove Theorem 3.6, which states that the solution to model (3) converges towards the solution to model (4) as $\tau \to 0^+$.

In the previous section, the time of existence $T > 0$ depends *a priori* on the norm of $\mathbf{v}$, which in turn depends on τ thanks to (3e). More precisely, in the proof of existence, we can see that the time T depends only on $\|\mathbf{v}\|_{L^2_T; H^{s+1}}$. Note that according to Remark 5.2, this norm could blow up as $\tau \to 0^+$. Our first goal consists in finding a bound to ensure that the time of existence does not depend on τ. In the last subsection, we perform the asymptotic analysis to obtain the convergence of model (3) to model (4).

6.1 Uniform Bound on the Final Time of Existence

Let $\tau > 0$ be given. Let $\mathbf{u}$, M, $\mathbf{v}$, and N as in Theorem 3.3 (i). According to Remark 5.2, $\mathbf{v}$ satisfies

$$(23) \qquad \|\mathbf{v}\|_{L^2_T; H^{s+1}} \leq C \left(\|\mathbf{b}(M) \cdot \mathbf{u}\|_{L^2_T; H^s} + \frac{1}{\tau} \|N\|_{L^2_T; H^s} \right).$$

The right-hand side blows up as $\tau \to 0^+$. The goal of the following results is to prove more precise estimates. First let us prove the next Lemma:

Lemma 6.1. *Under the assumptions of Theorem 3.3 (i), N satisfies the follow-ing inequality:*

$$
\left(\frac{1}{\sqrt{\tau}}\|N\|_{L_T^\infty;H^s}\right)^2 + \left(\frac{1}{\tau}\|N\|_{L_T^2;H^s}\right)^2
$$

(24)
$$
\leq C\sqrt{T}\left(\|\mathbf{b}(M)\cdot\mathbf{u}\|_{L_T^2;H^s} + \frac{1}{\tau}\|N\|_{L_T^2;H^s}\right) \times \left(\frac{1}{\sqrt{\tau}}\|N\|_{L_T^\infty;H^s}\right)^2
$$

$$
+ C\|\mathbf{d}(M)\cdot\mathbf{u}\|_{L_T^2;H^s}^2 + \left(\frac{1}{\sqrt{\tau}}\|N_0\|_{H^s}\right)^2.
$$

where $C > 0$ does not depend on τ.

Proof. We consider the equation satisfied by $\dfrac{N}{\sqrt{\tau}}$:

(25)
$$
\partial_t\left(\frac{N}{\sqrt{\tau}}\right) + \nabla\cdot\left(\mathbf{v}\frac{N}{\sqrt{\tau}}\right) = \frac{\mathbf{d}(M)\cdot\mathbf{u}}{\sqrt{\tau}} - \frac{1}{\tau}\left(\frac{N}{\sqrt{\tau}}\right),
$$

Let $m \in \mathbb{N}$ such that $m \leq s$. Apply ∂_x^m to (25), multiply by $\partial_x^m(1/\sqrt{\tau})N$ and apply Lemma 4.6 to $\partial_x^m\nabla\cdot(\mathbf{v}(1/\sqrt{\tau})N)\partial_x^m(1/\sqrt{\tau})N$, sum over $m \leq s$ and use (23). This leads to

$$
\frac{1}{2}\partial_t\left(\frac{1}{\sqrt{\tau}}\|N\|_{H^s}\right)^2 \leq C\left(\|\mathbf{b}(M)\cdot\mathbf{u}\|_{H^s} + \left(\frac{1}{\tau}\|N\|_{H^s}\right)\right)\left(\frac{1}{\sqrt{\tau}}\|N\|_{H^s}\right)^2
$$

$$
+ C\|\mathbf{d}(M)\cdot\mathbf{u}\|_{H^s}\left(\frac{1}{\tau}\|N\|_{H^s}\right) - \frac{1}{\tau}\left(\frac{1}{\sqrt{\tau}}\|N\|_{H^s}\right)^2.
$$

Applying Young's inequality, we obtain for almost every time $t \in [0, T]$:

$$
\frac{1}{2}\partial_t\left(\frac{1}{\sqrt{\tau}}\|N\|_{H^s}\right)^2 \leq C\left(\|\mathbf{b}(M)\cdot\mathbf{u}\|_{H^s} + \left(\frac{1}{\tau}\|N\|_{H^s}\right)\right)\left(\frac{1}{\sqrt{\tau}}\|N\|_{H^s}\right)^2
$$

$$
+ \frac{1}{2}\left(C^2\|\mathbf{d}(M)\cdot\mathbf{u}\|_{H^s}^2 + \frac{1}{\tau}\left(\frac{1}{\sqrt{\tau}}\|N\|_{H^s}\right)^2\right) - \frac{1}{\tau}\left(\frac{1}{\sqrt{\tau}}\|N\|_{H^s}\right)^2,
$$

then we integrate in time between 0 and t and we take the supremum for $t \in [0, T]$ to obtain

$$
\left(\frac{1}{\sqrt{\tau}}\|N\|_{L_T^\infty;H^s}\right)^2 + \left(\frac{1}{\tau}\|N\|_{L_T^2;H^s}\right)^2
$$

$$
\leq C\left(\|\mathbf{b}(M)\cdot\mathbf{u}\|_{L_T^1;H^s} + \frac{1}{\tau}\|N\|_{L_T^1;H^s}\right) \times \left(\frac{1}{\sqrt{\tau}}\|N\|_{L_T^\infty;H^s}\right)^2
$$

$$
+ C\|\mathbf{d}(M)\cdot\mathbf{u}\|_{L_T^2;H^s}^2 + \left(\frac{1}{\sqrt{\tau}}\|N_0\|_{H^s}\right)^2,
$$

and we estimate the L_T^1-norm by the L_T^2-norm to conclude the proof. $\qquad\square$

The previous Lemma makes it possible to prove the following result:

Lemma 6.2. *Assume the assumptions of Theorem 3.3 (i) hold. Denote by*

$$Y_1 := \|\mathbf{u}\|_{L_T^\infty; H^s},$$

$$Y_2 := \sqrt{\|M\|^2_{L_T^\infty; H^{s-1}} + \|M\|^2_{L_T^2; H^s}},$$

$$Y_3 := \|\xi\|_\infty,$$

$$Y_4 := \sqrt{((1/\sqrt{\tau})\|N\|_{L_T^\infty; H^s})^2 + ((1/\tau)\|N\|_{L_T^2; H^s})^2}.$$

Then there exists a constant $C > 0$ which does not depend on $\tau > 0$ such that $\mathbf{Y} := (Y_1, Y_2, Y_3, Y_4)$ satisfies the following estimates

(26)
$$Y_i^2 \leq F(T, \mathbf{Y}), \qquad i = 1, \cdots, 4,$$

where

$$F_1(T, \mathbf{Y}) = \left(\|\mathbf{u}_0\|^2_{H^s} + C\sqrt{T}\,(Y_1 Y_2 + Y_4)\right) \exp\left(C\sqrt{T}\,(Y_1 Y_2 + Y_4)\right),$$

$$F_2(T, \mathbf{Y}) = \left[1 + \left(\|M_0\|^2_{H^{s-1}} + CT\,(Y_1^2 + Y_3^2)\right) \exp\left(CT\,(1 + Y_1^2 + Y_3^2)\right)\right]$$
$$\times \left[1 + CT\,(1 + Y_1^2 + Y_3^2)\right] + 1 + \|M_0\|^2_{H^{s-1}} + CT\,(Y_1^2 + Y_3^2),$$

$$F_3(T, \mathbf{Y}) = |\xi_0|^2 + CTY_1^2 \exp\left(CT\right),$$

$$F_4(T, \mathbf{Y}) = C\left[\sqrt{T}Y_4^2\,(Y_1 Y_2 + Y_4) + F_1(T, \mathbf{Y})^2 F_2(T, \mathbf{Y})^2\right] + \left(\frac{1}{\sqrt{\tau}}\|N_0\|_{H^s}\right)^2.$$

Proof. The estimates on Y_1^2, Y_2^2, and Y_3^2 are simply consequence of stability estimates on $\mathcal{U}, \mathcal{M}$, and Ξ given by Proposition 4.9, 4.12, and 4.13. For the estimates on Y_4^2, the estimate (24) leads to

$$Y_4^2 \leq C\left[\sqrt{T}Y_4^2\,(Y_1 Y_2 + Y_4) + Y_1^2 Y_2^2\right] + \left(\frac{1}{\sqrt{\tau}}\|N_0\|_{H^s}\right)^2,$$

and we use (26) to bound $Y_1^2 Y_2^2$ by $F_1(T, \mathbf{Y})^2 F_2(T, \mathbf{Y})^2$. □

Now we can prove that, for T small enough, $\mathbf{Y}$ is uniformly bounded with respect to τ. For any $R > 0$ one has

$$\lim_{T \to 0^+} F_i(T, (R, R, R, R))$$

$$= \begin{cases} \|\mathbf{u}_0\|^2_{H^s}, & \text{if } i = 1, \\ 2(1 + \|M_0\|^2_{H^{s-1}}), & \text{if } i = 2, \\ |\xi_0|^2, & \text{if } i = 3, \\ \left(2\,C\|\mathbf{u}_0\|^2_{H^s}(1 + \|M_0\|^2_{H^{s-1}}) + \frac{1}{\sqrt{\tau}}\|N_0\|_{H^s}\right)^2, & \text{if } i = 4. \end{cases}$$

Assume there exists $C > 0$ such that

$$\forall \tau > 0, \qquad \left(\frac{1}{\sqrt{\tau}} \|N_0\|_{H^s} \right)^2 \leq C,$$

then we take

$$R = \sqrt{2 \max \left(\|\mathbf{u}_0\|_{H^s}^2, 2(1 + \|M_0\|_{H^{s-1}}^2), |\xi_0|^2, 2C \|\mathbf{u}_0\|_{H^s}^2 (1 + \|M_0\|_{H^{s-1}}^2) + C},$$

and we obtain that there exists $T > 0$, which depends only on R, such that $Y_i^2 \leq R^2$ for $1 \leq i \leq 4$. We thus have proved the following result

Proposition 6.3. *Assume the assumptions of Theorem 3.3 (i) hold. If there exists $C > 0$ such that*

$$\forall \tau > 0, \qquad \|\mathbf{u}_0\|_{H^s}^2 + \|M_0\|_{H^{s-1}}^2 + |\xi_0|^2 + \left(\frac{1}{\sqrt{\tau}} \|N_0\|_{H^s} \right)^2 \leq C,$$

then there exists $R > 0$ and $T > 0$ such that

$$\forall \tau > 0, \qquad \left(\frac{1}{\sqrt{\tau}} \|N\|_{L_T^\infty ; H^s} \right)^2 + \left(\frac{1}{\tau} \|N\|_{L_T^2 ; H^s} \right)^2 \leq R^2,$$

$$\|\mathbf{u}\|_{L_T^\infty ; H^s}^2 \leq R^2,$$

$$\|M\|_{L_T^\infty ; H^{s-1}}^2 + \|M\|_{L_T^2 ; H^s}^2 \leq R^2,$$

$$\|\xi\|_\infty^2 \leq R^2.$$

Therefore the time of existence of the solution to (3) is independent of τ.

In order to finish the asymptotic analysis, we also need estimates on the time derivative of $\mathbf{u}$, M, ξ, and N:

Corollary 6.4. *Under the assumptions of Proposition 6.3, there exists $C_R > 0$, such that for any $\tau > 0$ small enough*

(i) $\|\partial_t \mathbf{u}\|_{L_T^2 ; H^{s-1}}^2 \leq C_R,$
(ii) $\|\partial_t M\|_{L_T^2 ; H^{s-1}}^2 \leq C_R,$
(iii) $\|\partial_t \xi\|_\infty^2 \leq C_R,$
(iv) $\|\partial_t N\|_{L_T^2 ; H^{s-1}}^2 \leq C_R \left(\tau + \left(\frac{1}{\sqrt{\tau}} \|N_0\|_{H^s} \right)^2 \right).$

Proof. (i) and (iii) are consequences of Eqs. (3a), (3j), and Proposition 6.3.

To prove (ii), differentiate in time Eq. (3h) and apply Proposition 4.11 with $s' = s - 1$ and

$$\tilde{M} := \partial_t M,$$
$$\tilde{M}_0 := 0,$$
$$\mathbf{w}_1 := \xi \nabla(\mathbf{p} \cdot \mathbf{u}),$$
$$\mathbf{w}_2 := M \partial_t \mathbf{w}_1,$$
$$a := -(\eta \mathbf{p} + C_0 \mathbf{s}) \cdot \mathbf{u},$$
$$b := \partial_t (\eta \mathbf{p} \cdot \mathbf{u}) + M \partial_t a.$$

Then Proposition 6.3 and previous estimates on $\partial_t \mathbf{u}$ and $\partial_t \xi$ leads to (ii).

To prove (iv), we denote by $\tilde{N} := \partial_t N$, then $\tilde{N}$ satisfies

$$\partial_t \tilde{N} + \nabla \cdot \left(\mathbf{v} \tilde{N} \right) = -\nabla \cdot \left(\partial_t \mathbf{v} N \right) + \partial_t \left(\mathbf{d}(M) \cdot \mathbf{u} \right) - \frac{1}{\tau} \tilde{N}.$$

Applying Lemma 4.6 leads to

$$\frac{1}{2} \|\tilde{N}\|_{H^{s-1}}^2 \leq \left[C \|\mathbf{v}\|_{H^s} - \frac{1}{\tau} \right] \|\tilde{N}\|_{H^{s-1}}^2$$
$$+ C \left(\|\partial_t \mathbf{v}\|_{H^s} \|N\|_{H^s} + \|\partial_t \left(\mathbf{d}(M) \cdot \mathbf{u} \right)\|_{H^{s-1}} \right) \|\tilde{N}\|_{H^{s-1}},$$

By using Eq. (3e) and Proposition 6.3, we have the following estimates

(27)
$$\|\mathbf{v}\|_{L_T^\infty; H^s} \leq C_R \left(1 + \frac{1}{\sqrt{\tau}} \right),$$

and for almost every $t \in [0, T]$:

$$\|\partial_t \mathbf{v}\|_{H^s} \|N\|_{H^s} \leq C_R \left(\|\partial_t \left(\mathbf{b}(M) \cdot \mathbf{u} \right)\|_{H^{s-1}} + \frac{1}{\sqrt{\tau}} \|\tilde{N}\|_{H^{s-1}} \right),$$

these estimates lead to

$$\frac{1}{2} \|\tilde{N}\|_{H^{s-1}}^2 \leq \left[C_R \left(1 + \frac{1}{\sqrt{\tau}} \right) - \frac{1}{\tau} \right] \|\tilde{N}\|_{H^{s-1}}^2$$
$$+ C_R \left(\|\partial_t \left(\mathbf{b}(M) \cdot \mathbf{u} \right)\|_{H^{s-1}} + \|\partial_t \left(\mathbf{d}(M) \cdot \mathbf{u} \right)\|_{H^{s-1}} \right) \|\tilde{N}\|_{H^{s-1}}.$$

Apply Young's formula to

$$C_R \left(\|\partial_t \left(\mathbf{b}(M) \cdot \mathbf{u} \right)\|_{H^{s-1}} + \|\partial_t \left(\mathbf{d}(M) \cdot \mathbf{u} \right)\|_{H^{s-1}} \right) \|\tilde{N}\|_{H^{s-1}},$$

then for τ small enough, $\tilde{N}$ satisfies the following estimate:

$$\|\tilde{N}\|_{H^{s-1}}^2 + \frac{1}{\tau} \|\tilde{N}\|_{H^{s-1}}^2 \leq C_R \left(\|\partial_t \left(\mathbf{b}(M) \cdot \mathbf{u} \right)\|_{H^{s-1}}^2 + \|\partial_t \left(\mathbf{d}(M) \cdot \mathbf{u} \right)\|_{H^{s-1}}^2 \right).$$

Integrate the previous estimate in time between 0 and t and take the supremum for $t \in [0, T]$ to obtain

$$\|\tilde{N}\|_{L_T^\infty; H^{s-1}}^2 + \frac{1}{\tau} \|\tilde{N}\|_{L_T^2; H^{s-1}}^2$$
$$\leq \|\tilde{N}(0, \cdot)\|_{H^{s-1}}^2 + C_R \left(\|\partial_t \left(\mathbf{b}(M) \cdot \mathbf{u} \right)\|_{L_T^2; H^{s-1}}^2 + \|\partial_t \left(\mathbf{d}(M) \cdot \mathbf{u} \right)\|_{L_T^2; H^{s-1}}^2 \right).$$

Based on Proposition 6.3 and previous estimates on $\partial_t \mathbf{u}$ and $\partial_t M$, there exists $C_R > 0$ such that for any $\tau > 0$ small enough

(28)
$$\|\tilde{N}\|_{L_T^\infty; H^{s-1}}^2 + \frac{1}{\tau} \|\tilde{N}\|_{L_T^2; H^{s-1}}^2 \leq \|\tilde{N}(0, \cdot)\|_{H^{s-1}}^2 + C_R.$$

We focus on the term $\|\tilde{N}(0,\cdot)\|^2_{H^{s-1}}$. Based on Eq. (3c), $\tilde{N}(0,\cdot)$ satisfies

$$\tilde{N}(0,\cdot) + \nabla \cdot (\mathbf{v}(0,\cdot)N_0) = \mathbf{d}(M_0) \cdot \mathbf{u}_0 - \frac{1}{\tau}N_0,$$

then we have the following estimate

$$\|\tilde{N}(0,\cdot)\|_{H^{s-1}} \le C\|\mathbf{v}(0,\cdot)\|_{H^s}\|N_0\|_{H^s} + C\|M_0\|_{H^{s-1}}\|\mathbf{u}_0\|_{H^{s-1}} + \frac{1}{\tau}\|N_0\|_{H^{s-1}}.$$

By using Eq. (27), we have

$$\|\tilde{N}(0,\cdot)\|^2_{H^{s-1}} \le C_R\left(1 + \frac{1}{\tau^2}\|N_0\|^2_{H^s}\right),$$

then multiply (28) by τ and omit the non-negative term $\|\tilde{N}\|^2_{L^\infty_T;H^{s-1}}$ to obtain

$$(29) \qquad \|\tilde{N}\|^2_{L^2_T;H^{s-1}} \le C_R\left(\tau + \frac{1}{\tau}\|N_0\|^2_{H^s}\right).$$

$\square$

6.2   The Limit Case for $\tau \to 0$

Proposition 6.3 makes it possible to pass to the limit as $\tau \to 0^+$ and implies also that N converges to 0 in $L^\infty_T; H^s$. However the assumption that $(1/\sqrt{\tau})\|N_0\|_{H^s} \le C$ is not sufficient to prove the convergence of the whole solution $((\mathbf{u}^\tau, M^\tau, \xi^\tau), \mathbf{v}^\tau, N^\tau)$. We need to suppose that $(1/\sqrt{\tau})\|N_0\|_{H^s} \to 0$ as $\tau \to 0^+$ to prove Theorem 3.6. The following Lemma ends the proof of Theorem 3.6:

Lemma 6.5. *For any $\tau > 0$, let X_0^τ, N_0^τ, X_0 be as in Theorem 3.3 and Theorem 3.6 and denote by*

- *(X^τ, N^τ) the solution to $(X^\tau, N^\tau) = \Phi((X^\tau, N^\tau), (X_0^\tau, N_0^\tau), \tau)$,*
- *X the solution to $X = \Psi(X, X_0)$.*

Then $\lim_{\tau \to 0^+} \|X^\tau - X\|^2_{\mathcal{E}^{2,s-1}_T} = 0$.

Proof. Assumptions and Proposition 6.3 ensures that there exists $R > 0$ (depending only on X_0^τ, N_0^τ, and X_0) such that for any $\tau > 0$, X^τ, $(1/\tau)N^\tau$, and X are bounded by R.

Denote by $(\mathbf{u}^\tau, M^\tau, \xi^\tau) := X^\tau$ and by $(\mathbf{u}, M, \xi) := X$. Remind the Lipschitz estimates on $\mathcal{U}, \mathcal{M}$, and Ξ:

$$\|\mathbf{u}^\tau - \mathbf{u}\|_{L^2_T;H^{s-1}}$$
$$\le C_R T\left(\|\mathbf{u}_0^\tau - \mathbf{u}_0\|^2_{H^{s-1}} + \|\mathbf{v}^\tau - \mathbf{v}\|^2_{L^2_T;H^s} + \|M^\tau - M\|^2_{L^2_T;H^{s-1}}\right),$$

$$\|M^\tau - M\|^2_{L^2_T;H^{s-1}} \le C_R\left(\|M_0^\tau - M_0\|^2_{H^{s-2}} + \|\mathbf{u}^\tau - \mathbf{u}\|^2_{L^2_T;H^{s-1}} + \|\xi^\tau - \xi\|^2_{L^2_T}\right),$$

$$\|\xi^\tau - \xi\|^2_{L^2_T} \le C_R T\left(|\xi_0^\tau - \xi_0|^2 + \|\mathbf{u}^\tau - \mathbf{u}\|^2_{L^2_T;L^1} + \|M^\tau - M\|^2_{L^2_T;L^1}\right).$$

We need to find an estimate on $\mathbf{v}^\tau - \mathbf{v}$. Observe that

$$\mathbf{v}^\tau - \mathbf{v} = \mathcal{V}(\mathbf{b}(M^\tau) \cdot \mathbf{u}^\tau - (1/\tau)N^\tau) - \mathcal{V}((\mathbf{b}(M) - \mathbf{d}(M)) \cdot \mathbf{u}),$$

then we have

$$\begin{aligned}
\mathbf{v}^\tau - \mathbf{v} = {} & \mathcal{V}((\mathbf{b}(M^\tau) - \mathbf{d}(M^\tau)) \cdot \mathbf{u}^\tau - (\mathbf{b}(M) - \mathbf{d}(M)) \cdot \mathbf{u}) \\
& + \mathcal{V}(\mathbf{d}(M^\tau) \cdot \mathbf{u}^\tau - (1/\tau)N^\tau),
\end{aligned}$$

and we obtain the following estimate:

$$\|\mathbf{v}^\tau - \mathbf{v}\|^2_{L^2_T;H^s} \le C_R\Big(\|\mathbf{u}^\tau - \mathbf{u}\|^2_{L^2_T;H^{s-1}} + \|M^\tau - M\|^2_{L^2_T;H^{s-1}} + \varepsilon^\tau\Big),$$

where $\varepsilon^\tau = \|\mathbf{d}(M^\tau) \cdot \mathbf{u}^\tau - (1/\tau)N^\tau\|^2_{L^2_T;H^{s-1}}$. By using Proposition 6.3 and Corollary 6.4 and by using the fact that $(1/\sqrt{\tau})\|N_0\|_{H^s} \to 0$, we obtain

$$\lim_{\tau \to 0^+} \|\partial_t N^\tau\|^2_{L^2_T;H^{s-1}} + \|\nabla \cdot (\mathbf{v}^\tau N^\tau)\|^2_{L^2_T;H^{s-1}} = 0,$$

then Eq. (3c) ensures that $\lim_{\tau \to 0^+} \varepsilon^\tau = 0$.

Gathering together all the previous estimates (for $M^\tau - M$, we use the estimates on $\mathbf{u}^\tau - \mathbf{u}$ and $\xi^\tau - \xi$ to obtain the T term) we obtain

$$\|X^\tau - X\|^2_{\mathcal{E}^{2,s-1}_T} \le C_R\Big(\|X_0^\tau - X_0\|^2_{\mathcal{E}^{s-1}_0} + T\|X^\tau - X\|^2_{\mathcal{E}^{2,s-1}_T} + \varepsilon^\tau\Big),$$

then we assume that $C_R T \le \frac{1}{2}$ to get

$$\|X^\tau - X\|^2_{\mathcal{E}^{2,s-1}_T} \le C_R\Big(\|X_0^\tau - X_0\|^2_{\mathcal{E}^{s-1}_0} + \varepsilon^\tau\Big),$$

this conclude the proof of the Lemma.   □

7   Conclusion

A constructive proof of the solution to the tumor growth model of Lefebvre *et al.* has been derived. The main idea of the proof lies in the fact that the tumor remains compactly supported in the domain of interest up to a given time. We proved that the minimum time for well-posedness can be bounded independently of the characteristic time τ of necrosis evacuation. This proves that the model is consistent with the model without necrosis. In particular, the solution to the model without necrosis is the limit of the solutions to the model with necrosis as $\tau \to 0$. This result ensures the continuity of the family of the considered tumor growth model, proving the consistency of the modeling.

References

1. Alinhac, S., Gérard, P.: Pseudo-Differential Operators and the Nash-Moser Theorem, vol. 82. American Mathematical Society (2007)
2. Ambrosi, D., Preziosi, L.: On the closure of mass balance models for tumor growth. Math. Models Methods Appl. Sci. **12**, 737–754 (2002)
3. Anderson, A.R., Chaplain, M.: Continuous and discrete mathematical models of tumor-induced angiogenesis. Bull. Math. Biol. **60**, 857–899 (1998)
4. Billy, F., et al.: A pharmacologically based multiscale mathematical model of angiogenesis and its use in investigating the efficacy of a new cancer treatment strategy. J. Theor. Biol. **260**, 545–562 (2009)
5. Bresch, D., Colin, T., Grenier, E., Ribba, B., Saut, O.: A viscoelastic model for avascular tumor growth. Discret. Continuous Dyn. Syst. Suppl. **2009**, 101–108 (2009)
6. Brezis, H.: Functional Analysis, Sobolev Spaces and Partial Differential Equations. Springer, Heidelberg (2010)
7. Byrne, H.M., Chaplain, M.: Growth of necrotic tumors in the presence and absence of inhibitors. Math. Biosci. **135**, 187–216 (1996)
8. Byrne, H., Preziosi, L.: Modelling solid tumour growth using the theory of mixtures. Math. Med. Biol. **20**, 341–366 (2003)
9. Chen, X., Cui, S., Friedman, A.: A hyperbolic free boundary problem modeling tumor growth: asymptotic behavior. Trans. Am. Math. Soc. **357**, 4771–4804 (2005)
10. Colin, T., Cornelis, F., Jouganous, J., Palussière, J., Saut, O.: Patient-specific simulation of tumor growth, response to the treatment, and relapse of a lung metastasis: a clinical case. J. Comput. Surgery **2**(1), 1–17 (2015). https://doi.org/10.1186/s40244-014-0014-1
11. Cui, S., Friedman, A.: Analysis of a mathematical model of the growth of necrotic tumors. J. Math. Anal. Appl. **255**, 636–677 (2001)
12. Drasdo, D., Höhme, S.: Individual-based approaches to birth and death in avascular tumors. Math. Comput. Model. **37**, 1163–1175 (2003)
13. Folkman, J.: Tumor angiogenesis: therapeutic implications. New Engl. J. Med. **285**, 1182–1186 (1971)
14. Friedman, A.: A hierarchy of cancer models and their mathematical challenges. Discret. Continuous Dyn. Syst. Ser. B **4**, 147–160 (2004)
15. Friedman, A., Hu, B.: Bifurcation from stability to instability for a free boundary problem arising in a tumor model. Arch. Ration. Mech. Anal. **180**, 293–330 (2006)
16. Gatenby, R.A., Gawlinski, E.T.: A reaction-diffusion model of cancer invasion. Can. Res. **56**, 5745–5753 (1996)
17. Hillen, T., Painter, K.J., Winkler, M.: Convergence of a cancer invasion model to a logistic chemotaxis model. Math. Models Methods Appl. Sci. **23**, 165–198 (2013)
18. Lefebvre, G., Cornelis, F., Cumsille, P., Colin, T., Poignard, C., Saut, O.: Spatial modelling of tumour drug resistance: the case of GIST liver metastases. Math. Med. Biol. http://imammb.oxfordjournals.org/content/early/2016/03/30/imammb.dqw002.abstract
19. Lorz, A., Lorenzi, T., Clairambault, J., Escargueil, A., Perthame, B.: Effects of space structure and combination therapies on phenotypic heterogeneity and drug resistance in solid tumors, arXiv preprint arXiv:1312.6237
20. Perthame, B., Vauchelet, N.: Incompressible limit of mechanical model of tumor growth with viscosity, arXiv preprint arXiv:1409.6007

21. Preziosi, L., Tosin, A.: Multiphase modelling of tumour growth and extracellular matrix interaction: mathematical tools and applications. J. Math. Biol. **58**, 625–656 (2009)
22. Saitou, T., Rouzimaimaiti, M., Koshikawa, N., Seiki, M., Ichikawa, K., Suzuki, T.: Mathematical modeling of invadopodia formation. J. Theor. Biol. **298**, 138–146 (2012)
23. Swanson, K.R., Bridge, C., Murray, J., Alvord, E.C.: Virtual and real brain tumors: using mathematical modeling to quantify glioma growth and invasion. J. Neurol. Sci. **216**, 1–10 (2003)
24. Tosin, A.: Initial/boundary-value problems of tumor growth within a host tissue. J. Math. Biol. **66**, 163–202 (2013)
25. Ward, J.P., King, J.R.: Mathematical modelling of drug transport in tumour multicell spheroids and monolayer cultures. Math. Biosci. **181**, 177–207 (2003)

Mathematical Modeling and Experimental Verification of the Proneural Wave

Yoshitaro Tanaka[1] and Tetsuo Yasugi[2(✉)]

[1] Department of Complex and Intelligent Systems, School of Systems Information Science, Future University Hakodate, 116-2 Kamedanakano-cho, Hakodate, Hokkaido 041-8655, Japan
`y-tanaka@fun.ac.jp`
[2] Mathematical Neuroscience Unit, Institute for Frontier Science Initiative, Kanazawa University, 13-1 Takaramachi, Kanazawa-shi, Ishikawa 920-8640, Japan
`tetsuo.yasugi@staff.kanazawa-u.ac.jp`

Abstract. Spatio-temporal pattern formation during development is regulated by interactions of multiple signaling pathways. To understand complex signaling networks, we used the *Drosophila* visual system as a model because neural differentiation progresses in a spatiotemporally ordered manner. During the development of the visual system, a wave of differentiation, called the proneural wave, sweeps across the brain surface and determines the timing of differentiation of neuroepithelial cells into neuroblasts, which are neural stem cells in *Drosophila*. Propagation of the proneural wave is regulated through a combination of signaling pathways, including the Notch, EGF, and JAK/STAT. We combined mathematical modeling with *in vivo* experiments, the results of which revealed that Notch-mediated lateral inhibition and EGF-mediated reaction diffusion determine the speed of progression of the proneural wave. We reported that JAK/STAT signaling has a noise-canceling function to assure robust neuroblast differentiation. Furthermore, we introduced a continuation method from spatially discretized models while conserving the cell size and lattice. This mathematical method enables us to introduce information from spatially discrete to spatially continuous models, rendering it suitable for applications in both experimental and mathematical analyses. Our interdisciplinary studies have revealed new functions of signaling pathways that have previously been difficult to address by conventional biological experiments.

Keywords: *Drosophila* · Proneural wave · Mathematical modeling · Continuation method

1 Introduction

Spatio-temporal pattern formation of multicellular organisms is regulated through the inter- and intracellular communications of the signaling pathways.

In many cases, several signaling pathways act on the same developmental processes and show complex mutual interactions. Therefore, the interactions among signaling pathways have been difficult to address solely through biological experiments. To describe the mechanisms of a spatio-temporal pattern formation, it has become popular during the past few decades to formulate mathematical models by describing the function of each signaling pathway and the interaction among multiple pathways.

To theoretically and experimentally investigate the dynamic interaction of signaling pathways, the developing *Drosophila* visual system provides an excellent model (Fig. 1A) [1–3]. During the early stages of larval development, neuroepithelial cells (NEs) proliferate, and these NEs later differentiate into neuroblasts (NBs), which are neural stem-like cells in *Drosophila* [4,5]. A differentiation wave called the "proneural wave" (PW) sweeps across the brain surface and defines the timing of differentiation from NEs to NBs (Fig. 1A, B). The progression starts at the medial edge of the NE sheet and extends toward the lateral side. The differentiating "wavefront" cells start expressing Achaete-Scute Complex (AS-C) proneural transcription factors, such as Scute, Lethal of Scute (L'sc), and Asense (Ase) [5,6]. Among them, L'sc shows a transient expression in cells at the transition interface between NEs and NBs, and this transient L'sc expression acts as a trigger for NB differentiation (Fig. 1C) [6]. During the progression of the PW, several signaling pathways, such as EGF, Notch, JAK/STAT, and Hippo, play major roles [2,6–9]. The EGF and Notch signaling pathways are activated in the wavefront cells (Fig. 1C). EGF signaling is required for PW progression and NB differentiation [9]. Meanwhile, Notch signaling inhibits precocious PW progression [8–13]. Unpaired (Upd), a ligand of JAK/STAT signaling, is expressed in lateral NEs and generates an activity gradient of JAK/STAT signaling, which is higher in lateral NEs and lower in medial NEs (Fig. 1C). JAK/STAT signaling also acts as a negative regulator of PW progression [6,14]. Hippo signaling regulates the proliferation of NEs and promotes the progression of PW [7,8,15]. Although the functions of each signaling pathway and the interactions among the pathways have been extensively studied, the regulation of unidirectional NB differentiation remains difficult to explain (Fig. 1D). Hence, we formulated mathematical models to understand the interactions among the EGF, Notch, and JAK/STAT pathways in the progression of PW.

In this paper, we report that a mathematical model that includes the interaction between Notch and EGF can recapitulate the PW progression *in silico*. In addition, the mathematical model shows resistance to noise by including the function of JAK/STAT signaling, suggesting that JAK/STAT signaling may cancel the noise *in vivo*. This assumption from mathematical modeling is confirmed through *in vivo* experiments. We further show a continuation method from spatially discretized models. This versatile approach enables us to more effectively include cell proliferation or cell death during numerical simulations. These results suggest that combining mathematical modeling with *in vivo* experiments
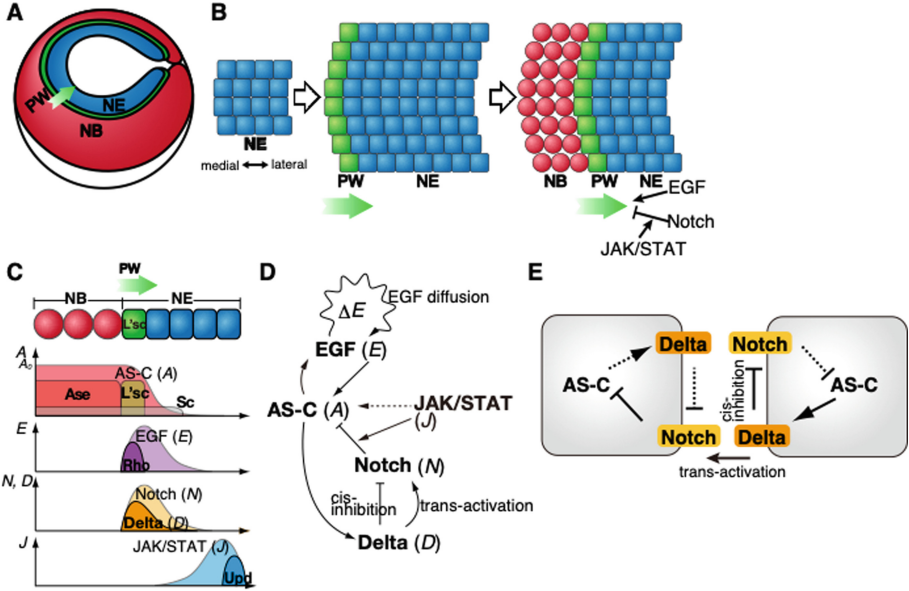
Fig. 1. Progression of the proneural wave. (A) Schematic of the larval optic lobe. NE, NB, and PW represent a neuroepithelial cell, neuroblast, and proneural wave, respectively. (B) Development of optic lobe during the larval stages. (C) Activation of AS-C (*A*), EGF signaling (*E*), Notch signaling (*N*), Delta (*D*), and JAK/STAT signaling (*J*). (D) Genetic interaction among AS-C (*A*), EGF signaling (*E*), Notch signaling (*N*), Delta (*D*), and JAK/STAT signaling (*J*). (E) Notch signaling between adjacent cells.

will enhance our knowledge on the interaction of multiple signaling pathways and its regulation of spatio-temporal patterning during development.

2   Mathematical Model of the PW

To understand the mechanism of PW progression, we first focused on the interaction between Notch and EGF signaling and formulated a mathematical model [16]. The function of Notch signaling in neural development is known as a lateral inhibition (Fig. 1E) [17,18]. Binding of the Delta ligand expressed in neighboring cells to the Notch receptor activates Notch signaling and inhibits AS-C expression. This effect is called a *trans-activation*. It is also known that Delta and Notch expressed in the same cell bind together and inactivate the Notch signaling, which is referred to as *cis-inhibition* [19–21]. AS-C proteins induce the Delta expression. During PW progression, Delta is expressed in the wavefront cells and activates Notch signaling in neighboring cells (Fig. 1C) [9]. Because the major components of Notch signaling, including Delta, Notch, and AS-C, are all involved in PW progression, we introduced the effect of Notch signaling by

applying a lateral inhibition system in the mathematical model. The secretion of the EGF ligand is spatially restricted by the function of the protease Rhomboid (Rho), which is also a target of EGF signaling [9]. Because it can be presumed that the activation of EGF signaling is dependent on the concentration of the diffusible EGF ligand, we described the function of EGF signaling using a reaction diffusion system [22]. In addition, *in vivo* experiments also showed mutual activation between EGF signaling and AS-C [9,16]. Based on this biological evidence, we formulated a mathematical model to elucidate the dynamics of the interaction between Notch and EGF signaling during PW progression [16]:

$$
\begin{cases}
\dfrac{\partial E}{\partial t} = d_e \Delta E - k_e E + a_e A (A_0 - A), \\[2mm]
\dfrac{dN_{i,j}}{dt} = -k_n N_{i,j} + d_t \displaystyle\sum_{l,m \in \Lambda_{i,j}} D_{l,m} - d_c N_{i,j} D_{i,j}, \\[2mm]
\dfrac{dD_{i,j}}{dt} = -k_d D_{i,j} + a_d A_{i,j} (A_0 - A_{i,j}), \\[2mm]
\dfrac{dA_{i,j}}{dt} = e_a (A_0 - A_{i,j}) \max\{E_{i,j} - N_{i,j}, 0\},
\end{cases}
\qquad (x,y) \in \Omega,\ t > 0, \qquad (1)
$$

where $\Omega = [0, L_x] \times [0, L_y]$ is a calculation region with positive constants L_x and L_y, and $E = E(x, y, t)$ is a composite variable for the concentration of the EGF ligand and activation of EGF signaling. Here, $N_{i,j} = N_{i,j}(t)$ and $D_{i,j} = D_{i,j}(t)$ represent the activity of Notch signaling and the amount of Delta protein in the ith and jth cells at time $t > 0$, respectively. In addition, $N_{i,j}$ is influenced by its degradation ($k_n N_{i,j}$), *trans-activation* by Delta expressed in the neighboring lth and mth cells ($d_t \sum_{l,m \in \Lambda_{i,j}} D_{l,m}$), and *cis-inhibition* by Delta expressed in the ith and jth cell ($d_c N_{i,j} D_{i,j}$). Moreover, $D_{i,j}$ is regulated by its degradation ($k_d D_{i,j}$) and receives a positive input from AS-C ($a_d A_{i,j}(A_0 - A_{i,j})$), and $A_{i,j} = A_{i,j}(t)$ is a variable for the level of differentiation and reflects the expression of AS-C in the ith and jth cell at time t. Further, $A_{i,j}$ is positively regulated by $E_{i,j}$ and negatively regulated by $N_{i,j}$.

Numerical simulations of the above model recapitulate the PW progression. When we set adequate parameters, the simulation shows a unidirectional differentiation wave (Fig. 2A) [16]. In addition, numerical simulations can reproduce the phenotypes of EGF, Notch, or Delta mutants. These results suggest that the combination of Notch-mediated lateral inhibition and EGF-mediated reaction diffusion adequately explains the progression of PW *in vivo*.

We next analyzed the spatio-temporal patterning of the Notch activity. In the context of lateral inhibition, AS-C-expressing cells activate Notch signaling and inhibit neuronal differentiation in neighboring cells. This lateral inhibition mechanism generates a complementary pattern of Notch-ON cells and AS-C expressing cells, which is commonly known as a salt-and-pepper pattern (Fig. 1E). However, during PW progression, wavefront cells express both the AS-C and Notch target genes (Fig. 2C). This contradicts the conserved mechanism of Notch-mediated lateral inhibition. We challenged this paradox by changing the parameters in the mathematical model and found that reducing the EGF activation shows a complementary pattern of AS-C-expressing cells and Notch-ON
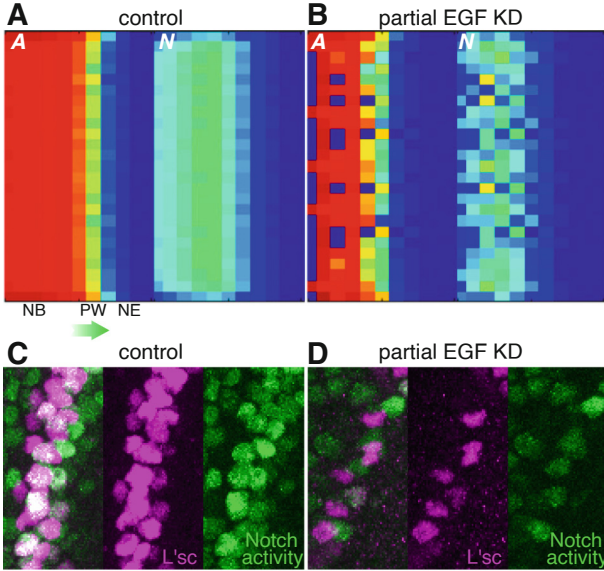
Fig. 2. A partial reduction of the EGF activity shows the salt-and-pepper-like pattern in the activation of Notch signaling. (A, B) Simulation results of control (A) and partial EGF knockdown (B) conditions. The activation of A and N is shown. (C, D) Experimental results of control (C) and partial EGF knockdown (D) conditions. Expression of L'sc (magenta) and $E(spl)m\gamma$-GFP (green, Notch activity marker) is shown. (Color figure online)

cells (Fig. 2B). We confirmed this prediction from the simulation by decreasing the EGF activity *in vivo* (Fig. 2D). This result suggests that EGF signaling cancels the formation of a salt-and-pepper pattern, which is mediated through Notch signaling.

Notch signaling is conserved among the species and plays diverse roles in development, homeostasis, and cancer [23]. Although similar key regulators act in Notch signaling, they exhibit different outcomes. A salt-and-pepper pattern is shown in the sensory organ precursor formation in *Drosophila*, and a striped pattern appears in the segmentation in vertebrates [18,24,25]. Our study results demonstrate that Notch signaling generates a pulse wave when combined with EGF signaling and regulates the timing of the neural stem cell formation in the *Drosophila* visual system.

3   Noise Canceling Function Using JAK/STAT

Although the mathematical model applied to the interaction between Notch and EGF recapitulated the states of the wild type and mutant *in vivo*, it showed weakness against noise. The addition of a small amount of noise for E in the undifferentiated NE region causes an ectopic NB differentiation, in addition

to the original PW (Fig. 3A). These simulation results suggest that a noise-canceling mechanism ensuring a robust PW progression exists. As a candidate mechanism, we focused on the function of JAK/STAT signaling based on previous reports. First, JAK/STAT signaling generates an activity gradient that is high in the lateral side and low in the medial side within the NE region [6]. Second, a loss-of-function of JAK/STAT signaling accelerates the wave progression, whereas an ectopic activation of JAK/STAT signaling delays the progression [6]. Third, JAK/STAT signaling positively regulates the expression of the Notch target genes in the optic lobe (Fig. 1D) [26]. Based on these findings, we revised the fourth equation of the mathematical formula by including the function of JAK/STAT signaling [27]:

$$\frac{dA_{i,j}}{dt} = e_a(A_0 - A_{i,j})\max\{E_{i,j} - N_{i,j} - k_{in}J_{\infty}, 0\},$$

where $J = J(x, y, t)$ represents the activation of JAK/STAT signaling, and k_{in} is a positive constant for the regulation rate of JAK/STAT signaling for the Notch target genes. We induced the role of JAK/STAT signaling in inhibiting AS-C expression by activating the function of Notch signaling (Fig. 1D). In addition, we defined the function of JAK/STAT signaling by the reaction diffusion system as JAK/STAT signaling creates an activity gradient. We imposed $J_{\infty} = J_{\infty}(x, y)$ as a stationary state for the following reaction diffusion model:

$$\begin{cases} \dfrac{\partial J}{\partial t} = d_i \Delta J - k_i J, \quad t > 0, \quad (x, y) \in \Omega, \\ \dfrac{\partial J}{\partial y}(x, 0, t) = \dfrac{\partial J}{\partial y}(x, L_y, t) = 0, \quad x \in [0, L_x], \\ \dfrac{\partial J}{\partial x}(0, y, t) = 0, \quad J(L_x, y, t) = J_0, \quad y \in [0, L_y], \end{cases}$$

where d_i, k_i, and J_0 are the diffusion coefficients of the JAK/STAT signaling, degradation rate, or positive constant corresponding to the JAK/STAT activation on the lateral side, respectively.

Next, we conducted a numerical simulation based on the revised model. In the original model, a small perturbation for E causes stochastic NB differentiation, and the differentiation wave is absent. By contrast, in the revised model, including the function of JAK/STAT, the PW progresses unidirectionally even in the presence of noise for E. This result indicates that the revised model, including the function of JAK/STAT signaling, shows resistance to EGF perturbation, and there is a possibility that JAK/STAT signaling is able to cancel the noise to assure a normal PW progression *in vivo*. To confirm this possibility, we reduced the activity of JAK/STAT signaling by inducing RNAi against *Stat92E*, which is the only *STAT* gene in *Drosophila*. Compared with the control, *Stat92E* RNAi brains show an ectopic and random L'sc expression and NB differentiation in a stochastic manner (Fig. 3B, C). These *in silico* and *in vivo* results suggest that JAK/STAT signaling is required to prevent spontaneous NB differentiation by suppressing the effect of noise [27].
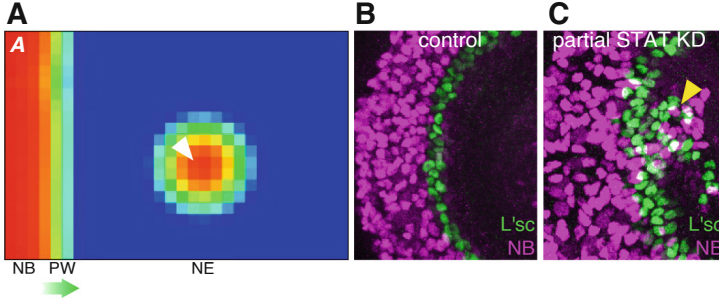
Fig. 3. JAK/STAT signaling is required for preventing spontaneous NB differentiation. (A) Simulation results from the mathematical model that excludes the effect of JAK/STAT signaling. A minor perturbation of EGF activity in the NE region (white arrowhead) induces ectopic NB differentiation. Activation of A is shown. (B, C) Experimental results of control (B) and partial STAT knockdown (C) conditions. The yellow arrowhead indicates the ectopic expression of L'sc (green) and Deadpan (magenta, NB marker). (Color figure online)

During the development of multicellular organisms, the behavior of each cell is influenced by stochastic noise. Even in the presence of noise, spatio-temporal patterning progresses in a robust manner. Therefore, noise resistance mechanisms are crucial during development [28]. However, it has been challenging to address the mechanism of noise regulation because of the limitation of approaches for noise detection. The mechanism of noise-resistant reproducibility in vertebrate somite formation has recently been elucidated by combining mathematical modeling with *in vivo* experiments [29,30]. These accumulating data will expand the field of noise-canceling mechanisms in multicellular systems.

4 Continuation Method from Spatially Discretized Models

As introduced in the previous sections, the discrete model of PW on square or hexagonal lattices, as shown in Fig. 4, was proposed. In this section, we describe a continuation method for spatially discretized models containing the intercellular interaction and reaction terms while conserving the shapes and sizes of the cells and lattices. This detailed method is reported in our previous study [31]. In this section, we label the mathematical models with discrete spatial independent variables as discrete models and those with continuous spatial independent variables as continuous models. Furthermore, we do not distinguish between the spatial and intercellular interactions.

4.1 Scalar Equation in One-Dimensional Space

Labeling the ith cell as c_i, $(i = 1, \ldots, N)$ with a uniform length $l > 0$, we suppose N cells are packed in a one-dimensional space. Let $u_i = u_i(t)$ be the

A   **B**
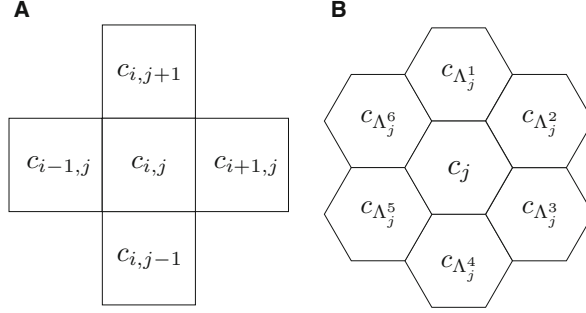
Fig. 4. Schematic figures of the (A) square and (B) hexagonal lattices with indexes.

concentration or density of some substances on c_i at time $t > 0$. Imposing the periodic boundary condition $u_{i\pm N}(t) = u_i(t)$, $(i = 1, 2, \ldots, N)$, we consider the following discrete model in this subsection:

$$\begin{cases} u_{i,t} = f\left(u_{i-[\frac{N-1}{2}]}, \cdots, u_i, \cdots, u_{i+[\frac{N-1}{2}]}\right) + g(u_i), & t > 0, \quad i = 1, \ldots, N, \\ u_i(0) = u_{i,0}, \end{cases}$$

$$\text{(P}_D\text{)}$$

where $f : \mathbb{R}^{2[N-1/2]+1} \to \mathbb{R}$ and $g : \mathbb{R} \to \mathbb{R}$ are functions corresponding to the intercellular interaction and reaction, respectively, and $[\cdot]$ is a Gauss symbol. Although the intercellular interaction f can be influenced by cells other than the neighboring cells, the intercellular interaction f includes a typical form of intercellular interactions as $f = f(u_{i-1}, u_i, u_{i+1})$. The one-dimensional space is set as follows:

$$\mathbb{T} := [0, Nl].$$

If f is linear, the function f is then generally defined in the following manner:

$$f\left(u_{-[\frac{N-1}{2}]}, \cdots, u_0, \cdots, u_{[\frac{N-1}{2}]}\right) = \sum_{i=-[\frac{N-1}{2}]}^{[\frac{N-1}{2}]} a_i u_i, \qquad (2)$$

where $\{a_i\}_{i=-[(N-1)/2]}^{[(N-1)/2]}$ are constants. Typical examples of function f include diffusion, a lateral inhibition such as a Delta-Notch interaction, and planar cellular polarity [32] as given by the following:

$$f_\Delta(u_{i-1}, u_i, u_{i+1}) = \frac{u_{i-1} - 2u_i + u_{i+1}}{l^2},$$

$$f_{\text{lat}}(u_{i-1}, u_{i+1}) = \frac{-u_{i-1} - u_{i+1}}{2},$$

$$f_{\text{pcp}}(u_{i-1}, u_i, u_{i+1}) = \sin(u_{i-1} - u_i) + \sin(u_{i+1} - u_i).$$

As introduced in [33, 34], we will utilize the piecewise constant functions for our continuation method. For equation (P_D) with $i = 1, \ldots, N$ on each cell c_i, we define the characteristic function as

$$\chi_{c_i}(x) = \begin{cases} 1, \, x \in c_i, \\ 0, \, x \notin c_i, \end{cases}$$

and define the following:

$$u(x, t) := \sum_{i=1}^{N} u_i(t)\chi_{c_i}(x).$$

For the continuous method of the discrete model, we set the following assumption:

For any N, there exists a unique global solution $u(x, t) \in C([0, T], L^1(\mathbb{T}))$ of (P_D).

By changing the variable in the ith equation (P_D) by multiplying the unknown function u_i by the characteristic function $\chi_{c_i}(x)$, and adding $u_i(t)\chi_{c_i}(x)$ with respect to $i = 1, \cdots, N$, we have the following:

$$u_t = f\left(\sum_{i=1}^{N} u_{i-[\frac{N-1}{2}]}(t)\chi_{c_i}(x), \cdots, \, u, \cdots, \sum_{i=1}^{N} u_{i+[\frac{N-1}{2}]}(t)\chi_{c_i}(x)\right) + g(u).$$

Because we can compute

$$\sum_{i=1}^{N} u_{i+j}\chi_{c_i}(x) = \sum_{i=1}^{N} u_i\chi_{c_i}(x + jl) = u(x + jl, t)$$

for $j = 0, \pm 1, \cdots, \pm N$, we obtain

$$\begin{cases} u_t = f\left(u\left(x - \left[\dfrac{N-1}{2}\right]l, t\right), \cdots, u, \right. \\ \qquad \left. \cdots, u\left(x + \left[\dfrac{N-1}{2}\right]l, t\right)\right) + g(u), \quad x \in \mathbb{T}, \, t > 0, \qquad (P_S) \\ u(x, 0) = u_0(x) = \displaystyle\sum_{i=1}^{N} u_i(0)\chi_{c_i}(x), \qquad\qquad x \in \mathbb{T}. \end{cases}$$

In addition, because the spatially independent variable is continuous, the discrete model (P_D) is successfully converted into a continuous model. The equation of (P_S) is pointwise equivalent to equation (P_D). Thus, if the initial conditions of equations (P_D) and (P_S) are the same by imposing $u_0(x) := u(x, 0) = \sum_{i=1}^{N} u_i(0)\chi_{c_i}(x)$, the solutions to both equations are equivalent.

Furthermore, to apply the continuous model to the experiments and analyze them in a convenient manner, we approximate the shift operator using the convolution on the mollifier. We define the shift operator as follows:

$$\tau_l u(x) := u(x + l).$$

The shift operator is regarded as the convolution of the shifted Dirac Delta function $\delta_l := \tau_l \delta = \delta(x + l)$, and we can describe the model (P_S) as follows:

$$u_t = f\left(u * \delta_{-[\frac{N-1}{2}]l}, \cdots, u, \cdots, u * \delta_{[\frac{N-1}{2}]l}\right) + g(u).$$

Herein, we suppose that the Dirac Delta function is periodic with Nl, that is, $\delta(x) = \delta(x + Nl)$, and we define the convolution $k * v$ with respect to x in $\mathbb{T}$ as follows:

$$(k * v)(x) := \int_{\mathbb{T}} k(x - y)v(y)dy,$$

where $\mathbb{T}$ can be replaced with a given region in this study. Setting the Friedrichs mollifier with a small parameter $0 < \varepsilon \ll 1$ as

$$\rho_\varepsilon(x) := \frac{1}{\varepsilon}\rho\left(\frac{1}{\varepsilon}x\right), \quad \rho(x) := \begin{cases} C_0 \exp\left(-\frac{1}{1-|x|^2}\right), & |x| < 1, \\ 0, & |x| \geq 1 \end{cases}$$

and using a constant for normalization of the integration $C_0 > 0$, we assume that ρ_ε is also periodic with Nl. We use the symbol $\boldsymbol{\rho}_\varepsilon$ for the mollifier in the higher-dimensional case. Approximating the Dirac Delta function using the mollifier $\rho_\varepsilon(x)$, we have

$$u_t^\varepsilon = f\left(u^\varepsilon * \rho_{\varepsilon, -[\frac{N-1}{2}]l}, \cdots, u^\varepsilon, \cdots, u^\varepsilon * \rho_{\varepsilon, [\frac{N-1}{2}]l}\right) + g(u^\varepsilon),$$

where the shifted mollifier is given by $\rho_{\varepsilon,l} := \rho_\varepsilon(x + l)$. Further, because the solution to this equation depends on ε, we denote the unknown variable as $u^\varepsilon(x, t)$. If the intercellular interaction f is linear, we derive the typical nonlocal evolution equation by summarizing the kernel of the convolution as follows:

$$\begin{cases} u_t^\varepsilon = K * u^\varepsilon + a_0 u^\varepsilon + g(u^\varepsilon), & x \in \mathbb{T}, \ t > 0, \\ u^\varepsilon(x, 0) = u_0(x) = \sum_{i=1}^{N} u_i(0)\chi_{c_i}(x), & x \in \mathbb{T}, \end{cases} \tag{P_ε}$$

where

$$K = \sum_{j=-[\frac{N-1}{2}], j \neq 0}^{[\frac{N-1}{2}]} a_j \tau_{jl} \rho_\varepsilon. \tag{3}$$

Therefore, the profile of K depends on the function f and the lattice shape. This type of nonlocal evolution has been analyzed in numerous studies [35,36]. Similarly, the proposed continuation method can be applied to the case of the systems and in higher dimensions.

4.2   Singular Limit Analysis

In this subsection, we demonstrate that the solution to (P_ε) is sufficiently close to that of (P_S) in $L^2(\mathbb{T})$ based on a singular limit analysis. We first assume that f is a form of (2). For the condition g, we assume that there exist positive constants g_0, g_2, g_4 and a non-negative constant g_1, g_3 such that for $u \in \mathbb{R}$

$$g(u)u \leq -g_0|u|^{p+1} + g_1|u|^3 + g_2|u|^2,$$
$$|g_u(u) + pg_0|u|^{p-1}| \leq g_3|u| + g_4,$$
$$p \geq 3 \text{ or } g_1 = g_3 = 0 \text{ if } 2 < p < 3.$$

A typical example of g is $g(u) = u(1 - u^2)$, where $g_0 = g_2 = g_4 = 1$, $g_1 = g_3 = 0$, and $p = 3$.

We can show the uniqueness and global existence of the solutions of (P_S) and (P_ε).

Proposition 1. *Assume that f is given by (2), and $\sup_{j \in \{-[(N-1)/2],\ldots,[(N-1)/2]\}}$ $|a_j| < \infty$. There exists a unique solution $u \in C[(0,\infty), L^\infty(\mathbb{T})]$ to (P_S) with an initial datum $u_0 \in L^\infty(\mathbb{T})$. Furthermore,*

$$\sup_{0 \leq t < \infty} \|u(\cdot, t)\|_{L^\infty(\mathbb{T})} < C_1, \tag{4}$$

where C_1 is a positive constant.

Proposition 2. *Assume that K is given by (3), and $\sup_{j \in \{-[(N-1)/2],\ldots,[(N-1)/2]\}}$ $|a_j| < \infty$. There exists a unique solution $u^\varepsilon \in C[(0,\infty), L^\infty(\mathbb{T})]$ of (P_ε) with an initial datum $u_0 \in L^\infty(\mathbb{T})$. In addition,*

$$\sup_{0 \leq t < \infty} \|u^\varepsilon(\cdot, t)\|_{L^\infty(\mathbb{T})} < C_2, \tag{5}$$

where C_2 is a positive constant independent of ε.

For the solutions to the models (P_S) and (P_ε), we have the following error estimate:

Theorem 1. *Suppose the same assumptions as in Propositions 1 and 2. Let $u(x,t)$ and $u^\varepsilon(x,t)$ be the solutions to (P_S) and (P_ε) with the initial datum $u(x,0) = u^\varepsilon(x,0) = u_0(x) = \sum_{i=1}^N u_i(0)\chi_{c_i}(x) \in L^\infty(\mathbb{T})$, respectively. Then, for any time $T > 0$ and any small positive constant ε,*

$$\sup_{0 < t < T} \|u^\varepsilon(\cdot, t) - u(\cdot, t)\|_{L^2(\mathbb{T})} \leq \sqrt{\frac{C_4}{C_3}\left(e^{C_3 T} - 1\right)} \sup_{|y| < \varepsilon, t > 0} \|\tau_y u - u\|_{L^2(\mathbb{T})},$$

where C_3 and C_4 are positive constants independent of ε. Thus, we have

$$\|u^\varepsilon(\cdot, t) - u(\cdot, t)\|_{L^2(\mathbb{T})} \to 0$$

as $\varepsilon \to +0$ for any $0 < t < T$.

The proof is based on the energy method using the boundedness of the global solutions (4) and (5), and the classical Gronwall inequality. From this estimation, the solution to the continuous model (P_ε) converges to that of (P_S) in a $L^2(\mathbb{T})$ space as ε tends toward 0. This implies that the solution of the nonlocal evolution equation can approximate the solution of the discrete model.

Corollary 1. *Assume that f is global Lipschitz continuous, that is, there exists a positive constant L such that*

$$\left| f\left(u_{-[\frac{N-1}{2}]}, \cdots, u_0, \cdots, u_{[\frac{N-1}{2}]} \right) - f\left(v_{-[\frac{N-1}{2}]}, \cdots, v_0, \cdots, v_{[\frac{N-1}{2}]} \right) \right|$$
$$\leq L \sum_{j=-[\frac{N-1}{2}]}^{[\frac{N-1}{2}]} |u_j - v_j|, \tag{6}$$

and $f(\mathbf{0}) = 0$ ($\mathbf{0} \in \mathbb{R}^N$). Then, for the solutions to (P_S) and (P_ε) with (6), Proposition 1, Proposition 2, and Theorem 1 hold. 1 hold.

This corollary suggests that the convergence Theorem 1 is guaranteed in the form of f, such as f_{pcp}.

4.3   Application to the Discrete Model of PW

In this subsection, by applying our proposed continuation method to the discrete model (1), we investigated the generation of patterns by the derived continuous model through numerical simulations. Although an optic lobe has a hemispherical shape, as shown in Fig. 1 A, we first consider the case of the discrete model of (1) on two-dimensional planes. For the model of (1) using the characteristic functions as in the previous subsection, we change the variables to

$$D(x,y,t) := \sum_{i,j=1}^{N} D_{i,j}(t)\chi_{c_{i,j}}(x,y), \quad N(x,y,t) := \sum_{i,j=1}^{N} N_{i,j}(t)\chi_{c_{i,j}}(x,y),$$
$$A(x,y,t) := \sum_{i,j=1}^{N} A_{i,j}(t)\chi_{c_{i,j}}(x,y).$$

In this modeling, we assume the following:

> The trigger of differentiation at each point in the cells is determined by the value of EGF instead of the value of the integration of EGF in a cell. (A1)

Then, approximating the shift operators with the Dirac Delta function based on the convolutions of the mollifier, we have the following continuous models:

$$\begin{cases} \dfrac{\partial E}{\partial t} = d_e\Delta E - k_e E + a_e A(A_0 - A), \\[2mm] \dfrac{\partial N}{\partial t} = -k_n N + d_t K * D - d_c ND, \\[2mm] \dfrac{\partial D}{\partial t} = -k_d D + a_d A(A_0 - A), \\[2mm] \dfrac{\partial A}{\partial t} = e_a(A_0 - A)\max\{E - N, 0\}, \end{cases} \quad \text{in } \Omega \times \{t > 0\}. \tag{7}$$
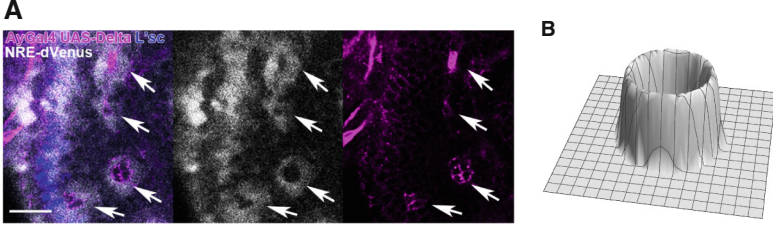
Fig. 5. (A) Notch activity as visualized using *NRE-dVenus* (white) is elevated in cells adjacent to the clones expressing *UAS-Delta* under the control of *AyGal4* (magenta) owing to the *trans*-activation, but is repressed in cells expressing *UAS-Delta* owing to the *cis*-inhibition (arrows) [31]. The wave front of the PW is visualized by L'sc (blue). Scale bar = 20 µm. (B) Profile of the radially symmetric kernel (8) with $\varepsilon = 0.7$. (Color figure online)

where kernel K is the linear sum of the shifted mollifiers depending on the shape of the lattice. We also impose the local term of the max function of the fourth equation based on the assumption (A1). We then define the division points as

$$\Lambda^k(n) := \left(l\sin\left(\frac{2\pi(k-1)}{n}\right),\ l\cos\left(\frac{2\pi(k-1)}{n}\right)\right),\quad (k = 1, \ldots, n).$$

These points divide the circumference of the concentric circles into n equal parts. We define the shift operators as

$$\tau_{\Lambda^k(n)}u(x,y) := u\left(x + l\sin\left(\frac{2\pi(k-1)}{n}\right),\ y + l\cos\left(\frac{2\pi(k-1)}{n}\right)\right).$$

If the lattice shapes are square or hexagonal, the forms of the corresponding kernel are given by

$$K(x,y) = \sum_{k=1}^{4}(\tau_{\Lambda^k(4)}\boldsymbol{\rho}_\varepsilon)(x,y),\quad K(x,y) = \sum_{k=1}^{6}(\tau_{\Lambda^k(6)}\boldsymbol{\rho}_\varepsilon)(x,y),$$

respectively.

4.4 Radially Symmetric Kernel

Activation of Notch signaling is induced by binding the Notch receptor to the Delta ligand expressed in adjacent cells (Fig. 1E). Therefore, the activation of Notch signaling can be affected by the shape of the cell membrane. To examine whether the shape of the activated region of the Notch signaling shows an isotropic or anisotropic pattern, we investigated the activation of such signaling when Delta is artificially expressed. Notch signaling was activated in a group of cells, forming a concentric distribution pattern adjacent to Delta-expressing
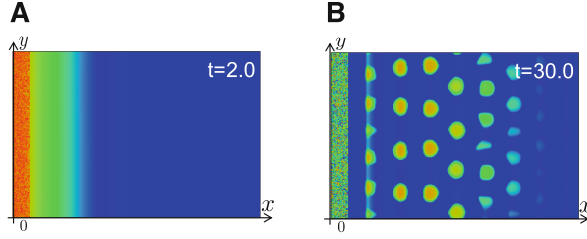
Fig. 6. Results of the numerical simulations for the state of the differentiation A in the continuous model (7) with the kernel corresponding to the averaged cell (8). Parameters are described in [31]. (A) PW with $a_e = 3.0$ and (B) salt-and-pepper pattern with $a_e = 0.4$.

cells (Fig. 5A). This result suggests that the shape of the cells does not affect the spatial activation pattern of the Notch signaling *in vivo*.

Based on the experimental results, we propose radially symmetric kernels as

$$K(x,y) = \frac{1}{2\pi l}\rho_\varepsilon(\sqrt{x^2 + y^2} - l).$$ (8)

The profile of this kernel is shown in Fig. 5B. The nonlocal operator becomes radially symmetric when using this shape of kernel. Figure 6 shows the numerical results of the model of (7) with (8). The wild type of the PW and the salt and pepper patterns can be replicated using this continuous model, as shown in Fig. 6A and B, respectively. These numerical results correspond to those of Fig. 2.

4.5   Description of Discrete Model on Sphere Surface

As the optic lobe has a hemispherical shape and the PW sweeps across the surface, as described in Sect. 1, it is natural to construct a discrete model for the PW on a spherical surface. However, mathematical studies of the PW on a 2-D plane have been discussed because it is technically difficult in general to deal with discrete models mathematically on a spherical surface owing to the discreteness. In this case, our continuation method can overcome these difficulties and enables us to handle the model on the spherical surface as a continuous model equation. In practice, by applying the continuation method with a radially symmetric kernel with radius $r > 0$ in (8), we can compute the continuous model (7) on a spherical surface using the spectrum method [31]. We can calculate the following model of the PW on a spherical surface numerically:

$$\begin{cases} \dfrac{\partial E}{\partial t} = d_e \Delta_{r\mathbb{S}^2} E - k_e E + a_e A(A_0 - A), \\ \dfrac{\partial N}{\partial t} = -k_n N + d_t K *_{r\mathbb{S}^2} D - d_c ND, \end{cases} \quad \text{in } r\mathbb{S}^2 \times \{t > 0\}, \quad (9)$$

A

B
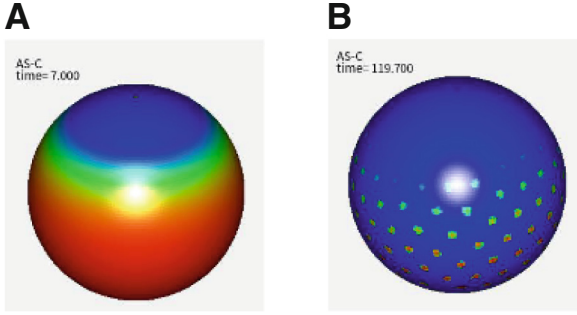
Fig. 7. Results of the numerical simulations for the state of the differentiation A in the continuous model on the spherical surface (11). The parameters are the same as those in Fig. 6 and $r = 10.0$ and $k_{in}J \equiv 1.0 \times 10^{-3}$. (A) PW with $a_e = 2.0$. (B) Salt-and-pepper pattern with $a_e = 0.4$.

where the equations of D and A are the same as in equation (1), and $r\mathbb{S}^2$ is a sphere with radius $r > 0$ and $K : [0, 2r] \to \mathbb{R}$ is defined as

$$K(x) := \rho_\varepsilon(x - l), \quad x \in [0, 2r].$$

In addition, the Laplace-Beltrami operator $\Delta_{r\mathbb{S}^2}$ on a general sphere with radius $r > 0$ is given by

$$\Delta_{r\mathbb{S}^2} = \frac{1}{r^2}\Delta_{\mathbb{S}^2}.$$

The convolution operator on a sphere $*_{r\mathbb{S}^2}$ is computed as

$$K *_{r\mathbb{S}^2} u(x) := \int_{r\mathbb{S}^2} K(|x - y|)u(y)d\Omega_r(y),$$
$$= r^2 \int_{\mathbb{S}^2} K_r(|x - y|)u_r(y)d\Omega(y),$$
$$= K_r *_{\mathbb{S}^2} u_r(x),$$

where

$$K_r(|\cdot|) := K(r|\cdot|), \quad u_r(x) := u(rx) \ (x \in \mathbb{S}^2). \tag{10}$$

Here, $d\Omega_r$ is denoted by the standard measure of $r\mathbb{S}^2$, and $*_{\mathbb{S}^2}$ is the convolution on the unit sphere. The details of the calculation are described in [31]. According to the calculation, we can rewrite equation (9) on the unit sphere as follows:

$$\begin{cases} \dfrac{\partial E_r}{\partial t} = \dfrac{d_e}{r^2}\Delta_{\mathbb{S}^2} E_r - k_e E_r + a_e A_r(A_0 - A_r), \\ \dfrac{\partial N_r}{\partial t} = -k_n N_r + d_t r^2 K_r *_{\mathbb{S}^2} D_r - d_c N_r D_r, \\ \dfrac{\partial D_r}{\partial t} = -k_d D_r + a_d A_r(A_0 - A_r), \\ \dfrac{\partial A_r}{\partial t} = e_a(A_0 - A_r)\max\{E_r - N_r - k_{in}J_r, 0\}, \end{cases} \quad \text{in } \mathbb{S}^2 \times \{t > 0\}, \tag{11}$$

where the notations of the unknown variables are based on (10). Through the numerical simulation of Fig. 7, the parameters of which are the same as those in Fig. 6, we obtain similar numerical results of the propagation of AS-C as the case of a 2-D plane when $r = 10.0$.

5   Discussion

In this paper, we introduced our interdisciplinary studies using the PW in the *Drosophila* visual system. We combined mathematical modeling with an experimental analysis and showed that the combination of Notch-mediated lateral inhibition and EGF-mediated reaction diffusion systems regulates the timing of neural stem cell differentiation. A further improvement of the mathematical model through the inclusion of the JAK/STAT function points to the possibility that JAK/STAT signaling can eliminate biological noise. Based on this prediction, we manipulated the JAK/STAT activity *in vivo* and confirmed that JAK/STAT signaling prevents spontaneous neural stem cell differentiation caused by noise. In both studies, we conducted simulations on mathematical models to recapitulate different situations *in vivo* and develop new biological predictions for analysis. To verify the predictions, we partially decreased the activity of EGF or JAK/STAT and found new functions of these pathways (Fig. 2D, 3C). Typically, biologists attempt to completely eliminate the functions of the target genes. However, our results show that we may find new functions of signaling pathways or molecules by gradually changing their activities. This is an interesting perspective for future biological research using mathematical modeling.

We also proposed a versatile continuation method from spatially discretized models. We applied this method to a mathematical model of the PW and confirmed that the numerical calculation of the continuous model shows equivalent results to those of the discrete model. We can easily include the effect of cell proliferation by using continuous models and expand the simulation results from a 2-D plane to a 3-D spherical surface. In addition, Hippo signaling inhibits NE proliferation and promotes NB differentiation [7,8,15]. Future studies including the function of Hippo signaling, based on a mathematical model, will reveal the spatio-temporal coupling of the proliferation and differentiation of undifferentiated NEs.

The biological processes of multicellular organisms are regulated by the complex intercellular communication of signaling pathways. It is often difficult to predict the behavior of each signaling pathway and the final phenotype if the functions of one or more pathways are compromised. Mathematical modeling can be a powerful tool to understand the dynamic functions of signaling pathways. The mathematical method described above is not specific to studies of the PW and is also useful for understanding many different biological systems. As the functions of Notch, EGF, and JAK/STAT are conserved, we can easily formulate similar mathematical models for other systems. A continuation method developed from discrete models conserving the cell size and lattice will enable us to efficiently conduct numerical calculations, both qualitatively and quantitatively. Finally, we can better understand the molecular basis of a wide variety of

biological systems by combining mathematical modeling with an experimental verification.

References

1. Yasugi, T., Nishimura, T.: Temporal regulation of the generation of neuronal diversity in Drosophila. Dev. Growth Differ. **58**(1), 73–87 (2016)
2. Sato, M., Suzuki, T., Nakai, Y.: Waves of differentiation in the fly visual system. Dev. Biol. **380**(1), 1–11 (2013)
3. Sato, M., Yasugi, T., Trush, O.: Temporal patterning of neurogenesis and neural wiring in the fly visual system. Neurosci. Res. **138**, 49–58 (2019)
4. Nassif, C., Noveen, A., Hartenstein, V.: Early development of the Drosophila brain: III. The pattern of neuropile founder tracts during the larval period. J. Comput. Neurol. **455**(4), 417–434 (2003)
5. Egger, B., Boone, J.Q., Stevens, N.R., Brand, A.H., Doe, C.Q.: Regulation of spindle orientation and neural stem cell fate in the Drosophila optic lobe. Neural Dev. **2**, 1 (2007)
6. Yasugi, T., Umetsu, D., Murakami, S., Sato, M., Tabata, T.: Drosophila optic lobe neuroblasts triggered by a wave of proneural gene expression that is negatively regulated by JAK/STAT. Development **135**(8), 1471–1480 (2008)
7. Kawamori, H., Tai, M., Sato, M., Yasugi, T., Tabata, T.: Fat/Hippo pathway regulates the progress of neural differentiation signaling in the Drosophila optic lobe. Dev. Growth Differ. **53**(5), 653–667 (2011)
8. Reddy, B.V., Rauskolb, C., Irvine, K.D.: Influence of fat-hippo and notch signaling on the proliferation and differentiation of Drosophila optic neuroepithelia. Development **137**(14), 2397–2408 (2010)
9. Yasugi, T., Sugie, A., Umetsu, D., Tabata, T.: Coordinated sequential action of EGFR and Notch signaling pathways regulates proneural wave progression in the Drosophila optic lobe. Development **137**(19), 3193–3203 (2010)
10. Weng, M., Haenfler, J.M., Lee, C.Y.: Changes in Notch signaling coordinates maintenance and differentiation of the Drosophila larval optic lobe neuroepithelia. Dev. Neurobiol. **72**(11), 1376–1390 (2012)
11. Wang, W., Liu, W., Wang, Y., Zhou, L., Tang, X., Luo, H.: Notch signaling regulates neuroepithelial stem cell maintenance and neuroblast formation in Drosophila optic lobe development. Dev. Biol. **350**(2), 414–428 (2011)
12. Orihara-Ono, M., Toriya, M., Nakao, K., Okano, H.: Downregulation of Notch mediates the seamless transition of individual Drosophila neuroepithelial progenitors into optic medullar neuroblasts during prolonged G1. Dev. Biol. **351**(1), 163–175 (2011)
13. Ngo, K.T., et al.: Concomitant requirement for Notch and JAK/STAT signaling during neuro-epithelial differentiation in the Drosophila optic lobe. Dev. Biol. **346**(2), 284–295 (2010)

14. Wang, W., Li, Y., Zhou, L., Yue, H., Luo, H.: Role of JAK/STAT signaling in neuroepithelial stem cell maintenance and proliferation in the Drosophila optic lobe. Biochem. Biophys. Res. Commun. **410**(4), 714–720 (2011)
15. Richter, C., Oktaba, K., Steinmann, J., Muller, J., Knoblich, J.A.: The tumour suppressor L(3)mbt inhibits neuroepithelial proliferation and acts on insulator elements. Nat. Cell Biol. **13**(9), 1029–1039 (2011)
16. Sato, M., Yasugi, T., Minami, Y., Miura, T., Nagayama, M.: Notch-mediated lateral inhibition regulates proneural wave propagation when combined with EGF-mediated reaction diffusion. Proc. Natl. Acad. Sci. U.S.A. **113**(35), E5153–5162 (2016)
17. Simpson, P.: Lateral inhibition and the development of the sensory bristles of the adult peripheral nervous system of Drosophila. Development **109**(3), 509–519 (1990)
18. Artavanis-Tsakonas, S., Rand, M.D., Lake, R.J.: Notch signaling: cell fate control and signal integration in development. Science **284**(5415), 770–776 (1999)
19. Miller, A.C., Lyons, E.L., Herman, T.G.: cis-Inhibition of Notch by endogenous Delta biases the outcome of lateral inhibition. Curr. Biol. **19**(16), 1378–1383 (2009)
20. del Alamo, D., Schweisguth, F.: Notch signalling: receptor cis-inhibition to achieve directionality. Curr. Biol. **19**(16), R683–684 (2009)
21. Sprinzak, D., et al.: Cis-interactions between Notch and Delta generate mutually exclusive signalling states. Nature **465**(7294), 86–90 (2010)
22. Wiley, H.S., Shvartsman, S.Y., Lauffenburger, D.A.: Computational modeling of the EGF-receptor system: a paradigm for systems biology. Trends Cell Biol. **13**(1), 43–50 (2003)
23. Bolos, V., Grego-Bessa, J., de la Pompa, J.L.: Notch signaling in development and cancer. Endocr. Rev. **28**(3), 339–363 (2007)
24. Liao, B.K., Oates, A.C.: Delta-Notch signalling in segmentation. Arthropod Struct. Dev. **46**(3), 429–447 (2017)
25. Barad, O., Hornstein, E., Barkai, N.: Robust selection of sensory organ precursors by the Notch-Delta pathway. Curr. Opin. Cell Biol. **23**(6), 663–667 (2011)
26. Wang, H., Chen, X., He, T., Zhou, Y., Luo, H.: Evidence for tissue-specific JAK/STAT target genes in Drosophila optic lobe development. Genetics **195**(4), 1291–1306 (2013)
27. Tanaka, Y., Yasugi, T., Nagayama, M., Sato, M., Ei, S.I.: JAK/STAT guarantees robust neural stem cell differentiation by shutting off biological noise. Sci. Rep. **8**(1), 12484 (2018)
28. Arias, A.M., Hayward, P.: Filtering transcriptional noise during development: concepts and mechanisms. Nat. Rev. Genet. **7**(1), 34–44 (2006)
29. Horikawa, K., Ishimatsu, K., Yoshimoto, E., Kondo, S., Takeda, H.: Noise-resistant and synchronized oscillation of the segmentation clock. Nature **441**(7094), 719–723 (2006)
30. Naoki, H., Akiyama, R., Sari, D.W.K., Ishii, S., Bessho, Y., Matsui, T.: Noise-resistant developmental reproducibility in vertebrate somite formation. PLoS Comput. Biol. **15**(2), e1006579 (2019)
31. Ei, S., Ishii, H., Sato, M., Tanaka, Y., Wang, M., Yasugi, T.: A continuation method for spatially discretized models with nonlocal interactions conserving size and shape of cells and lattices. J. Math. Biol. **81**, 981-1028 (2020)
32. Ayukawa, T., et al.: Dachsous-dependent asymmetric localization of spiny-legs determines planar cell polarity orientation in Drosophila. Cell Rep. **8**, 610–621 (2014)

33. Doumic, M., Goudon, T., Lepoutre, T.: Scaling limit of a discrete prion dynamics model. Commun. Math. Sci. **7**, 839–865 (2009)
34. Laurençot, P., Mischler, S.: From the discrete to the continuous coagulation-fragmentation equations. Proc. Roy. Soc. Edinb. Sect. A. **132**(5), 1219–1248 (2002)
35. Bates, P.W., Fife, P.C., Ren, X., Wang, X.: Traveling waves in a convolution model for phase transitions. Arch. Rational Mech. Anal. **138**, 105–136 (1997)
36. Coville, J., Dupaigne, L.: On a non-local equation arising in population dynamics. Proc. Roy. Soc. Edinb. Sect. A **137**, 727–755 (2007)

Exploring Similarity Between Embedding Dimension of Time-Series Data and Flows of an Ecological Population Model

Daiki Kumakura[1] and Shinji Nakaoka[2(✉)]

[1] Graduate School of Life Science, Hokkaido University, Sapporo, Japan
dkumakura@eis.hokudai.ac.jp
[2] Faculty of Advanced Life Science, Hokkaido University,
Kita 10 Nishi 8 Kita-ku, Sapporo, Hokkaido, Japan
snakaoka@sci.hokudai.ac.jp

1 Introduction

Cancer cells interact with tissue cells in a complex manner. Immune cells had that initially participated in eliminating cancer cells are often educated to become assisting cancer growth. Identifying causal relationship of cellular interactions that mediate cancer progression is crucial to understand how cancer cells grow, evolve, and persist. A mathematical model that describes dynamics of cancer cell population is constructed based on a given causal relationship among model ingredients. Mathematical modeling has been employed to explain cancer progression patterns in terms of dynamical system.

Time-series analysis provides prediction of a future state of a time-evolving process such as cancer progression. A nonlinear time-series analysis method called empirical dynamic modeling (EDM) has been recently applied in various fields. EDM has model-free analysis to estimate causality that arose from interactions among components. Convergent cross mapping (CCM) is a method which analyzes system's behavior by reconstructing a state space of a system from time-series data without assuming any mathematical equations. Empirical dynamic modeling (EDM) is a model-free method to infer causal relationships from time-series data. EDM has been recently extensively applied in various fields because of its usefulness and versatility.

Despite a variety of mathematical approaches have been available, less are investigated to combine mathematical modeling and model-free analysis method. In this chapter, we proposes a novel approach to bridge mathematical modeling and model-free causal inference method. We show that optimal embedding dimension of observed time-series data determined by simplex projection exhibits similarity with dynamical flow of a trajectory. In other words, pattern similarity represented as the emergence of naturally clustered sub-regions on heatmap is find between embedding dimension and vector field.

The organization of this chapter is as follows. In the next section, we introduce basics of empirical dynamic modeling. Then we show pattern similarity can be observed for two different population dynamics model representing ecological interactions of species.

2   What is Empirical Dynamic Modeling?

Can we capture relationships among populations from observed data? The better we understand these relationships, the better we will be able to implement interventions. This chapter lets us describe the applicability of empirical dynamic modeling (EDM), which has been increasingly used in ecology. Among various ecological studies, time-series data analysis of interacting populations has gained considerable attention. These studies often focus on identifying relation of the interactions among components, as a graph. In network analysis, the relationship among components in a given state is inferred from observed data, and represented as a network diagram. Although an inferred network may help to understand the relationship of a given ecological community, the inferred network is often represented as an undirected graph. In other words, no information regarding the orientation of effect is present. Therefore, even if we could know a relationship among components, it remains unclear whether the relationship represents a causal relationship.

Quantification of intervention effects is one of the most exciting aspects of time series analysis. Intervention effect quantifies how much intervention on a causal factor changes the outcome factor when there is a causal relationship among components. Intervention effect has been studied in medicine, economics, and statistical science, referred to as causal inference. In the causal inference study, a causal relationship is generally represented by drawing a directed acyclic graph (DAG).

Time-series data analysis often faces difficulty in collecting samples that contain all potentially important variables involved in a target ecosystem (e.g., grasses, rabbits, and foxes in the three-species ecological example) [1]. The theory of state-space reconstruction (SSR) [2,4] based on Takens' embedding theorem can provide a sophisticated solution to this problem [2]. Takens' theorem ensures to reconstruct an attractor that is equivalent to the original attractor if enough length of time-series data for a single variable are available. In practice, an attractor is reconstructed by projecting the original attractor to a state space with E dimensional time-delayed coordinates of an observed species X, in which a state vector contains E time-lagged species states [3]. In other words, vectors consist of from time-delayed values of a single variable, $\{X_t, X_{t-\tau}, ..., X_{t-(E-1)}\}$, where X_t is the population density of species X at time t. Note that τ is the time step and E is the embedding dimension.

Empirical dynamic modeling (EDM) is a collection of practical tools that apply to observed time-series data. EDM has several characteristic features: It determines the complexity (dimensionality) of a system, distinguishing nonlinear dynamical systems from linear stochastic systems, and quantifying nonlinearity (i.e., state dependence), identifying causal variables, forecasting, tracking the strength and sign of interaction, and exploring the scenario of external perturbation [5]. These methods are suitable for analyzing complex systems because they do not explicitly assume governing equations. Despite the potential usefulness, explicit formulation of governing equations often faces difficulty in making reasonable *a priori* assumptions about underlying mechanisms. In the next

section, we introduce how to utilize EDM to time-series data with special focus on convergent cross mapping (CCM).

3   Inference of Causal Relationships: Example

Among the EDM methods, convergent cross mapping (CCM) analyzes a system's behavior by reconstructing the state space of a system from time-series data without assuming any mathematical equations. Reconstruction of a dynamical system's attractor by applying Takens' embedding theorem to time series data assumed to be generated from a nonlinear dynamical system [1]. Causality (i.e., changing one causes another to change) is inferred from a couple of attractors reconstructed from observations of two variables in multivariate time series data [2]. The basic principle of cross-mapping involves reconstructing system states from two-time series variables and then quantifying the correspondence between them using nearest neighbor forecasting [3]. For each selected variable, an attractor is reconstructed by delay embedding proposed in Takens' theorem. Then, one on another's effect is measured by evaluating the error of the correlation coefficient (Cross Map Skill) between the estimated time series and the actual time series.

Hereafter we consider the following coupled logistic maps composed of two variables, denoted by X and Y:

$$X(t+1) = X(t)[3.8 - 2.8X(t)],$$
$$Y(t+1) = Y(t)[3.5 - 0.35X(t) - 3.1Y(t)]. \tag{1}$$

Synthetic time-series data are generated from system (1), and plotted in Fig. 1. Note that the synthetic data should indicate a direction from X to Y.
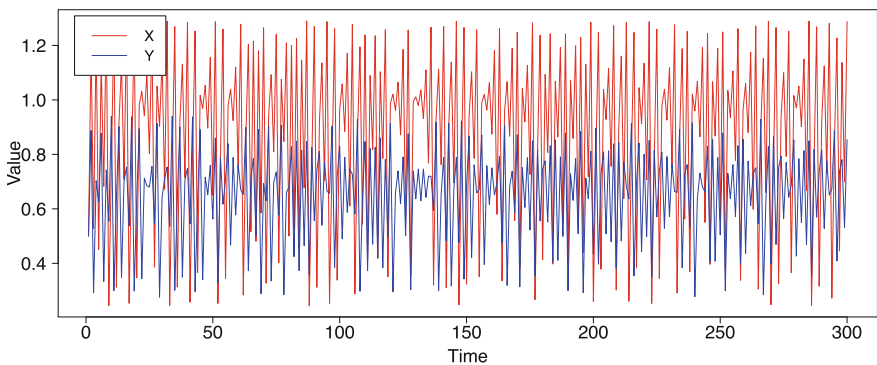

Fig. 1. Time series of coupled logistic maps. Red and blue lines represent the time series data of X and Y, respectively.

A workflow of CCM analysis is as follows. First, the optimal embedding dimension is determined. Let us denote the optimal embedding dimension of X and Y by E_x and E_y, respectively. For each variable (X and Y), the predicted value of Y is calculated from the time-series data of X in E_x, followed by calculating cross-map skill (CMS) as a measure of prediction accuracy from the correlation coefficient with the measured value of Y. This procedure is repeated for Y, and with increasing sample size, two CMSs are computed, one for Y predicted from X and one for X predicted from Y.

In the first step, the dimensionality of a dynamical system can be determined by simplex projection [4,5]. When using simplex projection, a time series dataset is typically divided into two halves, where one half (X) is used as the library set for out-of-sample forecasting and the rest are used for the prediction set (Y) [2]. Following this procedure, the nearest neighbor is selected based on the Euclidean distance between the target point and the other points. What we do here is to find a point that shows "similar behavior" to the target point. Finding the nearest neighbors corresponds to finding the points that show similar behavior in the time series data. The second step is to calculate the weights at each nearest neighbor and the predictions from these weights. Simplex projection with different values of E are used to determine the best embedding dimension according to the prediction skill. There exist several options to evaluate the predictive skill of simplex projection, such as the correlation coefficient (ρ), the mean absolute error (MAE), and root mean square error (RMSE) between the observed value and predicted value (Fig. 2). In this case, $E = 2$ is the optimal embedding dimension.

The third step is to evaluate the error of the correlation coefficient (CMS). Following Takens' theorem, an attractor reconstructed from a univariate embedding (SSR with a single variable) gives a one-to-one map to the original system. Since the reconstructed attractor has a one-to-one map to the original manifold, it is natural that all reconstructed manifolds are mapped one-to-one. Based on this idea, Sugihara et al. developed a cross-mapping algorithm to test the causal relationship between pairs of variables in a dynamical system [2,6–9]. The algorithm uses the time lag of another variable to predict one variable's current quantity and the other way around. If two variables belong to the same dynamical system (i.e., if they are causally related), then the cross-mapping between them must *converge*. Here the word "convergence" indicates that CMS improves as library size increases [5]. To confirm the cross-mapping convergence, the state space is reconstructed using different library sizes randomly subsampled from time-series data. Here, the maximum library size equals to all points in the time-series data.

For synthetic time-series data generated from system, prediction accuracy by cross-mapping was calculated from the correlation coefficient between the measured and predicted values (Fig. 3). The correlation coefficient increased with
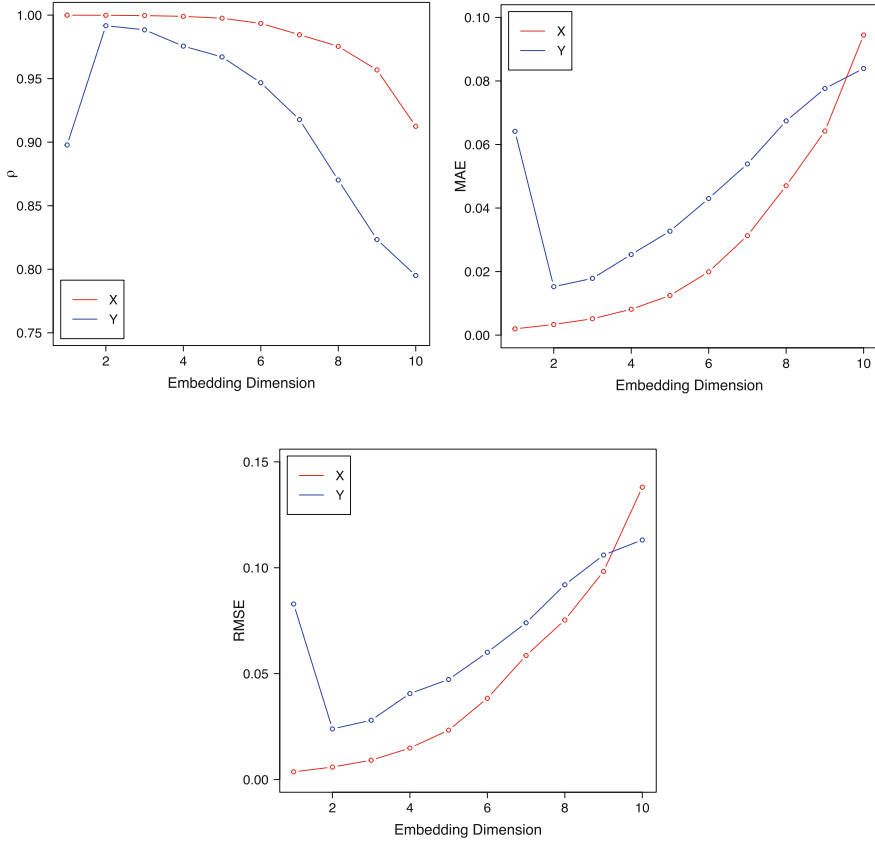
Fig. 2. Predictive skills using simplex projection and embedding dimension. Predictive skills are evaluated by correlation coefficient (ρ), the mean absolute error (MAE), and root mean square error (RMSE).

the increasing library size. In particular, the predicted and measured values of Y predicted from the time-series data of X approached 1 as the library size increases (see the red line in Fig. 3). On the other hand, the predicted and measured values of X from the data of Y as described by the blue line in Fig. 3 are low, suggesting that there exists a directionality only from X to Y.

As demonstrated in this section, CCM allows us to infer causal relationship between two components from multivariate time-series data.
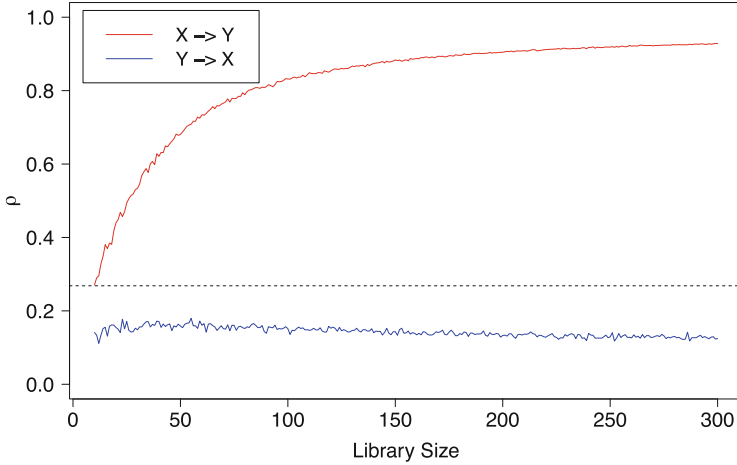
Fig. 3. Forecasting skills with different library sizes for convergent cross mapping (CCM). These skills are evaluated by correlation coefficient (ρ). Red and blue lines represent the library size of Y cross-map X (i.e., correlation coefficient of X predicted by Y) and X cross-map Y (i.e., correlation coefficient of Y predicted by X). The dash lines represents the linear correlation coefficient.

4 Pattern Similarity Between Optimal Embedding Dimension and Flow

In this section, we show that EDM can be used draw a phase diagram which is similar to a flow (vector-field) of a dynamical system. We consider two ecological species, denoted by x and y. We assume that x is not affected by y. More specifically, we consider the following system of differential equations:

$$\begin{aligned}
\frac{dx}{dt} &= x(a - bx), \\
\frac{dy}{dt} &= by(1 + x - y),
\end{aligned} \qquad (2)$$

Note that x is affected by x only, while y is affected by both x and y. We calculate an optimal embedding dimension for different initial values using simplex projection. Each of top panels in Fig. 4 describes a heatmap of optimal embedding dimension for different initial values. Interestingly, the right panel exhibits a similar pattern to the vector field of system (2). Note that nullcline and equilibrium point are clearly drawn in the heatmap of optimal embedding dimension. Although the generation mechanism of pattern similarity still remains currently unknown, these heuristic findings suggest that optimal embedding dimension of information for the flow of a dynamical system may capture nullclines and equilibrium.
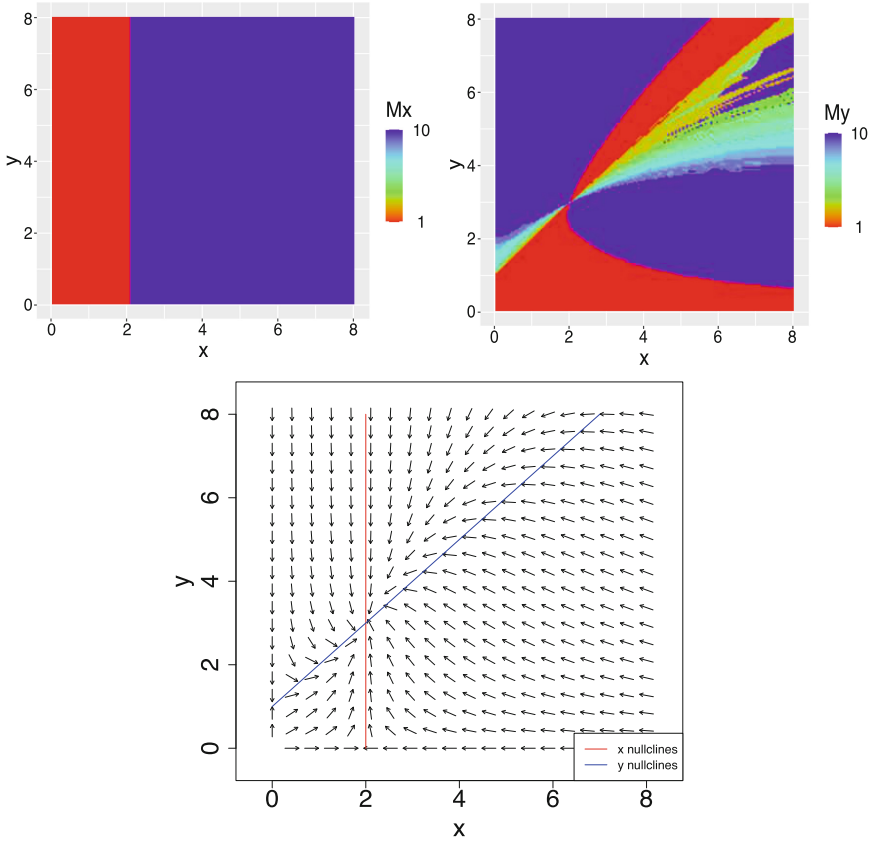
Fig. 4. Heatmaps of optimal embedding dimension for different initial values (top-left and top-right) and vector field of system (2) (bottom). The parameters are $a = 0.04$ and $b = 0.02$ and time step is set to 400 points.

Next, we consider a different mathematical model to check whether the heuristic findings shown in Fig. 4 can be observed as well. More specifically, we consider a Holling type II prey-predator model:

$$
\begin{aligned}
\frac{dx}{dt} &= rx\left(1 - \frac{x}{K}\right) - \frac{axy}{1 + hx}, \\
\frac{dy}{dt} &= \frac{bxy}{1 + hx} - cy,
\end{aligned}
\tag{3}
$$

where variables x and y denote the population density of prey and predator, respectively.

Note that system (3) can undergo Hopf bifurcation by changing b as a bifurcation parameter, known as the paradox of enrichment. In other words, system (3) can exhibit qualitatively different dynamical behaviors. Hence we generated three different synthetic time-series datasets by changing parameter b to check

whether the heatmap of optimal embedding dimension can capture the structure of the dynamical system.

More specifically, we selected two numerical values $b = 0.0120$ and $b = 0.0124$: the former value represents a situation that every trajectory converges to the unique stable coexistence equilibrium (Case1: stable) while the latter represents a situation that trajectories converge to a periodic orbit (Case2: unstable).

For each case, we calculated simplex projection for the synthetic time-series data generated from system (3) for different initial values. We examine how the values of the optimal embedding dimension change (represented in panels of Fig. 5). Interestingly, each heatmap exhibits a similar pattern to the vector field of system (3).

To quantitatively evaluate observed pattern similarities for systems (2) and (3), several values were arbitrarily picked up from case 1 (stable) and case 2 (unstable), respectively. Taking E_x and E_y as the magnitude of the optimal embedding dimension of X and Y, we define the following evaluation index:

$$M := \frac{m - Min(m)}{Max(m) - Min(m)}, \tag{4}$$

where $m := \sqrt{(E_x)^2 + (E_y)^2}$. Note that index M represents the magnitude of each optimal embedding dimension scaled by the minmax normalization [10].
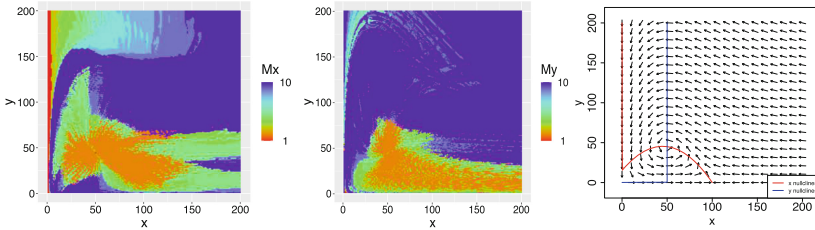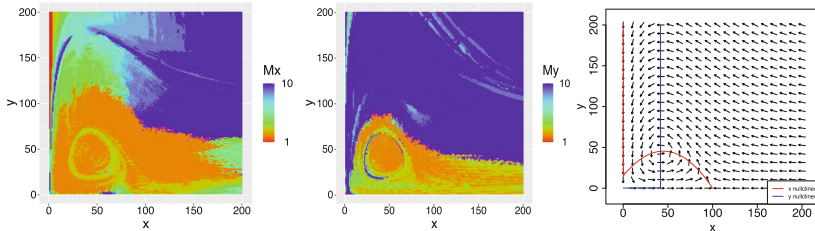
Fig. 5. Heatmaps of optimal embedding dimension [left/middle] and vector field [right] for Case 1 (stable) [top] and Case 2 (unstable) [bottom]. The parameters are $r = 0.03$, $K = 100$, $a = 0.002$, $h = 0.1$, $c = 0.1$, and $b = 0.0120$ (Stable) or $b = 0.0124$ (Unstable). Time step is set to 1000 points.
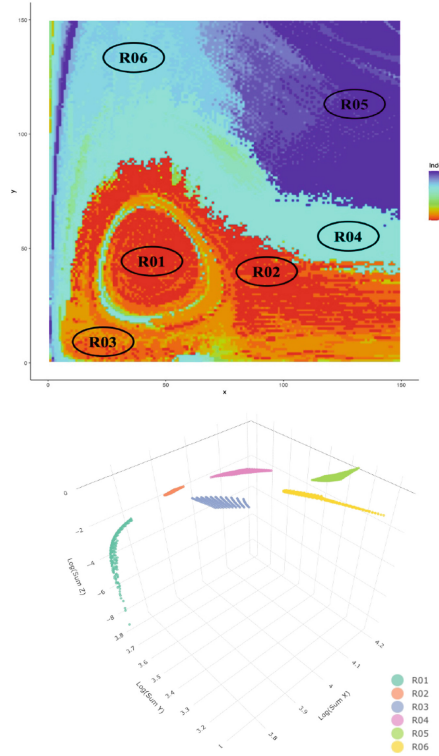
Fig. 6. The heatmap of evaluation index M [top panel] and 3D scatter plot z [bottom] for case 2 (unstable equilibrium), the corresponding. The entire region is naturally classified into six inclusion such region (R01–R06) by the optimal embedding dimension (different color panels). Note that each label (R01–R06) in the top panel corresponds to the labels in the bottom panel.

Based on the index, we compare and verify the similarity of population dynamics in regions with the same index value. On the other hand, to quantitatively evaluate the magnitude of flow speed for each trajectory, we define Z as an evaluation index (the bottom panel of Fig. 6):

$$Z := \sqrt{\frac{dx}{xt}^2 + \frac{dy}{xt}^2},$$ (5)

By comparing heatmap of M and 3D scatterplot of Z, we find an interesting observation that the entire region is naturally (without clastering) classified into six exclusive sub-regions.

Note that optimal embedding dimension using simplex projection is higher when trajectories are always close to each other (i.e., equilibrium). On the other hand, optimal embedding dimension is lower for trajectories showing moderate or rapid change (i.e., transition state).

5   Concluding Remarks

Mathematical oncology has recently contributed to achieve the following three significant milestones: (1) establishment of precise and reproducible predictions for the spatio-temporal progression of cancer, (2) avoidance and reduction of treatment resistance, and (3) integration of knowledge-based mathematical models with machine learning [11]. Despite the spreading availability of enormous data, we often face challenges to define what constitutes appropriate data. The current big data available in the field of cancer research do not necessarily cover every aspect but are often limited to specific time and space, environment, and context. Therefore, appropriate data collection is indispensable for building an accurate prediction model. For instance, when investigating the relationship among patient epidemiological characteristics [12], biopsy samples [13,14] and biomarkers, it is often inevitable to construct a prediction model based on inperfect data because biomarkers are often sensitive to clinically unobservable events such as the onset of metastases [15] and false-positive diagnoses [16]. Although empirical dynamic modeling (EDM) has initially been utilized in population dynamics study, the scope of its application has been spreading to the other field other than ecology because of its versatility: reconstructing of the state space of a system from observations of time series data and performs model-free analysis [17–20]. A typical field of application includes brain science [21,22]. An extended application of EDM to cancer research may make it possible to explore the relationship between patient conditions and biomarkers, or between molecular and cellular interactions from observed data.

In this chapter, we focused on empirical dynamic modeling (EDM). The present study has revealed a heuristic finding on relationship between optimal embedding dimension of nonlinear time-series data and vector field of a dynamical system. Although it is still not clear, the origin of the similarity observed in Sect. 4 might be possibly due to dependence on transient dynamics. Further considerations are left for our future work to obtain reasonable interpretations. If nonlinear time-series data of cancer population dynamics are available, the heuristic finding presented in this study may help to infer trajectories of cancer cell dynamics progression from time-series data of cancer cell dynamics based on the similarity to an optimal embedding dimension.

References

1. Mougi, A. (ed.): Diversity of Functional Traits and Interactions: Perspectives on Community Dynamics. Springer, Singapore (2020)
2. Takens, F.: Detecting strange attractors in turbulence. In: Rand, D., Young, L.-S. (eds.) Dynamical Systems and Turbulence, Warwick 1980. LNM, vol. 898, pp. 366–381. Springer, Heidelberg (1981). https://doi.org/10.1007/BFb0091924
3. McCann, K.S., Gellner, G. (eds.): Theoretical Ecology: Concepts and Applications. Oxford University Press, Oxford (2020)
4. Deyle, E.R., Sugihara, G.: Generalized theorems for nonlinear state space reconstruction. PLoS One **6**(3), e18295 (2011)
5. Chang, C.-W., Ushio, M., Hsieh, C.: Empirical dynamic modeling for beginners. Ecol. Res. **32**(6), 785–796 (2017). https://doi.org/10.1007/s11284-017-1469-9
6. Sugihara, G., et al.: Detecting causality in complex ecosystems. Science **338**(6106), 496–500 (2012)
7. Ushio, M., et al.: Fluctuating interaction network and time-varying stability of a natural fish community. Nature **554**, 360–363 (2018)
8. Sugihara, G., May, R.M.: Nonlinear forecasting as a way of distinguishing chaos from measurement error in time series. Nature **344**(6268), 734–741 (1990)
9. Hsieh, C.-H., Glaser, S.M., Lucas, A.J., Sugihara, G.: Distinguishing random environmental fluctuations from ecological catastrophes for the north pacific ocean. Nature **435**(7040), 336–340 (2005)
10. Gajera, V., Shubham, Gupta, R., Jana, P.K.: An effective Multi-Objective task scheduling algorithm using Min-Max normalization in cloud computing. In: 2016 2nd International Conference on Applied and Theoretical Computing and Communication Technology (iCATccT), pp. 812–816, July 2016
11. Rockne, R.C., et al.: The 2019 mathematical oncology roadmap. Phys. Biol. **16**(4), 041005 (2019)
12. de Koning, H.J., et al.: Benefits and harms of computed tomography lung cancer screening strategies: a comparative modeling study for the U.S. preventive services task force. Ann. Int. Med. **160**(5), 311–320 (2014)
13. Curtius, K., Hazelton, W.D., Jeon, J., Georg Luebeck, E.: A multiscale model evaluates screening for neoplasia in Barrett's esophagus. PLoS Comput. Biol. **11**(5), e1004272 (2015)
14. Hori, S.S., Lutz, A.M., Paulmurugan, R., Gambhir, S.S.: A model-based personalized cancer screening strategy for detecting early-stage tumors using blood-borne biomarkers. Cancer Res. **77**(10), 2570–2584 (2017)
15. Hanin, L., Pavlova, L.: Optimal screening schedules for prevention of metastatic cancer. Stat. Med. **32**(2), 206–219 (2013)
16. Ryser, M.D., Worni, M., Turner, E.L., Marks, J.R., Durrett, R., Shelley Hwang, E.: Outcomes of active surveillance for ductal carcinoma in situ: a computational risk analysis. J. Natl. Cancer Inst. **108**(5) (2016)
17. Tani, N., et al.: Small temperature variations are a key regulator of reproductive growth and assimilate storage in oil palm (Elaeis guineensis). Sci. Rep. **10**(1), 650 (2020)
18. Haaga, K.A., Brendryen, J., Diego, D., Hannisdal, B.: Forcing of late Pleistocene ice volume by spatially variable summer energy. Sci. Rep. **8**(1), 11520 (2018)
19. Luo, L., Cheng, F., Qiu, T., Zhao, J.: Refined convergent cross-mapping for disturbance propagation analysis of chemical processes. Comput. Chem. Eng. **106**, 1–16 (2017)

20. Wismüller, A., Wang, X., DSouza, A.M., Nagarajan, M.B.: A framework for exploring Non-Linear functional connectivity and causality in the human brain: mutual connectivity analysis (MCA) of Resting-State functional MRI with convergent Cross-Mapping and Non-Metric clustering, July 2014
21. Tajima, S., Yanagawa, T., Fujii, N., Toyoizumi, T.: Untangling brain-wide dynamics in consciousness by cross-embedding. PLoS Comput. Biol. **11**, e1004537 (2015)
22. Tajima, S., Mita, T., Bakkum, D.J., Takahashi, H., Toyoizumi, T.: Locally embedded presages of global network bursts. PNAS **114**, 9517–9522 (2017)

Mathematical Modeling for Angiogenesis

Tatsuya Hayashi[(✉)]

Graduate School of Information Science and Technology, Hokkaido University,
Sapporo, Japan
`thayashi@ist.hokudai.ac.jp`

Abstract. Angiogenesis is the morphogenetic phenomenon in which new blood vessels emerge from an existing vascular network and configure a new network. To understand complex movements of endothelial cells and molecular processes that drive angiogenic morphogenesis, time-lapse live imaging of dynamic collective cell migration and mathematical modeling have proven highly informative. This paper focuses on recent mathematical models for the dynamics of endothelial cells during angiogenesis and presents the importance of both repulsive and attractive two-body interactions by showing results of simulation.

1 Introduction

Angiogenesis is a phenomenon that new blood vessels are formed by sprouting from existing vessels. Branch elongation and bifurcation during angiogenesis are driven by collective motion of endothelial cells (ECs). Angiogenesis occurs in response to tissue ischemia or increased oxygen demand during various processes such as wound healing, placenta formation and tumor growth. Therefore, elucidation of mechanisms of angiogenesis is essential to expand our knowledge about physiological and pathological phenomena.

Collective cell migration in morphogenesis is often regulated by leader cells, which are accompanied by other follower cells that uniformly migrate. As for angiogenic elongation, an EC called a "tip cell", is commonly thought to migrate in the direction of new vessel [1,2]. The adjacent ECs are assumed to follow the tip cell as stalk cells connected to each other through cell-cell junctions. However, experiments with time-lapse live imaging have revealed that cell migration during angiogenic morphogenesis involves complex behavior. Individual ECs exhibit dynamic and heterogeneous motion, move forwards and backward along the path of the elongation and change often their positions even at the tips. This 'cell mixing' effect was observed in both *in vitro* and *in vivo* experiments [3,4]. Furthermore, Sugihara *et al.* observed the dynamics of ECs in sprouting blood vessels of zebrafish and found that the movement of tip cells depends on the presence of stalk cells within a proper distance [5]. For a tip cell and stalk cells moving forward along the elongating branch, the isolated tip cell stopped moving after a laser shot ablated the follower EC. However, the tip cell started moving again when another EC approached it. This result suggests that the

interaction between ECs plays an essential role in the complex multicellular dynamics in angiogenesis. To uncover hidden laws driving angiogenic morphogenesis, Takubo *et al.* analyzed EC behaviors in an *in vitro* angiogenic sprouting assay using mouse aortic explants [6]. Time-lapse imaging of sprouting from cell sheets around tissue explants showed directional collective cell movements with frequent U-turns. Imaging of isolated branches with basal cell sheets removed revealed that a constant supply of migrating cells is required for ECs to branch forward.

A lot of mathematical models for angiogenesis have been proposed from various points of view: a hybrid model of cell migration on an elastic matrix of fibers [7], a mesoscopic lattice-based stochastic model in relation to deterministic continuous models [8], a phase-field continuous model of sprouting angiogenesis described by compact partial differential equations [9], and continuous model described by differential equations [10]. A stochastic states model and the differential equation model corresponding to its continuous limit have been discussed to explain the observation in the dynamics of ECs along an elongating branch [5]. Matsuya *et al.* focused on the effects of cell-to-cell interaction and proposed a one-dimensional discrete model that incorporates deterministic two-body interaction between ECs, which do not consider stochastic fluctuation and a gradient distribution of angiogenic factors such as vascular endothelial growth factor (VEGF) [11]. This model has succeeded in explaining complex EC behaviors by cell-to-cell interactions. Takubo *et al.* quantitatively verified the two-body interaction, which had not been quantified in the one-dimensional model. Furthermore, they extended the model to take into account the interaction, which is thought to be caused by the polarity of ECs.

In Sect. 2, we present the one-dimensional model proposed by Matsuya et al. and show numerical simulation results. A power-law scaling behavior in this model is shown and analyzed. We present the extended model and a parameter estimation in Sect. 3. Section 4 is devoted to concluding remarks.

2   Discrete Dynamics System Model for Angiogenesis

The system is essentially two dimensional because murine aortic rings were embedded and ECs were cultured in collagen gel placed in a shallow petri dish. We neglect the effects of anastomosis(reconstruction of vessels) and cell division of ECs in neogenetic vessels. Actually cell division is rarely observed in the time span of the experiment (∼5% a day). We consider formation of one of the newly generated blood vessel networks which arise from the aortic ring. We suppose that there is no neogenetic vessel sprouts in a certain direction according to the supply of ECs for $t > 0$. The nth ($n = 0, 1, 2, \dots$) EC comes to the origin of this neogenetic vessel network at time step $t = \sum_{i=1}^{n} a_i$ with an initial velocity $v_{ini}(n) \geq 0$, where $a_i \in \mathbb{Z}_+$ is the time interval between the incidence of ith EC and that of $(i-1)$th EC. Here, we focus on the dynamics of ECs only in the first neogenetic vessel and the effects of two-body interactions between ECs in a branch. Interactions among ECs are quite complicated and have not been well uncovered. We assume that the interaction between ECs is caused by direct contact
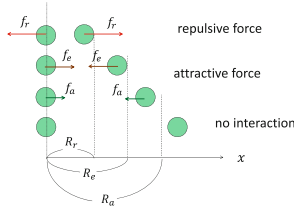
Fig. 1. Schematic figure of two-body interaction in the present model.

of their membranes; chemical signals or mechanical force induced by cell-to-cell contact yields the driving force of ECs. For short distance, the interaction force will turn out to be repulsive due to excluded volume effect, while it will turn out to be attractive if the distance becomes larger because of the interaction with pseudopodia. Thus the mathematical model we present here is given as

$$x_n^{t+1} - x_n^t = v_n^t \tag{1}$$

$$v_n^{t+1} - v_n^t = -\gamma v_n^t + \sum_{k \neq n} F\left(x_n^t - x_k^t\right), \tag{2}$$

where $x_n^t \geq 0$ is the position of the nth EC at time step $t \in \mathbb{Z}_+$, the time unit ($\Delta t = 1$) may correspond to the specific response time, the parameter $\gamma (0 < \gamma < 1)$ denotes the coefficient of conflict, and F denotes the two-body interaction between ECs.

The interaction F is adopted the following simple form by taking the three characteristic lengths R_r, R_e, R_a into account:

$$F(x) := \begin{cases} \mathrm{sgn}(x)f_r & (0 < |x| \leq R_r) \\ -\mathrm{sgn}(x)f_e & (R_r < |x| \leq R_e) \\ -\mathrm{sgn}(x)f_a & (R_e < |x| \leq R_a) \\ 0 & (R_a < |x|) \end{cases} \tag{3}$$

where $\mathrm{sgn}(x) := x/|x|$ and f_r, f_e, f_a are the positive constant for interaction strengths (Fig. 1). Although the case $x_n^t = x_k^t$ ($n \neq k$) may be possible in principle, practically this model can neglect this case in numerical simulation.

Equation (1) means that v_n^t is the velocity of the nth EC at time step t and (2) is the discrete analogue of the Newtonian equation of motion. We do not consider the effect that ECs in the neogenetic vessels go back into the existing aortic ring, and x_n^t has to take non-negative value. To avoid back flow of ECs into the source, we reset $x_n^{t+1}=0$ and $v_n^{t+1} = 0$ if $x_n^{t+1} \leq 0$ in (1). In order to see

(a) Repulsive force only   (b) Attractive force only   (c) Both
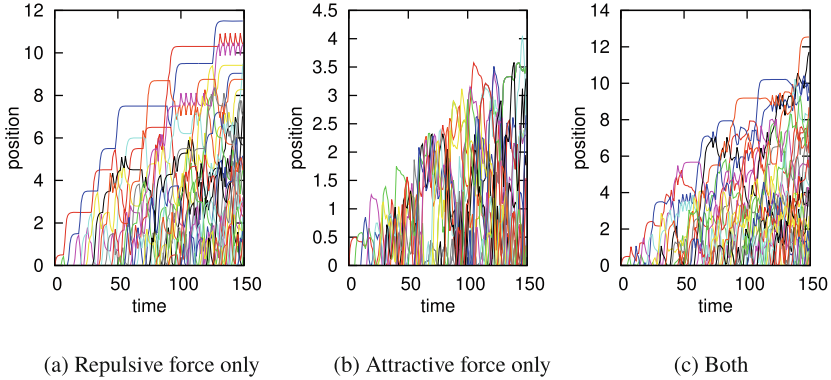
Fig. 2. Trajectories of EC movements during elongation with parameters $R_r = 0.2, R_e = 0.4, R_a = 0.7, \gamma = 0.6, a = 5, v_{ini} = 0.3, v_{max} = 1.0$ and (a) Repulsive force only: $f_r = 0.6, f_e = 0, f_a = 0$, (b) Attractive force only: $f_r = 0, f_e = 0.15, f_a = 0.05$ and (c) Both: $f_r = 0.6, f_e = 0.15, f_a = 0.05$.

the effects of repulsive and attractive interactions, we simulated (1) and (2) for three types of two-body interactions: (a) only repulsive ($f_e \rightarrow -f_e, f_a \rightarrow -f_a$ in (1), (b) only attractive ($f_r \rightarrow -f_r$), and (c) both interactions given in (1). A typical result is shown in Fig. 2, where we put $a_i = a$(constant) and $v_{ini}(i) = v_{ini}$ (constant) for all i.

When interaction is only repulsive, the distribution of ECs is fairly uniform as shown in Fig. 2(a), while if interaction is only attractive, ECs clump together as in Fig. 2(b). In case both repulsive and attractive interactions coexist as is supposed in this model, ECs clearly show the cell mixing behavior and the distribution of ECs is sufficiently uniform. The cell mixing behavior is also seen in Fig. 2(a), though it is less frequent than in Fig. 2(c). As a consequence, repulsive interaction between ECs is necessary for smoothing the distribution of ECs and attractive interaction enhances the cell mixing behavior in the dynamics of ECs. Figure 4 shows the time dependence of the reaching position of ECs, that is, the position of an EC at the tip. As shown in Fig. 4(b), it almost scales as $t^{2/3}$ for different strengths of attractive interaction. In fact, we can find that this exponent 2/3 is observed almost irrespective of the parameters for interactions, supply rate, and initial velocity. In particular, the data of numerical simulation closely fit, the curves $\propto t^{2/3}$ in the case of no attractive interaction. For random walk, the reaching position scales as $t^{1/2}$, while it scales as t^1 for wave propagation. The exponent 2/3 suggests that the ECs in the present model show the dynamics between random walk and wave propagation. The theoretical explanation of this universal exponent is given in Appendix.

(a) Repulsive force only   (b) Attractive force only   (c) Both
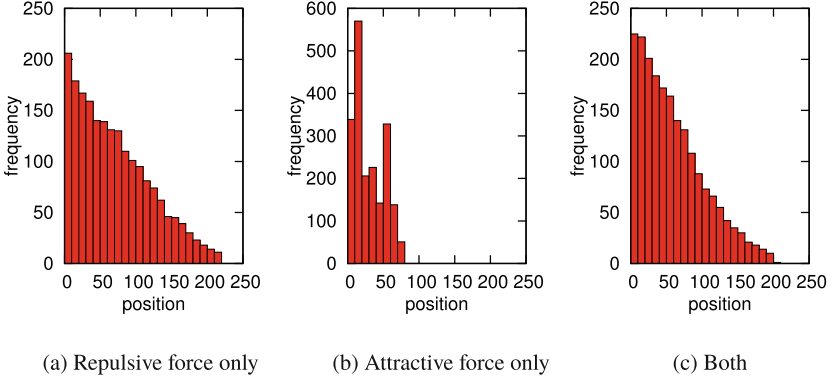
Fig. 3. Distributions of ECs at time step $t = 10^4$. Parameters are the same as those in Fig. 2.

3 A Two-Dimensional Model Considering the Anisotropic Nature of Two-Body Interactions

Under the assumption of simple two-body interactions between ECs, the mathematical model discussed in previous section successfully reproduced the cell mixing effects. However, the two-body interaction is not quantitatively validated. In this section, we present the parameter estimation of the model from the position data of ECs obtained by an automated cell tracking system. We first extended the one-dimensional model to a two-dimensional one as follows,

$$x_n^{t+1} - x_n^t = v_n^t \tag{4}$$

$$v_n^{t+1} - v_n^t = -\gamma v_n^t + \sum_{k \neq n} F\left(\left\|x_n^t - x_k^t\right\|\right) \frac{x_n^t - x_k^t}{\left\|x_n^t - x_k^t\right\|}, \tag{5}$$

where $x_n^t \in \mathbb{R}^2$ and $v_n^t \in \mathbb{R}^2$ are the position and the velocity of the nth EC at time step t, respectively, and $\gamma > 0$ denotes the coefficient of damping. The interaction term is isotropic, which depends only on the relative positions $x_n^t - x_k^t$ between two ECs. We estimate the parameter γ and the force function F from the experimental data of the time-lapse live imaging of ECs. The interaction between ECs are supposed to be short-range rather than long-range force. Therefore, let us consider the rectangular kernel on bounded support as the density kernel,

$$F(x) = \sum_{k=0}^{N-1} b_k \left(\theta \left(x - k \frac{R_d}{N} \right) - \theta \left(x - (k+1) \frac{R_d}{N} \right) \right), \tag{6}$$

Here R_d is the upper bound distance of cell-to-cell interaction, the range $[0, R_d]$ is divided into N equal intervals, and θ denotes the step function:

$$\theta(x) := \begin{cases} 1 & (x > 0) \\ 0 & (x \leq 0) \end{cases} \tag{7}$$
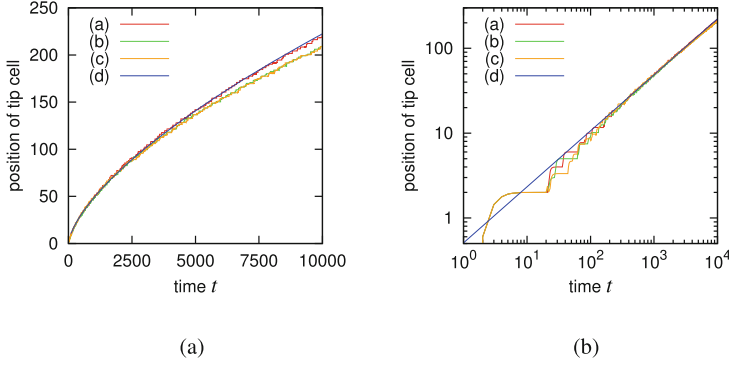
Fig. 4. (a) The parameters are $R_r = 0.2, R_e = 0.4, R_a = 0.7, f_r = 0.6, f_a = 0, v_{ini} = 0, \gamma = 0.6, v_{max} = 1.0, \langle a \rangle = 5$, and (red curve) $f_e = 0$, (green curve) $f_e = 0.2$, (orange curve) $f_e = 0.4$. The blue curve satisfies $y = 0.5092 t^{0.6601}$. (b) Log-log plot of the four curves in (a). The straight line satisfies $\ln(y) = 0.6601 \ln(t) - 0.6749$, which is fitted to the red curve. "$\langle a \rangle = 5$" means that the injection period is random with average period 5.

Given N and R_d, we minimize the following error function E for the estimation of the parameter γ and $b_k (k = 0, 1, \ldots, N-1)$:

$$E = \sum_t \sum_n \left\| \left(\overline{v}_n^{t+1} - \overline{v}_n^t \right) - \left(-\gamma \overline{v}_n^t + \sum_{k \neq n} F \left(\| \overline{x}_n^t - \overline{x}_k^t \| \right) \frac{\overline{x}_n^t - \overline{x}_k^t}{\| \overline{x}_n^t - \overline{x}_k^t \|} \right) \right\|^2, \qquad (8)$$

where $\overline{x}_n^t$ is experimentally obtained cell position of nth EC at time t, and $\overline{v}_n^t$ is the velocity as numerical difference. Since E is a quadratic polynomial of $N + 1$ variables γ and $\{b_k\}_{k=0}^{N-1}$, the minimum of E is unique.

Figure 5 shows the estimated function F and potential from F when $N = 25$ and $R_d = 50\mu m$. ECs experience distance-dependent interactions: with repulsive force in ~8 μm and attractive force in 8~30 μm. Since each EC has its own volume, proximity of two cells may produce the repulsive force as a result of excluded volume effects. On the other hand, the attractive force may reflect contact-dependence acceleration.

Furthermore, since the shape of an EC is anisotropic, we consider anisotropy of cellular interactions. The presence of ECs moving backward produces different pattern of directionality as follows: (i) two ECs move into the opposite direction apart from each other, (ii) two ECs move into the opposite direction approaching each other, (iii) two ECs move in the same direction. Based on these classifications, we extended Eq. (4) to the following equation.

$$v_n^{t+1} - v_n^t = -\gamma v_n^t + \sum_{k \neq n} F_1 \left(\| x_n^t - x_k^t \| \right) \frac{x_n^t - x_k^t}{\| x_n^t - x_k^t \|} \theta \left((x_n^t - x_k^t) \cdot v_n^t \right) \theta \left(-(x_n^t - x_k^t) \cdot v_k^t \right)$$

$$+ \sum_{k \neq n} F_2 \left(\| x_n^t - x_k^t \| \right) \frac{x_n^t - x_k^t}{\| x_n^t - x_k^t \|} \theta \left(-(x_n^t - x_k^t) \cdot v_n^t \right) \theta \left((x_n^t - x_k^t) \cdot v_k^t \right)$$
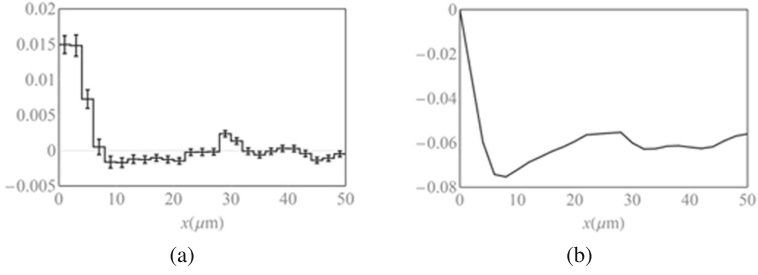
Fig. 5. (a) Estimated force $F(x)$ with $R_d = 50$, $N = 25$. (b) $-\int_0^x F(\mu)d\mu$, potential of (a).
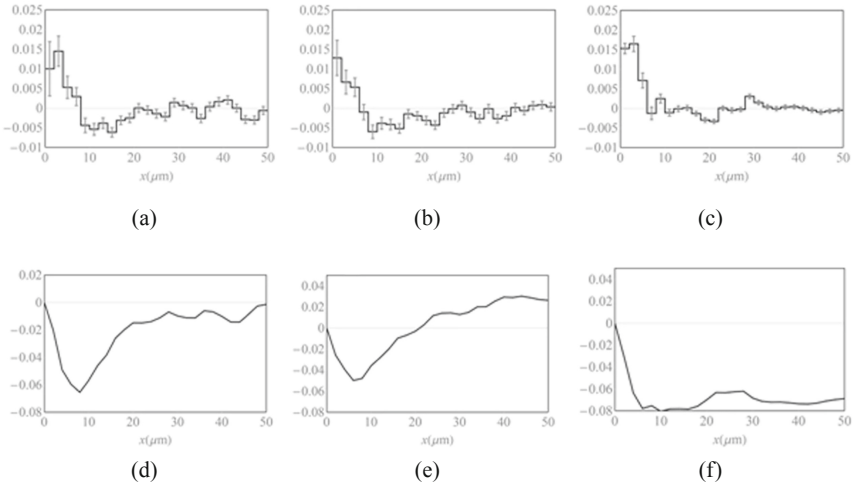
Fig. 6. Estimated force (a) $F_1(x)$, (b) $F_2(x)$, (c) $F_3(x)$. These functions were obtained in accordance with experimental results used in the estimation of $F(x)$ (Fig. 5). Potentials of each forces, (d) $-\int_0^x F_1(\mu)d\mu$, (e) $-\int_0^x F_2(\mu)d\mu$, (f) $-\int_0^x F_3(\mu)d\mu$, respectively.

$$+ \sum_{k \neq n} F_3 \left(\left\| x_n^t - x_k^t \right\| \right) \frac{x_n^t - x_k^t}{\left\| x_n^t - x_k^t \right\|} \theta \left(\left(x_n^t - x_k^t \right) \cdot v_n^t \right) \theta \left(\left(x_n^t - x_k^t \right) \cdot v_k^t \right)$$

$$+ \sum_{k \neq n} F_3 \left(\left\| x_n^t - x_k^t \right\| \right) \frac{x_n^t - x_k^t}{\left\| x_n^t - x_k^t \right\|} \theta \left(- \left(x_n^t - x_k^t \right) \cdot v_n^t \right) \theta \left(- \left(x_n^t - x_k^t \right) \cdot v_k^t \right)$$

where the centered dot '$\cdot$' is the inner product and three force functions F_1, F_2, F_3, which correspond to the three patterns (i), (ii) and (iii), respectively, were estimated by a similar method as above. Figures 6(a)–(c) show the estimated three forces. In F_1 and F_2, both repulsion ($\sim 8\,\mu$m) and attraction ($8 \sim 30\,\mu$m) were evident. By contrast, F_3 contained only a repulsive component in $\sim 8\,\mu$m with

no evident attractive component. Figures 6(d)–(f) are the integrals of Figs. 6(a)–(c) respectively, that is, potential. While Fig. 6(d) and (e) clearly indicate the positive slope (8~30 μm), Fig. 6(f) shows relatively flat in the region 6~50 μm. Hence, it is suggested that an attractive interaction occurs between a pair of a cell moving forward and backward, resulting in accelerated cell movement when passing each other. On the contrary for lateral cells, attractive force is not much driven.

4   Concluding Remarks

In this paper, we have discussed a discrete dynamical model for angiogenesis which fits well some aspects of collective cell migration during angiogenesis. The dynamics of each ECs is assumed to be mainly ruled by deterministic two-body interactions which consist of short-range repulsion due to excluded volume effect and long-range force through pseudopodia and described by a one-dimensional discrete Newtonian equation of motion. Under this interaction, the tip position of a neogenetic vessel at time step t, $l(t)$, develops as $l(t) \propto t^{2/3}$. We have given an interpretation on this value of exponent, 2/3, based on the equation of continuity and a hypothesis of existence of a scaling function. Although this model has succeeded in explaining complex EC behaviors by cell-to-cell interactions based on simple Newtonian dynamics, the assumption of two-body interactions is not quantitatively validated. Furthermore, anisotropic nature of two-body interactions, which may be caused by cellular polarity, is not considered. The parameter estimation discussed in Sect. 3 revealed distance-dependent intercellular forces; a repulsive force in ~8 μm and attractive force in 8~20 μm, which are consistent with the assumption of the one-dimensional model. Theses results suggest that the deterministic two-body interaction between ECs is an essential factor in complex EC behaviors such as cell mixing. However, these models deal with the early stage of angiogenesis and have not included chemotaxis, lumen formation, and remodeling of blood vessels, which are important in construction of *in vivo* blood vessel networks. Realistic mathematical modeling for angiogenesis and its application to medicine are an important issue. Development of the models by incorporating these factors is expected to uncover novel mechanisms and provide a theoretical framework for clinical trials targeting angiogenesis in the future.

Appendix

Here, we explain the scaling law of the position of an EC at the tip according to the method in [11]. Let $\rho(x,t)$ be the density of the ECs at time t and position x. In continuum limit, $\rho(x,t)$ satisfies the equation of continuity:

$$\frac{\partial \rho(x,t)}{\partial t} + \frac{\partial}{\partial x}\left(\rho(x,t)v(x,t)\right) = 0, \tag{9}$$

where $v(x, t)$ is the field of velocity ECs at (x, t). From (1), in quasi equilibrium, we may approximate $v(x, t)$ as

$$v(x, t) \sim \frac{1}{\gamma} \int F(x - y)\rho(y, t)dy. \tag{10}$$

If $\rho(x, t)$ is a smooth function of x, we can expand

$$\rho(y, t) = \rho(x, t) + \frac{\partial \rho(x, t)}{\partial x}(y - x) + \frac{\partial^2 \rho(x, t)}{\partial x^2}\frac{(y - x^2)}{2} + \cdots. \tag{11}$$

We further assume that higher derivatives of $\rho(x, t)$ takes smaller absolute values than its first derivate $\frac{\partial \rho(x, t)}{\partial x}$. In fact, as shown in Figs. 3(a) and 3(c), the density $\rho(x, t)$ is approximately a linear function, which implies that its higher order derivatives are negligible. Since $F(x)$ is an odd function, neglecting the higher order terms, we have

$$v(x, t) \sim \frac{1}{\gamma} \int (y - x)F(x - y)\rho(y, t)\frac{\partial \rho(x, t)}{\partial x}dy =: A_{\text{eff}}\frac{\partial \rho(x, t)}{\partial x}, \tag{12}$$

where A_{eff} is a constant depending on the parameter $\gamma, f_r, f_e, f_a, R_r, R_e, R_a$. Hence, (9) gives

$$\frac{\partial \rho(x, t)}{\partial t} + A_{\text{eff}}\frac{\partial}{\partial x}\left(\rho(x, t)\frac{\partial \rho(x, t)}{\partial x}\right) = 0. \tag{13}$$

Suppose that $\rho(x, t)$ has a scaling form with exponents α, β as

$$\rho(x, t) = t^\alpha G\left(x/t^\beta\right). \tag{14}$$

Then, from (13), we have

$$t^{\alpha-1}\left\{\alpha G(X) - \beta X G'(X)\right\} + t^{2(\alpha-\beta)}A_{\text{eff}}\left\{G'(X)^2 + G(X)G''(X)\right\} \sim 0 \ (X := x/t^\beta).$$

Hence, under the assumption of the scaling form (14), we find that

$$\alpha - 1 = 2(\alpha - \beta) \tag{15}$$

Since the number of ECs increases linearly in t,

$$\int_0^{l(t)} \rho(x, t)dx = \frac{t}{\langle a \rangle}, \tag{16}$$

where $l(t)$ is the position of the tip at which $\rho(x, t) = 0$ and a is the average injection rate of ECs, and we have

$$t^{\alpha+\beta} \int_0^{X_l} G(X)dX = \frac{t}{\langle a \rangle}, \tag{17}$$

The constant X_l is considered to be the first 0 of $G(X)$ for $X > 0$ (or a cut-off length), and $l(t) = X_l t^\beta$. Since the integral of $G(X)$ over X does not depend on time t, we have

$$\alpha + \beta = 1. \tag{18}$$

From (15) and (18), we obtain

$$\alpha = \frac{1}{3}, \beta = \frac{2}{3}. \tag{19}$$

Therefore, $l(t) \propto t^{2/3}$ and the reaching position of ECs scales as $t^{2/3}$.

References

1. Holderfield, M.T., Hughes, C.C.: Crosstalk between vascular endothelial growth factor, notch, and transforming growth factor-beta in vascular morphogenesis. Circ. Res. **102**, 637–652 (2008)
2. Smet, F.D., Segura, I., Bock, K.D., Hohensinner, P.J., Carmeliet, P.: Mechanisms of vessel branching: filopodia on endothelial tip cells lead the way. Arterioscler. Thromb. Vasc. Biol. **29**, 639–649 (2009)
3. Arima, S., et al.: Angiogenesis morphogenesis driven by dynamic and heterogeneous collective endothelial cell movement. Development **138**, 4763–4776 (2011)
4. Jakobsson, L., et al.: Endothelial cells dynamically compete for the tip cell position during angiogenic sprouting. Nat. Cell Biol. **12**, 943–953 (2010)
5. Sugihara, K., et al.: Autonomy and non-autonomy of angiogentic cell movements revealed by experiment-driven mathematical modeling. Cell Rep. **13**, 1814–1827 (2015)
6. Takubo, N., et al.: Cohesive and anisotropic vascular endothelial cell motility driving angiogenic morphogenesis. Sci. Rep. **9**, 9304 (2019)
7. Stéphanou, A., Floc'h, S.L., Chauvière, A.: A hybrid model to test the importance of mechanical cues driving cell migration in angiogenesis. Math. Model. Nat. Phenom. **10**, 142–165 (2015)
8. Spill, F., Guerrero, P., Alarcon, T., Maini, P.K., Byrne, H.M.: Mesoscopic and continuum modelling of angiogenesis. J. Math. Biol. **70**(3), 485–532 (2014). https://doi.org/10.1007/s00285-014-0771-1
9. Santos-Oliveira, P., et al.: The force at the tip-modelling tension and proliferation in sprouting angiogenesis. PLoS Comput. Biol. **11**, e1004436 (2015)
10. Mada, J., Matsuya, K., Yura, F., Kurihara, H., Tokihiro, T.: A mathematical modeling of angiogenesis. JSIAM **26**, 105–123 (2016)
11. Matsuya, K., Yura, F., Mada, J., Kurihara, H., Tokihiro, T.: A discrete mathematical model for angiogenesis. SIAM J. Appl. Math. **76**, 2243–2259 (2016)

Floating Potential Boundary Condition in Smooth Domains in an Electroporation Context

A. Collin, S. Corridore, and C. Poignard[✉]

INRIA, Bordeaux INP, CNRS, Univ. Bordeaux, IMB,
UMR 5251 351 Cours de la Libération, 33400 Talence, France
`clair.poignard@inria.fr`

Abstract. In electromagnetism, a conductor that is not connected to the ground is an equipotential whose value is implicitly determined by the constraint of the problem. It leads to a nonlocal constraints on the flux along the conductor interface, so-called floating potential problems. Unlike previous numerical study that tackle the floating potential problems with the help of advanced and complex numerical methods, we show how an appropriate use of Steklov-Poincaré operators enables to obtain the solution to these partial differential equations with a non local constraint as a linear (and well-designed) combination of $N + 1$ Dirichlet problems, N being the number of conductors not connected to a ground potential. In the case of thin highly conductive inclusions, we perform an asymptotic analysis to approach the electroquasistatic potential at any order of accuracy. In particular, we show that the so-called floating potential approaches the electroquasistatic potential with a first order accuracy. This enables us to characterize the configurations for which floating potential approximation has to be used to accurately solve the electroquasistatic problem.

Keywords: Floating potential · Dirichlet to Neumann operator · Thin conductive layer · Asymptotic analysis

1 Introduction

The computation of the electroquasistatic electric field in high contrasted domains is a research field which is active for several decades in both electrical engineering and applied mathematics research areas [1,3,4,9,12]. The interest has increased a lot for the last decade with the use of pulsed electric field for clinical ablation [5,7,8]. In particular, in the context of the insertion of multiple needles, the influence of the inactive electrods on the electric field distribution has to be precisely accounted to accurately determine the ablation region. The

focus of this paper is to present an effective and rigorous way to compute the
static electric field in the case of highly conductive thin inclusions.

The electroquasistatic theory states that the surface of a highly conductive
conductor is an equipotential surface, whose value is determined implicitly by
the constraints of the problem. This is the so-called floating potential problem
which has been studied for several decades. In [1] Amann *et al.* have shown that
the penalization method, which consists in imposing a high conductivity in the
inclusion provides a less accurate electric potential than a well-designed numer-
ical method for the floating potential problem. This result may seem strange,
since the penalization is somehow the model of the real problem, while the float-
ing potential is a perfect conductor approximation. Thus it is natural to wonder
how the floating potential approaches the real electric potential, whether there is
a relation between the size and the conductivity of the high conductive material
which prevents the use of this approximation, and if it is possible to increase the
accuracy with an asymptotic analysis. The aim of this paper is to address these
questions for thin and highly conductive inclusions.

1.1   Preliminary Numerical Observations on Concentric Disks

As preliminary, we investigate the observations of Amann *et al.* on a simplistic
case, for which an explicit solution is available. We consider the case of a dielectric
(low) conductive material Ω which is the annulus of radii $r_0 \in (0,1)$ and 1
and with conductivity equal to 1, surrounded by a high conductive sheet $\mathcal{O}_\varepsilon$
of thickness ε, and whose conductivity –after nondimensionalisation– is of order
$1/\varepsilon^\ell$, where $\ell = 1$ or 2 and ε is a small parameter. The electroquasistatic potential
u_ε satisfies the following elliptic problem

$$\frac{1}{r}\partial_r(r\partial_r u_\varepsilon) + \frac{1}{r^2}\partial_\theta^2 u_\varepsilon = 0 \quad \text{in} \quad (\{r_0 < r < 1\} \cup \{1 < r < 1+\varepsilon\}) \times \mathbb{R}/(2\pi\mathbb{Z}), \tag{1a}$$

with the following transmission conditions:

$$u_\varepsilon|_{r=1-} - u_\varepsilon|_{r=1+} = 0, \qquad \partial_r u_\varepsilon|_{r=1-} - \frac{1}{\varepsilon^\ell}\partial_r u_\varepsilon|_{r=1+} = 0, \tag{1b}$$

and the boundary conditions

$$\partial_r u_\varepsilon|_{r=1+\varepsilon} = 0, \qquad u_\varepsilon|_{r=r_0} = 1 + e^{i\theta}. \tag{1c}$$

The corresponding floating potential problem consists in finding $(u, \alpha) \in H^1(\Omega) \times \mathbb{Z}$ such that

$$\frac{1}{r}\partial_r(r\partial_r u) + \frac{1}{r^2}\partial_\theta^2 u = 0 \quad \text{in} \quad \{r_0 < r < 1\} \times \mathbb{R}/(2\pi\mathbb{Z}), \tag{2a}$$

with the boundary conditions

$$u|_{r=1} = \alpha, \qquad \text{such that} \quad \int_0^{2\pi} \partial_r u(1, \theta)\, d\theta = 0, \tag{2b}$$

$$u|_{r=r_0} = 1 + e^{i\theta}, \tag{2c}$$

To prevent errors due to numerical computations, it is convenient to give the expression of the solution u^{exact} to Problem (1). In $\{r_0 < r < 1\} \times \mathbb{R}/(2\pi\mathbb{Z})$, u^{exact} reads:

$$u_\varepsilon^{exact}(r,\theta) = \frac{\varepsilon r_0 e^{i\theta}}{d(r_0,\varepsilon)} \left(\left(\varepsilon^{l+1} + 2\varepsilon^l + 2\varepsilon^{l-1} - \varepsilon - 2\right) r + \frac{(\varepsilon^{l+1} + 2\varepsilon^l + 2\varepsilon^{l-1} + \varepsilon + 2)}{r} \right) + 1,$$

and in $\{1 < r < 1 + \varepsilon\} \times \mathbb{R}/(2\pi\mathbb{Z})$ it reads

$$u_\varepsilon^{exact}(r,\theta) = \frac{2\varepsilon^l r_0 e^{i\theta}}{d(r_0,\varepsilon)} \left(r + \frac{(\varepsilon+1)^2}{r} \right) + 1,$$

where $d(r_0,\varepsilon) = 2\varepsilon^l r_0^2 (1 + (\varepsilon+1)^2) - \varepsilon(r_0^2 - 1)(\varepsilon^{l+1} + 2\varepsilon^l + 2\varepsilon^{l-1} + \varepsilon + 2)$.

This solution is then compared with the numerical resolution by standard second order finite difference scheme. This enables us to compare simultaneously how the solution to Problem (1) is approached by the solution to Problem (2), and how accurate is the standard second order numerical scheme for Problem (1). Numerical results are shown in Fig. 1. Two main observations arise from these simplistic simulations.

First, for $\ell = 1$, the floating potential does not approach the solution to Problem (1), while it does with an order of accuracy in $O(\varepsilon)$ for $\ell = 2$, which means that floating potential cannot be used to approach the electric potential when the ratio R_{length} of the thickness of the conductor divided by the characteristic length of the dielectric is of the same order as the ratio R_{cond} of the conductivity of the dielectric divided by the conductivity of the high conductive sheet. Second, one can see that when ε becomes too small compared with the mesh grid, the numerical solution to the Problem (1) is not accurate, which provides an explanation to the statement by Amann *et al.* that the penalization method is less accurate than the floating potential.

1.2   Outline of the Paper

As shown on the previous simplistic example, the direct resolution of the electroquasistatic problem in a domain with highly conductive inclusion leads to *ill-conditioned* matrix and floating potentials are preferred to avoid the computational cost. The numerical resolution of such floating potential problems has been studied for several decades. One can cite for instance the paper by Dular *et al.* [3], where the authors proposed a finite element method, which consists in enriching the finite elements space with specific functions defined on the nodes of the interfaces Γ_k. Amann *et al.* proposed in [1] a boundary element method to tackle the problem using single boundary layer integral formulation of the solution. Note that recently, a hybrid Galerkin method has been proposed by Sala *et al.* for a similar problem in the context of ocular hemodynamic, the electric potential being replaced by the Darcy pressure [11].

The aim of the paper is twofold. On the one hand, after the proof of the well-posedness of the floating potential problem in the case of N multiple highly
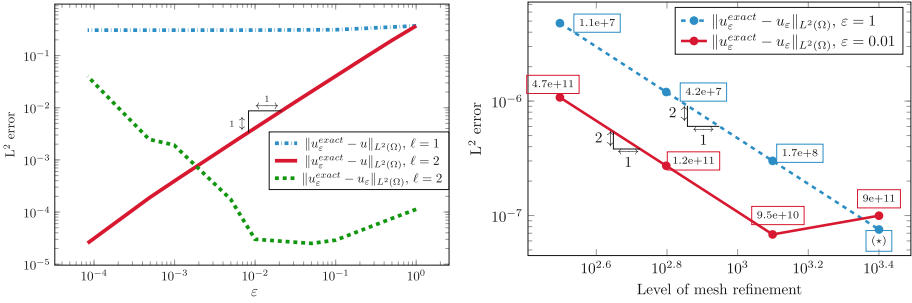
Fig. 1. (Left): Comparison of the explicit solution u_ε^{exact} to Problem (1) with the floating potential problem for $\ell = 1$ (dashed and dotted blue line) and 2 (red line), and comparison of the explicit and the numerical solutions (1) (green dashed line) as ε tends to zero. One can see that for $\ell = 1$ the floating potential is not accurate: the conductive sheet is too thin to be an equipotential. For $\ell = 2$, the floating potential approaches the exact solution with an order of accuracy in $O(\varepsilon)$. Due a high *condition number* of the matrix, a direct numerical resolution of Problem (1) gives a worse approximation for smaller ε. (Right): Numerical convergence with the steps $(d\theta, dr) \in \{(314, 200), (628, 400), (1256, 800), (2512, 1600)\}$ of the second order scheme to solve Problem (1) for $\varepsilon = 1$ (dashed blue line) and $\varepsilon = 0.01$ (red line). Condition number of the matrix for the discretization of Problem (1) grows considerably when ε approaches zero. With small discretization steps the instability increases and the numerical solution has lower accuracy. $(\star)$ value not available due to not reasonable computational cost to compute it. (Color figure online)

conductive inclusions, we propose a new numerical strategy to tackle the floating potential problem. Unlike the previous works cited above, our numerical strategy does not require any new specific numerical method. More precisely, it consists in characterising the solution to the floating potential problem as a linear combination of $N + 1$ explicit Dirichlet problems thanks to the definition of well designed Steklov-Poincaré operators. On the second hand, we propose an asymptotic analysis of the electroquasistatic potential in the case of a highly conductive thin inclusion, in the asymptotic regime where the ratio of the conductivities R_{cond} is of order ε^2, while the ratio R_{length} is of order ε. In particular, we prove the convergence of the asymptotic approximation at any order as ε goes to 0.

2 Analysis and Computation of the Floating Potential Problem

Even though the use of well-designed numerical methods can be useful, they require deep changes in the computing software that prevent the use of standard softwares, which have been designed for Dirichlet, Neumann and/or Robin conditions in most cases. In the following, we show that the solution to the floating

potential problem can be obtained as the linear combination of $N + 1$ independent potentials with Dirichlet conditions. The parallelization of the independent problem implies that the floating potential is almost reduced to a Dirichlet problem, and the problem does not necessarily require the use of advanced numerical strategies.

Let us state precisely the problem. Let $\mathcal{O}$ be a domain of $\mathbb{R}^d$, $d = 2, 3$ and let $(\mathcal{O}_k)_{k=1}^N$ be N highly conductive inclusions embedded in $\mathcal{O}$. We denote by Γ_{out} the outer boundary of $\mathcal{O}$, and by Γ_k the boundary of $\mathcal{O}_k$ for $k = 1, \cdots N$. Define $\Omega = \mathcal{O} \setminus \cup \overline{\mathcal{O}_k}$. Let $\sigma \in L^\infty(\Omega)$ be the conductivity map of Ω which satisfies for a given constant $a > 0$

$$a \leq \|\sigma\|_{L^\infty(\Omega)} \leq 1/a.$$

Given $(g_k)_{k=1}^N \in \mathbb{R}$ and $f \in H^{-1}(\Omega)$, the floating potential problem[1] consists in finding the $N + 1$-uple $(u, \alpha_1, \cdot, \alpha_N) \in H^1(\Omega) \times \mathbb{R}^N$ such that

$$-\nabla \cdot (\sigma \nabla u) = f \quad \text{in } \Omega, \qquad u|_{\Gamma_{\text{out}}} = 0, \tag{3a}$$

and on Γ_k, for $k = 1, \cdots N$

$$u|_{\Gamma_k} = \alpha_k, \qquad \int_{\Gamma_k} \sigma \partial_n u \, ds = g_k. \tag{3b}$$

2.1   Existence and Uniqueness of *Floating Potential* Problem

Even though the well-posedness of Problem (3) has been addressed by Amann *et al.* in [1] for one inclusion, we present a variant proof for N inclusions that will lead to our simple numerical strategy.

For $i = 1, \cdots, N$, we consider the following Steklov-Poincaré operators defined as

$$\Lambda_{\text{out}}^{(i)} : H^{-1}(\Omega) \longrightarrow H^{-1/2}(\Gamma_i)$$

$$f \qquad \longmapsto \quad \sigma \partial_n v|_{\Gamma_i} \quad \text{s. t.} \quad \begin{cases} -\nabla \cdot (\sigma \nabla v) = f \quad \text{in } \Omega, \\ v|_{\Gamma_{\text{out}}} = 0, \quad v|_{\Gamma_\ell} = 0, \quad \text{for } \ell = 1, \cdots, N. \end{cases}$$

For $k = 1, \cdots, N$, we define $\Lambda_k^{(i)}$ by

$$\Lambda_k^{(i)} : H^{1/2}(\Gamma_k) \longrightarrow H^{-1/2}(\Gamma_i)$$

$$\gamma \qquad \longmapsto \quad \sigma \partial_n v|_{\Gamma_i} \quad \text{s. t.} \quad \begin{cases} -\nabla \cdot (\sigma \nabla v) = 0 \quad \text{in } \Omega, \\ v|_{\Gamma_i} = \gamma, \\ v|_{\Gamma_{\text{out}}} = 0, \qquad v|_{\Gamma_\ell} = 0, \quad \text{for } \ell \neq i. \end{cases}$$

If it exists, the solution $(u, \alpha_1, \cdots, \alpha_N)$ to Problem (3) satisfies

$$\sigma \partial_n u|_{\Gamma_i} = \sum_{\ell=1}^N \alpha_\ell \Lambda_\ell^{(i)}(1) + \Lambda_{\text{out}}^{(i)}(f), \quad \text{for } i = 1, \cdots, N,$$

---

[1] Note that if the inclusion $\mathcal{O}_k$ is isolated, then g_k is nothing but 0.

and the nonlocal constraints (3b) read

$$g_i = \sum_{\ell=1}^{N} \alpha_\ell \int_{\Gamma_i} \Lambda_\ell^{(i)}(1)ds + \int_{\Gamma_i} \Lambda_{\text{out}}^{(i)}(f)ds, \qquad \text{for} i = 1, \cdots, N. \qquad (4)$$

Denoting by $\mathcal{M} = (\mathcal{M}_{ij})_{i,j=1,\cdots,N}$ the matrix defined as

$$\mathcal{M}_{ij} = \int_{\Gamma_i} \Lambda_j^i(1)ds, \qquad (5a)$$

and $\mathcal{B} = (\mathcal{B}_i)_{i=1,\cdots,N}$ the vector defined as

$$\mathcal{B}_i = g_i - \int_{\Gamma_i} \Lambda_{\text{out}}^i(f)ds. \qquad (5b)$$

Then equality (4) reads

$$\mathcal{M} \begin{pmatrix} \alpha_1 \\ \vdots \\ \alpha_N \end{pmatrix} = \mathcal{B}, \qquad (5c)$$

and the proof of the well-posedness of Problem (3) is reduced to proving the invertibility of $\mathcal{M}$.

Proposition 1. *Let Ω be a domain of $\mathbb{R}^d$, $d = 2, 3$. Let us endow the space $(L^2(\Omega))^d$, $d = 2, 3$ with the scalar product $<\cdot, \cdot>_{(L^2(\Omega))^d}$ defined by*

$$<F, G>_{(L^2(\Omega))^d}^\sigma = \int_\Omega \sigma F \cdot G \, dx, \qquad \forall (F, G) \in (L^2(\Omega))^d.$$

The matrix $\mathcal{M}$ defined by (5a) is a Gram matrix of the linearly independent vectors $\nabla v_1, \cdots, \nabla v_N$ of $(L^2(\Omega))^d$, where the functions $(v_\ell)_{\ell=1}^N$ are defined by

$$\begin{cases} -\nabla \cdot (\sigma \nabla v_\ell) = 0 & \text{in } \Omega, \\ v_\ell|_{\Gamma_\ell} = 1, \\ v_\ell|_{\Gamma_{\text{out}}} = 0, & v_\ell|_{\Gamma_k} = 0, \quad \text{for} k \neq \ell. \end{cases} \qquad (6)$$

Therefore $\mathcal{M}$ is invertible and there exists a unique $N+1$-uple $(u, \alpha_1, \cdots, \alpha_N) \in H^1(\Omega) \times \mathbb{R}^N$ solution to Problem (3).

Proof. Observe first that thanks to the Dirichlet boundary conditions on Γ_k for $k = 1, \cdots, N$, the vectors $(v_\ell)_{\ell=1}^N$ are linearly independent in $H^1(\Omega)$, hence the vectors $\nabla v_1, \cdots, \nabla v_N$ are linearly independent in $(L^2(\Omega))^d$.

By definition of $\mathcal{M}$ and by construction of v_i, one has

$$\mathcal{M}_{ij} = \int_{\Gamma_i} \sigma \partial_n v_j v_i dx = \int_\Omega \sigma \nabla v_j \cdot \nabla v_i \, dx.$$

Thus $\mathcal{M}$ is a Gram matrix of linearly independent vectors of $(L^2(\Omega))^d$, it is therefore invertible (see for instance [2]). $\qquad \square$

2.2   Numerical Strategy to Solve the Floating Potential Problem

Proposition 1 leads to a simple characterization of the solution to Problem (3), and thus a simple numerical strategy which is as follows.

- Compute v_ℓ given defined by (6) for $\ell = 1, \cdots, N$ and compute v_{out}, which is the solution in $H_0^1(\Omega)$ to

$$\begin{cases} -\nabla \cdot (\sigma \nabla v_{\text{out}}) = f & \text{in } \Omega, \\ v_{\text{out}|\partial\Omega} = 0. \end{cases} \tag{7}$$

- Compute $(\mathcal{M}_{ij})$ and $(\mathcal{B}_{ij})$ given by (5a)–(5b) or equivalently

$$\mathcal{M}_{ij} = \int_\Omega \sigma \nabla v_i \cdot \nabla v_j \, dx, \qquad \mathcal{B}_i = g_i - \int_\Omega \sigma \nabla v_{\text{out}} \cdot \nabla v_i \, dx,$$

and deduce $(\alpha_1, \cdots, \alpha_N)$ by solving the linear system (5c).
- Then the solution u to the floating potential problem (3) is obtained by the following linear combination:

$$u = v_{\text{out}} + \sum_{\ell=1}^{N} \alpha_\ell v_\ell.$$

In other words, to compute u one just has to solve $N+1$ independent Dirichlet problems, which can be easily parallelized.

3   Asymptotic Analysis and Generalization of the Floating Potential Problem for Thin Highly Conductive Sheets

3.1   The Conductivity Problem

In this section, we present the electroquasistatic problem in the case of one *thin high conductive* inclusion. We consider the asymptotic regime where the ratio between the dielectric/low conductive material R_{cond} is 2 order of magnitude greater than the ratio of the characteristic length R_{length} of the dielectric/low conductive material divided by the (small) thickness of sheet.

More precisely, we consider a smooth bounded domain Ω of $\mathbb{R}^d$, $d = 2$ or 3, which represents a conductive domain with a hole. We denote by Γ_{out} the external boundary of Ω, and by Γ the inner boundary corresponding the interface between Ω and the inner hole. The domain Ω is complemented with a thin highly conducting sheet coating the hole, and denoted by $\mathcal{O}_\varepsilon$, where ε is the ratio between the small thickness of the conductive sheet and the characteristic length of Ω. In addition we assume that the magnitude of the highly conductive sheet is of order $1/\varepsilon^2$. The domain $\mathcal{O}_\varepsilon$ may represent a inner passive electrode or a highly conductive thin inclusion as a surgical clip. We denote by Ω_ε the assembly $\Omega_\varepsilon = \Omega \cup \Gamma \cup \mathcal{O}_\varepsilon$, and Γ_ε is the interface between Ω_ε and the hole. Figure 2 provides a schematic of the geometrical framework.
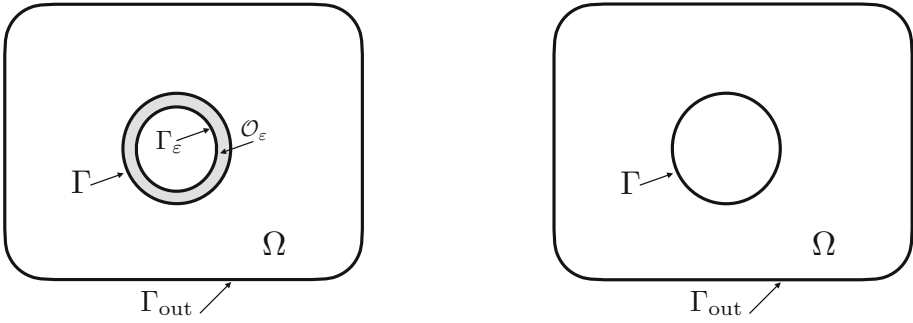
Fig. 2. Schematics of the *toy model*. (Left): The domain with one thin highly conductive inclusion of thickness ε. The domain $\mathcal{O}_\varepsilon$ may represent a inner passive electrode or a highly conductive thin inclusion as a surgical clip. (Right): The domain Ω in the limit $\varepsilon = 0$.

The nondimensionalized conductivity[2] map σ_ε of the domain Ω_ε is given by

$$\sigma_\varepsilon(x) = \begin{cases} \sigma(x), & \text{if} \quad x \in \Omega, \\ \varepsilon^{-2}, & \text{if} \quad x \in \mathcal{O}_\varepsilon, \end{cases} \tag{8}$$

where σ is a strictly positive function in Ω.

The electroquasistatic potential u_ε in Ω satisfies the following elliptic problem

$$-\nabla \cdot (\sigma_\varepsilon \nabla u_\varepsilon) = \mathbb{1}_\Omega f \quad \text{in} \quad \Omega \cup \mathcal{O}_\varepsilon, \tag{9a}$$

with the transmission conditions on Γ:

$$u_{\varepsilon|\Gamma^+} - u_{\varepsilon|\Gamma^-} = 0, \qquad \sigma \partial_n u_{\varepsilon|\Gamma^+} - \frac{1}{\varepsilon^2} \partial_n u_{\varepsilon|\Gamma^-} = 0, \tag{9b}$$

and the boundary conditions

$$\partial_n u_{\varepsilon|\Gamma_\varepsilon} = 0, \qquad u_{\varepsilon|\Gamma_{\text{out}}} = 0, \tag{9c}$$

where the source term $f \in H^{-1}(\Omega)$. The following a priori estimate holds.

Proposition 2 (A priori estimate). *Let Ω and $\mathcal{O}_\varepsilon$ be smooth connected domains. Denote by $\Omega_\varepsilon = \Omega \cup \Gamma \cup \mathcal{O}_\varepsilon$. Let $f \in H^{-1}(\Omega)$. There exists a unique solution u_ε to Problem* (9) *in $H^1(\Omega_\varepsilon)$. Moreover there exists a constant $C > 0$ independent of ε such that*

$$\|u_\varepsilon\|_{H^1(\Omega)} + \frac{1}{\varepsilon}\|\nabla u_\varepsilon\|_{L^2(\mathcal{O}_\varepsilon)} \leq C\|f\|_{H^{-1}(\Omega)}.$$

---

[2] To simplify notation, we consider the non dimension conductivity map σ_ε, which is the conductivity map divided by the characteristic conductivity of the domain, which might the average of the conductivity on the low conductive domain.

Proof. The well-posedness of the elliptic problem (9) is standard by a straightforward application of the Lax-Migram lemma. The proof of the estimate is based on standard Poincaré estimate [6] in Ω since $u_\varepsilon|_\Omega \in H^1(\Omega)$ is such that $u_\varepsilon|_{\Gamma_{\text{out}}} = 0$. Indeed, multiplying by u_ε and integrating by parts leads to

$$\int_\Omega \sigma |\nabla u_\varepsilon|^2 dx + \frac{1}{\varepsilon^2} \int_{\mathcal{O}_\varepsilon} |\nabla u_\varepsilon|^2 dx \leq \|f\|_{H^{-1}(\Omega)} \|u_\varepsilon\|_{H^1(\Omega)} \leq C \|f\|_{H^{-1}(\Omega)} \|\nabla u_\varepsilon\|_{L^2(\Omega)},$$

where C is independent of ε, which ends the proof. $\square$

The goal of this section is to provide the asymptotic expansion of u_ε as ε goes to 0.

3.2 Local Coordinates and Laplace Operator

To perform the asymptotic expansion it is natural to introduce the following change of variables which straightens up the thin inclusion. More precisely, let $\mathbf{x_T} = (\xi_1, \xi_2)$ be a system of local coordinates on $\Gamma = \{\Psi(\mathbf{x_T})\}$, where Ψ is a mapping of Γ. By abuse of notation, we denote by $\mathbf{x_T} \in \Gamma$ the point $\Psi(\mathbf{x_T}) \in \Gamma$. We define the following map Φ by

$$\Phi(\mathbf{x_T}, \xi_3) = \Psi(\mathbf{x_T}) + \xi_3 \, \mathbf{n}(\mathbf{x_T}) \quad \forall (\mathbf{x_T}, \xi_3) \in \Gamma \times \mathbb{R},$$

where $\mathbf{n}$ is the outer normal vector of Γ. The layer $\mathcal{O}_\varepsilon$ is parameterized by

$$\mathcal{O}_\varepsilon = \{\Phi(\mathbf{x_T}, \xi_3) \, | \, (\mathbf{x_T}, \xi_3) \in \Gamma \times (0, \varepsilon)\}.$$

The Euclidean metric tensor $(g_{ij})_{i\,j=1,2,3}$, defined as

$$g_{ij} = \langle \partial_i \Phi, \partial_j \Phi \rangle$$

reads as follows [10]

$$g_{33} = 1, \quad g_{\alpha 3} = g_{3\alpha} = 0 \quad \forall \alpha \in \{1, 2\},$$
$$g_{\alpha\beta}(\mathbf{x_T}, \xi_3) = g^0_{\alpha\beta}(\mathbf{x_T}) + 2\xi_3 \, b_{\alpha\beta}(\mathbf{x_T}, \xi_3) + \xi_3^2 \, c_{\alpha\beta}(\mathbf{x_T}, \xi_3) \quad \forall \alpha, \beta \in \{1, 2\}^2,$$

where

$$g^0_{\alpha\beta} = \langle \partial_\alpha \Psi, \partial_\beta \Psi \rangle, \; b_{\alpha\beta} = \langle \partial_\alpha \mathbf{n}, \partial_\beta \Psi \rangle, \; c_{\alpha\beta} = \langle \partial_\alpha \mathbf{n}, \partial_\beta \mathbf{n} \rangle.$$

The Laplace-Beltrami operator Δ_g in the system of local coordinates of $\mathcal{O}_\varepsilon$ reads then

$$\Delta_g = \frac{1}{\sqrt{g}} \sum_{i,j=1,2,3} \partial_i(\sqrt{g} g^{ij} \partial_j),$$

where $(g^{ij}) = (g_{ij})^{-1}$ and g the absolute value of the tensor metric determinant. Define $\forall \ell \in \mathbb{N}$ the coefficients

$$a^\ell_{ij} = \partial_3^\ell \left(\frac{\partial_i(\sqrt{g}\, g^{ij})}{\sqrt{g}} \right)\Bigg|_{\xi_3=0}, \qquad \forall (i,j) \in \{1,2,3\}^2,$$
$$A^\ell_{\alpha\beta} = \partial_3^\ell \left(g^{\alpha\,\beta} \right)\big|_{\xi_3=0}, \qquad \forall (\alpha, \beta) \in \{1, 2\}^2,$$

and let S_Γ^ℓ be the surface differential operator of order 2 on Γ defined as

$$S_\Gamma^\ell = \sum_{\alpha,\beta=1,2} a_{\alpha\beta}^l \partial_\beta + A_{\alpha\beta}^l \partial_\alpha \partial_\beta.$$

Remark 1. *As noticed in* [10], *the operator S_Γ^0 is nothing but the surface Laplace-Beltrami operator on Γ, so $S_\Gamma^0 = \Delta_\Gamma$. Moreover a_{33}^0 is the sum of the principal curvatures of Γ, in other words, denoting by $\mathcal{H}$ the mean curvature of Γ one has $a_{33}^0 = 2\mathcal{H}$.*

The Laplace-Beltrami operator in $\mathcal{O}_\varepsilon$ can be rewritten as

$$\Delta_g = \partial_3^2 + \sum_{l \geq 0} \frac{\xi_3^l}{l!}(a_{33}^l \partial_3 + S_\Gamma^l) \quad \forall(\mathbf{x_T}, \xi_3) \in \Gamma \times (0,\varepsilon).$$

Performing the change of variable $\eta = \xi_3/\varepsilon$, we denote by $\Phi_\varepsilon(\mathbf{x_T}, \eta) = \Phi(\mathbf{x_T}, \varepsilon\eta)$, and we obtain

$$\Delta_g = \frac{1}{\varepsilon^2}\partial_\eta^2 + \frac{1}{\varepsilon}a_{33}^0 \partial_\eta + \sum_{l \geq 0} \varepsilon^l \frac{\eta^l}{l!}\left(\frac{\eta}{l+1}a_{33}^{l+1}\partial_\eta + S_\Gamma^l\right) \quad \forall(\mathbf{x_T}, \eta) \in \Gamma \times (0,1).$$

3.3   Formal Expansion

Denote by U_ε the electroquasistatic potential in local coordinates in $\mathcal{O}_\varepsilon$:

$$U_\varepsilon(\mathbf{x_T}, \eta) = u_\varepsilon \circ \Phi(\mathbf{x_T}, \varepsilon\eta), \qquad (\mathbf{x_T}, \eta) \in \Gamma \times (0,1).$$

Thanks to this change of variables, Problem (9) reads as follows

$$\begin{cases} -\nabla \cdot (\sigma \nabla u_\varepsilon) = f & \text{in } \Omega, & \text{(10a)} \\ -\Delta_g U_\varepsilon = 0 & \text{on } \Gamma \times (0,1), & \text{(10b)} \\ u_\varepsilon|_\Gamma = U_\varepsilon|_{\eta=0} \circ \Psi^{-1}, & & \text{(10c)} \\ \sigma\, \partial_n u_\varepsilon|_\Gamma = \varepsilon^{-3}\, \partial_\eta U_\varepsilon|_{\eta=0} \circ \Psi^{-1}, & & \text{(10d)} \\ \partial_\eta U_\varepsilon|_{\eta=1} = 0, & & \text{(10e)} \\ u_\varepsilon|_{\Gamma_{\text{out}}} = 0. & & \text{(10f)} \end{cases}$$

We are now ready to derive formally the expansion. Set the following Ansatz:

$$u_\varepsilon(x) = \sum_{k \geq 0} \varepsilon^k u_k(x), \qquad \forall x \in \Omega, \tag{11a}$$

$$U_\varepsilon(\mathbf{x_T}, \eta) = \sum_{k \geq 0} \varepsilon^k \mathfrak{u}_k(\mathbf{x_T}, \eta), \qquad \forall(\mathbf{x_T}, \eta) \in \Gamma \times (0,1). \tag{11b}$$

Injecting the formal series in Problem ([10](#)) and identifying the terms with the same power in ε lead to the following relations for any $p \geq 0$,

$$-\nabla \cdot (\sigma \nabla u_p) = \delta_p f \text{ in } \Omega, \tag{12a}$$

$$\partial_\eta^2 \mathfrak{u}_p = -a_{33}^0 \partial_\eta \mathfrak{u}_{p-1} - \sum_{l=0}^{p-2} \frac{\eta^l}{l!} \left(\frac{\eta}{l+1} a_{33}^{l+1} \partial_\eta \mathfrak{u}_{p-2-l} + S_\Gamma^l \mathfrak{u}_{p-2-l} \right) \text{ on } \Gamma \times (0,1), \tag{12b}$$

$$u_{p|_\Gamma} = \mathfrak{u}_{p|_{\eta=0}}, \tag{12c}$$

$$\sigma \, \partial_n u_{p-3|_\Gamma} = \partial_\eta \mathfrak{u}_{p|_{\eta=0}}, \tag{12d}$$

$$\partial_\eta \mathfrak{u}_{p|_{\eta=1}} = 0, \tag{12e}$$

$$u_{p|_{\Gamma_{\text{out}}}} = 0, \tag{12f}$$

where δ_p is the Kronecker symbol equal to 1 if $p = 0$ and 0 elsewhere, and with the convention u_p and $\mathfrak{u}_p$ are 0 if $p \leq 0$.

3.3.1   Derivation of the 0th and 1rst Order Coefficients

Using ([12b](#)) with $p = 0$ together with the boundary condition ([12e](#)), implies that $\partial_\eta \mathfrak{u}_0 = 0$ and thus $\mathfrak{u}_0 = \mathfrak{u}_0(\mathbf{x_T})$, and then similarly $\partial_\eta \mathfrak{u}_1 = 0$ and thus $\mathfrak{u}_1 = \mathfrak{u}_1(\mathbf{x_T})$. Then using ([12b](#)) for $p = 2$ implies that

$$\partial_\eta^2 \mathfrak{u}_2 = -\Delta_\Gamma \mathfrak{u}_0(\mathbf{x_T}).$$

The boundary conditions ([12d](#))–([12e](#)) imply thus that $\partial_\eta \mathfrak{u}_2 = 0$ and $-\Delta_\Gamma \mathfrak{u}_0 = 0$. Therefore we infer that $\mathfrak{u}_0$ is a constant denoted by α_0 and thus $u_{0|_\Gamma} = \alpha_0$. Then using ([12b](#)) for $p = 3$ implies that

$$\partial_\eta^2 \mathfrak{u}_3 = -\Delta_\Gamma \mathfrak{u}_1(\mathbf{x_T}), \tag{13}$$

since $\partial_\eta \mathfrak{u}_2 = 0$, and $S_\Gamma^1 \mathfrak{u}_0 = 0$. We thus infer thanks to ([12e](#)) that

$$\int_\Gamma \partial_\eta \mathfrak{u}_3(\mathbf{x_T}, 1) d\mathbf{x_T} = -\int_\Gamma \Delta_\Gamma \mathfrak{u}_1 = 0,$$

from which we infer using ([12d](#)) the floating potential problem:

$$\text{Find} (u_0, \alpha_0) \in H^1(\Omega) \times \mathbb{R} \text{ such that}$$
$$-\nabla \cdot (\sigma \nabla u_0) = f, \qquad \text{in } \Omega, \qquad u_{0|_{\Gamma_{\text{out}}}} = 0, \tag{14a}$$

$$u_{0|_\Gamma} - \alpha_0 = 0, \qquad \text{such that} \qquad \int_\Gamma \sigma \partial_n u_0 \, ds = 0. \tag{14b}$$

Note also that the derivation process leads

$$\mathfrak{u}_0 = \alpha_0, \quad \partial_\eta \mathfrak{u}_1 = \partial_\eta \mathfrak{u}_2 = 0. \tag{15a}$$

To get the 1rst order coefficient, since $\partial_\eta \mathfrak{u}_1 = 0$, using ([13](#)) with ([12d](#)) implies that

$$\partial_\eta \mathfrak{u}_3(\mathbf{x_T}, \eta) = (1 - \eta) \Delta_\Gamma \mathfrak{u}_1, \qquad \text{and} \qquad \Delta_\Gamma \mathfrak{u}_1 = \sigma \partial_n u_{0|_\Gamma},$$

thus one can write $\mathfrak{u}_1 = g_1(\mathbf{x_T}) + \alpha_1$ where g_1 is uniquely determined by

$$\Delta_\Gamma g_1 = \sigma \partial_n u_{0|_\Gamma}, \qquad \int_\Gamma g_1 ds = 0,$$

and thanks to (12c), $u_{1|_\Gamma} - \alpha_1 = g_1 \circ \Psi^{-1}$. It remains to determine the constant α_1. Using (12b) with $p = 4$, one has

$$\partial_\eta^2 \mathfrak{u}_4 = -a_{33}^0 \partial_\eta \mathfrak{u}_3 - \sum_{l=0}^{2} \frac{\eta^l}{l!} \left(\frac{\eta}{l+1} a_{33}^{l+1} \partial_\eta \mathfrak{u}_{2-l} + S_\Gamma^l \mathfrak{u}_{2-l} \right)$$
$$= -(1-\eta)a_{33}^0 \Delta_\Gamma \mathfrak{u}_1 - \Delta_\Gamma \mathfrak{u}_2 - \eta S_\Gamma^1 \mathfrak{u}_1,$$

and thanks to (12e) one infers

$$\partial_\eta \mathfrak{u}_4 = -\left(\eta - \eta^2/2 - 1/2\right) a_{33}^0 \Delta_\Gamma \mathfrak{u}_1 - (\eta-1)\Delta_\Gamma \mathfrak{u}_2 - (\eta^2/2 - 1/2) S_\Gamma^1 \mathfrak{u}_1.$$

Note that since $\mathfrak{u}_2$ is not determined, the above equality does not define $\partial_\eta \mathfrak{u}_4$. However, integrating over Γ and using (12d), we obtain

$$\int_\Gamma \sigma \partial_n u_1 \, ds = \frac{1}{2} \int_\Gamma \left(a_{33}^0 \Delta_\Gamma \mathfrak{u}_1 + S_\Gamma^1 \mathfrak{u}_1 \right) ds = \frac{1}{2} \int_\Gamma \left(a_{33}^0 \Delta_\Gamma g_1 + S_\Gamma^1 g_1 \right) ds,$$

and then (u_1, α_1) is the solution to the following problem:

Find $(u_1, \alpha_1) \in H^1(\Omega) \times \mathbb{R}$ such that:
$$-\nabla \cdot (\sigma \nabla u_1) = 0, \qquad \text{in } \Omega, \qquad u_{1|_{\Gamma_{\text{out}}}} = 0,$$
$$u_{1|_\Gamma} - \alpha_1 = g_1 \circ \Psi^{-1}, \qquad \text{such that} \qquad \int_\Gamma \sigma \partial_n u_1 ds = h_1,$$

where g_1 and h_1 are given by

$$\Delta_\Gamma g_1 = \sigma \partial_n u_{0|_\Gamma}, \qquad \int_\Gamma g_1 ds = 0,$$
$$h_1 = \frac{1}{2} \int_\Gamma a_{33}^0 \Delta_\Gamma g_1 + S_\Gamma^1 g_1 ds.$$

Then one also has

$$\mathfrak{u}_1(\mathbf{x_T}) = g_1(\mathbf{x_T}) + \alpha_1, \qquad \partial_\eta \mathfrak{u}_2 = 0, \qquad \partial_\eta \mathfrak{u}_3 = (1-\eta)\Delta_\Gamma g_1.$$

3.3.2 Derivation of the Coefficients at Any Order k by Induction

Assume that there exists a smooth enough function g_k defined on Γ such that $\int_\Gamma g_k ds = 0$ and a constant h_k such that (u_k, α_k) is the solution to the following problem:

Find $(u_k, \alpha_k) \in H^1(\Omega) \times \mathbb{R}$ such that
$$-\nabla \cdot (\sigma \nabla u_k) = \delta_k f, \qquad \text{in } \Omega, \qquad u_{k|_{\Gamma_{\text{out}}}} = 0,$$
$$u_{k|_\Gamma} - \alpha_k = g_k \circ \Psi^{-1}, \qquad \text{such that} \qquad \int_\Gamma \sigma \partial_n u_k ds = h_k,$$

and assume that the following profile terms $\mathfrak{u}_\ell$ for $\ell = k, k+1, k+2$ read as

$$\mathfrak{u}_\ell(\mathbf{x_T}, \eta) = P_{\ell-1}(\mathbf{x_T}, \eta) + g_\ell(\mathbf{x_T}) + \alpha_\ell,$$

$$\int_\Gamma \partial_\eta \mathfrak{u}_{k+3}(\mathbf{x_T}, 0) = h_k,$$

where $P_{\ell-1}$ is a given polynomial of order $\ell - 1$ in η and vanishing in $\eta = 0$, for $\ell = k, k+1, k+2$, and g_ℓ and α_ℓ are unknown for $\ell = k+1, k+2$, with the constraint $\int_\Gamma g_\ell ds = 0$.

Then, using (12b)–(12e) with $p = k+3$, we infer that for any $r \in (0,1)$

$$\partial_\eta \mathfrak{u}_{k+3}(\mathbf{x_T}, r) - \int_r^1 \Delta_\Gamma \mathfrak{u}_{k+1} d\eta = \int_r^1 a_{33}^0 \partial_\eta \mathfrak{u}_{k+2} + a_{33}^1 \eta \partial_\eta \mathfrak{u}_{k+1}$$

$$+ \sum_{l=1}^{k+1} \frac{\eta^l}{l!} \left(\frac{\eta}{l+1} a_{33}^{l+1} \partial_\eta \mathfrak{u}_{k+1-l} + S_\Gamma^l \mathfrak{u}_{k+1-l} \right) d\eta.$$

We thus infer that $\partial_\eta \mathfrak{u}_{k+3}$ is polynomial of order $k+2$ or in other words $\mathfrak{u}_{k+3}$ reads as

$$\mathfrak{u}_{k+3}(\mathbf{x_T}, \eta) = P_{k+2}(\mathbf{x_T}, \eta) + g_{k+3}(\mathbf{x_T}) + \alpha_{k+3},$$

where P_{k+2} is explicitly given by the above equality vanishes in $\eta = 0$, and g_{k+3} is not determined but its mean value over Γ is 0 and α_{k+3} is a still undetermined constant. Using (12d) and the recurrence hypothesis, we also infer

$$-\Delta_\Gamma g_{k+1} = -\sigma \partial_n u_k + \int_0^1 \eta \Delta_\Gamma P_k(\mathbf{x_T}, \eta) d\eta$$

$$+ \int_0^1 a_{33}^0 \partial_\eta \mathfrak{u}_{k+2} + a_{33}^1 \eta \partial_\eta \mathfrak{u}_{k+1} \sum_{l=1}^{k+1} \frac{\eta^l}{l!} \left(\frac{\eta}{l+1} a_{33}^{l+1} \partial_\eta \mathfrak{u}_{k+1-l} + S_\Gamma^l \mathfrak{u}_{k+1-l} \right) ds,$$

which entirely determines g_{k+1} using the recurrence assumption since $\int_\Gamma g_{k+1} ds = 0$. It remains to determine the constant α_{k+1}. Using (12b)–(12e) with $p = k+4$ we infer that

$$\int_\Gamma \partial_\eta \mathfrak{u}_{k+4} ds = \int_\Gamma \int_\eta^1 a_{33}^0 \partial_\eta \mathfrak{u}_{k+3} + \sum_{l=0}^{k+2} \frac{r^l}{l!} \left(\frac{r}{l+1} a_{33}^{l+1} \partial_\eta \mathfrak{u}_{p-2-l} + S_\Gamma^l \mathfrak{u}_{p-2-l} \right) dr ds,$$

and (12d) leads to

$$\int_\Gamma \sigma \partial_n u_{k+1} ds = \int_\Gamma \int_0^1 a_{33}^0 \partial_\eta \mathfrak{u}_{k+3} + \sum_{l=0}^{k+2} \frac{r^l}{l!} \left(\frac{r}{l+1} a_{33}^{l+1} \partial_\eta \mathfrak{u}_{p-2-l} + S_\Gamma^l \mathfrak{u}_{p-2-l} \right) dr ds := h_{k+1}.$$

The condition (12c) implies then that (u_{k+1}, α_{k+1}) is the solution to the following problem:

Find $(u_{k+1}, \alpha_{k+1}) \in H^1(\Omega) \times \mathbb{R}$ such that
$$-\nabla \cdot (\sigma \nabla u_{k+1}) = 0, \quad \text{in } \Omega, \quad u_{k+1}|_{\Gamma_{\text{out}}} = 0,$$

$$u_{k+1}|_\Gamma - \alpha_{k+1} = g_{k+1} \circ \Psi^{-1}, \quad \text{such that} \quad \int_\Gamma \sigma \partial_n u_{k+1} ds = h_{k+1},$$

Remark 2. *It is worth noting that thanks to Proposition 1, the elementary problems are well-posed at any order.*

3.3.3   Proof of the Expansion

Let us now prove the convergence of the expansion.

Theorem 1. *Let $N \geq 0$. Let $f \in \mathcal{C}^\infty(\Omega)$, such that the above inductive process to obtain the coefficients of the expansion (11) holds at any order. Let u_ε be the smooth solution to Problem (9). Let $u_{\varepsilon,N}$ be the function defined by*

$$u_{\varepsilon,N} = \begin{cases} \sum_{k=0}^N \varepsilon^k u_k, & in\ \Omega, \\[2mm] \sum_{k=0}^{N+2} \varepsilon^k \mathfrak{u}_k \circ \Phi_\varepsilon^{-1}, & in\ \mathcal{O}_\varepsilon, \end{cases}$$

where the functions $u_k, \mathfrak{u}_k$ are defined by the above inductive process.

Then there exists a constant C_N independent of ε such that

$$\|u_\varepsilon - u_{\varepsilon,N}\|_{H^1(\Omega)} + \frac{1}{\varepsilon}\|\nabla(u_\varepsilon - u_{\varepsilon,N})\|_{L^2(\mathcal{O}_\varepsilon)} \leq C_N \varepsilon^{N+1}.$$

Proof. Note that by hypothesis on f, $u_N \in \mathcal{C}^\infty(\Omega)$ and $\mathfrak{u}_N \in \mathcal{C}^\infty(\Gamma \times (0,1))$ (as well as their traces on Γ and derivatives) are uniformly bounded independently of ε.

Denote by $v_\varepsilon = u_\varepsilon - u_{\varepsilon,N}$. By construction of the expansion coefficients, v_ε satisfies the following problem:

$$\begin{cases} -\nabla \cdot (\sigma \nabla v_\varepsilon) = 0, & in\ \ \Omega, & (16\mathrm{a}) \\[1mm] -\Delta v_\varepsilon = \Delta u_{\varepsilon,N}\ (= O_{L^\infty(\Omega)}(\varepsilon^{N+1})), & in\ \ \mathcal{O}_\varepsilon, & (16\mathrm{b}) \\[1mm] v_\varepsilon|_{\Gamma^-} - v_\varepsilon|_{\Gamma^+} = 0, & & (16\mathrm{c}) \\[1mm] \sigma \partial_n v_\varepsilon|_{\Gamma^-} - \dfrac{1}{\varepsilon^2}\partial_n v_\varepsilon|_{\Gamma^+} = \sigma \partial_n u_{\varepsilon,N}|_{\Gamma^-} - \dfrac{1}{\varepsilon^2}\partial_n u_{\varepsilon,N}|_{\Gamma^+}\ (= O_{L^\infty(\Gamma)}(\varepsilon^N)), & (16\mathrm{d}) \\[1mm] \partial_n v_\varepsilon|_{\Gamma_\varepsilon} = 0, & & (16\mathrm{e}) \\[1mm] v_\varepsilon|_{\Gamma_{\mathrm{out}}} = 0. & & (16\mathrm{f}) \end{cases}$$

Using the fact that

$$\|O_{L^\infty(\Omega)}(\varepsilon^N)\|_{L^2(\mathcal{O}_\varepsilon)} \leq C\varepsilon^{N+1/2},$$

multiplying by v_ε and integrating lead to

$$\int_\Omega \sigma|\nabla v_\varepsilon|^2 dx + \frac{1}{\varepsilon^2}\int_{\mathcal{O}_\varepsilon}|\nabla v_\varepsilon|^2 dx \leq C\left(\varepsilon^{N+1/2}\|v_\varepsilon\|_{L^2(\mathcal{O}_\varepsilon)} + \varepsilon^{N+1}|v_\varepsilon|_{L^2(\Gamma)}\right).$$

Since the diameter of Ω_ε is bounded below by the diameter of Ω, uniform Poincaré estimate holds for any function in $H^1(\Omega_\varepsilon)$ vanishing on Γ_{out}. Thus

thanks to Dirichlet trace estimate, there exists a constant C independent of ε such that

$$\int_\Omega \sigma |\nabla v_\varepsilon|^2 dx + \frac{1}{\varepsilon^2} \int_{\mathcal{O}_\varepsilon} |\nabla v_\varepsilon|^2 dx \leq C \left(\varepsilon^{N+1/2} \|\nabla v_\varepsilon\|_{L^2(\Omega_\varepsilon)} + C\varepsilon^{N+1} |v_\varepsilon|_{L^2(\Gamma)} \right)$$

$$\leq C\varepsilon^{N+1/2} \|\nabla v_\varepsilon\|_{L^2(\Omega_\varepsilon)},$$

hence

$$\|u_\varepsilon - u_{\varepsilon,N}\|_{H^1(\Omega)} + \frac{1}{\varepsilon} \|\nabla(u_\varepsilon - u_{\varepsilon,N})\|_{L^2(\mathcal{O}_\varepsilon)} \leq C_N \varepsilon^{N+1/2}.$$

We similarly have

$$\|u_\varepsilon - u_{\varepsilon,N+1}\|_{H^1(\Omega)} + \frac{1}{\varepsilon} \|\nabla(u_\varepsilon - u_{\varepsilon,N+1})\|_{L^2(\mathcal{O}_\varepsilon)} \leq C_N \varepsilon^{N+3/2}.$$

Observing that $w_{\varepsilon,N}$ defined by $w_{\varepsilon,N} = u_{\varepsilon,N+1} - u_{\varepsilon,N}$, satisfies

$$\|w_{\varepsilon,N}\|_{H^1(\Omega)} + \frac{1}{\varepsilon} \|\nabla w_{\varepsilon,N}\|_{L^2(\mathcal{O}_\varepsilon)} \leq C_N \varepsilon^{N+1},$$

we infer the result. □

4 Conclusion

In this paper, we have proposed an asymptotic analysis to approach accurately the solution to the electroquasistatic potential in a smooth domain with a highly conductive inclusion. We have shown that the so-called floating potential approaches the electroquasistatic potential with a first order accuracy, and we have given the expansion at any order. For the sake of simplicity, we have only considered the case where the relative thickness of the inclusion is of order ε and the ratio of the conductivities (the conductivity of the conductive inclusion divided by the conductivity of the domain) is of order $1/\varepsilon^2$. It is worth noting that in the case of higher conductive thin inclusions – that is for ratios of the conductivities of order $1/\varepsilon^{2+s}$, with $s > 0$ – the floating potential provides an approximation of order $\varepsilon^{1+\lfloor s \rfloor}$, since the terms u_i for $i = 1, \cdots, \lfloor s \rfloor$ vanish. This observation, which easily comes from the formal derivation of Sect. 3.3 is left to the reader.

This paper also provides an efficient numerical method to compute accurately the floating potential problem in the case of N highly conductive inclusions, by replacing the PDE with nonlocal constraints on the total flux along the interfaces by the resolution of $N + 1$ Dirichlet problems uncoupled, the solution of the floating potential problem being obtained thanks to the inversion of a definite Gram matrix of size N. This efficient and rigorous approach has been used recently by the authors and colleagues in [12].

References

1. Amann, D., Blaszczyk, A., Of, G., Steinbach, O.: Simulation of floating potentials in industrial applications by boundary element methods. J. Math. Ind. **4**(1), 1–15 (2014). https://doi.org/10.1186/2190-5983-4-13

2. Boyd, S., Vandenberghe, L.: Introduction to Applied Linear Algebra. Cambridge University Press, Cambridge (2018)

3. Dular, P., Henrotte, F., Meys, B., Genon, A., Legros, W.: Une méthode naturelle de traitement des potentiels flottants associée a la méthode des élements finis. J. Phys. III **7**(11), 2201–2209 (1997)

4. Erdozain, A., Péron, V., Pardo, D.: Asymptotic models for the electric potential across a highly conductive casing. Comput. Math. Appl. **76**, 1975–2000 (2018)

5. Gallinato, O., De Senneville, B.D., Seror, O., Poignard, C.: Numerical Workflow of Irreversible Electroporation for Deep-Seated Tumor. Physics in Medicine and Biology **64**(5), 055016 (2019)

6. Gilbarg, D., Trudinger, N.S.: Elliptic Partial Differential Equations of Second Order. Springer, Heidelberg (2001). https://doi.org/10.1007/978-3-642-61798-0. Reprint of the 1998 edition

7. Marčan, M., Pavliha, D., Kos, B., Forjanič, T., Miklavčič, D.: Web-based tool for visualization of electric field distribution in deep-seated body structures and planning of electroporation-based treatments. Biomed. Eng. Online **14**(3), S4 (2015)

8. O'Brien, T.J., et al.: Cycled pulsing to mitigate thermal damage for multi-electrode irreversible electroporation therapy. Int. J. Hyperthermia **36**(1), 952–962 (2019)

9. Péron, V., Schmidt, K., Duruflé, M.: Equivalent transmission conditions for the time-harmonic Maxwell equations in 3d for a medium with a highly conductive thin sheet. SIAM J. Appl. Math. **76**(3), 1031–1052 (2016)

10. Perrussel, R., Poignard, C.: Asymptotic expansion of steady-state potential in a high contrast medium with a thin resistive layer. Appl. Math. Comput. **221**, 48–65 (2013)

11. Sala, L., Prud'homme, C., Guidoboni, G., Szopos, M.: Ocular mathematical virtual simulator: a hemodynamical and biomechanical study towards clinical applications. J. Coupled Syst. Multiscale Dyn. **6**(3), 241–247 (2018)

12. Voyer, D., Corridore, S., Collin, A., Scorretti, R., Poignard, C.: Numerical modeling of floating potentials in electrokinetic problems using an asymptotic method. IEEE Trans. Magn. **56**, 1–4 (2020)

Free Boundary Problem of Cell Deformation and Invasion

Nuha Loling Othman[1(✉)] and Takashi Suzuki[2]

[1] Faculty of Computer Science and Information Technology,
Universiti Malaysia Sarawak, 94300 Kota Samarahan, Sarawak, Malaysia
`zzt230c@gmail.com`
[2] Center for Mathematical Modeling and Data Science, Osaka University,
1-3 Machikaneyama-cho, Toyonaka, Osaka 560-8531, Japan
`suzuki@sigmath.es.osaka-u.ac.jp`

Abstract. A novel approach of free boundary problem of invadopodia formation and invasion is proposed in this paper. The modeling of invadopodia formation and invasion of cell involving the interaction across plasma membrane is considered. The formation is formulated by Stefan problem approach which is known as free boundary problem where the boundary membrane is priori unknown. Changes in cell membrane will lead to protrusions of cell membrane. A normal growing cell in tissue on an organ will be altered into cancerous cells after some processes of mutation in genes. We proposed level set method to indicate the moving plasma membrane and to represent the behavior of the cell interface. An efficient and a straightforward enthalpy method (phase change problem) is then used to provide the description of the cell membrane diffusion. We successfully show the formation of invadopodia and migration of a single cell modeling.

1 Introduction

A tumor is an abnormal lump or growth of tissue located in clusters in different body part which can cause malignant or benign tumor. In this study, we focus on tumor cell deformation and invasion across tissue boundaries. Tumor cell invasion is the capacity of tumor cells to disrupt the basement membrane (BMs) and penetrate the underlying stroma. It depends on the capability of cancer cells to breach the basement membrane, remodel extracellular matrix (ECM) and migrate through meshwork [20]. In order for a primary solid tumor to be developed, it begins with a single normal cell being transformed into cancer cell through multiple certain key genes mutation. An individual tumor cell has the potential over successive divisions to develop into a cluster (or nodule) of tumour cell [2].

Invadopodia are dynamic actin-rich plasma membrane protrusions that degrade the extracellular matrix through the local deposition of proteases involved in cancer cell invasiveness and metastasis. It has a shape of a small punctuated finger which we called protrusion and formed during cell invasion.

Based on several reports [19], cancer cells can form few (1–10) invadopodia with lifetime in the range from several tens up to 60 and size measuring between 0.05 up to $2\,\mu$m [17]. From biological point of view, invadopodia formation involves specific signaling pathways in cell, that results from extracellular stimuli, which in addition, it is the interaction of specific chemical between cell membrane and the extracellular matrix [9]. In this study, we present *in silico* model of a single cell deformation from a normal cell in a tissue or organ in human body that will transform into cancer cell. The modeling of this cell incorporate the interaction between signal in the inner cell and, ligand outside the cell and this interaction occurs across the cell membrane.

2   Cell-Deformation-ECM Degradation

Invadopodia formed by tumor cells at contact sites between invasive tumor cells and in contact with ECM. Invadopodia present at the basal surfaces of cells and capable of crossing the extracellular barriers. It triggers matrix proteolytic activity and is capable of penetrating through basement membranes (BMs). It also continues with stromal invasion and intravasation to enter the blood, see Fig. 1 a) and b).

Invadopodia core proteins consisting of cortactin, cofilin and N-WASP form an initial nucleus or core structure are first binding the tip to ECM [18]. It is a dynamic extension of plasma membrane where it mimic the contact sites that form between tumor cells and the BMs during cell invasion [20].

The formation of invadopodia begins when matrix metallopeptidases (MMPs) generate a domain (DIII) from ECM macromolecule laminin-5 (Ln-5)γ2 where DIII fragment will bind the epidermal growth factor (EGFR) and stimulate the cell scattering and migration [15,16]. MMPs plays a crucial role in tissue remodeling such that membrane type 1-matrix metalloproteinases (MT1-MMP) is an essential to ECM component macromolecule disruption via degradation. MT1-MMP processed Ln-5γ2 chain which is an ECM substrate for cell adhesion, promotes migration and invasion of epithelial and tumor cells [16]. Based on [20], MT1-MMP expression is important not only in proteolytic activity but also in the formation of invadopodia.

EGFR bind directly to filamentous actin (F-actin) via its cytoplasmic domain with no other proteins involved [7]. From [1], the F-actin structural polarity during actin assembly has an implications on the rate, and direction of filament growth at the opposite ends of the actin filament. EGF ligand bind to EGFR to induced signalling transduction pathways. It trigger a reactions path which linked through several elements from membrane till nucleus which are sufficient enough for actin polymerization and matrix degradation. These pathways appear to converge at the level of the Rho family GTPases and Cdc42 [3]. Both RhoA and Cdc42 regulate matrix degradation through a mechanism which involves the delivery of MT1-MMP to the invadopodia and activates local matrix degradation [8,13].
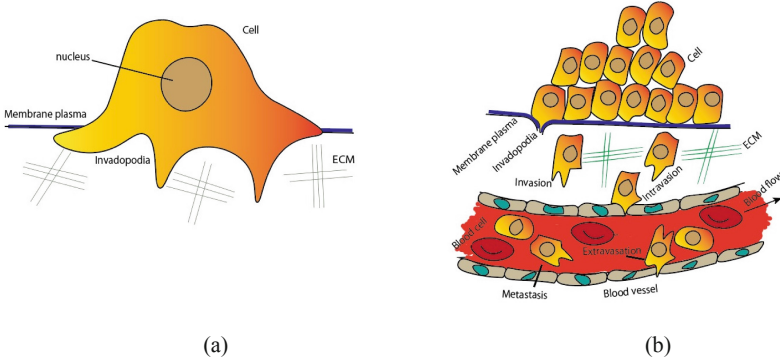
(a)   (b)

Fig. 1. a) An invasive cancer cell with invadopodia and b) Metastasis: invasion of tumor cell to blood vessel.

3   Individual Cell Model

In this section, we describe the mathematical modeling of a single cell deformation that describe the protrusions formation process, see Fig. 2. From [9], we define ECM is on the outside domain of the cell. Assume MT1-MMP enzymes flux denoted by $g(x,t)$ be given at any time on the cell membrane. It generates a flux degraded matrix (called ligands, c_*) on the cell boundary which will diffuse in the extracelullar medium. When bound to the cell membrane, the ligands will generate a signal σ which diffuses inside the cell. We describe the problem in Eulerian approach for this single cell model problem. Let $\psi(x,t)$ be a function for detecting the cell membrane is defined in the entire domain Ω. Define plasma membrane as

$$\Gamma_t = \{x \in \Omega | \psi(x,t) = 0\}. \tag{1}$$

where Ω be Lipschitz domain indicating the cancer cell with smooth boundary $\partial\Omega$ and x is a particle on the moving interface Γ_t.

The plasma membrane location is detected by the zero level set function, ψ which satisfies

$$\psi_t(x,t) + \upsilon \cdot \nabla\psi(x,t) = 0 \tag{2}$$

be smooth level set function and υ is the plasma membrane velocity on the interface

$$\upsilon = \gamma_n(\nabla\sigma - \nabla c_*) \qquad \text{on } \Gamma_t \tag{3}$$

where γ_n is a positive constant, σ is the gradient of signal inside the cell and c_* is the gradient of ligand outside cell. Hence, from (2) and (3),

$$\psi_t + \upsilon \cdot \nabla\psi = 0 \qquad \text{on } \Gamma_t. \tag{4}$$

We know the plasma membrane of the cell will either shrinks or expands. Degradation of ECM c by MMPs f happened on the plasma membrane Γ_t and produces

ligands (ECM fragment). The chemical reaction between this ECM and MMPs are formulated by

$$c_t + \nabla \cdot vc = -\kappa_c f c, \qquad\qquad c_{*t} + \nabla \cdot vc_* = \kappa_c f c \qquad\qquad \text{on} \ \bigcup_{0<t<T} \Gamma_t \times \{t\} \ (5)$$

where κ_c is reaction rate diffusion coefficent. We restrict c_* and σ outside and inside the cell. Hence, we defined f and σ inside the cell,

$$\sigma_t = d_\sigma \Delta \sigma \ \text{ in } \ \bigcup_{0<t<T} \omega_n^t \times \{t\}, \qquad\qquad \sigma|_{\Gamma_t} = c_* \ \text{ on } \ \bigcup_{0<t<T} \omega_n^t \times \{t\}$$

$$f_t = d_f \Delta f + k_f \sigma - \lambda_f f \ \text{ in } \ \bigcup_{0<t<T} \omega_n^t \times \{t\}. \tag{6}$$

Since there are no changes on MMPs density while cutting through fiber proteinases of ECM, it holds that

$$c_{*t} = d_{c_*} \Delta c_* \ \text{ in } \ Q_c, \quad \frac{\partial c_*}{\partial \nu} = g \ \text{ on } \ \bigcup_{0<t<T} \omega_c^t \times \{t\}. \tag{7}$$

3.1   Classical Solution Scheme

In this section, define $\omega_n^t = \{x \in \Omega | \psi(x,t) < 0\} \subset\subset \Omega$ as be one domain inside cell. Hence,

$$Q_n = \bigcup_{0<t<T} \omega_n^t \times \{t\} \tag{8}$$

and $\omega_c^t = \{x \in \Omega | \psi(x,t) > 0\}$ as an outside cell. Thus,

$$Q_c = \bigcup_{0<t<T} \omega_c^t \times \{t\}. \tag{9}$$

If the solution of $y = y(t)$ to

$$\frac{dy}{dt} = v(y,t), \qquad y|_{t=s} = x$$

is denoted by $y = U(t,s)x$. Then we have

$$\frac{D\psi}{Dt} = \psi_t + v \cdot \nabla = -(\nabla \cdot v)\psi.$$

The plasma membrane location is detected by the zero level set function and ψ is defined in the entire domain which satisfies

$$\psi_t(x,t) + \frac{dx}{dt} \cdot \nabla\psi(x,t) = 0 \tag{10}$$

be smooth level set function and $\frac{dx}{dt} = v(x,t)$ is the driving force of plasma membrane movement at the interface and defined by

$$v = \gamma_n (\nabla \sigma - \nabla c_*) \qquad\qquad \text{on} \ \ \Gamma \tag{11}$$

where γ_n is a positive constant, σ is the gradient of signal inside the cell and c_* is the gradient of ligand outside cell. Since velocity v is only defined on the boundary, it would be difficult for the domain to increase the volume of its shape and can cause discontinuities. As the plasma membrane is taken by the zero level set function, velocity extension is define in the whole domain to avoid discontinuities as

$$(\nabla\psi \cdot \nabla)w = 0, \quad \forall x \in \Omega, \qquad w \in (x, y)$$
$$w = v \quad \Gamma \tag{12}$$

where

$$v|_{\psi(x,t)=0} = \nabla\sigma|_{\psi(x,t)=0} - \nabla c_*|_{\psi(x,t=)=0}.$$

Hence, from (10) and (11),

$$\psi_t + v \cdot \nabla\psi = 0 \qquad \text{on } \Gamma. \tag{13}$$

To detect the membrane location, we define membrane boundary as

$$\Gamma = \{x \in \Omega | \psi(x, t) = 0\}. \tag{14}$$

where $\Omega \subset \mathbb{R}^N$, $N = 1, 2, \ldots$ be Lipschitz domain indicating the cancer cell and its environment with smooth boundary $\partial\Omega$ and x is a particle on the moving interface Γ. Based on Stefan problems, Γ is either pulled into interior region of a cell or pushed out towards the outer region of a cell.

Define f as MMPs and c as ECM, during cell transformation, f degrade c on the plasma membrane Γ and produces ligands (ECM fragment). Since MMPs act as a cutting tool for fiber-proteinases, there will be no changes on the MMPs density on the boundary. This act causes ligands to be produced in the domain outside cell.

When bound to the cell membrane, ligands will generate signal that will diffuse inside the cell that lead to actin polymerization. Actin polymerization is the key to protrusion at the leading edge and is counted by the gradient of inner sginal. This process will lead to the following equations,

$$\sigma_t = d_\sigma\Delta\sigma \text{ in } Q_n, \qquad \sigma|_{\Gamma_t} = c_* \text{ on } \Gamma$$
$$f_t = d_f\Delta f + k_f\sigma - \lambda_f f \qquad \text{in } Q_n. \tag{15}$$

Liouville's theorem guarantees the total mass of conservation of f, is conserved. Hence, produce the following derivations on the boundary

$$d_f\frac{\partial f}{\partial v} + (v \cdot v)f = 0 \qquad\qquad \text{on } \Gamma = \bigcup_{0<t<T} \Gamma_t \times \{t\}. \tag{16}$$

As there are no changes on MMPs density while cutting through fiber proteinases of ECM, it holds that

$$c_{*t} = d_{c_*}\Delta c_* \text{ in } Q_c, \quad c_*|_{\partial\Omega} = 0, \quad \frac{\partial c_*}{\partial v} = g \text{ on } \Gamma. \tag{17}$$

3.2   Free Boundary Problem

Proposedly, we extended the domain of applications to free boundary problem in order to simulate cell protrusions formation. We transformed the cell model from Fig. 2 into a simple cell model, see Fig. 3. From [9], free boundary problem makes it possible to localize membrane precisely while the velocity of the protrusion formation is not imposed but it is unknown of the PDE systems. Therefore, we treated cell membrane as free boundary surface to separate any activity happening in intracellular and extracellular regions.
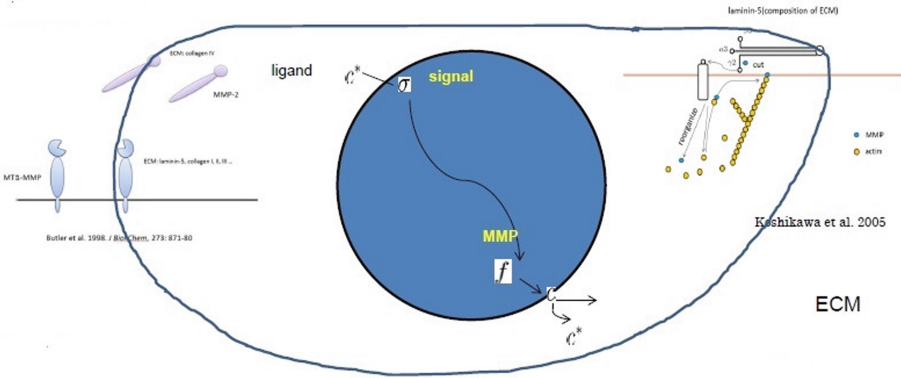
Fig. 2. An individual cell model

Let MT1-MMP be given at any time on the cell membrane. It generates a flux of degraded matrix called ligands denoted as c_* on the cell boundary and these ligands will diffuse in the extracellular medium. When bound to the cell membrane, ligands will generate a signal σ which will diffuse inside cell and the membrane is then transported by the normal velocity at the interface [9]. Thus, generation of signal for actin polymerization is represented by

$$d_\sigma^{-1}\sigma_t = \Delta\sigma \qquad \text{in } Q_n, \qquad \sigma\mid_{\partial\omega_c^t} = c_* \qquad (18)$$

and degradation of ECM becomes

$$d_{c_*}^{-1}c_{*t} = \Delta c_* \qquad \text{in } Q_c, \qquad \frac{\partial c_*}{\partial v} = 0 \qquad (19)$$

where $d > 0$ is a diffusion coefficient. Consider the core part problem of the cell. Let $\sigma = c_* = g(x,t)$ where the value is known. Define,

$$\theta = \begin{cases} \sigma \text{ in } Q_n = \{\psi < 0\} \\ c_* \text{ in } Q_c = \{\psi > 0\}. \end{cases} \qquad (20)$$
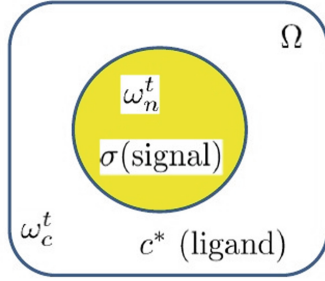
Fig. 3. A simple cell model

Now, we define the free boundary condition (Stefan condition). If g is continuous and diffuse where $\pm\psi > 0$ if and only if $\pm g > 0$, it holds that

$$\theta = g, \qquad v = -[\nabla\theta]_-^+ . \tag{21}$$

Therefore,

$$\gamma_n^{-1}\psi_t = -\gamma_n^{-1}(v \cdot v)\frac{\partial\psi}{\partial v}$$
$$= \left(\frac{\partial c_*}{\partial v} - \frac{\partial\sigma}{\partial v}\right)\frac{\partial\psi}{\partial v}$$
$$= \left[\frac{\partial\theta}{\partial v}\right]_-^+ \frac{\partial\psi}{\partial v}$$

where $\theta = g = c_*$ on Γ.

4   Numerical Scheme

4.1   Weak Form Derivation

In this section, we want to solve the modeling of invadopodia formation and migration of a single cell. The mathematical model used to solve these problems are based on the enthalpy formulation. From [6,11], the problems are described to be time dependent differential equations that satisfy boundary conditions at unknown interface where it has to be determined as part of the solution. Let $\Omega \subset \mathbb{R}^N$, $N = 1, 2, \ldots$ be a smooth bounded domain. Let

$$H(u)_t = \Delta u \qquad \text{in} \ \ Q = \Omega \times (0, T) \tag{22}$$
$$u \mid_{\partial\Omega} = 0, \qquad u \mid_{t=0} = u_0(x)$$

where H is the enthalpy function and $u = u(x, t)$ is the temperature distribution. Let $\varphi \in H^1(\Omega)$ be trial function,

$$-\int_\Omega \left(\frac{\partial}{\partial x}\frac{\partial u}{\partial x} + \frac{\partial}{\partial y}\frac{\partial u}{\partial y}\right)\varphi - \int_\Omega H(u)_t \varphi = 0.$$

Using integration by parts,

$$-\int_{\Omega} \frac{\partial}{\partial x}\left(\varphi \frac{\partial u}{\partial x}\right) + \frac{\partial}{\partial y}\left(\varphi \frac{\partial u}{\partial y}\right) - \left(\frac{\partial u}{\partial x}\frac{\partial \varphi}{\partial x} + \frac{\partial u}{\partial y}\frac{\partial \varphi}{\partial y}\right) - H(u)_t \varphi \, d\Omega = 0$$

Hence,

$$\int_{\Omega} (\nabla u \cdot \nabla \varphi) - H(u)_t \varphi \;\; d\Omega - \int_{\partial\Omega} (\nabla u) \cdot \varphi v \, d\Omega = 0.$$

4.2   Stefan Problems - Enthaply Formulation

Typically, Stefan problems involved in the evolution of smooth boundaries or interfaces between different phases of a pure substances that arises from the unstable solidification [5]. Define the temperature field is given by $u : Q = \Omega \times (0, T)$ and its evolution is given by

$$H(u)_t = \Delta u \qquad\qquad \text{in } Q \setminus \Gamma \tag{23}$$
$$[u]_-^+ = 0, \qquad\qquad [H(u)]_-^+ = \ell \qquad\quad \text{on } \Gamma$$

where $\Gamma = \{\Phi = 0\}$. On jump condition Γ, it holds

$$\ell v = -\left[k_+ \frac{\partial u_+}{\partial v} - k_- \frac{\partial u_-}{\partial v}\right]$$

where ℓ is the latent heat solidification, $k\pm$ are the constant of thermal diffusivities of the material on Ω and v is the outward normal vector. The jump is taken between solid to liquid or otherwise. Setting $\ell \neq 1$. Thus, we simplified problem into finding $u(x, t)$ and Γ_t such that,

$$v = -\frac{1}{\ell}\left[\frac{\partial u}{\partial v}\right]_-^+, \qquad\qquad x \in \Gamma. \tag{24}$$

Define the outward normal vector, v by

$$v = \nabla\Phi / |\nabla\Phi| \tag{25}$$

and curvature term κ by

$$\kappa = \nabla v = \nabla \cdot \left(\frac{\nabla\Phi}{|\nabla\Phi|},\right)$$

Rewrite the expression v from (24) and (25),

$$v = -[\nabla u] \cdot v = -[\nabla u] \cdot \left(\frac{\nabla\Phi}{|\nabla\Phi|}\right)$$

where v is the jump $[\nabla u]$ taken between two regions; solid to liquid or otherwise. Hence, from (13), we obtain,

$$\Phi_t + v \cdot \nabla\Phi = 0, \qquad\qquad v = (v \cdot v) v$$

where $v \cdot v$ is the Stefan condition.

   The total mass of conservation is guaranteed by Liouville's theorem of the first volume of enthalpy H between two regions must be equal during the process of physical or chemical changes.

Theorem 1 (Liouville's Theorem). *Assume that $\Omega \subset \mathbb{R}^N$, $N = 1, 2, \dots$ and boundary $\partial\Omega$. Let $\varphi \in C_0^\infty(Q)$ be an arbitrary constant and $\Omega_t^\pm \{\pm\Phi(\cdot, t) > 0\}$,*

$$\frac{d}{dt} \int_{\Omega_t^\pm} H(u)_t \varphi = \int_{\Omega_t^\pm} H(u)_t \varphi$$

$$+ H(u)\varphi_t \quad dx \pm \int_{\partial\Omega_t^\pm} H(u)\varphi v \cdot v \tag{26}$$

$$= \pm \int_{\partial\Omega_t^\pm} \varphi \frac{\partial u}{\partial v} - \frac{\partial \varphi}{\partial v} u + H(u)v \cdot v\varphi \, dS$$

$$+ \int_{\Omega_t^\pm} u\Delta\varphi + H(u)\varphi_t \, dx$$

Hence,

$$\frac{d}{dt} \int_\Omega H(u)\varphi = \int_\Omega u\Delta\varphi + H(u)\varphi_t \, dx$$

$$\Rightarrow \int \int_\Omega u\Delta\varphi + H(u)\varphi_t \, dxdt = 0$$

where dS denotes the surface element.

4.3 Degenerate Parabolic Equations

Define $X = L^1(\Omega)$. Let $f : \mathbb{R} \to \mathbb{R}$ be a Lipschitz continuous non-decreasing function on every bounded intervals satisfying $f(0) = 0$. Then the heat equation,

$$\begin{aligned}
v_t &= \Delta f(v), && \text{in } Q \\
f(v)|_{\partial\Omega} &= 0, && \text{on } \partial\Omega \\
v|_{t=0} &= v_0(x)
\end{aligned} \tag{27}$$

describe few phenomena including free boundary problem. By assumption from [4] We put $\mathcal{L} = -\Delta$ with

$$\mathcal{L} = -\Delta, \quad D(\mathcal{L}) = \{z \in W_0^{1,1}(\Omega) \mid \Delta z \in L^1(\Omega)\}$$

and $Av = -\Delta f(v)$ by

$$D(A) = \{v \in X | f(v) \in D(\mathcal{L})\}. \tag{28}$$

Consider initial value problem,

$$\frac{dv}{\partial t} + Av = 0 \tag{29}$$

$$v(0) = v_0$$

in X. Generate a contraction semi-group in X, denoted by $\{\mathcal{T}_t\}_{t>0}$. If (29) has a solution for every $v_0 \in L^1(\Omega)$, define $v = v(\cdot, t) \equiv \mathcal{T}_t v_0 \in ([0, +\infty), L^1(\Omega))$ as the nonlinear semi-group.

Hence,

$$\mathcal{T}_t v_0 = s - \lim_{k \to \infty} H\left(\frac{t}{k}\right)^k v_0, \tag{30}$$

where $\mathcal{T}_t v_0$ is uniform and bounded on intervals t and strongly differentiable almost everywhere. Therefore, (30) can be considered as "generalized solution" of (29). Suppose that A does not change rapidly and integral term by quasistatic approximation and integral term in (29) is relatively small, then we define $H'(0) = A$. Hence the solution of (29) can be simplify as $H(t)_g = e^{t\Delta} f(g)$ as the semigroup operator generated by $-A$.

Let A be the maximal monotone operator. Given any $\theta_0 \in D(A)$ exists a unique function

$$\begin{aligned} \theta = \theta_0 &\in L^\infty(\Omega \times (0,T)) \\ \theta(0) &= \theta_0. \end{aligned} \tag{31}$$

Moreover,

$$\|\theta(t)\| \le \|\theta_0\| \qquad \|H(\theta)_t\| = \|A\theta(t)\| \le \|A\theta_0\|, \qquad \forall t > 0.$$

However, $\zeta_\pm(\xi,t) = \lim_{x \to \xi, \pm\psi(x,t)>0} \zeta(x,t)$, $\zeta(x,t) \in \Gamma$. From (18), (19), and (20), let $\theta = f(v)$ if and only if $v = H(\theta)$, then,

$$H_g(\theta)_t = \Delta\theta \quad \text{in } Q/\Gamma, \qquad \left.\frac{\partial\theta}{\partial v}\right|_{t=0} = 0 \tag{32}$$

where

$$H_g(\theta) = \begin{cases} d_{c_*}^{-1}\theta + \ell \text{ in } \{\theta > g\} \\ d_\sigma^{-1}\theta - \ell \text{ in } \{\theta < g\}. \end{cases}$$

since $\ell > 0$ and $v > 0$.

5   Numerical Simulation and Results

We start our numerical experiments to verify our methods. This section is divided into two parts; level set method and enthalpy formulation (phase change formulation).

Since we treated the problem as free boundary, level set is suitable to deal with membrane cell to indicate the membrane interface as it is easy to implement with low computational cost. Even though the calculation of curvature and velocity of interface in order to indicate the plasma membrane interface is straightforward using level set method, when two interfaces between outer and inner cell are close to each other, the discontinuity in the derivatives of level set function between the these two interfaces can effect the estimation of velocity and curvature. Thus, we define the velocity extension to the whole domain in order to avoid singularities and instabilities as in Sect. 3.1.

While phase field method (enthalpy formulation) employ phase field variable that varies smoothly from zero to unity between two phases over the diffuse interface region which has a small but numerically resolvable thickness [21]. Thus, it provide the diffuse description of vanishing thickness of membrane interface between outer and inner cell.

We will discuss the results obtained from the simulations. All numerical calculations and simulations has been done in FreeFem++ [12].

5.1   Level Set Methods

Numerical works for free boundary problem of this model face a crucial difficulty in dealing with moving boundary. First, we implement level set method to a single cell model. Let level set function $\psi = \psi(\cdot, t)$ be smooth level function. Recall from Sect. 3.1.

Assume that there is no signal density at the start of the computation. ECM will degrade and produce ligands outside cell that diffuse and the density of ligands will bind to receptor and generate a signal inside cell. Signal density diffuse inside the cell and leads to actin polymerization.

From (18) and (19) we define the boundary data as:

1. Test I: Let $\sigma = c_* = g = 0.1 \, [2 + \cos(3\pi(x+y)) \cos(\pi(x+0.3))]$ [10] and the solution of level set as $\psi = 0.05 \times \tanh(((x-y)^{1/2} - R)/\epsilon h)$ where $\epsilon = 2$ and $h = 0.3$ [14].
2. Test II: We then do some modification on the equations from Test I.
   Let $\sigma = c_* = g = 0.01 \, [2 + \sin(2\pi(x+y)) \cos(\pi(x+0.2))]$ and the solution of level set become, $\psi = 0.05 \times \sinh(((x-y)^{1/2} - R)/\epsilon h)$ where $\epsilon = 5$ and $h = 0.2$.
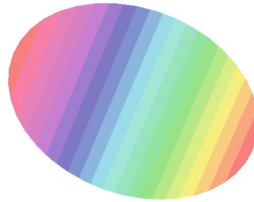

Fig. 4. Initial cell shape

Figure 4 shows the initial shape of a cell and Fig. 5a) and 5b) show the existence of invadopodia and protrusion formed at the boundary of the cell from Test I and II. The displacement of the membrane due to presence of signal gradient that has been stimulated from the interactions between membrane and the surrounding ECM cause the existence of protrusion.
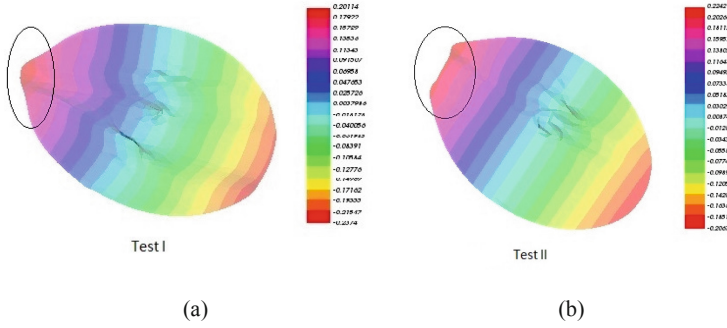
Fig. 5. a) and b) Simulation of cell deformation leads to invadopodia formation based on Test I and II.

5.2   Cell Deformation: Free Boundary Conversion

During phase change process between outer and inner cell, abrupt changes can happen at phase interfaces of a cell between outside and inner cell which can produce singularities and instabilities. Here, invadopodia will perforate and pass through collagen walls which have complex appearances.

Let the plasma membrane be time dependent. Therefore, simulation of enthalpy formulation is done based on time dependent with an implicit time scheme. As time is self discretized, the simulation process takes place through discrete time steps. Phase change starts when invadopodia begin to perforate and penetrate through cell to go outside the cell which we called invasion that is easy to see based on 2-dimensional rather than 3-dimensional. Let

$$
\begin{aligned}
H_g(\theta)_t &= \Delta\theta \qquad \text{in} \ \ Q = \Omega \times (0, T) \\
\frac{\partial\theta}{\partial\nu}\bigg|_{\partial\Omega} &= 0, \\
\theta|_{t=0} &= \theta_0(x) \geq 0
\end{aligned}
\tag{33}
$$

where

$$
H_g(\theta) = \begin{cases} \alpha_+\theta + \ell \ \text{in} \ \{\theta > g\} \\ \alpha_-\theta - \ell \ \text{in} \ \{\theta < g\} \end{cases}.
$$

We discretize the problem based on time discretization, N_{t+1} time steps into $t_n = t_0 + n\Delta t$, $n = 0, 1, \ldots, N_t$ by denoting the time step size and implicit Euler time discretization is applied to problem (33). For $n = 0, 1, \ldots, N_t$, find $\theta^{n+1} \approx \theta(\cdot, t_{n+1})$ such that

$$\frac{\theta^{n+1}}{\delta t} - \nabla \cdot (\kappa \nabla \theta^{n+1}) = f^{n+1} + \frac{\theta^n}{\delta t}, \qquad in \ \ Q = \Omega \times (0, T)$$

$$\frac{\partial \theta^{n+1}}{\partial \nu} = 0, \qquad on \ \ \partial \Omega_t \tag{34}$$

$$\theta^{n+1}|_{t=0} = \theta_0(x) \geq 0.$$

5.3   Enthalpy Formulation

In this problem, the density of signals and ligands are not time dependent but the plasma membrane is treated as free boundary and time dependent. From (33) we define enthalpy $\nu = H_g(\theta)$ by,

$$f(\nu) = \begin{cases} \alpha_-^{-1}(\nu + \ell), & \nu < \ell \\ 0, & -\ell \leq \nu \leq \ell \\ \alpha_+^{-1}(\nu - \ell), & \ell < \nu. \end{cases} \tag{35}$$

if and only if $\theta = f_g(\nu) = f(\nu) + g$. Hence,

$$\nu_t = \Delta f(\nu) + \Delta g \qquad in \ \ Q \tag{36}$$

$$\frac{\partial}{\partial \nu} f(\nu) \Big|_{\partial \Omega} = 0 \qquad \frac{\partial g}{\partial \nu} \Big|_{\partial \Omega} = 0$$
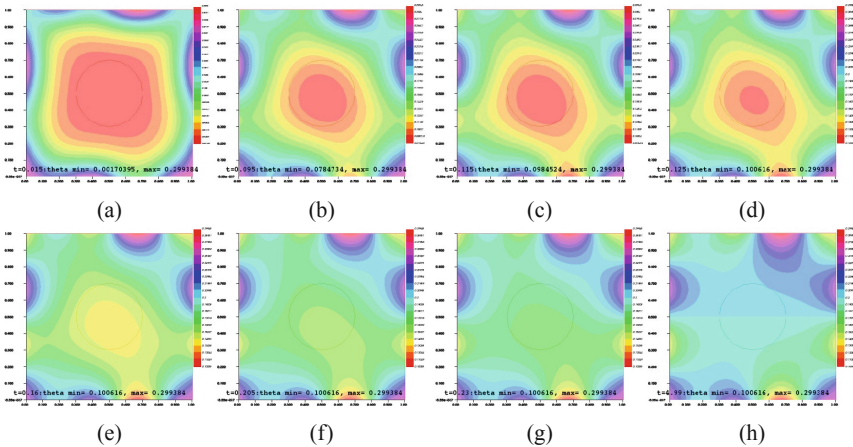
$$\nu|_{t=0} = \nu_0(x) \geq 0.$$

Fig. 6. A signal inside cell activated by ligand outside cell, start to produce invadopodia and migration happened from Test I.
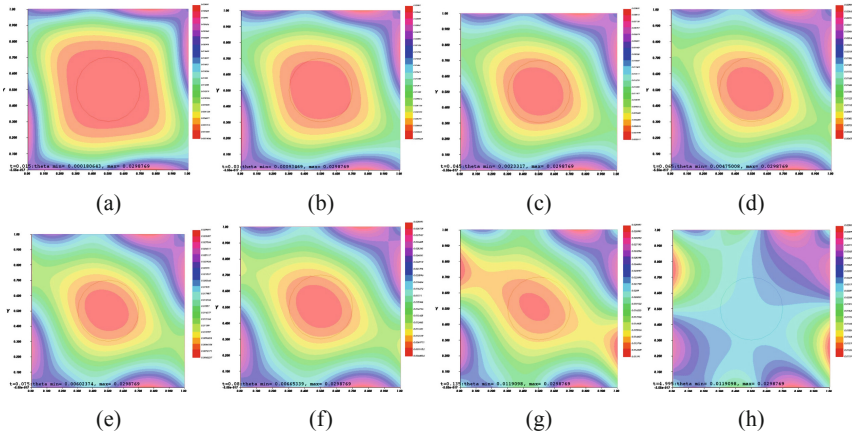
Fig. 7. Protrusion of invadopodia and migration of a cell from Test II .

Theorem 2. *Let Ω be an open bounded domain subset $\mathbb{R}^N$, $N = 1, 2$ with boundary $\partial\Omega$ is at least C^2. Let g be a nonnegative solution that g is bounded in $L^1(0, T; L^\infty(\Omega))$. Hence, Δg is also bounded in $L^1(0, T; L^\infty(\Omega))$. Assume that triangular structure guarantees that it is easily bounded for positive time from $L^1(\Omega) \to L^\infty(\Omega)$. Therefore, there exists at least one weak solution that is continuous from $[0, \infty)$ into $L^1(\Omega)$. Since, a priori $L^1(\Omega)$-estimates hold uniformly in time of solution (36), therefore, $v \in L^\infty(0, \infty; L^p(\Omega))$, $1 \le p < \infty$.*

Similarly, as in Sect. 5.2, we discretize the problem (36) into

$$\frac{v^{n+1}}{\delta t} - \nabla \cdot (\kappa \nabla f^{n+1}) - \nabla \cdot (\kappa \nabla g^{n+1}) = h^{n+1} + \frac{v^n}{\delta t}, \qquad \text{in } Q = \Omega \times (0, T)$$

$$\frac{\partial f^{n+1}}{\partial v} = 0, \qquad \frac{\partial g^{n+1}}{\partial v} = 0 \qquad \text{on } \partial\Omega_t \qquad (37)$$

$$v^{n+1}|_{t=0} = v_0(x) \ge 0.$$

An enzyme MT1-MMP will degrade extracellular matrix (ECM) and produces ligands that diffuse and bind to membrane receptors. This process distrupted the architecture of the plasma membrane. Hence, generate signal inside cell that diffuse and lead to actin polymerization. Phase change starts on the plasma membrane during this process and invadopodia start to protrude at the cell membrane and migrate.

Figure 6, 7, 8 and 9 show cell deformation process when mutation happens to a normal cell before it turns into cancer cell. Invasion starts in cancer cell after protrusion of invadopodia and starts to break away from the main cell. The changes and movement on cell is the consequence from the interactions between cell membrane and surrounding ECM that stimulates the existence of ligands and then activate the signal gradient. As time increases, the cell migrates to the nearby areas as to settle and grows in different parts of the body and become
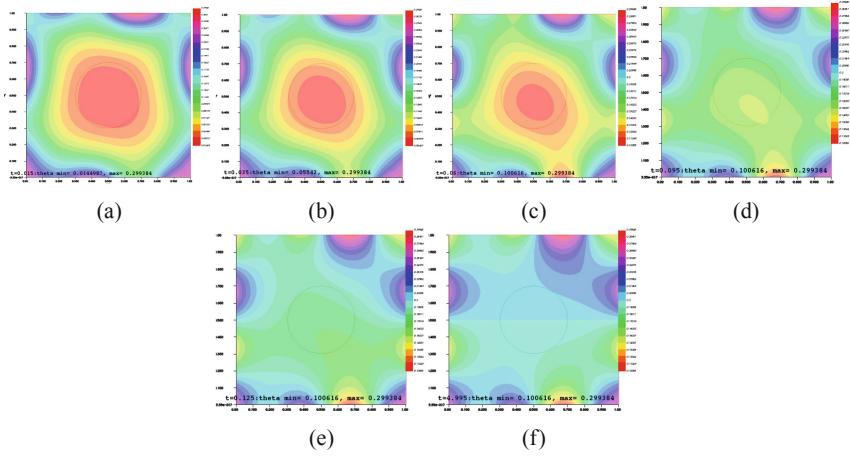
Fig. 8. Invasion process start faster from Fig. 6.
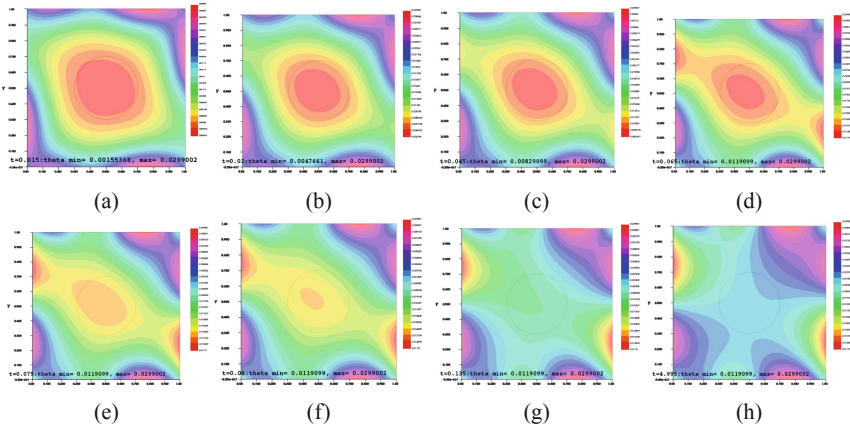
Fig. 9. A signal inside cell activated by ligand outside cell and start to produce invadopodia. Cancer cell start migrating to other cells faster than Fig. 7.

dispersed. However, the results from Fig. 8 and 9 show that the phase change of cell membrane from Eq. (36) is much more faster than Eq. (33). Equation (36) explains why the phase change problem from Fig. 8 and 9 happened faster than Fig. 6 and 7. In Eq. (36), we considered the concentration of MT1-MMP, f embedded in cell membrane degrades the ECM by contact and, taken signal density to be equal as function $g(x, t)$ which also represents MT1-MMP at any time t on the interface. While Eq. (33) only considers the density of signal or ligand based on Eq. (20).

As protrusion happened, the cell starts migrating through disrupted membrane, the protrusion velocity decreases, indicating the stabilization of invadopo-

dia formation. Phase change interface position decreases on increasing time and the density of signal decreases due to being away from the main cell.

6   Conclusion

We developed a numerical approach to solve Stefan problem of invadopodia formation using level set and enthalpy formulation (phase change problems). All described methods are implemented using FreeFem++. Level set is used to detect membrane location by zero level function of ψ and phase change problems in cancer cell has been developed using enthalpy formulation. The enthalpy method is demonstrated to be proficient and accurate in dealing with this type of problem. Both methods are used to solve cancer cell deformation and invasion numerically where protrusions appeared by the existence of invadopodia and invasion happened when cancer cell starts to spread to a different part of the cell.

References

1. Admon, M.A.B., et al.: Mathematical modeling and simulation in an individual cancer cell associated with invadopodia formation. Ph.D. thesis, PHD Thesis, Osaka University, Japan (2015)
2. Anderson, A.R., Chaplain, M.A., Newman, E.L., Steele, R.J., Thompson, A.M.: Mathematical modelling of tumour invasion and metastasis. Comput. Math. Methods Med. **2**(2), 129–154 (2000)
3. Beaty, B.T., Condeelis, J.: Digging a little deeper: the stages of invadopodium formation and maturation. Eur. J. Cell Biol. **93**(10–12), 438–444 (2014)
4. Berger, A.E., Brezis, H., Rogers, J.C.: A numerical method for solving the problem. RAIRO. Analyse numérique **13**(4), 297–312 (1979)
5. Chen, S., Merriman, B., Osher, S., Smereka, P.: A simple level set method for solving Stefan problems. J. Comput. Phys. **135**(1), 8–29 (1997)
6. Crank, J.: The Mathematics of Diffusion. Oxford University Press, Oxford (1979)
7. Den Hartigh, J.C., Van Bergen En Henegouwen, P.M., Verkleij, A.J., Boonstra, J.: The EGF receptor is an actin-binding protein. J. Cell Biol. **119**(2), 349–355 (1992)
8. Eddy, R.J., Weidmann, M.D., Sharma, V.P., Condeelis, J.S.: Tumor cell invadopodia: invasive protrusions that orchestrate metastasis. Trends Cell Biol. **27**(8), 595–607 (2017)
9. Gallinato, O., Ohta, M., Poignard, C., Suzuki, T.: Free boundary problem for cell protrusion formations: theoretical and numerical aspects. J. Math. Biol. **75**(2), 263–307 (2016). https://doi.org/10.1007/s00285-016-1080-7
10. Gallinato, O., Poignard, C.: Superconvergent second order cartesian method for solving free boundary problem for invadopodia formation. J. Comput. Phys. **339**, 412–431 (2017)
11. Groot, R.D.: Second order front tracking algorithm for Stefan problem on a regular grid. J. Comput. Phys. **372**, 956–971 (2018)

12. Hecht, F.: New development in freefem++. J. Numer. Mathe. 20(3–4), 251–266 (2012)
13. Jacob, A., Prekeris, R.: The regulation of MMP targeting to invadopodia during cancer metastasis. Front. Cell Dev. Biol. **3**, 4 (2015)
14. Kennedy, D.: Level set methods for two-phase flows with fem (2014)
15. Koshikawa, N., Giannelli, G., Cirulli, V., Miyazaki, K., Quaranta, V.: Role of cell surface metalloprotease MT1-MMP in epithelial cell migration over laminin-5. J. Cell Biol. **148**(3), 615–624 (2000)
16. Koshikawa, N., Minegishi, T., Sharabi, A., Quaranta, V., Seiki, M.: Membrane-type matrix metalloproteinase-1 (MT1-MMP) is a processing enzyme for human laminin $\gamma2$ chain. J. Biol. Chem. **280**(1), 88–93 (2005)
17. Murphy, D.A., Courtneidge, S.A.: The 'ins' and 'outs' of podosomes and invadopodia: characteristics, formation and function. Nat. Rev. Mol. Cell Biol. **12**(7), 413–426 (2011)
18. Pourfarhangi, K.E., Bergman, A., Gligorijevic, B.: ECM cross-linking regulates invadopodia dynamics. Biophys. J . **114**(6), 1455–1466 (2018)
19. Saitou, T., Rouzimaimaiti, M., Koshikawa, N., Seiki, M., Ichikawa, K., Suzuki, T.: Mathematical modeling of invadopodia formation. J. Theor. Biol. **298**, 138–146 (2012)
20. Sakurai-Yageta, M., et al.: The interaction of IQGAP1 with the exocyst complex is required for tumor cell invasion downstream of Cdc42 and RhoA. J. Cell Biol. **181**(6), 985–998 (2008)
21. Tan, L., Zabaras, N.: A level set simulation of dendritic solidification with combined features of front-tracking and fixed-domain methods. J. Comput. Phys. **211**(1), 36–63 (2006)

Multi-level Mathematical Models for Cell Migration in Confined Environments

Luigi Preziosi[✉] and Marco Scianna

Politecnico di Torino, 10134 Torino, Italy
{luigi.preziosi,marco.scianna}@polito.it
https://staff.polito.it/luigi.preziosi/

Abstract. The aim of this contribution is to put together in a systematic way several approaches operating at different scales that were recently developed to describe the phenomenon of physical limit of migration, that occurs when the environment surrounding cells results restrictive, and to apply it to tumour growth and invasion. In particular, we will present: (i) a mechanical model of the behaviour of a cell within a microchannel that gives a blockage criterium for its penetration; (ii) a cellular Potts model to describe the dependence of the speed of a malignant cell from the mechanical characteristics both of its compartments (i.e., nucleus and cytosol) and of its environment; (iii) a multiphase model embodying such effects; (iv) the proper interface conditions to implement to deal with tumour invasion across matrix membranes and cell linings.

Keywords: Cell migration · Cancer modelling · Extracellular matrix · Nucleus elasticity · Cell deformability

1 Introduction

Cell migratory ability is crucial in many physiological processes, occurring both during embryonic development and in adult life. In pathological conditions, cell motile behaviour is involved in chronic inflammatory diseases, such as artheriosclerosis, and in cancer growth. In particular, malignant cells have to migrate through confined environments, full of steric obstacles and physical barriers, whose opening and space available for locomotion might be substantially limited. It is the case of (i) dense extracellular matrix (ECM) regions, constituted by tightly-packed collagenous bundles, (ii) layers or membranes of non-malignant cells, that even compartmentalize the pathological tissue from the surrounding host (e.g., a mesothelial membrane prevents ovary tumour spreading), and (iii) walls of blood or lymphatic vessels, that have to be penetrated by cancer individuals to initiate the metastatic cascade.

In all these situations, tumour cells can achieve significant movement by squeezing through the available space. In this process, experimental evidence widely shows that cell cytoplasm is very flexible and is able to accommodate

nearly any pore size. On the contrary, the cell nucleus, being one order of magnitude stiffer than the surrounding cytosolic region, might not be able to adapt so well its shape to pores smaller than its diameter. As a result, the locomotion of the entire cell might be blocked. The critical pore size below which cells remain trapped has been denoted in the experimental literature as the *physical limit of migration* [28] and has been empirically estimated to be of the order of 10% of the relaxed nucleus cross-section.

One way to describe such a difficulty consists in observing that tumour cells need to do some work to deform their nucleus to be able to penetrate through constraining geometries. This energetic cost may become prohibitive when these constrictions become too small. In these cases, the nuclear deformability becomes a limiting factor for the overall cell migration [27, 29]. In order to circumvent this difficulty, malignant cells produce matrix degrading enzymes (MDEs), that are capable to digest ECM components. This action has the effect of widening the pores of the fiber network, making the migration condition less restrictive and allowing the cell to escape and invade the surrounding tissue.

In the present contribution, we will put together several approaches dealing with cell migration in confined environments, that we have recently developed. The aim is to organically give the reader a summary of the results obtained at different scales of examination and to highlight the links between them. In particular, we will start from descriptions at the single-cell level getting information that will be then upscaled and nested in macroscopic models analyzing growth and invasion of entire multicellular tumour masses. In more details, in the following section, we will focus on the mechanics of a single cell and on the evaluation of the work it has to do to penetrate a microchannel. This will give us a blockage criterium depending on the mechanical characteristics both of the cell and of the matrix microstructure. In Sect. 3, we will use a cellular Potts model to mimick cell motion within different extracellular enviroments, including microchannels, regular fiber networks and micropillar arrays that are used in *in vitro* experiments. The resulting outcomes will give a relationship between cell speed, cell deformability and some structural characteristics of the surrounding extracellular elements. In Sect. 4, we will nest the information obtained at the single-cell level in a multiphase continuum mechanics model, so that the macroscopic invasive behavior of a tumour mass will be properly linked to specific microscopic characteristics of the component malignant cells. Finally, in Sect. 5, we will show how such models can be applied to problems involving basal membranes, cell linings and sheets that compartimentalise *in situ* tumours and have to be broken up to give rise to further invasion.

2   Mechanical and Geometrical Conditions for Cell Penetration in Narrow Channels

We first start to focus on cell-level mechanisms. In this respect, we deal with a bi-compartmental individual, i.e., differentiated in the nucleus and the surrounding cytoplasm. The nucleus is the stiffest component: its deformability is mainly

regulated both by the chromatin structure and by lamin intermediate filaments that form a part of its envelope. The cytoplasm, contained in the plasmamembrane (PM), is made of a complex mixture of cytoskeletal filaments, dissolved macro-molecules, and water. It also contains many organelles and sub-structures that are fundamental for a wide range of cell functions and is much more flexible than the nucleus [8,9].

As already recalled in the Introduction, the cell and its nucleus have to deform when crawling within three-dimensional confining environments, such as ECM regions where the typical distance between collagenous fibers is small enough. It is clear that the possibility of success in this action mainly depends on two characteristics

(i) the ability of the cell to exert sufficiently high traction forces to pull its body ahead carrying its nucleus along;
(ii) the mechanical properties of the nucleus itself.

In fact, the deformability of the cytoplasm is not an issue here, because it has practically no difficulties in squeezing anywhere.

This process is modeled and analyzed in [10] and [11] in the simplified scenario of an individual cell entering a cylindrical microchannel, that has a diameter smaller than the size of the nucleus. The cell is assumed to exert traction forces where its membrane is in contact with the walls of the external structure. The deformation achieved by the nucleus is then prescribed with the obvious constraint that its cross section perpendicular to the direction of motion has to fit the cross section of the microchannel.

Our basic assumption is that, in order to have microchannel invasion, the work that can be performed by the cell to pull itself within the cylinder must be larger than the energy needed to obtain sufficient squeezing of the nucleus. As mentioned above, the cytoplasm is instead treated as an inviscid liquid that can easily adapt to fit any channel size, so that the energetic contribution related to its deformation is neglected. Entering in more details, the energy provided to the cell can derive both by the activation of its acto-myosin contraction machinery joined with the formation of integrin-mediated adhesion bonds and by passive stresses exterted on the individual by external elements (e.g., pressure from surrounding cells in the case of multicellular aggregates or fluid pressure in microfluidic devices). Such two types of contributions are hereafter denoted with $\mathcal{W}_{active}$ and $\mathcal{W}_{passive}$, respectively.

The energy needed for nuclear morphological variations is given by the sum of two components, the former ($\mathcal{W}_S$) relative to the deformation of the elastic membrane, the latter ($\mathcal{W}_V$) to the compression of the internal genetic material, described as a neo-Hookean elastic solid. The energy required to squeeze in a sufficient way the nucleus to pass through the microchannel is then compared with the work that can be performed by the cell to pull itself within the cylinder, that is

$$\mathcal{W}_{active} + \mathcal{W}_{passive} > \mathcal{W}_S + \mathcal{W}_V. \tag{1}$$

In order to compute the terms in Eq. (1), some assumptions need be made are necessary. Experimental evidences [28] suggest that, when the cell is forced to

fit in a cylindrical microchannels of restricting geometries, the nucleus takes an elongated shape oriented along the cell longer axis, that resembles an ellipsoid or a sigar with a cylindrical inner part ending with two spherical caps. Despite the geometrical difference, in [11] we show that the energy required to achieve these two different configurations is practically identical. So, one can consider a prolate ellipsoid, with minor semi-axes equal to the radius of the channel pore, i.e., R_p, with the same volume $V = \frac{4}{3}\pi R_n^3$ as the spherical shape the nucleus had before entering the microchannel.

In [10] and [11] the internal bulk of the nucleus is described as a neo-Hookean incompressible material for which

$$\mathcal{W}_V = \int_{V_{sphere}} W_V \, dV = \int_{V_{sphere}} \frac{\mu}{2} \left(\text{tr} \, \mathbf{C} - 3 \right) dV \,, \tag{2}$$

where $\mathbf{C}$ is the Cauchy-Green strain tensor that in the case of a deformation into an ellipsoid is simply

$$\mathbf{C} = \text{diag} \left\{ \frac{R_p^2}{R_n^2}, \frac{R_p^2}{R_n^2}, \frac{R_n^4}{R_p^4} \right\} \,. \tag{3}$$

This gives

$$W_V = \frac{2}{3}\mu\pi R_n^3 \left(2\hat{R}_p^2 + \frac{1}{\hat{R}_p^4} - 3 \right) \,, \tag{4}$$

where $\hat{R}_p = R_p/R_n$. Of course, there are no conceptual difficulties in using different constitutive laws, such as Gent's constitutive model

$$W_V = -\frac{\mu}{2} K \ln \left(1 - \frac{\text{tr} \, \mathbf{C} - 3}{K} \right) \,,$$

or Ogden's constitutive model written in terms of principal stretches λ_j

$$W_V = \sum_{i=1}^{3} \frac{\mu_i}{\alpha_i} \left[\lambda_1^{\alpha_i} + \lambda_2^{\alpha_i} + (\lambda_1\lambda_2)^{-\alpha_i} - 3 \right] \,,$$

or the one that takes into account of compressibility

$$W_V = \frac{\mu}{2} \left[(\det \mathbf{C})^{-1/3} \text{tr} \, \mathbf{C} - 3 - \ln(\det \mathbf{C}) \right] + \frac{\kappa}{2} \left[(\det \mathbf{C})^{1/2} - 1 \right]^2 \,.$$

Actually, Ogden's models are found to fit best the mechanical response of biological materials. However, it makes sense to use more complicated constitutive models when there are enough experimental evidences suggesting that one model is better than others. This knowledge at present is not available yet.

Following [7], in [10] the energy required to deform the nuclear surface area (i.e., the nuclear envelope) is taken to be equal to

$$\mathcal{W}_S = \lambda(\Delta S)(\Delta S)^2. \tag{5}$$

In Eq. (5), ΔS is the increment in the surface area resulting from the passage from the initial spherical shape to the final ellipsoidal configuration whereas $\lambda(\Delta S)$ is an increasing function of the increment of surface area, or possibly constantly equal to λ_0. This is done to include the observation that there is a maximum possible area extension of the nuclear envelope, that the underlying lamin network is able to achieve due to the stretched configuration. In the case of a deformation into an ellipsoid

$$\Delta S = 2\pi R_p^2 \left(1 + \frac{h_e}{R_p e} \sin^{-1} \sqrt{1 - \frac{R_p^2}{h_e^2}} \right) - 4\pi R_n^2 \tag{6}$$

where $h_e = \dfrac{R_n^3}{R_p^2}$ is the longest semi-axis of the prolate ellipsoid.

The other relevant component to be evaluated in Eq. (1) is the work $\mathcal{W}_{active}$ done by the traction forces that involve both formation of integrin-mediated adhesion bonds with the extra-cellular matrix (ECM) and actomyosin-mediated contraction to propel the nucleus forward. What is known by traction force microscopy [2,6,16,20] is that traction forces are exerted mainly in the regions close to the head and to the tail of polarized cells and that the traction force deriving from single cell-ECM bond is about 10 pN. Thus, the total force also depends on the extension of the surface of contact composed by ECM ligands (i.e., the portion α_m of the channel surface the cell can be actually bound to) and on the density of integrins that are expressed and activated over this area, denoted by ρ_b. Then, $\mathcal{W}_{active}$ can be evaluated by computing the work done by adhesion forces F_z to pull the nucleus completely in from the entrance of the microchannel, that is, for a distance

$$\Delta L = 2\frac{R_n^3}{R_p^2} - R_n + \sqrt{R_n^2 - R_p^2}.$$

Referring to [11] for more details, the above procedure allows to specify Eq. (1) and to determine a criterium able to describe when a cell with undeformed nucleus radius R_n can penetrate a cylindrical microchannel with a cross-section area A_p. The criterium involves the dimensionless numbers

$$G = \frac{\rho_b \alpha_m F}{\mu} \qquad \text{and} \qquad \beta = \frac{\lambda_0 R_n}{\mu}. \tag{7}$$

The former compares quantities related to traction forces with the nucleus shear modulus μ. Hence, large G's correspond, for instance, to larger traction forces, better ability to adhere to the substratum, or softer cell nuclei. The latter is proportional to the ratio between μ and the stiffness of the nuclear membrane quantified, as seen in Eq. (5), by λ_0. So, β becomes important when the membrane stiffness (times the nucleus radius) is substantially larger than the nucleus shear modulus.

Introducing the normalized counterparts of cell radius and microchannel cross section

$$\hat{R}_c = \frac{R_c}{R_n} \qquad \text{and} \qquad \hat{A}_p = \frac{A_p}{\pi R_n^2},$$

the criterium reads as

$$G = \frac{\rho_b \alpha_m F}{\mu} < \frac{a(\hat{A}_p) + 8\pi\beta b(\hat{A}_p)}{c(\hat{A}_p) L(\hat{A}_p, \hat{R}_c)} := \bar{G}, \qquad (8)$$

where

$$a(\hat{A}_p) = \frac{2}{3}\hat{A}_p + \frac{1}{3\hat{A}_p^2} - 1,$$

$$b(\hat{A}_p) = \left[\frac{\hat{A}_p}{2}\left(1 + \frac{\sin^{-1}\sqrt{1 - \hat{A}_p^3}}{\hat{A}_p^{3/2}\sqrt{1 - \hat{A}_p^3}} \right) - 1 \right]^2,$$

$$c(\hat{A}_p) = \frac{2}{\hat{A}_p} - 1 + \sqrt{1 - \hat{A}_p},$$

and

$$L(\hat{A}_p, \hat{R}_c) = \frac{4\hat{R}_c^3 - 3\hat{A}_p - 2\hat{A}_p^{3/2} - 2 - 2(1 - \hat{A}_p)^{3/2}}{3\sqrt{\hat{A}_p}}.$$

It can be noticed that if the effect of the stiffness of the nuclear membrane is neglected, i.e., $\beta = 0$, the r.h.s. of (8) is a function of geometric quantities only, namely the normalized channel cross section $\hat{A}_p$ and cell size (through L) whereas all relevant mechanical characteristics are contained in the l.h.s. in G.

More importantly and independently from its specific form, the criterium allows to discriminate whether a cell is able to squeeze through a narrow passage or not. In particular, as sketched in Fig. 1, given a cell of radius R_c (normalized with respect to the nucleus of radius R_n), one can identify in the parameter space $(G, \hat{A}_p)$ a "no-pass" region (shaded in Fig. 1). For instance, knowing the density ρ_b of expressed and activated integrins on the contact surface, the portion α_m of the channel available to form bonds, the cytoskeletal traction force F generated by a single bond and, finally, the mechanical properties of the nucleus (i.e., its shear modulus μ and the envelope stiffness β), moving rightward along the dotted arrow for a given G (path in blue in Fig. 1) it is possible to identify the minimum cross section of ECM channels that can be penetrated by the cell.

Conversely, knowing the characteristic dimensions of the ECM pores, of the cell, and of the nucleus, moving first upward on the graph along the dashed arrow it is possible to identify the minimum value of the parameter G that the cell must have in order to be able to penetrate the matrix environment. For instance, for constant adhesion parameters, this means that the nucleus must be soft enough (i.e., μ has to be below a threshold value) or the traction force must be strong enough (i.e., F has to be above a threshold value).

Such a criterium may represent a plausible explanation of different behaviours occurring in a malignant cell population, which yields to moving and non-moving clones due to differentiated nucleus stiffness or cell traction abilities.
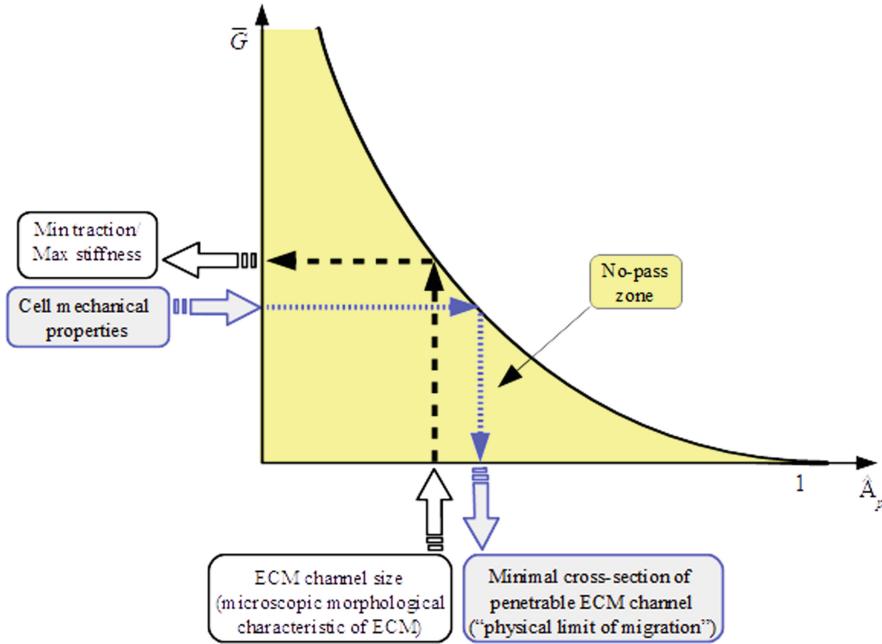
Fig. 1. Schematic representation of the biological interpretation of the relation between $\bar{G}$ and $\hat{A}_p = A_p/(\pi R_n^2)$ for given values of β and of the cell radius. The region below the curve identifies the set of parameters for which the cell cannot enter inside the ECM pore.

3   Cell Migration Speed in Constrained Environments

The model described in the previous section gives a criterium that determines whether a cell is able or not to enter a microchannel or a fibrous network according to its ability to do the required work. In order to get a dynamic view of this process, one can instead use individual cell-based approaches. One of them is the cellular Potts model (CPM), that is a grid-based stochastic method able to mimic cell dynamics using a stochastic algorithm for energy minimization. In particular, the CPM represents cell-level objects as patches of domain grid sites sharing the same identification number. The fundamental assumption is that cell behavior and interactions with the local microenvironment can be described by a *hamiltonian* function: at each time-step, the system configuration is then updated according to a modified Metropolis method for Monte Carlo-Boltzmann dynamics, i.e., cell behaviors that require more energy are more unlikely to happen.

The advantage of this approach for the problem of our interest consists in the possibility to relate the speed of a tumour cell within constraining enviroments both to the mechanical characteristics of its main compartments (i.e., nucleus and cytoplasm) and to the geometry of the surrounding elements. In

particular, in [23–25], we focused on cell motion inside different typologies of matrix structures: microchannels, fiber networks, and microfluidic-based devices characterized by the presence of constrictions formed by arrays of pillars, as shown in Fig. 2(A-B-C).

Independently of the specific geometry, the generalized energy H establishing cell behavior is given by the sum of two contributions:

$$H = H_{adhesion} + H_{shape}. \tag{9}$$

$H_{adhesion}$ is the general extension of the Steinberg's differential adhesion hypothesis. It takes into account both the generalized contact tension between the nucleus and the cytoplasm within the cell and the effective adhesion between the migrating individual and the extracellular components. H_{shape} instead sums the energetic components that describe the geometrical attributes of the two subcellular compartments included in the model, say $H_{surface}^{nucleus}$, $H_{surface}^{cytosol}$, $H_{volume}^{nucleus}$ and $H_{volume}^{cytosol}$. Referring to [23–26] for the specific contributions used, generally speaking they take the form of elastic energetic penalties that increase when the two cell subunits deviate from their relaxed configuration. In this respect, the elastic modulus of $H_{surface}^{nucleus}$ (resp., $H_{surface}^{cytosol}$) measures the deformation potential of the nucleus (resp., of the cytosol), whereas the elastic modulus of $H_{volume}^{nucleus}$ (resp., $H_{volume}^{cytosol}$) measures the compressibility of the nucleus (resp., of the cytosol). To model sustained cell migration Eq. (9) may also include energetic terms relative to chemotactic stimuli and/or inertial locomotion, as done in [24] and [25].

The discrete nature of the CPM also allows to reproduce in details the geometry of the extracellular environment. For instance, it is possible to easily represent both single matrix fibers, therefore tuning their characteristic distance (Fig. 2(A)), and microchannels with different openings or with different distributions of structural pillars (Fig. 2(B-C)).

Numerical results relative to the different scenarios consistently show that cell migration is completely inhibited in the case of prohibitively small environmental pores. In the case of matrix constrictions whose size is not negligible but remains smaller than the diameter of the nucleus, cell speed mainly depends on the deformability of its voluminous organelle. When the size of the narrow passages exceeds nucleus diameter, cell velocity instead relies on cytoplasmic dynamics. Finally, when the dimension of environmental constrictions is large enough, the migratory capacity of the cell drops, because of its difficulty to build adhesion bonds and to exert efficient traction forces. In this respect, simulation outcomes reveal that maximal cell velocity is achieved in the case of pore sizes slightly larger than then nuclear mean dimension but smaller than the diameter of the overall individual. Such outcomes are summarized in Fig. 2(D).

The proposed CPMs also show that when the nucleus is squeezing through a small enough constriction, its side edges are characterized by significant inwards stresses. Outwards forces are instead active at the trailing and leading borders, as put in evidence in Fig. 2(E). As soon as the intracellular organelle has overcome the mid point of the constriction, the inward stresses momentarily point almost

towards the direction of cell movement, thereby acting as a further instantaneous push for cell locomotion, see again Fig. 2(E).
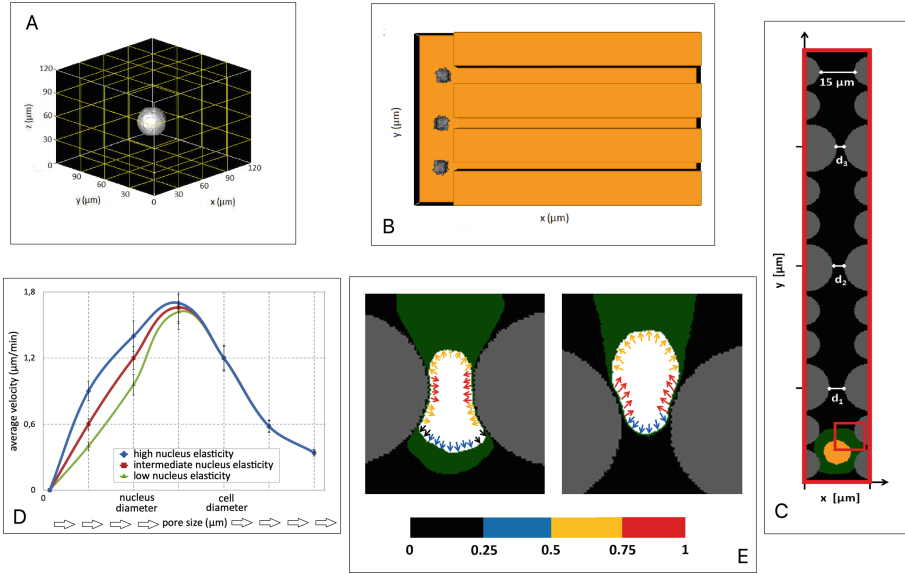
Fig. 2. Cellular Potts model reproducing single cell migration in selected confined environments: (A) regular scaffold of matrix fibers, (B) microchannels with different widths, and (C) microfluidic device formed by arrays of fixed pillars. (D) Cell speed vs characteristic pore size for different nucleus stiffness. (E) Force field at the nuclear membrane during cell penetration within a narrow passage.

4   Nesting Cell-Level Information in Multiphase Models of Tumour Growth

As already mentioned in the Introduction, tumour cells live in an environment made of several constituents, such as interstitial liquid, capillary and lymphatic vessels, ECM fibers, in addition to several other tissue cells. One way to describe such an heterogeneity from a macroscopic point of view and to take into account of mechanical issues was originally proposed in [4], devoted to the development of a model based on the theory of mixture and of deformable porous media. Recent developments of the model presented in [18,19] are aimed at the validation of the results with experimental data on tumours growing under compression. Referring to [21] for more details on the mechanical framework the model is based upon, the evolution law for the tumour cell population stems from a mass balance equation

$$\frac{\partial \phi_c}{\partial t} + \nabla \cdot (\phi_c \mathbf{v}_c) = \gamma_c(\phi_c, \mathbf{C})\phi_c - \delta_c(\phi_c, \mathbf{C})\phi_c, \tag{10}$$

where ϕ_c is the volume ratio occupied by cells and $\mathbf{v}_c$ is their velocity. The growth and death terms, i.e., γ_c and δ_c, respectively, may depend on nutrients and growth factors (generically denoted by the vector $\mathbf{C} = (C_1, \ldots, C_n$ where n is the number of chemical factors of interest) and on the volume ratio itself. For instance, when contact inhibition of growth is taken into account γ_c vanishes for $\phi_c \geq \phi_{max}$, ϕ_{max} being a sort of carrying capacity describing the fact that when cells feel a compression larger than a threshold, they do not duplicate any longer.

In order to determine $\mathbf{v}_c$, Eq. (10) can be joined with a momentum balance equation, that actually writes as a force balance equation because inertial effects can be neglected in growth phenomena. Without entering in detail that can be found, for instance, [21] when the mechanical interaction of the tumour mass with the extracellular fluid can be neglected compared with the one with the ECM, and the ECM can be described as a rigid substratum, this approach is able to determine the velocity of malignant cells as

$$\mathbf{v}_c = -\mathbf{M}_{cm}\nabla\Sigma(\phi_c), \tag{11}$$

where $\Sigma(\phi_c)$ describes the mechanical response of cells under compression, e.g., due to growth, whereas $\mathbf{M}_{cm}$ is the motility tensor related to cell-ECM interaction. The model (10) can be therefore rewritten, in its simplest version, as

$$\frac{\partial \phi_c}{\partial t} = \nabla \cdot [\phi_c \mathbf{M}_{cm}\nabla\Sigma(\phi_c)] + \gamma_c(\phi_c, \mathbf{C})\phi_c - \delta_c(\phi_c, \mathbf{C})\phi_c. \tag{12}$$

The crucial term on which we want to focus here is the motility tensor that, in order to simplify the discussion, is hereafter assumed to be isotropic, i.e., $\mathbf{M}_{cm} = M_{cm}\mathbf{I}$ where $\mathbf{I}$ is the identity tensor. On the basis of the experiments described in [28] and of the discussion done in previous sections (see for instance, Eq. (8)), we can affirm that

  (i) it depends on the characteristic ECM pore cross section A_p
 (ii) there exists a threshold pore cross section A_0 that establishes a physical limit for cell migration (i.e., cells cannot penetrate an ECM passage whose dimension is lower than A_0).

In addition, cell speed has been experimentally shown in [28] to increase linearly for small values of the quantity $A_p - A_0$. Recalling (11), this suggests that, close to A_0, M_{cm} behaves as

$$M_{cm} = m(A_p(\mathbf{x}) - A_0)_+, \tag{13}$$

where $(f)_+ = (f + |f|)/2$ is the positive part of f, so that when $A_p(\mathbf{x}) < A_0$ the motility coefficient vanishes.

However, cell speed can not increase indefinitely, but it must saturate or present a biphasic behaviour, as shown in Sect. 3 and in Fig. 2(D). This suggests to set

$$M_{cm} = m\frac{(A_p(\mathbf{x}) - A_0)_+}{\left(1 + \frac{A_p(\mathbf{x}) - A_0}{A_1}\right)^n}, \tag{14}$$

where the coefficient A_1 can be evaluated from experiments in the following way:

(i) If cell speed saturates, i.e., $n = 1$, then A_1 is identified by the motility asymptotic value divided by m;

(ii) If there is an optimal pore size $A_{p,max}$ favouring cell migration as shown in Fig. 2(D), corresponding to $n > 1$, then $A_1 = (n-1)(A_{p,max} - A_0)$.

The model (10) describing tumour growth in a constraining environment can be therefore specified as

$$\frac{\partial \phi_c}{\partial t} = \nabla \cdot \left[m \frac{(A_p(\mathbf{x}) - A_0)_+}{\left(1 + \frac{A_p(\mathbf{x}) - A_0}{A_1}\right)^n} \phi_c \nabla \Sigma(\phi_c) \right] + \gamma_c(\phi_c, \mathbf{C}) \phi_c - \delta_c(\phi_c, \mathbf{C}) \phi_c. \quad (15)$$

As we have discussed in Sect. 2, the value of A_0 is not constant but actually depends on (i) nucleus size and elasticity, (ii) nuclear membrane stiffness, (iii) the effective adhesion between malignant cells and matrix elements, and (iv) the ability of malignant cells to exert traction forces. So, a dependence like the one in Fig. 1 is expected if we replace the force F in G with a macroscopic measure of cell stress having both an active and a passive origin.

It can be noticed that Eq. (15) reduces to a simple growth model without any space derivative when and where $A_p(\mathbf{x}) \leq A_0$.

The model can be also applied to the case of tumour invasion of highly heterogeneous tissues in presence of discontinuities in ECM density and organization, i.e., in pore size. In such situations, the motility coefficient m can be discontinuous and proper interface conditions, namely continuity of fluxes and of pressure, must be imposed.

This is done in the simulations reported in Fig. 3, where a malignant mass grows in a very heterogeneous environment, e.g., a glandular or a fatty tissue, with jump discontinuities in ECM pore sizes. In this respect, the matrix pore size is $100 \ \mu m^2$, i.e., substantially larger than the nucleus cross section, outside the ellipsoidal regions, whereas it drops up to 20 times within the ellipsoids. In the simulation shown in the left column, the typical interfiber distance within the ellipsoids is $4.5 \ \mu m$: tumour cells have indeed difficulties in penetrating such denser regions, but they finally achieve full invasion. At the other extremum, in the right column, the ellipsoidal regions are not penetrable because they mimic an ECM network with interfiber distance close to $2.5 \ \mu m$, i.e., characterized by $A_p < A_0$. So, when cells arrive at the boundaries of these areas, they can not move in.

In this specific simulation setting, the stress-free volume ratio is $\phi_0 = 0.5$ (i.e., $\Sigma(\phi_0) = 0$) and compression inhibits growth at $\phi_{max} = 0.7$. It can be finally noticed that the healthy tissue is compressed by the growing tumour. To focus on the effect of ECM heterogeneity, nutrients are assumed to be fully available and growth factors are not considered.

5   Tumour Invasion Across Membranes

In the initial stages of cancer progression, non-invasive dysplastic cells locally proliferate and form a carcinoma *in situ* that is separated from the physiological tissue by membrane-like structures. For instance, ductal carcinoma *in situ*

(a) $t = 30\,\text{days}$

(b) $t = 50\,\text{days}$

(c) $t = 70\,\text{days}$
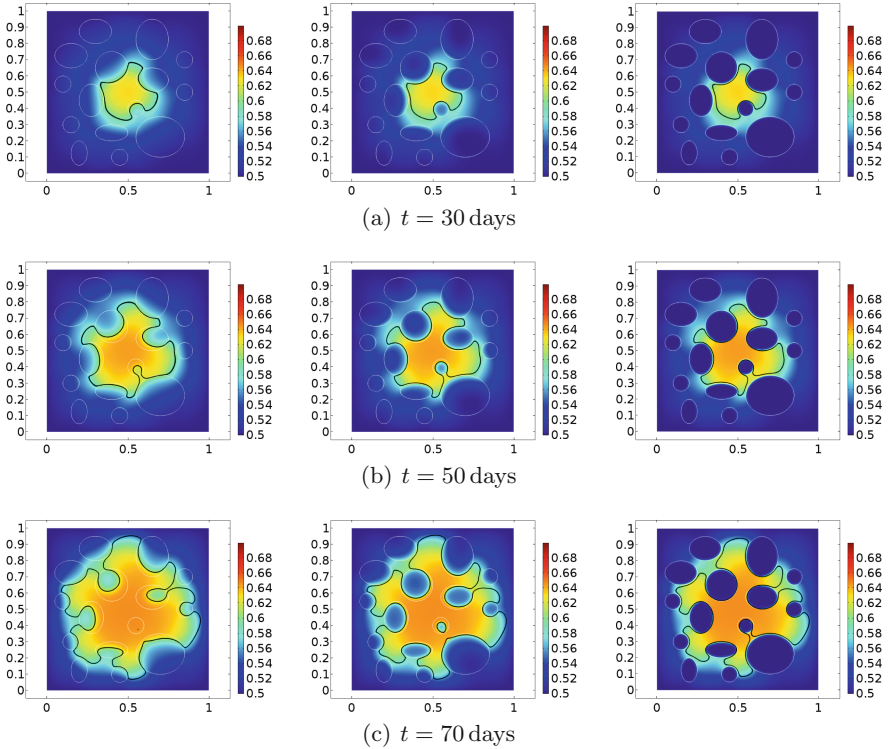
Fig. 3. Tumour growth (delimited by the black line) in an heterogeneous environment. In particular, the ellipsoidal regions represent dense matrix regions, characterized by different values of charactiristic pore size A_p. Left column: $A_p = 16\,\mu\text{m}^2$, which corresponds to a typical interfiber distance equal to $\approx 4.5\mu\text{m}$. Middle columns: $A_p = 7\,\mu\text{m}^2$, which corresponds to a typical interfiber distance equal to $\approx 3\mu\text{m}$. Right column: $A_p = 5\,\mu\text{m}^2 < A_0 = 6\,\mu\text{m}^2$, which corresponds to a typical interfiber distance equal to $\approx 2.5\mu\text{m}$. In all cases, the pore dimension characterizing the regions outside the ellipsoids is $A_p = 100\,\mu\text{m}^2$, which is larger than the typical nucleus cross section.

grows in a breast duct, endocrine pancreatic tumours in the islets of Langherans, uterin tumours at its wall, the myometrium, and similarly for prostate, ovary, bladder tumours, an so on. All these lesions are contained by a basal membrane, that is a thin, dense and highly cross-linked sheet-like network of ECM macromolecules that underlies, amongst others, all epithelial and endothelial layers (see [14] and [15] for a more complete description). Only small molecules such as nutrients and other chemical factors are able to passively diffuse across the basal membrane, since its characteristic pore size is of the order of $50\,\text{nm}$ (see [14] and [22]). Such a structural barrier can be also crossed by immune cells [13], that are very soft and therefore able to considerably deform.

In principle, also in this situations, one could use the same modelling approach used in the previous section, e.g., Eq. (12), extending it to account for

tumour cell transmigration across basal membranes. However, their cross section is substantially smaller than typical cell dimensions. So, from the computational viewpoint, it is not convenient to build a numerical grid adapted to its thickness; rather, it is much better to model its action through suitable interface conditions. With this aim in mind, in [3,5] a suitable limit procedure is proposed to replace the basal membrane with an effective zero thickness interface. In particular, the correct interface conditions than need be imposed at the membrane are proved to be the following

$$M_{cm}^{in}\phi_c^{in}\mathbf{n}\cdot\nabla\Sigma(\phi_c^{in}) = M_{cm}^{out}\phi_c^{out}\mathbf{n}\cdot\nabla\Sigma(\phi_c^{out}) = \widehat{M}_{bm}[\Pi(\phi_c^{out}) - \Pi(\phi_c^{in})], \quad (16)$$

where ϕ_c^{in} and ϕ_c^{out} are as usual the tumour volume fractions on the two sides of the membrane (say, D_{in} and D_{out}) and $\Pi'(\phi_c) = \phi_c\Sigma'(\phi_c)$ (primes stand for derivative), while $\mathbf{n}$ identifies the outward normal to the membrane (see Fig. 4). The first equality in (16) represents the usual continuity of mass flux across the interface that is to be expected. On the other hand, the second equality takes into account of the reduced motility across the basal membrane. Like M_{cm}^{in} and M_{cm}^{out}, $\widehat{M}_{bm}$ inherits the same structure as in (14). However, it is expected that while the formers are not restrictive, the latter usually is. Specifically, for prohibitively small pore cross sections of the basal membrane, i.e., below the mentioned physical limit of migration cross section A_0, $\widehat{M}_{bm}$ vanishes yielding the classical no-flux conditions

$$M_{cm}^{in}\phi_c^{in}\mathbf{n}\cdot\nabla\Sigma(\phi_c^{in}) = M_{cm}^{out}\phi_c^{out}\mathbf{n}\cdot\nabla\Sigma(\phi_c^{out}) = 0. \quad (17)$$

It can also be noticed that (16) is a generalization of the classical Kedem-Katchalsky interface condition. In fact, formally speaking, if $\Sigma(\phi_c) = \Sigma_0\ln\frac{\phi_c}{\phi_0}$ (which is experimentally unphysical as a relation describing the mechanical response of cell to compression), then Eq. (15) reduces to a linear, though heterogeneous, diffusion equation and the condition (16) reads as

$$M_{cm}^{in}\mathbf{n}\cdot\nabla\phi_c^{in} = M_{cm}^{out}\mathbf{n}\cdot\nabla\phi_c^{out} = \widehat{M}_{bm}(\phi_c^{out} - \phi_c^{in}), \quad (18)$$

i.e., the classical Kedem-Katchalsky interface condition used to describe the diffusion of molecules through permeable membranes.
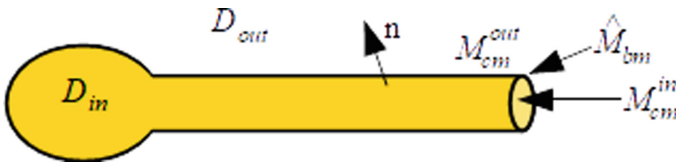

Fig. 4. Notation for basal membrane problem.

The application of the interface condition (16) to the model proposed in the previous section indeed allows to relate macroscopic tumour invasion or segregation by basal membranes to microscopic determinants, such as the mechanical

characteristic of the nuclear envelope and the stiffness of the nuclear bulk, the traction ability of malignant cells, in addition to the typical membrane pore size.

However, some cancer cells can acquire the ability to produce matrix degrading enzymes (MDEs) that digest collagen fibers constituting the basal membrane. In this way, malignant individuals are able to widen ECM pores or even to perforate the basal membrane and invade the adjacent tissue, thus switching to a more aggressive and metastatic phenotype. From the modelling point of view, this means that A_p in (13) or (14) increases and that Eq. (16) might pass from a no-flux interface condition (i.e., Eq. (17) when A_p is below A_0 and therefore $\widehat{M}_{bm} = 0$) to a flow condition.

Specifically, we can assume that

$$\frac{\partial A_p}{\partial t} = \mu(\bar{A}_p - A_p) + \eta C_{MDE},\tag{19}$$

where C_{MDE} defines the local amount of tumour-secreted MDEs and $\bar{A}_p$ is the physiological pore area of the basal membrane that is restored by the action of ECM producing cells, mainly fibroblasts, at a rate μ, e.g., when $C_{MDE} = 0$. In Eq. (19), η is instead related to the rate at which MDEs enlarge the membrane pore size.

The evolution of MDEs can then be classically modelled by the following reaction-diffusion equation

$$\frac{\partial C_{MDE}}{\partial t} = D\nabla^2 C_{MDE} + p(A_p)\phi_c - qC_{MDE},\tag{20}$$

where D is the diffusion coefficient of MDEs, q the degradation or wash-out rate, and p the production rate by tumour cells. It can also depend on the local pore area, which means that MDEs are produced only if needed. As MDEs are small, then they can easily pass through the pores of the basal membrane, so that continuity of concentration and flux can be assumed there.

In order to show the applicability of the model (15) joined with (16) we also add (19) and (20) to describe the invasion process of an ovarian tumour. These tumours originate either on the surface of the ovary or in the fallopian tube. Referring to [1] and [17] for more details on the phenomenological cascade of events, the invasion process from the primary tumour starts with the degradation of the basement membrane underling the ovarian capsule (i.e., the ovarian surface epithelium) by the production of MDEs. Cancer cells can subsequently break through the ovarian capsule as single cells or, more frequently, as aggregates. Such multicellular masses grow and passively move in the peritoneal cavity. Some ovarian cancer individuals may eventually reach the walls of the cavity and attach to the mesothelial cells that constitute the peritoneal lining. This fraction of tumour cells can then (i) degrade the basement membrane underling the mesothelium by secreting MDEs and (ii) cleave cell-cell adhesion molecules (e.g., N-cadherins) that hold mesothelial cells together by producing other enzymes such as CD-44 and CD-157 [17]. This leads to the retraction of mesothelial cells at the cancer cells' attachment sites and brings about the formation of foci of

(a) $t = 15\,\text{days}$ (b) $t = 25\,\text{days}$

(c) $t = 35\,\text{days}$ (d) $t = 50\,\text{days}$
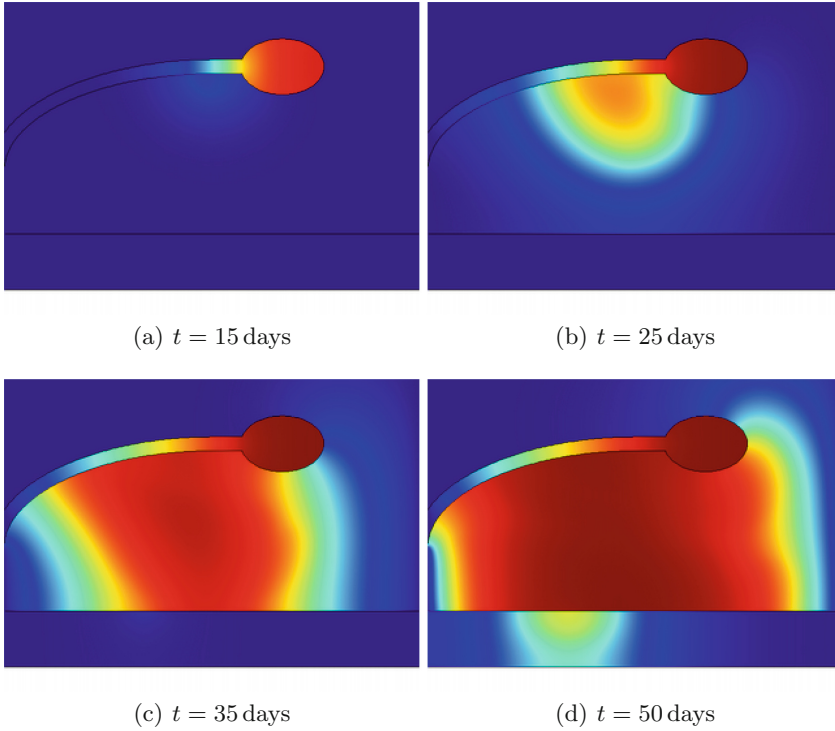
Fig. 5. Invasion of mesothelial layer by an ovary cancer originating at the start of the fallopian tube with final infiltration of the mesothelial cell lining.

invasion, which enable the malignant individuals to invade the healthy tissue adjacent to the peritoneum and form secondary tumours [12].

The ovarian capsule and the peritoneal lining consist of layers of epithelial cells attaching to the ECM. So, their size is much smaller that the characteristic size of the ovary and of the peritoneal cavity. For this reason, it is convenient to represent both of them as thin membranes and to use the effective interface condition (16) with different coefficients $\widehat{M}_{bm}$. The former has in fact a thicker ECM while the latter also involves the presence of a sheet of mesothelial cells, whose adhesion can loosen upon because of CD-44 and CD-157 activity.

In Fig. 5 the structure of the ovary is self-evident, while the mesothelial lining is represented by the lower horizontal line. Invasion starts at the beginning of the fallopian tube and continues through the peritoneal cavity till it reaches the mesothelial lining. Referring to [5] for a deeper discussion of the process, we want here to notice how well the model passes from a no-flux interface condition (17), where the membrane is intact or nearly intact, to condition (16). In the former case the solution is obviously discontinuous, while in the latter the jump discontinuity decreases in time and the pores in the membrane become wider and wider.

One can also notice that, at the early stages of the phenomenon, the mesothelial layer behaves as a solid wall containing the malignant mass, but it eventually breaks up due to the action of tumour-produced MDEs that allow cancer cell infiltration.

References

1. Ahmed, N., Thompson, E.W., Quinn, M.A.: Epithelial-mesenchymal interconversions in normal ovarian surface epithelium and ovarian carcinomas: an exception to the norm. J. Cell. Physiol. **213**, 581–588 (2007)
2. Ambrosi, D., Duperray, A., Peschetola, V., Verdier, C.: Traction patterns of tumor cells. J. Math. Biol. **58**, 163–181 (2009)
3. Arduino, A., Preziosi, L.: A multiphase model of tumour segregation in situ by a heterogeneous extra-cellular matrix. Int. J. Nonlinear Mech. **75**, 22–30 (2015)
4. Byrne, H., Preziosi, L.: Modeling solid tumour growth using the theory of mixtures. Math. Med. Biol. **20**, 341–366 (2004)
5. Chaplain, M.A.J., Giverso, C., Lorenzi, T., Preziosi, L.: Interface conditions for a tumour growth model with Basal Membrane. SIAM J. Appl. Math. **79**, 2011–2031 (2019)
6. Dembo, M., Wang, Y.L.: Stresses at the cell-to-substrate interface during locomotion of fibroblasts. Biophys. J. **76**, 2307–2316 (1999)
7. Evans, E.A., Waugh, R., Melnik, L.: Elastic area compressibility modulus of red cell membrane. Biophys. J. **16**, 585–595 (1976)
8. Friedl, P., Wolf, K., Lammerding, J.: Nuclear mechanics during cell migration. Curr. Opin. Cell. Biol. **23**, 55–64 (2011)
9. Gerlitz, G., Bustin, M.: The role of chromatin structure in cell migration. Trends Cell. Biol. **21**, 6–11 (2011)
10. Giverso, C., Arduino, A., Preziosi, L.: How nucleus mechanics and ECM topology influence the invasion of single cells and multicellular aggregates. Bull. Math. Biol. **80**, 1017–1045 (2018)
11. Giverso, C., Grillo, A., Preziosi, L.: Influence of nucleus deformability on cell entry into cylindrical structures. Biomech. Model. Mechanobiol. **13**(3), 481–502 (2013)
12. Giverso, C., Scianna, M., Preziosi, L., Lo Buono, N., Funaro, A.: Individual cell-based model for in-vitro mesothelial invasion of ovarian cancer. Math. Model. Nat. Phen. **5**, 203–223 (2010)
13. Huber, A.R., Weiss, S.J.: Disruption of the subendothelial basement membrane during neutrophil diapedesis in an in vitro construct of a blood vessel wall. J. Clin. Invest. **83**, 1122–1136 (1989)
14. Kalluri, R.: Basement membranes: structure, assembly and role in tumour angiogenesis. Nat. Rev. Cancer **3**, 422–433 (2003)
15. Kelley, L.C., Lohmer, L.L., Hagedorn, E.J., Sherwood, D.R.: Traversing the basement membrane in vivo: A diversity of strategies. J. Cell Biol. **204**, 291–302 (2014)
16. Legant, W.R., Miller, J.S., Blakely, B.L., Cohen, D.M., Genin, G.M., Chen, C.S.: Measurement of mechanical tractions exerted by cells in three-dimensional matrices. Nat. Methods **7**, 969–971 (2010)
17. Lengyel, E.: Ovarian cancer development and metastasis. Am. J. Pathol. **177**, 1053–1064 (2010)
18. Mascheroni, P., Boso, D., Preziosi, L., Schrefler, B.A.: Evaluating the influence of mechanical stress on anticancer treatments through a multiphase porous media model. J. Theor. Biol. **421**, 179–188 (2017)

19. Mascheroni, P., et al.: Predicting the growth of glioblastoma multiforme spheroids using a multiphase porous media. Biomech. Model. Mechanobiol. **15**, 1215–1228 (2016)
20. Peschetola, V.: Time-dependent traction force microscopy for cancer cells as a measure of invasiveness. Cytoskeleton **70**, 201–214 (2013)
21. Preziosi, L., Vitale, G.: Mechanical aspects of tumour growth: Multiphase modelling, adhesion, and evolving natural configurations. In: Ben Amar, M., Goriely, A., Müller, M.M., Cugliandolo, L.F. (eds.) New Trends in the Physics and Mechanics of Biological Systems, pp. 177–228. Oxford University Press (2011)
22. Rowe, R.G., Weiss, S.: Breaching the basement membrane: who, when and how? Trends Cell Biol. **18**, 560–574 (2008)
23. Scianna, M., Preziosi, L., Wolf, K.: A cellular Potts model simulating cell migration on and in matrix environments. Math. Biosci. Eng. **10**, 235–261 (2013)
24. Scianna, M., Preziosi, L.: Modeling the influence of nucleus elasticity on cell invasion in fiber networks and microchannels. J. Theor. Biol. **317**, 394–406 (2013)
25. Scianna, M., Preziosi, L.: A cellular Potts model for the MMP-dependent and -independent cancer cell migration in matrix microtracks of different dimensions. Comput. Mech. **53**(3), 485–497 (2013)
26. Scianna, M., Prezios, L.: A Cellular Potts Model analyzing cancer cell migration across constraining pillar arrays. Axioms **10**, 32 (2021)
27. te Boekhorst, V., Preziosi, L., Friedl, P.: Plastiticy of cell migration in vivo and in silico. Ann. Rev. Cell Dev. Biol. **32**, 491–526 (2016)
28. Wolf, K., et al.: Physical limits of cell migration: control by ECM space and nuclear deformation and tuning by proteolysis and traction force. J. Cell Biol. **201**, 1069–1084 (2013)
29. Wolf, K.: Multi-step pericellular proteolysis controls the transition from individual to collective cancer cell invasion. Nat. Cell. Biol. **9**, 893–904 (2007)

Mathematical Modeling of Cancer Signaling Addressing Tumor Heterogeneity

Shigeyuki Magi[✉]

Division of Cell Physiology, Toho University School of Medicine,
Ohmori-nishi 5-21-16, Ota-ku, Tokyo, Japan
shigeyuki.magi@med.toho-u.ac.jp

Abstract. One of the obstacles for cancer therapies is the heterogeneity of cancers. Heterogeneity in signal transduction within the same cell population contributes to drug resistance and stemness, and the diversity of cancer subtypes contributes to different therapeutic efficacy between individuals. However, the whole mechanisms associated with heterogeneity in signal transduction are poorly understood. In this review, I introduce several mathematical modeling studies to deal with cell-to-cell variability and diversity of cancer subtypes. Mathematical modeling studies to analyze the heterogeneity of signal transduction should provide new insights that will promote the next generation of cancer therapies, such as overcoming drug resistance and personalized medicine.

1 Introduction

Intracellular signaling induced by extracellular stimuli such as growth factors plays an important role in the physiological proliferation and differentiation of cells. On the other hand, abnormal activation of the signaling contributes to cancer survival and malignant transformation. Various molecular-targeted drugs have been developed to target mutated growth factor receptors and protein kinases responsible for downstream signaling. However, the efficacy of therapeutic agents are greatly influenced by the two heterogeneity properties of cancers; Non-genetic cell-to-cell variability and variability among cancer subtypes or individuals (Fig. 1). Non-genetic cell-to-cell variability means intratumor heterogeneity without genetic alteration; i.e., heterogeneity within the same cancer cell population without genetic heterogeneity, in which each cell behaves differently to external stimuli. This variability is known to be one of the sources of drug resistance. Although cancer is a disease driven by genetic mutations, cellular phenotypes in the presence of anti-cancer agents such as growth arrest, drug resistance, or stemness are initially regulated by the structure and spatiotemporal dynamics of signaling networks without genetic mutation [23]. Therefore, if signaling dynamics targeted by an anti-cancer agent are heterogeneous between individual cells, there may be a chance for some cells to differentiate in an undesirable phenotype such as drug resistance, even if a major population of the cells was killed.

Variability of cancer subtypes and individuals mean inter-tumor diversity with genetic differences, i.e., a diversity generated among cell populations with different genetic backgrounds due to genetic mutations or individual differences. It is responsible for differences in the efficacy of therapeutic agents. It is anticipated that the technologies stratifying individual patients and cancer subtypes for personalized medicine based on genetic mutation and expression levels of biomarkers. From the above background, a mathematical model of cancer signaling that can support drug discovery research in the future requires not only simulating ideal cells that behave like an average of the whole cell population, but also reproducing tumor heterogeneity in the model. In this review, we will introduce mathematical modeling studies that help us understand (i) non-genetic cell-to-cell variability and (ii) diversity among cancer subtypes.
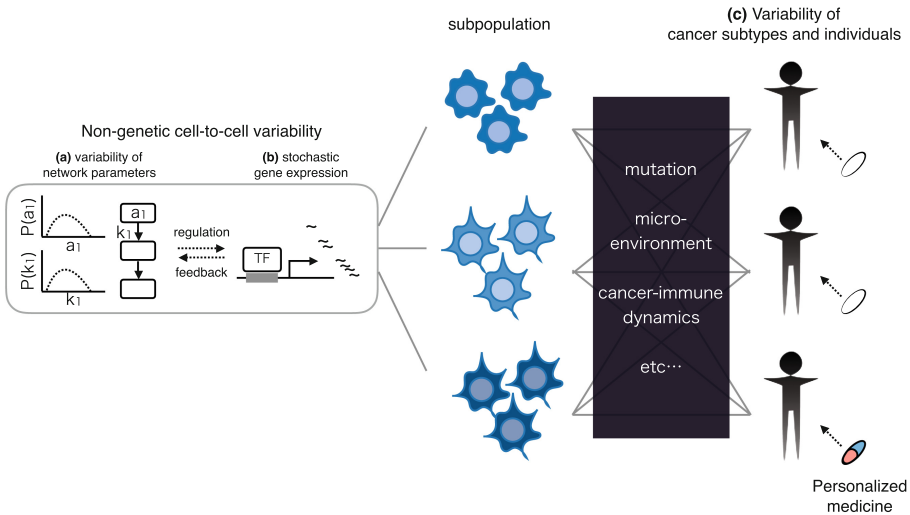
Fig. 1. Hierarchy of cancer heterogeneity. Non-genetic cell-to-cell variability are generally classified into the variability of signaling network parameters **(a)** and stochastic fluctuation in gene expression systems **(b)**. These variabilities produce subpopulations with different characteristics. Variabilities of cancer subtypes and individuals **(c)** are partially provided by cell-to-cell variability, but other factors such as genetic mutations and interaction with immune cells or cancer-associated fibroblast much contribute to the variabilities. a_1, k_1, and TF represent a concentration of a molecule, a parameter in a chemical reaction, and an abbreviation of a transcription factor, respectively.

2   Modeling of Non-genetic Cell-to-Cell Variability in Cancer Signaling

The sources of heterogeneity within a cell population are thought to be broadly classified into two types; intrinsic noise and extrinsic noise. These terms are firstly

defined and experimentally measured by quantifying the expression levels of two fluorescent proteins regulated by the same promoter at a single-cell level [9]. According to the dual-reporter method, two components of total noise (η^2_{total}), intrinsic noise (η^2_{int}), and extrinsic noise (η^2_{ext}) were defined as follows:

$$\eta^2_{total} = \eta^2_{int} + \eta^2_{ext}, \quad \eta^2_{int} = \frac{\langle (\mathbf{a} - \mathbf{b})^2 \rangle}{2\langle \mathbf{a} \rangle \cdot \langle \mathbf{b} \rangle}, \quad and \quad \eta^2_{ext} = \frac{\langle \mathbf{ab} \rangle - \langle \mathbf{a} \rangle \cdot \langle \mathbf{b} \rangle}{\langle \mathbf{a} \rangle \cdot \langle \mathbf{b} \rangle}. \quad (1)$$

The i-th elements of the vectors $\mathbf{a}$ and $\mathbf{b}$, a_i and b_i, denote the measurements of two fluorescent molecules of the i-th cell, respectively. Angle bracket denotes means over the cell population. The sources of extrinsic noise include the differences in cell cycle phase, cell size, concentrations of cellular components, and microenvironment. In this review, the term "extrinsic noise" is used in the sense of the variabilities of reaction coefficients and abundances of biochemical species between individual cells. These variabilities are thought to produce differences in developmental cell fate decisions and responses to chemotherapeutic agents through downstream gene expression [1,4,12,34].

Intrinsic noise is a stochastic process of intracellular components and can be observed as the uncorrelated fluctuations between two fluorescent proteins in the dual-reporter method. Ozbudak et al. experimentally showed that the variance of the expression levels in a cell population is proportional to the mean expression level [32]. Their results mean that the larger the average expression of the reaction molecules, the more the dispersion of the reaction products is dominated by extrinsic noise. In fact, it has been shown that the contribution of extrinsic noise in the MAPK signaling pathway is much larger than intrinsic noise [20]. On the other hand, intrinsic noise should be considered when the amount of chemical species in a reaction is few.

2.1   Modeling of Extrinsic Noise

A signal transduction system is a sequence of biochemical reactions described by such as low of mass action and Michaelis-Menten equation, has been described as an ordinary differential equations (ODE) model. Traditional mathematical models on signal transduction have been developed to reproduce the averaged temporal dynamics of chemical species in a cell population obtained by western blotting [17,22,29]. Considering extrinsic noise in the ODE model, it must be assumed that the parameters in the model are not identical but differ among every individual cell. Therefore, the construction and validation of the model considering extrinsic noise require experimental data at single-cell resolution to constrain the parameter distribution.

Single-cell experimental data can be broadly classified into two types: snapshot data from flow cytometry (reviewed in section V in [5]), mass cytometry (section VIII.3 in [5] and [15,28]), or imaging cytometry (section VIII.1 in [5] and [37]), and time-lapse data from live-cell imaging [11]. These data provide us different information about the cells. Snapshot data contains the expression or activation levels of molecules in more than thousands of cells and are suitable for measuring the dispersion and correlation of multiple molecules in a cell

population, but does not contain the trajectories of individual cells because the data in different time points are not obtained from an identical cell population by technical reasons; in most cases, the cells must be physically fixed or lysed in the process of sampling. On the other hand, time-lapse can trace the temporal changes of individual cells, but it is difficult to measure a large number of cells and molecules simultaneously.

Some modeling studies based on snapshot data have used a parametric distribution of parameters to represent single-cell data. Filippi et al. analyzed the cell-to-cell variability of the MAPK cascade based on the assumption that the 20 parameters in the MEK-ERK phosphorylation model follow a log-normal distribution [10]. They measured the total amount of doubly phosphorylated MEK and ERK, denoted respectively by $x_{i,t}^*$ and $y_{i,t}^*$, in cells $1 \leqq i \leqq N_t$ at each time point t. $\theta_{i,t}$ denotes a vector of 20 parameters of the i-th cell at time t. The distribution of the parameters across the cell population is assumed a log-normal distribution with mean μ_θ and covariance matrix Σ_θ. Besides, they assumed no correlation between parameters and the covariance matrix is diagonal $\Sigma_\theta = diag(\sigma_\theta^2)$ because of the computational cost. To approximate the two moments of the distribution $p(\{x_{i,t}^*, y_{i,t}^*\}_{i,t}|\mu_\theta, \Sigma_\theta^2)$, they used the Unscented Transformation (UT) [21]. UT is an algorithm that allows us to approximate the moments of the output of a non-linear function given the moments of the input. Based on the UT algorithm, they set up a series of weighed particles called sigma points in the variable space with the capturing both the mean μ_θ, and the variances σ_θ^2, and solved ODEs at each sigma point separately. By comparing the posterior distribution of the coefficient of variation of each parameter, they found variables that do or don't contribute to cell-to-cell variability in ERK phosphorylation. Magi et al. also hypothesized that the number of molecules in the model follows a log-normal distribution in their study on cell-to-cell variability of growth factor signaling [26]. They simulated the ODE model based on the initial values obtained by Monte Carlo sampling that takes into account the correlation between two molecular species which could be experimentally measured and predicted the mechanism of PHLDA1 molecule as a negative feedback regulator in growth factor receptor signaling.

The researches listed above assume that the parameters in the model follow a unimodal distribution, and therefore cannot take into account the existence of subpopulations. To address this issue, Hasenauer et al. [16] reported ODE constrained mixture modeling, a combined method of mixture distribution modeling at each time point and ODE modeling of time series mean dynamics of each subpopulation. Experimental snapshot data can be interpreted as a summation of subpopulations by conventional Gaussian mixture modeling,

$$p(y|\theta) = \sum_{i=1}^{m} w_i N(y|\mu_i, \Sigma_i) \quad with \quad \theta = \{(w_i, \mu_i, \Sigma_i)\}_{i=1}^{m}, \tag{2}$$

where y is a measured quantity of a molecule, θ is a parameter set of Gaussian mixture model including probability weights w_i, mean μ_i, and variance Σ_i of the i-th subpopulation. They also described the "average dynamics" of cells in the i-th subpopulation using ODE modeling,

$$\dot{x}_i = f(x_i, \xi_i, u), \quad x_i(0) = x_0(\xi_i, u), \quad i = 1, ..., m \quad (3)$$

in which $x_i(t) \in \mathbb{R}_+^{n_x}$ is the state of the i-th subpopulation at time t, $\xi_i \in \mathbb{R}_+^{n_\xi}$ is the parameter vector of the i-th subpopulation, and $u(t) \in \mathbb{R}_+^{n_u}$ is the experimental condition. The vector field f encodes the biochemical pathways and x_0 models the dependence of the initial condition on subpopulation parameters and experimental conditions. Assuming that interaction and transition between subpopulations can be neglected, the dynamics of the whole cell population are calculated by the weighted dynamics of each subpopulation. This method constrains the mean value of subpopulation by the ODE model (3), and thereby establishes a mechanistic link between different experimental conditions or time points based on ODE models and differences among subpopulations based on mixture modeling. However, since the component covariances $\Sigma_i = \Sigma_i(t, u)$, which summarise cell-to-cell variability within the i-th subpopulation and measurement noise, are not constrained by the ODE model, cell-to-cell variability within the subpopulation cannot be related to the chemical reaction network. Besides, this method is only applicable to one-dimensional measurements.

Thus they developed another approach that can capture cell-to-cell variability within subpopulations and fully leverage the correlation information in multivariate data [25]. In this method, the parameter distributions in the ODE model such as initial conditions or kinetic rates, are described by mixture distributions represented by the mean and covariance of the subpopulations to cover different levels of heterogeneity (Fig. 2). Each cell j has cellular properties encoded in the parameter vector ψ^j, are considered to be drawn from a mixture distribution, as follows:

$$\boldsymbol{\psi}^j \sim \sum_s w_s N(\beta_s, \mathbf{D}_s), \quad (4)$$

with subpopulation weight w_s, mean β_s, and covariance $\mathbf{D}_s$ for subpopulation $s = 1, ..., N$. The subpopulation parameters β_s and $\mathbf{D}_s$ classify the variability of property $\boldsymbol{\psi}^j$ as indicated in the top of Fig. 2.

These approaches enable quantifying the contributions of neuronal subpopulations, culture conditions, and expression levels of signaling proteins to the cell-to-cell variability of nerve growth factor-induced signal transduction. The method introduced above assumes that biochemical parameters follow a predefined distribution, and estimates hyperparameters such as variance and mean that define the distribution. However, there are two major limitations of the parametric models described above. First, parametric formulations become analytically intractable when the component of the subpopulation and the chemical reaction model becomes complex. This problem has been addressed by parameter reduction techniques such as ignoring the covariance between variables or restricting the number of dimensions of variables, but such manipulations may result in the loss of important information in multivariate single-cell data. Second, the model likely to be incorrect if the assumption that the distribution of parameters can be pre-defined distribution is not accurate.
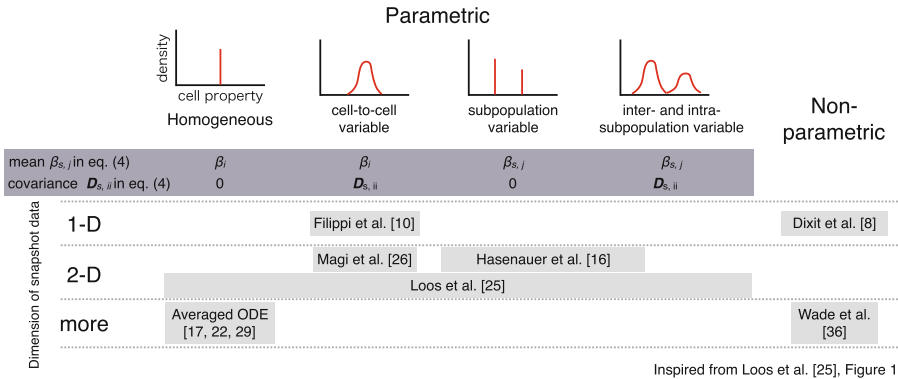
Fig. 2. Overview of ODE modeling study for cancer signaling considering extrinsic noise. The approaches are largely classified by modeling strategy (parametric or non-parametric) and the dimension of measurements. Parametric approaches are further classified by the assumptions to the distribution of single-cell property: **homogeneous**, the property being the same for the whole cell population; **cell-to-cell variable**, the property having a unimodal distribution; **subpopulation variable**, the population can be separated into subpopulations, but, within each subpopulation, the property does not vary; and **inter-and intra-subpopulation variable**, the property splitting the population into sub-populations and also varying between cells within a subpopulation.

Other ODE modeling studies have used non-parametric descriptions of the distributions. Dixit et al. developed a framework for non-parametric estimation of parameter distributions, MERIDIAN, based on the maximum entropy distribution [8]. Briefly, they firstly binned experimentally measured distribution into the fraction ϕ_k of cells that populate the kth abundance bins. On the other hand, they simulate dynamical trajectory based on distinct parameters obtained by Markov chain Monte Carlo sampling and estimate the predicted fraction ψ_k as the fraction of sampled trajectories for which dynamical trajectory passed through the kth bin. Parameter distribution was investigated by performing entropy maximization so that all predicted fractions ψ_k agree with those from experimental measurements, ϕ_k. Using this framework, they inferred parameter distribution in the growth factor-regulated Akt phosphorylation model. Wade et al., recently reported a non-parametric framework for parameter estimation of multidimensional single-cell modeling called DISCO (Distribution-Independent Single-Cell ODE modeling) [36]. They simulate the trajectories of many individual cells and calculate the maximum mean discrepancy (MMD) [14], which represents the similarity between the distribution of experimental and simulation results. Let $\mathcal{H}$ is the unit ball in a reproducing kernel Hilbert space with associated kernel k. Given m samples from a distribution X and n samples from a distribution Y, an empirical estimate of MMD between X and Y is

$$MMD_b[\mathcal{H}, X, Y] = [\frac{1}{m^2} \sum_{i,j=1}^{m^2} k(x_i, x_j) - \frac{2}{mn} \sum_{i,j=1}^{m,n} k(x_i, y_j) + \frac{1}{n^2} \sum_{i,j=1}^{n^2} k(y_i, y_j)].$$

(5)

By minimizing the sum of MMD where kernel k is the Gaussian kernel in all time points as a cost function, they reproduced experimental data of MAPK signaling dynamics in HEK293T monitored by multiplexed mass cytometry of more than 11 chemical species and optimize parameter set of MAPK singling model.

In summary, many powerful methods for model-based analysis of extrinsic noise, both parametric and non-parametric, have been proposed in the last decade. It has been shown that a parametric model may be sufficient for small-scale experimental data focusing on only a few molecules, while a distribution-free approach is useful for higher-order experimental data such as mass cytometry Fig. 2. It is now possible to measure the expression levels of thousands of genes simultaneously by single-cell sequencing. Once the solution of the computational cost problem and the experimental techniques to obtain higher-order data at the protein level like those available in mRNA level are established, the application of the distribution-free approach will provide new biological insights in the future.

2.2   Modeling of Intrinsic Noise

Although whether and how intrinsic noise in transcription machinery determines cell fate decisions are not well understood, gene expression systems with intrinsic noise are usually simulated with stochastic simulation such as the Gillespie algorithm [13]. The Gillespie algorithm draws the time elapsed until the next event by given propensity function of reaction, and then determines the next event from all available events. By running this simulation multiple times independently, intrinsic noise-derived cell-to-cell variability can be evaluated. The simplest model of gene expression can be written as a six-reaction model governed by the following parameters: the initiation rate into the transcription state, k_{on}; the rate where the promoter switches off, k_{off}; the rates of transcription and translation, k_m, and k_p, respectively; the degradation rates of mRNAs and proteins, γ_m, and γ_p, respectively (Fig. 3, more complex models are reviewed in [35]). Stochastic simulation of the simplest model can recapture one of the fundamental properties in gene expression systems celled "transcriptional bursting" which results from intrinsic noise in each reaction step. Although the general definition of transcriptional bursting is vague, it refers to the occurrence of transcriptional response in a series of short pulses of a few minutes in a period when no transcription occurs. Such discontinuous behavior cannot be explained by deterministic ODE models. There are two main types of characterization of transcriptional bursting that can contribute to the increase in non-genetic cell-to-cell variability: bursting frequency determined by k_{on} and bursting size (the

number of generated mRNAs at a pulse) determined by $\frac{k_m}{k_{off}}$. These parameters can be inferred by experimental data of single-molecule RNA fluorescence in-situ hybridization (FISH) or single-cell RNA techniques [24,31]. Some experimental researches confirmed that the bursting frequency is controlled by histone acetylation [30], especially H3K27Ac in the enhancer region [24], or transcription elongation factors [31]. In contrast, bursting size correlates to the presence of TATA box [24], RNA polymerase level, and cell size [33]. These factors may need to be taken into account in the stochastic simulation of gene expression systems

There is a case that intrinsic noise-derived transcriptional noise can be a drug target. A drug discovery research focusing on this transcriptional noise found several candidate compounds that inhibit human immunodeficiency virus (HIV) replication. Dar et al. searched for compounds that change only the coefficient of variation without changing the expression level of the fluorescent protein which is encoded downstream of the HIV long terminal repeat promoter [6]. They found some chromatin modifying compounds increased intrinsic noise in HIV gene expression systems and showed these compounds synergized with a transcriptional activator to enhance HIV reactivation. Their finding may contribute to an HIV treatment strategy that tries to re-activate the latent virus to a replicative phenotype which is sensitive to antiretroviral therapy [7].

However, it remains unclear that the simplest model is sufficient for explaining transcriptomic variability in human cells, especially in human cancer cells. In luminal breast cancer cells, the expression level of histone demethylase KDM5B, which erases transcriptionally active methylation in histone H3K4, is associated with transcriptomic heterogeneity [18]. Their finding is not explained by only using the simplest model of the gene expression process (Fig. 3) because high expression level of KDM5B may increase k_{off} and thereby reduce the bursting size in the model. Other researchers also reported that gene expression levels regulated by polycomb repressive complex showed non-genetic cell-to-cell variability [3], suggesting that epigenetic changing increase of k_{off} does not necessarily reduce the variability of gene expression.

Another possible source of intrinsic noise is RNA degradation rate (γ_m). Baudrimont, et al., investigated the contribution of RNA degradation to both intrinsic and extrinsic noise in gene expression systems [2]. They concluded that fluctuation of degradation rate in unstable RNAs is buffered by stable expression of exonuclease XRN1 which targets unstable RNAs, while ribonucleases targeting stable RNA have large fluctuation. In other words, intrinsic noise in RNA degradation is fine-tuned by extrinsic noise in the expression levels of RNases. Taken together, we should consider the extrinsic variability of gene expression systems in addition to intrinsic noise, or expand when discussing transcriptional cell-to-cell variability.
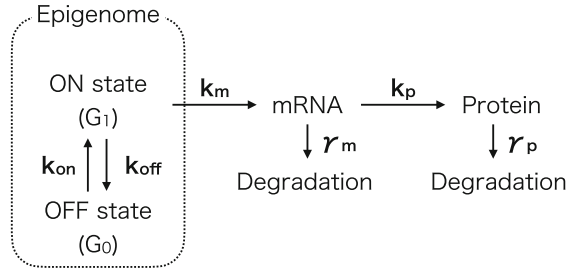
Fig. 3. Simple scheme of stochastic gene expression model. This model consists of six biochemical reactions: switching ON/OFF of epigenetic status, and production/degradation of mRNAs and proteins.

3 Modeling of Variability Among Cancer Subtypes

Variability among cancer cell types generated by the difference of genetic mutation and polymorphism beyond non-genetic factors. At present, it is very difficult to simulate the process of generating variability of cancer subtypes at a molecular resolution. However, if we focus on not modeling the process but the results of molecular differences in cancer subtypes including the difference of gene expression levels and enzymatic activities caused by a genetic mutation, we can deal with them in the same way as the extrinsic noise framework. Namely, even if some genetic mutation alters gene expression profiles or generates point-mutated or fusion oncoproteins, these can be conceptually represented on a model as the difference of molecular expression levels or reaction constants. Imoto et al. have developed BioMASS (Modeling and Analysis of Signaling Systems), a simulation platform that reproduces the dynamics of growth factor signaling across cell types using the RNA-seq expression data of 19 genes responsible for growth factor signaling as input [19]. The platform assumes that kinetic parameters such as transport, binding, and phosphorylation rates are identical across cell types, and estimated each kinetic parameter using the signal transduction dynamics of three breast cancer cells with different subtypes as training data. Using the estimated parameters, they successfully reproduced the signaling dynamics of a cancer cell line that was not used for training. The platform also provides functions for sensitivity analysis of reaction parameters and initial conditions with high usability for experimental biologists.

Considering genetic mutations that affect molecular function such as constitutive active mutations, it may be necessary to check the possibility that reaction constants may differ among cell types. In this case, we must be careful not to overfit simulation results to experimental data. Merkle et al. successfully inferred common and cell type-specific parameters by applying L1 regularization in machine learning, incorporating a penalty in the objective function based on the number of cell type-specific parameters, to parameter estimation in the model [27]. They recapitulated erythropoietin-induced JAK-STAT signaling in non-small cell lung cancer and erythroid progenitor cells and revealed a poten-

tial target to inhibit only the signaling in tumor cells. Their approach has the potential to mathematically reveal not only the diversity among cancer cells but also the differences between normal cells and tumor cells that are associated with side effects of anticancer drugs.

4   Conclusion

In this review, we have listed examples of studies that analyze tumor heterogeneity at various levels by using mathematical modeling. This field has matured during the last decade, and new methods are still being proposed. However, there is still much room for improvement to obtain useful biological findings from the model-based analysis, such as adopting hypotheses that are consistent with actual experimental data, using accurate modeling parameter obtained from single-molecule measurements, and developing software tools that are easy to use for everyone, including experimental researchers. I believe that these challenges can be remedied by greater cooperation between mathematical oncologists and experimental researchers than has been possible to date.

References

1. Albeck, J.G., Burke, J.M., Aldridge, B.B., Zhang, M., Lauffenburger, D.A., Sorger, P.K.: Quantitative analysis of pathways controlling extrinsic apoptosis in single cells. Mol. Cell **30**(1), 11–25 (2008)
2. Baudrimont, A., Jaquet, V., Wallerich, S., Voegeli, S., Becskei, A.: Contribution of RNA degradation to intrinsic and extrinsic noise in gene expression. Cell Rep. **26**(13), 3752-3761.e5 (2019)
3. Carcamo-Orive, I., et al.: Analysis of transcriptional variability in a large human iPSC library reveals genetic and non-genetic determinants of heterogeneity. Cell Stem Cell **20**(4), 518-532.e9 (2017)
4. Chen, J.Y., Lin, J.R., Cimprich, K.A., Meyer, T.: A two-dimensional ERK-AKT signaling code for an NGF-triggered cell-fate decision. Mol. Cell **45**(2), 196–209 (2012)
5. Cossarizza, A., et al.: Guidelines for the use of flow cytometry and cell sorting in immunological studies (second edition). Eur. J. Immunol. **49**(10), 1457–1973 (2019)
6. Dar, R.D., Hosmane, N.N., Arkin, M.R., Siliciano, R.F., Weinberger, L.S.: Screening for noise in gene expression identifies drug synergies. Science **344**(6190), 1392–1396 (2014)
7. Deeks, S.G.: HIV: shock and kill. Nature **487**(7408), 439–440 (2012)
8. Dixit, P.D., Lyashenko, E., Niepel, M., Vitkup, D.: Maximum entropy framework for predictive inference of cell population heterogeneity and responses in signaling networks. Cell Syst. **10**(2), 204-212.e8 (2020)
9. Elowitz, M.B., Levine, A.J., Siggia, E.D., Swain, P.S.: Stochastic gene expression in a single cell. Science **297**(5584), 1183–1186 (2002)
10. Filippi, S., et al.: Robustness of MEK-ERK dynamics and origins of cell-to-cell variability in MAPK signaling. Cell Rep. **15**(11), 2524–2535 (2016)

11. Gaudet, S., Miller-Jensen, K.: Redefining signaling pathways with an expanding single-cell toolbox. Trends Biotechnol. **34**(6), 458–469 (2016)

12. Gerosa, L., et al.: Receptor-driven ERK pulses reconfigure MAPK signaling and enable persistence of drug-adapted BRAF-mutant melanoma cells. Cell Syst. **11**(5), 478-494.e9 (2020)

13. Gillespie, D.T.: Stochastic simulation of chemical kinetics. Annu. Rev. Phys. Chem. **58**(1), 35–55 (2007)

14. Gretton, A., Borgwardt, K.M., Rasch, M.J., Schölkopf, B., Smola, A.: A kernel two-sample test. J. Mach. Learn. Res. **13**, 723–773 (2012)

15. Hartmann, F.J., Bendall, S.C.: Immune monitoring using mass cytometry and related high-dimensional imaging approaches. Nat. Rev. Rheumatol. **16**(2), 87–99 (2020)

16. Hasenauer, J., Hasenauer, C., Hucho, T., Theis, F.J.: ODE constrained mixture modelling: a method for unraveling subpopulation structures and dynamics. PLoS Comput. Biol. **10**(7), e1003686 (2014)

17. Hatakeyama, M.: A computational model on the modulation of mitogen-activated protein kinase (MAPK) and Akt pathways in heregulin-induced ErbB signalling. Biochem. J. **373**(Pt 2), 451–463 (2003)

18. Hinohara, K., et al.: KDM5 histone demethylase activity links cellular transcriptomic heterogeneity to therapeutic resistance. Cancer Cell **35**(2), 330–332 (2019)

19. Imoto, H., Zhang, S., Okada, M.: A computational framework for prediction and analysis of cancer signaling dynamics from RNA sequencing data-application to the ErbB receptor signaling pathway. Cancers (Basel) **12**(10), 2878 (2020)

20. Iwamoto, K., Shindo, Y., Takahashi, K.: Modeling cellular noise underlying heterogeneous cell responses in the epidermal growth factor signaling pathway. PLoS Comput. Biol. **12**(11), e1005222-18 (2016)

21. Julier, S.J.: The scaled unscented transformation. In: Proceedings of 2002 American Control Conference, vol. 6, pp. 4555–4559. IEEE (2002)

22. Kholodenko, B.N., Demin, O.V., Moehren, G., Hoek, J.B.: Quantification of short term signaling by the epidermal growth factor receptor. J. Biol. Chem. **274**(42), 30169–30181 (1999)

23. Kolch, W., Halasz, M., Granovskaya, M., Kholodenko, B.N.: The dynamic control of signal transduction networks in cancer cells. Nat. Rev. Cancer **15**(9), 515–527 (2015)

24. Larsson, A.J.M., et al.: Genomic encoding of transcriptional burst kinetics. Nature **565**(7738), 251–254 (2019)

25. Loos, C., Moeller, K., Fröhlich, F., Hucho, T., Hasenauer, J.: A Hierarchical, Data-Driven Approach to Modeling Single-Cell Populations Predicts Latent Causes of Cell-To-Cell Variability. Cell Syst. **6**(5), 593-603.e13 (2018)

26. Magi, S.: Transcriptionally inducible Pleckstrin homology-like domain, family A, member 1, attenuates ErbB receptor activity by inhibiting receptor oligomerization. J. Biol. Chem. **293**(6), 2206–2218 (2018)

27. Merkle, R., et al.: Identification of cell type-specific differences in erythropoietin receptor signaling in primary erythroid and lung cancer cells. PLoS Comput. Biol. **12**(8), e1005049-34 (2016)

28. Mistry, A.M., Greenplate, A.R., Ihrie, R.A., Irish, J.M.: Beyond the message: advantages of snapshot proteomics with single-cell mass cytometry in solid tumors. FEBS J. **286**(8), 1523–1539 (2019)

29. Nakakuki, T., et al.: Ligand-specific c-Fos expression emerges from the spatiotemporal control of ErbB network dynamics. Cell **141**(5), 884–896 (2010)

30. Nicolas, D., Zoller, B., Suter, D.M., Naef, F.: Modulation of transcriptional burst frequency by histone acetylation. Proc. Natl. Acad. Sci. U.S.A. **115**(27), 7153–7158 (2018)
31. Ochiai, H., et al.: Genome-wide kinetic properties of transcriptional bursting in mouse embryonic stem cells. Sci. Adv. **6**(25), eaaz6699 (2020)
32. Ozbudak, E.M., Thattai, M., Kurtser, I., Grossman, A.D., van Oudenaarden, A.: Regulation of noise in the expression of a single gene. Nat. Genet. **31**(1), 69–73 (2002)
33. Padovan-Merhar, O., et al.: Single mammalian cells compensate for differences in cellular volume and DNA copy number through independent global transcriptional mechanisms. Mol. Cell **58**(2), 339–352 (2015)
34. Spencer, S.L., Gaudet, S., Albeck, J.G., Burke, J.M., Sorger, P.K.: Non-genetic origins of cell-to-cell variability in TRAIL-induced apoptosis. Nature **459**(7245), 428–432 (2009)
35. Tunnacliffe, E., Chubb, J.R.: What is a transcriptional burst? Trends Genet. **36**(4), 288–297 (2020)
36. Wade, J.D., Lun, X.K., Bodenmiller, B., Voit, E.O.: Multidimensional single-cell modeling of cellular signaling. bioRxiv **30**, 857–70 (2020)
37. Zanella, F., Lorens, J.B., Link, W.: High content screening: seeing is believing. Trends Biotechnol. **28**(5), 237–245 (2010)

Mathematical Modelling of Cancer Invasion: A Review

Nikolaos Sfakianakis and Mark A. J. Chaplain[✉]

School of Mathematics and Statistics, University of St Andrews,
St Andrews KY16 9SS, Scotland
{n.sfakianakis,majc}@st-andrews.ac.uk

Abstract. A defining feature of cancer is the capability to spread locally into the surrounding tissue, with cancer cells spreading beyond any normal boundaries. Cancer invasion is a complex phenomenon involving many inter-connected processes at different spatial and temporal scales. A key component of invasion is the ability of cancer cells to alter and degrade the extracellular matrix through the secretion of matrix-degrading enzymes. Combined with excessive cell proliferation and cell migration (individual and collective), this facilitates the spread of cancer cells into the local tissue. Along with tumour-induced angiogenesis, invasion is a critical component of metastatic spread, ultimately leading to the formation of secondary tumours in other parts of the host body. In this paper we present an overview of the various mathematical models and different modelling techniques and approaches that have been developed over the past 25 years or so and which focus on various aspects of the invasive process.

1 Introduction

In their ground-breaking paper *The Hallmarks of Cancer*, Hanahan and Weinberg (2000) identified six essential alterations in cell physiology that distinguish cancer cells/tissue from normal cells/tissue. Tissue invasion and metastasis was one of these key "hallmarks". Although the first use of the term "metastasis" can be traced back to Jean Claude Recamier in his 1829 book *"Recherches sur le traitement du cancer sur la compression méthodique simple ou combinée et sur l'histoire générale de la meme maladie"* (Recamier 1829), tissue invasion by cancer cells goes back to classical antiquity, with the phenomenon recognised by Hippocrates and Galen (among others). The word cancer itself derives from the Latin *cancer, -cri (m)* meaning crab, in turn derived from the Greek καρκίνος [cf. *carcinoma*] also meaning crab. The physicians of classical antiquity already recognised the distinctive spreading pattern of an invasive cancer, with cellular projections into the surrounding tissue like the arms of a crab.

An excellent historical overview of the biology of cancer metastasis can be found in the article by Talmadge and Fidler (Talmadge and Fidler 2010), while an overview of the core aspects of invasion can be found in the articles of Hanahan and Weinberg (Hanahan and Weinberg 2000, 2011) and the review article of Friedl and Wolf (Friedl and Wolf 2003).

The mathematical modelling of cancer invasion, part of the broader topic of mathematical oncology, may have a somewhat shorter history than its biological/pathological counterpart, but nonetheless mathematical models of cancer cell migration and invasion have the potential to shed light on this complex phenomenon and can play a role in improving treatment protocols. The purpose of this review paper is to give an overview of the key developments in the mathematical modelling of cancer invasion starting in the mid-1990s. Before embarking on this task, we first of all give a brief description of the main cellular processes involved in cancer invasion.

2   Biological Background

Cancer invasion is a complex process involving numerous interactions between the cancer cells and the *extracellular matrix* (ECM) (cf. the tumour microenvironment) facilitated by matrix degrading enzymes. Along with active cell migration (both individual and collective) and increased/excessive proliferation, these processes enable the local spread of cancer cells into the surrounding tissue. Any encounter with blood or lymphatic vessels (cf. tumour-induced angiogenesis, lymph-angiogenesis) in the tumour microenvironment initiates the spread of the cancer to secondary locations in the host, i.e., metastasis or metastatic spread.

Critical steps in the invasion-metastatic cascade include the following:

- metastatic cells arise within a population of neoplastic/tumourigenic cells as a result of genomic instabilities;
- vascularization of the primary solid tumour through tumour-induced angiogenesis;
- detachment of any metastatic-competent cells that have already evolved;
- migration of the metastatic cells;
- local invasion of cancer cells into the surrounding tissue, requiring adhesion to and subsequent degradation of ECM components;
- transport of metastatic cells either travelling individually or as emboli composed of tumour cells (homotypic) or of tumour cells and host cells (heterotypic);
- metastatic cells survive their journey in the circulation system;
- adhesion/arrest of the metastatic cells at the secondary site, cells or emboli arrest either because of physical limitations (i.e. too large to traverse a lumen) or by binding to specific molecules in particular organs or tissues;
- escape from the blood circulation (extravasation);
- proliferation of the metastatic tumour cells;
- growth of the secondary tumour in the new organ.

Further details of the invasion-metastasis process (and also extensive biological/clinical references) can be found in the papers of Hanahan and Weinberg (2000, 2011), Friedl and Wolf (2003), Valster et al. (2005), Nyström et al. (2005), Talmadge and Fidler (2010).

In the next section we present a number of mathematical models which have been developed since the mid-1990s, exploring a range of issues associated with cancer invasion and using a range of different mathematical approaches and techniques.

3   Mathematical Models of Cancer Invasion

3.1   Early ODE and PDE Models

We start with the seminal paper of Gatenby ([1995](#)) where he proposes a macroscopic mathematical model in which the tumour is viewed as a dynamic community of malignant cells, rather than a collection of individual cells, interacting and competing for resources with the normal tissue. This allows for an analytical insight in the mechanisms by which an initially small malignancy grows to replace a much larger and stable population of normal cells. In particular the author proposes the following model

$$
\begin{cases}
\dfrac{dN_1}{dt} = r_1 N_1 \dfrac{K_1 - N_1 - a_{12} N_2}{K_1} \\[2mm]
\dfrac{dN_2}{dt} = r_2 N_2 \dfrac{K_2 - N_2 - a_{21} N_1}{K_2}
\end{cases}
\tag{1}
$$

where N_1, N_2 represent the populations of cancer and normal cells respectively, r_1, r_2 the intrinsic growth rates of each population, and K_1, K_2 the carrying capacities or maximum numbers of cells from each population which can occupy the tissue and be supported by the environment. Furthermore a_{12}, a_{21} are the competition coefficients that measure the effects on the population N_2 (respectively N_1) from the presence of N_1 (respectively N_2).

Further to the fundamental formulations introduced in ([1](#)), Gatenby and Gawlinski ([1996](#)) made the modelling assumption that tumour-induced alteration of microenvironmental pH provides a mechanism for cancer invasion. In particular they propose the following reaction-diffusion system:

$$
\begin{cases}
\dfrac{\partial N_1}{\partial t} = \nabla \cdot \left(D_{N_1}[N_2] \nabla N_1 \right) + r_1 N_1 \left(1 - \dfrac{N_1}{K_1} - a_{12} \dfrac{N_2}{K_2} \right) - d_1 L N_1 \\[2mm]
\dfrac{\partial N_2}{\partial t} = \nabla \cdot \left(D_{N_2}[N_1] \nabla N_2 \right) + r_2 N_2 \left(1 - \dfrac{N_2}{K_2} - a_{21} \dfrac{N_1}{K_1} \right) \\[2mm]
\dfrac{\partial L}{\partial t} = D_3 \nabla^2 L + r_3 N_2 - d_3 L
\end{cases}
\tag{2}
$$

where N_1, N_2 represent the density of the normal and neoplastic tissue respectively, and L the excess concentration of H$^+$ ions. $d_1 L$ is the death rate of the normal tissue due to excess acid concentration.

Investigations of the structure and dynamics of the proposed model demonstrate a transition from benign to malignant growth analogous to the adenoma-carcinoma progression. Accordingly, the authors conclude that their model predicts crossover behaviour that is consistent with clinical observations on the

growth of *in-situ* tumours before the development of an invasive phenotype. Their model moreover predicts a variable interfacial structure, including a previously unrecognised hypocellular interstitial gap in some malignancies, and show some evidence in support of this prediction in both clinical observations and in vitro experiments.

In a follow-up paper, Gatenby et al. (2006) consider a direct simplification of the model (2). Namely, they consider a healthy tissue that is well organised and regulated in an organ and will therefore be immovable i.e. $D_{N_1}[N_2] = 0$; and the diffusivity of the cancer cells $D_{N_2}[N_1] = D_2\left(1 - \frac{N_1}{K_1}\right)$ attains the value D_2 in the absence of healthy tissue and the value zero when the density of the healthy tissue N_1 is at carrying capacity K_1.

This simpler model allows the authors to perform numerical simulations that provide testable predictions concerning the morphology of cellular and extracellular dynamics at the interface between tumour and host. On the other hand, *in-vivo* experiments confirm the presence of peritumoral acid gradients as well as cellular toxicity and ECM degradation in the normal tissue exposed to the acidic microenvironment. They conclude that their acid-mediated invasion model (2) can provide a description mechanism to link altered glucose metabolism with the ability of cancer cells to form invasive tumours.

Along similar lines of modelling, Perumpanani et al. (1996) proposed a cancer invasion model that accounts for the competition between the invasive cancer cells, the non-invasive cancer cells, the normal tissue, and the ECM. They moreover account for the proteases responsible for the degradation of the ECM and the product of proteolysis.

In particular, the model they propose reads as:

$$
\begin{cases}
\dfrac{\partial n}{\partial t} = k_1 n \left(k_2 - n - m - u\right) + \dfrac{\partial}{\partial x}\left[\Theta(c)\left(\Gamma_n(u,m,n)\dfrac{\partial u}{\partial x}\right)\right] \\[2ex]
\dfrac{\partial m}{\partial t} = k_4 m \left(k_5 - n - m - u\right) + \dfrac{\partial}{\partial x}\left[\Theta(c)\left(\Gamma_n(u,m,n)\dfrac{\partial m}{\partial x}\right)\right] \\[2ex]
\dfrac{\partial u}{\partial t} = k_4 u \left(k_5 - n - m - u\right) \\[1ex]
\qquad + \dfrac{\partial}{\partial x}\left[\Theta(c)\left(\Gamma_u(u,m,n)\dfrac{\partial u}{\partial x} - k_{17}u\dfrac{\partial c}{\partial x} - k_{16}u\dfrac{\partial s}{\partial x}\right)\right] \\[2ex]
\dfrac{\partial c}{\partial t} = -k_8 pc \\[1ex]
\qquad + \dfrac{\partial}{\partial x}K\left[c\,\Theta(c)\left(\Gamma_n\left(\dfrac{\partial u}{\partial x} + \dfrac{\partial m}{\partial x}\right) + \Gamma_u\dfrac{\partial u}{\partial x} - k_{17}u\dfrac{\partial c}{\partial x} - k_{16}u\dfrac{\partial s}{\partial x}\right)\right] \\[2ex]
\dfrac{\partial s}{\partial t} = k_{21}pc + D_s\dfrac{\partial^2 s}{\partial x^2} \\[2ex]
\dfrac{\partial p}{\partial t} = k_1 uc - k_{12}p - k_{13}pu - k_{14}pc + D_p\dfrac{\partial^2 p}{\partial x^2}
\end{cases}
\tag{3}
$$

where n represents the concentration of the normal cells, m the non-invasive cancer cells, u the invasive cancer cells, c a generic ECM protein (e.g. *collagen, vitronectin* or other), s the product of the ECM proteolysis, and p a generic protease. Moreover, Θ is the ramp function

$$\Theta(c) = \begin{cases} k_{26}, & 0 < c < k_{27} \\ \dfrac{k_{28} - c}{k_{28} - k_{27}}, & k_{27} < c < k_{28} \\ 0, & k_{28} < c \end{cases} \tag{4}$$

and

$$\Gamma_n = k_3 \frac{k_{18}}{k_{19} + k_{25}(k_{25}n + k_{25}m + k_{20}u)} \tag{5}$$

$$\Gamma_u = k_6 \frac{k_{18}}{k_{19} + k_{20}(k_{25}n + k_{25}m + k_{20}u)} \tag{6}$$

In a follow-up work, Perumpanani et al. (1998) investigate further the degradation of the ECM. During the invasion, a gradient of ECM fragments is established counter to the direction of the invasion. This results in anti-invasive chemotactic attraction which opposes the haptotaxis migration of the cancer cell towards higher ECM concentrations. They then conclude that the invasion potential of the cancer cells depends on the action of *matrix metalloproteinases* (MMPs) in "a biphasic manner"; excessive degradation of the ECM can lead to the opposite than the invasion effect.

For u, c, p, s representing the concentrations of HT1080 cells, intact *fibronectin*, MMP-2, and the MMP-2-digested soluble *fibronectin* respectively, the model reads as

$$\begin{cases} \dfrac{\partial u}{\partial t} = k_1 u(k_2 - u) - \dfrac{\partial}{\partial x}\left(k_3 \psi(s) u \dfrac{\partial s}{\partial x} - k_4 \chi(c) u \dfrac{\partial c}{\partial x}\right) \\ \dfrac{\partial c}{\partial t} = -k_5 pc \\ \dfrac{\partial s}{\partial t} = k_5 k_6 pc + h(p,s) + D_s \dfrac{\partial^2 s}{\partial x^2} \\ \dfrac{\partial p}{\partial t} = k_7 uc - k_8 pu - k_9 p + D_p \dfrac{\partial^2 p}{\partial x^2} \end{cases} \tag{7}$$

where k_i, s are positive constants and the functions $\psi(s)$, and $\chi(c)$ represent the extend of chemo- and haptotaxis respectively. The proteolysis of the *fibronectin* is represented by $-pc$ and $h(p,s)$ the continued action of the proteases.

Furthermore, Perumpanani et al. (1999) develop and analyse a model for malignant invasion, that combines proteolysis and haptotaxis; a common feature of these two mechanisms is that they can be produced by contact with the ECM. Namely, the model they study reads:

$$\begin{cases} \dfrac{\partial u}{\partial t} = f(u) - k_3 \dfrac{\partial}{\partial x}\left(u\dfrac{\partial c}{\partial x}\right) \\[3mm] \dfrac{\partial c}{\partial t} = -g(c,p) \\[3mm] \dfrac{\partial p}{\partial t} = h(u,c) - Kp \end{cases} \tag{8}$$

where u, c, and p represent the concentrations of the invasive cancer cells, the ECM, and the matrix degrading proteases, and where

$$f(u) = k_1\, u(k_2 - u), \quad g(c,p) = k_4\, pc, \quad h(u,c) = k_5\, uc,$$

with $k_1, \ldots, k_5, K \geq 0$.

Compared with the previous works of these authors, i.e. Perumpanani et al. (1996, 1998), special characteristic of the model (8) is the absence of cancer cell diffusion. In the search for travelling wave solutions, the model (8) is reduced to a system of ordinary differential equations (ODEs) which the authors then study using phase plane analysis. They are able to demonstrate that the model admits a family of travelling waves with speeds depending on the ECM concentration, and hence identify an expected qualitative property on behalf of cancer invasion.

Following the steps laid in Perumpanani et al. (1996), Marchant et al. (2000, 2001) address a haptotaxis model that accounts for three variables: the concentration u of the invasive cells, the connective tissue c, and of the proteases p. In the non-dimensional form the model they study takes the form:

$$\begin{cases} \dfrac{\partial u}{\partial t} = u(1 - u) - \dfrac{\partial}{\partial x}\left(u\dfrac{\partial c}{\partial x}\right) \\[3mm] \dfrac{\partial c}{\partial t} = -pc \\[3mm] \dfrac{\partial p}{\partial t} = \dfrac{1}{\varepsilon}(uc - p) \end{cases}, \tag{9}$$

where $0 < \varepsilon$ represents the relative timescale of the dynamics of the protease p versus the cell growth dynamics. The time variable t is scaled so that u grows as $O(1)$ to the carrying capacity of unity; the space variable x is scaled so that the rate of haptotaxis is of the same order, p is scaled so that c dissolves on the same timescale and, c is scaled so that p and uc are of the same order in the p-equation. This implies that the p timescale is relatively much faster, so that $0 < \varepsilon \ll 1$ is small. This allows the authors to re-model the proteases dynamics, i.e. p-equation in (9), into

$$p = uc$$

and accordingly (9) recasts to:

$$\begin{cases} \dfrac{\partial u}{\partial t} = u(1 - u) - \dfrac{\partial}{\partial x}\left(u\dfrac{\partial c}{\partial x}\right) \\[3mm] \dfrac{\partial c}{\partial t} = -uc^2 \end{cases} \tag{10}$$

The authors were then able to identify a host of travelling wave solutions in the system (10), among which (discontinuous) shock waves. The latter being of a particularly high interest as, according to the authors, the sharpness of the invading profile better approximates the sharp invasion front observed experimentally in cancer growth.

In a follow-up work Marchant et al. (2006) adopted the sequence of models (3), (7), and (8) to obtain the following haptotaxis invasion model

$$\begin{cases} \dfrac{\partial u}{\partial t} = ru(1 - \dfrac{u}{U_0}) - kuc - \chi \dfrac{\partial}{\partial x}\left(u\dfrac{\partial c}{\partial x}\right) \\ \dfrac{\partial c}{\partial t} = -\alpha pc \\ \dfrac{\partial p}{\partial t} = \beta uc - \gamma p \end{cases} \tag{11}$$

where u represents the concentration of tumour cells; c the concentration of the ECM, and p the concentration of a matrix-degrading protease.

With arguments similar as in the case of (9), the authors were able to reduce the model (11) to a two-equation system similar to (10) that exhibits discontinuous solutions, and is able to reproduce the biphasic behaviour first seen in (3).

In a different approach, still though within the general modelling of cancer invasion, Swanson et al. (2000), develops further a mathematical model of *glioma* growth—the most common type of brain tumour—previously proposed in a series of papers by Cruywagen et al. (1995), Tracqui et al. (1995), and Woodward et al. (1996).

The proposed model describes the time evolution of of the glioma cell population based solely on proliferation and diffusion. It is comprised of a single equation, namely,

$$\frac{\partial c}{\partial t} = \nabla \cdot (D(\mathbf{x})\nabla c) + \rho c \tag{12}$$

where $c(\mathbf{x}, t)$ represents the density of the glioma cells, and where the Fickian diffusivity depends on the local tissue

$$D(\mathbf{x}) = \begin{cases} D_g, & \mathbf{x} \in \text{grey matter} \\ D_w, & \mathbf{x} \in \text{white matter} \end{cases}, \quad D_w > D_g.$$

The authors argue that, although the linear proliferation term ρc lacks a saturation effect (like e.g. a logistic term) that would make it more accurate, still it is adequate for the time scale of the experiment considered. The previously observed fit of the model predictions with *in-vivo computerised tomography* (CT) scan measurements, is further investigated under the availability of information regarding the local composition of the brain in grey and white matter.

In a follow up work Swanson et al. (2003) introduce chemotherapy in the model (12), administered in the form of a time dependent decay of the tumour cell population c. Namely, the authors propose the model

$$\frac{\partial c}{\partial t} = \nabla \cdot (D(\mathbf{x})\nabla c) + \rho c - G(t)c \tag{13}$$

where the therapy schedule G is given by

$$G(t) = \begin{cases} k, & \text{during administration periods} \\ 0, & \text{otherwise} \end{cases}$$

Besides chemotherapy though, the authors consider the effect of surgical resection in the treatment of high- and low-grade gliomas. The mathematical approach they followed has allowed them to demonstrate that any local treatment of a diffusely invading glioma will fail, since the invasion is still more peripheral than any localizable treatment can reach.

In a follow-up work, Swanson (2008) studied further the model (12) discussed in Swanson et al. (2000, 2003), and compared its predictions against *in vitro* experimental measurement data.

The authors then argue that the model sufficiently describes the key dynamics of gliomas *in-vitro* and that these results provide a foundation for using this model for more complicated scenarios *in-vivo*. In any case, they argue, that they have obtained with their model a better understanding of glioma cell behaviour since the model provides a means for quantification of experimental observations.

3.2   A Hybrid Continuum-Discrete Model

In the next milestone in the evolution towards hybrid invasion models, Anderson et al. (2000) propose a blend of continuum deterministic modelling and discrete stochastic modelling in 1- and 2- space dimensions.

The continuum model they study examines the migratory response of cancer cells to self-generated haptotaxis gradients. Namely, the authors consider cancer cell mediated production and activation of *matrix degrading enzymes* (MDEs), the ensuing degradation of the ECM, and the subsequent haptotaxis response of the cancer cells to the induced gradient of the matrix. The model itself reads as follows

$$\begin{cases} \dfrac{\partial n}{\partial t} = D_n \nabla^2 n - \chi \nabla \cdot (n \nabla f) \\ \dfrac{\partial f}{\partial t} = -\delta m f \\ \dfrac{\partial m}{\partial t} = D_m \nabla^2 m + \mu n - \lambda m \end{cases} \tag{14}$$

where n, f, m, denote the densities of the cancer cells, the ECM, and the MDEs respectively, and D_n, D_m and χ the diffusion and haptotaxis coefficients respectively.

They can verify with their model that the cancer cells are split in two groups: those driven primarily by diffusion that form a propagating front and degrade the matrix, and those driven by haptotaxis that follow the gradient formed in

the ECM. The self-generated haptotaxis effect is still present when a heterogeneous ECM is considered, although not clearly seen due to the pre-existing ECM gradients.

The authors formulate also a discrete model which tracks the positions of migratory cancer cells while accounting for the extracellular stimuli (haptotaxis in this instance). The model reads as follows:

$$
\begin{cases}
n_{l,m}^{q+1} = P_0 n_{l,m}^q + P_1 n_{l+1,m}^q + P_2 n_{l-1,m}^q + P_3 n_{l,m+1}^q + P_4 n_{l,m-1}^q \\[2mm]
P_0 = 1 - \dfrac{4kD}{h^2} - \dfrac{k\gamma}{h^2}\left(f_{l+1,m}^q + f_{l-1,m}^q - 4f_{l,m}^q + f_{l,m+1}^q + f_{l,m-1}^q\right), \\[2mm]
P_1 = \dfrac{kD}{h^2} - \dfrac{k\gamma}{4h^2}\left(f_{l+1,m}^q - f_{l-1,m}^q\right) \\[2mm]
P_2 = \dfrac{kD}{h^2} + \dfrac{k\gamma}{4h^2}\left(f_{l+1,m}^q - f_{l-1,m}^q\right) \\[2mm]
P_3 = \dfrac{kD}{h^2} - \dfrac{k\gamma}{4h^2}\left(f_{l,m+1}^q - f_{l,m-1}^q\right) \\[2mm]
P_4 = \dfrac{kD}{h^2} + \dfrac{k\gamma}{4h^2}\left(f_{l,m+1}^q - f_{l,m-1}^q\right)
\end{cases}
\tag{15}
$$

where $P_0, \cdots, P_4$ are termed directional transition rates. In the above k, h represent the time- and space-step of the discretisation method.

This discrete version allows the authors to track individual cells as they move in the two-dimensional tissue. They can then make remarks on the migration of the cancer cells which have important implications in metastasis.

The authors also combine the discrete and continuum versions of their models, acting in different scales of the cancer invasion, and compare the model predictions with clinical observations of cancer invasion in breast cancer.

3.3 A Model of Trophoblast Invasion

Further in the macroscopic tissue invasion, although not cancerous, Byrne et al. (2000) present a mathematical model that describes the initial stages of placental development during which trophoblast cells begin to invade the uterine tissue as a continuous mass of cells.

The proposed model accounts for the density of the trophoblast cells $n(x,t)$, trophoblast-derived proteases $u(x,t)$, and uterine tissue $\rho(x,t)$, and reads as

$$
\begin{cases}
\dfrac{\partial n}{\partial t} = D_n \dfrac{\partial}{\partial x}\left(n^2 \dfrac{\partial n}{\partial x}\right) - \chi \dfrac{\partial}{\partial x}\left(n \dfrac{\partial v}{\partial x}\right) + k_1 n(1 - n - p) \\[2mm]
\dfrac{\partial u}{\partial t} = D_u \dfrac{\partial^2 u}{\partial x^2} + k_2 un(1 - n) - k_3 uv \\[2mm]
\dfrac{\partial v}{\partial t} = D_v \dfrac{\partial^2 v}{\partial x^2} + k_4 u\rho - k_3 uv \\[2mm]
\dfrac{\partial \rho}{\partial t} = k_5 \rho(1 - n - \rho) - k_6 u\rho
\end{cases}
\tag{16}
$$

where D_n, D_u, $D_v > 0$, $\chi > 0$ are the corresponding linear diffusion and hapto-taxis coefficients, k_1, k_2, $k_5 > 0$ the logistic proliferation rates, and k_3, k_4, $k_6 > 0$ are kinetic rate parameters.

The mathematical analysis of a simpler submodel that the authors under-take, describes the final stages of normal embryo implantation and suggests that as the timescale of interest increases, the dominant migratory mechanism of the trophoblasts switches from chemotaxis to nonlinear random motion. More precisely, the initial invasion of the system is dominated by the chemotactic response of the trophoblast cells to the inhibitor w. In addition, when the pro-tease is relaxing to a uniform steady state, chemotaxis plays an important role in defining the depth of penetration of the trophoblasts while the limiting profile adopted is determined by nonlinear random motility.

3.4   An Individual-Based Cellular Potts Model

Switching back to cancer invasion, Turner and Sherratt (2002) develop a discrete model of malignant invasion using a thermodynamic argument. They employ an extension of the Potts model to simulate a population of malignant cells experiencing interactions due to both homotypic and heterotypic adhesion while also secreting proteolytic enzymes and experiencing a haptotactic gradient.

Specifically, the authors consider a square lattice and assign at every point (i, j) a label σ_{ij}. Neighbouring lattice sites with the same value of σ are assumed to lie within the same cell. The interaction between the cell surfaces follows from the coupling constants $J_{\tau(\sigma_{ij}),\tau(\sigma_{i'j'})}$, which account for the energy/strength of the interaction between adjacent points with different values of σ_{ij} (i.e. of different cells). This is described in the first term in the total energy H:

$$H = \sum_{ij} \sum_{i'j'} J_{\tau(\sigma_{ij}),\tau(\sigma_{i'j'})} \left\{ 1 - \delta_{\sigma_{ij},\sigma_{i'j'}} \right\} + \sum_{\sigma} \lambda \left(u_\sigma - V_T \right)^2 \tag{17}$$

The second term describes the energy required for the growth and mechanical deformation of the cells where v_σ is the volume of the cell σ, V_T is the target volume, and λ the corresponding Lagrange-multiplier. Furthermore, the model accounts for haptotaxis by attaching in every lattice point a parameter f_{ij} that accounts for the local density of the ECM protein concentration.

The overall energy change is then calculated as

$$\Delta H_{ij} = \Delta H_{1,ij} + \Delta H_{2,ij} + k_H(f_{i'j'} - f_{ij}) \tag{18}$$

where $k_H > 0$ represents the strength of haptotaxis, and where $\Delta H_{1,ij}$, $\Delta H_{2,ij}$ correspond to the surface and mechanical energy changes between the two con-formations H_1 and H_2, given by the corresponding total energy formulas (17).

With this approach the authors demonstrate that the morphology of the invading front is influenced by changes in the adhesiveness parameters, and detail how the invasiveness of the tumour is related to adhesion. Their model suggests

that cell-cell adhesion has less of an influence on invasion compared to cell-matrix adhesion, and that increases in both proteolytic enzyme secretion rate and the coefficient of haptotaxis act in synergy to promote invasion. By including cell proliferation, they extend their algorithm for cell division rates that depend on changes in the relative magnitudes of homotypic and heterotypic cell-cell adhesiveness.

3.5   A Model of the Urokinase-Plasminogen uPA System

Further on the macroscopic description, Chaplain and Lolas (2005) present a mathematical model of the invasion of the ECM by cancer cells through the secretion of MDEs. The model focuses specifically on the role of the urokinase plasminogen activation system and is more complex than other mathematical models of invasion, in the sense that it accounts for more key biological components of tissue invasion.

Denoting the cancer cell density by c, the urokinase plasminogen activator (uPA) concentration by u, the plasminogen activator inhibitor-1 (PAI-1) concentration by p, the plasmin concentration by m and the ECM substrate (*vitronectin* in this case) density by v, the model reads as:

$$\begin{cases} \dfrac{\partial c}{\partial t} = D_c \dfrac{\partial^2 c}{\partial x^2} - \dfrac{\partial}{\partial x}\left(\chi_c c \dfrac{\partial u}{\partial x} + \zeta_c c \dfrac{\partial p}{\partial x} + \xi_c c \dfrac{\partial v}{\partial x} \right) + \phi_{13} cu + \mu_1 c \left(1 - \dfrac{c}{c_0} \right) \\[2mm] \dfrac{\partial v}{\partial t} = -\delta vm + \phi_{21} up - \phi_{22} vp + \mu_2 v \left(1 - \dfrac{v}{v_0} \right) \\[2mm] \dfrac{\partial u}{\partial t} = D_u \dfrac{\partial^2 u}{\partial x^2} - \phi_{31} pu - \phi_{33} cu + a_{31} c \\[2mm] \dfrac{\partial p}{\partial t} = D_p \dfrac{\partial^2 p}{\partial x^2} - \phi_{41} pu - \phi_{42} pv + a_{41} m \\[2mm] \dfrac{\partial m}{\partial t} = D_m \dfrac{\partial^2 m}{\partial x^2} - \phi_{51} pu - \phi_{52} pv + a_{53} uc \end{cases} \qquad (19)$$

where $D_c, D_u, D_p, D_m \geq 0$ and $\chi_c, \zeta_c, \xi_c > 0$ are the diffusion and taxis coefficients, μ_1, μ_2 the cell proliferation and matrix reconstruction rates, and the rest of the parameters are the kinetic rate parameters.

The main achievement of this model is that fairly simple mathematical representation of the binding interactions of the components of the plasminogen activation system coupled with cell migration were able to capture the main characteristic effects of the system in cancer progression and invasion. The results show a very rich dynamic spatio-temporal behaviour which are in line with recent experimental results, that show that when breast cells become malignant, plasmin is activated on their membrane and their morphology is changed from sheet-like structures to multicellular heterogeneous masses.

3.6   Modelling the Role of Acidity in Invasion

With a series of papers, Smallbone et al. (2005, 2007, 2008) turn their attention
to the role of acidity in cancer invasion and connect with the previous works
of Gatenby et al. (2006). Smallbone et al. (2005). In particular, they develop a
simple model of three-dimensional tumour growth to examine the role of *acidosis*
in the interaction between normal and tumour cell populations. The tumours
under investigation are assumed to be at the first avascular and early vascular
stages and in effect, expect the formation of necrotic cores. The model they
discuss reads

$$\begin{cases} \dfrac{\partial H}{\partial t} = D_H \nabla^2 H + F_H \\ \dfrac{dR_2^3}{dt} = S\left(R_2^3 - R_1^3\right) - LR_1^3 \end{cases} \tag{20}$$

where H represents the concentration of the acid, $D_H > 0$ represent the diffusion
coefficient and F_H the combined rate of acid production and removal from the
system. The second equation stems after an assumption of rotational symmetry
on the tumour—which is assumed to be of radius R_2—and the formation of
a (rotational symmetric) necrotic core—with radius R_1. The proliferation term
$S\left(R_2^3 - R_1^3\right)$ refers solely to the living part of the tumour, the only part of the
tumour where proliferation takes place.

   With this modelling setting, the authors are able to observe a number of
different behaviours. The analysis they perform predicts three regimes of tumour
growth. If the rate of acid removal from the tumour is insufficient, there is growth
followed by auto-toxicity, resulting in a benign tumour. This is found always to
occur in an avascular tumour. A vascular tumour displays sustained growth, and
invades the whole of the normal tissue space. If the tumour is sufficiently small,
there is no growth as the acid perturbations cannot to induce normal cell death.

3.7   Modelling the Role of Cell-Cell Adhesion Using PDEs

Armstrong et al. (2006) move away from the interactions between the cancer cells
and the tumour microenvironment, and turn their attention to the interactions
between the cancer cells themselves. Accordingly, they develop a macroscopic
model of cell-cell adhesion by considering the movement of cells in response to
the adhesive forces generated through transcellular binding proteins.

   Namely, for $u(t, x)$, $v(t, x)$, $t \geq 0$ and $x \in \mathbb{R}$ denoting the population densities
of two cell types, the model reads:

$$\begin{cases} \dfrac{\partial}{\partial t} u = \dfrac{\partial^2}{\partial x^2} u - \dfrac{\partial}{\partial x}\left(uK^u(u,v)\right) \\ \dfrac{\partial}{\partial t} v = \dfrac{\partial^2}{\partial x^2} v - \dfrac{\partial}{\partial x}\left(vK^v(u,v)\right) \end{cases} \tag{21}$$

where the adhesion terms K^u, K^v encompass both self- and cross-population adhesion for the u and v cell family respectively, and read:

$$K^u(u, v) = S^u \int_{-1}^{1} g^{uu}\left(u(x + x_0), v(x + x_0)\right) \omega^{uu}(x_0)dx_0$$

$$+ C \int_{-1}^{1} g^{uv}\left(u(x + x_0), v(x + x_0)\right) \omega^{uu}(x_0)dx_0$$

$$K^v(u, v) = S^v \int_{-1}^{1} g^{vv}\left(u(x + x_0), v(x + x_0)\right) \omega^{vv}(x_0)dx_0$$

$$+ C \int_{-1}^{1} g^{vu}\left(u(x + x_0), v(x + x_0)\right) \omega^{uv}(x_0)dx_0$$

Here S^u, S^v and C represent the self-adhesive strength of the populations u and v, and the cross-adhesive strength between the populations, respectively. Differences in cell geometry can be modelled through the specific choices of S^u, S^v and C as well as of g^{uu}, g^{uv}, g^{vv} and ω^{uu}, ω^{uv}, ω^{vv}.

The authors employ both analytical and numerical techniques to demonstrate the that (21) can predict the aggregation behaviour of a disassociated adhesive cell populations and can replicate the different types of cell sorting behaviour that is observed experimentally. The authors argue that the resulting aggregation and pattern formation phenomena is a direct consequence of the relative strengths of self-population and cross-population adhesive bonds in the model.

Further on the modelling of cell-cell and cell-matrix interactions, Gerisch and Chaplain (2008) explore the spatio-temporal evolution of cancer invasion by cell-cell adhesion and haptotaxis by accounting for local and non-local contributions in the cell-cell adhesion tensor.

For a single family of cancer cells, the model the authors propose reads as

$$\begin{cases} \dfrac{\partial c}{\partial t} = \nabla \cdot \left(D_1 \nabla c - c\mathcal{A}\left\{\underline{u}(t, \cdot)\right\}\right) + \mu_1 c\left(1 - c - v\right) \\[2mm] \dfrac{\partial v}{\partial t} = -\gamma m v + \mu_2\left(1 - c - v\right) \\[2mm] \dfrac{\partial m}{\partial t} = \nabla \cdot \left(D_3 \nabla m\right) + \alpha c - \lambda m \end{cases} \tag{22}$$

where the non-local cell-cell adhesion term $\mathcal{A}\left\{\underline{u}(t, \cdot)\right\}$ is defined for $x \in \mathbb{R}$, as:

$$\mathcal{A}\left\{\underline{u}(t, \cdot)\right\}(x) = \frac{1}{R} \int_0^R \sum_{k=0}^{1} \underline{\eta}(k) \cdot \Omega(r) g(\underline{u}(t, x + r\underline{\eta}(k))))dr$$

where $\underline{\eta}(k) = (-1)^k$, $k = 0, 1$. In a two dimensional extension, $\mathbf{x} \in \mathbb{R}^2$ the authors define the non-local cell-cell adhesion term to be

$$\mathcal{A}\left\{\underline{u}(t, \cdot)\right\}(\mathbf{x}) = \frac{1}{R} \int_0^R r \int_0^{2\pi} \underline{\eta}(\theta) \cdot \Omega(r) g(\underline{u}(t, \mathbf{x} + r\underline{\eta}(\theta))))d\theta dr$$

where $\eta(\theta) = (\cos\theta, \sin\theta)^{\mathrm{T}}$ is the unit outer normal vector corresponding to the angle θ.

Furthermore Domschke et al. (2014) extend (22) to a two-cancer-cell species non-local as follows:

$$
\begin{cases}
\dfrac{\partial c_1}{\partial t} = \nabla \cdot \left(D_{1,1}\nabla c_1 - c_1 \mathcal{A}_1 \left\{ t, x, \underline{u}(t, \cdot) \right\} \right) + \mu_{1,1} c_1 \left(1 - \rho(\mathbf{u}) \right) + M_{1,1}(t, \mathbf{u}) c_1 \\[2mm]
\dfrac{\partial c_2}{\partial t} = \nabla \cdot \left(D_{1,2}\nabla c_2 - c_2 \mathcal{A}_2 \left\{ t, x, \underline{u}(t, \cdot) \right\} \right) + \mu_{1,2} c_2 \left(1 - \rho(\mathbf{u}) \right) + M_{2,1}(t, \mathbf{u}) c_1 \\[2mm]
\dfrac{\partial v}{\partial t} = -\gamma m v + \mu_2 \left(1 - \rho(\mathbf{u}) \right)^+ \\[2mm]
\dfrac{\partial m}{\partial t} = \nabla \cdot (D_3 \nabla m) + \alpha_1 c_1 + \alpha_2 c_2 - \lambda m
\end{cases}
\tag{23}
$$

Another extension that the model (23) introduces to (22) is the possibility for a change of adhesion properties during the growth of the caner; this is achieved through time-dependent cell-cell and cell-matrix adhesion functions.

Numerical experiments of both (22) and (23) demonstrate a range of heterogeneous dynamics which are qualitatively similar to the invasive growth patterns observed experimentally in a number of different types of cancer, such as *tumour infiltrative growth patterns* (INF).

3.8   Multiscale Moving Boundary Models of Cancer Invasion

Amalgamating the previous ideas of mutliscale interactions between the cancer cells and their microenvironment, Trucu et al. (2013), Peng et al. (2017), Shuttleworth and Trucu (2019a, 2019b, 2019c) formulate in a series of papers a moving boundary two-scale model for cancer invasion of the tissue. Their approach combines the macroscopic dynamics of the distributions of cancer cells and of the surrounding ECM, and microscopic scale dynamics of the MDEs, produced by the individual cancer cells. These microscopic scale dynamics are assumed to take place at the interface of the cancer cells and the ECM and give rise to a moving boundary at the macroscopic scale.

To be more specific, Peng et al. (2017) consider the macroscopic *urokinase* model (19), which was earlier introduced by Chaplain and Lolas (2005). In its original derivation, the macroscopic equation for the urokinase u reads as

$$
\frac{\partial u}{\partial t} = D_u \frac{\partial^2 u}{\partial x^2} - \phi_{31} p u - \phi_{33} c u + a_{31} c.
$$

The approach of the authors amounts to reconsidering the u-equation in, what they call "microscopic regime", as follows:

$$
\frac{\partial u}{\partial \tau} = D_u \frac{\partial^2 u}{\partial x^2} - \phi_{31} p u + \left(-\phi_{33} u + a_{31} \right) f_1^{\epsilon Y}(y, \tau)
$$

where the "source" $f_1^{\epsilon Y}$ of the urokinase is given in terms of the cancer cell concentration c by:

$$
f_1^{\epsilon Y}(y, \tau) = \frac{1}{\lambda \left(B(y, \gamma) \cap \Omega(t_0) \right)} \int_{B(y,\gamma) \cap \Omega(t_0)} c(x, t_0 + \tau) dx
$$

where λ is the usual Lebesgue measure and γ represents the maximal thickness of the outer proliferating rim, and $\Omega(t_0)$ the physical space occupied by the tumour.

The proposed modelling framework allows the authors to study the changes in the macroscopic scale morphology of the tumour caused by the dynamical urokinase processes occurring in the microscopic scale along the invasive edge of the tumour.

3.9   A Framework for Modelling the Metastatic Spread of Cancer

Even more recently, the hybrid cancer and tissue modelling led Franssen et al. (2019) to study the metastatic process, and to present a mathematical modelling framework that captures the interconnected processes of invasion and metastatic spread of individual cancer cells in a spatially explicit manner a multigrid, hybrid, individual-based approach. This framework accounts for the spatiotemporal evolution of mesenchymal- and epithelial-like cancer cells, *membrane-type-1 matrix metalloproteinase* (MT1-MMP) and the diffusible *matrix metalloproteinase-2* (MMP-2), and for their interactions with the ECM.

The authors consider a modelling and computational representation of an organism comprised of a number of compartments, each one representing a separate organ. One of the organs is designated as the primary spatial domain—where the initial tumour is located—and assign locations within it to function as entry points into the vasculature. Similarly they impose a spatial map of exit locations from the vasculature to secondary locations organs. This allows cancer cells to use the vasculature and travel from the primary tumour site to the metastatic sites.

Within every organ the authors consider the following dimensional cancer growth/invasion model:

$$\begin{cases} \dfrac{\partial c_E}{\partial t} = d_E \nabla^2 c_E - \phi_E \nabla \cdot (c_E \nabla w) \\[2mm] \dfrac{\partial c_M}{\partial t} = d_M \nabla^2 c_M - \phi_M \nabla \cdot (c_M \nabla w) \\[2mm] \dfrac{\partial m}{\partial t} = d_m \nabla^2 m + \theta c_M - \lambda m \\[2mm] \dfrac{\partial w}{\partial t} = -\left(\gamma_1 c_M + \gamma_2 m \right) w \end{cases} \tag{24}$$

where $c_E(t, x, y)$, $c_m(t, x, y)$ represent the two-dimensional densities of the epithelial-like and mesenchymal-like cancer cells respectively. The MMP-2 concentration is represented by $m(t, x, y)$, and the density of the ECM by $m(t, x, y)$. The diffusion of the epithelial-, mesenchymal-like cancer cells and the diffusible MMPs is assumed ot be linear with diffusivities d_E, d_M and d_m respectively. ϕ_E and ϕ_M are the haptotaxis sensitivities of the epithelial- and mesenchymal-like cancer cells respectively. Finally θ_m, λ_m and γ_1, γ_2 are the production and decay rates of the MMPs, the degradation rates of the ECM.

With a series of numerical experiments, the authors were able to reproduce a number qualitative observations/phenomena and quantitative measurements

made in *in vivo* experimental settings in human oral squamous carcinoma cells invasion in myoma tissue.

In a follow up work, Franssen and Chaplain (2020) propose an extension of (24), where besides the multiorgan and metastatic conformation of the two phenotypic states of epithelial- and mesenchymal-like cancer cells, they also consider a partial-EMT phenotype. They allow for the switching between these phenotypic states via EMT (locally) and MET (in the metastatic site) and account for the likelihood of spread of cancer cells to the various secondary sites. They also consider the maladaptation of metastasized cancer cells at the secondary sites and the effect of the immune response by accounting for cancer cell dormancy and death. They achieve this by considering a discrete-continuous approach along the lines proposed by Anderson et al. (2000) and presented here in (14).

3.10   A Novel Hybrid Continuum-Discrete Multiscale Model of Invasion

We close this review with most recent and genuinely hybrid modelling of cancer invasion. Sfakianakis et al. (2020) propose a modelling framework to study the combined invasion of the ECM by two types of cancer cells, the epithelial- and the mesenchymal-like cancer cells. The proposed framework is a *genuinely hybrid multiscale model* that treats the epithelial-like cancer cells in a macroscopic and deterministic fashion and the mesenchymal-like cancer cells in an atomistic and stochastic way.

This modelling framework is a coupled system of macroscopic deterministic PDEs and Stochastic Differential Equations (SDEs) for the migration of the individual mesenchymal-like cancer cells.

The macroscopic sub-model—for the time evolution of the macroscopic quantities, such as the ECM, MMPs, and the densities of the epithelial-like cancer cells—reads as follows:

$$
\begin{cases}
\dfrac{\partial}{\partial t} c^\alpha(\mathbf{x}, t) = D_\alpha \Delta c^\alpha(\mathbf{x}, t) - \mu_\alpha^{\mathrm{EMT}}(\mathbf{x}, t) c^\alpha(\mathbf{x}, t) + \mu_\beta^{\mathrm{MET}}(\mathbf{x}, t) c^\beta(\mathbf{x}, t) \\
\qquad\qquad + \rho_c^\alpha c^\alpha(\mathbf{x}, t) \left(1 - c^\alpha(\mathbf{x}, t) - c^\beta(\mathbf{x}, t) - v(\mathbf{x}, t) \right), \\[4pt]
\dfrac{\partial}{\partial t} m(\mathbf{x}, t) = D_m \Delta m(\mathbf{x}, t) + \rho_m^\alpha c^\alpha(\mathbf{x}, t) + \rho_m^\beta c^\beta(\mathbf{x}, t) - \lambda_m m(\mathbf{x}, t) \\[4pt]
\dfrac{\partial}{\partial t} v(\mathbf{x}, t) = - \left(\lambda_v^\alpha c^\alpha(\mathbf{x}, t) + \lambda_v^\beta c^\beta(\mathbf{x}, t) \right) m(\mathbf{x}, t) v(\mathbf{x}, t),
\end{cases}
\tag{25}
$$

where $\mu_\alpha^{\mathrm{EMT}}(\mathbf{x}, t) = \mu_\alpha \mathcal{X}_{\mathcal{E}(t)}(\mathbf{x})$, $\mu_\beta^{\mathrm{MET}}(\mathbf{x}, t) = \mu_\beta \mathcal{X}_{\mathcal{M}(t)}(\mathbf{x})$, with $\mathcal{E}(t), \mathcal{M}(t) \subset \Omega$, and D_α, μ_α, μ_β, $\rho_c^\alpha \geq 0$, and D_m, ρ_m^α, ρ_m^β, $\lambda_m \geq 0$ constants. Alternative approaches could also be considered, e.g. an ECM-density dependent production of the MMPs by the cancer cells, and λ_v^α, $\lambda_v^\beta \geq 0$ constants. Possible extensions of the model could include non-diffusible MMPs, MC-only matrix degradation, matrix reconstruction, and other biologically relevant processes.

The stochastic submodel—responsible for the migration of the individual mesenchymal-like cancer cells—reads:

$$d\mathbf{X}_t^p = \mu\left(\mathbf{X}_t^p, t\right) dt + \sigma\left(\mathbf{X}_t^p, t\right) d\mathbf{W}_t^p, \quad \text{for } p \in P, \tag{26}$$

where $\mathbf{X}_t^p$ represents the position vector of the mesenchymal-cell with index $p \in \{1, \ldots, N(t)\}$, $\mathbf{W}_t^p$ is a Wiener process with independent components, μ and σ^2 are the *drift* and *diffusion* coefficients that encode the modelling assumptions made on the directed and random parts of the motion of the mesenchymal-cells.

The coupling between the macroscopic and stochastic submodels (25) and (26) is happening via phase transition operators that connect the isolated cellular description with the density formulation:

$$\left\{(\mathbf{x}_p(t), m_p), \ p = 1, \ldots, N(t)\right\} \rightleftarrows c(\mathbf{x}, t)$$

$$m_p(t) = \int_{M_p} c(\mathbf{x}, t) d\mathbf{x}, \qquad \mathbf{x}_p(t) = \text{ the (bary-)centre of } M_p$$

This approach allows them to reproduce, in a very natural way, fundamental qualitative features, of the current biomedical understanding of cancer invasion, that are not easily captured by classical modelling approaches, for example, the invasion of the ECM by self-generated gradients and the formation of EC invasion islands outside of the main body of the tumour.

With the atomistic stochastic sub-model, they reproduce a sustainable invasion of the ECM by means of a *self-induced haptotaxis gradient*; this verifies the experimentally invasion behaviour and at the same time it serves as verification of the propagating invasion front seen in numerical simulations of macroscopic deterministic cancer invasion models.

With the full model, they reproduce the spread of the tumour and the invasion of the ECM in the form of invasion "islands". These are well known to appear in many cases of cancer, outside the main body of the tumour, and are quite difficult to reproduce by either macroscopic or atomistic cancer invasion models. With this approach these invasion "islands" are a naturally emerging property of modelling framework, which has very recently been used to model oral squamous cell carcinoma cell migration and invasion in an in vitro organotypic invasion assay experiment (Franssen et al. 2021).

4 Discussion and Conclusion

In a prescient statement from 50 years ago, Judah Folkman (the "father" of tumour-induced angiogenesis and angiogenesis research) stated that the interactions between tumour cells and endothelial cells *"...may constitute a highly integrated ecosystem. In this ecosystem the mitotic index of the two cell populations may depend on each other."* (Folkman 1971). This viewpoint was echoed in the 2011 paper of Hanahan and Weinberg, where they note: *"When viewed from this perspective, the biology of a tumor can only be understood by studying*

the individual specialized cell types within it as well as the "tumor microenvironment" that they construct during the course of multistep tumorigenesis. This depiction contrasts starkly with the earlier, reductionist view of a tumor as nothing more than a collection of relatively homogeneous cancer cells, whose entire biology could be understood by elucidating the cell-autonomous properties of these cells." (Hanahan and Weinberg 2011).

The first paper discussed in this review (Gatenby 1995) considered the interactions of cancer cells with the host tissue precisely from this "ecological" perspective. The subsequent papers reviewed here also take a "holistic approach" to the problem, focussing on the complex dynamic interactions between the (solid) tumour and the tumour microenvironment (between the cancer cells and normal cells of the host tissue). The results of these mathematical modelling efforts (both analytical and computational) have helped to elucidate some of the details of the interplay between cancer cells and normal tissue during invasion across a range of spatial and temporal scales. Insight into how better treatment protocols could be developed have arisen from the results of several models e.g. changing the level of acidity within the tumour or interrupting the hypoxia-glycolysis-acidosis cycle (Smallbone et al. 2005, 2007, 2008), estimating the amount of healthy tissue to resect during breast cancer surgery (Anderson et al. 2000), estimating the depth of invasion and its relation to cell adhesion (Turner and Sherratt 2002), and estimating the depth of spread of gliomas into brain tissue (Swanson et al. 2000, 2003; Swanson 2008). Moreover, the complexity of cancer invasion has necessitated the development of new modelling approaches resulting in advances on the mathematical side over and above the biological insight provided.

While a lot of the insight from the modelling has been qualitative in nature, the recent work of Franssen et al. (2021), focussing on modelling cell invasion in a 3D organotypic assay with a novel hybrid continuum-discrete model, indicates a possible way to combine and include real data from *in vitro* experiments, parameterise the model accurately and robustly, calibrate the model and then use the model to make further predictions on the *in vitro* system, while opening up possible avenues to make use of this as a platform to simulate *in vivo* invasion in a predictive and quantitative manner cf. Brady and Enderling (2019).

References

Anderson, A.R.A., Chaplain, M.A.J., Newman, E.L., Steele, R.J.C., Thompson, A.M.: Mathematical modelling of tumour invasion and metastasis. Comput. Math. Methods Med. **2**(2), 129–154 (2000)

Armstrong, N.J., Painter, K.J., Sherratt, J.A.: A continuum approach to modelling cell-cell adhesion. J. Theor. Biol. **243**(1), 98–113 (2006)

Brady, R., Enderling, H.: Mathematical models of cancer: when to predict novel therapies, and when not to. Bull. Math. Biol. **81**, 3722–3731 (2019)

Byrne, H.M., Chaplain, M.A.J., Pettet, G.J., McElwain, D.L.S.: An analysis of a mathematical model of trophoblast invasion. Appl. Math. Lett. **14**, 1005–1010 (2000)

Chaplain, M.A.J., Lolas, G.: Mathematical modelling of cancer cell invasion of tissue: the role of the urokinase plasminogen activation system. Math. Models Methods Appl. Sci. **15**(11), 1685–1734 (2005)

Cruywagen, G.C., Woodward, D.E., Tracqui, P., Bartoo, G.T., Murray, J.D., Alvord Jr., E.C.: The modelling of difusive tumors. J. Biol. Syst. **3**, 937–945 (1995)

Domschke, P., Trucu, D., Gerisch, A., Chaplain, M.A.J.: Mathematical modelling of cancer invasion: implications of cell adhesion variability for tumour infiltrative growth patterns. J. Theor. Biol. **361**, 41–60 (2014)

Folkman, J.: Tumor angiogenesis: therapeutic implications. New Engl. J. Med. **285**, 1182–1186 (1971)

Franssen, L.C., Chaplain, M.A.J.: A mathematical multi-organ model for bidirectional epithelial-mesenchymal transitions in the metastatic spread of cancer. IMA J. Appl. Math. **85**, 724–761 (2020)

Franssen, L.C., Lorenzi, T., Burgess, A.E.F., Chaplain, M.A.J.: A mathematical framework for modelling the metastatic spread of cancer. Bull. Math. Biol. **81**, 1965–2010 (2019)

Franssen, L.C., Sfakianakis, N., Chaplain, M.A.J.: A novel 3D atomistic-continuum cancer invasion model: in silico simulations of an in vitro organotypic invasion assay. J. Theor. Biol. (2021, in press)

Friedl, P., Wolf, K.: Tumour-cell invasion and migration: diversity and escape mechanisms. Nat. Rev. Cancer **5**, 362–374 (2003)

Gatenby, R.A.: Models of tumor-host interaction as competing populations: implications for tumor biology and treatment. J. Theor. Biol. **176**(4), 447–455 (1995)

Gatenby, R.A., Gawlinski, E.T.: A reaction-diffusion model of cancer invasion. Cancer Res. **56**(24), 5745–5753 (1996)

Gatenby, R.A., Gawlinski, E.T., Gmitro, A.F., Kaylor, B., Gillies, R.J.: Acid-mediated tumor invasion: a multidisciplinary study. Cancer Res. **66**(10), 5216–5223 (2006)

Gerisch, A., Chaplain, M.A.J.: Mathematical modelling of cancer cell invasion of tissue: local and non-local models and the effect of adhesion. J. Theor. Biol. **250**(4), 684–704 (2008)

Hanahan, D., Weinberg, R.A.: The Hallmarks of Cancer. Cell **100**, 57–70 (2000)

Hanahan, D., Weinberg, R.A.: The hallmarks of cancer: the next generation. Cell **144**, 646–671 (2011)

Marchant, B.P., Nornbury, J., Perumpanani, A.J.: Traveling shock waves arising in a model of malignant invasion. SIAM J. Appl. Math. **60**(2), 463–476 (2000)

Marchant, B.P., Nornbury, J., Sherratt, J.A.: Travelling wave solutions to a haptotaxis-dominated model of malignant invasion. Nonlinearity **14**, 1653–1671 (2001)

Marchant, B.P., Norbury, J., Byrne, H.M.: Biphasic behaviour in malignant invasion. Math. Med. Biol. **23**, 173–196 (2006)

Nyström, M., Thomas, G.J., Stone, I.C., Mackenzie, M., Hart, I.R., Marshall, J.F.: Development of a quantitative method to analyse tumour cell invasion in organotypic culture. J. Pathol. **205**, 468–475 (2005)

Peng, L., Trucu, D., Lin, P., Thompson, A., Chaplain, M.A.J.: A multiscale mathematical model of tumour invasive growth. Bull. Math. Biol. **79**(3), 389–429 (2017)

Perumpanani, A.J., Sherratt, J.A., Norbury, J., Byrne, H.M.: Biological inferences from a mathematical model for malignant invasion. Invas Metast **16**, 209–221 (1996)

Perumpanani, A.J., et al.: Extarcellular matrix-mediated chemotaxis can impede cell migration. Proc. R. Soc. London B **265**, 2347–2352 (1998)

Perumpanani, A.J., Sherratt, J.A., Norbury, J., Byrne, H.M.: A two parameter family of travelling waves with a singular barrier arising from the modelling of extracellular matrix mediated cellular invasion. Phys. D **126**, 145–159 (1999)

Recamier, J.C.: Recherches sur le traitement du cancer sur la compression méthodique simple ou combinée et sur l'histoire générale de la meme maladie. Tome Second. Paris, Chez Gabon, Libraire-Editeur (1829)

Sfakianakis, N., Madzvamuse, A., Chaplain, M.A.J.: A hybrid multiscale model for cancer invasion of the extracellular matrix. Multisc. Model. Simul. **18**(2), 824–50 (2020)

Shuttleworth, R., Trucu, D.: Multiscale dynamics of a heterotypic cancer cell population within a fibrous extracellular matrix. J. Theor. Biol. **486**, 1–22 (2019a)

Shuttleworth, R., Trucu, D.: Multiscale modelling of fibres dynamics and cell adhesion within moving boundary cancer invasion. Bull. Math. Biol. **81**, 2176–2219 (2019b)

Shuttleworth, R., Trucu, D.: Cell-scale degradation of peritumoural extracellular matrix fibre network and its role within tissue-scale cancer invasion. Bull. Math. Biol. **82**, 1–47 (2019c)

Smallbone, K., Gavaghan, D.J., Gatenby, R.A., Maini, P.K.: The role of acidity in solid tumour growth and invasion. J. Theor. Biol. **235**, 476–484 (2005)

Smallbone, K., Gatenby, R.A., Gillies, R.J., Maini, P.K., Gavaghan, D.J.: Metabolic changes during carcinogenesis: potential impact on invasiveness. J. Theor. Biol. **244**, 703–713 (2007)

Smallbone, K., Gatenby, R.A., Maini, P.K.: Mathematical modelling of tumour acidity. J. Theor. Biol. **255**, 106–112 (2008)

Swanson, K.R.: Quantifying glioma cell growth and invasion in vitro. Math. Comput. Model. **47**, 638–648 (2008)

Swanson, K.R., Alvord Jr., E.C., Murray, J.D.: A quantitative model for differential motility of gliomas in grey and white matter. Cell Prolif. **33**, 317–329 (2000)

Swanson, K.R., Bridge, C., Murray, J.D., Alvord Jr., E.C.: Virtual and real brain tumors: using mathematical modeling to quantify glioma growth and invasion. J. Neurol. Sci. **216**, 1–10 (2003)

Talmadge, J.E., Fidler, I.J.: Aacr centennial series: the biology of cancer metastasis: historical perspective. Cancer Res. **70**, 5649–5669 (2010)

Tracqui, P., Cruywagen, G.C., Woodward, D.E., Bartoo, G.T., Murray, J.D., Alvord Jr., E.C.: A mathematical model of glioma growth: the effect of chemotherapy on spatio-temporal growth. Cell Prolif. **28**, 17–31 (1995)

Trucu, D., Lin, P., Chaplain, M.A.J., Wang, Y.: A multiscale moving boundary model arising in cancer invasion. Multisc. Model. Simul. **11**(1), 309–335 (2013)

Turner, S., Sherratt, J.A.: Intercellular adhesion and cancer invasion: a discrete simulation using the extended Potts model. J. Theor. Biol. **216**(1), 85–100 (2002)

Valster, A., Tran, N.L., Nakada, M., Berens, M.E., Chan, A.Y., Symons, M.: Cell migration and invasion assays. Methods **37**, 208–215 (2005)

Woodward, D.E., Cook, J., Tracqui, P., Cruywagen, G.C., Murray, J.D., Alvord Jr., E.C.: A mathematical model of glioma growth: the effect of extent of surgical resection. Cell Prolif. **29**, 269–288 (1996)

The First Step Towards the Mathematical Understanding of the Role of Matrix Metalloproteinase-8 in Cancer Invasion

Anna Wilson, Thomas Williams, and Nikolaos Sfakianakis[✉]

School of Mathematics and Statistics, Mathematical Institute,
University of St Andrews, St Andrews, KY16 9SS, UK
{aw291,tjw8,n.sfakianakis}@st-andrews.ac.uk

Abstract. The role of matrix metalloproteinases-8 (MMP-8) in the cancer progression is quite complex, with contradictory indications as to whether it suppresses or assists the local growth of cancer. In addition, while other types of MMPs appear in either soluble or (cancer cell) membrane-bound form MMP-8 seems to appear in both. We take the first step in unravelling this dual nature of MMP-8 by shedding some mathematical light into its properties. To this end, we develop a mathematical model to investigate the impact of both soluble and membrane-bound MMPs in the early stages of local invasion of cancer cells. We propose an extension to a previously developed three-dimensional, hybrid atomistic-collective, cancer invasion model that allows the description of individual cancer cells along side with macroscopic tissue representations, and for the natural transition between these phases. We further assume that the soluble MMPs are produced by *polymorphonuclear neutrophils*, that pre-exist in the environment, and that they get activated by the cancer cells. The membrane-bound MMPs are expressed on the membrane of the cancer cells and along with the soluble MMPs, participate in the degradation of the *extracellular matrix* and, in effect, directly influence the migration of the cancer cells in what is understood to be a self-generated haptotaxis invasion strategy. With a series of numerical experiments and simulations we investigate the potential of the model in producing various invasion patterns, some resembling, qualitatively, to experimental invasion assays.

Keywords: Cancer invasion · Metalloproteinases · Polymorphonuclear neutrophils · Mathematical models · Partial differential equations · Stochastic differential equations · Genuinely hybrid models

1 Introduction

Cancer cells are different from normal cells, in that, among others, they develop capabilities that allow them to escape the body of tumour and migrate in the healthy tissue. This process, i.e. the local tissue invasion has been identified

as one of the *hallmarks of cancer*, (Hanahan and Weinberg 2000, 2011). It is understood that the invasion of the local tissue is a key process in more than 90% of cancer related deaths, (Sporn 1996).

Cancer types may be grouped in a number of ways, one of which is with respect to the organ from which they originate. Using such categorisation, the most prevalent types of cancer are *carcinomas*. As the malignancy of a carcinoma increases, a set of typical progressions are commonly seen. We refer here to but a few, a loss of cell-to-cell adhesion is caused by lower levels of *cadherin*, and various additional proteins, which affect the cell-to-matrix adhesion (Hanahan and Weinberg 2011). This matrix is understood to be the *extracellular matrix* (ECM), a collection of macromolecules which provide structure and integrity to the tissues and organs. The ECM can be "invaded" by cancer cells in a proteolytic or non-proteolytic fashion. Protease-dependent invasion utilises *matrix metalloproteinases* (MMPs) as well as a *cathespins* and *serine* proteases, to degrade the ECM, and to create a preferential environment for the progression of cancer (Wolf and Friedl 2011).

MMPs are the key enzyme in the degradation of the ECM, (Itoh and Nagase 2002). There have currently been identified 23 different types of MMPs and which are usually categorised into *collagenases, gelatinases, stromelysins, matrilysins*, membrane-type (MT-MMPs), and others depending on their structural domains, (Wang and Khali 2018). Although traditionally MMPs were thought to aid the progression, and in particular the invasion, of cancer there are certain cases where it has been shown that MMP-8 and MMP-11 are oncosuppressive, (Noël et al. 2012). More specifically, in humans MMP-8 is oncosuppressive in the breast and skin tissues, (Gutierrez-Fernanez et al. 2008), however they are a sign of poor prognosis in ovarian, and gastric cancers, (Juurikka et al. 2019; Van Lint and Libert 2006).

MMP-8 is a collagenase, originally thought to be produced only by *polymorphonuclear neutrophils* (PMNs). However, although PMNs are the most common source of MMP-8, it is known that they are produced by fibrolast and plasma and oral epithelial cells, (Van Lint and Libert 2006). MMP-8 is thought to have a role in managing inflammation through tissue remodelling and wound healing, Owen et al. (2004b).

Often MMPs are divided in to membrane bound and soluble (or diffusable), however MMP-8 and MMP-9 can be produced in both forms. All MMP-8 expressing cells have the ability to produce the pro-proteinase which allows the soluble form to be developed, and PMNs or mature white blood cells, can produce a membrane bound form on their surface, as well as the soluble type (Craig et al. 2014). The form of MMP-8 that is produced depends on the presence of a degranulating agonist which activates the pro-MMP-8 and triggers the movement from the granules it was stored in, to the plasma membrane. Both forms of MMP-8 are similar, but with a key difference in how they interact with *tissue inhibitors of metalloproteinases* (TIMPs). TIMP-1 is able to inhibit soluble MMP-8 however membrane bound MMP-8 has a greater resistance to it (Wang et al. 2019).

MMP-8 is predominantly produced by neutrophils (Sirniö et al. 2018). More generally, *leukocytes* are a type of blood cell, of which PMN-leukocytes or *neutrophils* (also referred to as white blood cells), are the most common type (Di Carlo et al. 2001). Neutrophils are produced in the bone marrow and the extramedullary tissues, by *common myeloid progentors* (CMP) (Hidalgo et al. 2019). The neutrophil life cycle has multiple stages, but of interest to us are mature neutrophils which are capable of producing MMP-8. There are large discrepancies in the estimates for the half life of neutrophils with estimates varying between 6 h and 5 days. The number of neutrophils produced per kg is of the order of $1 - 2 \times 10^9$, or $3 - 6 \times 10^9$ per litre of blood Borregaard (2016). The density of neutrophils is $\geq$1.080 g/ml (Zipursky et al. 1976).

The Metalloproteinases and the Progression of Cancer

The MMPs are fundamental in key alterations that take place in the tumour microenvironment during the progression of cancer. These alterations involve, among others, the degradation of the adjacent tissue and the components of the basal membrane, the secretion of growth factors and the activation of surface receptors, and more. These interactions with the ECM have an impact on the cancer cells' response to the local tissue, in particular the cancer cells become less adherent and hence more migratory.

To be more specific, the roles the MMPs can play, during the progression of the cancer, depend on the stage of tumour progression. In early stages, the proteolysis of MMP-3 and MMP-7 contributes to cellular proliferation, but later, the cleavage of *E-cadherin* activates the motility of the cancer cells facilitating metastasis (Chabottaux and Noel 2007). In contrast, MMP-8 has a protective effect as it diminishes the metastatic potential of breast cancer cells (Decock et al. 2008), but in the case of the overexpression of MMP-2 and -9, which indicates an unfavourable prognosis as it degrades type 4 collagen, located in the basal membranes, and induces the expression of angiogenic factors (Gonzalez et al. 2008).

The local invasion of the tumours depends on the degradation of the proteins of the basal membranes, such as type 4 or 5 collagen, and the proteolysis of type 1, 2, or 3 interstitial collagen present in the connective tissue that surrounds the tumour cells (Rucci et al. 2011). In addition, the MMPs intervene in angiogenesis, promoting the migration of the endothelial cells, liberating *vascular endothelial growth factor* (VEGF) and other proangiogenic factors of the ECM, such as fibroblast growth factors (FGF)-2 and *transforming growth factor* (TGF-β), which also favour the proliferation and migration of these cells (Hua et al. 2011). The transcription of the MMPs is induced by inflammatory cytokines, such as *interleukin* IL-1, IL-6, *tumor necrosis factor* (TNF-α), and growth factors such as *epidermal growth factor* (EGF), *hepatyocyte growth factor* (HGF), and TGF-β, giving them a preponderant role in the chronic inflammation which is present in the tumour microenvironment. Other factors, such as TGF-α and IL-4 inhibit their expression, and can be considered as therapeutic targets for cancer, (Kessenbrock et al. 2010).

It is hence understood that the role of MMP-8 in the progression of cancer is quite complex. So, our aim in this paper is to shed some mathematical light into these complex dynamics by formulating and discussing a first mathematical model that considers both soluble and membrane-bound MMPs, (Wang et al. 2019; Owen et al. 2004a).

2   Model Description

The model we formulate a three-dimensional, hybrid atomistic-continuum model that accounts for the MMP-assisted degradation of the ECM and invasion strategy of the cancer cells. The present model is based upon the previous works by Sfakianakis et al. (2020), Franssen et al. (2021) where a two- and three-dimensional hybrid atomistic-continuum invasion strategy of the ECM was developed. in the atomistic/individual-cell scale the dynamics were dictated by a system of *stochastic differential equations* (SDE)s, whereas the collective/macroscopic scale dynamics are governed by one or more *partial differential equations* (PDEs).

The novelty of the current model is to contribute to these previous works by primarily accounting for the compound degradation of the ECM by both types of MMPs, soluble and membrane-bound. A further addition to the model is the inclusion PMNs—throughout the tissue—as the source of soluble MMPs. This adds to the level of detail and biological realism.

The hybrid nature of the our model incorporates simultaneously multiple biological scales, i.e. the continuum macroscopic scale, where a density description is more appropriate, and the microscopic scale of discrete cells, where an individual description and a stochastic approach is better fitted. For the number of cancer cells which we consider in the present paper, which is in the order of 10^2 cells, a density description is not appropriate. We assume hence that these cells can be described by a SDE, and furthermore, as was previously done by Sfakianakis et al. (2020), Franssen et al. (2021), the cancer cells are able to interact with the density components of the model—namely, the ECM, the soluble and membrane-bound MMPs and the PMNs—through a phase transition process which is described in some detail in Appendix 5.1.

In effect, the cancer invasion model we formulate is comprised of two parts: a density- and an individual-based submodel.

Density-Based Submodel

We consider $\Omega \subset \mathbb{R}^3$ to be a Lipschitz domain and denote by $c(\mathbf{x}, t)$, $m_b(\mathbf{x}, t)$, $m_s(\mathbf{x}, t)$, $n(\mathbf{x}, t)$, and $w(\mathbf{x}, t)$, with $\mathbf{x} \in \Omega$ and $t \geq 0$, the corresponding densities of the cancer cells (whenever the density description of the cancer cells is appropriate), the membrane bound and soluble MMPs, the PMNs, and the ECM, respectively.

- The cancer cells are primarily described through their individual-cell formulation. Still, their corresponding density formulation, denoted by c participates in the evolution of other model components. We deduce their density description from their individual-cell formulation—using the *individual-cell-to-density* transition that is discussed in Appendix 5.1—which reads

$$c(\mathbf{x}, t) = \sum_{p \in \mathcal{P}(t)} \frac{m_p(t)}{K} \mathcal{X}_{K_p(t)}(\mathbf{x}). \tag{1a}$$

  Here $m_p(t)$ is the mass of the cancer cell $p \in \mathcal{P}(t) = \{1, \ldots, N(t)\}$, $K_p(t) \subset \Omega$ is the physical space it occupies at time t, and $K = |K_p(t)|$ the (assumed uniform with respect to p) size/volume of the cancer cells. Further details of this transition are provided in Appendix 5.1.
- The membrane bound MMPs are expressed solely on the membrane of the cancer cells. We assume, for the sake of simplicity, that the same number of MMPs is expressed on every cell at any given time. We denote their density by m_b and account for them through the relation

$$m_b(\mathbf{x}, t) = \sum_{p \in \mathcal{P}(t)} a\, \mathcal{X}_{K_p(t)}(\mathbf{x}) \tag{1b}$$

  where $K_p(t) \subset \Omega$ the physical space that the cell $p \in \mathcal{P}(t) = \{1, \ldots, N(t)\}$ occupies; $\mathcal{X}_{K_p(t)}$ the corresponding characteristic function; and a represents the "number" of MMPs on the surface of every cell.
- We assume that the PMNs pre-exist in the tissue, and that, for the sake of simplicity, they evolve in a time-scale much slower than the experiment under consideration. This allows to consider them being in a quasi-steady state; hence we model their evolution by

$$\frac{\partial}{\partial t} n(\mathbf{x}, t) = 0 \tag{1c}$$

- We assume that the soluble MMPs are produced by the PMNs, disperse freely in the tissue, and undergo molecular decay. We model their time evolution through

$$\frac{\partial}{\partial t} m_s(\mathbf{x}, t) = D_s \Delta m_s(\mathbf{x}, t) + r_s n(\mathbf{x}, t) - d_s m_s(\mathbf{x}, t) \tag{1d}$$

  where $r_s > 0$, $d_s > 0$, are the constant production and decay rates respectively, and $D_s > 0$ their (linear) diffusivity.
- We also assume that the extracellular tissue is well established, healthy, and stable, hence, its constituents can be considered to be an immovable component of the system that neither diffuses nor otherwise translocates; it is moreover assumed not to be reconstructed in any way. It is only expected

to be degraded by both the soluble and the membrane-bound MMPs. These
assumptions are encoded in the equation:

$$
\frac{\partial}{\partial t} w(\mathbf{x}, t) = - \left(\lambda_s \underbrace{m_s(\mathbf{x}, t) \sum_{p \in \mathcal{P}(t)} \mathcal{X}_{K_p(t)}(\mathbf{x})}_{\text{soluble MMPs/cancer cells complex}} + \lambda_b \underbrace{m_b(\mathbf{x}, t)}_{\text{membrane bound MMPs}} \right) w(\mathbf{x}, t)
$$

$$
= - \left(\lambda_s m_s(\mathbf{x}, t) \sum_{p \in \mathcal{P}(t)} \mathcal{X}_{K_p(t)}(\mathbf{x}) + \lambda_b a \sum_{p \in \mathcal{P}(t)} \mathcal{X}_{K_p(t)}(\mathbf{x}) \right) w(\mathbf{x}, t)
$$

$$
= - (\lambda_s m_s(\mathbf{x}, t) + \lambda_d) \sum_{p \in \mathcal{P}(t)} \mathcal{X}_{K_p(t)}(\mathbf{x}) w(\mathbf{x}, t) \tag{1e}
$$

where λ_s, $\lambda_b > 0$ and $\lambda_d = \lambda_b a$ is the effective degradation rate of the ECM
by the membrane bound MMPs.

The density sub-model is augmented with initial conditions, the construction of
which is discussed in Sect. 3 and in Appendix 6.

Individual-Cell-Based Submodel

The cancer cells are modelled as a collection of individual cells that migrate
through the tissue by performing a biased random motion. The biased part of
their motion is due to their haptotactic response of the cells' migratory mecha-
nism to gradients of ECM-bound chemoattractants and cellular adhesion sites,
while the random part of the motion is understood as a manifestation of the
cells' tendency to investigate its surrounding; the latter is modelled as a Brow-
nian motion. We don't consider here any direct interaction between the cancer
cells or between the cancer cells and the surrounding tissue.

We model these properties following the previous works (Sfakianakis et al.
2020; Franssen et al. 2021), where we also refer for more detail. At any given
time $t \geq 0$, we consider a system of $N(t) \in \mathbb{N}$ cancer cells, for which we account
their positions and masses i.e.

$$
\{ (\mathbf{x}_p(t), m_p(t)) \in \Omega \times [0, \infty) \}, \quad p \in P = \{1, \ldots, N(t)\}. \tag{2}
$$

Their migration is modelled by a system of SDEs and accounts for the biased
and the random part of the motion of the cancer cells, namely a directed motion
component that represents the haptotactic response of the cells to gradients of
ECM-bound adhesion sites, and a random motion that is modelled as a Brownian
motion. Namely,

$$
d\mathbf{X}_t^p = \mu(\mathbf{X}_t^p, t)dt + \sigma(\mathbf{X}_t^p, t)d\mathbf{W}_t^p, \quad \text{for } p \in P, \tag{3}
$$

where $\mathbf{X}_t^p$ represents the position of the individual-cell in the tissue $\Omega \subset \mathbb{R}^3$, and $\mathbf{W}_t^p$ is a Wiener process. The *drift* term μ encodes the directed (or biased) part of the motion, whereas the *diffusion* term σ encodes its random component. We refer to (Sfakianakis et al. 2020, Franssen et al. 2021) for a thorough discussion on the formulation of the μ and σ.

The individual cancer cells serve as carriers of the membrane bound MMPs (1b) and participate in the degradation of the ECM through the activation of the soluble MMPs (1e). Yet, the their migration equation (3) does not include any of these interactions. Instead, these are accounted for in the following way: at any given time t the cancer cells are transformed to a density profile via the *individual-cell-to-density* operator and participate in the dynamics of the system (1b)–(1e). The converse is also possible, this density profile of the cancer cells c is transformed into individual cells via the *individual-cell-to-density* operator. We refer to Appendix 5.3 and to (Sfakianakis et al. 2020; Franssen et al. 2021) for a thorough discussion of the coupling of the two biological phases.

3   Parametrisation, Simulations, and Results

For the numerical treatment of the coupled system of deterministic PDEs (1a)–(1e) and SDEs (3) we employ an elaborate numerical solver that has been previously described in Sfakianakis et al. (2020), Franssen et al. (2021) and in Kolbe et al. (2016), Sfakianakis et al. (2017). We refer to these papers and the references therein for more detail. Moreover, we note that all numerical simulations and visualisations were conducted using MATLAB (2019).

For all experiments, we consider the domain

$$\Omega = [-0.05, 0.05]^3 \subset \mathbb{R}^3$$

in cm and perform the numerical simulations for the time period $t \in [0, 6]$ days.

In this series of experiments we consider $N = 400$ individual cancer cells, of the same mass m_p, for $p = 1, \ldots, N$, initially placed (with some random perturbations) close to the centre of the domain, Ω, cf. Fig. 1. As no cell-mitosis, or other cell-number or cell-mass altering processes are assumed, we expect that their number and mass will not change with time, i.e. for all $t \geq 0$, $N(t) = N$ and $m_p(t) = m_p$, $p = 1, \ldots, N$, see also (2) and the parameter Table 1.

On the membrane of the cancer cells we consider an amount a of membrane-bound MMPs, this is assumed to be the same for all N cancer cells and not to change with time, see also (1b). This is directly involved in the degradation of the ECM, cf. (1e) and the parameter Table 1.

Table 1. Basis parameter set, used in all experiments unless otherwise indicated.

	Description	Value	Range	Reference
s	Maximum cancer cell speed	$2.16 \, \mathrm{cm\,d^{-1}}$	1.83×10^{-5}–$3.83 \times 10^{-5} \, \mathrm{cm\,s^{-1}}$	Butler et al. (2010)
m_{ref}	Cancer cell reference mass	$2.3 \times 10^{-9} \, \mathrm{g\,cell^{-1}}$	2.3×10^{-9}–$3.3 \times 10^{-9} \, \mathrm{g\,cell^{-1}}$	Park et al. (2008)
$|V_0|$	Cancer reference volume	$2.3 \times 10^{-9} \, \mathrm{cm^3}$	2.2×10^{-9}–$5.2 \times 10^{-9} \, \mathrm{cm^3}$	Puck et al. (1956)
w_{max}	Maximum (initial) ECM density	$1.06 \, \mathrm{g\,cm^{-3}}$	1.02–$1.05 \, \mathrm{g\,cm^{-3}}$	ICRP (2009)
n_{max}	Maximum (initial) PMN density	$1.08 \, \mathrm{g\,cm^{-3}}$	0.9–$1.10 \, \mathrm{g\,cm^{-3}}$	ICRP (2009)
σ	Cancer cell diffusion coefficient	$0.1 \, \mathrm{cm\,d^{-1/2}}$		Our choice
μ	Cancer cell drift coefficient	$0.1 \, \mathrm{cm^2\,d^{-1}}$		Our choice
λ_s	Soluble MMP ECM degradation rate	$1 \times 10^{-2} \, \mathrm{M\,cm^{-3}\,d^{-1}}$		Our choice
λ_d	Membrane-bound MMP ECM degradation rate	$1 \times 10^{-2} \, \mathrm{M\,cm^{-3}\,d^{-1}}$		Our choice
a_s	Initial soluble MMP ratio	9×10^{-2}		Our choice
D_s	Soluble-MMP diff	$1 \times 10^{-4} \, \mathrm{cm\,d^{-1/2}}$		Our choice
r_s	Soluble-MMP prod	$5 \, \mathrm{M\,d^{-1}}$		Our choice
d_s	Soluble-MMP decay	$4.5 \times 10^{-1} \, \mathrm{M\,d^{-1}}$		Our choice

The ECM, denoted by w in (1e), is represented by a three-dimensional landscape that is initially randomly structured with values, in compliance to ICRP (2009), within a biologically relevant range, cf. Table 1. We assume that the ECM predates the experiments of cancer invasion considered here. Although randomly constructed, we use the same ECM in all our numerical investigations, unless otherwise stated, as we want to produce results that are directly comparable.

Similarly, the PMNs, denoted by n in (1c), are represented by a three-dimensional concentration that is also initially randomly distributed, in compliance with Zipursky et al. (1976), within a biologically relevant range, cf. Table 1. As with the ECM, we also consider that the PMNs predate the invasion experiments considered here. The PMN concentration is randomly produced, still, for the sake of comparison between the numerical experiments, we employ the same PMN in all our investigations.

The construction of the initial PMN and ECM concentrations is quite elaborate and we refer to Appendix 6 and the previous works (Sfakianakis et al. 2020; Franssen et al. 2021) for a detailed discussion.

The soluble-MMPs, denoted by m_s in (1d) and (1e), are understood to be a product of the PMNs, independently of the action of the cancer cells. Since the PMNs predate the invasion experiments considered here, so do the soluble-MMPs. For the sake of simplicity, we assume that their initial concentration is

given as a fraction of the initial PMN concentration, i.e.

$$m_s(\mathbf{x}, 0) = a_s n(\mathbf{x}, 0), \quad \mathbf{x} \in \Omega \tag{4}$$
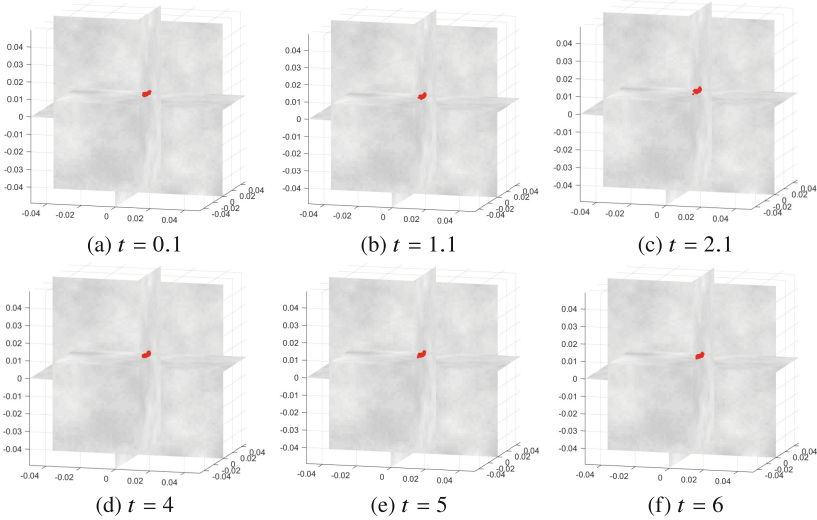
where $a_s > 0$ is a constant, cf. Table 1.

(a) $t = 0.1$ (b) $t = 1.1$ (c) $t = 2.1$

(d) $t = 4$ (e) $t = 5$ (f) $t = 6$

Fig. 1. Experiment 1—No ECM degradation: Showing here is the time evolution of the $N = 400$ cancer cells within the domain Ω along with the ECM (grey background) plotted at the three main planes $x = 0$, $y = 0$, $z = 0$. Due to the lack of matrix degradation, the cancer cells do not migrate away from their initial placement, they rather converge to a location of local maximum of ECM density around which they then perform small oscillations. It is clear that in with this parameter set, haptotaxis dominates over the random migration.

Throughout this work, we do not allow the individual cancer cells to leave the domain Ω. Instead, every time a cancer cell escapes, it is returned to its last known position within Ω and is allowed to resume its biased random motion according to (3). Accordingly, we do not impose any boundary conditions on the membrane-bound MMPs as the "inherit" those from the individual cancer cells. Also, no boundary conditions are needed for the PMNs and the ECM as they are assumed to be immovable components of the system. Finally, we consider zero Neumann boundary conditions for the soluble-MMPs.

The parameters we employ are extracted from the relevant biomedical literature, although the aim of this paper is not to reproduce realistic biological scenarios. These are summarised in Table 1 together with the corresponding literature sources.

Experiment 1— No ECM Degradation

This first experiment experiment serves primarily as a benchmark for the ones that follow. We completely knockout the ability of the cancer cells to degrade the ECM, neither from membrane-bound nor from soluble MMPs. This is achieved by setting the ECM degradation parameters $\lambda_s = \lambda_d = 0$ in parameter set Table 1. As a result, see Fig. 1, the cancer cells do not migrate and rather converge to a position of local maximum of the ECM around which they then perform oscillatory motions of small magnitude. With this experiment it becomes clear that, in this parameter set the haptotaxis dominates over the random cell migration.

(a) $t = 0.1$ (b) $t = 1.1$ (c) $t = 2.1$

(d) $t = 4$ (e) $t = 5$ (f) $t = 6$
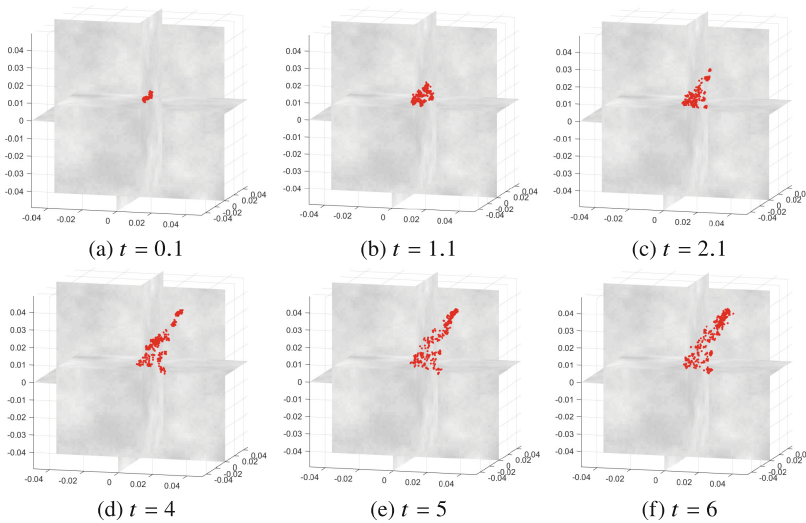
Fig. 2. Experiment 2—Membrane-bound MMP only ECM degradation: As in Fig. 1, showing here is the time evolution of the $N = 400$ cancer cells within the domain Ω along with the ECM (grey background). This time though, the membrane-bound MMP mediated ECM degradation is responsible for the self-sustained migration of the cancer cells that we witness. We can also see a collective invasion behaviour unfolding despite the fact that there is no cell-cell adhesion or other form of "communication" between the cancer cells.

Experiment 2— Membrane-Bound MMP only ECM Degradation

In this experiment we knockout the ability of cancer cells to activate the soluble-MMPs, and, as a result, the ECM is degraded exclusively by the membrane-bound MMPs. This is achieved by setting the soluble-MMP ECM degradation parameter $\lambda_s = 0$ in parameter Table 1. As a result, and when comparing with the previous Experiment 1, the cancer cells migrate further as they degrade the ECM at their current location and, subsequently, respond in haptotaxis way to

the newly formed ECM gradients. This style of cell migration is often charac-
terised/termed as *self-generated haptotaxis strategy*, see Fig. 2, a phenomenon
that is expected in the cancer invasion of the tissue. It is furthermore so that the
migration of the cancer cells follow a direction that is dictated by the "original"
gradients of the ECM (cf. Experiment 5), and by some few "leading" cells.

(a) $t = 0.1$ (b) $t = 1.1$ (c) $t = 2.1$

(d) $t = 4$ (e) $t = 5$ (f) $t = 6$
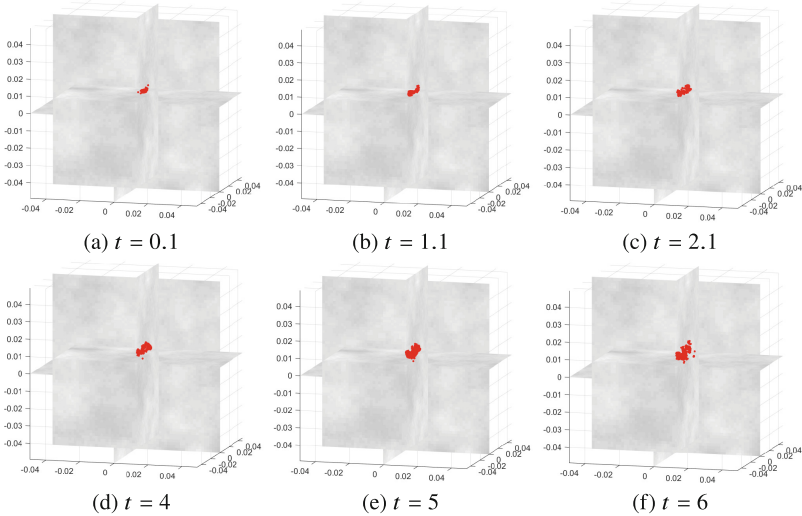
Fig. 3. Experiment 3—Soluble MMP only ECM degradation: Comparing these sim-
ulation results with the membrane-bound MMP only ECM degradation in Fig. 2 it
becomes apparent the current migration strategy is less efficient; still it is not negligi-
ble, as can be seen when compared with the no-degradation case in Fig. 1.

Experiment 3— Soluble MMP only ECM Degradation

In this experiment we knockout the ability of the cancer cells to degrade the
matrix using their membrane-bound MMPs; this comes in contrast to the Exper-
iment 2; and as a result the ECM is degraded exclusively by the action of the acti-
vated soluble MMP-mediated ECM. This is achieved by setting the membrane-
bound MMP ECM degradation parameter $\lambda_d = 0$ in parameter Table 1. As it
is expected that lower rather than higher concentrations of soluble MMPs are
present in the environment we accordingly set the initial MMP concentrations
to a moderate value, relative to the PMNs. This is achieved by setting the ini-
tial soluble MMP ratio $a_s = 0.09$. It becomes clear with this experiment, see
Fig. 3, that the cancer cells migrate further than they do in the case of no ECM
degradation, i.e. with Experiment 1 and Fig. 1, but still remain much closer to
their initial location than they do in the case of membrane-bound MMPs, cf.
Experiment 2 and Fig. 2.
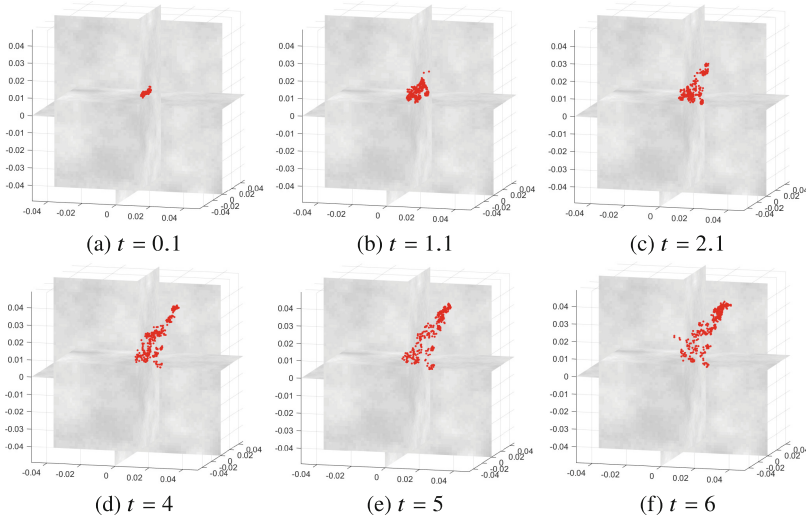
Fig. 4. Experiment 4—Both MMP Types ECM Degradation: When both types of MMPs participate in the degradation of the ECM, it becomes apparent that the effect of the membrane-bound MMP ECM degradation on the migration strategy of the cancer cells, dominates over contribution of the the soluble MMPs. The direction of the (again collective migration) is dictated by the original gradient of the ECM, and it is enhanced to a sustained invasion by both types of MMP. The soluble-MMPs have a slight, but still visible, impact in widening the spread of the cancer cell migration.

Experiment 4— Both MMP Types ECM Degradation I

In this experiment, we allow for ECM degradation by both types of MMPs with degradation parameters as reported in Table 1. The overall effect resembles more the membrane-bound only migration pattern as in Experiment 2 and Fig. 2 rather than the soluble only MMP migration of Experiment 3 and Fig. 3. It can be seen that the average direction of the cancer cell migration is similar to the membrane-bound case Fig. 2, since this is primarily influenced by the pre-existing gradients on the ECM—enhanced of course by the degrading action of the MMPs. A more careful investigation indicates that the leading cells play a relatively less prominent role in the invasion; this can be seen by the wider spread of the (still collective and directed) cancer cell migration through the tissue.

Experiment 5— Both MMP Types ECM Degradation II

This is a similar experiment to the previous one, i.e. Experiment 4, except for the fact that we employ a different (but still randomly produced in the same fashion) initial concentration of the ECM. As can be seen in Fig. 5, and compared with Fig. 4, the cancer cells perform again a collective migration indicating that this particular migration strategy is qualitatively robust and independent of the ECM.

(a) $t = 0.1$ (b) $t = 1.1$ (c) $t = 2.1$

(d) $t = 4$ (e) $t = 5$ (f) $t = 6$
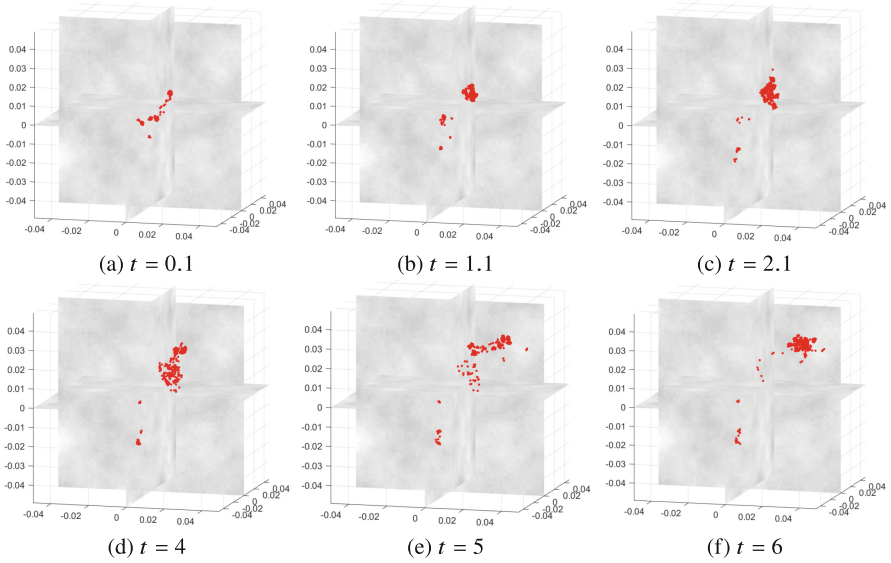
Fig. 5. Experiment 5—Both MMP types ECM degradation II: Although the ECM is different here than in Experiment 4, the are qualitatively similar, cf. Fig. 4. This is a strong indicates that the particular migration strategy, along with the chosen parameter values, is quite robust and independent of the ECM.

Experiment 6— Cluster Migration Pattern

In this last experiment we investigate the effect that the magnitude of the adhesion and diffusion coefficients. This experiment is understood to be the first step in a new direction of study, where realistic parameter values are estimated based on experimental data. Still, we include it in the current paper as it provides a useful insight on the wealth of invasion patterns that our modelling approach can produce. In more detail, we decrease the values of the two cancer cell migration parameters σ and μ to half their previous value reported in Table 1, namely we set $\sigma = 5 \times 10^{-2}$ and $\mu = 5 \times 10^{-2}$. We notice that this reduction of the "aggressiveness" in the migration of the cancer cells leads to a larger spread of the cancer cells. Still they form small clusters, of few cancer cells each, that move in a coherent way; these clusters "flock" together in what seems to be a uniform direction. This is a very interesting invasion pattern that resembles, qualitatively, to observation made in *in vitro* invasion assays, see e.g. (Nurmenniemi et al. 2009).

4   Discussion

It was understood in the past that MMPs assist in cancer invasion, still, it has been shown recently that in certain animals, humans among those, MMP-8 is
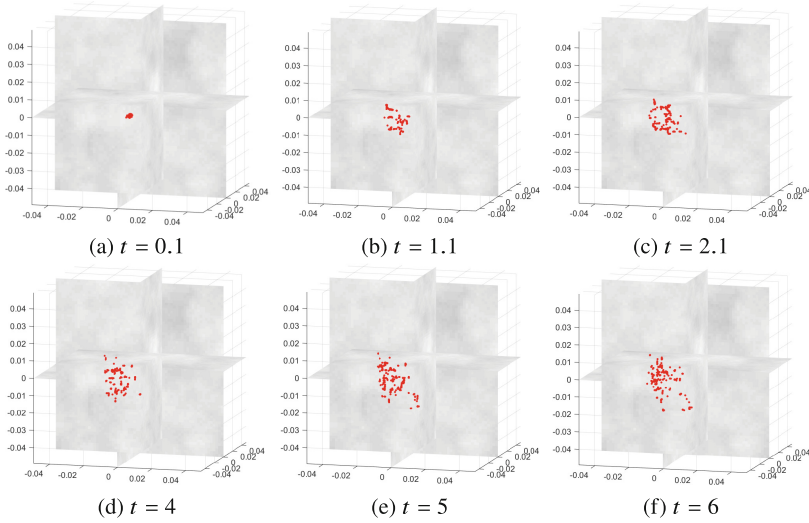
Fig. 6. Experiment 6—Cluster migration pattern: Reducing the cancer cell migration parameters μ and σ to half the values used in the Experiments 4 and 5, we notice a widening of the spread of the cancer cells, the formation of small clusters, of a few cancer cells each, and a "flocking" of those clusters. This last remark will certainly spawn a new study, as it resembles with experimental observations in invasion assays.

oncosuppressive in breast and skin tissues, whereas it is a sign of poor prognosis in ovarian, and gastric cancers, (Gutierrez-Fernanez et al. 2008; Juurikka et al. 2019; Van Lint and Libert 2006). Most, out of the 23 known types of MMPs, can be classified either as membrane-bound or soluble, however MMP-8 can be produced in both forms. MMP-8 expressing cells have the ability to produce the pro-proteinase which allows the soluble form to be developed. PMNs in particular—that are the most common source of MMP-8—can produce a membrane-bound form on their surface, as well as the soluble type, (Van Lint and Libert 2006; Craig et al. 2014).

Our objective in the current paper was to take the first step to mathematically unravel this complex role of MMP-8 in cancer. With this in mind we have investigated aspects of the dynamical behaviour of soluble and membrane-bound MMPs in the degradation of the ECM.

We have based our model derivation on previous works, (Sfakianakis et al. 2020; Franssen et al. 2021), These PDEs account for the evolution of the ECM, the PMNs and the soluble MMPs, but they are coupled to the individual cell scale via specialised phase transition operators, cf. Appendix 5.1. The transition between the two phases, the individual-cell and collective-continuum phases takes place in real time and is dynamically exploited.

The novelty that the current model adds to the previous works, (Sfakianakis et al. 2020, Franssen et al. 2021), lies primarily with the compound degradation of the ECM by both types of MMPs, soluble and membrane-bound. This is

encoded in (1e) where we do the modelling approximations of a) the *in-situ* activation, by the cancer cells, of the soluble MMPs, and b) the tautochronous degradation of the ECM by both the activated-soluble and the membrane-bound MMPs.

With our numerical simulations, we were able to exhibit the potential of this particular modelling approach and the effect that the two ECM degradation types have in the migration of the cancer cells and the invasion of the healthy tissue. In some more detail, although it is not our objective in this paper to do a specialised parameter estimation, we were still able identify—and comparatively evaluate—the difference between membrane-bound and soluble MMP degradation, cf. Figs. 2 and 3. Even more, combining both ECM degradation types MMPs we were able to verify a consistent invasion strategy of the cancer cells, in the form of a large collective migration, independent of the initial distribution of the ECM, cf. Figs. 4 and 5. We should note again, at this point that no cell-cell adhesion is assumed throughout this work, so this collective behaviour on behalf of the cancer cells is understood to be an emerging property of their synchronous action on the ECM. Furthermore, by reducing the migratory "aggressiveness" of the cancer cells we were able to lead the system to the formation of numerous small and robust clusters of cancer cells, each one migrating through the tissue as a coherent unit, cf. Fig. 6. This last experiment is of particular interest as it reproduces, qualitatively, a known tissue invasion pattern which is not easily "captured" through mathematical approach.

In closing, we note that this first step in the modelling of the complex ECM degradation by membrane-bound and soluble MMPs, has clearly indicated the potential of this particular modelling approach in the mathematical modelling of the MMP-8 dynamics. It will serve as a building block for follow-up works as they account for more biochemically realistic scenarios, and, possibly, with the inclusion of experimental and other measurement data.

Appendix

5   Phase Transition Operators

5.1   Individual-Cell-to-Density Transition Operator

Let $\left\{(\mathbf{x}_p^{\text{M}}, m_p^{\text{M}}), \ p \in P\right\}$ be a collection of individual cells. Using (13) and (14), we define the *individual-cell-to-density* operator $\mathcal{F}$ as

$$\left\{(\mathbf{x}_p^{\text{M}}, m_p^{\text{M}}), \ p \in P\right\} \xrightarrow{\mathcal{F}} c(\mathbf{x}, t). \tag{5}$$

To define the function $c(\mathbf{x}, t)$, we go through all the cancer cells and consider their corresponding density formulation according to (12). The support K_p of every cell overlaps with several of the partition cells M_i, $i \in I$. We assign the corresponding portion of the cell's mass to every partition cell M_i:

$$m_p^{\text{M}}\big|_{M_i} = \frac{m_p^{\text{M}}}{K} \big|K_p \cap M_i\big|. \tag{6}$$

In a similar fashion, we account for the contribution of all cells $p \in P$ to a partition cell M_i:

$$c_i(t) = \sum_{p \in P} \frac{1}{K} m_p^{\text{M}}\big|_{M_i} \overset{(6)}{=} \sum_{p \in P} \frac{m_p^{\text{M}}(t)}{K^2} |K_p \cap M_i|, \quad \text{for } i \in I. \tag{7}$$

In view of equations (12) and (7), we deduce the density function $c(\mathbf{x}, t)$ over the full domain Ω to be

$$c(\mathbf{x}, t) = \sum_{i \in I} c_i(t) \mathcal{X}_{M_i}(\mathbf{x}), \quad \mathbf{x} \in \Omega. \tag{8}$$

5.2   Density-to-Individual-Cell Transition Operator

Given a density function $c = c(\mathbf{x}, t)$, we define the *density-to-individual-cell* operator $\mathcal{B}$ for a general individual cell as

$$c(\mathbf{x}, t) \overset{\mathcal{B}}{\longrightarrow} \{(\mathbf{x}_p(t), m_p(t)), \ p \in P\}. \tag{9}$$

We assign one cell with mass

$$m_i(t) = \int_{M_i} c(\mathbf{x}, t) d\mathbf{x} \tag{10}$$

and position

$$\mathbf{x}_i(t) = \text{ the (bary-)centre of } M_i \tag{11}$$

to every cube partition cell M_i, $i \in I$.

5.3   Hybrid Formulation of Cancer Cells

We assume that the domain Ω is sufficiently large and regular to be uniformly partitioned as $\Omega = \bigcup_{i \in I} M_i$, where every M_i, $i \in I$ is a translation of a generic cube $K_0 \subset \mathbb{R}^3$, representing the volume occupied by a single biological cell. This partition allows to represent every scalar (measurable) density function $c : \Omega \times (0, \infty) \to \mathbb{R}$ by its simple-function decomposition

$$\sum_{i \in I} c_i(t) \mathcal{X}_{M_i}(\mathbf{x}), \tag{12}$$

where $\mathcal{X}_{M_i}$ is the characteristic function of $M_i \subset \Omega$, and $c_i(t)$ the mean value of $c(\cdot, t)$ over M_i, i.e.

$$c_i(t) = \frac{1}{K} \int_{M_i} c(\mathbf{x}, t) d\mathbf{x}, \tag{13}$$

where K is the volume of K_0 and, effectively, of M_i.

Accordingly, the hybrid description upon which this work is based reads

$$(\mathbf{x}_p(t), m_p(t)) \longleftrightarrow \frac{m_p(t)}{K} \mathcal{X}_{K_p}(\mathbf{x}), \quad p \in P, \tag{14}$$

where $\mathbf{x}_p(t)$ and $m_p(t)$ represent the time-dependent position and mass of the individual cell; K_p is the translation of the generic cube K_0 with centre $\mathbf{x}_p$; and $K = |K_p| = |K_0|$ is the volume of these cubes. Based on (14), the transition between the two cell phases is conducted by the *individual-cell-to-density* and the *density-to-individual-cell* transition operators.

6 Construction of the Initially Randomly Structured ECM and PMN

We use the following technique to construct the three-dimensional randomly structured initial ECM and PMN densities that we use in our simulations. For the sake of simplicity we describe here the one-dimensional case, over the domain $[0, 1)$, and refer to Fig. 7 for a graphical representation of the same process in two-dimensional domains.

At first, a coarse approximation of the ECM or PMN is decided by setting the number of major "hills" and "valleys" in the density of the matrix. Should this number be 8 (to coincide with Fig. 7), the first approximation to the ECM or PMN is set

$$\sum_{i=1}^{8} c_i^{(8)} \mathcal{X}_{C_i^{(8)}}(x), \quad x \in [0, 1),$$

where $C_i^{(8)}$, with $|C_i^{(8)}| = \Delta x^{(8)}$ for $i = 1, ..., 8$, represent the 8 computational cells of the uniform discretization of $[0, 1)$, and where the coefficients $c_i^{(8)}$ are uniformly distributed random numbers within $[0, 1)$. When we globally refine (by bisection), the domain $[0, 1)$ is discretized by 16 equivalent computational cells $C_i^{(16)}$, $i = 1, ..., 16$. Accordingly, the ECM or PMN concentration is approximated by the simple/piecewise constant function

$$\sum_{i=1}^{16} c_i^{(16)} \mathcal{X}_{C_i^{(16)}}(x), \quad x \in [0, 1).$$

The new coefficients $c_i^{(16)}$ interpolate—with the addition of some random noise—between the previous values, i.e.

$$c_i^{(16)} = \left(1 + 0.002 \left(r_i^{(16)} - 0.5\right)\right) \frac{c_{\lfloor i/2 \rfloor}^{(8)} + c_{\lfloor i/2 \rfloor+1}^{(8)}}{2}, \quad i = 1 \ldots 16,$$

where $\lfloor \cdot \rfloor$ represents the Gauss floor function, and where $r_i^{(16)}$ are uniformly distributed random numbers within $[0, 1)$. The first and last coefficients, $c_1^{(16)}$ and $c_{16}^{(16)}$, are computed periodically with respect to the $c_{\cdot}^{(8)}$ values. The rescaling factor 0.002 is chosen so that the multiplicative randomness/noise is adjusted to 0.1% of the interpolated value. A similar refinement process is iterated until the desired resolution of the domain is reached. Then values of the ECM or PMN density are rescaled within their biological range of a minimum and maximum ECM or PMN density.

(a) 8×8 (b) 16×16 (c) 32×32

(d) 64×64 (e) 128×128 (f) 256×256
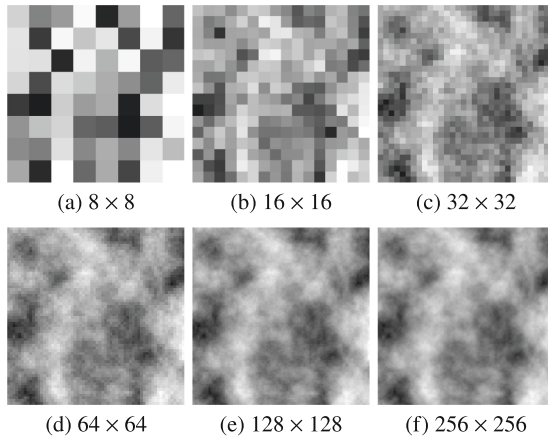
Fig. 7. Construction of the randomly-structured ECM or PMN with a sequence of grid refinements steps. The first stage of this process is the construction of a random 8×8 grid (top left panel) with values normally distributed in $[0, 1]$. This grid is progressively refined to the final (for this case) resolution of 256×256 (bottom right panel). At every refinement step the number of computational cells is doubled along each dimension and the new values are obtained by a) averaging the values of the neighboring cells of the coarser grid, and b) adding some random and normally distributed noise. Periodic interpolations are employed at the "boundary" the discretization domain. It can be clearly seen that the coarse structure of the ECM that was randomly chosen in the 8×8 matrix is still visible in the refined 256×256 grid.

References

Borregaard, N.: Neutrophils role in innate immunity. Encycl. Immunobiol. **1**, 281–288 (2016)

Butler, K.L., et al.: Burn injury reduces neutrophil directional migration speed in microfluidic devices. PloS One **5**(7), e11921 (2010)

Chabottaux, V., Noel, A.: Breast cancer progression: insights into multifaceted matrix metalloproteinases. Clin. Exp. Metastasis **24**, 647–656 (2007)

Craig, V.J., et al.: Mononuclear phagocytes and airway epithelial cells: novel sources of matrix metalloproteinase-8 (MMP-8) in patients with idiopathic pulmonary fibrosis. PloS One **9**(5) (2014). https://doi.org/10.1371/journal.pone.0097485

Decock, J., et al.: Plasma MMP1 and MMP8 expression in breast cancer: protective role of MMP8 against lymph node metastasis. BMC Cancer **8**, 8–77 (2008)

Di Carlo, E., Forni, G., Lollini, P., Colombo, M.P., Modesti, A., Musiani, P.: The intriguing role of polymorphonuclear neutrophils in antitumor reactions. Blood **97**(2), 339–345 (2001). https://doi.org/10.1182/blood.V97.2.339

Franssen, L.C., Sfakianakis, N., Chaplain, M.A.J.: A novel 3D atomistic-continuum cancer invasion model: in silico simulations of an in vitro organotypic invasion assay. J. Theor. Biol. **522**, 110677 (2021)

Gonzalez, L.O., et al.: Study of matrix metalloproteinases and their tissue inhibitors in ductal in situ carcinomas of the breast. Histopathology **4**, 403–415 (2008)

Gutierrez-Fernanez, A., et al.: Matrix metalloproteinase-8 functions as a metastasis suppressor through modulation of tumor cell adhesion and invasion. Cancer Res. **68**(8), 2755–2763 (2008). https://doi.org/10.1158/0008-5472.CAN-07-5154

Hanahan, D., Weinberg, R.A.: The hallmarks of cancer. Cell **100**(1), 57–70 (2000). https://doi.org/10.1016/s0092-8674(00)81683-9

Hanahan, D., Weinberg, R.A.: Hallmarks of cancer: the next generation. Cell **144**(5), 646–674 (2011). https://doi.org/10.1016/j.cell.2011.02.013

Hidalgo, A., Chilvers, E.R., Summers, C., Koenderman, L.: The neutrophil life cycle. Trends Immunol. **40**(7), 584–597 (2019). https://doi.org/10.1016/j.it.2019.04.013

Hua, H., Li, M., Luo, T., Yin, Y., Jiang, Y.: Matrix metalloproteinases in tumorigenesis: an evolving paradigm. Cell. Mol. Life Sci. **23**, 3853–3868 (2011)

ICRP. Adult reference computational phantoms. Ann. ICRP **110**(39(2)) (2009)

Itoh, Y., Nagase, H.: Matrix metalloproteinases in cancer. Essays Biochem. **38**(1), 21–36 (2002). https://doi.org/10.1042/bse0380021

Juurikka, K., Butler, G.S., Salo, T., Nyberg, P., Åström, P.: The role of MMP8 in cancer: a systematic review. Int. J. Mol. Sci. **20**(18) (2019). https://doi.org/10.3390/ijms20184506

Kessenbrock, K., Plaks, V., Werb, Z.: Matrix metalloproteinases: regulators of the tumor microenvironment. Cell **141**, 52–67 (2010)

Kolbe, N., Kat'uchová, J., Sfakianakis, N., Hellmann, N., Lukáčová-Medvid'ová, M.: A study on time discretization and adaptive mesh refinement methods for the simulation of cancer invasion: the urokinase model. Appl. Math. Comput. **273**, 353–376 (2016)

MATLAB. MATLAB version 9.7.0 (R2019b). The MathWorks Inc., Natick, Massachusetts (2019)

Noël, A., et al.: New and paradoxical roles of matrix metalloproteinases in the tumor microenvironment. Front. Pharmacol. **3**(1) (2012). https://doi.org/10.3389/fphar.2012.00140

Nurmenniemi, S., et al.: A novel organotypic model mimics the tumor microenvironment. Am. J. Pathol. **175**(3), 1281–1291 (2009)

Owen, C.A., Hu, Z., Lopez-Otin, C., Shapiro, S.D.: Membrane-bound matrix metalloproteinase-8 on activated polymorphonuclear cells is a potent, tissue inhibitor of metalloproteinase-resistant collagenase and serpinase. J. Immunol. **172**(12), 7791–7803 (2004a). https://doi.org/10.4049/jimmunol.172.12.7791

Owen, C.A., Hu, Z., Lopez-Otin, C., Shapiro, S.D.: Membrane-Bound Matrix Metalloproteinase-8 on Activated Polymorphonuclear Cells Is a Potent, Tissue Inhibitor of Metalloproteinase-Resistant Collagenase and Serpinase. J. Immunol. **172**(12), 7791–7803 (2004b). https://doi.org/10.4049/jimmunol.172.12.7791

Park, K., et al.: 'Living cantilever arrays' for characterization of mass of single live cells in fluids. Lab Chip **8**(7), 1034–1041 (2008)

Puck, T.T., Marcus, P.I., Cieciura, S.J.: Clonal growth of mammalian cells in vitro: Growth characteristics of colonies from single hela cells with and without a "feeder" layer. J. Exp. Med. **103**(2), 273–284 (1956)

Rucci, N., Sanita, P., Angelucci, A.: Roles of metalloproteases in metastatic niche. Curr. Mol. Med. **11**, 609–622 (2011)

Sfakianakis, N., Kolbe, N., Hellmann, N., Lukáčová-Medvid'ová, M.: A multiscale approach to the migration of cancer stem cells: mathematical modelling and simulations. Bull. Math. Biol. **79**(1), 209–235 (2017)

Sfakianakis, N., Madzvamuse, A., Chaplain, M.A.J.: A hybrid multiscale model for cancer invasion of the extracellular matrix. Multiscale Model. Simul. **18**(2), 824–850 (2020)

Sirniö, P., et al.: High-serum MMP-8 levels are associated with decreased survival and systemic inflammation in colorectal cancer. Br. J. Cancer **119**(1), 213–219 (2018). https://doi.org/10.1038/s41416-018-0136-4

Sporn, M.B.: The war on cancer. Lancet **347**(9012), 1377–1381 (1996). https://doi.org/10.1016/s0140-6736(96)91015-6

Van Lint, P., Libert, C.: Matrix metalloproteinase-8: cleavage can be decisive. Cytokine Growth F R **17**(4), 217–223 (2006). https://doi.org/10.1016/j.cytogfr.2006.04.001

Wang, X., Khali, R.A.: Chapter eight - matrix metalloproteinases, vascular remodeling, and vascular disease. Adv. Pharmacol. **81**(1), 241–330 (2018). https://doi.org/10.1016/bs.apha.2017.08.002

Wang, X., Rojas-Quintero, J., Wilder, J., Tesfaigzi, Y., Zhang, D., Owen, C.A.: Tissue inhibitor of metalloproteinase-1 (TIMP-1) promotes PMN pericellular proteolysis by anchoring matrix metalloproteinase-8 and -9 to PMN surfaces. J. Immunol. **202**(11), 3267–3281 (2019). https://doi.org/10.4049/jimmunol.1801466

Wolf, K., Friedl, P.: Extracellular matrix determinants of proteolytic and non-proteolytic cell migration. Trends Cell Biol. **21**(12), 736–744 (2011). https://doi.org/10.1016/j.tcb.2011.09.006

Zipursky, A., Bow, B., Seshadri, R.S., Brown, E.J.: Leukocyte density and volume in normal subjects and in patients with acute lymphoblastic leukemia. Blood **48**(3), 361–371 (1976)

Biological Prediction

Mathematical Modeling of the Dimerization of EGFR and ErbB3 in Lung Adenocarcinoma

Takeshi Ito[1(✉)], Takashi Suzuki[2], and Yoshinori Murakami[1]

[1] Division of Molecular Pathology, The Institute of Medical Science,
The University of Tokyo, 4-6-1 Shirokanedai, Minato-ku, Tokyo 108-8639, Japan
`t-ito@ims.u-tokyo.ac.jp`
[2] Center for Mathematical Modeling and Data Science, Osaka University,
1-3 Machikaneyama, Toyonaka, Osaka 560-8531, Japan

Abstract. The most common driver mutations in lung adenocarcinoma occur in the *EGFR* gene. Gefitinib, an EGFR tyrosine kinase inhibitor, is an effective therapy for lung adenocarcinoma with *EGFR* mutations. However, resistant tumors inevitably arise. One of the mechanisms conferring gefitinib resistance is the amplification of the *MET* gene, which is observed in 5–22% of all cases. A previous study suggested that MET overexpression may cause gefitinib resistance through ErbB3, and most likely through the formation of EGFR-ErbB3 heterodimers. In this study, we focused on the dimer formation of EGFR and ErbB3 in lung adenocarcinoma cells and built a mathematical model using ordinary differential equations. To simulate the dimerization process of EGFR and ErbB3, we determined the molecular concentrations of each on the cell surface by flow cytometry and estimated unknown reaction constants by dimensional analysis. Our mathematical model would provide a quantitative understanding of dimer formation, one which cannot be obtained by a molecular biology methods.

Keywords: Dimerization · EGFR · ErbB3 · Dimensional analysis

1 Introduction

The epidermal growth factor receptor (EGFR), also known as ErbB1, is a tyrosine kinase receptor for epidermal growth factor (EGF) and several other ligands. EGFR can form a homo- or heterodimer with other ErbB family members. Upon ligand binding, EGFR homo- or heterodimers undergo autophosphorylation and/or transphosphorylation on multiple tyrosine residues to activate downstream signaling cascades, including mitogen-activated protein kinase (MAPK), phosphoinositide-3 kinase (PI3K), and signal transducer and activator of transcription (STAT) pathways [1]. Activating mutations in the *EGFR* gene, which drive cancer cell proliferation, are frequently observed in a variety of cancers including non-small-cell lung cancer (NSCLC) [2]. ErbB3, another

ErbB family member, is a receptor for Neuregulin 1 and 2, and can also form a homo- or a heterodimer with other ErbB family members. ErbB3 homodimers would be non-functional because ErbB3 lacks intrinsic kinase activity and require transphosphorylation by its dimerization partners to gain activity. Importantly, the EGFR-ErbB3 and ErbB2-ErbB3 heterodimers play important roles in the growth and survival of cancer cells [3].

In East Asia, *EGFR* mutations are observed in approximately half of all NSCLC cases and especially in lung adenocarcinoma cases. Gefitinib (Iressa), an EGFR tyrosine kinase inhibitor, is an approved first-line therapy for lung adenocarcinomas with *EGFR* mutations. However, most cases acquire gefitinib resistance within a year [4]. One mechanism which confers gefitinib resistance is the amplification of the *MET* gene, which is observed in 5–22% of the cases. Overexpression of MET, a tyrosine kinase receptor for hepatocyte growth factor (HGF), causes gefitinib resistance by activating the PI3K pathway through ErbB3 in a ligand-independent manner [5]. To understand the dimerization and phosphorylation status of each receptor tyrosine kinase in gefitinib resistance by *MET* amplification, we performed a simulation of molecular reactions using a mathematical model and showed the limited contribution of ErbB3 in gefitinib resistance [6]. Herein, we focus on the mathematical modeling of the dimerization of EGFR and ErbB3, and describe methods to determine the molecular concentrations and reaction constants to simulate the dimerization process in lung adenocarcinoma cells.

2   Mathematical Modeling of the Dimerization of EGFR and ErbB3

EGFR and ErbB3 form homo- and heterodimers with one another with three possible types of dimers; EGFR-EGFR, ErbB3-ErbB3, and EGFR-ErbB3. When EGFR (ErbB1) and ErbB3 were represented as B1 and B3, respectively, for simplicity, molecular reactions of dimerization can be described as follows:

$$B1 + B1 \leftrightarrow B1B1,$$
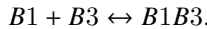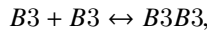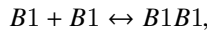
$$B3 + B3 \leftrightarrow B3B3,$$

$$B1 + B3 \leftrightarrow B1B3.$$

In these equations, the rate constants of association between B1 and B1, between B3 and B3, and between B1 and B3 in the absence of their ligands were defined as k_1, k_2, and k_3, respectively. The dissociation rate constants of B1B1, B3B3, and B1B3 were also defined as l_1, l_2, and l_3, respectively. The effects of ligands on dimerization were not considered because *MET*-driven gefitinib resistance is ligand-independent. In addition, we assumed that EGFR and ErbB3 localization was restricted to the plasma membrane which is homogeneous.

Evolution equations of the concentration of each molecule were derived from the laws of mass action and mass conservation as represented by the following

ordinary differential equations (ODEs):

$$\frac{d}{dt}[B1] = -k_1[B1]^2 + 2l_1[B1B1] - k_3[B1][B3] + l_3[B1B3] \tag{1}$$

$$\frac{d}{dt}[B3] = -k_2[B3]^2 + 2l_2[B3B3] - k_3[B1][B3] + l_3[B1B3] \tag{2}$$

$$\frac{d}{dt}[B1B1] = \frac{1}{2}k_1[B1]^2 - l_1[B1B1] \tag{3}$$

$$\frac{d}{dt}[B3B3] = \frac{1}{2}k_2[B3]^2 - l_2[B3B3] \tag{4}$$

$$\frac{d}{dt}[B1B3] = k_3[B1][B3] - l_3[B1B3] \tag{5}$$

By assuming that the reaction network is closed, the following equations were obtained from the law of mass conservation concerning EGFR and ErbB3:

$$\frac{d}{dt}([B1] + 2[B1B1] + [B1B3]) = 0 \tag{6}$$

$$\frac{d}{dt}([B3] + 2[B3B3] + [B1B3]) = 0 \tag{7}$$

To simulate EGFR and ErbB3 dimerization using the ODEs (1)–(5), we determined the concentrations of EGFR and ErbB3 in a lung adenocarcinoma cell line and estimated the reaction constants as described below.

3   Quantification of Cell-Surface EGFR and ErbB3

The number of EGFR and ErbB3 molecules on the cell surface can be quantified by flow cytometry using specific antibodies and calibration beads [7]. For example, the Quantum Simply Cellular kit consists of 5 bead populations, 1 blank and 4 with increasing levels of an anti-mouse IgG antibody. The fluorescence intensity of each bead population after incubating with a mouse monoclonal anti-EGFR antibody and an FITC-conjugated anti-mouse IgG secondary antibody was analyzed by flow cytometry (Fig. 1A). A calibration curve was obtained by plotting the number of antibodies (i.e., Antibody Binding Capacity) against the normalized fluorescence intensity of each bead population (Fig. 1B).

Next, flow cytometric analyses of HCC116 (colon cancer), HaCaT (keratinocyte), and A431 (epidermoid carcinoma) cell lines, which exhibit differential expression of EGFR [8], were performed using an anti-EGFR antibody and an FITC-labeled secondary antibody (Fig. 1C). The number of cell-surface EGFRs was estimated to be 2.6×10^5, 3.5×10^6, and 7.9×10^6, respectively, in a unit of *Antibody Binding Capacity*, from the median fluorescence intensities. These values were close to the previously published values of 2.2×10^5, 8.7×10^5, and 1.65×10^6 cell^{-1}, respectively [8]. These data confirmed that we could successfully estimate the number of cell-surface EGFR molecules by flow cytometry.

Subsequently, we investigated the number of cell-surface EGFRs in HCC827 cell line, which harbors an *EGFR* mutation and is commonly used as a model of gefitinib resistance in lung adenocarcinoma. Using flow cytometry, we estimated the number of cell-surface EGFRs on HCC827 cells to be $5.0 \times 10^5 \, \text{cell}^{-1}$ (Fig. 1C). Moreover, the concentration of cell-surface EGFRs was calculated as $4.2 \times 10^{-12} \, \text{mol/dm}^2$ assuming a surface area of $2.0 \times 10^3 \, \mu\text{m}^2$ in HCC827 cells. The unit of mol/dm^2, which is referred to as D, was used as a molar concentration in 2 dimensions according to a previous study [9]. In addition, we estimated the number of cell-surface ErbB3s in HCC827 cells to be $3.6 \times 10^3 \, \text{cell}^{-1}$ with a cell surface concentration of $3.0 \times 10^{-14} \, D$ [6]. This quantification method cannot distinguish monomers from dimers of EGFR and ErbB3. Consequently, the concentration of each molecule represents the sum of monomers and dimers. Therefore, the following equations are obtained from the Eqs. (6) and (7).

$$[B1] + 2[B1B1] + [B1B3] = 4.2 \times 10^{-12} \tag{8}$$

$$[B3] + 2[B3B3] + [B1B3] = 3.0 \times 10^{-14} \tag{9}$$

4   Estimation of the Reaction Constants by Dimensional Analysis

Regarding the previously published reaction constants, the equilibrium constant of EGFR dimerization (k_1/l_1) was determined to be $4.8 \times 10^{10} \, D^{-1}$ by single-molecule imaging of the binding of fluorescent-labeled EGF to the surface of HeLa cells [10] or to be $5.3 \times 10^{11} \, D^{-1}$ by analyzing the binding of radiolabeled EGF to the surface of CHO cells [9]. The dissociation rate constant (l_1) was determined as $1.24 \, \text{s}^{-1}$ by single particle tracking of the fluorescent-labeled anti-EGFR antibody bound to A431 cells [11]. In similar experiments, the equilibrium constant of ErbB3 dimerization (k_2/l_2) was determined to be $1.7 \times 10^{12} \, D^{-1}$ in MCF7 breast cancer cells [12] and the dissociation rate constant (l_2) was shown to be $1.08 \, \text{s}^{-1}$ in SKBR3 breast cancer cells [13]. Therefore, k_1 and k_2 were calculated as 6.0×10^{10} (or $6.6 \times 10^{11}) \, D^{-1}\text{s}^{-1}$ and $1.9 \times 10^{12} \, D^{-1}\text{s}^{-1}$, respectively. In contrast, the reaction constants of EGFR-ErbB3 heterodimerization, k_3 and l_3, have not been reported. Since the dissociation rate constant of the ErbB2-ErbB3 heterodimer was similar to that of the ErbB3 homodimer (l_2) [13], the dissociation rate constant of EGFR-ErbB3 (l_3) was assumed to be equal to l_2. The value of k_3 was estimated by dimensional analysis as follows.

In Eq. (2), dt, which corresponds to the time taken in the reactions involving ErbB3, was assumed to be 1 s because the dissociation rate constants of ErbB3 homodimerization (l_2) and EGFR-ErbB3 heterodimerization (l_3) are approximately $1 \, \text{s}^{-1}$. In addition, if all of the EGFR and ErbB3 molecules were assumed to be monomers, $[\text{B1}] = 4.2 \times 10^{-12}$, $[\text{B3}] = 3.0 \times 10^{-14}$, and $[\text{B1B1}] = [\text{B1B3}] = 0$ according to Eqs. (8) and (9). By substituting these values into the both sides of Eq. (2), the following expressions were obtained:

$$\frac{d}{dt}[B3] = \left| \frac{3.0 \times 10^{-14}}{1} \right| \tag{10}$$
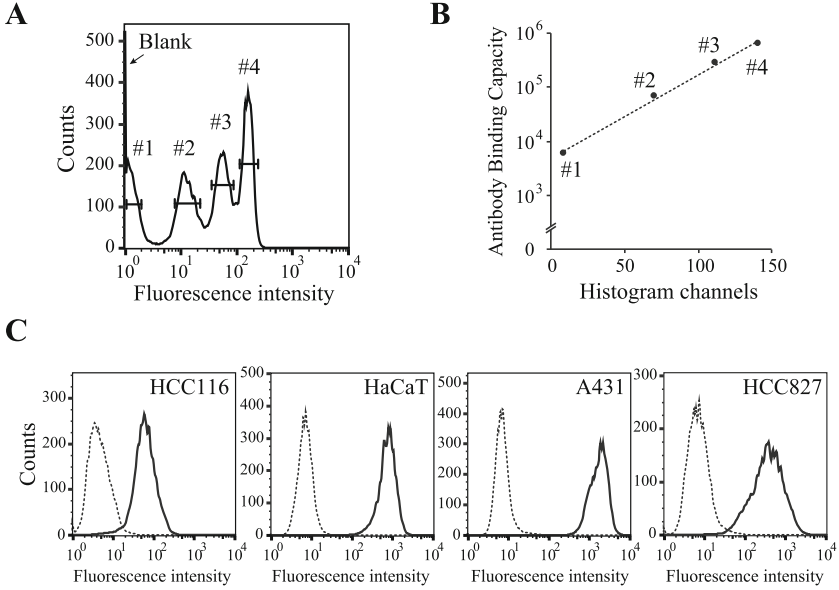
A

B

C

Fig. 1. Quantification of cell-surface EGFR molecules using Quantum Simply Cellular anti-mouse IgG beads. (A) One blank and four labeled beads with increasing amounts of anti-mouse IgG antibody were incubated with an anti-EGFR antibody and an FITC-conjugated secondary antibody. The fluorescence intensity of each bead was analyzed by flow cytometry. (B) The normalized fluorescence intensity values of the labeled beads were plotted against the numbers of anti-mouse IgG antibody molecules labeled on the beads, termed Antibody Binding Capacity. (C) The fluorescence intensity of HCC116, HaCaT, A431, and HCC827 cells were analyzed by flow cytometry after labelling with an anti-EGFR antibody (solid line) or normal mouse IgG (dotted line).

$$-k_2[B3]^2 + 2l_2[B3B3] - k_3[B1][B3] + l_3[B1B3] =$$
$$-1.9 \times 10^{12} \bullet (3.0 \times 10^{-14})^2 + 0 - k_3 \bullet 4.2 \times 10^{-12} \bullet 3.0 \times 10^{-14} + 0 \qquad (11)$$

Based on expressions (10) and (11), k_3 was estimated to be 2.2×10^{11} D^{-1}s^{-1}.

5 Simulation Results

A simulation of the dimerization of EGFR and ErbB3 in HCC827 cells was performed using the ODEs (1)–(5) and the estimated molecular concentration and reaction constants. All of the EGFR and ErbB3 molecules were assumed to be monomers in the initial conditions. The results of the simulation at $t = 0$–10 s are shown in Fig. 2. Dimerization of EGFR and ErbB3 reached equilibrium after approximately 1 s, and the amount of each molecule at equilibrium was; EGFR: 4.3×10^5, ErbB3: 2.1×10^3, EGFR-EGFR: 3.7×10^4, ErbB3-ErbB3: 31, EGFR-ErbB3: 1.5×10^2 cell^{-1}. These results suggest that the number of EGFR homodimers is approximately 25 times higher than the EGFR-ErbB3 heterodimers,

and that only a few ErbB3 homodimers are formed in lung adenocarcinoma cells. Moreover, we have shown that the ODEs can be explicitly solved and that the concentration of each molecule can be derived theoretically by classification as either monomers (EGFR and ErbB3) or dimers (EGFR-EGFR, ErbB3-ErbB3, and EGFR-ErbB3) [14].
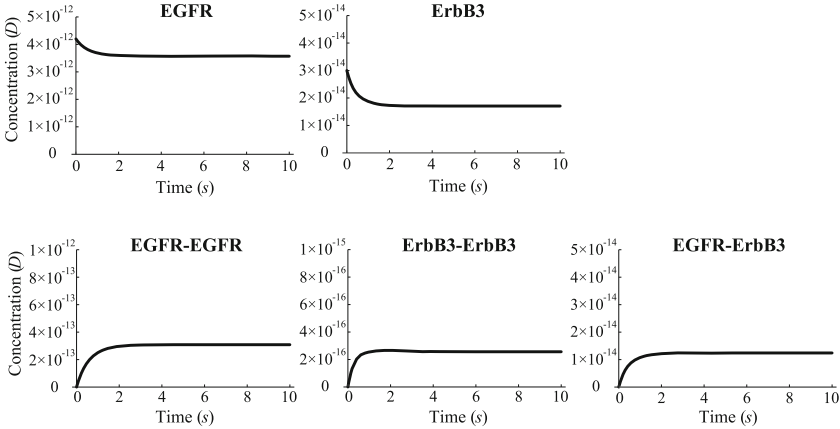
Fig. 2. A simulation of the time-course of dimerization of EGFR and ErbB3 on the surface of HCC827 cells. All of EGFR and ErbB3 molecules are assumed to be monomers at $t = 0$. The x- and y-axis represent the time and the concentration of each molecule on the cell surface, respectively.

6   Discussion

In this study, we built a mathematical model of the dimerization of EGFR and ErbB3 on the surface of lung adenocarcinoma cells in the absence of their ligands. We also described the methods to quantify their molecular concentrations on the cell surface and to estimate unknown reaction constants by dimensional analysis. This approach is useful for simulating a variety of molecular reactions on the cell surface and our model would provide a quantitative understanding of dimer formation, which cannot be analyzed by a common biological approach.

The EGFR-ErbB3 heterodimer has higher mitogenic activity than the EGFR homodimer partly because the heterodimer is more likely to be recycled to the cell surface after endocytosis [15]. The EGFR-ErbB3 heterodimer is reported to be involved in the resistance of cancer cells to gefitinib, an EGFR tyrosine kinase inhibitor, or cetuximab, an anti-EGFR antibody [5,16]. In our previous study, we simulated the dimer formation and phosphorylation of EGFR, ErbB3, and MET in HCC827 gefitinib-resistant (GR) cells, which acquired resistance to gefitinib by *MET* amplification. Although ErbB3 activation induced by MET was reported to be essential for gefitinib resistance, our simulation showed that the number of active EGFR-ErbB3 dimers was only less than 1% of active MET

homodimers. Since knockdown of ErbB3 did not sensitize HCC827 GR cells to gefitinib and the cells were also resistant to AZD8931, a dual inhibitor against EGFR and ErbB3, we concluded that the contribution of ErbB3 to gefitinib resistance by MET is rather limited [6]. It would be important to further investigate the ratio of the EGFR-ErbB3 heterodimer to the EGFR or MET homodimer by experiments using single-molecule imaging or other techniques.

In lung adenocarcinoma cells with *EGFR* mutation, the formation of an EGFR homodimer and an EGFR-ErbB3 heterodimer would cause phosphorylation of EGFR, ErbB3, and its downstream effectors, thereby promoting cell proliferation and survival. On the other hand, in cells with wild-type *EGFR* alleles, ligand-independent EGFR dimer formation caused some EGFR phosphorylation but this was not enough to activate its downstream signaling [17]. Therefore, to apply this mathematical model to cells with wild-type EGFR, ligands for EGFR and ErbB3 should also be considered. In the presence of EGF, the equilibrium constant of EGFR dimerization (k_1/l_1) is about 12 times smaller and the dissociation rate constant (l_2) is about 4.5 times smaller in the absence of EGF [9,11] (Table 1). This is probably due to the conformational changes in EGFR in response to EGF binding [18]. Thus, the dynamics of the dimerization of EGFR and ErbB3 are likely quite different depending on the presence or absence of their ligands.

A more detailed simulation including the involvement of other ErbB family proteins, turnover of the receptors, and activation of downstream signaling would be useful to gain a full understanding of EGFR and ErbB3 functions in cancer cells. Further studies are required for the development of such an extended model.

Table 1. Reaction constants of the homodimerization of EGFR in the presence or absence of EGF.

Constant (unit)	w/o EGF	w/EGF	Reference
k_1/l_1 (D^{-1})	5.3×10^{11}	4.5×10^{10}	[9]
l_1 (s^{-1})	1.24	0.273	[11]
k_1 (D$^{-1}s^{-1}$)	6.6×10^{11}	1.2×10^{10}	Calculated

References

1. Hynes, N.E., Lane, H.A.: ERBB receptors and cancer: the complexity of targeted inhibitors. Nat. Rev. Cancer **5**, 341–354 (2005)
2. Sharma, S.V., Bell, D.W., Settleman, J., Haber, D.A.: Epidermal growth factor receptor mutations in lung cancer. Nat. Rev. Cancer **7**, 169–181 (2007)

3. Baselga, J., Swain, S.M.: Novel anticancer targets: revisiting ERBB2 and discovering ERBB3. Nat. Rev. Cancer **9**, 463–475 (2009)
4. Rotow, J., Bivona, T.G.: Understanding and targeting resistance mechanisms in NSCLC. Nat. Rev. Cancer **17**, 637–658 (2017)
5. Engelman, J.A., Zejnullahu, K., Mitsudomi, T., et al.: MET amplification leads to gefitinib resistance in lung cancer by activating ERBB3 signaling. Science **316**, 1039–1043 (2007)
6. Ito, T., Kumagai, Y., Itano, K., et al.: Mathematical analysis of gefitinib resistance of lung adenocarcinoma caused by MET amplification. Biochem. Biophys. Res. Commun. **511**, 544–550 (2019)
7. Serke, S., van Lessen, A., Huhn, D.: Quantitative fluorescence flow cytometry: a comparison of the three techniques for direct and indirect immunofluorescence. Cytometry **33**, 179–187 (1998)
8. Novy, Z., Barta, P., Mandikova, J., et al.: A comparison of in vitro methods for determining the membrane receptor expression in cell lines. Nucl. Med. Biol. **39**, 893–896 (2012)
9. Macdonald, J.L., Pike, L.J.: Heterogeneity in EGF-binding affinities arises from negative cooperativity in an aggregating system. Proc. Natl. Acad. Sci. U.S.A. **105**, 112–117 (2008)
10. Teramura, Y., Ichinose, J., Takagi, H., et al.: Single-molecule analysis of epidermal growth factor binding on the surface of living cells. EMBO J. **25**, 4215–4222 (2006)
11. Low-Nam, S.T., Lidke, K.A., Cutler, P.J., et al.: ErbB1 dimerization is promoted by domain co-confinement and stabilized by ligand binding. Nat. Struct. Mol. Biol. **18**, 1244–1249 (2011)
12. Hiroshima, M., Saeki, Y., Okada-Hatakeyama, M., Sako, Y.: Dynamically varying interactions between heregulin and ErbB proteins detected by single-molecule analysis in living cells. Proc. Natl. Acad. Sci. U.S.A. **109**, 13984–13989 (2012)
13. Steinkamp, M.P., Low-Nam, S.T., Yang, S., et al.: ErbB3 is an active tyrosine kinase capable of homo- and heterointeractions. Mol. Cell. Biol. **34**, 965–977 (2014)
14. Itano, K., Ito, T., Kawasaki, S., et al.: Mathematical modeling and analysis of ErbB3 and EGFR dimerization process for the gefitinib resistance. JSIAM Lett. **10**, 33–36 (2018)
15. Lenferink, A.E., Pinkas-Kramarski, R., van der Poll, M.L., et al.: Differential endocytic routing of homo- and hetero-dimeric ErbB tyrosine kinases confers signaling superiority to receptor heterodimers. EMBO J. **17**, 3385–3397 (1998)
16. Schoeberl, B., Faber, A.C., Li, D., et al.: An ErbB3 antibody, MM-121, is active in cancers with ligand-dependent activation. Cancer Res. **70**, 2485–2494 (2010)
17. Byrne, P.O., Hristova, K., Leahy, D.J.: EGFR forms ligand-independent oligomers that are distinct from the active state. J. Biol. Chem. **295**, 13353–13362 (2020)
18. Endres, N.F., Das, R., Smith, A.W., et al.: Conformational coupling across the plasma membrane in activation of the EGF receptor. Cell **152**, 543–556 (2013)

Selective Regulation of the Insulin-Akt Pathway by Simultaneous Processing of Blood Insulin Pattern in the Liver

Hiroyuki Kubota[✉]

Division of Integrated Omics, Research Center for Transomics Medicine, Medical Institute of
Bioregulation, Kyushu University, 3-1-1 Maidashi,
Higashi-ku, Fukuoka 812-8582, Fukuoka, Japan
kubota@bioreg.kyushu-u.ac.jp

Abstract. Insulin exhibits several temporal patterns, such as the 10- to 15-min pulsatile (minutes), additional (hours), and basal (days) secretions, leading to selective insulin responses *in vivo*; however, the mechanisms by which different temporal patterns of insulin selectively regulate downstream molecules remain unknown. Revealing the mechanisms of selective regulation by temporal patterns of insulin is pivotal for understanding insulin actions *in vivo*.

We examined selective regulation of the insulin-Akt pathway and its mechanisms in the liver under hyperinsulinemic-euglycemic clamp conditions. We obtained time series data of the insulin-Akt pathway molecules using different stimulation patterns and developed a mathematical model that could reproduce these data. We found that all temporal patterns of the blood insulin levels are encoded into the insulin receptor (IR), and downstream molecules selectively and simultaneously decode them via protein kinase B (Akt or PKB). Mathematical modeling revealed the mechanisms via differences in network structures, sensitivity, and time constants. Moreover, we simulated the type II diabetes mellitus (T2DM) condition using the model and found that abnormal blood insulin patterns might contribute to the pathogenesis and/or progression of T2DM. Given that almost all hormones exhibit distinct temporal patterns, temporal coding may be a general principle of system homeostasis by hormones.

1 Temporal Patterns of the Blood Insulin Level

Almost all hormones exhibit distinct temporal patterns that are important for their functions [1]. Insulin is a well-studied hormone that exhibits several secretion patterns, such as the 10- to 15-min pulsatile secretions (minutes) [2, 3], the additional secretion (hours) which is observed in response to meals, and the basal secretion (days) which is a low constant secretion observed during fasting [4]. The importance of these insulin secretion patterns has been reported: 13 min of pulsatile insulin stimulation was more effective than continuous stimulation in regulating hepatic glucose production *in vivo* [5, 6]. Moreover, the relationship between insulin secretion abnormalities and type 2 diabetes mellitus (T2DM) has also been reported: the 10- to 15-min pulsatile secretion was diminished in T2DM patients [3], and both the additional and basal secretions were

increased (hyperinsulinemia) in the early stages of T2DM patients [4]. Furthermore, a discrepancy is observed in patients with the early stages of T2DM: the ability to suppress the blood glucose levels decreases, whereas the liver stores a lot of fat, both of which are activated by insulin [7].

In the hepatoma cell line, Fao cells, the Akt pathway [8], metabolites [9], and gene expression [10] can be selectively regulated by insulin stimulation patterns. However, since Fao cells are derived from hepatoma cells, they are distinct from the normal liver cells; various liver responses were collapsed, revealed infinite proliferation, and their environmental conditions did not match the *in vivo* conditions. Therefore, whether different secretion patterns of insulin selectively regulate the responses in the liver remains unclear.

2   Obtaining Experimental Data

An experimental design that is suitable for its purpose is necessary to obtain good results. In particular, to develop a precise model, we require abundant data, including a lot of information, such as detailed time course data, dose response, and different stimulation patterns.

2.1   Animal Experiments

In this study, we focused on the temporal patterns of insulin *in vivo.* Therefore, insulin needs to be administered *in vivo* at the site of insulin secretion. Insulin is secreted from the pancreas and released into the portal vein, which delivers blood to the liver; however, because the portal vein is located deep inside the body, it is difficult to administer insulin through the portal vein. Hence, we administered insulin through the mesenteric vein, which led to the portal vein. Moreover, somatostatin was administered through the jugular vein to suppress endogenous insulin secretion. Since insulin lowers blood glucose level, we evaluated the blood glucose level every 5 min and maintained it a constant value by changing the glucose infusion rate through the jugular vein. In the present study, to develop a precise model, we administered insulin at three stimulation patterns (Fig. 1B); 1) constant infusion rate at three doses (step stimulation), 2) continuous increase stimulation (ramp stimulation), and 3) two-pulse stimulation (pulse stimulation). At the indicated time points, the rats were sacrificed, and their livers were obtained. Thereafter, we obtained time series data of the molecules via quantitative western blotting and qPCR analyses.

2.2   Different Temporal Patterns of Insulin-Akt Pathway Molecules

We measured phosphorylated insulin receptor (pIR), Akt (pAkt), S6K (pS6K), GSK3β (pGSK3β), FoxO1 (pFoxO1), and gene expression of G6Pase (*G6Pase*) (Fig. 1A and 1C), which play pivotal roles in metabolic responses in the liver [11].

We initially examined the responses using step stimulation (Fig. 1B and 1C) and observed sustained responses of pIR, pAkt, and pGSK3β in an insulin dose dependent manner. Furthermore, pFoxO1 and *G6Pase* exhibited similar sustained responses and
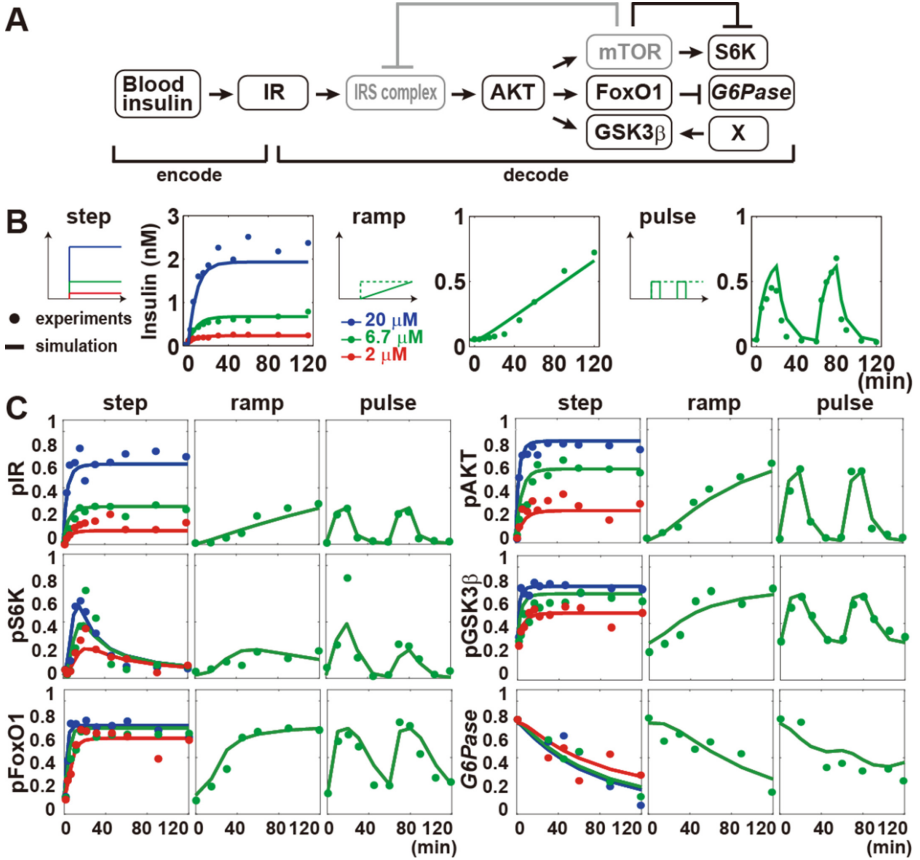
Fig. 1. Different temporal patterns of pIR, pAkt, pS6K, pGSK3β, pFoxO1, and *G6Pase* in the liver. (A) Schematic overview of the insulin-Akt pathway. (B) Time courses of the blood insulin levels in step, ramp, and pulse stimulations. (C) Time courses of pIR, pAkt, pS6K, pGSK3β, pFoxO1, and *G6Pase* in step, ramp, and pulse stimulation. (B, C) Lines and dots indicate simulation and experimental results (means), respectively. Blue, green, and red indicate time courses stimulated by 20, 6.7, and 2 μM insulin, respectively.

gradual decreases regardless of the insulin dose, respectively. According to our previous studies [8–10], these results indicated that the molecules responded to the concentration of the blood insulin levels. On the other hand, only pS6K exhibited transient responses by reacting to the increasing rate of the blood insulin levels. These different temporal patterns indicated that the insulin-Akt pathway molecules captured distinct properties of the temporal patterns of the blood insulin levels.

To confirm these characteristics, we examined responses using ramp stimulation. The ramp stimulation induced gradual changes in pIR, pAkt, pGSK3β, pFoxO1, and *G6Pase* and reached the same values as those of step stimulation regardless of the stimulation patterns (Fig. 1B and 1C), indicating that these molecules responded to the concentration of the blood insulin levels. In contrast, the transient response of pS6K decreased. Thus,

a higher increase in the blood insulin levels induced a remarkable transient response of pS6K and vice versa, indicating that pS6K responded to the increasing rate of the blood insulin levels.

To further confirm these characteristics, we examined the responses using pulse stimulation. The pulse stimulation induced two transient responses of pIR, pAkt, pGSK3β, and pFoxO1, similar to the blood insulin level (Fig. 1B and 1C), indicating that these molecules could rapidly follow changes in the blood insulin levels. Thus, these molecules responded to the concentration of blood insulin levels. In contrast, *G6Pase* revealed a similar response to step stimulation. Moreover, pS6K also exhibited two transient responses; however, the second peak was smaller than the first one, indicating that pS6K responded to the increasing rate of the blood insulin levels (see below).

The experiments using different insulin stimulation patterns revealed that the insulin-Akt pathway molecules in the liver are regulated by the temporal patterns of the blood insulin levels.

3   Developing the Insulin-Akt Pathway Model

To understand the selective regulation mechanisms, we developed an ordinal differential equation (ODE) model that can reproduce the behavior of the experimental results. Furthermore, we examined the responses of molecules in the progression of T2DM using this model.

3.1   Developing the Insulin-Akt Pathway Model

We developed an insulin-Akt pathway model based on our previous model (Fig. 1A) [8, 12]. In the present model, we made the following three changes; First, we incorporated IR, which was not considered in our previous model. Second, we carried out the degradation of insulin receptor substrate proteins (IRSs). It has been reported that protein levels of IRSs decrease in response to prolonged insulin exposure [13]; however, under our experimental conditions of mice within 2 h, no significant decrease was observed in the amount of IRSs. Therefore, we did not incorporate the degradation term of the IRSs in our present model. Third, we put a restriction on GSK3ß regulation. In our previous model, GSK3ß phosphorylation was only regulated by pAkt; however, the previous model could not reproduce the behavior of pGSK3ß in the liver. Therefore, we developed a model with an unknown molecule X, which regulates the phosphorylation of GSK3ß by an insulin independent pathways (Fig. 1A), such ILK and PKA. As a result of an investigation by the Akaike Information Criterion, we chose the model with regulation X. Recently, we found another difference, that is, a negative feedback loop from mTOR to the IRSs [14, 15]. We have confirmed the negative feedback loop in Fao cells in our previous study [8]; however, the parameter of the feedback loop in the current model is very small. Therefore, we experimentally confirmed whether the negative feedback loop played a pivotal role in the liver using the mTOR-specific inhibitor rapamycin, and found that the negative feedback loop was not effective or its effect was limited; an increase in pAKT was not observed, though phosphorylation of S6K was completely inhibited by rapamycin. These results indicate qualitative differences between the liver and Fao cells.

Even if the overall network structure remains conserved among different cell types, the quantitative differences (parameters) can cause different dynamics, leading to distinct temporal coding and decoding depending on the cell type.

3.2   Selective Regulation Mechanisms of the Insulin-Akt Pathway

Our model reproduced the characteristics of the aforementioned molecules (Fig. 1C). This indicated that our model captured the mechanisms by which insulin temporal patterns regulate the insulin-Akt pathway molecules in the liver. Therefore, we further investigated the type of information that the insulin-Akt pathway molecules responded and the manner in which these molecules decoded the information. If the signaling pathway does not carry out complicated information processing, correlation is a good index of information transfer efficiency. Therefore, to tackle these issues, we calculated the absolute value of the correlation coefficient (SIs) between insulin and a molecule in both experimental and simulation results (Fig. 2A).

According to our model, pIR, pAkt, pGSK3β, pFoxO1, and *G6Pase* can be assumed the same network structure, feed-forward (FF); however, the SIs differed (Fig. 2A), that is, those of pIR, pAkt, and pGSK3β were high, whereas those of pFoxO1 and *G6Pase* were moderate and low, respectively. The information transferred and untransferred to the molecules was assessed. Two indices characterize an FF, that is, the time constant (**T**) and EC_{50}. We calculated these values to understand these differences.

First, we calculated the apparent time constants of the molecules against insulin (Fig. 2B). The time constant indicates how rapidly the downstream molecule can follow changes in the upstream molecule. The time constant is defined as the time to reach 63.2% of the steady state by step stimulation and is the reciprocal of the dephosphorylation parameter in a linear system. A molecule with a small time constant can rapidly follow changes in the upstream molecule, indicating that the molecule can receive much information on the increasing rate. The only apparent time constant of *G6Pase* was large, indicating that only *G6Pase* cannot receive much information on the increasing rate of insulin.

Furthermore, we calculated the EC_{50s} of molecules against insulin (Fig. 2C, upper panel). EC_{50} is a half-maximal effective concentration, which provides 50% of the maximal response. EC_{50} is determined by a ratio between the parameters of phosphorylation and dephosphorylation. A molecule with a large EC_{50} can respond to a wide range of input, indicating that the molecule can receive much information on concentration. The largest EC_{50} of IR indicated that pIR can receive more information on concentration than the other molecules. On the other hand, because of the small EC_{50s}, pFoxO1 and *G6Pase* cannot receive much information on concentration. Considering that the maximum blood insulin level is approximately 1 nM, pIR, pAkt, and pGSK3β can receive enough information on the concentration of the blood insulin levels. To further investigate the mechanisms, we calculated the EC_{50s} of molecules against the molecules located just above them (Fig. 2C, lower panel). Interestingly, the EC_{50} of *G6Pase* against pFoxO1 was larger than those of pAkt, pGSK3β, and pFoxO1 against each upstream molecule. This indicated that *G6Pase* could potentially receive much information on the concentration of pFoxO1; however, since pFoxO1 did not receive much information on concentration, it could no longer transfer enough information to *G6Pase*.
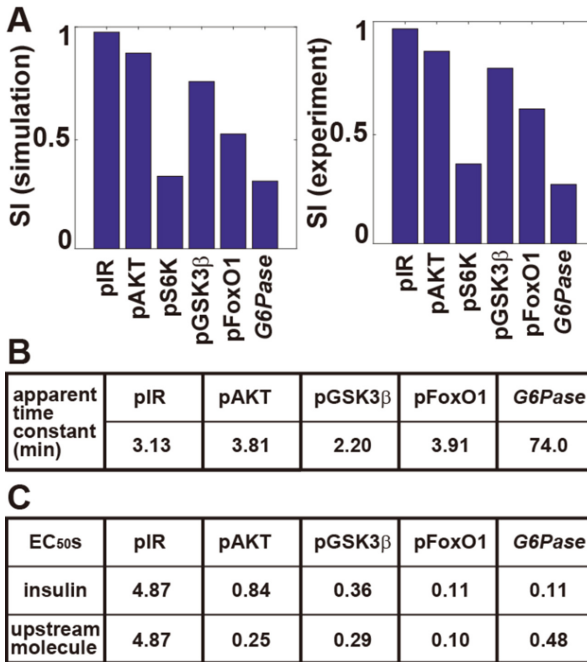
Fig. 2. Selective regulation mechanisms of the insulin-Akt pathway molecules. (A) The similarity indices (SIs) of the indicated molecules in simulation (left panel) and experiments (right panel). (B) The apparent time constant of the indicated molecules. (C) The EC_{50}s of the indicated molecules against insulin (upper) and the molecule located above them (lower).

In contrast to the aforementioned molecules, the network structure of pS6K is an incoherent feed-forward loop (IFFL) (Fig. 1A). During pulse stimulation, pS6K exhibited two transient responses similar to the other molecules (Fig. 1C); however, the second peak was smaller than the first one. This phenomenon is termed as the refractory period, which is a characteristic of IFFL; at the second stimulation, since the phosphatase activity activated by the first stimulation was retained, the kinase could not fully phosphorylate pS6K. Owing to the characteristics of IFFL, pS6K responded to the increasing rate, but it did not respond to the concentration of the blood insulin levels.

We investigated the regulatory mechanisms of the insulin-Akt pathway. Due to the small time constant and large EC_{50}, pIR, pAkt, and pGSK3β can receive much information on both the increasing rate and concentration of the blood insulin levels, indicating large SIs (Fig. 2A). Due to the small time constant and low EC_{50}, pFoxO1 can mainly receive information on the increasing rate, thereby indicating a moderate SI. Considering the large time constant and small EC_{50} against insulin, *G6Pase* can receive limited information on both the increasing rate and concentration of the blood insulin levels, thereby revealing a small SI. Furthermore, due to the different network structure, IFFL, pS6K can only receive information on the increasing rate of the blood insulin levels, thereby indicating a small SI.

3.3   Decoding of the Blood Insulin Level *In Vivo*

We found that the insulin-Akt pathway molecules selectively responded to the temporal patterns of the blood insulin levels in the liver and their mechanisms (Fig. 3). We further investigated the possible physiological roles of insulin function based on these characteristics.

pIR and pAkt: Owing to the small time constant and large EC_{50}, pIR and pAkt can receive much information on both the increasing rate and concentration of the blood insulin levels. Therefore, pIR and pAkt can respond to all secretion patterns (Fig. 3). Considering that IR is the "only gate" of the cell for insulin, blood insulin may encode much information into pIR. Thereafter, the information is transferred to Akt, which acts as the branch point of the pathway, without much attenuation of the information.

pGSK3β: Owing to the small time constant and large EC_{50}, pGSK3β can receive much information on both the increasing rate and concentration of the blood insulin levels. Therefore, pGSK3β has the ability to respond to all secretion patterns. Moreover, GSK3β should immediately regulate glycogen synthesis depending on the blood insulin levels, since glycogen in the liver acts as a blood glucose buffer [16]. In response to the additional secretion during high blood glucose, GSK3β immediately activates glycogen synthesis, and vice versa.

pFoxO1: Owing to the small time constant and small EC_{50}, pFoxO1 can mainly receive information on the increasing rate of the blood insulin levels. Therefore, although pFoxO1 cannot distinguish the concentration of the blood insulin levels effectively, it can respond to all secretion patterns. Considering that FoxO1 is a transcriptional factor [17], all gene expressions regulated by FoxO1, including *G6Pase*, may not be able to respond to information on the concentration of the blood insulin levels.

G6Pase: Owing to the large time constant and small EC_{50} against insulin, *G6Pase* can receive a little information on both the increasing rate and concentration of the blood insulin levels. Interestingly, *G6Pase* can potentially receive much information on the concentration of pFoxO1, because it possesses a large EC_{50} against the upstream molecule, pFoxO1; however, since pFoxO1 cannot receive much information on the concentration of the blood insulin levels, *G6Pase* cannot also receive much information. *G6Pase* responded to ramp and pulse stimulations similar to step stimulation (Fig. 1C); however, it could not distinguish the stimulation patterns, since *G6Pase* cannot receive much information on both the increasing rate and concentration of the blood insulin levels. As a result, *G6Pase* preferentially responds to the basal secretion, which is similar to ramp stimulation. Considering that *G6Pase* regulates gluconeogenesis, it may be used for regulating gluconeogenesis in days rather than in hours to avoid unnecessary consumption of energy.

pS6K: Owing to the network structure, IFFL, pS6K can only receive information on the increasing rate of the blood insulin levels. Therefore, pS6K can respond to the additional and 10- to 15-min pulsatile secretions, but not to the basal secretion. Considering that S6K regulates protein synthesis, S6K activates protein synthesis in response to the additional secretion when the blood is rich in nutrients, including amino acids.
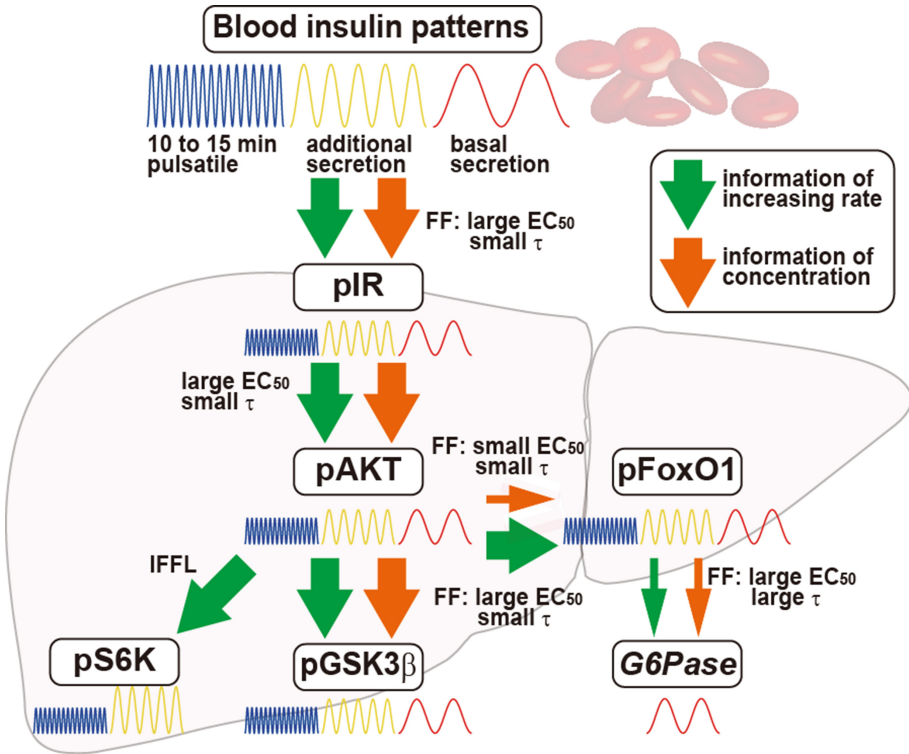
Fig. 3. Summary of the selective regulation mechanisms of the insulin-Akt pathway molecules in the liver.

4 Simulation of the T2DM Condition

We predicted the responses of the molecules in the early stages of T2DM patients using the aforementioned model. It has been reported that the expression level and/or activity of IR decreased (insulin resistance) in the early stages of T2DM patients [18, 19]. Moreover, the ratio between the basal and additional secretion in the healthy and early stages of T2DM patients remains the same [4]. In the early stages of T2DM patients, one large discrepancy was found, that is, both fatty acid synthesis and gluconeogenesis were increased [7]. Fatty acid synthesis is activated by insulin, whereas gluconeogenesis is suppressed. To address this issue, we used our model to predict T2DM progression.

We focused on the basal and additional secretion patterns in the simulation and approximated them using a sinusoidal curve (Fig. 4). Since it has been reported that the ratio between the additional and basal secretion remains the same between the healthy and early stages of T2DM patients, we maintained the same ratio in our model. Blue lines indicate normal IR phosphorylation activity with normal insulin stimulation (a normal condition) (Fig. 4). Yellow lines indicate 1/3 of the normal IR phosphorylation activity with normal insulin stimulation (the early stages of T2DM condition without insulin secretion increase). In the early stages of T2DM patients, the pancreas increases insulin secretion and recovers the responses to compensate for insulin resistance (red
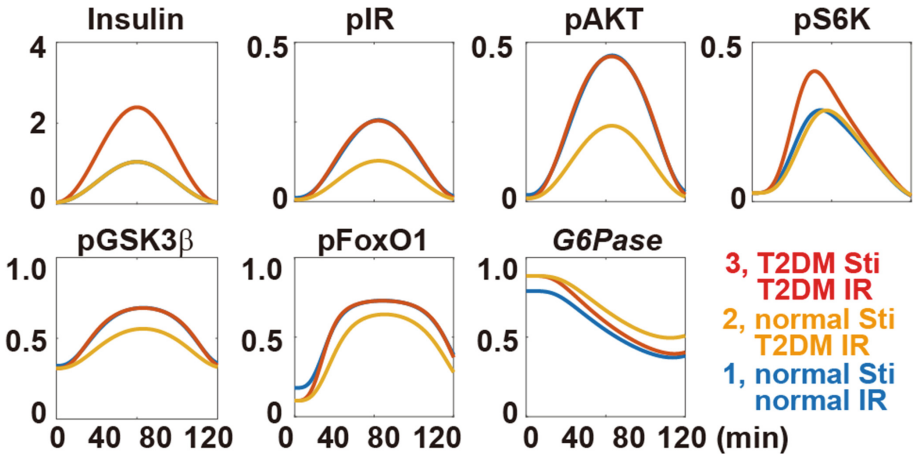
Fig. 4. Simulation of the T2DM condition. The basal and additional secretion patterns were approximated using a sinusoidal curve. Blue, orange, and red lines indicate normal IR phosphorylation activity with normal insulin stimulation, 1/3 of the normal IR phosphorylation activity with normal insulin stimulation, and 1/3 of the normal IR phosphorylation activity with 3.5 times insulin stimulation patterns, respectively. Notably, many of orange lines overlap with those of the blue lines.

lines); however, after a short duration, the pancreas is exhausted, and it cannot produce enough insulin, thereby impairing insulin secretion. This is a state of diabetes mellitus (yellow lines). Most responses in the early stages of T2DM condition (red lines) were recovered to those in the heathy condition (blue lines); however, interestingly, the basal levels of pFoxO1 and *G6Pase* increased, indicating the activation of gluconeogenesis. This was caused by the small EC_{50} of pFoxO1 against insulin (Fig. 2C and 3). There were slight differences between the blue and red lines for pIR and pAkt. The differences were enhanced by pFoxO1, with a small EC_{50}. Our model suggested that the small EC_{50} of pFoxO1 against the blood insulin levels might be the reason for the hyperactivation of gluconeogenesis in the early stages of T2DM.

5   Conclusions

In the early stages of T2DM patients, a discrepancy has been reported; the ability to suppress the blood glucose levels decreases, whereas the liver stores a lot of fat, both of which are activated by insulin [7]. Controlling both responses is important for T2DM treatment. In this study, we predicted that different sensitivity (EC_{50s}) against the blood insulin level might be a reason for the hyperactivation of gluconeogenesis in the early stage of T2DM patients. Prescribing insulin secretagogues, which increase insulin secretion, is a common treatment for T2DM. However, our model predicted that reducing the basal secretion rather than increasing insulin secretion might be effective for suppressing gluconeogenesis. This result may provide new insights into T2DM treatment.

Given that almost all hormones exhibit distinct temporal patterns [1], other hormones are also presumed to possess similar temporal coding properties. Thus, temporal coding

may be the general principle of system homeostasis by hormones. The secretion patterns of growth factors remain unclear; however, growth factors may also exhibit distinct secretion patterns, which are important for their functions. Therefore, the pathogenesis and/or progression of cancer is presumed to be affected by the temporal patterns of various hormones and growth factors. Perturbation of circadian rhythms has been reported to be associated with cancer pathogenesis [20]. The concept of temporal coding will provide new insights into the understanding and treatment of various cancer types.

References

1. Brabant, G., Prank, K., Schijfl, C.: Pulsatile patterns in hormone secretion. Trends Endocrinol. Metab. **3**, 183 (1992)
2. O'Meara, N.M.: Analytical problems in detecting rapid insulin secretory pulses in normal humans. Am. J. Physiol. **264**, E231 (1993)
3. O'Rahilly, S., Turner, R.G., Matthews, D.R.: Impaired pulsatile secretion of insulin in relatives of patients with non-ubsykub-dependent diabetes. N. Engl. J. Med. **318**, 1225 (1988)
4. Polonsky, K.S.: Twenty-four-hour profiles and pulsatile patterns of insulin secretion in normal and obese subjects. J. Clin. Invest. **81**, 442 (1988)
5. Bratusch-Marrain, P.R., Komjati, M., Waldhausl, W.K.: Efficacy of pulsatile versus continuous insulin administration on hepatic glucose production and glucose utilization in type I diabetic humans. Diabetes **35**, 922 (1986)
6. Grubert, J.M., et al.: Impact of continuous and pulsatile insulin delivery on net hepatic glucose uptake. Am. J. Physiol. Endocrinol. Metab. **289**, E232 (2005)
7. Brown, M.S., Goldstein, J.L.: Selective versus total insulin resistance: a pathogenic paradox. Cell Metab. **7**, 95 (2008)
8. Kubota, H., et al.: Temporal coding of insulin action through multiplexing of the AKT pathway. Mol. Cell **46**, 820 (2012)
9. Noguchi, R., et al.: The selective control of glycolysis, gluconeogenesis and glycogenesis by temporal insulin patterns. Mol. Syst. Biol. **9**, 664 (2013)
10. Sano, T., et al.: Selective control of up-regulated and down-regulated genes by temporal patterns and doses of insulin. Sci. Signal. **9**, ra112 (2016)
11. Whiteman, E.L., Cho, H., Birnbaum, M.J.: Role of Akt/protein kinase B in metabolism. Trends Endocrinol. Metab. **13**, 444 (2002)
12. Yugi, K., et al.: Reconstruction of insulin signal flow from phosphoproteome and metabolome data. Cell Rep. **8**, 1171 (2014)
13. Shah, O.J., Wang, Z., Hunter, T.: Inappropriate activation of the TSC/Rheb/mTOR/S6K cassette induces IRS1/2 depletion, insulin resistance, and cell survival deficiencies. Curr. Biol. **14**, 1650 (2004)
14. Boura-Halfon, S., Zick, Y.: Chapter 12 Serine kinases of insulin receptor substrate proteins. Vitam. Horm. **80**, 313 (2009)
15. Martin, J., Myers, G., White, M.F.: Insulin signal transduction and the IRS proteins. Annu. Rev. Pharmacol. Toxicol. **36**, 615 (1996)
16. Nawaz, A., Zhang, P., Li, E., Gilbert, R.G., Sullivan, M.A.: The importance of glycogen molecular structure for blood glucose control. iScience **24**, 101953 (2021)

17. Benchoula, K., Arya, A., Parhar, I.S., Hwa, W.E.: FoxO1 signaling as a therapeutic target for type 2 diabetes and obesity. Eur. J. Pharmacol. **891**, 173758 (2021)
18. Kubota, T., Kubota, N., Kadowaki, T.: Imbalanced insulin actions in obesity and type 2 diabetes: key mouse models of insulin signaling pathway. Cell Metab. **25**, 797 (2017)
19. Burant, C.F., Treutelaar, M.K., Buse, M.G.: Diabetes-induced functional and structural changes in insulin receptors from rat skeletal muscle. J. Clin. Invest. **77**, 260 (1986)
20. Ohdo, S., Koyanagi, S., Matsunaga, N.: Chronopharmacological strategies focused on chrono-drug discovery. Pharmacol. Ther. **202**, 72 (2019)

Mathematical Simulation of Linear Ubiquitination in T Cell Receptor-Mediated NF-κB Activation Pathway

Daisuke Oikawa[1], Naoya Hatanaka[2], Takashi Suzuki[3], and Fuminori Tokunaga[1(✉)]

[1] Department of Pathobiochemistry, Graduate School of Medicine, Osaka City University, Osaka, Japan
{oikawa.daisuke,ftokunaga}@med.osaka-cu.ac.jp
[2] Division of Mathematical Science, Department of Systems Innovation, Graduate School of Engineering Science, Osaka University, Toyonaka, Japan
n-hatanaka@sigmath.es.osaka-u.ac.jp
[3] Center for Mathematical Modeling and Data Science, Osaka University, Toyonaka, Japan
suzuki@sigmath.es.osaka-u.ac.jp

Abstract. The linear ubiquitin chain assembly complex (LUBAC), composed of the HOIP, HOIL-1L, and SHARPIN subunits, activates the canonical nuclear factor-κB (NF-κB) pathway through the Met1 (M1)-linked linear ubiquitination activity. On the course of the T cell receptor (TCR)-mediated NF-κB activation pathway, LUBAC transiently associates with and linearly ubiquitinates the CARMA1-BCL10-MALT1 (CBM) complex. In contrast, the linear ubiquitination of NEMO, a substrate of the TNF-α-induced NF-κB activation pathway, was limited in the TCR pathway. A linear ubiquitin-specific deubiquitinase (DUB), OTULIN, plays a major role in downregulating LUBAC-mediated TCR signaling. Mathematical modeling indicated that linear ubiquitination of the CBM complex accelerates the activation of IκB kinase (IKK), as compared with the activity induced by linear ubiquitination of NEMO alone. Moreover, simulations of the sequential linear ubiquitination of the CBM complex suggested that the allosteric regulation of linear (de)ubiquitination of CBM subunits is controlled by the ubiquitin-linkage lengths. Thus, unlike the TNF-α-induced NF-κB activation pathway, the TCR-mediated NF-κB activation in T cells has a characteristic mechanism to induce LUBAC-mediated NF-κB activation.

1 Involvement of LUBAC in TCR-Mediated NF-κB Activation

NF-κB is a crucial transcription factor controlling immune responses, inflammation, and anti-apoptosis [1, 2]. Therefore, impaired NF-κB activity is implicated in multiple diseases, including cancers, metabolic syndrome, and inflammatory, autoimmune, and neurodegenerative diseases. NF-κB activation is typically classified into canonical and non-canonical pathways [1, 2]. LUBAC is a ubiquitin ligase (E3) complex, comprising the HOIP, HOIL-1, and SHARPIN subunits (Fig. 1), that specifically generates the M1-linked linear ubiquitin chain through the E3 activity in HOIP. LUBAC linearly polyubiquitinates NF-κB essential modulator (NEMO) and receptor-interacting

serine/threonine protein kinase 1 (RIP1) upon stimulation by inflammatory cytokines, such as TNF-α and IL-1β, and activates the canonical NF-κB pathway [3–5]. Since NEMO contains a linear ubiquitin-specific binding site, the so called UBAN domain, the linear ubiquitin chain functions as a scaffold to recruit and activate the canonical IKK [6, 7]. LUBAC and its linear ubiquitination activity participate in several canonical NF-κB pathways induced by proinflammatory cytokines, pathogen-associated molecular patterns (PAMPs), and T cell receptor (TCR) pathways [8, 9], but not in the B cell receptor (BCR)-mediated canonical or the noncanonical NF-κB activation pathways [10, 11]. Importantly, LUBAC binds negative regulators of DUBs, such as OTULIN and CYLD-SPATA2 complex, through the N-terminal PUB domain of HOIP (Fig. 1) [12–14]. OTULIN, an ovarian tumor (OTU)-family DUB, directly binds to HOIP and exclusively cleaves M1-linked ubiquitin chains. OTULIN plays crucial roles in limiting cell death and inflammation [15]. Therefore, LUBAC is a unique E3-DUB complex to scrap-and-build linear ubiquitin chains.
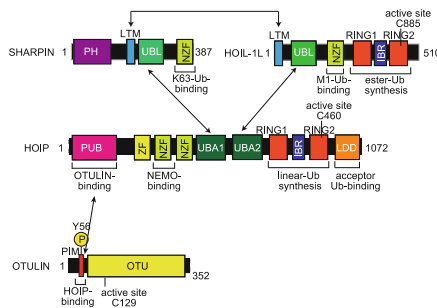
Fig. 1. Domain structure and functional regions of the LUBAC subunits, HOIL-1L, HOIP, and SHARPIN, and linear ubiquitin chain-specific DUB, OTULIN. LTM, LUBAC-tethering motif; UBL, ubiquitin-like; NZF, Npl4-type zinc finger; RING, really interesting new gene; IBR, in-between RING; PUB, PNGase/UBA or UBX; ZF, zinc finger; UBA, ubiquitin-associated; LDD, linear ubiquitin chain determining domain; PH, Pleckstrin-homology; PIM, PUB-interacting motif; OTU, ovarian tumor; P, phosphorylation.

TCR recognizes major histocompatibility complex (MHC) molecules expressed on the surface of antigen-presenting cells [16]. In the TCR-mediated NF-κB activation pathway, the protein tyrosine kinase ZAP70 is initially activated upon co-stimulation through TCR and CD28 [17], leading to the activation of protein kinase Cθ (PKCθ). Then, PKCθ phosphorylates the scaffold protein CARMA1 (CARD-containing MAGUK protein 1, also called CARD11 and Bimp3) (Fig. 2A) [18, 19]. The activated CARMA1 recruits heterodimers of B cell lymphoma 10 (BCL10) and the paracaspase mucosa-associated lymphoid tissue lymphoma translocation protein1 (MALT1) to form the oligomerized CARMA1-BCL10-MALT1 (CBM) complex, which functions as a scaffold to activate the NF-κB signaling(Fig. 2A) [18, 19]. In TCR signaling, LUBAC linearly ubiquitinates BCL10 [20–22], and MALT1 cleaves HOIL-1L upon stimulation [23, 24]. We here summarize our recently study on the cellular and mathematical analyses of LUBAC in the TCR-mediated NF-κB pathway [25].

1.1 Linear Ubiquitination of CBM Complex by LUBAC Induces TCR-Mediated NF-κB Activation

Using *HOIP*-deficient human leukemic T cell lymphoblast Jurkat cells (*HOIP*-KO), we identified that TCR-mediated NF-κB activation upon stimulation with agonistic anti-CD3 and anti-CD28 antibodies was markedly suppressed in *HOIP*-KO cells [25]. Whereas, the ZAP70 was similarly phosphorylated in parental and *HOIP*-KO cells upon TCR stimulation. In contrast, the phosphorylation of IKKα/β, which represents IKK activation, was strongly impaired by the ablation of *HOIP*. Thus, the LUBAC activity is involved downstream from ZAP70, and upstream from IKK activation (Fig. 2A). In the absence of LUBAC activity, the expression of IL-2 was suppressed, which caused the reduced T cell activation. Thus, LUBAC plays a pivotal role in the TCR-mediated NF-κB activation and T cell activation [25].

Upon TCR stimulation, endogenous LUBAC transiently binds with the CBM complex (Fig. 2A). Co-immunoprecipitation experiments indicated that HOIP, but not HOIL-1L or SHARPIN, bound to CARMA1 and MALT1, whereas the direct binding of LUBAC subunits with BCL10 was negligible. LUBAC reportedly linearly ubiquitinates BCL10 in the CBM complex [22], whereas we showed that CBM subunits were transiently linearly ubiquitinated after TCR stimulation with different time courses. Thus, MALT1 was initially linearly ubiquitinated after 15 min as the maximum, and subsequently, CARMA1 (20 min) and BCL10 (25 min) were linearly ubiquitinated (Fig. 2B) [25]. NEMO is a physiological substrate of LUBAC upon TNF-α stimulation [26], and it functions as a scaffold to recruit other IKK molecules [6]. The recruited and concentrated IKK molecules are then activated by *trans*-phosphorylation [7]. Indeed, NEMO was efficiently linearly ubiquitinated upon TNF-α stimulation, whereas the linear ubiquitination of NEMO was suppressed upon TCR stimulation. In contrast, MALT1 was linearly ubiquitinated by a TCR stimulation, but not by TNF-α stimulation. These results suggested that the CBM complex is the major substrate of LUBAC during TCR-mediated NF-κB activation. Furthermore, upon TCR stimulation, the canonical IKK activity reached the maximum after 15 min of stimulation, and declined thereafter, suggesting the linear ubiquitination of MALT1 triggers IKK activation (Fig. 2B) [25]. Collectively, these results suggested that the linear ubiquitination of the CBM complex by LUBAC correlates with the canonical IKK activation in the TCR-mediated NF-κB activation pathway.

1.2 OTULIN Is the Predominant Regulator of TCR-Mediated NF-κB Activation

DUBs, such as OTULIN and the CYLD-SPATA2 complex, bind to the PUB domain of HOIP and downregulate NF-κB activity by hydrolyzing the ubiquitin chains [12–14]. To examine the effect of these DUBs on the TCR-mediated NF-κB activation, we constructed *CYLD*- and *OTULIN*-deficient Jurkat cells. Upon TCR stimulation, the phosphorylation of NF-κB factors was enhanced in *OTULIN*-KO cells, but not in *CYLD*-KO cells. In *OTULIN*-KO cells, linear ubiquitination of MALT1 was augmented ~3-fold over that of the parental Jurkat cells [25]. In *OTULIN*-deficient cells, canonical IKK was transiently activated with a time course similar to that of the parental cells. These results suggested that OTULIN plays a major role in the downregulation of the LUBAC-mediated canonical NF-κB activation pathways in T cells.
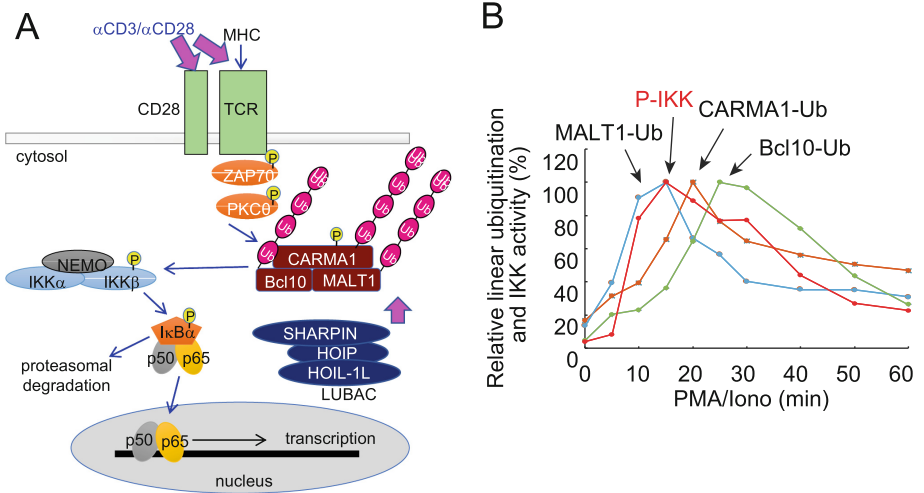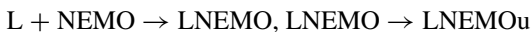
Fig. 2. Linear ubiquitination of CBM complex and resulting IKK activation. (A) Scheme for LUBAC-mediated linear ubiquitination of CBM complex in TCR pathway. (B) TCR-mediated linear ubiquitination of CBM complex and canonical IKK activation in Jurkat cells. Taking the maximum intensities of linear ubiquitination and IKK activity as 100%, the relative intensities are indicated.

2 Mathematical Simulation of Linear Ubiquitination-Mediated IKK Activation in TCR Pathway

To investigate the characteristics of LUBAC in the TCR-mediated NF-κB activation pathway, we mathematically considered the reaction of LUBAC-mediated IKK activation through the linear ubiquitination of NEMO and CBM (Fig. 3A). Since IKK is *trans*-activated by using the linear ubiquitin chain as a scaffold, the NEMO-mediated activation of IKK occurs between ubiquitinated IKKs or between ubiquitinated IKKs and non-ubiquitinated IKKs. On the other hand, the CBM-mediated activation of IKK occurs by contact between ubiquitinated CBM and IKKs that are not distinguished by their ubiquitination state. In addition, the mass conservation law for the LUBAC and CBM complex holds, because protein production and degradation are not considered. Then, we constructed mathematical models of NF-κB signaling based on the law of mass action [27]. In order to investigate the effect of the CBM complex on IKK activation in T cells, the following two models were constructed. The first was the CBM simplify model (CBM_SM), which includes the reaction of IKK activation depending on the linear ubiquitin chain of NEMO and the CBM complex. In this model, we simulated the effect of the CBM complex on the IKK activation by changing the parameters related to ubiquitination. The reaction involves the transient binding of LUBAC with NEMO or CBM, followed by the LUBAC-mediated linear ubiquitination of the proteins in the bound state.

L + NEMO → LNEMO, LNEMO → LNEMOu
L + CBM → LCBM, LCBM → LCBMu

A

B

Symbol	Value	Unit	Description
kc	1.482817	1/μM	CBM-LUBAC association
lc	0.770128	1/min	CBM-LUBAC dissociation
uc	0.217147	1/min	CBM ubiquitination
dc	0.178648	1/min	CBM deubiquitination
kN	1.210012	1/μM min	NEMO-LUBAC association
lN	0.813971	1/min	NEMO-LUBAC dissociation
uN	0.04963	1/min	NEMO ubiquitination
dN	0.399584	1/min	NEMO deubiquitination
pc	0.463834	1/μM^2 min	CBM-mediated IKK phosphorylation
pl	0.085297	1/μM min	NEMO-mediated IKK phosphorylation
dp	0.682746	1/min	IKK dephosphorylation
Ltot	0.379065	μM	amount of LUBAC
CBMtot	2.317712	μM	amount of CBM complex
IKKtot	0.178664	μM	amount of IKK

C

Fig. 3. Mathematical simulation of the effects of linear ubiquitination of the CBM complex and NEMO on the TCR-mediated IKK activation. (A) LUBAC ubiquitinates NEMO and the CBM complex. In this model, ubiquitination is assumed to be a first-order reaction. (B) Fitting result by GA. Solid lines represent simulation results, and dots represent experimental data. Figure 3A, 3B, and 3C are originally shown in Fig. 6A, Table 1, and Fig. 6B, respectively, of Ref. [25].

After dissociation, the LUBAC-bound NEMO or CBM was postulated to exist in a temporarily inactive form (prime symbol (′) represents inactive state).
LNEMO → L + NEMO′
LCBM → L + CBM′
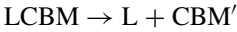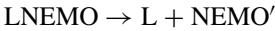
The linear ubiquitin chains are cleaved by DUBs, such as CYLD and OTULIN. Since CYLD and OTULIN stably bind LUBAC, LUBAC/NEMOu and NEMOu may have different deubiquitination coefficients. The model is characterized by the following equations, and parameters are shown in Fig. 3B;

$$\frac{dCBM}{dt} = -k_C\, CBM(t)(L_{tot} - LCBM(t) - LCBM_u(t) - LIKK(t) - LIKK_u(t))$$

$$\frac{dLCBM}{dt} = k_C\, CBM(t)(L_{tot} - LCBM(t) - LCBM_u(t) - LIKK(t) - LIKK_u(t))$$
$$- (u_C + l_C)\, LCBM(t) + d_C\, LCBM_u(t)$$

$$\frac{dLCBM_u}{dt} = u_C\, LCBM(t) - (d_C + l_C)\, LCBM_u(t)$$

$$\frac{dCBM_{du}}{dt} = l_C\, LCBM_u(t) - a\, d_C\, CBM_{du}(t)$$

$$\frac{dLIK}{dt} = k_N(L_{tot} - LCBM(t) - LCBM_u(t) - LIKK(t) - LIKK_u(t))\,(IKK_{tot} - IKK_u(t)$$
$$- LIKK(t) - LIKK_u(t) - IKK_p(t) - IKK_{up}(t) - IKKd(t) - IKKd_u(t))$$

$$-LIKK_p(t) - LIKK_{up}(t) - IKKd_p(t) - IKKd_{up}(t)\big) - (l_C + u_N)\, LIKK(t)$$
$$+ d_N\, LIKK_u(t) + d_p\, LIKK_p(t) - p_C(LCBM_u(t) + CBMd_u(t))\, LIKK(t)IKK_{tot}$$
$$- p_I\, LIKK(t)\big(LIKK_u(t) + IKK_u(t) + IKK_{up}(t) + IKKd_{up}(t)\big)$$

$$\frac{dLIKK_u}{dt} = u_N\, LIKK(t) - (d_N + l_C)\, LIKK_u(t) + d_p\, LIKK_{up}(t)$$
$$- p_C(LCBM_u(t) + CBMd_u(t))\, LIKK_u(t)\, IKK_{tot} - p_I\, LIKK_u(t)\, IKK_{tot}$$

$$\frac{dIKK_u}{dt} = -p_C(LCBM_u(t) + CBMd_u(t))\, IKK_u(t)\, IKK_{tot}$$

$$\frac{dIKKd}{dt} = l_C\, LIKK(t) + d_N\, IKKd_u(t) + d_p\, IKKd_p(t)$$
$$- p_C(LCBM_u(t) + CBMd_u(t))\, IKKd(t)\, IKK_{tot}$$
$$- p_I\, IKKd(t)\, \big(LIKK_u(t) + IKK_u(t) + IKK_{up}(t) + IKKd_{up}(t)\big)$$

$$\frac{dIKKd_u}{dt} = l_C\, LIKK_u(t) - d_N\, IKKd_u(t) + d_p\, IKKd_{up}(t)$$
$$- p_C(LCBM_u(t) + CBMd_u(t))\, IKKd_u(t)\, IKK_{tot} - p_I\, IKKd_u(t)\, IKK_{tot}$$
$$\frac{dIKK_p}{dt} = p_C(LCBM_u(t) + CBMd_u(t))\big(IKK_{tot} - IKK_u(t) - LIKK(t) - LIKK_u(t) - IKK_p(t)$$
$$- IKK_{up}(t) - IKKd(t) - IKKd_u(t) - LIKK_p(t) - LIKK_{up}(t) - IKKd_p(t)$$
$$- IKKd_{up}(t)\big)IKK_{tot}$$
$$+ p_I\big(IKK_{tot} - IKK_u(t) - LIKK(t) - LIKK_u(t) - IKK_p(t) - IKK_{up}(t)$$
$$- IKKd(t) - IKKd_u(t) - LIKK_p(t) - LIKK_{up}(t) - IKKd_p(t)$$
$$- IKKd_{up}(t)\big)\big(LIKK_u(t) + IKK_u(t) + IKK_{up}(t) + IKKd_{up}(t)\big)$$

$$\frac{dLIKK_p}{dt} = p_C(LCBM_u(t) + CBMd_u(t))\, LIKK(t)\, IKK_{tot}$$
$$+ p_I\, LIKK(t)\big(LIKK_u(t) + IKK_u(t) + IKK_{up}(t) + IKKd_{up}(t)\big) - d_p\, LIKK_p(t)$$
$$+ d_N\, LIKK_{up}(t)$$

$$\frac{dLIKK_{up}}{dt} = p_C(LCBM_u(t) + CBMd_u(t))\, LIKK_u(t)\, IKK_{tot} + p_I\, LIKK_u(t)\, IKK_{tot}$$
$$- \big(d_p + d_N\big)\, LIKK_{up}(t)$$

$$\frac{dIKK_{up}}{dt} = p_C(LCBM_u(t) + CBMd_u(t))\, IKK_u(t)\, IKK_{tot} + p_I\, IKK_u(t)\, IKK_{tot}$$
$$- \big(d_p + d_N\big)\, IKK_{up}(t)$$
$$\frac{dIKKd_p}{dt} = p_C(LCBM_u(t) + CBMd_u(t))\, IKKd(t)\, IKK_{tot}$$
$$+ p_I\, IKKd(t)\big(LIKK_u(t) + IKK_u(t) + IKK_{up}(t) + IKKd_{up}(t)\big) - d_p\, IKKd_p(t)$$
$$+ d_N\, IKKd_{up}(t)$$

$$\frac{dIKKd_{up}}{dt} = p_C(LCBM_u(t) + CBMd_u(t))\, IKKd_u(t)\, IKK_{tot} + p_I\, IKKd_u(t)\, IKK_{tot}$$

$$- \left(d_p + d_N \right) IKKd_{up}(t)$$

The parameters of CBM_SM were set by a genetic algorithm (GA), using experimental data of the ubiquitinated CBM complex and phosphorylated IKK (Fig. 3C) [25]. The estimation was performed 1,000 times with the setting to generate 1,000 generations. We set the estimation results such that the error from the experimental data is small and the concentrations of LUBAC, CBM, and IKK were close to the concentrations of general signal transduction factors (0.1 μM). However, all of the parameter settings were values larger than 0.1 μM, since proteins with different molecular weights accumulate and are locally concentrated on the linear ubiquitin chains, and T cells are smaller than general somatic cells. Importantly, the parameters obtained by the GA showed that the CBM complex is more likely to bind to LUBAC than NEMO ($k_C > k_N$) (Fig. 3B, C). Moreover, the ubiquitination rate of the CBM complex was faster than that of NEMO ($u_C > u_N$). These results suggested that IKK activation induced by the linear ubiquitination of the CBM complex plays a major role to activate IKK in T cells, by the linear ubiquitination of NEMO.

3 Mathematical Simulation for Linear Ubiquitination of CBM Complex Components

Finally, we constructed an expanded model to analyze the timing deviations in the linear ubiquitinations of CARMA1, BCL10, and MALT1. By focusing on the linear ubiquitination of the CBM complex, we constructed a model that distinguishes CARMA1, BCL10, and MALT1. The amounts of ubiquitinated proteins were then simulated. If the ubiquitination and deubiquitination rates of CARMA1, BCL10, and MALT1 were the same values, then the CBM detailed model (CBM_DM) is represented by the same model as the CBM_SM, by equating CARMA1, BCL10, and MALT1. In this model, we assumed that ubiquitination is a first-order reaction for simplicity (Fig. 4A).

The CBM_DM focused only on the ubiquitination reaction of the CBM complex to elucidate the mechanisms of timing shift of ubiquitination. CARMA1, BCL10, and MALT1 were distinguished, and the reaction coefficients of the ubiquitination of each protein were compared.

$$x_0'(t) = -k_0 x_0(t) \, LUBAC(t)$$

$$LUBAC'(t) = -k_0 x_0(t) \, LUBAC(t) \\ + l_0(x_1(t) + x_2(t) + x_3(t) + x_4(t) + x_5(t) + x_6(t) + x_7(t) + x_8(t))$$

$$x_1'(t) = k_0 x_0(t) \, LUBAC(t) - k_1 x_1(t) + l_1 x_2(t) - k_2 x_1(t) + l_2 x_3(t) - k_3 x_1(t) + l_3 x_4(t) \\ - l_0 x_1(t)$$

$$x_2'(t) = k_1 x_1(t) - l_1 x_2(t) - k_4 x_2(t) + l_4 x_5(t) - k_5 x_2(t) + l_5 x_6(t) - l_0 x_2(t)$$

$$x_3'(t) = k_2 x_1(t) - l_2 x_3(t) - k_6 x_3(t) + l_6 x_5(t) - k_7 x_3(t) + l_7 x_7(t) - l_0 x_3(t)$$

$$x'_4(t) = k_3x_1(t) - l_3x_4(t) - k_8x_4(t) + l_8x_6(t) - k_9x_4(t) + l_9x_7(t) - l_0x_4(t)$$

$$x'_5(t) = k_4x_2(t) - l_4x_5(t) + k_6x_3(t) - l_6x_5(t) - k_{10}x_5(t) + l_{10}x_8(t) - l_0x_5(t)$$

$$x'_6(t) = k_5x_2(t) - l_5x_6(t) + k_8x_4(t) - l_8x_6(t) - k_{11}x_6(t) + l_{11}x_8(t) - l_0x_6(t)$$

$$x'_7(t) = k_7x_3(t) - l_7x_7(t) + k_9x_4(t) - l_9x_7(t) - k_{12}x_7(t) + l_{12}x_8(t) - l_0x_7(t)$$

$$x'_8(t) = k_{10}x_5(t) - l_{10}x_8(t) + k_{11}x_6(t) - l_{11}x_8(t) + k_{12}x_7(t) - l_{12}x_8(t) - l_0x_8(t)$$

$$y'_1(t) = a(l_1y_2(t) + l_2y_3(t) + l_3y_4(t)) + l_0x_1(t)$$

$$y'_2(t) = a(-l_1y_2(t) + l_4y_5(t) + l_5y_6(t)) + l_0x_2(t)$$

$$y'_3(t) = a(-l_2y_3(t) + l_6y_5(t) + l_7y_7(t)) + l_0x_3(t)$$

$$y'_4(t) = a(-l_3y_4(t) + l_8y_6(t) + l_9y_7(t)) + l_0x_4(t)$$

$$y'_5(t) = a(-l_4y_5(t) - l_6y_5(t) + l_{10}y_8(t)) + l_0x_5(t)$$

$$y'_6(t) = a(-l_5y_6(t) - l_8y_6(t) + l_{11}y_8(t)) + l_0x_6(t)$$

$$y'_7(t) = a(-l_7y_7(t) - l_9y_7(t) + l_{12}y_8(t)) + l_0x_7(t)$$

$$y'_8(t) = a(-l_{10}y_8(t) - l_{11}y_8(t) - l_{12}y_8(t)) + l_0x_8(t)$$

As a result of fitting with the GA, the timing shifts of the peaks of MALT1, CARMA1, and BCL10 could be reproduced. However, in this simulation, the increase and decrease of ubiquitination levels did not match well. Therefore, more detailed modeling of ubiquitination is needed to solve this problem. Since ubiquitin is consecutively linked and its activity changes depending on its length, ubiquitination cannot be expressed well by the assumption of the first-order reaction. The model could be improved by considering the production levels of linear (de)-ubiquitination of MALT1, CARMA1, and BCL10 as a switch-like reaction; for example, by applying the Hill equation (Fig. 4B). These results indicated that length of the ubiquitin-linkage allosterically regulates the generation and degradation of linear ubiquitin chains.
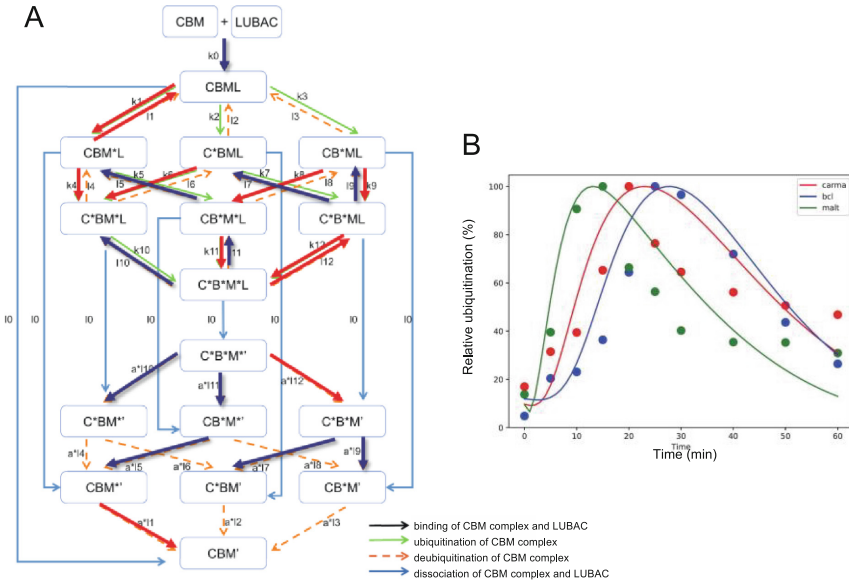
Fig. 4. Mathematical model for different linear ubiquitinations of the CBM complex. (A) Detailed reaction pathway of the ubiquitination of the CBM complex. The red lines show parameters that are larger than the average value. The blue lines show parameters that are smaller than the average value. (B) Fitting results by GA. The ubiquitination reaction is assumed to be a Hill function. Figure 4A and 4B are originally shown in Fig. 7A and 7C, respectively, of Ref. [25].

4   Conclusion

T cells play crucial roles in the host defence against pathogens and tumors, and TCR recognizes the MHC-bound antigen peptide fragments derived from them [16]. We initially identified that LUBAC is indispensable for the TCR-mediated NF-κB pathway and T cell activation. LUBAC physiologically associates with the CBM complex, and BCL10, MALT1, and CARMA1 are linearly ubiquitinated by LUBAC, suggesting that the CBM complex components are physiological substrates for LUBAC. Among them, the linear ubiquitination of MALT1 seems to precede the canonical IKK activation. Moreover, we determined that OTULIN plays a pivotal role in the suppression of TCR-mediated NF-κB activation.

The mathematical analysis of the NF-κB signaling pathway has provided a novel paradigm for spatiotemporal activation mechanism, target gene expression, feed-back inhibition, and cytosol-nucleus oscillation of the transcription factor, and various mathematical models have been proposed [28–30]. In contrast to TNF-α-mediated NF-κB activation pathway, the CBM complex, but not NEMO, was preferentially ubiquitinated by LUBAC upon TCR stimulation, and the mathematical analysis indicated that linear ubiquitination of the CBM complex stably promotes IKK activation. On the other hand, NEMO-mediated activation of IKK was required to increase the activation level of IKK. In addition, we identified the differences in the timing of ubiquitination between

CARMA1, BCL10, and MALT1 in the CBM complex, although its physiological function was not clear. The mathematical modeling suggested that by shifting the timing of the MALT1, CARMA1, and BCL10 ubiquitinations, the scaffolding of ubiquitin chains persists, and IKK can be stably activated due to the allosteric regulation. Moreover, DUBs, such as OTULIN, can quickly downregulate IKK and then restore it to the original state. Thus, these mathematical simulations were effective in characterizing the experimentally obtained features in TCR-mediated NF-κB pathway.

References

1. Zhang, Q., Lenardo, M.J., Baltimore, D.: 30 Years of NF-κB: a blossoming of relevance to human pathobiology. Cell **168**(1–2), 37–57 (2017). https://doi.org/10.1016/j.cell.2016.12.012

2. Hayden, M.S., Ghosh, S.: NF-κB, the first quarter-century: remarkable progress and outstanding questions. Genes Dev. **26**(3), 203–234 (2012). https://doi.org/10.1101/gad.183434.111

3. Sasaki, K., Iwai, K.: Roles of linear ubiquitinylation, a crucial regulator of NF-κB and cell death, in the immune system. Immunol. Rev. **266**(1), 175–189 (2015). https://doi.org/10.1111/imr.12308

4. Shimizu, Y., Taraborrelli, L., Walczak, H.: Linear ubiquitination in immunity. Immunol. Rev. **266**(1), 190–207 (2015). https://doi.org/10.1111/imr.12309

5. Ikeda, F.: Linear ubiquitination signals in adaptive immune responses. Immunol. Rev. **266**(1), 222–236 (2015). https://doi.org/10.1111/imr.12300

6. Rahighi, S., Ikeda, F., Kawasaki, M., Akutsu, M., Suzuki, N., Kato, R., et al.: Specific recognition of linear ubiquitin chains by NEMO is important for NF-κB activation. Cell **136**(6), 1098–1109 (2009)

7. Fujita, H., Rahighi, S., Akita, M., Kato, R., Sasaki, Y., Wakatsuki, S., et al.: Mechanism underlying IκB kinase activation mediated by the linear ubiquitin chain assembly complex. Mol. Cell Biol. **34**(7), 1322–1335 (2014). https://doi.org/10.1128/MCB.01538-13

8. Iwai, K., Fujita, H., Sasaki, Y.: Linear ubiquitin chains: NF-κB signalling, cell death and beyond. Nat. Rev. Mol. Cell Biol. **15**(8), 503–508 (2014). https://doi.org/10.1038/nrm3836

9. Rittinger, K., Ikeda, F.: Linear ubiquitin chains: enzymes, mechanisms and biology. Open Biol. **7**(4) (2017). https://doi.org/10.1098/rsob.170026

10. Sasaki, Y., Sano, S., Nakahara, M., Murata, S., Kometani, K., Aiba, Y., et al.: Defective immune responses in mice lacking LUBAC-mediated linear ubiquitination in B cells. EMBO J. **32**(18), 2463–2476 (2013). https://doi.org/10.1038/emboj.2013.184

11. Tokunaga, F., Nakagawa, T., Nakahara, M., Saeki, Y., Taniguchi, M., Sakata, S., et al.: SHARPIN is a component of the NF-κB-activating linear ubiquitin chain assembly complex. Nature **471**(7340), 633–636 (2011). https://doi.org/10.1038/nature09815

12. Elliott, P.R., Nielsen, S.V., Marco-Casanova, P., Fiil, B.K., Keusekotten, K., Mailand, N., et al.: Molecular basis and regulation of OTULIN-LUBAC interaction. Mol. Cell **54**(3), 335–348 (2014). https://doi.org/10.1016/j.molcel.2014.03.018

13. Schaeffer, V., Akutsu, M., Olma, M.H., Gomes, L.C., Kawasaki, M., Dikic, I.: Binding of OTULIN to the PUB domain of HOIP controls NF-κB signaling. Mol. Cell **54**(3), 349–361 (2014). https://doi.org/10.1016/j.molcel.2014.03.016

14. Elliott, P.R., Leske, D., Hrdinka, M., Bagola, K., Fiil, B.K., McLaughlin, S.H., et al.: SPATA2 Links CYLD to LUBAC, activates CYLD, and controls LUBAC signaling. Mol. Cell **63**(6), 990–1005 (2016). https://doi.org/10.1016/j.molcel.2016.08.001

15. Heger, K., Wickliffe, K.E., Ndoja, A., Zhang, J., Murthy, A., Dugger, D.L., et al.: OTULIN limits cell death and inflammation by deubiquitinating LUBAC. Nature **559**(7712), 120–124 (2018). https://doi.org/10.1038/s41586-018-0256-2

16. Alcover, A., Alarcon, B., Di Bartolo, V.: Cell biology of T cell receptor expression and regulation. Annu. Rev. Immunol. **36**, 103–125 (2018). https://doi.org/10.1146/annurev-immunol-042617-053429

17. Au-Yeung, B.B., Shah, N.H., Shen, L., Weiss, A.: ZAP-70 in signaling, biology, and disease. Annu. Rev. Immunol. **36**, 127–156 (2018). https://doi.org/10.1146/annurev-immunol-042617-053335

18. Thome, M., Charton, J.E., Pelzer, C., Hailfinger, S.: Antigen receptor signaling to NF-κB via CARMA1, BCL10, and MALT1. Cold Spring Harb. Perspect. Biol. **2**(9), a003004 (2010). https://doi.org/10.1101/cshperspect.a003004

19. Meininger, I., Krappmann, D.: Lymphocyte signaling and activation by the CARMA1-BCL10-MALT1 signalosome. Biol. Chem. **397**(12), 1315–1333 (2016). https://doi.org/10.1515/hsz-2016-0216

20. Dubois, S.M., Alexia, C., Wu, Y., Leclair, H.M., Leveau, C., Schol, E., et al.: A catalytic-independent role for the LUBAC in NF-κB activation upon antigen receptor engagement and in lymphoma cells. Blood **123**(14), 2199–2203 (2014). https://doi.org/10.1182/blood-2013-05-504019

21. Satpathy, S., Wagner, S.A., Beli, P., Gupta, R., Kristiansen, T.A., Malinova, D., et al.: Systems-wide analysis of BCR signalosomes and downstream phosphorylation and ubiquitylation. Mol. Syst. Biol. **11**(6), 810 (2015). https://doi.org/10.15252/msb.20145880

22. Yang, Y.K., Yang, C., Chan, W., Wang, Z., Deibel, K.E., Pomerantz, J.L.: Molecular determinants of scaffold-induced linear ubiquitinylation of B cell lymphoma/leukemia 10 (Bcl10) during T cell receptor and oncogenic caspase recruitment domain-containing protein 11 (CARD11) signaling. J. Biol. Chem. **291**(50), 25921–25936 (2016). https://doi.org/10.1074/jbc.M116.754028

23. Douanne, T., Gavard, J., Bidere, N.: The paracaspase MALT1 cleaves the LUBAC subunit HOIL1 during antigen receptor signaling. J. Cell Sci. **129**(9), 1775–1780 (2016). https://doi.org/10.1242/jcs.185025

24. Elton, L., Carpentier, I., Staal, J., Driege, Y., Haegman, M., Beyaert, R.: MALT1 cleaves the E3 ubiquitin ligase HOIL-1 in activated T cells, generating a dominant negative inhibitor of LUBAC-induced NF-κB signaling. FEBS J. **283**(3), 403–412 (2016). https://doi.org/10.1111/febs.13597

25. Oikawa, D., Hatanaka, N., Suzuki, T., Tokunaga, F.: Cellular and mathematical analyses of LUBAC involvement in T cell receptor-mediated NF-κB activation pathway. Front. Immunol. **11**, 601926 (2020). https://doi.org/10.3389/fimmu.2020.601926

26. Tokunaga, F., Sakata, S., Saeki, Y., Satomi, Y., Kirisako, T., Kamei, K., et al.: Involvement of linear polyubiquitylation of NEMO in NF-κB activation. Nat. Cell Biol. **11**(2), 123–132 (2009). https://doi.org/10.1038/ncb1821

27. Hatanaka, N., Seki, T., Inoue, J.I., Tero, A., Suzuki, T.: Critical roles of IκBα and RelA phosphorylation in transitional oscillation in NF-κB signaling module. J. Theor. Biol. **462**, 479–489 (2019). https://doi.org/10.1016/j.jtbi.2018.11.023

28. Hoffmann, A., Levchenko, A., Scott, M.L., Baltimore, D.: The IκB-NF-κB signaling module: temporal control and selective gene activation. Science **298**(5596), 1241–1245 (2002). https://doi.org/10.1126/science.1071914

29. Basak, S., Behar, M., Hoffmann, A.: Lessons from mathematically modeling the NF-κB pathway. Immunol. Rev. **246**(1), 221–238 (2012). https://doi.org/10.1111/j.1600-065X.2011.01092.x
30. Ohshima, D., Inoue, J., Ichikawa, K.: Roles of spatial parameters on the oscillation of nuclear NF-κB: computer simulations of a 3D spherical cell. PLoS ONE **7**(10), e46911 (2012). https://doi.org/10.1371/journal.pone.0046911

Time Changes in the VEGF-A Concentration Gradient Lead Neovasculature to Engage in Stair-Like Growth

Yukinobu Ito[1(✉)], Dhisa Minerva[2], Sohei Tasaki[3], Makoto Yoshida[1], Takashi Suzuki[2], and Akiteru Goto[1]

[1] Department of Cellular and Organ Pathology, Graduate School of Medicine, Akita University, 1-1-1 Hondo, Akita, Akita 010-8543, Japan
xing-xin@rhythm.ocn.ne.jp
[2] Center for Mathematical Modeling and Data Science, Osaka University, Osaka, Japan
[3] Institute for the Advanced Study of Human Biology, Kyoto University, Kyoto, Japan

Abstract. Arteriovenous malformations consist of tangles of arteries and veins that are often connected by a fistula. The causes of and mechanisms underlying the development of these clinical entities are not fully understood. We previously reported a novel in vivo angiogenesis model as a useful disease model of arteriovenous malformation. With this model, the arterial graft was collected from the left carotid artery and sutured to the left jugular vein as a patchwork. The neovasculature extended from the branch of the subclavian artery toward the arterial graft. We measured the neovasculature, which had sprouted from arterioles, in the tissue samples. In the present study, we collected the arterial patch graft and adipose tissue surrounding the arterial graft and examined the distribution of the VEGF concentration by an enzyme-linked immunosorbent assay. At the area most distant from the arterial graft, the VEGF-A concentration changed over time in a sine wave pattern that gradually attenuated. A mathematical model was then constructed using the results, and a mathematical simulation of the neovasculature growth was performed. The new vessels grew in a stair-like pattern in this simulation, a result that matched those obtained through histological measurements.

1 Introduction

Angiogenesis is a fundamental developmental and adult physiological process, requiring the coordinated action of a variety of growth factors and cell-adhesion molecules in endothelial and mural cells [1–3]. At present, VEGF-A and its receptors are the best-characterized signaling pathways in developmental angiogenesis [1–3]. VEGF-A is produced by most cells in the body but is upregulated under conditions of hypoxia [4,5]. In tumors, VEGF is produced by hypoxic

tumor cells, endothelial cells (ECs) and infiltrating myeloid cells, termed tumor-associated macrophages [5]. In mathematical oncology, mathematical modeling of tumor angiogenesis has been performed, and the Anderson-Chaplain equation is famous among such models [6]. In the mathematical modeling of tumor angiogenesis, VEGF is released by malignant tumors, and new blood vessels then sprout toward the tumor, expanding toward the site with the highest VEGF concentration.

However, in our in vivo angiogenesis model that we previously reported, new blood vessels sprouted from pre-existing arteries toward the arterial patch graft (Fig. 1a) and opened around the arterial graft. We herein report the change in the VEGF concentration in this angiogenesis model and propose a new mathematical model modified from the Anderson-Chaplain model.

2 Quantification and Fluctuations of VEGF in Our Angiogenesis Animal Model

2.1 Tissue Collection and VEGF Quantification

In the in vivo angiogenesis model developed by Ito et al., the arterial graft is sutured to the wall of the left common jugular vein in male rabbits to initiate angiogenesis [7]. In this model, we measured the VEGFA concentration of the tissue involved in angiogenesis to observe its space and time variation. In brief, two rabbits at each time point (5 min; 1 and 3 h; and 1, 3, 7, 10, and 14 days) after grafting were euthanized, and the arterial graft and fatty tissue were divided and collected from 8 areas (Fp and F1-7), as shown schematically in Fig. 1b.

Total protein was extracted from these collected tissues using a Minute Detergent-Free Total Protein Extraction Kit obtained from Invent Biotechnologies, Inc. (Plymouth, MN, USA). The VEGFA concentration in the tissue was measured using rabbit VEGFA enzyme-linked immunosorbent assay (ELISA) kits purchased from Cusabio Biotech Co., Ltd. (Wuhan, China). The concentration of VEGFA in each sample was calculated based on the recombinant protein-based standard curve. A Multiskan JX spectrophotometer (Thermo Fisher Scientific Inc., Yokohama, Japan) was used to measure the absorbance. All assays were performed in duplicate, and the mean value of the results was used in the analyses.

2.2 Dampened Oscillation of VEGF Concentration at F4/5

We measured the VEGF concentration in eight areas (Fp and F1-7). The VEGF concentration at Fp in each case was low and equal to that in serum. The VEGF concentrations at tissue areas of F4 and F5 were higher than in other areas, including Fp and F1, F2, and F3. Time-course analyses of the VEGF concentrations at F4 and F5 with an ELISA revealed repeated increases and decreases with gradual attenuation. The polynomial approximation of the fluctuation is shown
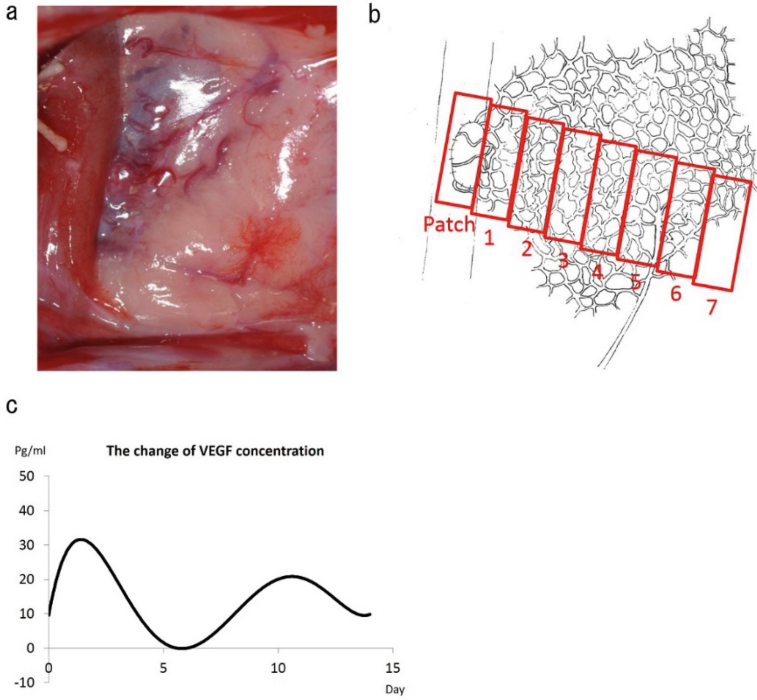
Fig. 1. The method of this study and the fluctuations of VEGF concentration

in Fig. 1c. The waveform of the VEGF concentration at F4 and F5 showed attenuation with oscillation. This pattern suggested the involvement of the formation of new blood vessels.

F4 and F5 are located approximately 1 to 1.5 cm from the common jugular vein, which is the site of a pre-existing arterial branch that nourishes the adipose tissue of the neck. We previously reported that new blood vessels sprouted from this pre-existing arterial branch near F4 and F5 [7]. In our angiogenesis model, new blood vessels originate from the pre-existing artery and head to Fp. Based on these observations, we suspect that VEGF is released from the area where new blood vessels sprout and grow.

3   Mathematical Modeling

3.1   VEGF Concentration and Sprouting Tip Cells in This Model

Our angiogenesis model incorporated two important components: the tip sprout and VEGF distributions. Let $n = n(x, t)$ and $c = c(x, t)$ be the sprout tip distribution and VEGF concentration, respectively, on a two-dimensional domain, $x = (x, y) \in R^2, \quad 0 \leq t \in R$. First, we will explain the mathematical equation for the VEGF distribution.

3.2 VEGF Concentration Equation

The highest VEGF concentration is located most closely to the area of pre-existing artery, F4 and F5. The VEGF concentration decreases as it approaches the arterial patch but can be high or low in different periods. The data in Fig. 1c show that the VEGF concentration is damped and oscillated in the area of F4 and F5. We therefore assumed the VEGF distribution to oscillate with the following pattern:

$$c = \begin{cases} \frac{c_1}{4}(1 + \sin(\pi(\frac{1}{2} - x)))(1 + \sin(2\pi\sigma t)) & (c_t > 0) \\ 0 & (c_t \leq 0) \end{cases}$$

where c_1, σ are constants that represent the peak concentration and oscillation speed, respectively.

3.3 Sprouting Tip Cell Distribution Equation

The sprout tip is assumed to migrate under the influence of random movement and chemotactic responses to VEGF. The general conservation equation is thus as follows:

$$n_t = d_n \Delta n - \nabla n v_n,$$

where d_n is a constant of random movement and $v_n = v_n(x, t)$ is the chemotactic velocity of the sprout tip.

Despite there being few sprouts growing from the arterial patch area to meet new blood vessels growing from nearby pre-existing vessels, those new blood vessels still reportedly extend from the nearby pre-existing vessel toward the arterial patch [7]. We assume that the sprouted tip migrates due to a gradient change in the VEGF concentrations. Thus, v_n has the following form:

$$v_n = c_t$$

This notion of velocity stems from the aggregation of the Dictyostelium model under a cyclic AMP (cAMP) non-dissipating wave. Dictyostelium continues to aggregate toward the center of the cAMP source, while the cAMP waves are emitted from the center in the opposite direction [8]. This means that the Dictyostelium becomes the driving force in the reverse direction of cAMP. Through this model, we can understand the three factors of signal gradient, moving speed, and gradient change at the same time.

First, let us assume that cAMP, which we consider to stand for VEGF in the angiogenesis model, is signal S, and the activator and inhibitor of the cellular derived from signal S are A and I, respectively. The following are then equations describing the chemical interactions between S-A-I

$$\frac{dA(t)}{dt} = k_a S(x, t) - \gamma_a A(t), \quad \frac{dI(t)}{dt} = k_i S(x, t) - \gamma_i I(t), \tag{1}$$

where k_a, k_i, γ_a, and γ_i are constants.

Through these *S*-*A*-*I* interactions, the output response of R as activation within the cell, denoted as R, is expressed as follows:

$$\frac{dR(t)}{dt} = F(R(t))A(t) - G(R(t))I(t), \tag{2}$$

where,

$$F(R(t)) = k_A \frac{(R_0 - R(t))}{(R_0 - R(t)) + K'_A}, \quad G(R(t)) = k_I \frac{R(t)}{R(t) + K'_I}$$

are ultrasensitive transfer functions [8].

In the steady state of (2), we find that

$$Q \equiv \frac{A}{I} = \frac{G}{F}(R). \tag{3}$$

Now, consider (2) as

$$\frac{dR(t)}{dt} = F(R)I(\frac{A}{I} - H(R))$$

where

$$H(R) = G(R)/F(R).$$

Second, we approximated the solution of A(t) and I(t). Define

$$E(t) \equiv A(t) - f(t - \epsilon)$$

where $\epsilon = \gamma_a^{-1}$ and

$$f(t - \epsilon) = \epsilon k_a S(t - \epsilon)$$

We take

$$\frac{dE}{dt} = g_\epsilon(t) - \frac{1}{\epsilon}E(t)$$

Since

$$g_\epsilon(t) = \frac{1}{\epsilon}(f(t) - f(t - \epsilon)) - f'(t - \epsilon) = o(1)$$

is local uniformly in $t, f \in C^1(R)$,

$$E(t) = e^{-\frac{t}{\epsilon}}E(0) + \int_0^t e^{-\frac{(t-s)}{\epsilon}} g_\epsilon(s)ds = e^{-\frac{t}{\epsilon}}E(0) + o(1)\epsilon(1 - e^{-\frac{t}{\epsilon}}) = o(\epsilon)$$

is also local uniformly in $t > 0$. This means A(t) can be approximated by $f(t - \epsilon)$ under the assumption of $\gamma_a \gg 1$. That is,

$$A(t) \sim \gamma_a^{-1} k_a S(l, t - \gamma_a^{-1}). \tag{4}$$

The same can be done to obtain an approximation of I(t).

The cell is assumed to have polarity at the front and back sides, which is represented by $x = \pm l$. We therefore have $A_\pm = A(\pm l, t)$ and $I_\pm = I(\pm l, t)$. With the approximation in (4), we have

$$\frac{dA_+}{dt} \sim \gamma_a^{-1} k_a S_t(l, t - \gamma_a^{-1}) \sim \gamma_a^{-1} k_a \gamma_a (S(l,t) - S(l, t - \gamma_a^{-1}))$$
$$\sim k_a S(l,t) - \gamma_a A_+(t)$$

as the approximation of (1). A_- and $I_\pm$ can be obtained by the same manner.

The activator and inhibitor are assumed to occur locally and globally, respectively. Thus, $A_\pm$ and $I_\pm$ are approximated as

$$A_\pm \sim \gamma_a^{-1} k_a S(\pm l, t - \gamma_a^{-1}), \quad I_\pm = I = \gamma_i^{-1} k_i S_{av}(t - \gamma_i^{-1}), \tag{5}$$

where

$$S_{av}(t) = \frac{1}{2}(S(l,t) + S(-l,t)).$$

Through a simple calculation, namely the activator/inhibitor ratio Q from (3), (5), and $\gamma_a, \gamma_i \gg 1$, we obtain the following:

$$Q_\pm(t) \sim Q_0\{1 + \frac{S_t(\pm l, t)}{S(\pm l, t)}(\gamma_i^{-1} - \gamma_a^{-1})\} \pm l \cdot \frac{S_x(\pm l, t) - \gamma_i^{-1} S_{xt}(\pm l, t)}{S(\pm l, t)}, \tag{6}$$

where $Q_0 = (k_a \gamma_i)/(k_i \gamma_a)$. From (5), we can see that the cell has polarity in the direction of $S_{xt} < 0$.

3.4 Numerical Simulation

An angiogenesis simulation was performed using the mathematical equation (Fig. 2a). We simulated from t = 1 to 14. The tip cells gradually moved, and the behavior of these cells represented the elongation of new blood vessels. Some of these tip cells formed a loop and then stopped growing. We measured the distance that the tip cells moved and presented it in Fig. 2b. New blood vessels showed a stair-like pattern of growth, and there was a point at which the growth plateaued. The growth of new blood vessels stopped at t = 10.

a

b
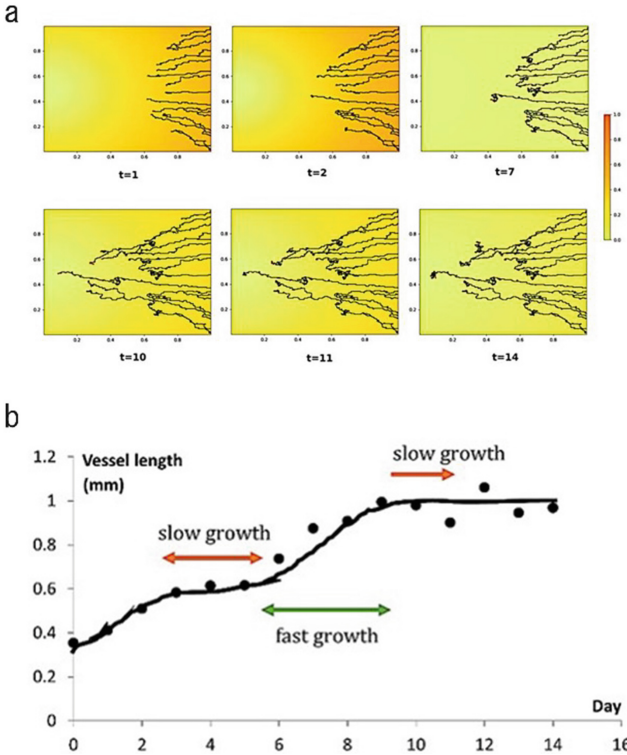
Fig. 2. The length of new blood vessels in the numerical simulation

4   The Histological Measurement of New Blood Vessels in Our Angiogenesis Models

New blood vessels sprout and grow from arterioles (Fig. 3a; red arrowhead: arteriole, yellow arrowhead: new blood vessels). In Fig. 3a, the distance between the dotted lines was considered to represent new blood vessels. This graph shows the average length of the new blood vessels from days 0 to 10 (Fig. 3b). The new blood vessels gradually grew until three days after the operation, but the length did not increase markedly from days 3 to 5; however, from days 5 to 10, the vessels grew again before ultimately reaching a plateau.

As previously reported, in this in vivo angiogenesis model, new blood vessels reach the arterial patch graft at day 10 and open around the graft. The blood in the new blood vessels flowed into the common jugular vein around the graft. Therefore, we speculate that the new blood vessels reached the arterial graft on day 10, at which point the angiogenesis process ceased. Measurements from days 10 to 14 should also be conducted.
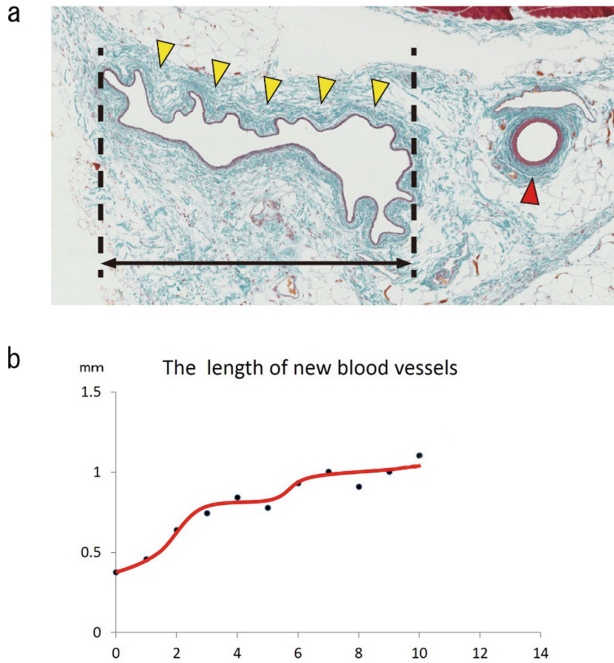
Fig. 3. The length of new blood vessels in the numerical simulation

5 Discussion

Our mathematical model of angiogenesis successfully depicted the growth of new vessels to fit the experimental data. The results of our mathematical simulation are similar to those in our previous work on the angiogenesis of arterial patch graft. Although it is a site of VEGF production different from tumor angiogenesis, it was possible to apply the pre-existing mathematical model by the resolution of chemotaxis paradox. With this improvement, our mathematical model of angiogenesis can be applied to not only tumor angiogenesis but also typical angiogenesis occurring in vivo.

VEGF was measured by an ELISA after extracting the total protein from tissue in the present study. While we are confident that most of the proteins were extracted, a small amount may still have remained. However, most of the VEGF was extracted, so any remaining protein was considered to have no significant influence on the fluctuation of the VEGF concentration.

The number of cases and time points for which VEGF was measured were not very large in the present study. Therefore, it is necessary to increase the number of cases and improve the accuracy of the VEGF fluctuations. In addition, the number of cases in which the length of new blood vessels was measured was insufficient and should be increased to three per time point in a future study.

Following such improvements, future studies should examine whether or not the experiment and mathematical simulation match.

References

1. Ferrara, N.: VEGF and the quest for tumour angiogenesis factors. Nat. Rev. Cancer **2**, 795–803 (2002)
2. Ferrara, N., Gerber, H.P., LeCouter, J.: The biology of VEGF and its receptors. Nat. Med. **9**, 669–676 (2003)
3. Yancopoulos, G.D., et al.: Vascular-specific growth factors and blood vessel formation. Nature **407**, 242–248 (2000)
4. Ferrara, N.: Vascular endothelial growth factor: basic science and clinical progress. Endocr. Rev. **25**, 581–611 (2004)
5. Claesson-Welsh, L., Welsh, M.: VEGFA and tumour angiogenesis. J. Intern. Med. **273**, 114–127 (2013)
6. Anderson, A.R., Chaplain, M.A.: Continuous and discrete mathematical models of tumor-induced angiogenesis. Bull. Math. Biol. **60**, 857–899 (1998)
7. Ito, Y., et al.: Neovasculature can be induced by patching an arterial graft into a vein: a novel in vivo model of spontaneous arteriovenous fistula formation. Sci. Rep. **8**, 3156 (2018)
8. Nakajima, A., Ishihara, S., Imoto, D., Sawai, S.: Rectified directional sensing in long-range cell migration. Nat. Commun. **5**, 5367 (2014)

Mathematical Modeling of Tumor Malignancy in Bone Microenvironment

Naoya Hatanaka[1], Mitsuru Futakuchi[2], and Takashi Suzuki[3(✉)]

[1] Graduate School of Engineering Science, Osaka University, Suita, Japan
n-hatanaka@sigmath.es.osaka-u.ac.jp
[2] Graduate School of Biomedical Sciences, Nagasaki University, Nagasaki, Japan
futakuch@nagasaki-u.ac.jp
[3] Center for Mathematical Modeling and Data Science, Osaka University, Suita, Japan
suzuki@sigmath.es.osaka-u.acjp

Abstract. We construct a multi-scaled mathematical model of tumor malignancy in bone microenvironment including tumor cells, osteoblasts, and ostoclasts underlined by NF-κB family, RANKL, RNK, and OPG molecules. Pathways causing change of the amounts of osteoblasts, osteoclast, and cancer cells are analyzed via numerical simulations.

1 Introduction

Bone maintains a normal state by repeating bone formation by osteoblasts and bone resorption by osteoclasts. RANKL, secreted by the osteoblastic line, induces the differentiation of the osteoclast lineage. When bone is decomposed and absorbed, TGF-β contained in the bone matrix is released, which promotes the differentiation of the osteoblast lineage. Due to such mutual relations, the bone mass is kept constant. However, when cancer cells metastasize to the bone microenvironment, their balance is lost.

In the tumor-bone microenvironment, interaction among cancer cells, osteoblasts, and osteoclasts has been shown to play important roles for the progression of bone metastatic lesions. The mesenchymal stem cells (MSC), the progenitors of osteoblasts, contribute to the regeneration of bone tissues [1,2]. Monocytic progenitors are well known to differentiate to osteoclasts from under inflammatory conditions [3] through cytokine stimulation such as M-CSF [4] and RANKL [5]. Cancer stem cells (CSCs) are a subpopulation of cancer cells which are able to self-renew and differentiate, which make them to be considered as the seeds of cancer, as they are responsible of cancer cells heterogeneity and chemoresistance [6].

RANKL, OPG and TGFβ are well known cytokines to be involved in the interaction of cancer cells, osteoblasts, and osteoclasts in the tumor-bone microenvironment [7,8]. It is found that RANKL expressed in osteoblasts promoted osteolysis associated with prostate cancer growth in the bone microenvironment [9]. TGFβ is released in the bone microenvironment by osteolysis

because TGFβ is stored in the bone matrix. TGFβ promotes the induction of osteoblasts associated with rat prostate cancer growth [10], MSCs [11–13], and RAW267.4 cell line, which is the precursor of osteoclasts [10,14]. TGFβ also promotes cell proliferation of rat prostate cancer [10] and mouse breast cancer [14]. Recently it is shown that TGFβ is involved in the induction of cancer stem cell in vivo [15].

In this study, we identify the factors that disrupt the equilibrium state in bone formation by constructing a mathematical model that includes the interaction between osteoblasts, osteoclasts, and cancer cells.

2   Modeling (1)

First, we construct a model of bone metabolism composed of osteoblast cell and osteoclast cell. The number of MSCs (X_1) changes by the physiological supply (m_0) and the consumption by the differentiation to osteoblasts (X_2). Similarly, the number of monocyte (X_3) changes by the supply (m_1) and the consumption of the differentiation to osteoclast (X_4). Amount of bone matrix (X_6) changes by the bone formation by osteoblasts (l_2) and bone destruction by osteoclasts (de) (Fig. 1 and Eq. (1)–(7) with $m_0 = m_0(X_7)$ and $m_1(X_9) = a_{m1}$) (Table 1).
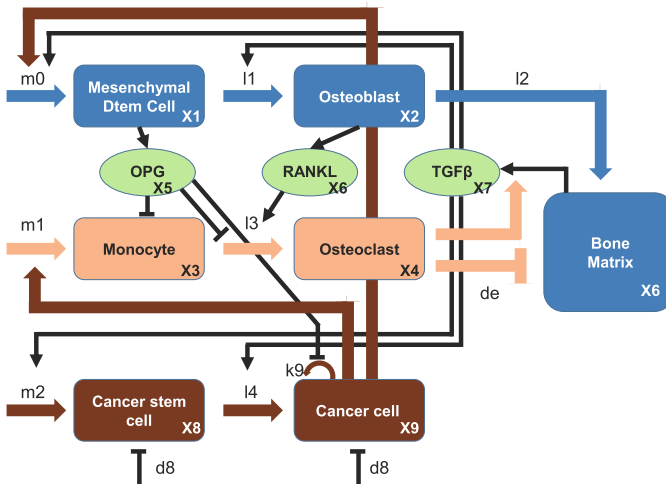
Fig. 1. Model diagram including bone metabolism and bone metastasis. It is composed of osteoblasts, osteoclasts, and cancer cells. Osteoblasts produce bone matrix and osteoclasts absorb bone. The growth of cancer cells is promoted by TGF-β released from the bone microenvironment.

$$\frac{dX_1}{dt} = m_0(X_7, X_9) - l_1(X_7)X_1 \tag{1}$$

$$\frac{dX_2}{dt} = l_1(X_7)X_1 - l_2X_2 \tag{2}$$

$$\frac{dX_3}{dt} = m_1(X_9) - l_3(X_5, RANKL)X_3 - d_1(X_5)X_3 \tag{3}$$

$$\frac{dX_4}{dt} = l_3(X_5, RANKL)X_3 - d_2X_4 \tag{4}$$

$$\frac{dX_5}{dt} = pX_1 - d_3X_5 \tag{5}$$

$$\frac{dX_6}{dt} = l_2X_2 - deX_4X_6 \tag{6}$$

$$\frac{dX_7}{dt} = tg(X_4)X_6 - d_4X_7 \tag{7}$$

$$\frac{dX_8}{dt} = m_2X_7 - d_8X_8 \tag{8}$$

$$\frac{dX_9}{dt} = l_4(X_8) + (k_9(X_5, X_7) - d_8)X_9 \tag{9}$$

As far as the infinitesimal variation upon the differentiation coefficientes is valid, we can assume the following linear relations of the change of these coefficients under the reaction of molecular level:

$$m_0(X_7) = a_m + b_mX_7 \tag{10}$$
$$l_1(X_7) = a_l + b_lX_7 \tag{11}$$
$$l_3(X_5, RANKL) = l_3(X_5, kX_2) = \lambda\frac{kX_2}{X_5 + kX_2} \tag{12}$$
$$d_3(X_5) = b_dX_5 \tag{13}$$
$$tg(X_4) = b_{tg}X_4 \tag{14}$$
$$l_4(X_8) = b_{l4}X_8 \tag{15}$$
$$k_9(X_5, X_7) = a_{k9} + b_{m2}X_7 \tag{16}$$

Table 1. Variables in the bone metastasis model

Valuable	Corresponding object
X_1	mesechymal stem cell
X_2	osteoblast
X_3	monocyte
X_4	osteoclast
X_5	OPG
X_6	bone matrix
X_7	TGFβ
X_8	cancer stem cell
X_9	cancer cell

3   Analysis via Simulations (1)

Although bone mass is a variable changing in time in the above bone metabolism model, it is regarded as a constant in a dynamic equilibrium realized in the normal state. It is the case of dX6/dt=0, where the amount of bone in the dynamic equilibrium state is determined by the number of osteoblasts and the number of osteoclasts. Since the solution cannot be obtained analytically, changes of this dynamical equilibrium are analyzed numerically. Since constant bone metabolism requires for each reaction to occur at the same rate, we put the parameters to be roughly 1, except for protein degradation faster than cell degradation. Thus d_3 and d_4 are set to be 10.

To execute sensitivity analysis, change of the equilibrium of the bone matrix is examined numerically when each parameter is changed in the range of 0.1 to 10 times. It is observed that the bone mass greatly increases when a_m and b_m increase, and that the bone mass decreases when m_1 increases. These parameters correspond to the supply of pre-osteoblasts and pre-osteoclasts, respectively. In contrast, change of the dynamical equilibrium is small relative to the perturbations of differentiation constants.

We thus conclude that even if the differentiation is promoted, the precursor cells used for differentiation are insufficient to promote reaction thereafter. In other words, bone mass abnormally increases or decreases by the metastasis of cancer, because cancer cells promote the supply of mesenchymal stem cell or that of monocyte, respectively.
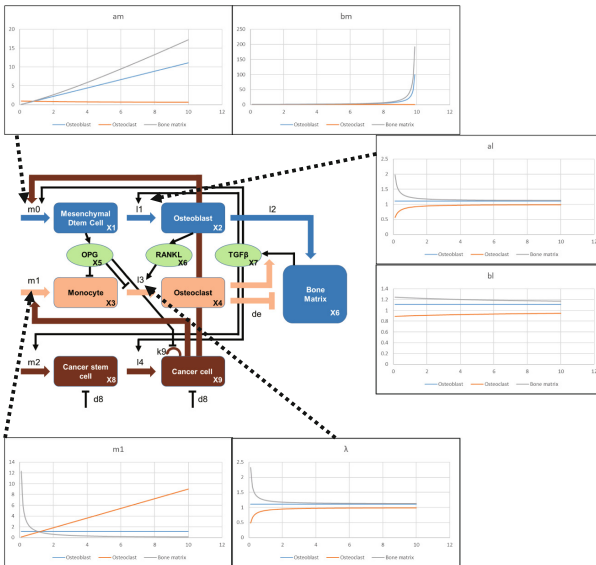
Fig. 2. Simulation of equilibrium bone matrix changing parameters related to the increase of osteoblasts and osteoclasts (Model 2). The horizontal axis represents the changing parameter and the vertical axis represents the equilibrium point of X_6 (bone matrix).

4 Modeling (2)

Next, we construct a model of the stage when cancer has metastasized to bone. We assume that the number of cancer cells (X_9) changes by the supply of the asymmetric cell division of CSC (X_8) and division of cancer cell, and decrease by the defense system by immune cells. From the above analysis of bone metabolism, it is necessary for m_0 or m_1 to induce abnormally increasing or decreasing of the bone mass, where cancer cells act on these pathways (Fig. 1 and Eq. (1)–(9) with $m_0 = m_0(X_9)$, $m_1 = m_1(X_9)$).

5 Analylsis via Simulations (2)

We investigate the change of bone mass due to the increase in cancer cells, putting $d_b = 0.01$ and $a_{k9} = 1$. Numerical simulations show the change of dynamical equilibrium when d_b decreases or a_{k9} increases due to immunosuppression and cancer malignancy. It is observed also that this equilibrium collapses around $a_{k9} = 10$, where cancer cells grow continuously (Fig. 2).

After this critcal point cancer cells are continuouosly proliferating, which results in the increase of osteoclast (the decrease of bone mass) under the presense osteolytic bone metastasis indicated by $m_0(X_9) = 0$. According to the type of cancer, actually, there arises either $m_0(X_9) = 0$ or $m_1(X_7) = 0$. In the model containing both pathways, however, osteoblastic bone metastasis or osteolytic bone metastases can switch in numerical simulations, depending on the nature of the cancer cells (Table 2).

Table 2. Summary of parameter values

Symbol	Value	Description
a_m	1	supply of mesenchymal stem cell
b_m	1	Promotion of mesenchymal stem cell supply by TGF-β
a_l	1	Differentiation of mesenchymal stem cell to osteoblasts
b_l	1	Promotion of differentiation of mesenchymal stem cell by TGF-β
m_1	1	supply of monocyte
λ	1	Differentiation of monocyte to osteoclasts
l_2	1	Bone matrix formation by osteoblasts
d_e	1	Osteoclast-induced osteolysis of bone matrix
p	1	OPG secretion from preosteoclasts
t_g	1	Release of TGF-β from bone matrix
d_1	1	Disappearance of monocyte
d_2	1	Disappearance of osteoclasts
d_3	10	OPG decomposition
d_4	10	Degradation of TGF-β
m_2	1	Cancer stem cell supply
b_{l4}	1	Asymmetric division of cancer stem cells into cancer cells
a_{k9}	1	Promotion of cancer cell growth by TGF-β
b_{k9}	1	Suppression of cancer cells by OPG
d_{8b}	1	Suppression of cancer stem cells by in vivo defense mechanism
d_{9b}	1	Suppression of cancer cells by in vivo defense mechanism

6   Conclusion

In the first model of bone metabolism, it is observed that the change of bone mass is large when there arises an abnormal pathway related to the supply of progenitor cells. Therefore, if the bone mass is abnormal, the treatment that suppresses the pathway related to supply rather than suppression of differentiation is considered to be more effective. In the second model, next, increase of the supply of cancer cells to osteoblasts or osteoclasts is switched between osteoblastic and osteolytic.

7   Discussions

Among many mathematical models on bone metastasis [16–18], novelty of our mathematical model are the following. (1) This model involves the mechanisms by the regulation of precursors and differentiated type of cancer cells, osteoblasts, and osteoclasts. (2) It reflects both osteolytic and osteoblastic bone metastasis. We shall provide quantitative data in a forthcoming paper to treat bone metastases in more details.

References

1. Pittenger, M.F., et al.: Multilineage potential of adult human mesenchymal stem cells. Science **284**(5411), 143–7 (1999)
2. Polak, J.M., Bishop, A.E.: Stem cells and tissue engineering: past, present, and future. Ann. N. Y. Acad. Sci. **1068**, 352–66 (2006)
3. Blair, H.C., Teitelbaum, S.L., Ghiselli, R., Gluck, S.: Osteoclastic bone resorption by a polarized vacuolar proton pump. Science **245**(4920), 855–7 (1989)
4. Wiktor-Jedrzejczak, W., Bartocci, A., Ferrante, A.W., Jr., Ahmed-Ansari, A., Sell, K.W., Pollard, J.W., Stanley, E.R.: Total absence of colony-stimulating factor 1 in the macrophage-deficient osteopetrotic (op/op) mouse. Proc. Natl. Acad. Sci. U S A. **87**(12), 4828–32 (1990)
5. Lacey, D.L., et al.: Osteoprotegerin ligand is a cytokine that regulates osteoclast differentiation and activation. Cell **93**(2), 165–76 (1998)
6. Wang, Y., et al.: Transforming growth factor-β regulates the sphere-initiating stem cell-like feature in breast cancer through miRNA-181 and ATM. Oncogene **30**(12), 1470–80 (2011)
7. Mundy, G.R.: Mechanisms of bone metastasis. Cancer **80**(8 Suppl), 1546–56 (1997)
8. Mundy, G.R.: Metastasis to bone: causes, consequences and therapeutic opportunities. Nat. Rev. Cancer **2**(8), 584–93 (2002)
9. Lynch, C.C., et al.: MMP-7 promotes prostate cancer-induced osteolysis via the solubilization of RANKL. Cancer Cell **7**(5), 485–96 (2005)
10. Sato, S., et al.: Transforming growth factor beta derived from bone matrix promotes cell proliferation of prostate cancer and osteoclast activation-associated osteolysis in the bone microenvironment. Cancer Sci. **99**(2), 316–23 (2008)

11. Hung, S.P., Yang, M.H., Tseng, K.F., Lee, O.K.: Hypoxia-induced secretion of TGF-β1 in mesenchymal stem cell promotes breast cancer cell progression. Cell Transplant. **22**(10), 1869–82 (2013)
12. Gao, P., et al.: Functional effects of TGF-β1 on mesenchymal stem cell mobilization in cockroach allergen-induced asthma. J. Immunol. **192**(10), 4560–4570 (2014)
13. Patel, S.A., Meyer, J.R., Greco, S.J., Corcoran, K.E., Bryan, M., Rameshwar, P.: Mesenchymal stem cells protect breast cancer cells through regulatory T cells: role of mesenchymal stem cell-derived TGF-beta. J. Immunol. **184**(10), 5885–94 (2010)
14. Futakuchi, M., et al.: Transforming growth factor-beta signaling at the tumor-bone interface promotes mammary tumor growth and osteoclast activation. Cancer Sci. **100**(1), 71–81 (2009)
15. Futakuchi, M., Lami, K., Tachibana, Y., Yamamoto, Y., Furukawa, M., Fukuoka, J.: The Effects of TGF-β Signaling on Cancer Cells and Cancer Stem Cells in the Bone Microenvironment. Int. J. Mol. Sci. **20**(20), 5117 (2019)
16. Garzón-Alvarado, D.A.: A mathematical model for describing the metastasis of cancer in bone tissue. Comput. Methods Biomech. Biomed. Eng. **15**(4), 333–46 (2012)
17. Munoz, A.I., Tello, J.I.: On a mathematical model of bone marrow metastatic niche. Math. Biosci. Eng. **14**(1), 289–304 (2017)
18. Ryser, M.D., Qu, Y., Komarova, S.V.: Osteoprotegerin in bone metastases: mathematical solution to the puzzle. PLoS Comput. Biol. **8**(10), e1002703 (2012)

Signaling Networks Involved in the Malignant Transformation of Breast Cancer

Mizuki Yamamoto[1(✉)] and Jun-ichiro Inoue[2]

[1] Research Center for Asian Infectious Diseases, The Institute of Medical Science, The University of Tokyo, Tokyo, Japan
mizuyama@ims.u-tokyo.ac.jp
[2] The University of Tokyo, Tokyo, Japan
jun-i@ims.u-tokyo.ac.jp

Abstract. Breast cancer stem cells (CSCs) are involved the malignant transformation of breast cancer, including metastasis, because they are more stress-resistant and have higher tumorigenicity than the surrounding breast cancer cells (non-CSCs). We aimed to elucidate the various signaling networks involved in the transformation of mammary epithelial cells into tumor cells based on literature review. We found that constitutive activation of the NF-κB pathway maintains CSCs in basal-like breast cancer, a subtype of triple-negative breast cancer, where NF-κB-mediated induction of JAG1 in non-CSCs results in the stimulation of Notch signaling in CSCs. On the other hand, epithelial-mesenchymal transition (EMT) and its reverse reaction, mesenchymal-epithelial transition (MET), are thought to be involved in breast cancer cell metastasis, which makes elucidating their regulatory mechanisms essential. We identified HCC38, a basal-like breast cancer cell line, as a suitable model to investigate such mechanisms, because EMT and MET are in intratumoral equilibrium with each other in HCC38. In the HCC38 study, we found that multiple signaling pathways between epithelial and mesenchymal cells are involved in the regulation of the dynamic equilibrium between EMT and MET. Mathematical simulation of these intracellular and intercellular signaling networks involved in the malignant transformation of breast cancer could lead to the elucidation of the mechanisms of tumor malignant transformation and the development of therapeutic targets.

Keywords: Triple-negative breast cancer · Basal-like breast cancer · Epithelial-mesenchymal transition · Signal transduction · Cell-cell interaction

1 Subtypes of Breast Cancer

Breast cancers are classified into four subtypes, including luminal-like, ERBB2-enriched, basal-like, and claudin-low breast cancers, based on their gene expression profiles [1–3]. Luminal-like breast cancers, which account for approximately 70% of all breast cancers, depend on signals downstream of the estrogen receptor (ER) and the progesterone receptor (PR) for survival and proliferation. Therefore, inhibitors of

these receptors, such as selective androgen receptor modulators, and of hormone synthesis, such as aromatase inhibitors, are effective, resulting in relatively good prognosis. ERBB2-enriched breast cancers, which account for about 20% of all breast cancers, are caused by genetic amplification of the oncogene *ERBB2 (HER2)* and depend on proliferation signals downstream of ERBB2. Herceptin, an anti-ERBB2 antibody, binds to ERBB2 overexpressed on the membrane of breast cancer cells and induces antibody-dependent cytotoxic immune cell activity, resulting in an antitumor effect. In contrast, triple negative breast cancer (TNBC), which does not express these therapeutic target molecules, including ER, PR, and ERBB2, is found in approximately 10% of breast cancer patients and includes basal-like breast cancer and claudin-low breast cancer subtypes. To date, there have been no molecular targeted therapies for TNBC, and chemotherapy is mainly used in these cases. In addition, prognosis for TNBC patients is poor due to the high malignancy of the cancer cells themselves, including their invasive potential [4].

2 Differentiation and Malignant Transformation of Normal Mammary Epithelial Cells

The mammary gland, origin of breast cancer, is formed by a ductal structure consisting of two types of epithelial cells. During gestation, luminal epithelial cells on the inner side of the lumen produce milk, while basal epithelial cells on the outer side transport the milk from the lumen to the nipple by contraction. These epithelial cells differentiate from a single mammary epithelial stem cell (MaSC) (Fig. 1). MaSCs differentiate into luminal and basal progenitor cells, and the two types of progenitor cells mature by active proliferation to form milk ducts. Each subtype of breast cancer arises from mammary epithelial cells at different stages of differentiation [5–7]. Hormone receptor-positive luminal-like breast cancer and ERBB2-enriched breast cancer develop from relatively well-differentiated luminal epithelial cells. On the other hand, claudin-low breast cancer originates from MaSCs, while basal-like breast cancer originates from luminal progenitor cells.
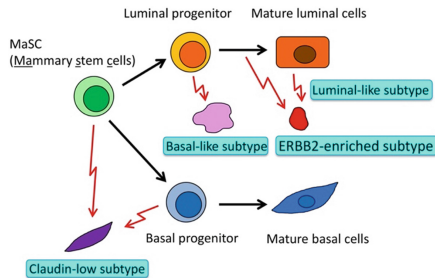
Fig. 1. Differentiation of normal mammary epithelial cell lineage and origins of each breast cancer subtype.

The two types of mammary epithelial cells, luminal and basal epithelial cells, comprise the mammary gland. These cells differentiate from a single mammary epithelial stem cell (MaSC). Different breast cancer subtypes arise from different mammary epithelial cells.

3 Signaling Networks that Maintain Cancer Stem Cells (CSCs)

3.1 Breast CSCs

Tumors are not a collection of cancer cells with uniform properties, but rather a "tissue" composed of a variety of cells that can repair themselves in response to external damage from surgery, drugs, and radiation therapy. This heterogeneity is not only due to the presence of normal tissues, such as stroma and tumor blood vessels, but is also see in the cancer cells. The ductal structure of some tumors is similar to that of normal tissues, suggesting that cancer cells, like normal cells, are undifferentiated cells that can differentiate and mature to form tumors. These undifferentiated cancer cells are named CSCs. CSCs are thought to maintain their differentiation potential because of their similarity to the undifferentiated normal cells, from which they originate. However, they also possess features such as stress tolerance and immune evasion. This ability of CSCs also leads to the recurrence, where new tumors are formed by the few remaining cancer cells after treatment (Fig. 2). Metastasis also requires the migration of one or more cancer cells from the primary tumor site to other organs through blood vessels and lymphatic vessels to form new tumors, and CSCs are also important for this purpose (Fig. 2). Therefore, understanding the nature of CSCs and constructing therapeutic strategies based on this is important for the eradication of the primary tumor and for the control of metastasis. The CSC hypothesis has been proposed for a long time, but with the development of flow cytometry technology, it has become possible to analyze individual cells based on the expression of surface antigens. CSCs from leukemia cells were first identified in 1997 [8]. In 2003, Al-hajj et al. isolated breast CSCs from solid tumors for the first time [9] using surface antigens of various tissue stem cells as indicators and evaluated their tumorigenicity in immunodeficient mice. They reported that CD24^{low}CD44^{high}EpCAM^{+} fraction in breast cancer cells showed higher tumorigenicity than other fractions. Subsequently, it was reported that breast CSCs demonstrated high sphere-forming ability in an anchorage-independent manner in floating cultures *in vitro* and high acetaldehyde dehydrogenase enzyme activity. Based on these characteristics, various methods have been used to culture breast CSCs, allowing us to investigate various CSC signal transduction pathways. Activation of PI3K/AKT signaling [10], IL6/STAT3 signaling [11], Notch signaling [12], transcription factors related to epithelial-mesenchymal transition (EMT) [13], IL8/CXCR1 signaling [14], and NF-κB signaling [15–17], as well as decreased expression of *let7* miRNAs [18] were observed in breast CSCs, indicating that these signaling pathways play an important role in tumorigenesis. Furthermore, it was reported that high expression of reactive oxygen species (ROS) scavenger enzymes resulted in resistance to radiotherapy [19], indicating the importance of CSCs. However, the activation and maintenance of these signaling pathways by breast CSCs is still unclear. Therefore, analyzing their similarity to undifferentiated normal mammary

epithelial cells, environmental factors surrounding CSCs, and metabolic effects is an important point of interest.
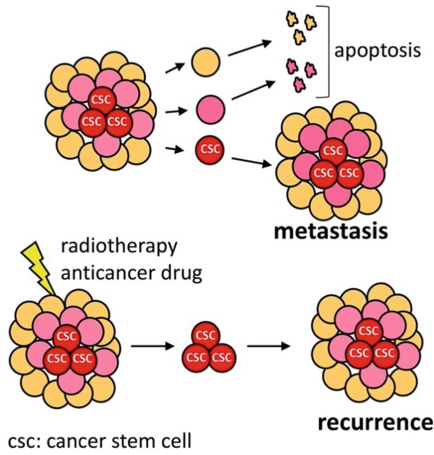

Fig. 2. Importance of cancer stem cells in metastasis and recurrence

Most cancer cells undergo cell death due to anoikis and stress when they leave the primary site. However, cancer stem cells are resistant to stress and migrate to distant organs and metastasize due to their ability to form new tumors. Furthermore, CSCs have been shown to be resistant to radiotherapy and anticancer drug treatments due to reactive oxygen species (ROS) scavenging and the activation of drug efflux pump mechanisms. Recurrence occurs when a few surviving CSCs form tumors.

3.2   Constitutive Activation of NF-κB in Breast Cancer

Although the transient activation of NF-κB is strictly regulated in normal cells, NF-κB is constitutively activated in various cancer types including breast cancer, pancreatic cancer, colon cancer and leukemia. The constitutive NF-κB activation induces cancer cell survival, proliferation, and metastasis. We have previously demonstrated that NF-κB is constitutively and strongly activated in TNBCs, including basal-like and claudin-low breast cancers, compared to luminal-like and ERBB2-enriched breast cancers, and NF-κB activation is mediated by overexpression of NF-κB-inducing kinase (NIK) [20]. Furthermore, we have shown that NIK overexpression in TNBC occurs because of disrupted epigenetic gene expression repression mechanisms [21]. In addition, since breast CSCs are involved in the malignant transformations of cells, leading to metastasis and recurrence, we reported the mechanism of breast CSC maintenance by basal-like breast cancer-specific NF-κB-JAG1-Notch signaling [22].

3.3 Maintenance of Breast CSCs via JAG1-Notch Signaling Induced by Constitutive NF-κB Activation

Prior to our report, several research groups have reported NF-κB activation in breast CSCs. For example, Iliopoulos et al. reported that the transformation of normal mammary epithelial cell line MCF10A cells by IL-6 treatment resulted in an NF-κB activation-dependent expansion of the breast CSC fraction [11], and Murohashi et al. reported that the CD24^{low} CSC fraction of MCF7 and basal-like breast cancer cell line HCC1954 cells showed stronger NF-κB activation than the CD24^{high} non-CSC fraction [17]. However, these reports suggest that NF-κB activation in CSCs induces their proliferation and survival. In contrast, we focused on the activation of signal transduction by interaction between CSC and non-CSC, since the expression of various ligand molecules is induced downstream of NF-κB [22]. We found that when basal-like breast cancer cells with enhanced NF-κB activation were co-cultured with the same breast cancer cells with unaltered NF-κB activation, the percentage of CSCs in the unaltered NF-κB group increased significantly. Under these conditions, the expression of Notch target genes increased in CSCs of co-cultured breast cancer cells with unaltered NF-κB activation. Therefore, we focused on Notch signaling. We found that JAG1, a Notch ligand, was induced by NF-κB activation in basal-like breast cancer. Furthermore, knockdown of JAG1 by RNAi suppressed the NF-κB-dependent increase of CSCs. Based on these results, we proposed a model for NF-κB-mediated maintenance of CSC populations in basal-like breast cancer, where NF-κB activation in non-CSCs surrounding CSCs induces expression of JAG1, which in turn activates Notch signaling in CSCs, thereby their maintenance (Fig. 3) [22]. Furthermore, since breast CSCs are thought to play an important role in metastasis, we analyzed the relationship between JAG1 expression and metastasis rate in clinical samples. The metastasis rate was significantly higher in the JAG1^{high} group compared to JAG1^{low} group in basal-like breast cancer, suggesting that Notch signaling may increase the number of breast CSCs *in vivo* [22]. In addition, progesterone secreted during the menstrual cycle and pregnancy induces the expression of RANK ligand (RANKL) in luminal epithelial cells, in turn stimulating RANK in basal epithelial cells, where NF-κB activation induces JAG1 expression. In other words, normal mammary epithelial cells are also involved in the maintenance of CSCs of basal-like breast cancer [22, 23].

In basal-like breast cancer, NF-κB activation is induced by the overexpression of NF-κB-inducing kinase (NIK) due to epigenetic abnormalities and by inflammatory cytokines, such as TNF-α, leading to JAG1 expression in cancer cells (non-cancer stem cells) that surround cancer stem cells (CSCs). JAG1 activates Notch signaling in breast CSCs and induces self-renewal or survival activities, thereby maintaining breast CSCs in tumors. Furthermore, surrounding normal cells, where NF-κB is activated due to pregnancy or inflammation, also express JAG1, suggesting that normal cells may also contribute to the maintenance of breast CSCs in the cancer microenvironment. This figure was originally shown in Fig. 8c of Ref. [22].
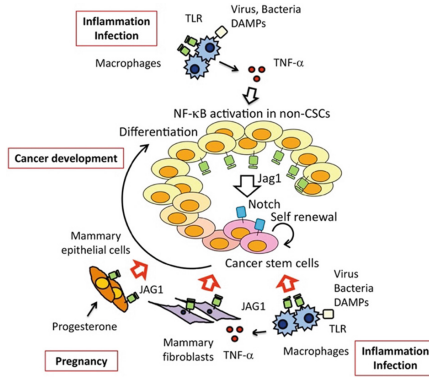
Fig. 3. Role of NF-κB-JAG1-Notch signaling in the maintenance of basal-like breast cancer stem cells

4   Signaling Network Regulating Intratumoral Bidirectional Transitions Between Epithelial and Mesenchymal Cells in TNBC

EMT and its reverse reaction, mesenchymal-epithelial transition (MET), are critical in breast cancer metastasis, along with CSC maintenance (Fig. 4) [24, 25]. EMT reduces cell-cell contact and promotes cell motility, allowing cancer cells to migrate from the primary lesion to nearby blood vessels and pass through the vessel wall. Since EMT and MET are dynamic processes, mesenchymal cancer cells that emerge from EMT transiently undergo MET and revert to epithelial cancer cells by interacting with other cancer and normal cells. Epithelial cancer cells may undergo EMT and reacquire the mesenchymal phenotype before invading the blood vessels. In other words, EMT and MET may be in equilibrium, and their equilibrium may be spatiotemporally regulated during the process of metastasis, especially during the period from the primary lesion occurrence to intravascular invasion and that from extravasation at the metastatic site to metastatic tumor formation. Studies using immortalized non-cancerous mammary epithelial cells have shown that the TGF-β and Wnt pathways cooperate to induce EMT [26]. However, the molecular mechanisms that regulate bidirectional EMT-MET equilibrium in breast cancer cells remain unclear. Since epithelial and mesenchymal cancer cell populations maintain an equilibrium state of interconversion in the basal-like breast cancer cell line HCC38, we analyzed the regulatory mechanism of the EMT-MET interconversion as a model system of *in vivo* metastasis [27].

Epithelial cancer cells, which form the primary tumor, have a high proliferative capacity, strong intercellular adhesion, but low cell motility. On the other hand, mesenchymal cancer cells have low proliferative activity and intercellular adhesion, but high viability and motility. In the primary tumor, EMT and MET are in equilibrium, and the emerging mesenchymal cells migrate to blood vessels and invade them. They then migrate within the blood vessel and exit the vessel at another location, where EMT and MET are again in equilibrium, and epithelial cells proliferate and form metastatic tumors.
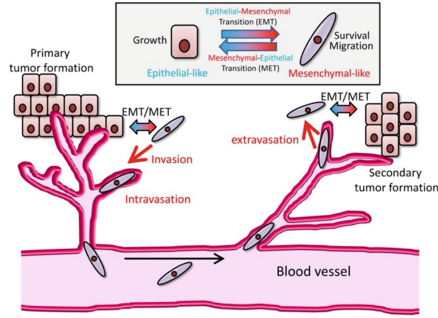
Fig. 4. Importance of epithelial-mesenchymal transition (EMT) and mesenchymal-epithelial transition (MET) in cancer metastasis

Fluorescence-activated cell sorter (FACS) analysis of HCC38 showed that there were two populations of cells, EpCAM$^+$CD44^{low} and EpCAM$^-$CD44^{high}, with a ratio of approximately 9:1. In addition to EpCAM, an epithelial cell marker, western blotting and immunostaining analysis showed that EpCAM$^+$ cells also express epithelial cell markers such as E-cadherin, ZO-1, and Claudin-1, while EpCAM$^-$ cells express mesenchymal cell markers such as vimentin and N-cadherin. Forced expression of ZEB1, a transcription factor that induces EMT, in HCC38 markedly increased EpCAM$^-$ cell numbers. These results indicate that EpCAM$^+$CD44^{low} and EpCAM$^-$CD44^{high} cells are epithelial and mesenchymal cells, respectively. Therefore, epithelial and mesenchymal cancer cells were maintained at a 9:1 ratio in HCC38 cells (Fig. 5).
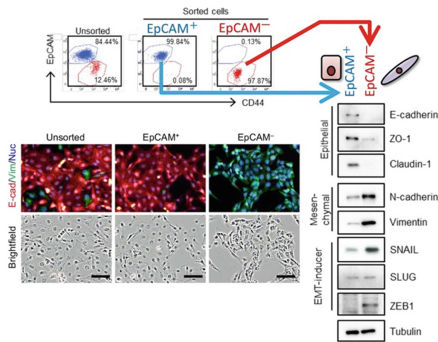
Fig. 5. Coexistence of epithelial and mesenchymal cell groups in HCC38

HCC38 cells were separated into EpCAM$^+$ and EpCAM$^-$ populations by FACS. Cells before and after FACS sorting were immunostained with antibodies against E-cadherin and vimentin. EpCAM$^+$ cells are E-cadherin$^+$ and vimentin$^-$, while EpCAM$^-$ cells are E-cadherin$^-$ and vimentin$^+$. Western blotting analyses revealed that EpCAM$^+$ cells were positive for epithelial markers (E-cadherin, ZO-1, and Claudin-1), while EpCAM$^-$ cells were positive for mesenchymal markers (N-cadherin and vimentin). This figure was originally shown in Fig. 1b, 1c, and 1g of Ref. [27].

More interestingly, when GFP was expressed only in EpCAM$^+$ epithelial cells, GFP$^+$ cells appeared in the EpCAM$^-$ mesenchymal population, and their ratio in the mesenchymal population increased over time. Conversely, GFP$^+$ cells appeared in the EpCAM$^+$ epithelial population over time when GFP was expressed only in EpCAM$^-$ mesenchymal cells. These results indicate that epithelial and mesenchymal cells are in equilibrium with each other in HCC38 cells. Furthermore, experiments where the ratio of EpCAM$^+$ to EpCAM$^-$ cells was artificially changed revealed that both epithelial and mesenchymal populations promote the migration of cells from other populations to their own (Fig. 6) [27]. Our data on the molecular mechanisms of equilibrium between epithelial and mesenchymal cell populations in HCC38 can be summarized as follows:

1) HCC38 maintains EpCAM$^+$ epithelial and EpCAM$^-$ mesenchymal cell populations at a fixed ratio of 9:1;
2) EMT occurs, and it is enhanced by mesenchymal cells;
3) MET also occurs, and it is enhanced by epithelial cells;
4) Knockdown of EMT-inducing transcription factors ZEB1 or SLUG significantly suppressed EMT, whereas knockdown of ZEB2 or SNAIL did not affect EMT;
5) Knockdown of ZEB1 or SLUG induced partial MET;
6) A JAK2/3 inhibitor suppressed EMT, but inhibitors against WNT, IL-8, NOTCH, p38, and IKKβ did not affect EMT;
7) A GSK3β inhibitor enhanced EMT;
8) Neutralizing antibodies against TGF-β inhibited EMT.

These results suggest that the TGF-β signaling pathway in epithelial cells and an unidentified pathway incorporating JAK2/3 in epithelial cells likely promote EMT by inducing ZEB1 expression or SLUG activation. On the other hand, the GSK3β-dependent pathway may negatively regulate EMT, thus suppressing the expression and activity of ZEB1 and SLUG. Interestingly, Wnt inhibitors, which suppress EMT in immortalized mammary epithelial cells, had no effect on EMT in HCC38 cells [27], suggesting that the regulatory mechanism of EMT differs between cancer and normal cells. The results of the inhibitor experiments suggest that various ligands expressed by mesenchymal cells in HCC38 may promote the EMT pathway or inhibit the EMT inhibitory pathway. TGF-β1 is highly expressed in HCC38 mesenchymal cells and is specifically induced during EMT in primary breast cancer, suggesting that TGF-β1 is a promising candidate for such a ligand. However, it is necessary to identify the signaling pathways that inhibit the expression of ZEB1 and CD44 [28]. Since the expression of ZEB1 and CD44 is repressed by various miRNAs, including the miR-200 family for ZEB1 [29] and miR-373 and 520c for CD44, signals inducing the expression of these miRNAs may be involved in MET promotion. The efficiency of EMT is approximately one order of magnitude higher than that of MET, while the proliferation of mesenchymal cells is significantly slower than that of epithelial cells. The migration rates of EMT and MET and the proliferation rates of the two populations may be influenced by their size, but are likely coordinated to maintain a fixed population ratio (Fig. 6) [27].

See Sect. 4 for details. EpCAM, epithelial cell adhesion molecule; GSK3β, glycogen synthase kinase 3β; SLUG, zinc finger protein SNAI2; TGF-β1, transforming growth
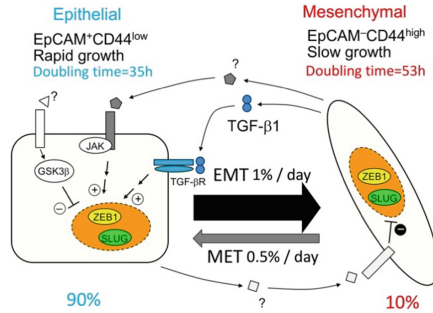
Fig. 6. Molecular mechanism of intra-tumoral equilibrium between epithelial and mesenchymal cell populations in HCC38.

factor-β1; TGF-βR, transforming growth factor-β receptor; ZEB1, zinc finger E-box-binding homeobox 1. This figure was originally shown in Fig. 7 of Ref. [27].

5   Conclusion

In this review, based on our studies, we describe the signaling networks involved in the malignant transformation of breast cancer from two perspectives: CSC maintenance and EMT. Both systems are regulated by the intercellular signaling networks spread between multiple cells and the intracellular signal networks in each cell. The factors involved in these signaling networks have only been partially explored, and the full picture will be elucidated by future molecular and cellular biological analyses. Mathematical simulations of these signaling networks will be used to elucidate the mechanisms of malignant tumor transformation and identify therapeutic targets.

References

1. Vargo-Gogola, T., Rosen, J.M.: Modelling breast cancer: one size does not fit all. Nat. Rev. Cancer **7**(9), 659–672 (2007)
2. Herschkowitz, J.I., Simin, K., Weigman, V.J., Mikaelian, I., Usary, J., Hu, Z., et al.: Identification of conserved gene expression features between murine mammary carcinoma models and human breast tumors. Genome Biol. **8**(5), R76 (2007)
3. Sorlie, T., Tibshirani, R., Parker, J., Hastie, T., Marron, J.S., Nobel, A., et al.: Repeated observation of breast tumor subtypes in independent gene expression data sets. Proc. Natl. Acad. Sci. U S A. **100**(14), 8418–8423 (2003)
4. Neve, R.M., Chin, K., Fridlyand, J., Yeh, J., Baehner, F.L., Fevr, T., et al.: A collection of breast cancer cell lines for the study of functionally distinct cancer subtypes. Cancer Cell **10**(6), 515–527 (2006)

5. Lim, E., Vaillant, F., Wu, D., Forrest, N.C., Pal, B., Hart, A.H., et al.: Aberrant luminal progenitors as the candidate target population for basal tumor development in BRCA1 mutation carriers. Nat Med. **15**(8), 907–913 (2009)

6. Molyneux, G., Geyer, F.C., Magnay, F.A., McCarthy, A., Kendrick, H., Natrajan, R., et al.: BRCA1 basal-like breast cancers originate from luminal epithelial progenitors and not from basal stem cells. Cell Stem Cell **7**(3), 403–417 (2010)

7. Visvader, J.E.: Cells of origin in cancer. Nature **469**(7330), 314–322 (2011)

8. Bonnet, D., Dick, J.E.: Human acute myeloid leukemia is organized as a hierarchy that originates from a primitive hematopoietic cell. Nat. Med. **3**(7), 730–737 (1997)

9. Al-Hajj, M., Wicha, M.S., Benito-Hernandez, A., Morrison, S.J., Clarke, M.F.: Prospective identification of tumorigenic breast cancer cells. Proc. Natl. Acad. Sci. U S A. **100**(7), 3983–3988 (2003)

10. Zhou, J., Wulfkuhle, J., Zhang, H., Gu, P., Yang, Y., Deng, J., et al.: Activation of the PTEN/mTOR/STAT3 pathway in breast cancer stem-like cells is required for viability and maintenance. Proc. Natl. Acad. Sci. U S A. **104**(41), 16158–16163 (2007)

11. Iliopoulos, D., Hirsch, H.A., Struhl, K.: An epigenetic switch involving NF-kappaB, Lin28, Let-7 MicroRNA, and IL6 links inflammation to cell transformation. Cell **139**(4), 693–706 (2009)

12. Harrison, H., Farnie, G., Howell, S.J., Rock, R.E., Stylianou, S., Brennan, K.R., et al.: Regulation of breast cancer stem cell activity by signaling through the Notch4 receptor. Cancer Res. **70**(2), 709–718 (2010)

13. Mani, S.A., Guo, W., Liao, M.J., Eaton, E.N., Ayyanan, A., Zhou, A.Y., et al.: The epithelial-mesenchymal transition generates cells with properties of stem cells. Cell **133**(4), 704–715 (2008)

14. Ginestier, C., Liu, S., Diebel, M.E., Korkaya, H., Luo, M., Brown, M., et al.: CXCR1 blockade selectively targets human breast cancer stem cells in vitro and in xenografts. J Clin Invest. **120**(2), 485–497 (2010)

15. Zhou, J., Zhang, H., Gu, P., Bai, J., Margolick, J.B., Zhang, Y.: NF-kappaB pathway inhibitors preferentially inhibit breast cancer stem-like cells. Breast Cancer Res. Treat. **111**(3), 419–427 (2008)

16. Liu, M., Sakamaki, T., Casimiro, M.C., Willmarth, N.E., Quong, A.A., Ju, X., et al.: The canonical NF-kappaB pathway governs mammary tumorigenesis in transgenic mice and tumor stem cell expansion. Cancer Res. **70**(24), 10464–10473 (2010)

17. Murohashi, M., Hinohara, K., Kuroda, M., Isagawa, T., Tsuji, S., Kobayashi, S., et al.: Gene set enrichment analysis provides insight into novel signalling pathways in breast cancer stem cells. Br. J. Cancer **102**(1), 206–212 (2010)

18. Yu, F., Yao, H., Zhu, P., Zhang, X., Pan, Q., Gong, C., et al.: let-7 regulates self renewal and tumorigenicity of breast cancer cells. Cell **131**(6), 1109–1123 (2007)

19. Diehn, M., Cho, R.W., Lobo, N.A., Kalisky, T., Dorie, M.J., Kulp, A.N., et al.: Association of reactive oxygen species levels and radioresistance in cancer stem cells. Nature **458**(7239), 780–783 (2009)

20. Yamaguchi, N., Ito, T., Azuma, S., Ito, E., Honma, R., Yanagisawa, Y., et al.: Constitutive activation of nuclear factor-kappaB is preferentially involved in the proliferation of basal-like subtype breast cancer cell lines. Cancer Sci. **100**(9), 1668–1674 (2009)

21. Yamamoto, M., Ito, T., Shimizu, T., Ishida, T., Semba, K., Watanabe, S., et al.: Epigenetic alteration of the NF-κB-inducing kinase (NIK) gene is involved in enhanced NIK expression in basal-like breast cancer. Cancer Sci. **101**(11), 2391–2397 (2010)

22. Yamamoto, M., Taguchi, Y., Ito-Kureha, T., Semba, K., Yamaguchi, N., Inoue, J.: NF-κB non-cell-autonomously regulates cancer stem cell populations in the basal-like breast cancer subtype. Nat. Commun. **4**, 2299 (2013)

23. Yamamoto, M., Abe, C., Wakinaga, S., Sakane, K., Yumiketa, Y., Taguchi, Y., et al.: TRAF6 maintains mammary stem cells and promotes pregnancy-induced mammary epithelial cell expansion. Commun. Biol. **2**, 292 (2019)
24. Heerboth, S., et al.: EMT and tumor metastasis. Clin. Transl. Med. **4**(1), 1–13 (2015). https://doi.org/10.1186/s40169-015-0048-3
25. Yu, M., Bardia, A., Wittner, B.S., Stott, S.L., Smas, M.E., Ting, D.T., et al.: Circulating breast tumor cells exhibit dynamic changes in epithelial and mesenchymal composition. Science **339**(6119), 580–584 (2013)
26. Scheel, C., Eaton, E.N., Li, S.H., Chaffer, C.L., Reinhardt, F., Kah, K.J., et al.: Paracrine and autocrine signals induce and maintain mesenchymal and stem cell states in the breast. Cell **145**(6), 926–940 (2011)
27. Yamamoto, M., Sakane, K., Tominaga, K., Gotoh, N., Niwa, T., Kikuchi, Y., et al.: Intratumoral bidirectional transitions between epithelial and mesenchymal cells in triple-negative breast cancer. Cancer Sci. **108**(6), 1210–1222 (2017)
28. Huang, Q., Gumireddy, K., Schrier, M., le Sage, C., Nagel, R., Nair, S., et al.: The microRNAs miR-373 and miR-520c promote tumour invasion and metastasis. Nat. Cell Biol. **10**(2), 202–210 (2008)
29. Wellner, U., Schubert, J., Burk, U.C., Schmalhofer, O., Zhu, F., Sonntag, A., et al.: The EMT-activator ZEB1 promotes tumorigenicity by repressing stemness-inhibiting microRNAs. Nat. Cell Biol. **11**(12), 1487–1495 (2009)

Data Science

Cell-Free Based Protein Array Technology

Ryo Morishita[1], Hirotaka Takahashi[2], and Tatsuya Sawasaki[2(✉)]

[1] CellFree Sciences. Co. Ltd., 3 Bunkyo-cho, Matsuyama 790-8577, Ehime, Japan
[2] Division of Cell-Free Sciences, Proteo-Science Center, 3 Bunkyo-cho, Matsuyama 790-8577,
Ehime, Japan
{takahashi.hirotaka.rn,sawasaki}@ehime-u.ac.jp

Abstract. Cell-free protein production technology can easily produce recombinant proteins from cDNA temples, because it is synthesized in a tube without cell culture. We developed a wheat cell-free protein production system from washed wheat embryos. Since our cell-free system is based on eukaryotic translational machinery, it is very suitable for synthesis of eukaryotic proteins such as human protein. Using this system, recently we made a protein array technology consisting of proteins synthesized in 384-well formatted plates, and then constructed human protein array consisting of more than 20,000 recombinant human proteins (20K-HuPA). In addition, combinations with AlphaScreen or magnetic plate technology promotes development of a new high-throughput and high-sensitive approach for identification of protein–protein or protein–antibody interaction. Herein, we demonstrate the results of protein interactomes and antibody validation by using protein array.

1 Importance of Protein–Protein Interactome

Proteins are the basic molecules responsible for the biological phenomena of all living organisms. Until now, proteins were thought to function alone, but recent many studies have revealed that many proteins function by interacting with other proteins to form multiple complexes [1]. In particular, in higher organisms such as humans, it has been found that the formation of protein complex is an important regulatory mechanism for protein function, and understanding of the protein complex is for elucidating higher-order functions of higher organisms. Therefore, finding a protein that interacts with the protein of interest has become an indispensable research for functional analysis of proteins. In addition, the protein complex is also expected to be drug targets because they function as switches for cell proliferation and response. In fact, in recent years, several inhibitors that inhibit formation of the complex such as ledipasvir known as hepatitis C virus therapeutic drug, have been put on the market and has shown great medicinal properties. The technique for comprehensively identifying interacting proteins is called interactome analysis. As mentioned above, this method is extremely important for the development of life science in general, from basic research to applied research such as drug discovery. Therefore, it is very important to understand how proteins interact with target proteins. Identification of partner proteins has been carried out by several technologies like the yeast two-hybrid system [2, 3], mass spectrometry analysis after immunoprecipitation

[4, 5], and cell-free based protein arrays that we have previously described [6, 7]. These methods provide many critical findings. Sine intracellular proteins are regulated by quite complicated systems like signalling transduction cascades, multiple technologies can strongly promote our understanding of cellular protein regulation.

1.1   Wheat Cell-Free Protein Production

In principle, if all proteins are prepared as a substrate, it is possible to identify partner proteins. Because complete genomic DNA sequencing of various species showed a gene set coding a protein, we can obtain DNA template for protein production. However, protein production is not so simple. Currently, three strategies are being used for protein production: chemical synthesis, in vivo expression, and cell-free protein synthesis. The first two methods have severe limitations. Chemical synthesis is not practical for the synthesis of peptides longer than 30 residues [8], and in vivo expression can produce only those proteins which do not significantly interfere with host cell physiology [9–11]. Cell-free translation systems, in contrast, can synthesize proteins with high speed and accuracy, approaching in vivo rates [12, 13], and they can express proteins that seriously interfere with cell physiology. However, they are relatively inefficient because of their instability [14].

More than 20 years ago, we found that plants contain endogenous inhibitors of translation [15] and we demonstrated that elimination of these inhibitors led to an extraordi-

Fig. 1. The mRNA synthesis from PCR-based cDNA template.

narily stable and efficient translation system [16]. However, in order to adapt the cell-free system to address the high-throughput needs of modern proteomics, several critical improvements were needed. More recently, we improved the system performance by examining the following critical design issues [17]: (a) optimization of the 5'- and 3'-UTRs of mRNA; (b) elimination of the 5'–7 mGpppG (cap) and poly(A)-tail (pA),

thereby increasing translation initiation; (c) design of PCR primers to generate transcription templates directly from *Escherichia. coli* cells carrying cDNAs (**Fig. 1**), thus bypassing the time-consuming cloning steps; (d) construction of an expression vector, specialized for the massive production of proteins; (e) continuous translation reactions; (f) robotic automation of the whole translation steps starting with transcription. These improvements provide a technology for highly productive eucaryotic cell-free protein production from wheat embryo.
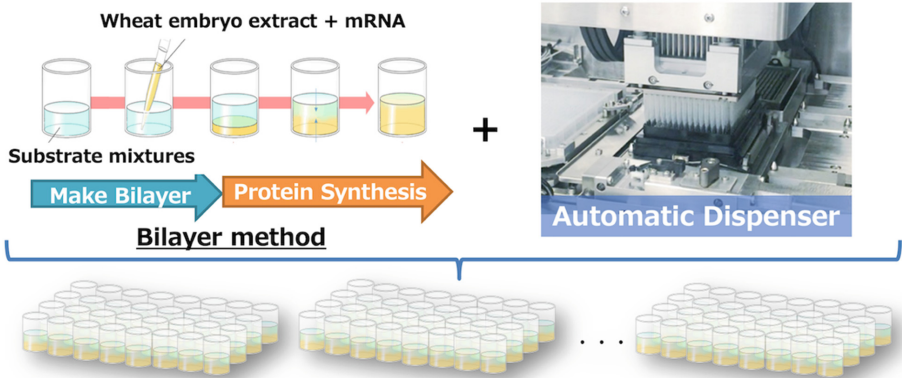
Fig. 2. Protein production on a 384-well plate using a wheat cell-free protein production method.

1.2 Cell-Free Based Protein Array

The wheat cell-free system is available to use PCR-based DNA template for large-size protein production such as human [17]. In addition, protein production by the cell-free system can carry out in a small well in 384-well plate [18], indicating that the cell-free system can prepare a large number of proteins. Furthermore, recent developments in DNA synthesis technology have been remarkable, and it has become possible to prepare a full-length cDNA set possessed by one species because it is possible to synthesize long DNA template found in higher eukaryotic genes. Therefore, the combination of the wheat cell-free system and a set of full-length cDNA can construct protein array (**Fig. 2**). Using this system, a set in which different cell-free synthetic proteins are mounted in each hole of a 96-hole or 384-hole plate is called a cell-free based protein array [18] (Fig. 3).

Fig. 3. Cell-free based protein array.

2   E3 Ubiquitin Ligase Protein Array

Protein ubiquitination plays crucial roles in numerous cellular processes, including cell growth, regulation of diverse signal transduction, and the development of disease [19–21]. It is mediated by three enzymatic reactions, the ubiquitin-activating enzyme E1, the ubiquitin-conjugating enzyme E2 and E3 ubiquitin ligase (E3). Because the substrate specificity of protein ubiquitination is widely thought to be determined mainly by E3 [22], identification of E3 interacting with target protein is a crucial step. To date, more than 600 E3s have been annotated in the human genome [23], and this diversity contributes to the specific recognition of numerous target proteins in eukaryotic cells. Identifying the E3 responsible for a target protein provides extensive information about the regulation mechanisms of half-life, localization, and functions in both the target proteins and the E3s in each biological phenomenon.

Assays based on living cells such as yeast, mammalian cultured cells, and model mouse are currently the primary tools used to identify combinations of E3s and their target proteins. Indeed, many physiologically important interactions between E3 and target protein were identified with various kinds of the cell-based assay [24–27]. However, because during the screening, a target protein is usually degraded immediately by 26S proteasomes after ubiquitination, the E3s of many target proteins—even widely studied proteins—remain unidentified. To overcome these situations, we developed a novel *in vitro* screening method by combining the cell-free based protein array and a high-throughput luminescence-based binding assay that is able to use crude protein samples (AlphaScreen) [7]. An E3 protein array consisting of 250 E3 ubiquitin ligases was made by the wheat cell-free system. To establish the high-throughput binding assay, we used an AlphaScreen, a luminescence-based interaction assay, to detect interaction between recombinant MDM2 and p53. This assay is performed in a 384-well format with only small amount (0.5 to 1.0 μL) of the crude translation mixtures from the wheat cell-free system without purification [28, 29]. As shown in Fig. **4**A, luminescent signal is obtained when FLAG-tagged E3 and biotinylated p53 are in proximity. Using this new method, we found novel E3s interacting with p53 (**Fig. 4**B). A several E3s in them induced ubiquitination of p53 (**Fig. 4**C). Therefore, these results demonstrated that the assay we developed is a powerful tool for the identification of novel E3s targeting proteins of interest. So far, the E3 protein array platform identified many E3s responsible for the proteins of interests. For examples, MIND bomb 2 (MIB2) has been identified as the responsible E3 involving with the proteolysis of a deubiquitinating enzyme, CYLD that negatively regulate NF-κB signaling through its deubiquitinating activity [30]. Interestingly, the array system revealed

that MIB2 also involved in the proteolysis of cellular FLICE-inhibitory protein (cFLIP) [31]. Furthermore, two E3s, STUB1 and RNF38 were identified as responsible E3s for RUNX1, a transcription factor correlating with development of hematopoietic neoplasms [32, 33]. These reports strongly indicated the robustness of the E3 array system.
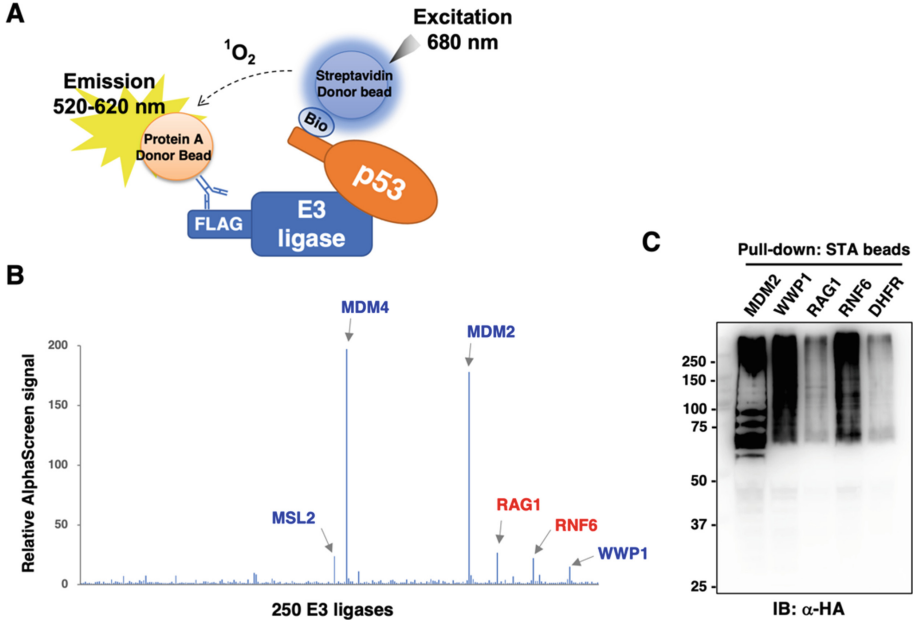

Fig. 4. Screening of E3 ubiquitin ligase interacting with p53. (A) Schematic diagram of the AlphaScreen assay. (B) The result of the AlphaScreen assay to detect the binding between p53 and 250 E3 ligases (E3s). Among the hit E3s with high AlphaScreen signal, the E3s that were already reported to bind to p53 are indicated in blue characters, and the E3s that were newly identified in the AlphaScreen are in red characters. (C) In vitro ubiquitination assay of p53 by hit E3s. Biotinylated p53 was mixed with each E3 and HA-tagged ubiquitin, and the ubiquitination reaction was carried out. Then the biotinylated p53 were pull-downed with streptavidin (STA) magnetic beads, and polyubiquitin chains on the p53 were detected by immunoblot analysis using anti-HA-antibody.

3 CF-PA^{2}Vtech (Cell-Free Based Protein Array for Antibody Validation)

A molecule of antibody has three special features: 1) high specificity, 2) high affinity, and 3) a high variety of recognition molecules [34–36]. Utilizing these features, the antibody is widely used to detect specific molecules such as proteins, peptides, nucleotides, or small chemical compounds in a broad range of biotechnological applications such as ELISA (enzyme-linked immunosorbent assay), immunoblotting, immunohistochemistry, and immunoprecipitation. In addition, the monoclonal antibody (mAb) has also been used in many medical therapies such as cancer immunotherapies [37, 38] and

infectious disease treatments [39–41]. In these utilizations of the antibody, especially for antibody drugs, the specificity of the antibody is the most important feature because the antibody is expected to recognize a single specific target molecule only. However, it is not easy to validate antibody specificity [42].

Since the antibody is widely used for multiple applications as described above, the validation methods are based on these applications. For example, an antibody for detecting a specific virus should be validated by using a wide variety of related viruses to prevent false-positive reactions. According to this concept, the best validation technique for an antibody against a specific human protein requires a method using all human proteins. However, it is impossible to collect all human proteins from cells or tissues because limited proteins are expressed in them. Thus, the cross-reactivity of a general antibody is based on limited data using several kinds of extracts from selected cells and/or tissues. A simple method for antibody validation using a wide-range of human proteins would provide useful information for researchers and medical doctors.

Previously, a human full-length cDNA set for wheat cell-free protein synthesis was reported [43]. All human recombinant proteins for the array were synthesized as a fusion form of N-terminal FLAG-GST (FG) protein by a wheat cell-free protein production system on 384-well (**Fig. 2**). In the construction of a protein array plate for antibody validation, about 14 kinds of FG-proteins were mixed with glutathione-conjugated magnetic beads, and then were washed four times with buffer to remove extra proteins from wheat embryo proteins. Because each well included about 14 kinds of proteins, CF-PA^{2}Vtech consists of a two-step screening, in which the first step is used to find positive mixed spot(s) and the second screening identifies individual positive clones.

For antibody validation, we used a protein array of a 1536-well format, in which about 14 kinds of proteins were captured on each well as a single spot, and a set consisted of a single plate. A notable feature of this format is that 19,712 human proteins were mounted on a single plate. Before screening, to investigate whether proteins could be captured on the 1536-well spot, a signal on each spot was detected by anti-FLAG antibody. Fluorescence intensity showed that more than 80% of wells were found within the high signal zone, indicating that a sufficient amount of FG-protein was captured in each well on a 1536-well array. Recently, many kinds of mAbs from rabbits have been widely used in cell biology. Thus, as an antibody for validation, we chose commercially available anti-PD-1 rabbit mAb (D4W2J, Cell Signaling Technology). Since this anti-PD-1 mAb has not been conjugated with the HRP enzyme, before the first screening, a background signal from rabbit-IgG-HRP mAb (NA934, GE Healthcare) used as a second antibody was analyzed. This pre-check indicated that a single spot (17–12, green colour) was provided by the rabbit-IgG antibody, indicating that this rabbit-IgG-HRP mAb has very low cross-reactivity with human proteins.

For the first screening (**Fig. 5**), anti-PD-1 mAb (100 ng/ml) was applied on a plate. After washing, rabbit-IgG-HRP mAb was also applied, and then the plate was treated with detection mixture after washing. On this human protein array, as a positive control, human PD-1 protein was mounted as two spots (02–46 and 02–48 shown as the blue colour on the right-upper area of a plate in **Fig. 5B**). The first screening results indicated five spots (red colour in **Fig. 5B**) as positive by imaging. Since the two spots on the right-upper area were human PD-1 protein (a blue ellipse), five spots (19–01, 19–46,

19–48, and 25–28) were found as positive mixture proteins in the human protein array. Detection of the PD-1 protein indicated that this screening worked well.
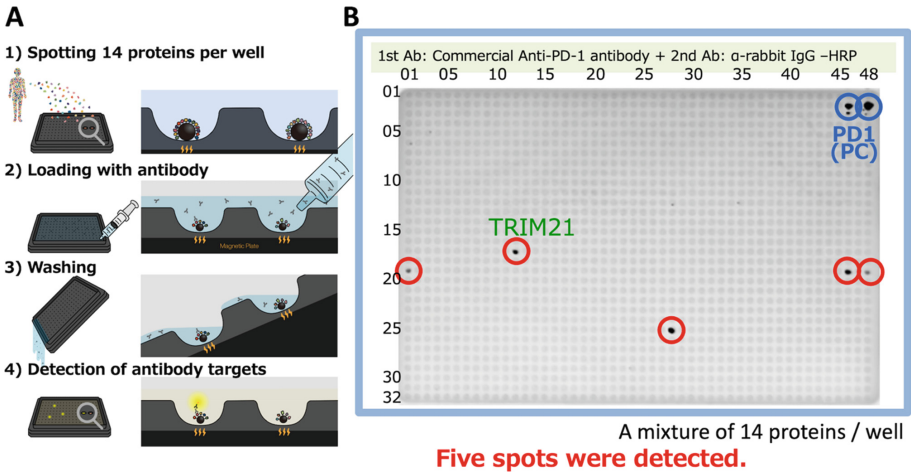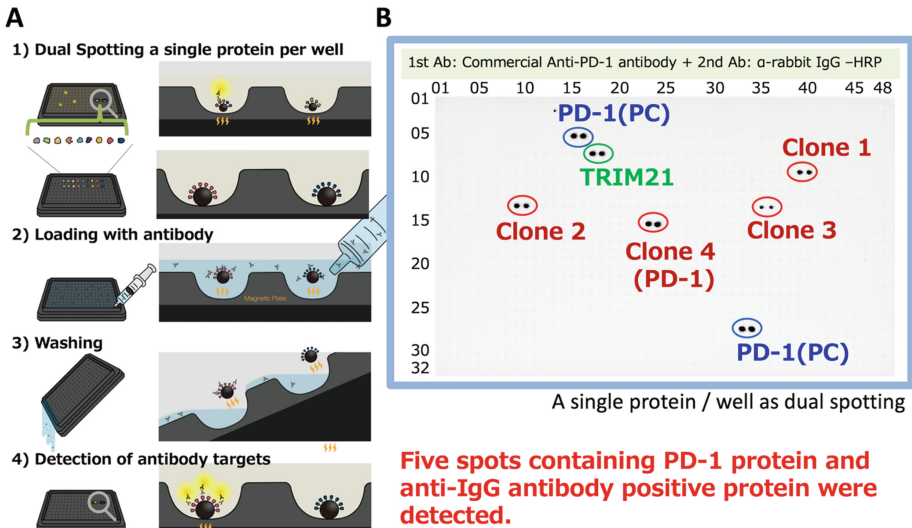

Fig. 5. The first screening procedure and results of cross-reactive antigen against anti-PD-1 antibody using CF-PA^{2}Vtech. (A) First screening procedure using CF-PA^{2}Vtech. 1) 19,712 human full-length proteins array onto one 1536-well plate with 14 proteins per well. 2) Antibody-containing solution is added and binding reaction is performed. 3) The plate is washed with TBST solution. 4) A chemiluminescence reagent is used for detection of binding signals. (B) The result images of the first screening using anti-PD-1 antibody by CF-PA^{2}Vtech. Five spots shown as black dots were positive. one spot was TRIM21 (green colour) reacting with secondary antibody. A blue ellipse indicates the spots of human PD-1 protein as a positive control (Color figure online).

Next, in the second screening (**Fig. 6**), a total of 170 proteins from the five positive and three border spots (17–44, 25–33, and 32–44 in **Fig. 5B**), three randomly selected spots (18–39, 26–35, and 31–33), 19 proteins, and control proteins including Venus (27–37/38) and PD-1 were individually spotted in a 1536-well plate as a dual spot. In the plate for the second screening, the PD-1 protein was used as a double dual spot (05–5/16 and 27–33/34) shown in the two blue ellipses in Fig. 5B. The same reaction condition as that of the first screening was used for this second screening. These results from a single image clearly indicated that four dual clones (09–39/40, 13–09/10, 13–35/36, and 15–23/24 shown as red ellipses) and TRIM21 (07–17/18, green ellipse) from the human protein array and two dual positive clones (two blue ellipses) reacted with anti-PD-1 mAb. Since TRIM21 has the ability to bind to IgG protein [44], this was considered background and not cross reactivation. Fortunately, all four positive spots from the first screening had one cross-reactive clone, indicating that the 1536-well formatted CF-PA^{2}Vtech is suitable for antigen screening against the antibody.

Fig. 6. The second screening procedure and results of cross-reactive antigen against anti-PD-1 antibody using CF-PA^{2}Vtech. (A) Second screening procedure using CF-PA^{2}Vtech. 1) Individual proteins from the first screening positive are re-arrayed a 1536-well plate with a single protein per well as each dual spot. 2) Antibody-containing solution is added and binding reaction is performed. 3) The plate is washing with TBST solution. 4) A chemiluminescence reagent is used for detection of binding signals. (B) The result images of the second screening using anti-PD-1 antibody by CF-PA^{2}Vtech. Four spots shown as black dots were positive. one spot was TRIM21 (green colour) reacting with secondary antibody. A blue ellipse indicates the spots of human PD-1 protein as a positive control (Color figure online).

4   Conclusion

In this review, we showed the two examples using the cell-free based protein array. Because they currently identified substrates or target antigen with its epitope, the cell-free based protein array would be very useful for screening of proteins interacting with target protein. If you have an interesting protein, the interactor screening using the protein array would provide the new insight with new partner protein(s).

References

1. Hartwell, L.H., Hopfield, J.J., Leibler, S., Murray, A.W.: From molecular to modular cell biology. Nature **402**, C47-52 (1999). https://doi.org/10.1038/35011540
2. Zhao, S., et al.: Screening and identification of host proteins interacting with Theileria annulata cysteine proteinase (TaCP) by yeast-two-hybrid system. Parasites Vectors, **10**, 536 (2017). https://doi.org/10.1186/s13071-017-2421-0
3. Li, J., et al.: Development of a membrane-anchored ligand and receptor yeast two-hybrid system for ligand-receptor interaction identification. Sci Rep **6**, 35631 (2016). https://doi.org/10.1038/srep35631

4. Ohshiro, K., et al.: Identification of a novel estrogen receptor-alpha variant and its upstream splicing regulator. Mol Endocrinol **24**, 914–922 (2010). https://doi.org/10.1210/me.2009-0413

5. Han, J., et al.: The identification of novel Protein-Protein interactions in liver that affect glucagon receptor activity. PLoS ONE **10**, e0129226 (2015). https://doi.org/10.1371/journal.pone.0129226

6. Nemoto, K., et al.: Tyrosine phosphorylation of the GARU E3 ubiquitin ligase promotes gibberellin signalling by preventing GID1 degradation. Nat. Commun. **8**, 1004 (2017). https://doi.org/10.1038/s41467-017-01005-5

7. Takahashi, H., et al.: Establishment of a wheat cell-free synthesized protein array containing 250 human and mouse E3 ubiquitin ligases to identify novel interaction between E3 ligases and substrate proteins. PLoS ONE **11**, e0156718 (2016). https://doi.org/10.1371/journal.pone.0156718

8. Blaschke, U.K., Silberstein, J., Muir, T.W.: Protein engineering by expressed protein ligation. Methods Enzymol **328**, 478–496 (2000). https://doi.org/10.1016/s0076-6879(00)28414-0

9. Henrich, B., Lubitz, W., Plapp, R.: Lysis of Escherichia coli by induction of cloned phi X174 genes. Mol Gen Genet **185**, 493–497 (1982). https://doi.org/10.1007/BF00334146

10. Golf, S.A., Goldberg, A.L.: An increased content of protease La, the lon gene product, increases protein degradation and blocks growth in Escherichia coli. J Biol Chem **262**, 4508–4515 (1987). PMID: 3549709

11. Chrunyk, B.A., Evans, J., Lillquist, J., Young, P., Wetzel, R.: Inclusion body formation and protein stability in sequence variants of interleukin-1 beta. J Biol Chem **268**, 18053–18061 (1993). PMID: 8394358

12. Kurland, C.G.: Translational accuracy in vitro. Cell **28**, 201–202 (1982). https://doi.org/10.1016/0092-8674(82)90336-1

13. Pavlov, M.Y., Ehrenberg, M.: Rate of translation of natural mRNAs in an optimized in vitro system. Arch Biochem Biophys **328**, 9–16 (1996). https://doi.org/10.1006/abbi.1996.0136

14. Roberts, B.E., Paterson, B.M.: Efficient translation of tobacco mosaic virus RNA and rabbit globin 9S RNA in a cell-free system from commercial wheat germ. Proc Natl Acad Sci USA **70**, 2330–2334 (1973). https://doi.org/10.1073/pnas.70.8.2330

15. Ogasawara, T., Sawasaki, T., Morishita, R., Ozawa, A., Madin, K., Endo, Y.: A new class of enzyme acting on damaged ribosomes: ribosomal RNA apurinic site specific lyase found in wheat germ. EMBO J **18**, 6522–6531 (1999). https://doi.org/10.1093/emboj/18.22.6522

16. Madin, K., Sawasaki, T., Ogasawara, T., Endo, Y.: A highly efficient and robust cell-free protein synthesis system prepared from wheat embryos: plants apparently contain a suicide system directed at ribosomes. Proc Natl Acad Sci USA **97**, 559–564 (2000). https://doi.org/10.1073/pnas.97.2.559

17. Sawasaki, T., Ogasawara, T., Morishita, R., Endo, Y.: A cell-free protein synthesis system for high-throughput proteomics. Proc Natl Acad Sci USA **99**, 14652–14657 (2002). https://doi.org/10.1073/pnas.232580399

18. Morishita, R., et al.: CF-PA^{2}Vtech: a cell-free human protein array technology for antibody validation against human proteins. Sci Rep. **9**(1), 19349 (2019). https://doi.org/10.1038/s41598-019-55785-5

19. Hershko, A., Ciechanover, A.: The ubiquitin system. Annu Rev Biochem. **67**, 425–479 (1998). https://doi.org/10.1146/annurev.biochem.67.1.425

20. Chen, Z.J., Sun, L.J.: Nonproteolytic functions of ubiquitin in cell signaling. Mol cell **33**(3), 275–286 (2009). https://doi.org/10.1016/j.molcel.2009.01.014

21. Lipkowitz, S., Weissman, A.M.: RINGs of good and evil: RING finger ubiquitin ligases at the crossroads of tumour suppression and oncogenesis. Nat Rev Cancer **11**(9), 629–643 (2011). https://doi.org/10.1038/nrc3120

22. David, Y., Ternette, N., Edelmann, M.J., Ziv, T., Gayer, B., Sertchook, R., et al.: E3 ligases determine ubiquitination site and conjugate type by enforcing specificity on E2 enzymes. J Biol Chem **286**(51), 44104–44115 (2011). https://doi.org/10.1074/jbc.M111.234559

23. Li, W., Bengtson, M.H., Ulbrich, A., Matsuda, A., Reddy, V.A., Orth, A., et al.: Genome-wide and functional annotation of human E3 ubiquitin ligases identifies MULAN, a mitochondrial E3 that regulates the organelle's dynamics and signaling. PLoS ONE **3**(1), e1487 (2008). https://doi.org/10.1371/journal.pone.0001487

24. Momand, J., Zambetti, G.P., Olson, D.C., George, D., Levine, A.J.: The mdm-2 oncogene product forms a complex with the p53 protein and inhibits p53-mediated transactivation. Cell **69**(7), 1237–1245 (1992). https://doi.org/10.1016/0092-8674(92)90644-r

25. Winston, J.T., Strack, P., Beer-Romero, P., Chu, C.Y., Elledge, S.J., Harper, J.W.: The SCFbeta-TRCP-ubiquitin ligase complex associates specifically with phosphorylated destruction motifs in IkappaBalpha and beta-catenin and stimulates IkappaBalpha ubiquitination in vitro. Genes Dev **13**(3), 270–283 (1999). https://doi.org/10.1101/gad.13.3.270

26. Locke, M., Tinsley, C.L., Benson, M.A., Blake, D.J.: TRIM32 is an E3 ubiquitin ligase for dysbindin. Hum Mol Genet **18**(13), 2344–2358 (2009). https://doi.org/10.1093/hmg/ddp167

27. Kronke, J., Fink, E.C., Hollenbach, P.W., MacBeth, K.J., Hurst, S.N., et al.: Lenalidomide induces ubiquitination and degradation of CK1alpha in del(5q) MDS. Nature **523**(7559), 183–188 (2015). https://doi.org/10.1038/nature14610

28. Takahashi, H., Nozawa, A., Seki, M., Shinozaki, K., Endo, Y., Sawasaki, T.: A simple and high-sensitivity method for analysis of ubiquitination and polyubiquitination based on wheat cell-free protein synthesis. BMC Plant Biol **9**, 39 (2009). https://doi.org/10.1186/1471-2229-9-39

29. Tadokoro, D., Takahama, S., Shimizu, K., Hayashi, S., Endo, Y., Sawasaki, T.: Characterization of a caspase-3-substrate kinome using an N- and C-terminally tagged protein kinase library produced by a cell-free system. Cell Death Dis **1**, e89 (2010). https://doi.org/10.1038/cddis.2010.65

30. Uematsu, A., et al.: The E3 ubiquitin ligase MIB2 enhances inflammation by degrading the deubiquitinating enzyme CYLD. J Biol Chem **294**(38), 14135–14148 (2019). https://doi.org/10.1074/jbc.RA119.010119

31. Nakabayashi, O., et al.: MIND bomb 2 prevents RIPK1 kinase activity-dependent and -independent apoptosis through ubiquitylation of cFLIPL. Commun Biol **4**(1), 80 (2021). https://doi.org/10.1038/s42003-020-01603-y

32. Yonezawa, T., et al.: The ubiquitin ligase STUB1 regulates stability and activity of RUNX1 and RUNX1-RUNX1T1. Biochem Biophys Res Commun **505**(3), 905–909 (2018). https://doi.org/10.1016/j.bbrc.2018.10.006

33. Yonezawa, T., Takahashi, H., Shikata, S., Sawasaki, T., Kitamura, T., Goyama, S.: The ubiquitin ligase RNF38 promotes RUNX1 ubiquitination and enhances RUNX1-mediated suppression of erythroid transcription program. J Biol Chem **292**(30), 12528–12541 (2017). https://doi.org/10.1074/jbc.M117.785675

34. Peng, H.P., Lee, K.H., Jian, J.W., Yang, A.S.: Origins of specificity and affinity in antibody-protein interactions. Proc Natl Acad Sci USA **111**, E2656-2665 (2014). https://doi.org/10.1073/pnas.1401131111

35. Kaplon, H., Reichert, J.M.: Antibodies to watch in 2019. MAbs **11**, 219–238 (2019). https://doi.org/10.1080/19420862.2018.1556465

36. de Taeye, S.W., Rispens, T., Vidarsson, G.: The ligands for human IgG and their effector functions. Antibodies **8**, 30 (2019). https://doi.org/10.3390/antib8020030

37. Ohaegbulam, K.C., Assal, A., Lazar-Molnar, E., Yao, Y., Zang, X.: Human cancer immunotherapy with antibodies to the PD-1 and PD-L1 pathway. Trends Mol Med **21**, 24–33 (2015). https://doi.org/10.1016/j.molmed.2014.10.009

38. Sharpe, A.H., Pauken, K.E.: The diverse functions of the PD1 inhibitory pathway. Nat Rev Immunol **18**, 153–167 (2018). https://doi.org/10.1038/nri.2017.108
39. Chan, C.E., Chan, A.H., Hanson, B.J., Ooi, E.E.: The use of antibodies in the treatment of infectious diseases. Singapore Med J **50**, 663–672 (2009). PMID: 19644620
40. Salazar, G., Zhang, N., Fu, T.M., An, Z.: Antibody therapies for the prevention and treatment of viral infections. NPJ Vaccines **2**, 19 (2017). https://doi.org/10.1038/s41541-017-0019-3
41. Sparrow, E., Friede, M., Sheikh, M., Torvaldsen, S.: Therapeutic antibodies for infectious diseases. Bull World Health Organ **95**, 235–237 (2017). https://doi.org/10.2471/BLT.16.178061
42. Bordeaux, J., et al.: Antibody validation. Biotechniques **48**, 197–209 (2010). https://doi.org/10.2144/000113382
43. Goshima, N., et al.: Human protein factory for converting the transcriptome into an in vitro-expressed proteome. Nat Methods **5**, 1011–1017 (2008). https://doi.org/10.1038/nmeth.1273
44. Mallery, D.L., McEwan, W.A., Bidgood, S.R., Towers, G.J., Johnson, C.M., James, L.C.: Antibodies mediate intracellular immunity through tripartite motif-containing 21 (TRIM21). Proc Natl Acad Sci USA **107**, 19985–19990 (2010). https://doi.org/10.1073/pnas.1014074107

Omics Data Analysis Tools for Biomarker Discovery and the Tutorial

Yosui Nojima[1(✉)] and Yoshito Takeda[2]

[1] Center for Mathematical Modeling and Data Science, Osaka University,
Toyonaka, Japan
nojima@sigmath.es.osaka-u.ac.jp
[2] Department of Respiratory Medicine and Clinical Immunology, Osaka University
Graduate School of Medicine, Suita, Japan

Abstract. Given the current progress in next-generation sequencing and mass spectrometry, considerable attention has been given to omics approaches and biomarker discovery to understand heterogeneous diseases. However, it is difficult to analyze them in the biological experimental community because the analysis processes are complicated. To address this problem, we have introduced and explained in this chapter the tools used for omics data analysis and how they are used.

Keywords: Biomarker · RNA-Seq analysis · Disease ontology · Metabolic networks

1 Introduction

While numerous biomarkers have been discovered for various diseases, their diagnostic and predictive abilities lack sensitivity and specificity in heterogeneous diseases [1,2]. In recent years, the use of high-throughput omics technologies has led to the rapid discovery of many candidate biomarkers [3]. Furthermore, the quest to uncover the mechanisms underlying complex biological processes and the proliferation of various high-throughput "omics" experiments has resulted in an unprecedented surge in the diversity, volume, and complexity of genomic, transcriptomic, proteomic, and metabolomic data among others [4]. Thus, these omics technologies are expected to provide breakthroughs in the research field of biomarker discovery.

In our recent study, combined metabolomic and transcriptomic analyses revealed a novel candidate biomarker for idiopathic pulmonary fibrosis (IPF), a chronic, progressive, and heterogeneous disease [5]. Mass spectrometry data analyses are mainly performed on a graphical user interface (GUI), whereas RNA-Seq data analyses are generally performed on a command line interface (CLI). Data analysis via CLI is complicated because CLI is not user friendly. In this chapter, we describe the tools that we used for RNA-Seq analysis in our previous study, and explain how to use them in CLI. Finally, we will introduce tools for subsequent analyses to provide biological understanding of metabolomic and transcriptomic data.

2 Downloading and Analysis of Public RNA-Seq Data

2.1 Gene Expression Omnibus

Gene expression omnibus (GEO, http://www.ncbi.nlm.nih.gov/geo/) is an international public repository for high-throughput microarray and next-generation sequence functional genomic data sets submitted by the research community [6] and is managed by the National Center for Biotechnology Information.

The descriptions below are the contents of the webpage of UC Berkley library [7] and are useful for better understanding the GEO.

1. The three main goals of GEO are to
    a. Provide a database of high-throughput functional genomic data.
    b. Support complete and well-annotated data deposits from the research community.
    c. Allow users to query, locate, review, and download studies and gene expression profiles of interest.
2. There are three types of GEO submitter records:
    a. A platform record describes an array or a sequencer and, for array-based platforms, a data table defines the array template. Sample records are linked to the platform records.
    b. A sample record describes the sample source, the protocols used in its analysis, and the expression data derived from it. Samples can only reference a single platform.
    c. A series record links together a group of related samples and describes a whole study.

2.2 How to Download RNA-Seq Data from GEO

To investigate the expression profile of pulmonary fibrosis-related genes, we obtained from GEO the public RNA-Seq data (GSE92592) of the lung tissues obtained from IPF patients (n = 20) and healthy controls (n = 19).

To download the raw RNA-Seq data (`.sra` file), we used `prefetch`, one of the programs of Sratoolkit (https://github.com/ncbi/sra-tools).

Use `--option-file` option to download multiple `.sra` files.

```
$ prefetch --option-file SraAccList.txt
```

`SraAccList.txt` is formatted as:

```
SRR5120902
SRR5120903
SRR5120904
...
SRR5120940
```

Then, `.sra` files were converted to `.fastq` files using `fastq-dump` which is a program of sratoolkit.

```
$ find . -name '*.sra' -exec fastq-dump --gzip
--split-files --outdir . /{} \;
```

2.3   RNA-Seq Analyses

We downloaded the RNA-Seq data from GEO as raw data and analyzed the data using the method described below.

2.3.1   Quality Control and Read Trimming

The data quality of the fastq files was verified with the FastQC tool (http://www.bioinformatics.babraham.ac.uk/projects/fastqc/). Read trimming was performed with Trimmomatic version 0.36 (http://www.usadellab.org/cms/?page=trimmomatic) [8] using the following command line.

```
$ java -jar trimmomatic-0.36.jar PE -threads
40 -phred33 read_1.fastq.gz read_2.fastq.gz
read_1_paired.fastq.gz read_1_unpaired.fastq.gz
read_2_paired.fastq.gz read_2_unpaired.fastq.gz
ILLUMINACLIP:Truseq_adapter.fa:2:30:10 LEADING:20
TRAILING:20 SLIDINGWINDOW:4:20 MINLEN:2
```

2.3.2   Genome Mapping

Trimmed reads were mapped to the reference human genome, GRCh38, available in the Ensembl genome database (https://asia.ensembl.org/Homo_sapiens/Info/Index) using STAR program version 2.7.0b (https://github.com/alexdobin/STAR) [9] with mismatch option `--outFilterMismatchNmax 2`. Prior to the genome mapping, the genome index was generated using the following command line.

```
$ mkdir star2.7.0b_index
$ STAR --runMode genomeGenerate --genomeDir
star2.7.0b_index/ --genomeFastaFiles
Homo_sapiens.GRCh38.dna.primary_assembly.fa --sjdbGTFfile
Homo_sapiens.GRCh38.92.gtf --runThreadN 40
```

Then, the genome mapping was run with the following command line.

```
$ STAR --runThreadN 40 --limitBAMsortRAM
187000000000 --outSAMtype BAM SortedByCoordinate
--outFilterMismatchNmax 2 --quantMode TranscriptomeSAM
GeneCounts --readFilesCommand gunzip -c --genomeDir
star2.7.0b_index/ --readFilesIn read_1_paired.fastq.gz
read_2_paired.fastq.gz --outFileNamePrefix star_output
```

2.3.3   Gene Abundance Calculation

RNA-seq by Expectation-Maximization software version 1.3.0 (https://github.com/deweylab/RSEM) [10] was used to calculate the expression values in transcripts per million (TPM). Prior to the gene abundance calculation, the reference for the calculation was built using the following command line.

```
$ mkdir rsem_ref
$ rsem-prepare-reference -p 40 --gtf
Homo_sapiens.GRCh38.92.gtf --star --star-path
[PATH/TO/STAR] Homo_sapiens.GRCh38.dna.primary_assembly.fa
rsem_ref/GRCh38
```

Then, TPM values were calculated with the following command line.

```
$ rsem-calculate-expression --num-threads
40 --paired-end --bam --no-bam-output
star_output_Aligned.toTranscriptome.out.bam
rsem_ref/GRCh38 rsem_output
```

2.3.4   Differentially Expressed Gene

Differentially expressed genes (DEGs) were defined by false discovery rate (FDR) and fold change (FC). P value was calculated by Welch's t-test, and FDR was calculated using Storey's method [11]. FC was removed by FC < 2.

The workflow of RNA-Seq analysis described in Sec. 2 is shown in **Fig. 1**.
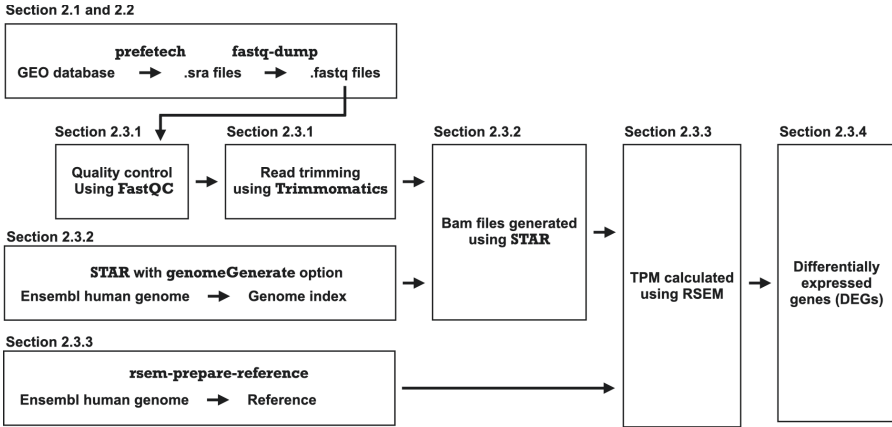
Fig. 1. The workflow of the downloading and analysis of public RNA-Seq data.

3   Disease Ontology

Disease ontology has been developed as a standardized ontology for human disease with the purpose of providing the biomedical community with consistent, reusable, and sustainable descriptions of human disease terms, phenotype characteristics, and related medical vocabulary disease concepts [12]. Using the information about disease ontology, disease enrichment analysis was performed using DOSE R package, which analyzed whether the input genes or proteins have the feature of any diseases. Generally, differentially expressed genes or proteins have the potential to be novel biomarker candidates. Thus, it is very important to know whether the features of the disease could be interpreted using these genes or proteins. ClusterProfiler R package was designed by considering the support of multiple ontologies/pathways, up-to-date gene annotation, multiple organisms, user's annotation data, and comparative analysis [13]. After obtaining the output results from DOSE, clusterProfiler provided the P value of each disease term using Fisher's exact test [14] according to the following equation:

$$P = \frac{{}_{a+b}C_a \times {}_{c+d}C_c}{{}_{a+b+c+d}C_{a+c}}$$

a, b, c and d are defined in Table 1.

Table 1. The number of genes or proteins in the input list and the number not in the input list

	In the input list	Not in the input list	Total
Associated genes or proteins	a	b	a + b
Unassociated genes or proteins	c	d	c + d
Total	a + c	b + d	a + b + c + d

a; the number of the associated genes or proteins in the input list
b; the number of the associated genes or proteins not included in the input list
c; the number of the unassociated genes or proteins in the input list
d; the number of the unassociated genes or proteins not included in the input list

4 Metabolic Networks

Metabolic networks describe the relationships between metabolites and the enzymes (proteins) that interact with them to catalyze a biochemical reaction [15].

MetaCore (Clarivate Analytics, Philadelphia, United States) is a commercial tool for functional analysis and visualization of different kinds of high-throughput omics data [16], which provide the core capabilities of precise pathway analysis, knowledge mining, simple bioinformatics, and effective visualizations in a comprehensive off-the-shelf package. High-quality 100% manually curated biological pathway data from peer-reviewed literature are used to accelerate drug development by rapidly generating and validating hypotheses for novel biomarkers, targets, and mechanisms of action [17].

We used "Metabolic Networks (Endogenous)", which is a function of MetaCore, to perform metabolic network analysis. The Enrichment Analysis "Metabolic Networks (Endogenous)" ontology only includes networks built around endogenous metabolic processes, that is, processes related to internal metabolic processes [18]. MetaCore is able to concurrently input the gene and metabolic list, and thus, both genes and metabolites are mapped in one network (**Fig.** 2). This function helps to better understand the metabolism and the related factors of the biomarker.
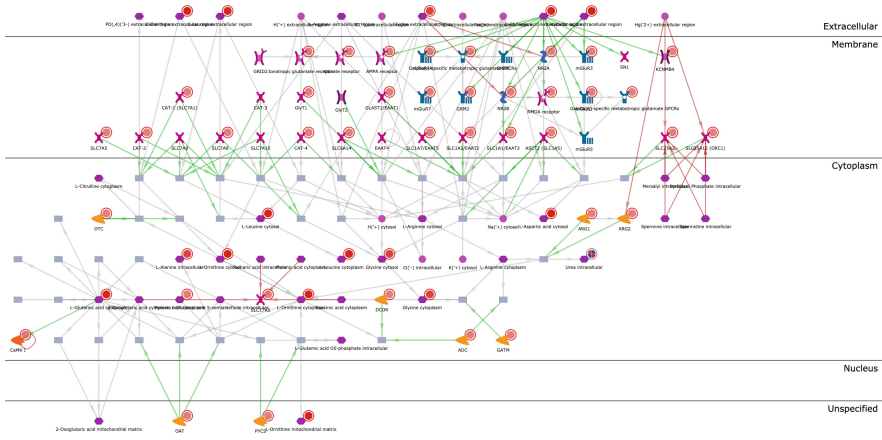
Fig. 2. An example of the metabolic network outputted from MetaCore. The green, red, and gray arrows indicate positive effect, negative effect, and unspecified effects, respectively. Closed red circles or mixed red/blue circles indicate differentially changed metabolites. Further explanations are provided at https://portal.genego.com/legends/MetaCoreQuickReferenceGuide.pdf. (Color figure online)

5   Conclusion

In this chapter, we have described RNA-Seq analysis tools and explained how to use them. We subsequently introduced tools and methods to biologically understand metabolomic and transcriptomic data. Using methods described in this chapter, we recently found that the proline and methionine in bronchoalveolar lavage fluid and serum are candidate diagnostic biomarkers for IPF, as our data suggest that proline and methionine-related genes are involved in their metabolism and transport [5]. Therefore, multi-layer combination omics studies have the potential to discover novel biomarker candidates and reveal mechanisms of biomarker involvement at different levels. We hope that this chapter will help researchers better understand and analyze omics data.

References

1. Zhao, Y.D., et al.: Metabolic heterogeneity of idiopathic pulmonary brosis: a metabolomic study. BMJ Open Respir. Res. **4**, e000183 (2017)
2. Zhang, Y., Kaminski, N.: Biomarkers in idiopathic pulmonary brosis. Curr. Opin. Pulm. Med. **18**, 441–446 (2012)
3. Quezada, H., Guzmán-Ortiz, A., Díaz-Sánchez, H., Valle-Rios, R., Aguirre-Hernández, J.: Omics-based biomarkers: current status and potential use in the clinic. Bol. Med. Hosp. Infant. Mex. **74**(3), 219–226 (2017)

4. Tripathi, L., Esaki, T., Itoh, M., Chen, Y.A., Mizuguchi, K.: Integrative analysis of multi-omics data. Encycl. Bioinform. Comput. Biol. 194–199 (2019)
5. Nojima, Y., Takeda, Y., Maeda, Y., Bamba, T., Fukusaki, E., Itoh, M., Mizuguchi, K., Kumanogoh, A.: Metabolomic analysis of fibrotic mice combined with public RNA-Seq human lung data reveal potential diagnostic biomarker candidates for lung fibrosis. FEBS Open Bio **10**(11), 2427–2436 (2020)
6. Barrett, T., Wilhite, S., Ledoux, P., Evangelista, C., Kim, I., Tomashevsky, M., Marshall, K., Phillippy, K., Sherman, P., Holko, M., Yefanov, A., Lee, H., Zhang, N., Robertson, C., Serova, N., Davis, S., Soboleva, A.: NCBI GEO: archive for functional genomics data sets–update. Nucleic Acids Res. **41**(D1), D991–D995 (2012)
7. Berkeley Library, University of California. (https://guides.lib.berkeley.edu/c.php?g=403317&p=6553361)
8. Bolger, A.M., Lohse, M., Usadel, B.: Trimmomatic: a flexible trimmer for illumina sequence data. Bioinformatics **3015**, 2114–2120 (2014)
9. Dobin, A., Davis, C.A., Schlesinger, F., Drenkow, J., Zaleski, C., Jha, S., Batut, P., Chaisson, M., Gingeras, T.R.: STAR: ultrafast universal RNA-seq aligner. Bioinformatics **29**(1), 1–21 (2013)
10. Li, B., Ruotti, V., Stewart, R.M., Thomson, J.A., Dewey, C.N.: RNA-Seq gene expression estimation with read mapping uncertainty. Bioinformatics **26**(4), 493–500 (2010)
11. Storey, J.D., Tibshirani, R.: Statistical significance for genomewide studies. Proc. Natl. Acad. Sci. U.S.A. **100**(16), 9440–9445 (2003)
12. Disease Ontology (https://disease-ontology.org/)
13. Slifka, M.K., Whitton, J.L.: Clinical implications of dysregulated cytokine production. J. Mol. Med. **78**(2), 74–80 (2000). https://doi.org/10.1007/s001090000086
14. Fisher, R.A.: On the interpretation of χ^2 from contingency tables, and the calculation of P. J. Roy. Stat. Soc. **85**(1), 87–94 (1922)
15. Castrillo, J.I., Pir, P., Oliver, S.G.: Yeast systems biology: towards a systems understand-ing of regulation of eukaryotic networks in complex diseases and biotechnology, pp. 343–365. Elsevier, Handbook of systems biology (2013)
16. Cambiaghi, A., Ferrario, M., Masseroli, M.: Analysis of metabolomic data: tools, current strategies and future challenges for omics data integration. Brief. Bioinform. **18**(3), 498–510 (2016)
17. MetaCore. (https://clarivate.com/cortellis/solutions/early-research-intelligence-solutions/)
18. Metabolic Networks (Endogenous). (https://support.clarivate.com/Endnote/s/article/MetaCore-Difference-between-Metabolic-network-and-Metabolic-network-endogenous?language=en_US/)

Integrative Network Analysis of Cancer Cell Signaling by High-Resolution Proteomics

Masaaki Oyama$^{(\boxtimes)}$ and Hiroko Kozuka-Hata

Medical Proteomics Laboratory, The Institute of Medical Science, The University of Tokyo,
4-6-1 Shirokanedai, Minato-ku, Tokyo 108-8639, Japan
{moyama,hata}@ims.u-tokyo.ac.jp

Abstact. Post-translational modifications (PTMs), such as phosphorylation, ubiquitination and acetylation, are known to be widely involved in the regulation of various biological processes through extensive diversification of each protein function at the cellular network level. Previous functional analyses of cancer cell signaling under a variety of experimental conditions revealed many of the key molecules and their associated protein modifications in relation to each type of cancer. In order to systematically discover critical modulators from diversified signaling molecules, we have developed a high-resolution mass spectrometry-based proteomics platform for integrative identification and quantification of multiple post-translational modifications from various types of cancer cells. In this chapter, we would like to highlight the potential impact of computational network dissection based on PTM-directed proteomic data towards systematic understanding of cellular signaling principles.

1 Shotgun Proteomics Enables Comprehensive Identification and Quantification of the Focused Protein Modifications

Signal transduction is known to play a diverse role in regulating complex biological events such as proliferation, differentiation and apoptosis. Protein modifications including phosphorylation, ubiquitination, and acetylation is known to regulate hub protein molecules, such as epidermal growth factor receptor (EGFR) and p53 in cancer cell signaling as described in the PTM knowledgebase [1]. Shotgun proteomic analysis of cellular protein-protein interaction networks revealed many of the key molecules and their associated protein modifications in relation to each biological context [2–8].

Based on the highly sensitive mass spectrometry technology, we have developed a high-resolution proteomics platform for integrative identification and quantification of multiple post-translational modifications (PTMs) from various types of cancer cells. Our analytical workflow allows us to perform comprehensive detection of representative protein modifications, such as phosphorylation, ubiquitination and acetylation, leading to system-wide extraction of significant molecules from large-scale PTM data in a statistical manner (Fig. 1).
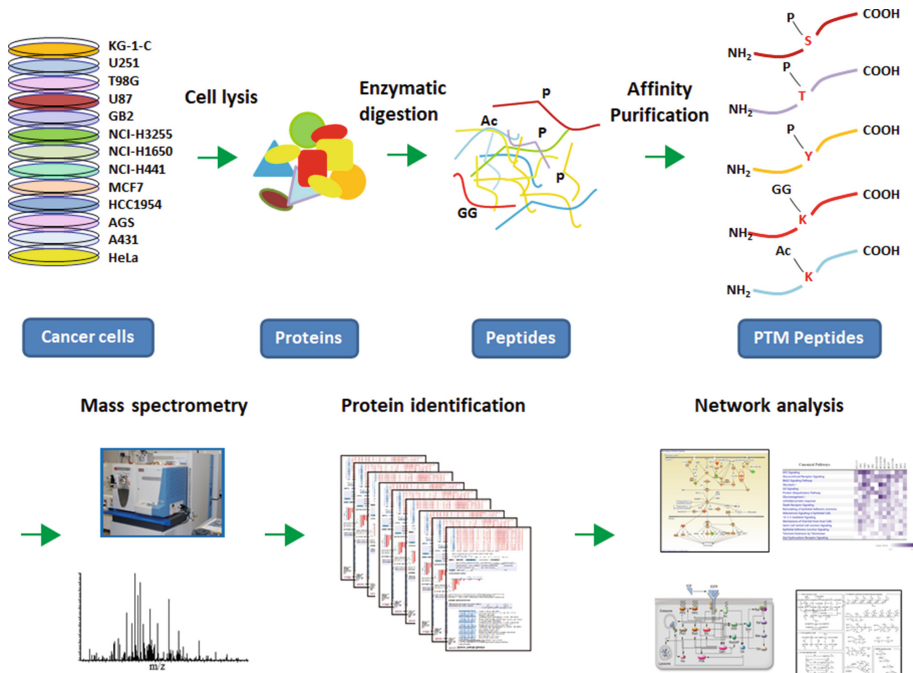
Fig. 1. Schematic workflow for integrative analysis of protein modifications by shotgun proteomics

2 Global Regulation of Cancer Cell Signaling Networks by Post-Translational Modification Dynamics

2.1 Phosphoproteomics

Recent technological advances regarding high-resolution quantitative proteomics, in combination with phosphorylation-directed protein/peptide enrichment methodology, have enabled us to grasp the dynamic status of phosphorylated cellular signaling molecules in a comprehensive and unbiased manner [9, 10]. Our in-depth phosphoproteome analysis of glioblastoma initiating cells led to identification of 6,073 phosphopeptides derived from 2,282 proteins and showed 516 up-regulated and 275 down-regulated phosphorylation sites upon epidermal growth factor (EGF) stimulation [11]. Very interestingly, the phosphorylation levels of the cellular molecules related to the ERK/MAPK and mTOR signaling pathways were dynamically changed in response to this external input (Fig. 2).

2.2 Lysine Modification Proteomics

Further in-depth proteomic analyses of protein lysine acetylation and ubiquitination based on shotgun mass spectrometric detection in combination with antibody-based affinity enrichment of lysine-modified peptides enabled global identification of more
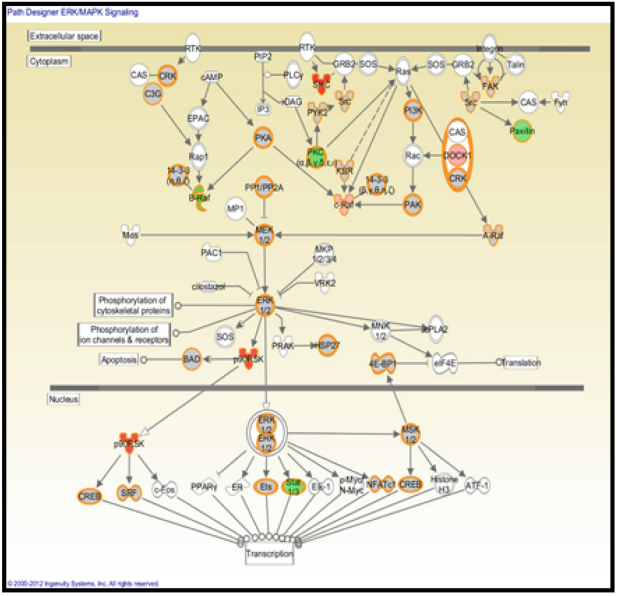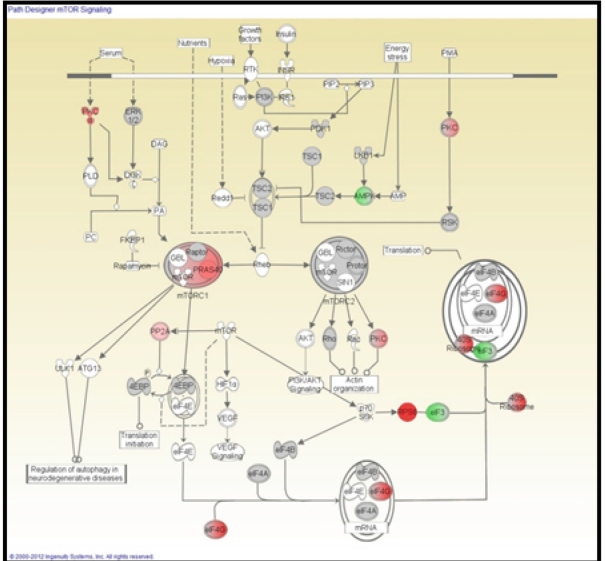
Fig. 2. Phosphorylation-dependent signaling regulation of human glioblastoma initiating cells in response to EGF stimulation. Pathway-level description of the phosphorylated molecules were visualized by Ingenuity Pathway Analysis (IPA) [12]. The red nodes indicate upregulated signaling effectors, whereas the green ones represent downregulated molecules.

than 6,000 ubiquitination and acetylation sites including 236 lysine residues regulated through both of the two modification modes [13]. The integrative pathway analysis of the large-scale lysine modification proteome data uncovered cell type-dependent lysine modification diversity at the cellular network level (Fig. 3). We found that that the EIF2 signaling pathway was relatively enriched in brain-derived cancer cell lines such as U251, T98G and U87 cells.
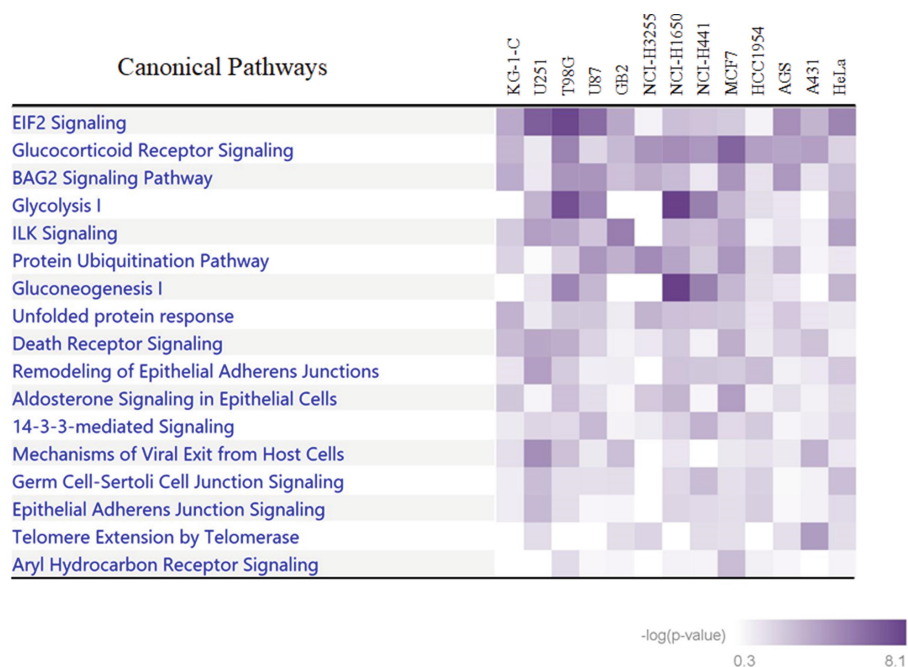
Fig. 3. IPA-based canonical pathway analysis of the dually lysine-modified proteins identified from each cancer cell line. The IPA canonical pathways relevant to the molecules modified with ubiquitination as well as acetylation are shown with the corresponding score ($-\log$ [p value]), adapted from Ref. [13].

2.3 Mathematical Modeling of Cellular Signaling Networks Based on PTM-Directed Quantitative Proteomic Data

The proteomics-oriented computational approaches have also opened up a new gate for mathematical modeling of cellular signaling networks involved in cancer. We developed a computational framework based on data assimilation and applied it for analyzing mutated EGFR signaling through phosphoproteomics-driven numerical modeling [14]. The hybrid functional petri net with extension (HFPNe) is a computational modeling architecture which can deal with discrete biological events as well as continuous ones and enables us to analyze temporal data on biological entities such as phosphorylated signaling molecules within the data assimilation framework (Fig. 4).
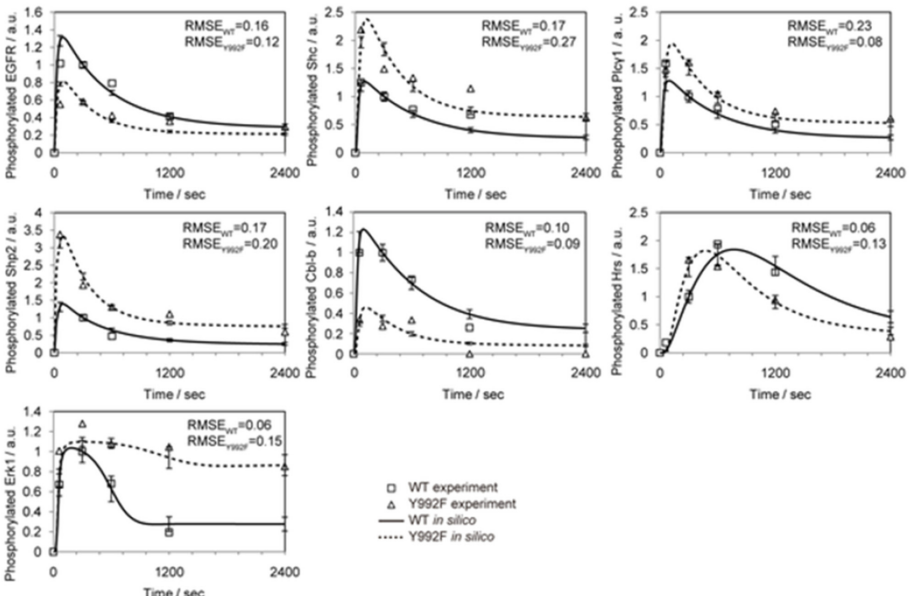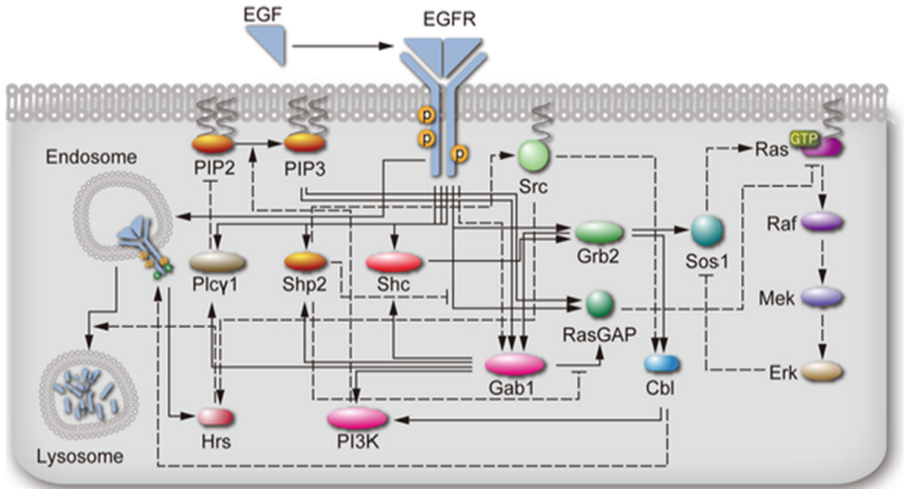
Fig. 4. Mathematical modeling of EGF signaling networks based on tyrosine phosphoproteome dynamics regarding NIH3T3 cells expressing full-length human EGFR (WT) and mutant EGFR with substitution of tyrosine to phenylalanine at position 992 (Y992F) upon EGF stimulation, adapted from Ref. [14].

The previous study based on the protein microarray analysis indicated that phosphorylated Y992 bound to multiple cellular proteins, serving as a multifunctional docking site of EGFR [15]. The HFPNe-based computational modeling of aberrant EGFR

(Y992F) signaling allowed us to reduce the factors responsible for mutational effect to several alterations in the reaction parameters and provided a mechanistic description of the signaling disorders at the network level (Fig. 5). Our mathematical model-based analyses indicated that Y992F mutation caused rapid EGFR degradation through the upregulation of EGFR ubiquitination and aberrant temporal activation of ERK1 by network-wide activation of tyrosine phosphorylation, which suggests that pY992 strengthens and attenuates phosphotyrosine singling by distinct regulatory mechanisms.
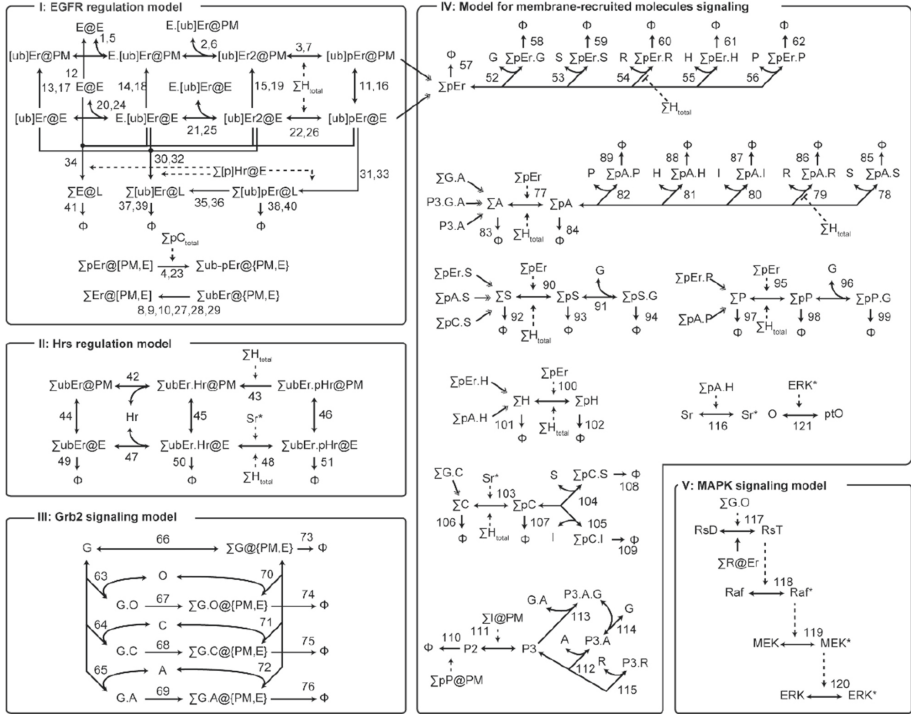
Fig. 5. Parameter-based evaluation of critical biochemical reactions in mutated EGFR signaling. The numbers attached to the arrows represent the reaction indexes of this simulation model. Each of the 38 estimated parameters in the Y992F model was reset to the value in the WT model, and the likelihood for the measured data was evaluated. The color bar shows the log-transformed fold change of the likelihood against the value in the original Y992F model, adapted from Ref. [14].
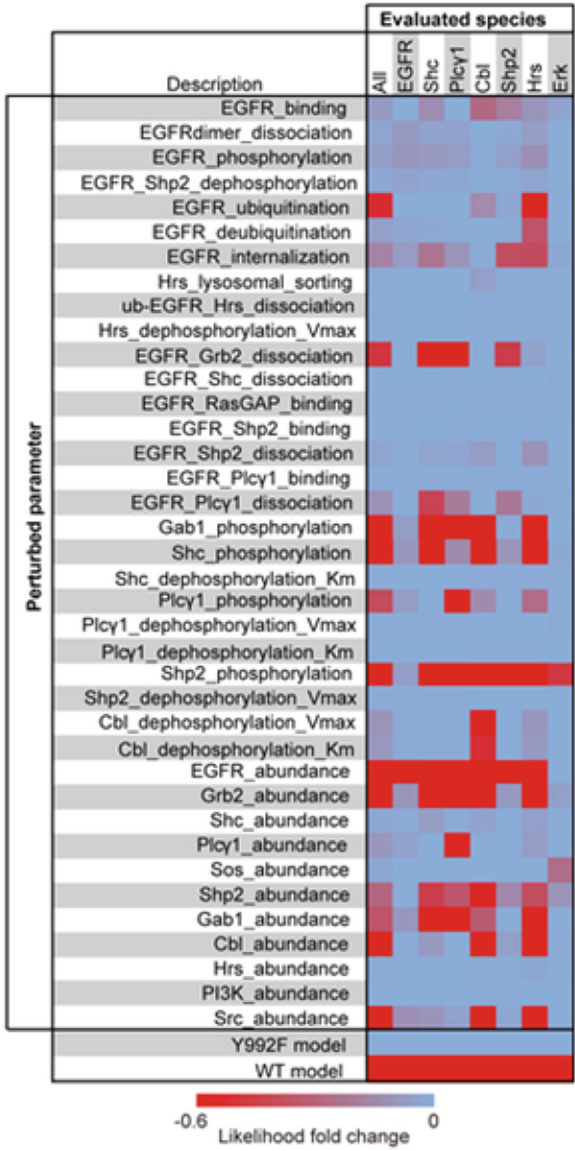
Fig. 5. (*continued*)

3 Future Prospects

Our high-resolution proteomic platform based on affinity enrichment of post-translationally modified peptides in combination with high-resolution mass spectrometry enabled us to unveil global phosphorylation and lysine acetylation/ubiquitination regulation in various types of human cancer cells. We consider that integrative network analysis based on multiple PTM-directed proteomic big data will lead to detailed dissection of

signaling dynamics and facilitate systematic visualization of complex signaling hubs related to each cell fate regulation [16–18].

References

1. Hornbeck, P.V., et al.: 15 years of PhosphoSitePlus®: integrating post-translationally modified sites, disease variants and isoforms. Nucleic Acids Res **47**, D433–D441 (2019)
2. Shibata, Y., et al.: p47 negatively regulates IKK activation by inducing the lysosomal degradation of polyubiquitinated NEMO. Nat Commun **3**, 1061 (2012)
3. Hirano, A., et al.: FBXL21 regulates oscillation of the circadian clock through ubiquitination and stabilization of cryptochromes. Cell **152**, 1106–1118 (2013)
4. Ohta, M., et al.: Direct interaction of Plk4 with STIL ensures formation of a single procentriole per parental centriole. Nat Commun **5**, 5267 (2014)
5. Inoue, D., Nishimura, K., Kozuka-Hata, H., Oyama, M., Kitamura, T.: The stability of epigenetic factor ASXL1 is regulated through ubiquitination and USP7-mediated deubiquitination. Leukemia **29**, 2257–2260 (2015)
6. Inoue, D., et al.: A novel ASXL1-OGT axis plays roles in H3K4 methylation and tumor suppression in myeloid malignancies. Leukemia **32**, 1327–1337 (2018)
7. Oishi, K., Yamayoshi, S., Kozuka-Hata, H., Oyama, M., Kawaoka, Y.: N-Terminal acetylation by NatB Is required for the shutoff activity of influenza a virus PA-X. Cell Rep **24**, 851–860 (2018)
8. Tatebayashi, K., et al.: Osmostress enhances activating phosphorylation of Hog1 MAP kinase by mono-phosphorylated Pbs2 MAP2K. EMBO J **39**, e103444 (2020)
9. Oyama, M., et al.: Temporal perturbation of tyrosine-phosphoproteome dynamics reveals the system-wide regulatory networks. Mol Cell Proteomics **8**, 226–231 (2009)
10. Oyama, M., et al.: Integrated quantitative analysis of the phosphoproteome and transcriptome in tamoxifen-resistant breast cancer. J Biol Chem **286**, 818–829 (2011)
11. Kozuka-Hata, H., et al.: Phosphoproteome of human glioblastoma initiating cells reveals novel signaling regulators encoded by the transcriptome. PLoS ONE **7**, e43398 (2012)
12. Krämer, A., Green, J., Pollard, J., Jr., Tugendreich, S.: Causal analysis approaches in ingenuity pathway analysis. Bioinformatics **30**, 523–530 (2014)
13. Kozuka-Hata, H., et al.: System-wide analysis of protein acetylation and ubiquitination reveals a diversified regulation in human cancer cells. Biomolecules **10**, 411 (2020)
14. Tasaki, S., et al.: Phosphoproteomics-based modeling defines the regulatory mechanism underlying aberrant EGFR signaling. PLoS ONE **5**, e13926 (2010)
15. Jones, R.B., Gordus, A., Krall, J.A., MacBeath, G.: A quantitative protein interaction network for the ErbB receptors using protein microarrays. Nature **439**, 168–174 (2006)
16. Kozuka-Hata, H., Tasaki, S., Oyama, M.: Phosphoproteomics-based systems analysis of signal transduction networks. Front Physiol **2**, 113 (2012)

17. Narushima, Y., et al.: Integrative Network Analysis Combined with Quantitative Phospho-proteomics Reveals TGFBR2 as a Novel Regulator of Glioblastoma Stem Cell Properties. Mol Cell Proteomics **15**, 1017–1031 (2016)
18. Narushima, Y., Kozuka-Hata, H., Tsumoto, K., Inoue, J., Oyama, M.: Quantitative phosphoproteomics-based molecular network description for high-resolution kinase-substrate interactome analysis. Bioinformatics **32**, 2083–2088 (2016)

Distance-Matrix-Based Extraction of Motility Features from Functionally Heterogeneous Cell Populations

Naotoshi Nakamura[1,2(✉)] and Ryo Yamada[2]

[1] Center for Mathematical Modeling and Data Science, Osaka University,
Toyonaka, Japan
n-nakamura@sigmath.es.osaka-u.ac.jp
[2] Department of Statistical Genetics, Center for Genomic Medicine,
Kyoto University, Kyoto, Japan
ryamada@genome.med.kyoto-u.ac.jp

Abstract. It has recently been recognized that seemingly identical cell populations can exhibit functional heterogeneity *in vivo*. However, the unsupervised extraction of features to understand such heterogeneous cell behaviors has been a challenging task. Here, we present a novel, data-driven method to visualize cell heterogeneity as a set of points in a low-dimensional Euclidean space, based on a distance matrix between individual cells. The axes of this space serve as a guide for finding the characteristic features in the population. By using cell motility as an example, we show that our visualization can distinguish three types of simulated cell movements as separate clusters, without knowing *a priori* the mathematical models they follow. By applying our method to time-lapse two-photon imaging data of neutrophils, we successfully extract critical features that characterize different types of cell motility. We expect that our method would be applicable to other cellular phenotypes.

1 Introduction

Cell motility is observed in many types of cells and plays essential roles in a wide variety of biological phenomena, ranging from bacterial chemotaxis and wound healing with fibroblasts to immune cell migration and cancer cell metastasis [1]. It is often studied using the imaging data recorded with time-lapse microscopy. The method of analysis commonly employed for extracting the characteristic features related to cell motility from the imaging data involves fitting the motility of the entire cell population with a single equation of motion with noise, considering individual cells as different realizations of a stochastic process [2]. In this approach, we can obtain statistically robust results by gathering the data of all cells in the imaging field. However, it suffers from two major problems. First, the equations of motion that need to be used should be known beforehand. Second, it neglects cell-to-cell heterogeneity, which may have biological significance that is yet to be uncovered, as suggested in recent literature [3–6].

In this paper, we propose a new data-driven approach wherein no prior knowledge of cell models is necessary. Instead of fitting data to known mathematical models, we first extract and visualize the important axes that dominate the variability between cells. We can then use them as a guide to search for appropriate mathematical models of cell motility.

2   Problem Formulation

Here, we state our problem of extracting motility features using a simulated dataset consisting of three types of two-dimensional (2D) cell movements: 100 cells following random walk, 100 cells following persistent random walk, and 100 cells following Lévy walk (Fig. 1). We simulated the coordinates (x_t, y_t) of the same cells for 31 consecutive time frames ($t = 0, \ldots, 30$), so that the length of the cell trajectories is 31 for all cells. However, as we see later in the real dataset, the length can be different for different cells. Note that we ignore the cell size and treat individual cells as points. Details of the simulations are described in the Appendix.

We first consider the cell velocities, which are defined here as 2D vectors $(x_{t+1} - x_t, y_{t+1} - y_t)$ with discrete steps from time t to $t + 1$ ($t = 0, \ldots, 29$). We use this collection of velocities, expressed as a 30×2 matrix for each cell, as one type of input data. We also focus on the angles between adjacent velocities, $(x_{t+2} - x_{t+1}, y_{t+2} - y_{t+1})$ and $(x_{t+1} - x_t, y_{t+1} - y_t)$ ($t = 0, \ldots, 28$). These angles take values in $[-\pi, \pi)$. We use this collection of angles, expressed as a 29×1 matrix for each cell, as another type of input data. In general, the input data consists of a collection of k-dimensional vectors, expressed as an $n \times k$ matrix for each cell, where n is the number of observations.

Our goal is to condense these input data and obtain the characteristic features that can best explain cell-to-cell heterogeneity and distinguish different types of movements.
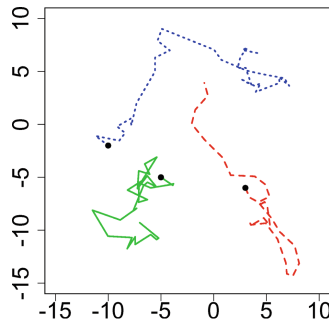

Fig. 1. Examples of simulated trajectories: random walk (solid green line); persistent random walk (dashed red line); and Lévy walk (dotted blue line). In this figure, the starting points (black dots) were shifted to prevent trajectories from overlapping. (Color figure online)

3   The Proposed Method

The proposed method is comprised of three steps (Fig. 2): (1) treat the input data (velocities or angles of cell trajectories) as random samples from a probability density, which can be regarded as a hidden phenotype of a cell; (2) construct a distance matrix (whose size is equal to the number of cells) between probability densities; (3) use multidimensional scaling to express each cell as a point in a low-dimensional Euclidean space.
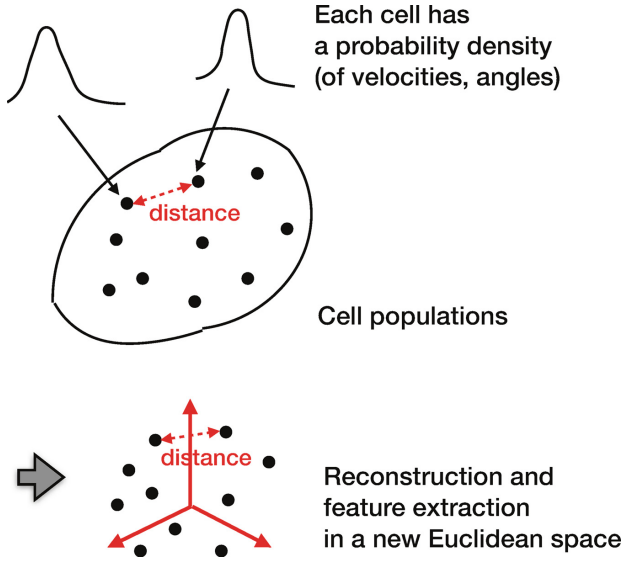

Fig. 2. The proposed method. The input data (such as velocities or angles of cell trajectories) are treated as random samples from a probability density. A distance matrix is constucted between these probability densities. Multidimensional scaling is then used to embed each point in a new Euclidean space.

3.1   Step 1

We assume that each cell i has its own probability density p_i, from which the input data S_i is randomly sampled. In the examples given in the previous section, the probability of velocities is defined on $\mathbb{R}^2$, and the probability of angles is defined on $[-\pi, \pi)$.

3.2   Step 2

We next calculate the distance between different cells by estimating the Jensen-Shannon divergence between p_i and p_j for all pairs (i, j) of cells:

$$JS(p_i||p_j) = \int_{\mathbb{R}^k} \left(\frac{1}{2} p_i \log \frac{2p_i}{p_i + p_j} + \frac{1}{2} p_j \log \frac{2p_j}{p_i + p_j} \right) d\boldsymbol{x},$$

where log indicates natural logarithm throughout the paper. We define the distance between cells i and j as the square root of this divergence. The square root of the Jensen-Shannon divergence is known to be a metric, which satisfies all the intuitive properties of a distance, including the triangle inequality [7].

We estimate the above divergence from the input data S_i and S_j as follows. By using the k nearest neighbors density estimation, we estimate the density of p_i and p_j, denoted by $\widehat{p}_i$ and $\widehat{p}_j$, respectively, at each sample point belonging to the input data. We find that

$$
\begin{aligned}
2JS(p_i\|p_j) &= \int_{\mathbb{R}^k} (p_i + p_j)\frac{p_i}{p_i + p_j} \log \frac{2p_i}{p_i + p_j}\, d\boldsymbol{x} \\
&+ \int_{\mathbb{R}^k} (p_i + p_j)\frac{p_j}{p_i + p_j} \log \frac{2p_j}{p_i + p_j}\, d\boldsymbol{x} \\
&= \mathbb{E}_{p_i}\left[\frac{p_i}{p_i + p_j} \log \frac{2p_i}{p_i + p_j}\right] + \mathbb{E}_{p_j}\left[\frac{p_i}{p_i + p_j} \log \frac{2p_i}{p_i + p_j}\right] \\
&+ \mathbb{E}_{p_i}\left[\frac{p_j}{p_i + p_j} \log \frac{2p_j}{p_i + p_j}\right] + \mathbb{E}_{p_j}\left[\frac{p_j}{p_i + p_j} \log \frac{2p_j}{p_i + p_j}\right],
\end{aligned}
$$

where $\mathbb{E}_p[\ ]$ denotes the expectation value over probability density p. Therefore, the divergence $JS(p_i\|p_j)$ can be estimated from the input data S_i and S_j as:

$$
\begin{aligned}
&\frac{1}{2\#S_i} \sum_{\boldsymbol{v}\in S_i} \left(\frac{\widehat{p}_i}{\widehat{p}_i + \widehat{p}_j} \log \frac{2\widehat{p}_i}{\widehat{p}_i + \widehat{p}_j} + \frac{\widehat{p}_j}{\widehat{p}_i + \widehat{p}_j} \log \frac{2\widehat{p}_j}{\widehat{p}_i + \widehat{p}_j}\right) + \\
&\frac{1}{2\#S_j} \sum_{\boldsymbol{v}\in S_j} \left(\frac{\widehat{p}_i}{\widehat{p}_i + \widehat{p}_j} \log \frac{2\widehat{p}_i}{\widehat{p}_i + \widehat{p}_j} + \frac{\widehat{p}_j}{\widehat{p}_i + \widehat{p}_j} \log \frac{2\widehat{p}_j}{\widehat{p}_i + \widehat{p}_j}\right).
\end{aligned}
$$

Since $x \log 2x + (1 - x) \log 2(1 - x)$ is nonnegative for $0 < x < 1$, the divergence estimated using the above formula is also nonnegative.

3.3   Step 3

Having obtained a distance matrix consisting of distances between all pairs of probability densities, we perform classical multidimensional scaling to place each sample in a new coordinate space according to the estimated distances. The first few coordinates are critical features that best express the cell-to-cell heterogeneity.

4   Results

4.1   Simulated Dataset

We tested our method to see if it can distinguish three types of simulated cell movements, namely random walk, persistent random walk and Lévy walk.

When we chose a set of velocities as the input data, we obtained Fig. 3A, where each point corresponds to a cell trajectory of either type. Here, the Lévy
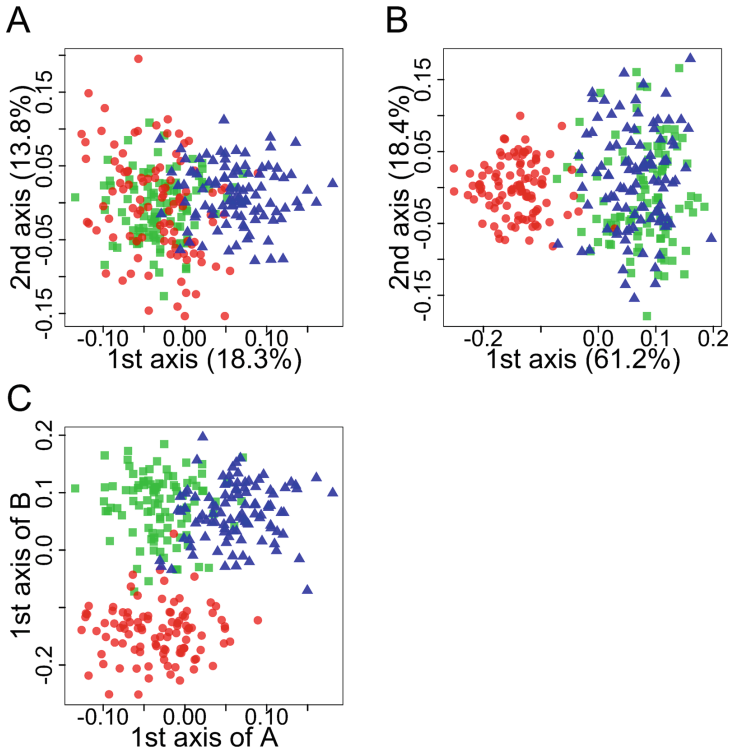
Fig. 3. Application of the proposed method to the simulated cell motility dataset: random walk (green squares); persistent random walk (red circles); and Lévy walks (blue triangles). (A) A set of velocities were given as the input data. (B) A set of angles between adjacent velocities were given as the input data. (C) The first axes of (A) and (B) were combined in the same plot. In (A) and (B), the proportions of the variance explained by each axis are also shown. (Color figure online)

walks (blue triangles) were separated from the other walks (multi-response permutation procedures, $p = 0.0001$ with 10,000 permutations), but the random walks (green squares) and persistent random walks (red circles) were indistinguishable ($p = 0.1417$). This is consistent with the fact that the theoretical distributions of velocities in random walks and persistent random walks are the same in our setting.

We also tried a set of angles between adjacent velocities as another type of input data. This time we obtained Fig. 3B, where the persistent random walks were well separated from the other walks ($p = 0.0001$), but the random walks and Lévy walks were not distinguishable ($p = 0.0247$). This is again consistent with the fact that the theoretical distributions of angles in random walks and Lévy walks are the same (the uniform distribution over $[0, 2\pi)$) in our setting.

By combining the first axes of these two plots, we were able to distinguish three types of cell movements (Fig. 3C).
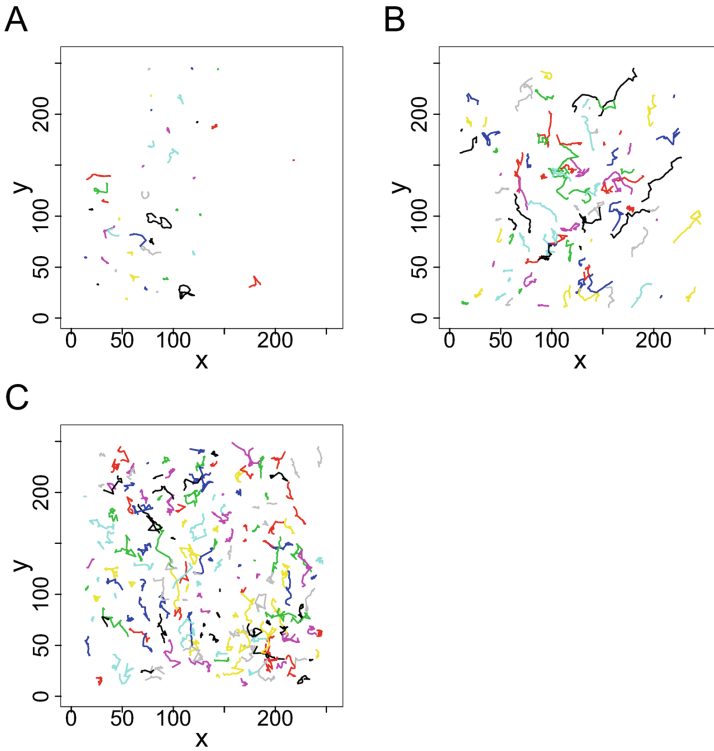
Fig. 4. Motility of neutrophils observed in mouse skin. (A) 8 h, (B) 12 h, and (C) 24 h after stimulation with PMA ($n = 41, 97, 183$ cells). The units of x and y are μm.

4.2   Real Dataset

We next applied our method to the real dataset of neutrophil motility (Fig. 4, details in the Appendix).

As in the simulation dataset, we first chose a set of velocities as the input data. The result (Fig. 5A) showed that the 8 h, 12 h and 24 h cell populations showed overlapping, but identifiable clusters (multi-response permutation procedures, $p = 0.0001$ with 10,000 permutations). Note that, because the multi-response permutation procedures test uses the original distance matrix (i.e. all the axes obtained from multidimensional scaling) for cluster separation, the separation is better than is suggested by Fig. 5A, which shows only the first and second axes.
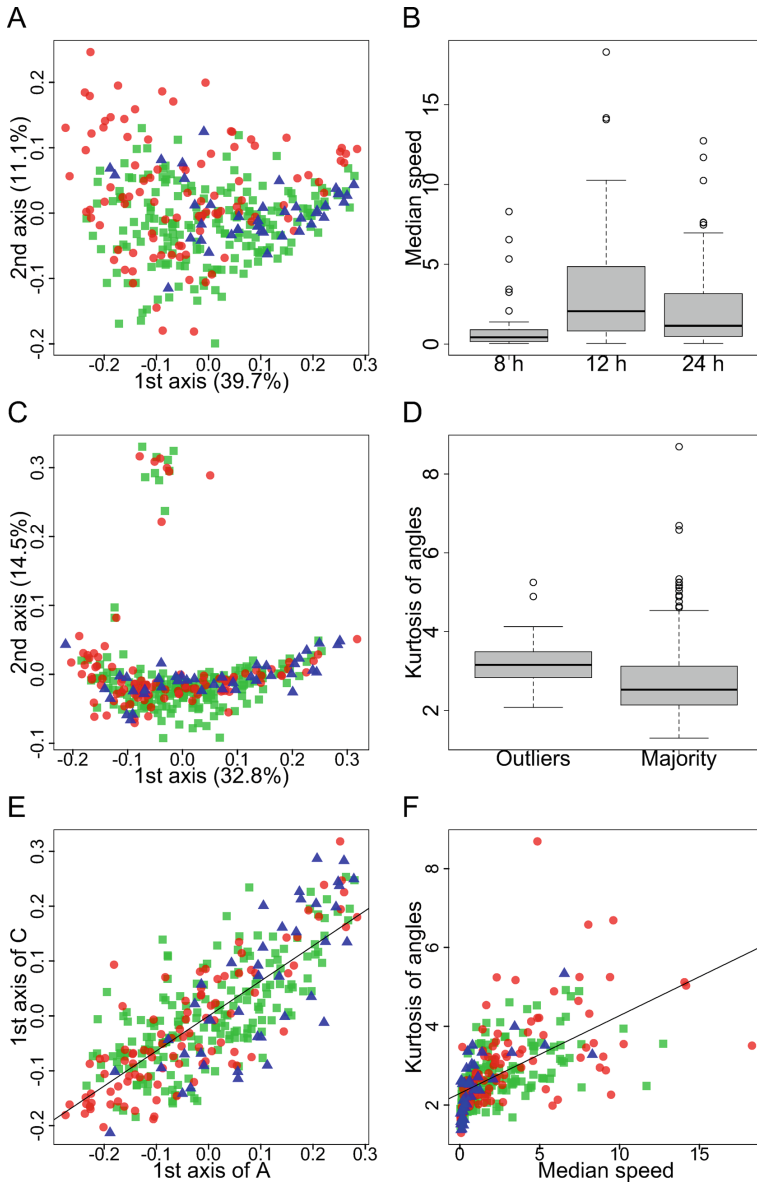
Fig. 5. Application of the proposed method to the neutrophil motility dataset: 8 h (blue triangles); 12 h (red circles); and 24 h (green squares). (A) A set of velocities were given as the input data. (B) Difference in median cell velocities between experimental conditions. (C) A set of angles between adjacent velocities were given as the input data. (D) Difference in kurtosis of angles between majority cells and outliers. (E) The first axes of (A) and (B) combined in the same plot. (F) Correlation between the median cell speed and kurtosis of angles. (Color figure online)

In our search for characteristic features correlated with the first axis of Fig. 5A, we find that the median cell speed differs between these populations (Fig. 5B). We also used a set of angles between adjacent velocities as another type of input data. The result (Fig. 5C) showed overlapping clusters that were less distinguishable than Fig. 5A (multi-response permutation procedures, $p = 0.0004$ with 10,000 permutations). However, this time, a small subset of outlier cells (defined by the values of the second axis being larger than 0.2) containing 12 h and 24 h cells was identified. The trajectories of the outlier cells are shown in Fig. 6.

After searching for characteristic features correlated with the first axis of Fig. 5C, we found that the angle distribution of these outlier populations has a higher kurtosis (characterized by heavier tails) compared with a majority of the cells (Fig. 5D). Interestingly, the first axis of Fig. 5A and the first axis of Fig. 5C were highly correlated with a correlation coefficient of 0.78 (Fig. 5E). The median cell speed and the kurtosis of the angles were also highly correlated with a correlation coefficient of 0.59 (Fig. 5F).

We note the difference in the shape of distributions in the multidimensional scaling space between the simulated dataset and the real dataset. The former (Fig. 3) is circular and homogeneous, whereas the latter (especially Fig. 5C) is separated and concave. This reflects the fact that the simulated dataset is generated from exactly the same parameter sets, while the real dataset consists of different types of neutrophils having presumably varied parameter sets.
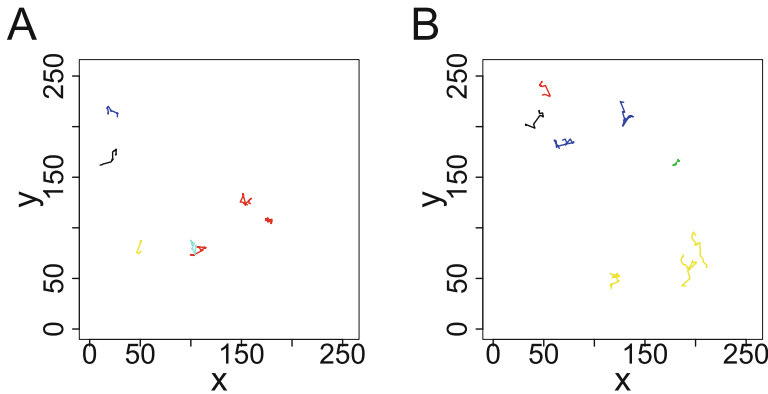

Fig. 6. Trajectories of outlier cells shown in Fig. 5C. (A) 12 h after PMA application. (B) 24 h after PMA application.

5   Conclusion

We have proposed a new method for detecting and visualizing cell-to-cell heterogeneity in a population, and have demonstrated its effectiveness using simulated and real datasets of cell motility. Our method is broadly applicable to cases

where the phenotype of individual cells (or in general, entities) can be expressed as a probability distribution [13].

We used the square root of the Jensen-Shannon divergence to quantify the difference between probability distributions. This divergence is derived from the Kullback-Leibler divergence $\int p_i \log \frac{p_i}{p_j} \, d\boldsymbol{x}$, which, compared with $\int \log \frac{p_i}{p_j} \, d\boldsymbol{x} = \int (\log p_i - \log p_j) \, d\boldsymbol{x}$, puts less weight on sparse areas where p_i is small. This is suitable for accentuating the dense, important areas in the distribution while ignoring the less important ones.

However, depending on the purpose of research, one might be interested in outliers in the distribution and might want to focus on them. For example, one possible application of this method is to detect errors in cell segmentation or tracking as outliers in the population. In such cases, other types of metrics, such as Wasserstein distances with appropriate weights (cost functions), might be useful.

7   Appendix

7.1   Simulated Dataset of Cell Motility

We simulated three types of 2D cell movements: random walk, persistent random walk and Lévy walk. To simulate the experimental data, all the cell movements were observed only at discrete time points ($t = 0, 1, \ldots, 30$).

Each step $(x_{t+1} - x_t, y_{t+1} - y_t)$ of a random walk was defined to be a vector whose x and y coordinates were independently chosen from the standard normal distribution $N(0, 1)$. Each step of a persistent random walk was defined to be a vector whose x and y coordinates independently follow an Ornstein-Uhlenbeck process $dX = -\frac{1}{2}X \, dt + dW_t$ (W_t is the Wiener process), with the initial step chosen randomly from the stationary distribution $N(0, 1)$. Each step of a Lévy walk was given by $(r \cos\theta, r \sin\theta)$, where the radius r was chosen with the probability density $p(r) = \begin{cases} r^{-3} & (r \geq \frac{1}{\sqrt{2}}) \\ 0 & (r < \frac{1}{\sqrt{2}}) \end{cases}$, and the angle θ was chosen from the uniform distribution over $[0, 2\pi)$. In all types of cell movements, the mean (expected) length of each step was equal to $\sqrt{2}$.

In the case of random walks, the individual step sizes are independently taken from the chi distribution with two degrees of freedom, whereas in the case of persistent random walks, they are correlated with their recent past history, as if they have a memory. In the case of Lévy walks, the individual step sizes are independently taken from a power-law probability distribution with heavy tails. The latter two walks have been previously reported as mathematical models of cell motility [8–10].

7.2   Real Dataset of Cell Motility

The real dataset used here is that of neutrophils at different time points (8 h, 12 h and 24 h) after an external stimulation of PMA to the mouse skin. In more detail, LysM-EGFP mice expressing fluorescent neutrophils were used to record cell motility. The ears of LysM-EGFP mice were treated with 30 μg/mL PMA (Phorbol 12-myristate 13-acetate), a stimulant of protein kinase C that causes contact dermatitis. After a period of 8, 12 or 24 hours, a group of neutrophils in close proximity to the skin was identified and observed for 40 min at 1-min intervals using two-photon microscopy. An in-house Python script was used to extract the individual 2D cell trajectories from the microscopy images [11,12]. All the cell trajectories with length > 30 (i.e. cells successfully tracked for more than 30 consecutive time frames) were used for this study. The maximum length of the cell trajectories was 40. Owing to the chemotaxis of the cells, different time points include different numbers of cells ($n = 41, 97, 183$ cells for 8 h, 12 h, 24 h).

7.3   Implementation of the Proposed Method in R

The k nearest neighbor density estimation was performed using the R package TDA. The value of k was taken to be 8; however, in cases where the maximum number of observations of a point exceeded 8, that maximum value was used as k. The simulation of an Ornstein-Uhlenbeck process was carried out using the R package sde. Classical multidimensional scaling was performed using the R command cmdscale. Multi-response permutation procedures were performed using the R package vegan. All the other calculations were performed in R.

References

1. Reig, G., Pulgar, E., Concha, M.L.: Cell migration: from tissue culture to embryos. Development **141**, 1999–2013 (2014)
2. Beltman, J.B., Marée, A.F.M., de Boer, R.J.: Analysing immune cell migration. Nat. Rev. Immunol. **9**, 789–798 (2009)
3. Samadani, A., Mettetal, J., van Oudenaarden, A.: Cellular asymmetry and individuality in directional sensing. Proc. Natl. Acad. Sci. **103**, 11549–11554 (2006)
4. Spencer, S.L., Gaudet, S., Albeck, J.G., Burke, J.M., Sorger, P.K.: Non-genetic origins of cell-to-cell variability in TRAIL-induced apoptosis. Nature **459**, 428–432 (2009)
5. Nakamura, N., Yamazawa, T., Okubo, Y., Iino, M.: Temporal switching and cell-to-cell variability in Ca^{2+} release activity in mammalian cells. Mol. Syst. Biol. **5**, 247 (2009)
6. Ohta, Y., Furuta, T., Nagai, T., Horikawa, K.: Red fluorescent cAMP indicator with increased affinity and expanded dynamic range. Sci. Rep. **8**, 1866 (2018)
7. Endres, D.M., Schindelin, J.E.: A new metric for probability distributions. IEEE Trans. Inf. Theory **49**, 1858–1860 (2003)
8. Campos, D., Méndez, V., Llposis, I.: Persistent random motion: uncovering cell migration dynamics. J. Theor. Biol. **267**, 526–534 (2010)

9. Jones, P.J., et al.: Inference of random walk models to describe leukocyte migration. Phys. Biol. **12**, 066001 (2015)
10. Harris, T.H., et al.: Generalized Lévy walks and the role of chemokines in migration of effector CD8+ T cells. Nature **486**, 545–548 (2012)
11. Ito, K., et al.: "Cell tracking based on global data association considering migration tendency". IPSJ SIG Technical Report, vol. 2017-MPS-112, no. 6, pp. 1–6 (2015)
12. Bise, R., Zhaozheng, Y., Kanade, T.: "Reliable cell tracking by global data association". In: 2011 IEEE International Symposium on Biomedical Imaging: From Nano to Macro, pp. 1004–1010 (2011)
13. Nakamura, N., et al.: "LAVENDER: latent axes discovery from multiple cytometry samples with non-parametric divergence estimation and multidimensional scaling reconstruction". bioRxiv, p. 673434 (2019)

Data Analytic Study of the Genetic Mechanism of Ovarian Carcinoma Using Single-Cell RNA-Seq Data

Shuji Kawasaki[1]([✉]), Hiroatsu Hayashi[2], and Yoko Tominaga[1]

[1] Iwate University, Morioka 020-8550, Japan
{shuji,tOminaga}@iwate-u.ac.jp
[2] University of Tokyo, Bunkyo, Tokyo 113-0032, Japan
hiroton-h@iam.u-tokyo.ac.jp

Abstract. This study aims to elucidate the underlying genetic mechanism for ovarian carcinoma using single-cell RNA-seq data. We propose a unique data-driven approach to understand the nature of the data as it is as far as possible. Precisely, we draw a scatter plot, called distance-direction expression pattern, and show it presents several channels of progresses of gene interactions. Then we apply it to the above data. As a result, we found that two channels are presented in the pattern, one for moderate exacerbation of TGF-β and the other for TGF-β-induced highly expressed genes that are more directly connected to cancer growth.

Keywords: sc RNA-seq data · Distance and direction of vectors · TGF-β

1 Introduction

This study aims to elucidate the genetic mechanisms underlying carcinogenesis in ovarian clear-cell carcinoma (OCCC), a historical type of clear-cell carcinoma, using single-cell RNA-sequencing (scRNA-seq) data from tumor samples.

In general, gene expression data obtained by scRNA-seq are large-scale having dimension of hundreds to thousands or more for cells and genes. In recent years, in order to reveal genetic mechanisms of life phenomena from such data, various analysis methods by tools or algorithms have been developed (see, for example, [1,2]). While they are making steady progress through repeated improvements, analysis of the data is still developing. In fact, in not a few cases, the results obtained are difficult to understand their plausibility or appropriateness. We would like here to adopt a data-driven method, to make data tell their identity or nature as they are, as far as possible.

In this study, we propose a novel approach in which expression vectors are presented in a kind of scatter plot, called distance-direction expression pattern (DDEP) that incorporate a concept of topology of expression vectors, and consider its characteristics and how to read it, to identify progresses of genetic

interactions. Then we apply it to the above data. As a result, we found that two channels are presented in the pattern, one for upstream toward TGF-β exacerbation and the other for downstream to TGF-β-induced highly expressed genes that are more directly connected to cancer growth.

2   Distance-Direction Pattern of the Expression

We have normalised the expression value dataset to a matrix of 298 cells × 12324 genes. Note that the analysis here is neither cell lineage estimation nor cell-to-cell analysis. In fact, it is a gene-to-gene analysis. We intend to elucidate genetic mechanism, i.e. progress of gene interactions from the expression data. A matrix of the above size has information of amount of 298×298 at most, as linear algebra tells. Working with 298 row vectors or 298 column vectors have essentially the same amount of information. Hence, the gene-to-gene analysis here must be able to provide an analysis method of the genetic mechanism with the same amount of information as cell-to-cell analysis.

We began our analysis by finding genes expressed in only a small number of cells, among the expression vectors $\boldsymbol{x}_k$ ($k = 1, \cdots, 12324$) of length 298. Then, we extracted the five genes shown in Table 1, all of which expressed only in four cells. No genes were expressed in three cells or fewer. There were no genes that have expressions only at three or less cells. For example, for the gene {1673, RP11-181E10.3} in the first row of the table, $\boldsymbol{x}_{1673}$ was expressed only in cells {34, 99, 123, 297} and 0 otherwise. Also, there were ten genes with exactly the same expression levels in the four cells, such as {305, RBBP4}, including {1673} itself. We will take the 21 genes in the fifth row, to exemplify further analysis. The four cells and 21 genes associated with {8185, RP11-141M1.3} are denoted by c(4-5) and g(4-5), respectively. For the usual inner product $(\boldsymbol{z}_1, \boldsymbol{z}_2)$ of two vectors $\boldsymbol{z}_1$ and $\boldsymbol{z}_2$, we use their correlation

$$<\boldsymbol{z}_1, \boldsymbol{z}_2> = \left(\frac{\boldsymbol{z}_1 - \bar{\boldsymbol{z}}_1}{\|\boldsymbol{z}_1 - \bar{\boldsymbol{z}}_1\|}, \frac{\boldsymbol{z}_2 - \bar{\boldsymbol{z}}_2}{\|\boldsymbol{z}_2 - \bar{\boldsymbol{z}}_2\|} \right) \qquad (\bar{\boldsymbol{z}}_i \text{ is the arithmetic mean of } \boldsymbol{z}_i).$$

We construct a scatter plot of expression vectors as shown in Fig. 1. Here we used the correlation of $\boldsymbol{x}_{8185}$ and $\boldsymbol{x}_k$, $\rho_k = <\boldsymbol{x}_k, \boldsymbol{x}_{8185}>$ for horizontal axis and the difference norms $\|\boldsymbol{x}_k - \boldsymbol{x}_{8185}\|$ for vertical axis, respectively. Since the difference norm is distance and the correlation corresponds to angle or direction of two vectors, we refer to this plot as *Distance-Direction Expression Pattern* (DDEP for short) of expression vectors. In the figure, it is observed that several stream-like patterns from bottom right to top left are formed. We call the patterns *layers* in this paper. Precisely, we used the sorted index k^* of k, according to the values of $\rho_k \in [-1, 1]$ so that $-1 \leqq \rho_{k^*(1)} \leqq \rho_{k^*(2)} \leqq \cdots \leqq \rho_{k^*(12324)} \leqq 1$ for the horizontal axis. Given that the DDEP represents a certain transition/flow of genetic expression, we sought to gain insight into the mechanism underlying ovarian carcinoma from various perspectives using the pattern. Note that this specific DDEP here is based on {8185}. Two vectors may not be near one another in the figure, even though the two have close interactions. Conversely,

Table 1. Five genes positively expressed in only four cells.

|	genes	cells	#	genes with same cell expressions
1	{1673, RP11-181E10.3}	{34, 99, 123, 297}	10	{{305, RBBP4}, {779, TUFT1}, {1673, RP11-181E10.3}, {2415, TMF1}, {3995, SLC39A7}, {5537, KAT6A}, {7084, RSU1}, {10568, DSC2}, {11705, PTOV1}, {12184, APP}}
2	{4204, FUT9}	{106, 253, 259, 280}	21	{{98, CLSTN1}, {115, UBIAD1}, {285, SERINC2}, {503, TM2D1}, {2326, IFRD2}, {2339, HEMK1}, {2608, ZBTB38}, {2855, WDR1}, {3293, RAI14}, {4204, FUT9}, {4221, ATG5}, {5562, MRPL15}, {5762, PHF20L1}, {5883, RRAGA}, {6361, TALDO1}, {6967, TMEM25}, {8170, PAN3}, {8764, UBE3A}, {9436, PRSS8}, {9505, KIFC3}, {10469, PYCR1}}
3	{4431, PSMG3-AS1}	{10, 42, 184, 210}	23	{{1082, CD46}, {1094, LPGAT1}, {1520, ZNF638}, {1535, DGUOK}, {1560, EVA1A}, {3230, SLC25A4}, {4131, ELOVL5}, {4431, PSMG3-AS1}, {6707, EFEMP2}, {6724, BRMS1}, {6777, MRPL21}, {7387, NFKB2}, {9267, ANKS3}, {9290, DEXI}, {9763, SLC25A11}, {10034, STARD3}, {10130, TMUB2}, {10409, TMC6}, {10950, PRELID3B}, {11028, DAZAP1}, {11152, MAP2K7}, {11939, PITPNB}, {12078, ACO2}}
4	{6211, RP11-545E17.3}	{54, 70, 78, 172}	28	{{130, PRDM2}, {558, BCL10}, {965, MRPS14}, {1107, SMYD2}, {1128, AIDA}, {1234, SCCPDH}, {2802, CTBP1}, {4162, TMEM30A}, {4174, PGM3}, {4657, WBSCR27}, {4910, C7orf49}, {5158, WDR45}, {5177, PHF8}, {5215, PIN4}, {6211, RP11-545E17.3}, {7112, ACBD5}, {7206, VPS26A}, {8519, DAAM1}, {8523, DHRS7}, {9041, TSPAN3}, {9450, DNAJA2}, {9582, CYB5B}, {10010, MRPL45}, {10663, PQLC1}, {11094, CTB-50L17.10}, {11515, SUPT5H}, {11634, SAE1}, {11953, NIPSNAP1}}
5	{8185, RP11-141M1.3}	{78, 221, 225, 233}	21	{{577, ZNF326}, {762, C1orf56}, {1509, PCYOX1}, {1886, SF3B1}, {3545, FNIP1}, {4285, HINT3}, {6448, PARVA}, {6721, RAB1B}, {6793, NUMA1}, {7359, DNMBP}, {7649, KIF21A}, {7901, UBE2N}, {7913, NTN4}, {7939, C12orf73}, {8185, RP11-141M1.3}, {8686, GLRX5}, {9192, SPSB3}, {9614, GLG1}, {9657, USP10}, {11250, DHPS}, {11705, PTOV1}}
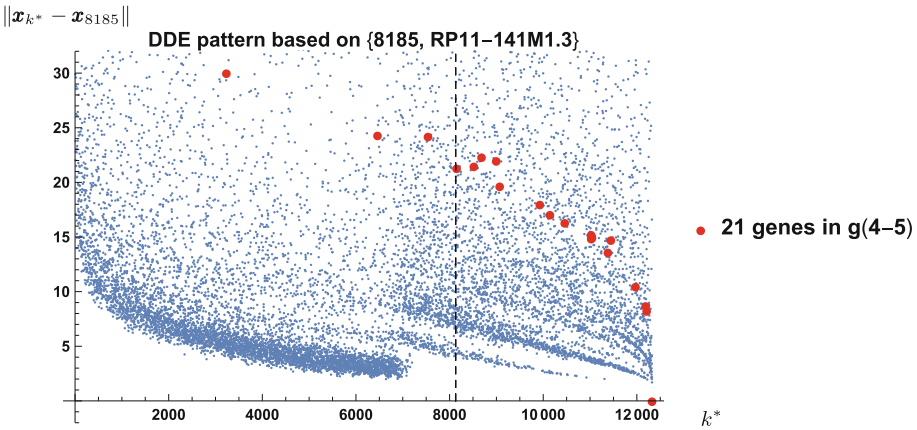
Fig. 1. Red dots indicate 21 genes in **g(4–5)**, among which, the bottom right one is {8185, RP11-141M1.3}. The black dotted line indicates $\rho_{k^*} = 0$, so that the left side region is $\rho_{k^*} < 0$ and the right side region $\rho_{k^*} > 0$. (Color figure online)

it is not necessarily true that two genes closely located in the figure have close interactions.

This DDEP is motivated by considering when two vectors are really close. An answer may be given by the Law of Cosine:

$$\|\boldsymbol{z}_1 - \boldsymbol{z}_2\|^2 = \|\boldsymbol{z}_1\|^2 + \|\boldsymbol{z}_2\|^2 - 2\|\boldsymbol{z}_1\|\|\boldsymbol{z}_2\| \cos\theta$$

for the angle θ between $\boldsymbol{z}_1$ and $\boldsymbol{z}_2$. If $\|\boldsymbol{z}_1 - \boldsymbol{z}_2\| \simeq 0$ and $\cos\theta \simeq 1$, then we have $\|\boldsymbol{z}_1\| \simeq \|\boldsymbol{z}_2\|$ and, in this case, $\boldsymbol{z}_1 \simeq \boldsymbol{z}_2$ as well. As a substitute for $\cos\theta$, we use the correlation in this paper.

Now, in the DDEP, we may consider that a progress of the interaction of gene expressions is taking place along with each of the layers from right bottom to left top, starting with {8185, RP11-141M1.3}, by the reason as follows:

- In each of the layers, the distance $\|\boldsymbol{x}_k - \boldsymbol{x}_{8185}\|$ basically increases from right bottom to left top. In a layer, the genes have exactly the same expression level at cells c(4-5)={78,221,225,233}. {8185, RP11-141M1.3} is expressed only at c(4-5) and is 0 at other cells c̄(4 − 5). Especially, in

$$\|\boldsymbol{x}_k - \boldsymbol{x}_{8185}\|^2 = \|\boldsymbol{x}_k - \boldsymbol{x}_{8185} \,|\, \mathtt{c(4\text{-}5)}\mathtt{c(4\text{-}5)}\|^2 + \|\boldsymbol{x}_k - \boldsymbol{x}_{8185} \,|\, \bar{\mathtt{c}}\mathtt{(4\text{-}5)}\|^2,$$

  the first term on the right hand side is a constant for g(4-5), so that the increase of $\|\boldsymbol{x}_k - \boldsymbol{x}_{8185}\|^2$ is 1 to 1 with the increase of $\|\boldsymbol{x}_k - \boldsymbol{x}_{8185} \,|\, \bar{\mathtt{c}}\mathtt{(4\text{-}5)}\|^2$ i.e. progress of $\boldsymbol{x}_k \,|\, \bar{\mathtt{c}}\mathtt{(4\text{-}5)}$, basically. Sometimes, there may be two genes g_1 and g_2 such that g_1 is expressed in cells in a subset $\mathtt{c}_1 \subset \mathtt{c(4\text{-}5)}$ and g_2 is expressed at cells in other subset $\mathtt{c}_2 \subset \bar{\mathtt{c}}\mathtt{(4\text{-}5)}$, with $\mathtt{c}_1 \cap \mathtt{c}_2 = \emptyset$. But, as shown in Fig. 2, such are only a few cases and we may consider the 1 to 1 property to hold in general. In the figure, the number of cells in the maximally same number of cells (MSCE) is basically decreasing from right to left and it is synchronous with the increase in the distance. Also, the shape of the curves seems to correspond with the shape of the distance curves in Fig. 2, respectively.

In addition, when we take the MSCE genes for $\boldsymbol{x}_{8185}$ in each of the layers, we have the genes depicted in Fig. 3. For example, the gene {6211, RP11-545E17.3} in the table has the MSCE as {8185, RP11-141M1.3} at 292 cells, and top 300 of such MSCE genes are located at right end of each of the layers in the top left figure. The location gradually moves to left over the four figures.

- If $\|\boldsymbol{x}_k - \boldsymbol{x}_{8185}\| \simeq \|\boldsymbol{x}_{8185}\|$, then the increase of $\|\boldsymbol{x}_k - \boldsymbol{x}_{8185}\|$ imply the same for $\|\boldsymbol{x}_{8185}\|$ as well, which in turn suggests the progress of expressions furthermore. This $\|\boldsymbol{x}_k - \boldsymbol{x}_{8185}\| \simeq \|\boldsymbol{x}_{8185}\|$ is actually right for genes in g(4-5), since

$$\|\boldsymbol{x}_k\|^2 = \|\boldsymbol{x}_k - \boldsymbol{x}_{8185}\|^2 + \|\boldsymbol{x}_{8185}\|^2$$

  and, $\|\boldsymbol{x}_k - \boldsymbol{x}_{8185}\|$ and $\|\boldsymbol{x}_k\|$ are both increasing and 1 to 1. For genes other than g(4-5), it is right for at least those k such that $\|\boldsymbol{x}_k - \boldsymbol{x}_{8185}\|$ are sufficiently larger than $\|\boldsymbol{x}_{8185}\|$, since $\|\boldsymbol{x}_k - \boldsymbol{x}_{8185}\| - \|\boldsymbol{x}_{8185}\| \leqq \|\boldsymbol{x}_k\| \leqq \|\boldsymbol{x}_k - \boldsymbol{x}_{8185}\| + \|\boldsymbol{x}_{8185}\|$. These relationships are easily understood since $\boldsymbol{x}_{8185}$ is expressed only at c(4-5).

When we think the progress of gene expressions as above, the progress may have 20–30 'types' corresponding to the number of layers. We would thus like to study genetic mechanism of the ovarian carcinoma through the DDEP, expecting that the 'types' may correspond to pathways of gene expression.
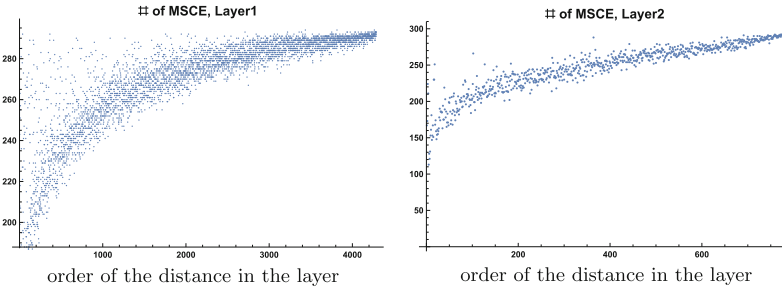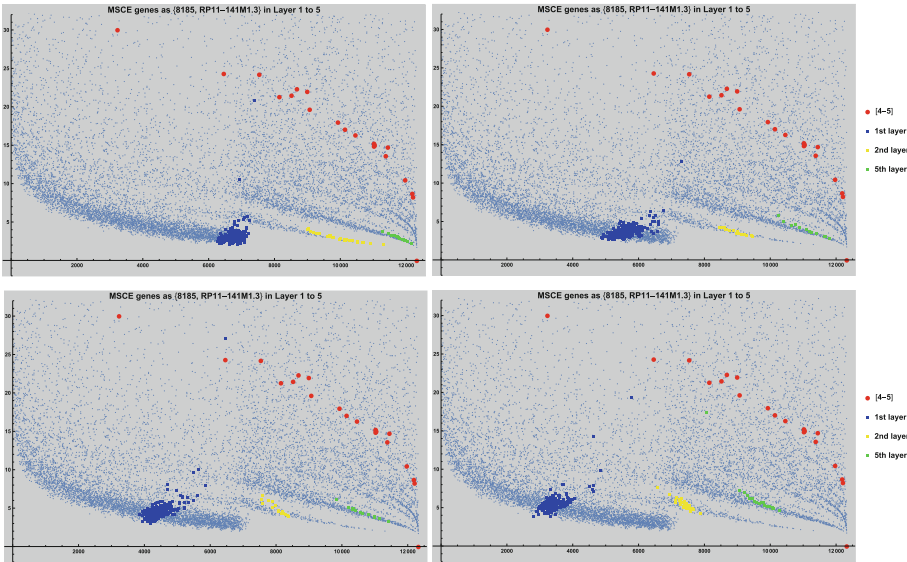
Fig. 2. Number of the MSCE cells in Layer 1 (left) and 2 (right). While the distance increases from right bottom to left top for each layer as in Fig. 1, the number decreases. This observation suggests that the distance increases through expressing at $\bar{c}(4-5)$, and thus progress of the expressions. The horizontal axis here is the order of distance of genes in the layer.

k	MSCE genes		k	MSCE genes		k	MSCE genes		k	MSCE genes	
1	{6211, RP11-545E17.3}	292	11	{12 245, B3GALT5-AS1}	289	21	{9964, ATAD5}	289	31	{8275, LMO7-AS1}	289
2	{7646, ALG10B}	291	12	{12 169, CH507-9B2.9}	289	22	{9725, RP11-961A15.3}	289	32	{8201, RP11-427J23.1}	289
3	{9901, ZNF286B}	290	13	{12 050, APOBEC3D}	289	23	{9707, RPH3AL}	289	33	{7881, LIN7A}	289
4	{8532, RP11-47I22.2}	290	14	{11 757, ZNF845}	289	24	{9587, CLEC18A}	289	34	{7787, RP11-977G19.11}	289
5	{6699, PCNXL3}	290	15	{11 654, TMEM143}	289	25	{9484, MT1B}	289	35	{7678, SENP1}	289
6	{4431, PSMG3-AS1}	290	16	{11 234, ZNF439}	289	26	{9050, HYKK}	289	36	{7477, FLJ37035}	289
7	{4204, FUT9}	290	17	{11 169, ZNF558}	289	27	{8902, C15orf65}	289	37	{7169, SGMS1-AS1}	289
8	{3647, CTD-2283N19.1}	290	18	{11 126, PSPN}	289	28	{8674, OTUB2}	289	38	{6945, AP000997.1}	289
9	{1673, RP11-181E10.3}	290	19	{10 686, SDCBP2-AS1}	289	29	{8494, CDKN3}	289	39	{6800, CLPB}	289
10	{586, FAM69A}	290	20	{10 660, RP11-800A18.4}	289	30	{8314, KDELC1}	289	40	{6790, FAM86C1}	289

Fig. 3. 300 MSCE genes for {8185, RP11-141M1.3}, $k = 1$ to 300, 1000 to 1300, 2000 to 2300 and 3000 to 3300 of the listed MSCE genes, top left to bottom right. The list indicates, for example, that {6211, RP11-545E17.3} has the MSCE at 292 cells, and such top 300 MSCE genes are located at right end of each of the layers in the top left figure. The location gradually moves to the left.

3   Genes Related to TGF-β Pathways

We expect that pathways related to TGF-β play a major role in our system based on preliminary study. Here, we examined how these genes are captured on the DDEP. For the TGF-β related genetic pathway, see e.g. [3] for exposition and [4] for an analysis of the pathways involved in ovarian cancer.

We first examined how the DDEP was composed based on the genes in `g(4-5)`. For each of $\boldsymbol{x}_k$, we took the norm of the subvectors $\boldsymbol{y}_k = \boldsymbol{x}_k \big| \texttt{c(4-5)}$ consisting of only the four cells `c(4-5)={78,221,225,233}`. We then sorted the norms according to magnitudes and plotted them as shown in Fig. 4. As in the figure, we can see some intervals wherein the norms have constant values. We set a certain threshold value for the jumps to distinguish the intervals. In Table 2, we list the genes for the first four intervals. We plotted the genes in each of the intervals on the DDEP, to produce Fig. 5. It is apparent that the genes in each interval correspond to one of the layers in the DDEP.

What is important here is that the order of the subnorms are exactly the same as the order of the layers from bottom to top in DDEP. Since the the latter, the order of distance, is the norm of a whole vector, the progress in terms of distance may be understood by the subvectors. This argument complements the notion of 'types' of progress of gene interaction in Sect. 2.

Next, in order to see a progress of gene interactions along the layers, we depicted four blocks of 500 MSCE genes for {`11544, TGFB1`}, as in Fig. 6. The blocks are taken by $k = 500 \times (j-1)+1, \cdots, 500 \times j$ (k is the order of genes having MSCE. See Fig. 3) and $j = 1, 7, 13, 20$. It shows the corresponding transition of interacting genes along with layers. We can observe that the MSCE genes are located close to {`11544, TGFB1`} only for the block $j = 20$, in which case genes with only small number of MSCEs are contained, while in other blocks having high MSCEs, MSCE genes are not necessarily located close to {`11544, TGFB1`} in the plane.

In the pattern, genes in the blocks seem to be approaching to {`11544, TGFB1`} from the bottom right to the top left, over j. It may be considered from

$$(\boldsymbol{x}_{11544}, \boldsymbol{x}_{8185}) = (\boldsymbol{x}_{11544} - \boldsymbol{x}_k, \boldsymbol{x}_{8185}) + (\boldsymbol{x}_k, \boldsymbol{x}_{8185}),$$

that genes are transiting from those approximately satisfying $(\boldsymbol{x}_{11544} - \boldsymbol{x}_k) \parallel \boldsymbol{x}_{8185}$ to those close to satisfying $(\boldsymbol{x}_{11544} - \boldsymbol{x}_k) \perp \boldsymbol{x}_{8185}$. That is, along with the layers, genes are losing the vector component parallel to $\boldsymbol{x}_{8185}$ and gaining the vector component perpendicular to $\boldsymbol{x}_{8185}$. The parallel component may be composed of a subvector composed almost of the MSCE. Thus, letting C_1 the subvector with MSCE component and C_2 the complementary subvector ($C_1 \cup C_2 = \{1, 2, \cdots, 298\}$, $C_1 \cap C_2 = \emptyset$), we have $(\boldsymbol{x}_{11544} - \boldsymbol{x}_k) \big| C_1 \equiv \boldsymbol{0}$ and

$$(\boldsymbol{x}_{11544} - \boldsymbol{x}_k, \boldsymbol{x}_{8185}) = \big(\boldsymbol{x}_{11544} - \boldsymbol{x}_k \big| C_2, \ \boldsymbol{x}_{8185} \big| C_2\big).$$

Using this argument, we may consider the origin of the components of $\boldsymbol{x}_{11544}$. Among the component, cells in $\boldsymbol{x}_{11544} | C_1$ may have received interactions from MSCE genes, so that $\boldsymbol{x}_{11544} | C_1$ had the same subvector component as the MSCE
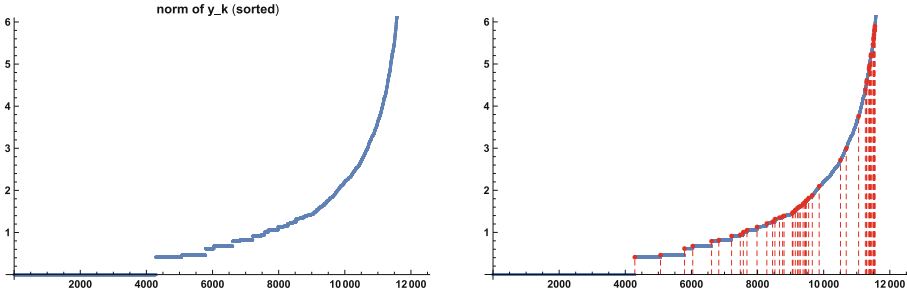
Fig. 4. Norm of $\boldsymbol{y}_k$, sorted according to magnitude. Genes corresponding to each of the pieces are specified.

Table 2. List of genes corresponding to each of the constant intervals.

piece	#	genes
piece1	4287	{1, 2, 3, 5, 9, 15, 16, 17, 19, 20, 22, 25, 30, 32, 37, 42, 45, 50, 53, 55, 59, 60, 69, 73, 75, 76, 77, 78, 80, 83, 84, 91, 97, 101, 109, 111, 120, 121, 122, 127, 131, 132, 133, 136, ≪4199≫, 12 224, 12 225, 12 226, 12 227, 12 228, 12 229, 12 230, 12 235, 12 239, 12 244, 12 246, 12 248, 12 249, 12 250, 12 251, 12 255, 12 259, 12 261, 12 263, 12 265, 12 266, 12 272, 12 273, 12 275, 12 277, 12 278, 12 279, 12 280, 12 281, 12 285, 12 287, 12 290, 12 293, 12 294, 12 296, 12 297, 12 300, 12 301, 12 308, 12 317, 12 318, 12 319, 12 321, 12 324}
piece2	777	{7, 33, 38, 46, 99, 116, 135, 144, 165, 205, 229, 239, 308, 330, 343, 349, 358, 367, ≪741≫, 12 065, 12 073, 12 074, 12 113, 12 130, 12 170, 12 181, 12 193, 12 198, 12 200, 12 205, 12 211, 12 233, 12 245, 12 253, 12 267, 12 288, 12 322}
piece3	726	{4, 8, 39, 63, 66, 105, 140, 145, 147, 158, 223, 237, 242, 266, 309, 326, 327, 332, ≪690≫, 11 978, 11 986, 12 013, 12 022, 12 140, 12 156, 12 183, 12 195, 12 196, 12 197, 12 219, 12 237, 12 242, 12 243, 12 254, 12 257, 12 295, 12 298}
piece4	249	{41, 47, 67, 106, 113, 200, 220, 234, 339, 446, 493, 549, 685, 847, 886, 956, 1039, ≪215≫, 11 656, 11 661, 11 698, 11 728, 11 730, 11 775, 11 805, 11 851, 11 877, 11 979, 12 001, 12 087, 12 091, 12 095, 12 161, 12 199, 12 264}

genes. We then investigated where the complementary subvector component $\boldsymbol{x}_{11544}|C_2$ came from. We took the top 1000 MSCE genes for {11544, TGFB1} and the union of each of the C_1 sets of cells; we denote the union again C_1. Then, we obtain the 262 genes shown as C_1 in Table 3 (top). We searched for genes that contain the complement subvector C_2 ($298 - 262 = 36$ cells). Twenty-two genes that had at least 10 MSCE cells were extracted, and are shown in Table 3 (middle). For example, the gene {233, HMGN2} has the same cellular expression level as {11544, TGFB1} at 10 cells $\{5, 71, 128, \cdots\}$. Here, the union of such cells over 22 genes becomes just the remaining 36 cells in C_2, as in Table 3 (bottom). $\boldsymbol{x}_{11544}|C_1$ is shared by the top MSCE genes and they are distributed as blue dots in Layer1 in Fig. 6 (j = 1). How about $\boldsymbol{x}_{11544}|C_2$? Where do the genes sharing C_2-component come from (see Fig. 7)? To see this, we examined their location in the DDEP. It is shown in Fig. 8. Figure 8 (left) indicates genes that have at least 10 C_2-MSCE cells and Fig. 8 (right) those having at least five.
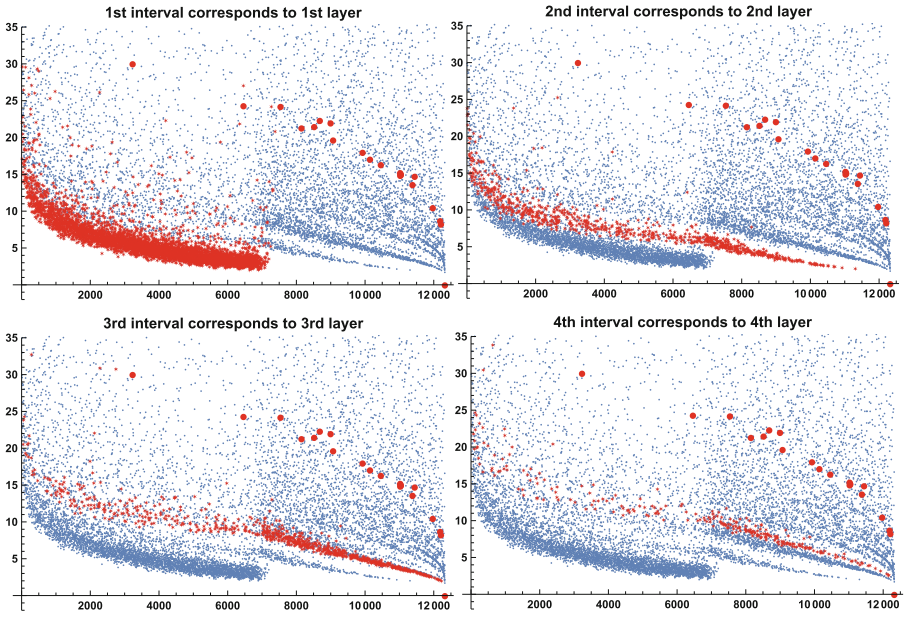
Fig. 5. Genes in the k-th interval in Fig. 4 corresponding to each of the layers in the DDEP: $k = 1$ to 4, top left to bottom right.
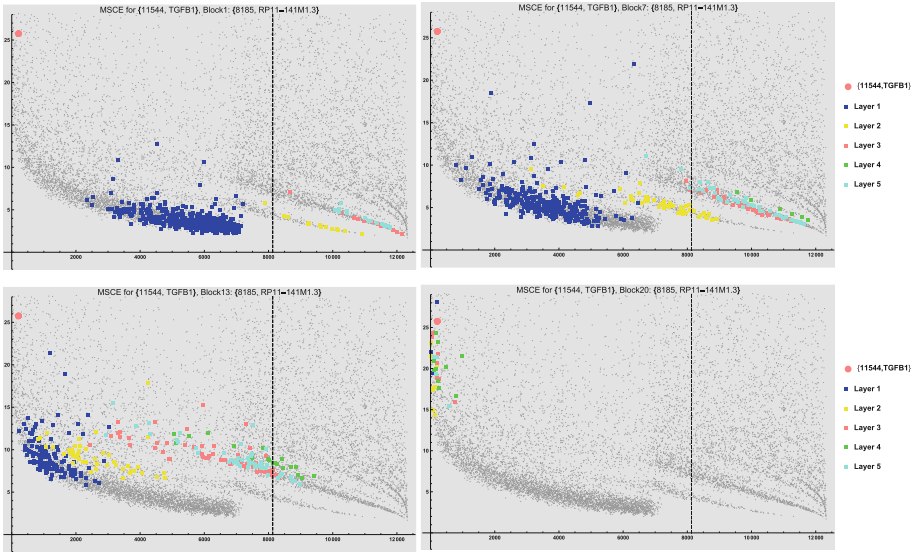

Fig. 6. Each of the blocks of 500 genes from the top of the MSCE genes and their intersection with layers: $j = 1, 7, 12, 20$, from left top to right bottom.

Table 3. Cells obtained by the union of all of C_1 cells for genes of the top 1000 MSCE genes. We write the union C_1 again. (middle) The top 22 genes containing cells with the same cellular expressions as $C_2 = \bar{C}_1$ (complement of C_1). (bottom) Union of the cells in (middle) becomes just C_2 (Note that $262 + 36 = 298$).

union of C1	262	{1, 2, 3, 4, 6, 8, 9, 10, 11, 12, 13, 14, 15, 16, 17, 18, 19, 20, 21, 22, 23, 24, 25, 26, 28, 29, 30, 31, 32, 33, ≪202≫, 262, 263, 265, 266, 267, 268, 269, 270, 271, 273, 274, 276, 278, 280, 281, 282, 283, 284, 285, 287, 288, 289, 290, 291, 293, 294, 295, 296, 297, 298}

genes	#	cells of same expressions
{233, HMGN2}	10	{5, 71, 128, 134, 159, 179, 210, 260, 264, 275}
{526, SRSF11}	10	{7, 75, 147, 185, 198, 210, 211, 236, 260, 272}
{1379, DPY30}	11	{27, 75, 147, 159, 166, 185, 211, 260, 275, 277, 286}
{2075, HDLBP}	13	{7, 27, 70, 71, 91, 128, 134, 166, 202, 236, 260, 277, 279}
{2710, AP2M1}	10	{27, 70, 71, 75, 128, 159, 166, 179, 236, 272}
{2726, IGF2BP2}	11	{62, 75, 81, 119, 134, 147, 228, 236, 260, 272, 292}
{3405, HEXB}	10	{70, 81, 85, 147, 185, 198, 202, 264, 275, 286}
{3769, CANX}	10	{5, 27, 70, 72, 91, 147, 179, 236, 260, 292}
{5210, NONO}	11	{7, 72, 75, 81, 91, 128, 179, 202, 264, 275, 286}

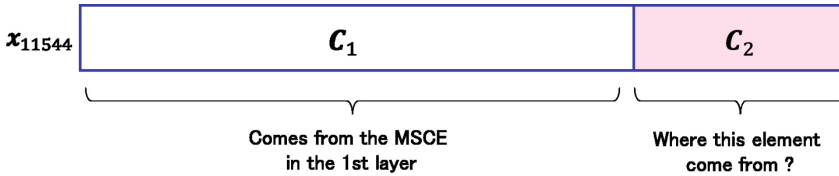| union of the cells =C2	36	{5, 7, 27, 62, 70, 71, 72, 75, 81, 82, 85, 91, 92, 119, 128, 134, 147, 157, 159, 166, 179, 185, 198, 202, 210, 211, 228, 236, 260, 264, 272, 275, 277, 279, 286, 292}

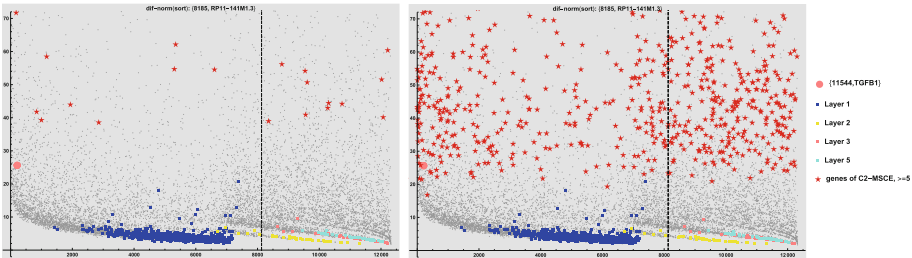**Fig. 7.** x_{11544} is considered to have the components C_1 and C_2.

Fig. 8. Genes in C_2-MSCE. (left) Red stars indicate those C_2-MSCE genes that have at least 10 MSCE cells, and similarly, (right) those that have al least 5 MSCE cells.

We can observe that C_2-MSCE genes are all located in the upper part of the figure, mostly higher than {11544, TGFB1}. These genes are those, with large distance, that have basically high expression levels, and are therefore in the phase of intensive exacerbation of certain pathways. We may then infer a

two stage process of {11544, TGFB1}; in the first, {11544, TGFB1} receives gene interactions and progresses through pathways along the layers, and in turn, it produces much stronger expressions of genes that are more directly connected to cancer formation.

On the contrary, C_1-MSCE genes for {11544, TGFB1}, indicated by the blue dots in Layer1 as in Fig. 6, have small distances $\|\boldsymbol{x}_k - \boldsymbol{x}_{8185}\|$ and are located on the lower part of the figures. This is partly because $\boldsymbol{x}_k - \boldsymbol{x}_{8185}|C_1$ cancels out, and hence we have $\|\boldsymbol{x}_k - \boldsymbol{x}_{8185}\| = \|\boldsymbol{x}_k - \boldsymbol{x}_{8185}|C_2\|$. However, the large values of distances for C_2-MSCE genes is due to the fact that $\|\boldsymbol{x}_k - \boldsymbol{x}_{11544}\| = \|\boldsymbol{x}_k - \boldsymbol{x}_{11544}|C_1\|$ has been largely exacerbated after {11544, TGFB1} in the gene interaction process. From Table 3 and the Law of Cosine

$$\|\boldsymbol{x}_k - \boldsymbol{x}_{8185}\|^2 = \|(\boldsymbol{x}_k - \boldsymbol{x}_{11544}) - (\boldsymbol{x}_{8185} - \boldsymbol{x}_{11544})\|^2$$
$$= \|\boldsymbol{x}_k - \boldsymbol{x}_{11544}\|^2 + \|\boldsymbol{x}_{8185} - \boldsymbol{x}_{11544}\|^2 - 2(\boldsymbol{x}_k - \boldsymbol{x}_{11544}, \boldsymbol{x}_{8185} - \boldsymbol{x}_{11544}),$$

it follows that the contribution of $\|\boldsymbol{x}_k - \boldsymbol{x}_{11544}\|^2$ in $\|\boldsymbol{x}_k - \boldsymbol{x}_{8185}\|^2$ is dominant (about 80–90%) and $(\boldsymbol{x}_k, \boldsymbol{x}_{11544})$ is approximately twice as large as $(\boldsymbol{x}_k, \boldsymbol{x}_{8185})$. The C_2-component of $\boldsymbol{x}_{11544}$, it is thus seen to make relevant C_2-MSCE genes jump to a status of strong exacerbation.

How about C_1-component? While Layers 2, 3, $\cdots$ are growing from the bottom right to the top left, they appear to contact on their way each other. For example, Layer 1 does not begin from right bottom but from the left side of the black dotted line representing $\rho_k = 0$. This may be understood as receiving the interactions from other layers, the genes in the right-hand end of Layer 1 have been activated, and Layer 1 is thus formed. In order to see this effect, we note some specific genes of Layer1 existing sparsely alone above the mainstream of Layer 1 in block $j = 1, 7, 13$ in Fig. 2 or 6. For example, Fig. 9 is an enlarged view of Layer 2 crossing Layer 1, around the right-hand end of Layer 1. In the figure, we can see a Layer 2 gene {6870, NOX4} having Layer 1 genes closely surrounding it. When we determine the surrounding genes, we set certain horizontal and vertical ranges. We may then consider that interactions in Layer 2 have progressed along the genes in the Layer, and the movement is then moved to Layer 1 by the surrounding genes. We took a series of MSCE cell sets for each of the surrounding genes and the union of the MSCE sets. In the union 284 out of a total of 298 cells coincide with {6870, NOX4}. Of course, if one takes a larger range to determine the surroundings, the number of MSCE cells will be larger. This situation is similar for other genes in layer 2 that have such surrounding genes (Tables 4 and 5).

To summarise, the above inferences may suggest a hypothesis, as follows. Starting from {8185, RP11-141M1.3}, gene expressions interactively progress along several layers. Each of the layers thus embraces a gradual exacerbation of expression values, which correspond to genetic pathways. However, sometimes a rapid exacerbation occurs, as in the C_2 process described above. The analysis in this study may list all relevant genes that are in the course of the layers or the bridges in a data analytic way. This is a better approach than searching for

Table 4. Values of terms in the Law of Cosine for $\|\boldsymbol{x}_k - \boldsymbol{x}_{8185}\|^2$. The rightmost column is $(\boldsymbol{x}_k - \boldsymbol{x}_{11544}, \boldsymbol{x}_{8185} - \boldsymbol{x}_{11544})$.

	$\|\boldsymbol{x}_k\|$	$(\boldsymbol{x}_k, \boldsymbol{x}_{8185})$	$(\boldsymbol{x}_k, \boldsymbol{x}_{11544})$	$\|\boldsymbol{x}_k - \boldsymbol{x}_{8185}\|$	$\|\boldsymbol{x}_k - \boldsymbol{x}_{11544}\|$	
{233, HMGN2}	3687.21	268.34	526.018	3652.63	3299.96	157.341
{526, SRSF11}	1861.48	200.488	452.	1848.93	1622.26	220.345
{1379, DPY30}	1943.14	217.208	415.934	1936.29	1776.06	253.562
{2075, HDLBP}	2952.03	256.701	635.079	2936.74	2346.66	38.6362
{2710, AP2M1}	1633.83	166.646	444.888	1614.96	1408.83	230.614
{2726, IGF2BP2}	6091.26	470.985	736.2	6078.18	5283.65	-63.5901
{3405, HEXB}	2988.27	273.77	554.78	2979.08	2543.49	115.885
{3769, CANX}	5159.93	392.784	893.614	5149.71	4037.48	-222.435
{5210, NONO}	1551.99	221.845	471.48	1547.73	1273.82	196.723
{5543, SMTM19}	1529.84	172.254	388.54	1521.78	1417.55	281.564

Table 5. (top) Genes surrounding {6870, NOX4}. (bottom) Union of MSCEs for the 27 genes.

surrounding genes of {6870,NOX4} in Layer1	27	{{17,TNFRSF18}, {482,LDLRAD1}, {885,C1orf204}, {1126,RP11-400N13.3}, {2729,TBCCD1}, {3007,SCD5}, {4862,AC005276.1}, {5073,NHS}, {5412,DEFB4A}, {6190,NAIF1}, ≪7≫, {8580,RP6-65G23.5}, {8771,RP11-680F8.3}, {8858,PATL2}, {9432,ZNF646}, {9484,MT1B}, {10028,STAC2}, {10856,DHX35}, {10920,LINC01272}, {12126,CITF22-92A6.1}, {12230,RIPPLY3}}

union of MSCEs of {6870,NOX4} in Layer1	284	{1, 2, 3, 4, 5, 6, 7, 8, 9, 10, 11, 12, 13, 14, 15, 16, 17, 18, 19, 20, 21, 22, 23, 24, 25, 26, 27, 28, 29, 30, 31, 32, 33, 34, 35, ≪214≫, 264, 265, 266, 267, 268, 269, 270, 271, 272, 273, 274, 275, 276, 277, 278, 279, 280, 281, 282, 283, 284, 285, 286, 287, 288, 289, 290, 291, 292, 293, 294, 295, 296, 297, 298}

relevant genes in the literature or databases, one by one. We would like to develop analytical methods for genetic mechanisms using DDEP in future research.

By continuing the analysis, one can see the interaction with {11544, TGFB1} propagated through Layer 1 by the C_1 component of the $\boldsymbol{x}_{11544}$, and was transmitted to Layer 2 via some bridging genes. Another component of $\boldsymbol{x}_{11544}$ rises above on the field to a higher position than $\boldsymbol{x}_{11544}$. These two processes may be considered to correspond to a small acceleration toward producing the expression of $\boldsymbol{x}_{8185}$, and a significant acceleration toward malignant alteration of TGF-β-related pathways. Further analysis on the vector field may elucidate the gene interactions and mechanism underlying the development of cancer.
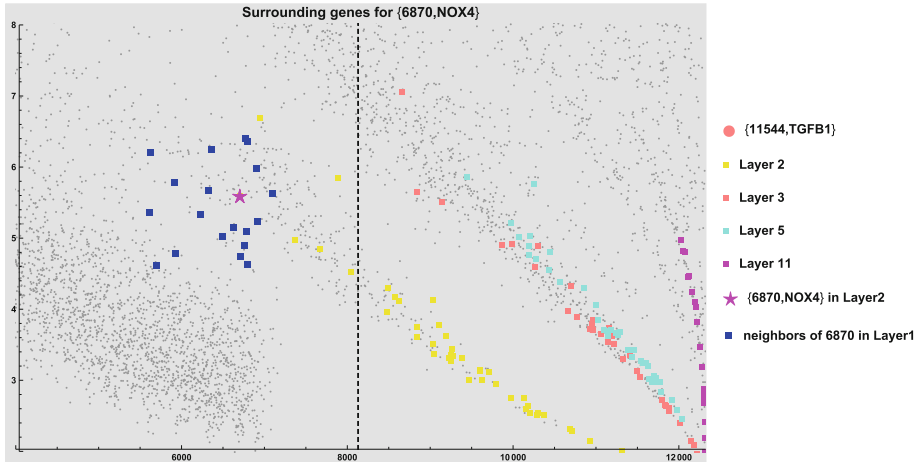
Fig. 9. Neighborhood of genes where Layer 1 and 2 crosses each other. For the extracted 27 genes, MSCEs for {6870, NOX4} are taken and then their union. The resulting cells of the union are 284 MSCE for {6870, NOX4} among 298.

References

1. Saelens, W., Canoodt, R., Todorov, H., Saeys, Y.: A comparison of single-cell trajectory inference methods. Nat. Biotechnol. **37**, 547–554 (2019)
2. Canoodt, R., Saelens, W., Saeys, Y.: Computational methods for trajectory inference from single-cell transcriptomics. Eur. J. Immunol. **46**, 2496–2506 (2016)
3. Komiyama, S., et al.: Expression of TGFβ1 and its receptors is associated with biological features of ovarian cancer and sensitivity to paclitaxel/carboplatin. Oncol Rep., 225 (2011). https://doi.org/10.3892/or.2011.1151
4. Miyazono, K., et al.: Intracellular and extracellular TGF-β signaling in cancer: some recent topics. Front. Med. **12**, 387–411 (2018)

Author Index